GLAVNOYE UPRAVLENIYE GIDROMETEOROLOGICHESKY SLUZHBY

PRI SOVETE MINISTROV SSSR

[MAIN ADMINISTRATION OF THE HYDROMETEOROLOGICAL SERVICE

OF THE COUNCIL OF MINISTERS OF THE USSR]

TRUDY GLAVNOY GEOFIZICHESKOY OBSERVATORII IMENI A. I. VOYEYKOVA

[TRANSACTIONS OF THE A. I. VOYEYKOV MAIN GEOPHYSICAL OBSERVATORY]

NUMBER 166

PROBLEMS RELATING TO INTERPRETATION OF WEATHER SATELLITE DATA

Under the Editorship of
M. I. Yudin,
Doctor of Physico-Mathematical Sciences,
and V. L. Gayevskiy,
Candidate of Geographic Sciences

GIDROMETEOROLOGICHESKOYE IZDATEL'STVO [GIMIZ]

[HYDROMETEOROLOGY PUBLISHING HOUSE]

LENINGRAD, 1964

(Translated under contract NAS 5-8010 for the Goddard Space Flight Center, Greenbelt, Md., by the Language Service Bureau, Inc., Washington, D.C., 1967)

UDK 535,247.1: 629,195.1 - 551.52: 629,195.1

N O T E

The Collection presents works carried out in 1961 - 1962, devoted to problems of the study of the atmosphere by means of weather satellites and to the interpretation and use of satellite data in meteorology.

The problems discussed in the articles offer new ways of approaching satellite meteorology and new perspectives for its development.

The Collection will be of interest to experts in the field of meteorology and related disciplines, and to candidates for advanced degrees and graduate students in geophysics.

TABLE OF CONTENTS

K. S. Shifrin and N. P. Pyatovskaya

SHORTWAVE RADIATION FIELD ABOVE TYPICAL UNDERLYING SURFACES[1)]

1. Introduction. The Interpolation Problem. Statement of the Problem

The use of artificial earth satellites (AES) in meteorology has created a number of new problems.

The present article will deal with the determination of the shortwave radiation for the earth--atmosphere system (E—A) by means of AES. Since the intensity of solar irradiation is well known, the problem consists in determining the flux of outgoing shortwave radiation (OSR) through a horizontal area at the upper boundary of the atmosphere, i.e., at an altitude of about 30 km. This will enable us to determine the amount of solar heat absorbed in a vertical column of air and by the earth's surface, and the part of this energy which can be consumed in weather-forming processes.

Unfortunately, the indirect data obtained from instruments mounted aboard the AES cannot provide the OSR flux for fundamental reasons, since the satellites orbit at altitudes considerably greater than 30 km. This applies to both narrow-sector and wide-sector instruments (NSI and WSI).

A narrow-sector receiver of shortwave radiation gives individual values of the brightnesses of small areas of the earth's surface under most diverse angles. A wide-sector receiver "sees" a vast area of the earth, and its data cannot be converted into values of radiance at individual points with the required degree of accuracy.

The use of direct measurements made by AES for any forecast, quantitative or synoptic, requires the solution of two problems.

1) A method must be found for the conversion from individual values

1) The work was carried out in 1961 and presented at a conference of the Main Administration of the Hydrometeorological Service on 10 January 1962.

of OSR intensities to OSR fluxes through a horizontal area at the upper boundary of the atmosphere. If photometric terms are used, the problem consists in calculating the energy radiance R of 1 cm^2 of the external surface of the earth's atmosphere from individual values of the energy brightness B measured by the instruments aboard the AES.

2) It is necessary to develop a method of conversion from the individual values of the radiances (fluxes) R, calculated at different points of the trajectory which are usually taken at random and at different times, into values of R at the nodes of a proper preselected grid. These values should be either synchronized or averaged in some equivalent manner. Knowing the values at the correct nodes, we can then construct maps of the OSR field which describe either this field at a single physical instant of time or an average field during a certain time interval.

These two problems make up the complete problem involving the development of a method of conversion of the information obtained from the AES into the OSR field.

Below, we shall deal only with the first problem. For this reason, we shall say a few words about the second problem in order to avoid returning to it.

The problem of interpolation is not specific for measurements made with an AES. It also arises in the plotting of a field of any meteorological element by means of its earth-bound measurements at certain random points (stations and posts). In view of the large number of data, the methods should be adapted to computers. Using a given program, the computer should carry out the space-time interpolation of a two-dimensional field at the nodes of a given grid, smoothing out its random nonrepresentative values, and should plot the maps of the field of this element.

The set of problems involved constitute a new chapter in meteorology which has been worked on intensively in the last few years and has been termed the method of objective analysis of meteorological fields.

The field is smoothed out by means of a polynomial of the second or third degree in horizontal coordinates (American method) or by means of a climatological average in the region of the node (Swedish method). A new method, the so-called optimum interpolation, has been developed at the Main Geophysical Observatory by L. S. Gandin. It is based on the idea of finding values providing the minimum mean square quadratic error of interpolation. The initial data are those on the statistical structure of the field of the element. Adopting the hypothesis that the field of deviations of the meteorological element from its norm is statistically homogeneous and isotropic, L. S. Gandin developed a method of interpolation for use with the electronic computer "Ural-1".

All these methods are of course fully applicable to our problem as well. In order to obtain an acceptable accuracy, it is important that neighboring values be fairly close to one another. More precisely, the methods of objective analysis may be applied to any set of original data, but in certain cases, the interpolation errors may be very large. One can indicate the "smoothness" of the original data for which the interpolation errors will not exceed a given magnitude. Because of the abrupt change in brightness which takes place with the sighting device mounted aboard the AES crosses the edge of a cloud, the boundary of a snow cover or a water reservoir, etc., we can obtain sufficiently smooth data only if we use averaged values of the brightness. This averaging may be performed directly with the optical instrument if the latter is equipped with an appropriate conical adapter, or during the treatment of the

observational data obtained from the NSI.

If the distance between the nodes of our grid - the lattice constant - is of the order of 300 km, and if the NSI scans the earth continuously, about 90 separate measurements should be averaged for each node. Actually, the number of points used for averaging is considerably smaller. It depends on the field of vision of the instrument and the location of the points aimed at, i.e., the frequency of interrogations. It is difficult to indicate a priori the values of the characteristics which will insure an adequate smoothness of the values, since it is necessary to have data on the statistics of the linear extent of the cloud systems, snow covers, water reservoirs, and generally, data on the statistical structure of the optical inhomogeneity of the atmosphere and earth's surface.

If smoothness is not obtained, the regions of averaging must be enlarged, but this leads either to an increase in the distance between the nodes of the grid, or to a loss of the necessary detail in the fields and maps of the OSR. At this point, we are faced with the important problem of determining the optimum field of vision and other parameters of the instrument, a complete solution of which can be given after sufficient information from the AES has been received. Let us add that without preliminary information on the OSR field, one should not use the methods of objective analysis either, since they require data on the statistical structure of the OSR field in the vicinity of a specific node.

The main problem consists in the fact that a method should be developed for converting the NSI readings to radiance values, i.e., a method should be indicated for handling the data of an NSI so that by using them one can obtain values of R within the required accuracy. Because of the large volume of information to be processed, the proposed method should be designed for use with computers.

The relation between the brightness B and flux R is given by the formula

$$R=\int_{(2\pi)} B(\theta, \varphi)\cos\theta d\omega. \tag{1.1}$$

From the formal point of view, the problem facing us is completely undefined, since we wish to find the total integral from one value of the function under the integral sign. Obviously, the conversion from B to R is possible only if the angular structure of the energy brightness is known under actual conditions. For instance, if it is found that the angular structure of the brightness of the E—A system is Lambertian, i.e., B is independent of the sighting angle θ and azimuth φ, then

$$R=\pi B; \tag{1.2}$$

this would mean that in order to obtain the OSR flux, it is necessary to simply multiply by π the data obtained from the NSI.

Unfortunately, this simple dependence does not occur. The structure of the brightness field of the system E—A depends on the relation between the brightness of the earth's surface and the brightness of the haze, and generally turns out to be rather complex. We shall study it for typical underlying surfaces: water, grass and snow. This constitutes the object of the present work. We shall consider the atmosphere as being a standard one, and in our numerical calculations we shall take the altitude of the AES to be H = 700 km, the field of vision of the NSI to be $\beta = 3^\circ$, and the field of vision of the WSI, $\theta = 130^\circ$ (this is the angle from which the earth is seen by an open receiver).

For a standard radiation model of the atmosphere, we shall take an optical thickness $\tau_o = 0.3$, a horizontal range of visibility at the earth's surface $S_o = 20$ km, and the amount of precipitated water and carbon dioxide,

respectively, w_{H_2O} = 2.1 g/cm^2, and w_{CO_2} = 264 atm cm.

2. Geometry of the Problem[1)]

Let us examine the geometrical relationships of the coordinates of the sighted point on the ground to the coordinates of the satellite and the sighting angles (Fig. 1).

We shall place the origin of the coordinates at the center of the earth O. The AES is located at point A. The plane ZOY is defined by the axis of rotation of the earth OZ and the direction OA, r is the earth's radius, and R is the distance from the AES to the center of the earth. The satellite is oriented, and its axis is directed along OA. The optical axis of the instrument aboard the AES is directed toward point C.

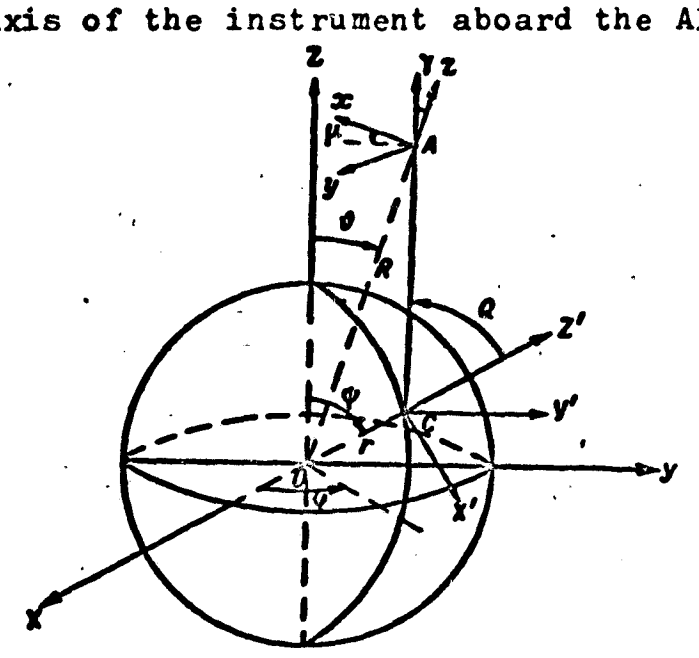

Fig. 1. Relationship between the angular coordinants on the AES and earth (general case).

We shall introduce a spherical coordinate system into the satellite. Axis Oz is directed along OA, and axis x lies in the orbital plane. Let γ and μ be the spherical coordinates formed by an arbitrary ray in the system of the satellite. Point C has coordinates ψ and φ in the frame of reference related to the center of the earth. The ray CA in the spherical frame of reference, in which the center is located at point C and axis Z' is directed toward the zenith, has the coordinates θ and δ. Axis

1) This section was written with the participation of V. Yu. Kolomiytsov.

Z' lies in the meridian plane and is directed toward the equator. Point A has the polar coordinates R and ϑ (in the reference frame related to the earth).

It can be shown that the following formulas are valid:

$$\cos\psi = \frac{-l\sin\vartheta\sin\gamma\cos\mu + (R - l\cos\gamma)\cos\vartheta}{r}, \tag{2.1}$$

$$\cos\varphi = -\frac{l\sin\gamma\sin\mu}{r\sin\psi}, \tag{2.2}$$

$$\cos\Theta = \frac{R\cos\gamma - l}{r}, \tag{2.3}$$

$$\cos\delta = \frac{1}{\sin\Theta}\left[\frac{\cos\Theta}{\operatorname{tg}\psi} - \frac{1}{\sin\psi}(\sin\gamma\cos\mu\sin\vartheta + \cos\gamma\cos\vartheta)\right]. \tag{2.4}$$

Here l is the length of segment CA

$$l = R\cos\gamma - \sqrt{r^2 - \sin^2\gamma R^2}. \tag{2.5}$$

If the axis of the instrument moves within the plane perpendicular to the orbital plane, we should set $\mu = \frac{\pi}{2}$ in the preceding formulas. In this case, it is convenient to introduce the angle α between the directions OA and OC. From the triangle OCA we immediately obtain some very simple formulas for the geometrical relations in latitude scanning:

$$\alpha = \arcsin\left(\frac{R}{r}\sin\gamma\right) - \gamma, \tag{2.6}$$

$$\psi = \arccos(\cos\vartheta\cos\alpha). \tag{2.7}$$

The sighting angle Θ will be

$$\Theta = \alpha + \gamma. \tag{2.8}$$

Formulas (2.6)-(2.8) make it possible to find the coordinates of point C and angle Θ from the coordinates of the AES (R, ϑ) and from angle γ.

3. Basic Photometric Relations

Narrow-sector receiver. Let s be the surface of the sighted area, $B(\Theta, \lambda)$, the spectral plane of the brightness (w/cm^2 ster. $\Delta\lambda$), s_0 the area of the input Θ of the receiver, the angle formed by the ray with

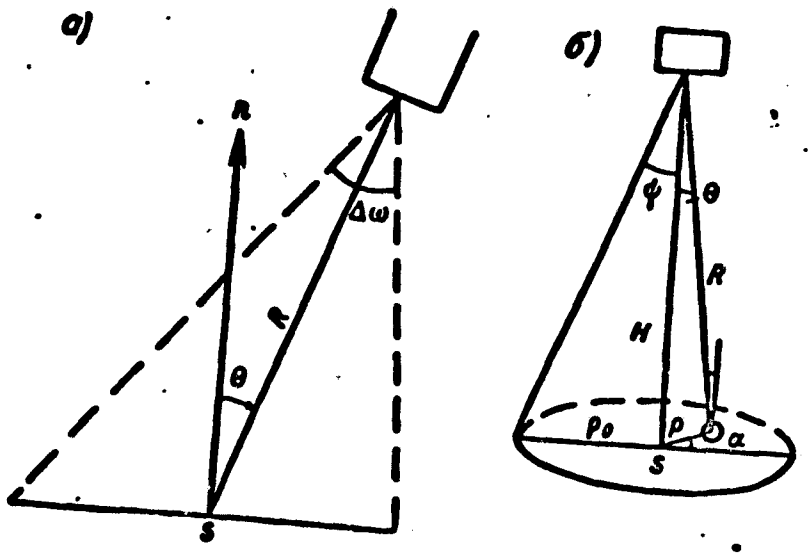

Fig. 2. Photometric relationships for an NSI (a) and a WSI (b).

the normal to the area s (Fig. 2a). The spectral density of the energy flux $F(\lambda)$ reaching the entrance pupil of the receiver will be

$$F(\lambda)=B(\theta, \lambda)s\cos\theta\frac{s_0}{R^2}. \tag{3.1}$$

Since

$$\frac{s\cos\theta}{R^2}=\Delta\omega \tag{3.2}$$

is the solid viewing angle of the receiver, then

$$F(\lambda)=B(\theta, \lambda)s_0\Delta\omega\frac{W}{\Delta\lambda}, \tag{3.3}$$

or, if we introduce $\eta(\lambda)$, the curve of the spectral sensitivity of the receiver (including the transmission of the optical system, filters, etc.), we obtain, for the energy flux reaching the receiver,

$$\Phi(\theta)=\int_{\lambda} F(\lambda)\eta(\lambda)d\lambda \quad W \tag{3.4}$$

$$\Phi(\theta)=\Delta\omega s_0\int_{\lambda} B(\theta, \lambda)\eta(\lambda)d\lambda=\Delta\omega s_0 B(\theta\bar{\lambda})\,\bar{\eta}. \tag{3.5}$$

In the last formula, we switched to the effective wavelength $\bar{\lambda}$ and to the effective transmission of the system $\bar{\eta}$

$$\bar{\eta}=\int_{\lambda}\eta(\lambda)d\lambda. \tag{3.6}$$

<u>Wide-sector receiver</u>. Let 2ψ be the viewing angle of the WSI. The meaning of the other symbols is apparent from Fig. 2b. Considering the plane of the receiver to be parallel to the earth, we have

$$F = s_0 \int_0^{2\pi} d\alpha \int_0^{\rho_0} \rho B(\rho, \alpha, \theta, \varphi) \cos^2\theta \frac{d\rho}{\rho^2 + H^2},$$
$$\rho_0 = H \operatorname{tg} \psi, \cos^2\theta = \frac{H^2}{H^2 + \rho^2}, \tag{3.7}$$
$$F = s_0 H^2 \int_0^{2\pi} d\alpha \int_0^{\rho_0} B(\rho, \alpha, \theta, \varphi) \frac{\rho d\rho}{(H^2 + \rho^2)^2}.$$

For the energy flux, we have

$$\Phi = \int F(\lambda) \eta(\lambda) d\lambda. \tag{3.8}$$

If the surface is homogeneous and Lambertian, then B = const and

$$F = s_0 H^2 B\pi \frac{\rho_0^2}{H^2 (H^2 + \rho_0^2)}. \tag{3.9}$$

If we introduce the viewing angle of the WSI

$$\Delta\omega = \frac{\pi\rho_0^2}{H^2}, \tag{3.10}$$

we find for F

$$F = s_0 \Delta\omega B \frac{H^2}{H^2 + \rho_0^2} = s_0 \Delta\omega \overline{B} \tag{3.11}$$

or

$$\Phi = \int F \eta d\lambda = s_0 \Delta\omega \overline{B(\lambda)} \overline{\eta}. \tag{3.12}$$

Formulas (3.5) and (3.12) establish the relation between the brightness of the surface and the magnitude of the signal Φ measured by the receiver.

The WSI signal was obtained by integrating over a very large area. It is unsuitable for obtaining a detailed picture of the OSR field.

Let us determine the fractions of the various parts in the total signal of the WSI. Assuming that the brightness of all the parts of the earth's surface within this field of vision of the WSI is the same and equal to B, the signal will be (Fig. 3)

$$\Phi = B \int_0^{\gamma_0} 2\pi H^2 \sin\theta \cos\theta d\theta = \frac{\pi H^2}{2} B(1 - \cos 2\gamma_0). \tag{3.13}$$

Here H is the height of the receiver above the earth's surface. The contribution of the various parts is given by the formula

$$\eta(\gamma) = \frac{\Phi(\gamma)}{\Phi(\gamma_0)} = \frac{1-\cos 2\gamma}{1-\cos \gamma_0}. \qquad (3.14)$$

We shall now assume that the luminous surface is Lambertian, but that the brightness of its various parts is determined by their illumination, which is different for different locations. If the receiver and the sun are at the zenith, the illumination of the different parts is given by the factor cos i (Fig. 3), and we have (with the symbols of Section 2)

$$\sin i = \frac{l}{r}\sin\gamma, \quad \sin\theta = (1+\alpha)\sin\gamma, \qquad (3.15)$$

where θ is the angle between the ray and the zenithal direction.

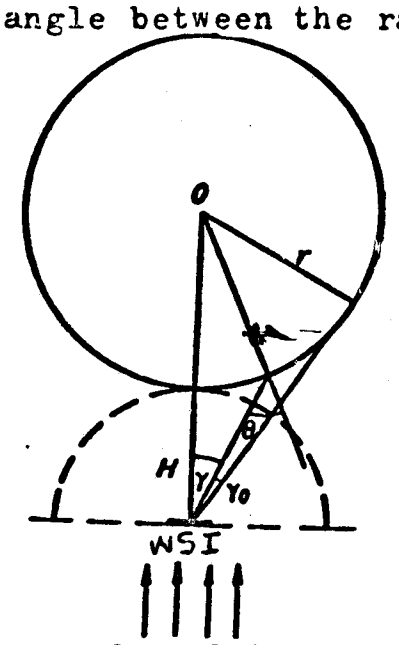

Fig. 3. Geometrical relationships for a WSI.

When γ changes from 0 to $\gamma_0 = 65^\circ$, angle changes from 0 to 90°, and the sun's altitude i, from 0 to 25°. The total signal of the WSI Φ^* will be

$$\Phi^*(\gamma_0) = \int_0^{2\pi} d\mu \int_0^{\gamma_0} B\cos\theta\sin\theta\, d\theta;$$
$$B = A_{3-A}\frac{I_0}{\pi}\cos i. \qquad (3.16)$$

Here A_{E-A} is the albedo of the E—A system, and I_0 is the solar constant.

As before, the fraction of the contribution of the various parts $\eta^*(\gamma)$ to the total signal will be

$$\eta^*(\gamma) = \frac{\Phi^*(\gamma)}{\Phi^*(\gamma_0)}. \qquad (3.17)$$

The graphs of the functions T and η^* versus the radius r (distance in kilometers from the base of the perpendicular) are given in Fig. 4.

We see that for the curve of η^*, 50% of the signal comes from an area with a radius of about 500 km, and that the fraction of the portion with a 150 km radius (one-half of the distance between the nodes) amounts to only 10%. It is evident that the use of data of open receivers for the determination of R from a square 300 km on one side is impossible. Data from NSI measurements are necessary.

4. Method of calculating the spectral density of brightness

General formula for brightness. Let us consider a parallel beam of solar rays of intensity $I_0(\lambda)$ incident at angle i to the zenith. The brightness B sighted by the receiver oriented downward is equal to the sum of the brightness caused by scattering in air B_1 and by the reflection from the sighted area of the earth's surface B_2:

$$B(\theta) = B_1(\theta) + B_2(\theta), \qquad (4.1)$$

$$B_1 = \frac{I_0(\lambda)}{\pi} D, \quad B_2 = \frac{r}{\pi} ET = \frac{I_0(\lambda)}{\pi} rB^*T. \qquad (4.2)$$

Here D is the brightness of the atmospheric haze, T is the transparency of the atmosphere, r is the albedo of the surface, and B^* is a function characterizing the conversion of the incident flux I_0 into the illumination on earth E (see Refs. 1, 2).

$$E = I_0 B^*,$$

where

$$B^* = \frac{2R_0 \cos i}{4 + (3 - \varkappa_1)(1 - A)\tau_0}, \qquad (4.3)$$

$$B(\lambda)=\frac{I_0(\lambda)}{\pi}[D+rB^*T]. \qquad (4.4)$$

The quantity $I_0(\lambda)$ is known [2], and the values of $r(\lambda)$ are assigned experimentally. In order to determine B, we have to know how to calculate the values of D, B^* and T.

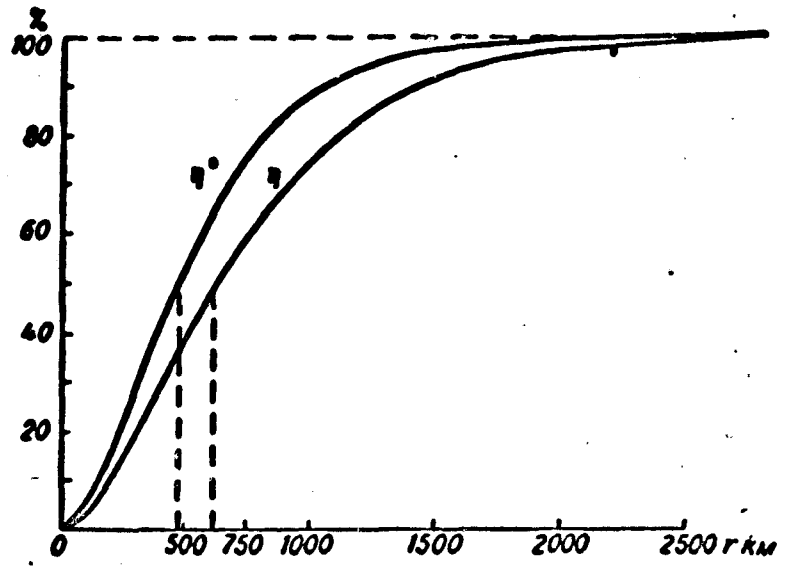

Fig. 4. Contribution of various parts of the earth's surface to the total signal of the WSI.

The method of calculating these quantities is given in Refs. [1-3]. It is based on a certain schematization of the processes of conversion of shortwave radiation in the atmosphere, and is illustrated in Table 1.

Table 1

Spectral region	Multiple scattering	Absorption
Visible $\lambda \leq 0.75\ \mu$	+	-
Infrared $\lambda > 0.75\ \mu$	-	+

For the coefficient of attenuation by an aerosol $b(z, \lambda)$, the following formula has been adopted:

$$b=b_1e^{-\beta z}+b_2. \qquad (4.5)$$

Here $b_1 e^{-\beta z}$ is the coefficient of scattering on a coarse-particle aerosol, $b_2 = 0.007$ 1/km on a "fine" aerosol, the latter being considered uniformly distributed over the entire troposphere. In calculating the

atmospheric transparency, both the scattering and the absorption in gases have been taken into account (in accordance with Ref. [3]).

The transmission function for the various layers was calculated by using the method of Ref. [3].

Calculation of the haze[1)]. In calculating the haze in the visible region of the spectrum in accordance with the concept presented in Ref. [1], instead of the exact formula

$$D^*(\lambda) = D(\lambda)\frac{I_0(\lambda)}{\pi} \tag{4.6}$$

we used the approximate formula (39*) from [1]

$$D^*(\lambda) \simeq D(0{,}550)\frac{I_0(\lambda)}{\pi}. \tag{4.7}$$

In order to evaluate the accuracy of formula (4.7), we compared the integrals for the visible region of the spectrum (0.4-0.75 μ) with the values of $D^*(\lambda)$ given by formulas (4.6) and (4.7). The haze averaged over the azimuth φ was examined for the following 300 cases: z[1, 2, 3, 5, 10 km], angles i[20, 40, 60, 80°] and Θ[0, 20, 40, 60, 85°], and albedo A[0, 0.2, 0.75].

In all these cases, the deviation of the approximate value from the exact value did not exceed a few percent. This means that for the visible region λ = 0.550 μ may be regarded as the effective wavelengths. With the above-indicated accuracy, the haze may be calculated here by means of formula (4.7).

In calculating the haze in the infrared region, we proceeded from the fact that in this case all the optical thicknesses are small ($\tau_0(\lambda) < < 0.2$). Therefore, we can simply write

---

1) This section was written in cooperation with V. Yu. Kolomiytsov.

$$D(\tau_0) \simeq D(0,2)\frac{\tau_0}{0,2}, \qquad (4.8)$$

i.e., introduce the dependence of D on λ through the dependence of τ_0 on λ. An estimate shows that for all $\lambda \geq 0.75\ \mu$ the error of this approximate formula does not exceed 10%. Using the tables of [1 and 2], which list the values of D (0.2), we can calculate $D(\tau_0)$ from formula (4.8) for any wavelengths in the infrared region. For the integral haze we have

$$B^{vih} = \frac{1}{\pi} D(\lambda_0) \int_{0,4}^{0,75} I_0(\lambda)\, d\lambda = \frac{0,863}{\pi} D(\lambda_0) \text{ cal/cm}^2 \text{ min ster}, \qquad (4.9)$$

since

$$\int_{0,4}^{0,75} I_0(\lambda)\, d\lambda = 0,863 \quad \text{cal/cm}^2 \text{ min};$$

$$B^{ik} = \frac{D(0,2)}{\pi \cdot 0,2} \int_{0,75}^{2,5} \tau_0(\lambda) I_0(\lambda)\, d\lambda = \frac{0,511}{\pi} D(0,2) \text{ cal/cm}^2 \text{ min ster};$$

since

$$\frac{1}{0,2} \int_{0,75}^{2,5} \tau_0(\lambda) I_0(\lambda)\, d\lambda = 0,511. \qquad (4.10)$$

Finally, we obtain for the integral haze (over the entire shortwave portion) B_1

$$B_1 = \frac{1}{\pi} [0,863 D(0,3) + 0,511 D(0,2)] \quad \text{cal/cm}^2 \text{ min ster}. \qquad (4.11)$$

D should be substituted into the first term for the values $\tau_0 = 0.3$ and $S_0 = 20$ km, and into the second term for $\tau_0 = 0.2$ and $S_0 = 20$ km.

Spectral indicatrixes of scattering. A correct choice of scattering indicatrixes is basic to a calculation of the haze. Thus far, we have taken the same indicatrix for all λ. The method of calculation can be refined if spectral indicatrixes are taken into account. They were calculated from the formulas of Ref. [1].

$$\varkappa(\gamma, \lambda) = \frac{p(\lambda)}{\tau_0(\lambda)} \varkappa_p(\gamma) + \frac{q(\lambda)}{\tau_0(\lambda)} \varkappa_s(\gamma, \lambda). \qquad (4.12)$$

Here $\varkappa(\gamma, \lambda)$ is a spectrally normalized indicatrix, γ is the angle of scattering, $\varkappa_p(\gamma)$ is the Rayleigh normalized indicatrix, $\varkappa_a(\gamma, \lambda)$ is the spectrally normalized aerosol indicatrix, and $\frac{p(\lambda)}{\tau_0}$ and $\frac{q(\lambda)}{\tau_0}$ are the "weights" with which both components are introduced into the total indicatrix (it is known that $\frac{p(\lambda)}{\tau_0} + \frac{q(\lambda)}{\tau_0} = 1$).

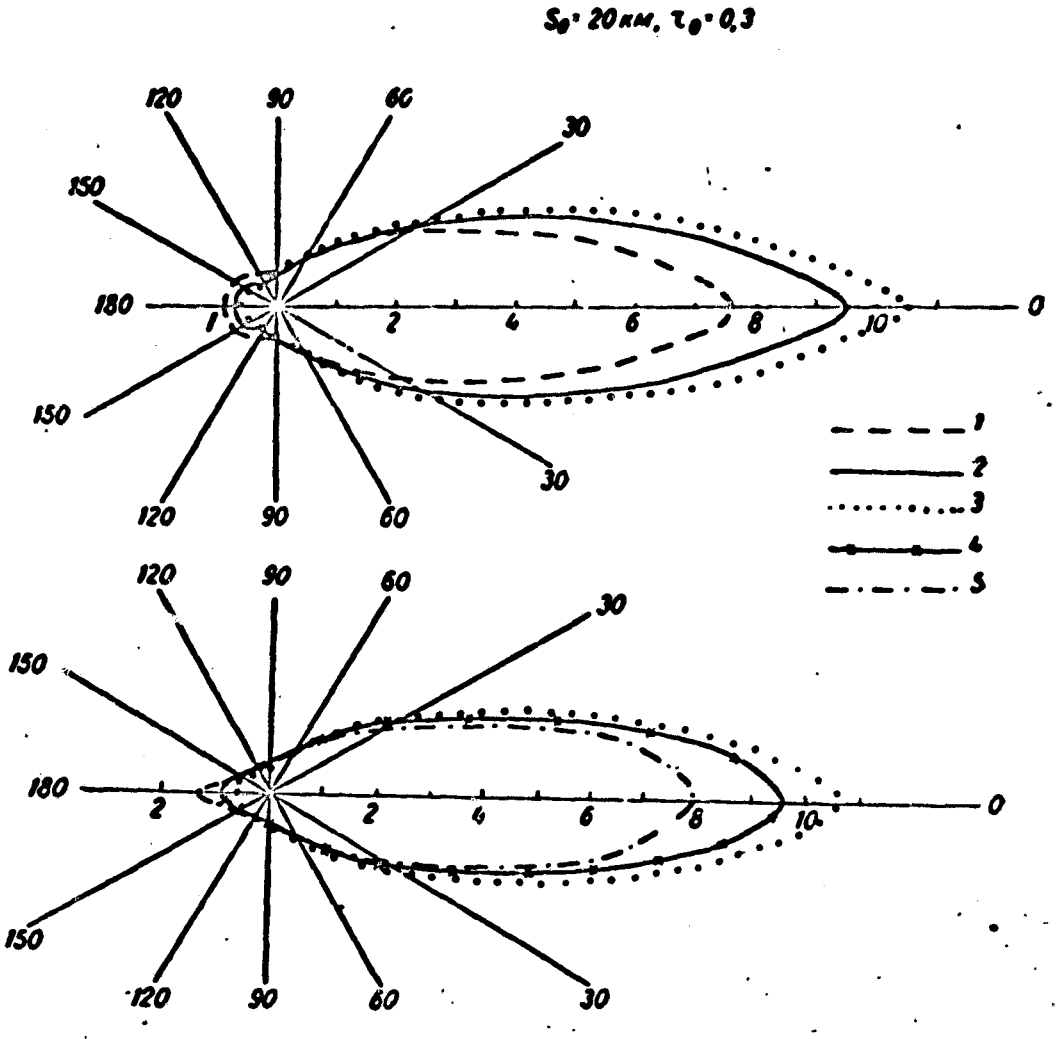

Fig. 5. Total spectral scattering indicatrixes for various wavelengths.

1–λ=0.4 μ; 2–λ=0.55 μ, 3–λ=0.82 μ, 4–λ=1.51 μ, 5–λ=2.45 μ.

In order to calculate $\varkappa(\gamma, \lambda)$ from (4.12), data on $\tau_0(\lambda)$, $p(\lambda)$, $q(\lambda)$, $\varkappa_a(\gamma, \lambda)$ are necessary. The values of $\tau_0(\lambda)$ were taken from Ref. [3], and we calculated those of $p(\lambda)$ and $q(\lambda)$ in the range of 0.4-2.5 μ from the formulas of Ref. [1] with an increment $\Delta\lambda = 0.05$ μ (for the visible region) and for the infrared region for λ values indicated in Ref. [3]. We calculated the data on $\varkappa_a(\gamma, \lambda)$ from the data of Ref. [9]. In this work,

the shape of the aerosol indicatrix is uniquely related to $S_0(\lambda)$. By determining $S_0(\lambda)$ for various λ's and assuming that the experimental data in Ref. [9] can be extended over the entire spectral region of 0.4-2.5 μ, we calculated the spectral indicatrixes $\varkappa_a(\gamma, \lambda)$ and then $\varkappa(\gamma, \lambda)$. Results of the calculations are given in Table 2 and Fig. 5. The last column of Table 2 gives the values of the parameter $\varkappa_1$ characterizing the degree of elongation of the indicatrix as calculated from the formula

$$\varkappa_1 = \frac{3}{2}\int_0^\pi \varkappa(\gamma)\sin\gamma\cos\gamma\, d\gamma.$$

It is interesting to note that as λ increases, the total indicatrix initially stretches up to $\lambda = 0.82\ \mu$, then begins to contract.

Calculation of the fluxes. The brightness of the reflected beam B_2 will be

$$B_2 = \int_{0.4}^{2.5} \frac{I_0(\lambda)}{\pi} rTB^* d\lambda \quad \text{cal/cm}^2 \text{ min. ster.} \tag{4.13}$$

For a flux due to the haze (R_1) and reflected from the earth's surface (R_2), we find the following working formula by using the trapezoidal formula:

$$R_{1.2} = 0{,}275\,[f_{1.2}(20^\circ) + f_{1.2}(40^\circ) + 1{,}12 f_{1.2}(60^\circ) + 0{,}625 f_{1.2}(85^\circ)] \quad \text{cal/cm}^2 \text{ min.}, \tag{4.14}$$

where the functions f are obtained by averaging the brightness over the azimuth φ

$$f_{1.2}(\theta) = \sin 2\theta\,[B_{1.2}(\theta, 0^\circ) + 2B_{1.2}(\theta, 90^\circ) + B_{1.2}(\theta, 180^\circ)]. \tag{4.15}$$

The total flux R will be

$$R = R_1 + R_2. \tag{4.16}$$

5. Results of the calculation of the field of shortwave radiation

The calculations were performed for zenithal distances of the sun i equal to 20, 40, 60, 80° and for different heights over the earth's

surface $0 \leq z \leq 10$ km and the spectral region of $0.4 \leq \lambda \leq 2.5\ \mu$. Three typical surfaces were considered: water, grass, and snow. For grass, use was made of experimental data on brightness coefficients borrowed from Refs. [4, 5]. The snow surface was assumed to be Lambertian, and data on its spectral albedo were taken from Ref. [8].

A problem of serious difficulty is that of r for water. It is known that for a real water surface, the reflection indicatrix is stretched in the direction of specular reflection. However, there are practically no reliable quantitative data on the brightness indicatrix of the sea (we are dealing here both with reflected light and with a beam emerging from the sea).

Observations show that the formation of a sea swell changes the angular structure of the reflected flux appreciably, making it less stretched, but that it has little effect on the magnitude of the reflected flux.

Therefore, for the albedo of a water surface, we adopted values obtained from calculations using Fresnel formulas [6], and the angular structure was assumed to be Lambertian.

Angular structure of the OSR field. By integrating with respect to λ the data on the spectral brightnesses calculated for the three studied surfaces by means of formulas (4.11) and (4.13), we obtained the brightness indicatrixes.

Let us examine the data for the OSR.

Fig. 6 illustrates the brightness indicatrixes of the haze above snow, grass and water for $i = 20, 40, 60$, and 80°. We shall note the appreciable anisotropy of the OSR field, reflecting the anisotropy of the atmospheric scattering indicatrix.

Table 2

Spectral indicatrixes (λ, γ)

λ μ	$\gamma°$																			π_1
	0	10	20	30	40	50	60	70	80	90	100	110	120	130	140	150	160	170	180	
0,40	7,52	5,72	3,24	2,39	1,62	1,17	0,893	0,704	0,603	0,555	0,546	0,571	0,622	0,682	0,754	0,824	0,881	0,921	0,935	0,843
0,45	8,22	6,23	3,97	2,53	1,69	1,20	0,906	0,697	0,586	0,530	0,516	0,539	0,580	0,626	0,688	0,747	0,797	0,834	0,846	0,937
0,50	8,92	6,61	4,24	2,64	1,76	1,23	0,920	0,693	0,573	0,503	0,499	0,502	0,540	0,575	0,627	0,675	0,720	0,754	0,765	1,060
0,55	9,57	6,82	4,41	2,72	1,82	1,27	0,924	0,696	0,565	0,491	0,472	0,480	0,503	0,541	0,585	0,633	0,669	0,701	0,712	1,147
0,60	9,84	7,04	4,51	2,78	1,86	1,27	0,926	0,698	0,557	0,482	0,459	0,466	0,493	0,515	0,550	0,595	0,632	0,667	0,676	1,204
0,65	10,14	7,17	4,54	2,82	1,88	1,28	0,932	0,699	0,555	0,478	0,451	0,458	0,480	0,493	0,527	0,575	0,609	0,647	0,650	1,229
0,70	10,36	7,31	4,63	2,86	1,90	1,29	0,933	0,700	0,556	0,472	0,444	0,446	0,464	0,478	0,502	0,552	0,586	0,631	0,641	1,265
0,72	10,37	7,34	4,64	2,86	1,89	1,29	0,937	0,705	0,556	0,472	0,444	0,446	0,460	0,475	0,500	0,550	0,585	0,631	0,642	1,268
0,76	10,41	7,36	4,64	2,86	1,89	1,30	0,938	0,710	0,558	0,471	0,442	0,443	0,456	0,472	0,492	0,544	0,582	0,631	0,642	1,274
0,82	10,56	7,39	4,64	2,86	1,89	1,31	0,938	0,712	0,559	0,473	0,443	0,442	0,448	0,461	0,479	0,532	0,575	0,635	0,650	1,283
0,85	10,64	7,40	4,60	2,85	1,89	1,31	0,939	0,714	0,563	0,473	0,443	0,441	0,448	0,461	0,478	0,532	0,578	0,637	0,658	1,279
0,93	10,55	7,35	4,56	2,85	1,88	1,31	0,939	0,714	0,567	0,475	0,445	0,442	0,447	0,457	0,470	0,531	0,580	0,648	0,676	1,273
1,01	10,48	7,30	4,50	2,84	1,88	1,31	0,940	0,728	0,574	0,479	0,452	0,446	0,450	0,455	0,470	0,535	0,595	0,671	0,715	1,264
1,13	10,33	7,11	4,39	2,82	1,86	1,31	0,943	0,736	0,589	0,486	0,466	0,458	0,457	0,461	0,475	0,544	0,615	0,709	0,775	1,235
1,24	10,15	7,02	4,26	2,77	1,84	1,30	0,947	0,743	0,604	0,499	0,467	0,469	0,468	0,469	0,486	0,565	0,646	0,747	0,827	1,200
1,31	9,90	6,90	4,15	2,75	1,83	1,30	0,951	0,745	0,6	0,503	0,480	0,472	0,476	0,478	0,494	0,567	0,666	0,770	0,863	1,176
1,44	9,75	6,89	4,13	2,74	1,82	1,30	0,958	0,747	0,622	0,508	0,485	0,479	0,489	0,485	0,502	0,578	0,678	0,798	0,905	1,165
1,51	9,55	6,88	4,09	2,71	1,81	1,30	0,962	0,751	0,624	0,517	0,496	0,479	0,495	0,490	0,507	0,588	0,693	0,816	0,941	1,152
1,53	9,52	6,88	4,05	2,68	1,80	1,30	0,964	0,758	0,625	0,524	0,496	0,487	0,499	0,491	0,509	0,590	0,694	0,818	0,951	1,143
1,60	9,36	6,82	4,05	2,63	1,79	1,29	0,975	0,761	0,628	0,529	0,500	0,491	0,506	0,499	0,515	0,594	0,713	0,850	0,987	1,132
1,68	9,27	6,81	4,04	2,68	1,79	1,28	0,981	0,762	0,632	0,530	0,504	0,495	0,508	0,501	0,523	0,601	0,721	0,863	1,03	1,127
1,81	8,96	6,76	4,02	2,63	1,78	1,28	0,982	0,763	0,640	0,535	0,514	0,504	0,521	0,509	0,534	0,619	0,739	0,892	1,08	1,106
1,93	8,72	6,72	3,97	2,59	1,77	1,28	0,985	0,770	0,649	0,543	0,521	0,514	0,532	0,523	0,546	0,634	0,757	0,927	1,14	1,086
2,09	8,54	6,65	3,93	2,59	1,75	1,27	0,990	0,776	0,656	0,552	0,522	0,523	0,539	0,526	0,556	0,644	0,773	0,944	1,18	1,070
2,19	8,35	6,56	3,88	2,58	1,73	1,26	1,000	0,778	0,660	0,561	0,523	0,524	0,543	0,533	0,564	0,654	0,784	0,965	1,23	1,053
2,45	7,92	6,48	3,84	2,52	1,72	1,26	1,010	0,780	0,673	0,571	0,537	0,536	0,543	0,544	0,583	0,674	0,804	1,003	1,30	1,028

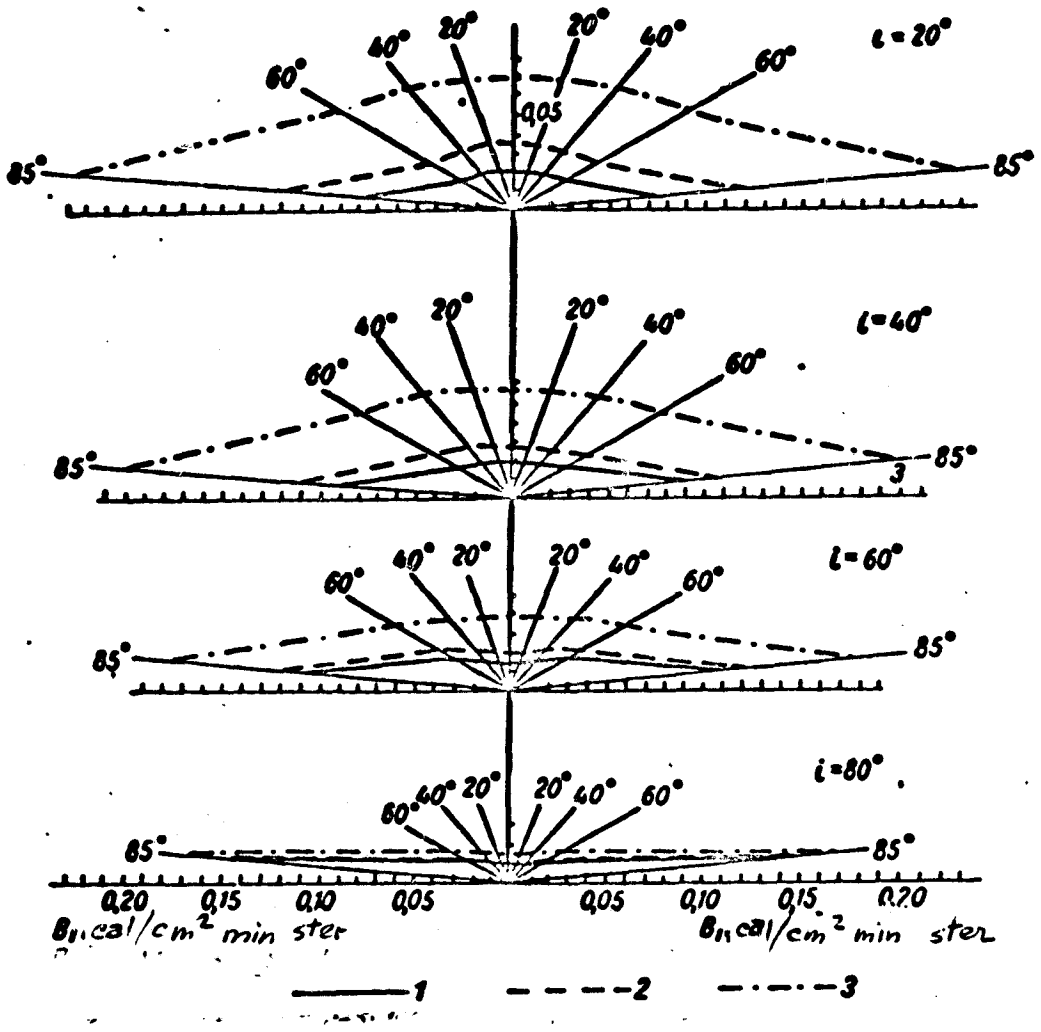

Fig. 6. Brightness indicatrixes of atmospheric haze over water (1), grass (2), and snow (3).

Fig. 7 gives the brightness indicatrixes determined by reflection from the earth's surface for the same cases as in Fig. 6. Fig. 8 gives the total OSR field.

Of major importance is the relation between the OSR flux and the brightness. As an illustration, we shall cite the relation $\varepsilon = \frac{B(60^\circ)}{R}$ for OSR for four values of i (20, 40, 60, 80°) and the three surfaces.

The values of ε in l/ster are given in Table 3.

For the angle θ under consideration, the highest deviation from $\varepsilon = 0.32$, corresponding to an isotropic reflection from the E—A system, amounts to about 20%. The deviations will be greater if averaging over

the sighting azimuth φ is not performed. This important problem is analyzed in more detail in Ref. [7].

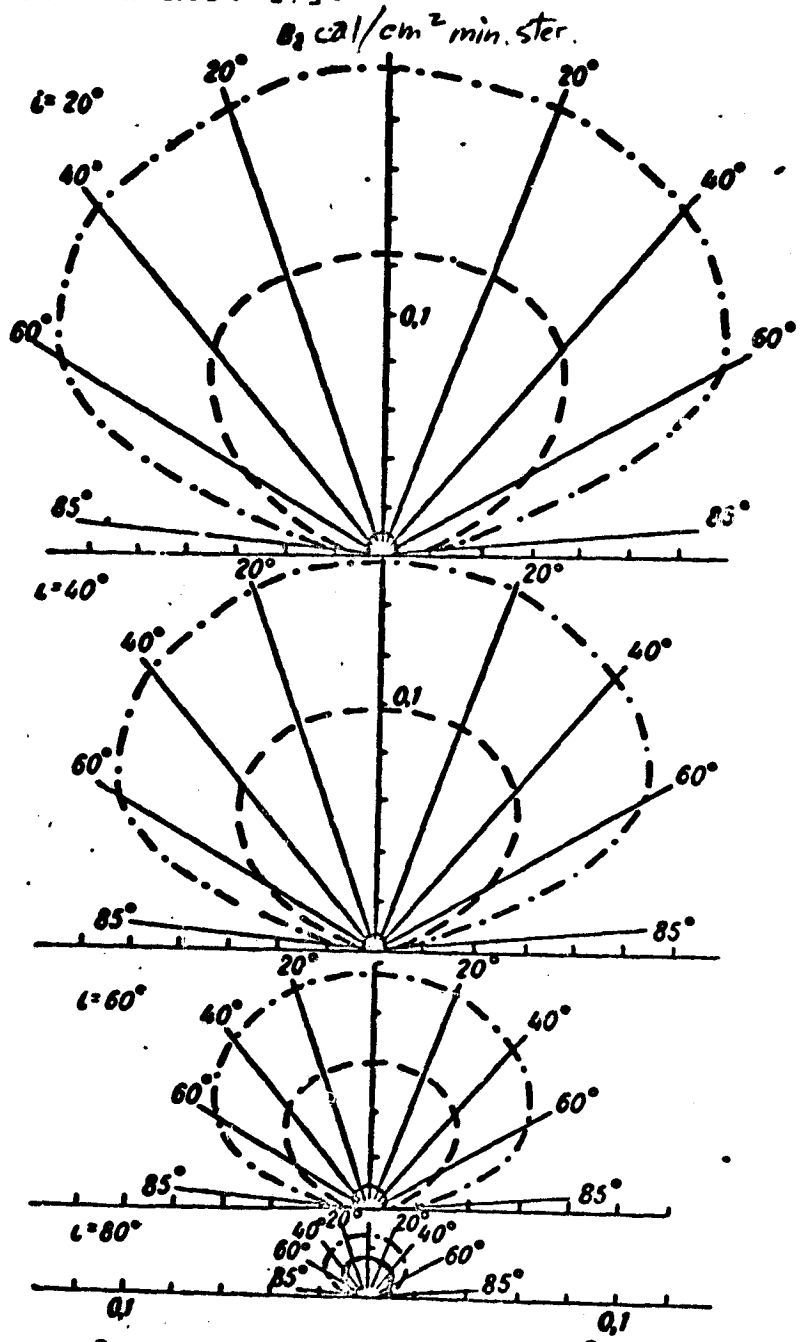

Fig. 7. Brightness indicatrixes caused by reflection from water (1), grass (2), and snow (3).

Spectral flux densities R(λ). We calculated the spectral density of ascending and descending fluxes for a family of z levels (0, 0.5, 1, 2, 3, 5, 10 km).

As an illustration, we shall examine the data on ascending fluxes.

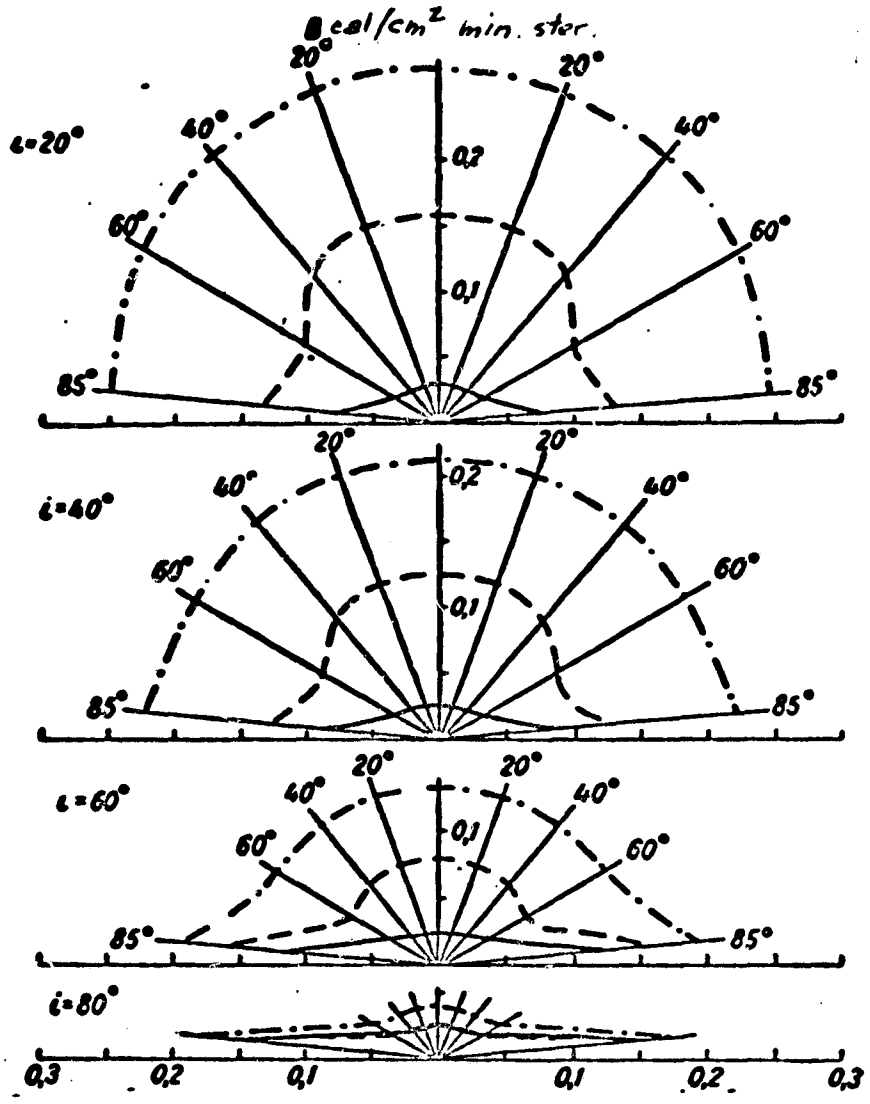

B cal/cm^2 min. ster. B cal/cm^2 min. ster.

——— 1 – – – – 2 —·—·— 3

Fig. 8. OSR field over water (1), grass (2), and snow (3).

They are shown in Fig. 9-11. Also given is the dependence of the ascending flux on the wavelength λ for all three surfaces for two limiting values of i (20 and 80°) and different heights z over the earth's surface. $\lambda\mu$ is plotted along the horizontal axis and $R(\lambda)$ in w/m^2 is plotted along the vertical axis for the interval $\Delta\lambda = 0.01\ \mu$. These figures show that as the reflection coefficient of the earth's surface increases, the ascending flux increases [owing to an increase in the term $R_2(z)$]. The spectral variation of $R(\lambda)$ for all three surfaces under consideration is mainly determined by the curves of $I_0(\lambda)$ and $r(\lambda)$. All three figures show two maxima (at λ equal to 0.45 and 0.55 μ) corresponding to the maxima of the

curve $I_0(\lambda)$, while Fig. 10 shows a third maximum at $\lambda = 0.75\ \mu$ for grass, due to the abrupt rise in the curve $r(\lambda)$ in the band of chlorophyll (about 0.7 μ). The spectral variation of $R(\lambda)$ is also appreciably affected by the transmission function T. The absorption bands of H_2O and CO_2 are visible on all three figures.

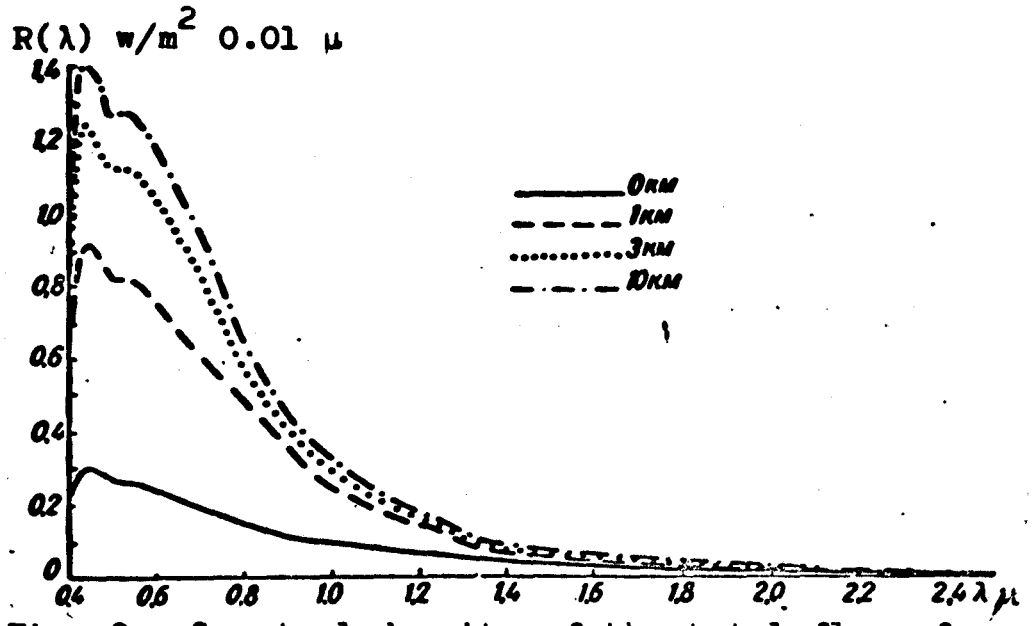

Fig. 9. Spectral density of the total flux of reflected radiation over water ($i = 20^\circ$).

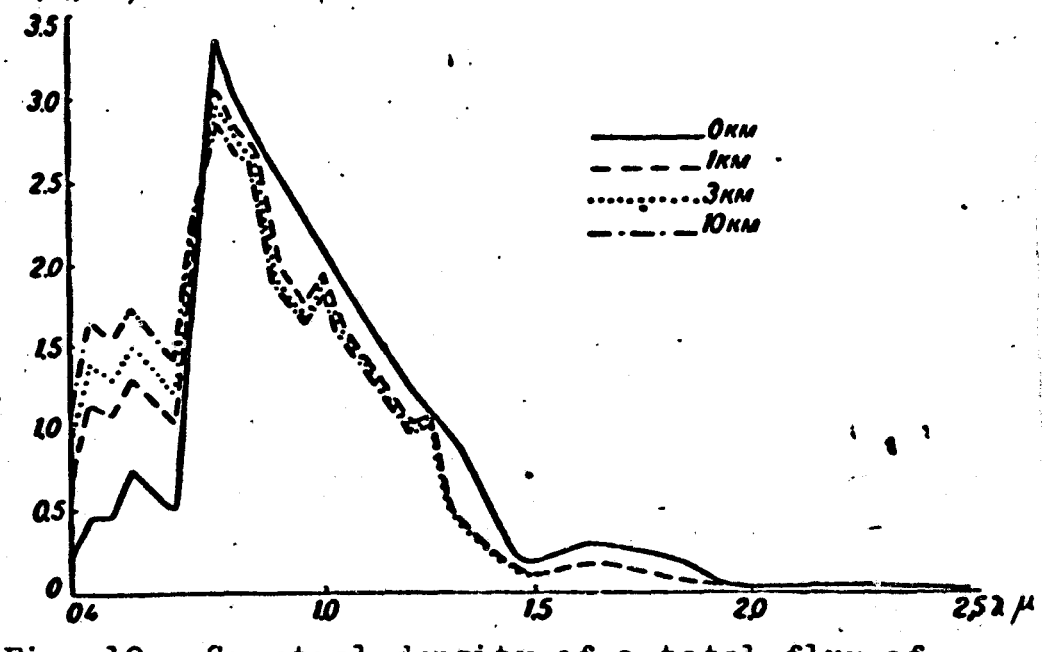

Fig. 10. Spectral density of a total flux of reflected radiation over grass ($i = 20^\circ$).

Table 3

i°	Water	Grass	Snow
20	0.36	0.28	0.33
40	0.37	0.29	0.33
60	0.38	0.32	0.34
80	0.36	0.34	0.35

The variation of $R(\lambda)$ with the height above the earth differs with the type of reflecting surface. Thus, in the case of water, for all i, $R(\lambda)$ increases with the height, and the increase is particularly great for the visible region of the spectrum (owing to the increase in the brightness of atmospheric haze). A similar variation was obtained in the case of grass for i equal to 80 and 60°. For i equal to 40 and 20° for grass in the infrared region, the variation of $R(\lambda)$ with the height was opposite. For snow at $i = 80$ and 60°, as z increased, $R(\lambda)$ increased for the entire spectrum considered, and for $i = 40$ and 20°, as z increased, $R(\lambda)$ decreased for $\lambda \leq 0.55\ \mu$. At $\lambda > 0.55\ \mu$, $R(\lambda)$ increased with z.

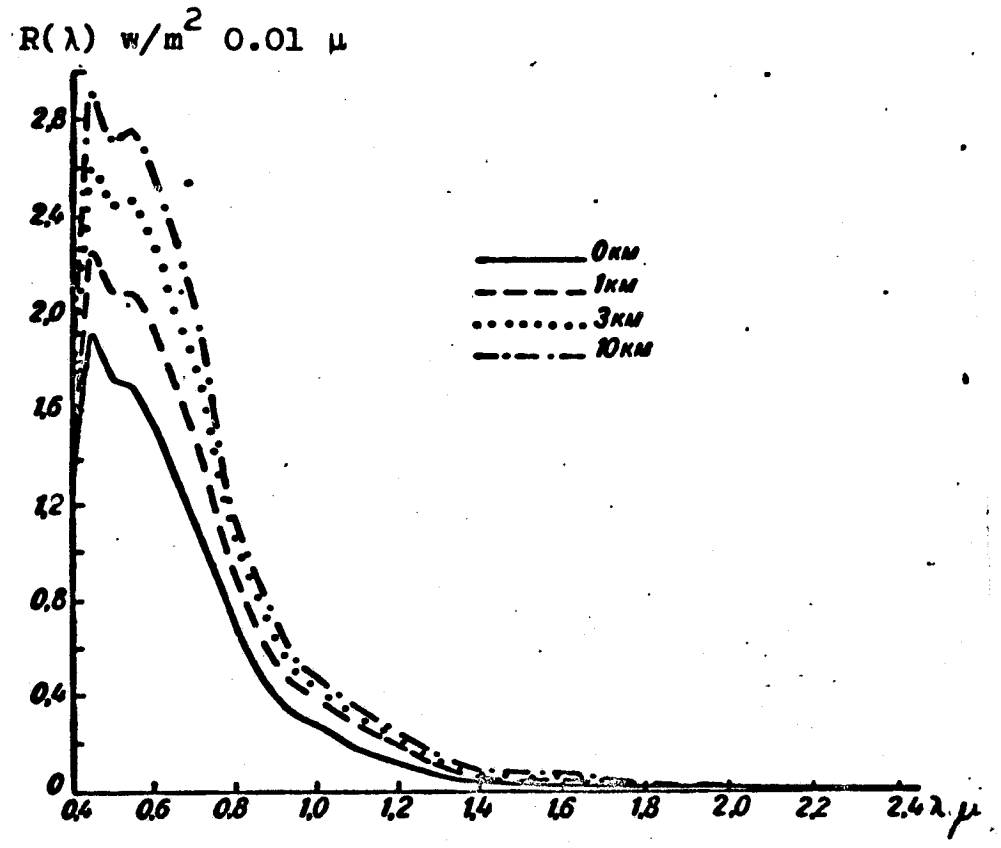

Fig. 11. Spectral density of a total flux of reflected radiation over snow ($i = 80^\circ$).

As i increases, the ascending flux $R(\lambda)$ decreases for grass and snow at all heights above the earth's surface and for all λ. For water, the albedo increases considerably with i, and as a result, the ascending flux for water changes little with an increase in i.

Integral fluxes. By integrating $R(\lambda)$ with respect to λ from 0.4 to 2.5 μ, we obtain the values of R_1, R_2 and R in cal/cm^2 min., (Tables 4-6).

Let us examine the structure of the integral ascending flux. Fig. 12-14 show the change of the ascending flux and both of its components with height, i.e., of the quantities R_1, R_2 and R for the three surfaces under consideration (snow, grass, water) for four i [20, 40, 60, 80°]. The values of the ascending fluxes in cal/cm^2 min are plotted along the vertical axis, and the height z is plotted in kilometers along the horizontal axis. It is evident from the figures that in all cases, the flux R_1 due to the atmospheric haze increases monotonically with the height from 0 (at $z = 0$), the most rapid increase in R_1 taking place in the lower layer of the troposphere (from 0 to 3 km); above 3 km, the increase in R_1 slows down somewhat.

On the contrary, the flux R_2 due to the reflection from the earth's surface decreases with the height for all the cases under consideration, and again the most rapid decrease of R_2 is observed in the lower layer of the troposphere (from 0 to 3 km), while above 3 km the change of R_2 with the height is small.

As z increases, the total ascending flux R for grass and water rapidly increases in all cases in the lower layer of the troposphere (from 0 to 3 km) and more slowly at levels above 3 km. It approaches asymptotically a constant value which may be termed the flux of outgoing shortwave radiation R_∞.

Table 4

Flux of ascending shortwave radiation flux due to haze at various levels, R_1 (cal/cm^2 min).

z km	$l = 20°$			$l = 40°$			$l = 60°$			$l = 80°$		
	water	grass	snow	water	grass	snow	water	grass	snow	water	grass	snow
0	0	0	0	0	0	0	0	0	0	0	0	0
0,5	0,0323	0,0518	0,106	0,0331	0,0437	0,0935	0,0235	0,0372	0,0671	0,0160	0,0185	0,0259
1,0	0,0481	0,0786	0,167	0,0496	0,0675	0,138	0,0435	0,0568	0,0939	0,0270	0,0305	0,0417
2,0	0,0639	0,103	0,215	0,0627	0,0887	0,180	0,0595	0,0767	0,132	0,0403	0,0450	0,0581
3,0	0,0718	0,114	0,238	0,0712	0,0992	0,200	0,0676	0,0861	0,148	0,0476	0,0529	0,0683
5,0	0,0784	0,124	0,254	0,0771	0,107	0,215	0,0751	0,0945	0,161	0,0553	0,0607	0,0716
10,0	0,0859	0,136	0,279	0,0853	0,119	0,235	0,0828	0,104	0,176	0,0725	0,0794	0,0995

Table 5

Flux of ascending shortwave radiation at various levels, caused by radiation reflected from the earth R_2 (cal/cm^2 min).

z km	$l = 20°$			$l = 40°$			$l = 60°$			$l = 80°$		
	water	grass	snow	water	grass	snow	water	grass	snow	water	grass	snow
0	0,0335	0,278	0,801	0,0312	0,221	0,630	0,0390	0,133	0,382	0,0396	0,0346	0,0976
0,5	0,0275	0,236	0,690	0,0254	0,186	0,533	0,0320	0,111	0,323	0,0325	0,0285	0,0841
1,0	0,0255	0,222	0,633	0,0236	0,175	0,499	0,0298	0,104	0,292	0,0305	0,0269	0,0750
2,0	0,0234	0,206	0,579	0,0217	0,164	0,458	0,0273	0,0980	0,263	0,0278	0,0252	0,0659
3,0	0,0226	0,200	0,555	0,0208	0,160	0,439	0,0263	0,0956	0,252	0,0268	0,0248	0,0629
5,0	0,0217	0,195	0,533	0,0200	0,154	0,422	0,0254	0,0992	0,250	0,0257	0,0240	0,0618
10,0	0,0207	0,190	0,508	0,0192	0,149	0,408	0,0243	0,0930	0,240	0,0248	0,0234	0,0617

Table 6

Total flux of ascending shortwave radiation at various levels R (cal/cm^2 min).

z km	$l = 20°$			$l = 40°$			$l = 60°$			$l = 80°$		
	water	grass	snow	water	grass	snow	water	grass	snow	water	grass	snow
0	0,0335	0,278	0,801	0,0312	0,221	0,630	0,0390	0,133	0,382	0,0396	0,0346	0,0976
0,5	0,0598	0,288	0,796	0,0585	0,230	0,632	0,0605	0,148	0,390	0,0485	0,0470	0,110
1,0	0,0736	0,301	0,800	0,0702	0,242	0,637	0,0733	0,162	0,392	0,0575	0,0578	0,117
2,0	0,0873	0,309	0,794	0,0844	0,253	0,638	0,0868	0,175	0,395	0,0681	0,0710	0,124
3,0	0,0944	0,314	0,793	0,0920	0,259	0,639	0,0939	0,182	0,400	0,0714	0,0775	0,128
5,0	0,100	0,320	0,787	0,0971	0,261	0,639	0,100	0,188	0,411	0,0810	0,0847	0,133
10,0	0,107	0,336	0,787	0,104	0,278	0,643	0,107	0,205	0,416	0,0973	0,1028	0,151
R_∞	0,115	0,340	0,780	0,112	0,284	0,650	0,115	0,220	0,425	0,100	0,112	0,162

For snow (i = 40, 60 and 80°) in the lower layer of the troposphere, R increases only slightly, and for i = 20°, it even decreases somewhat. Above 3 km, R remains practically constant, i.e., equal to R_∞. In Figs. 12-14, R_∞ is designated by a dotted line. The values of R_∞ are listed in Table 6.

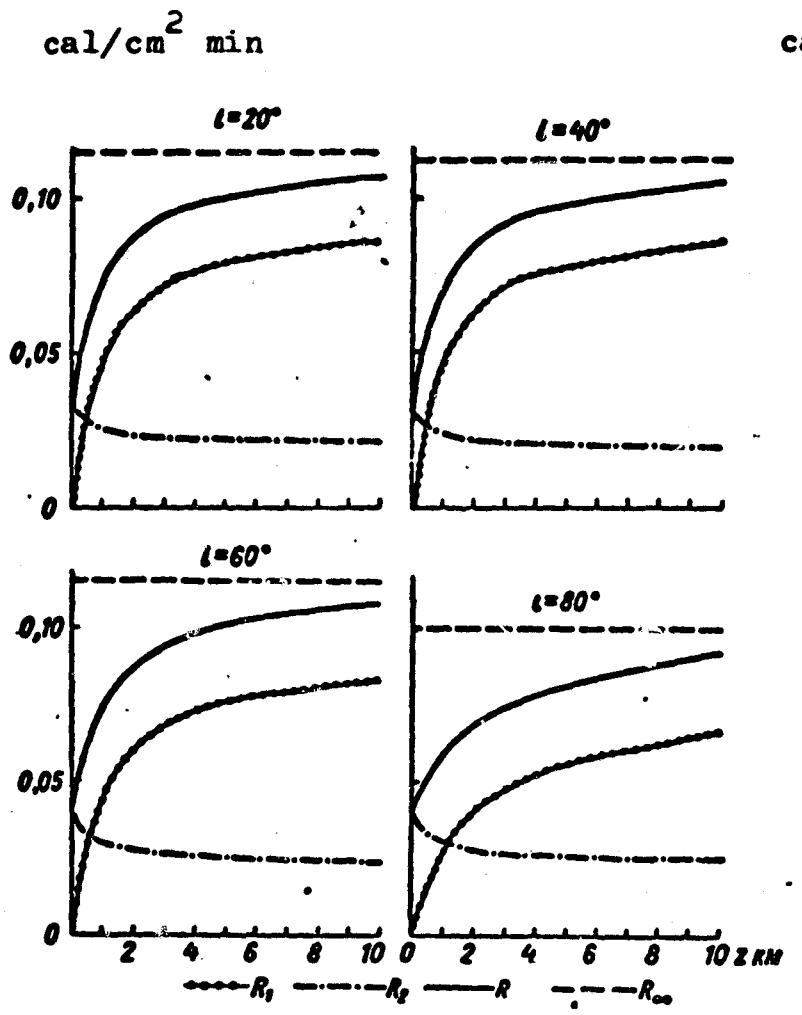

Fig. 12. Integral ascending flux of shortwave radiation versus altitude for water.

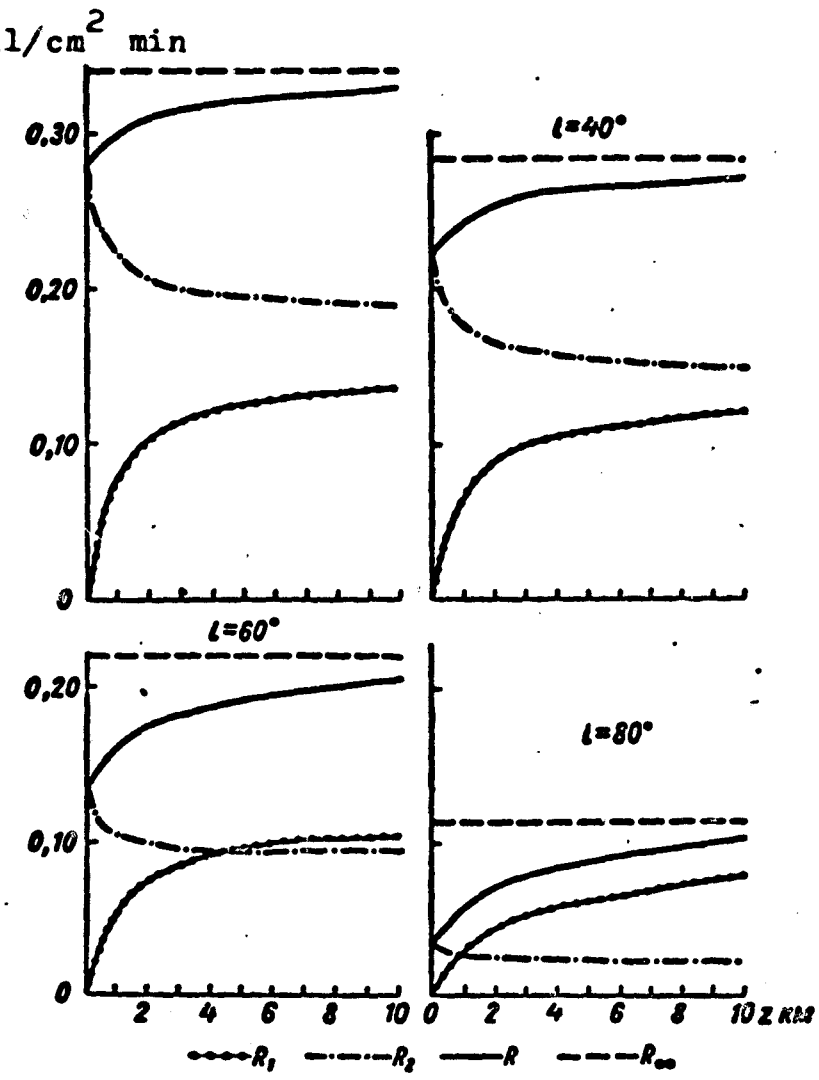

Fig. 13. Integral ascending flux of shortwave radiation versus altitude for grass.

It is evident that as the sun's altitude decreases, the OSR flux decreases more appreciably the greater the reflectivity of the earth's surface. For water, the OSR flux remains practically unchanged as i increases.

Data on the calculation of the descending fluxes are given in Tables 7 and 8.

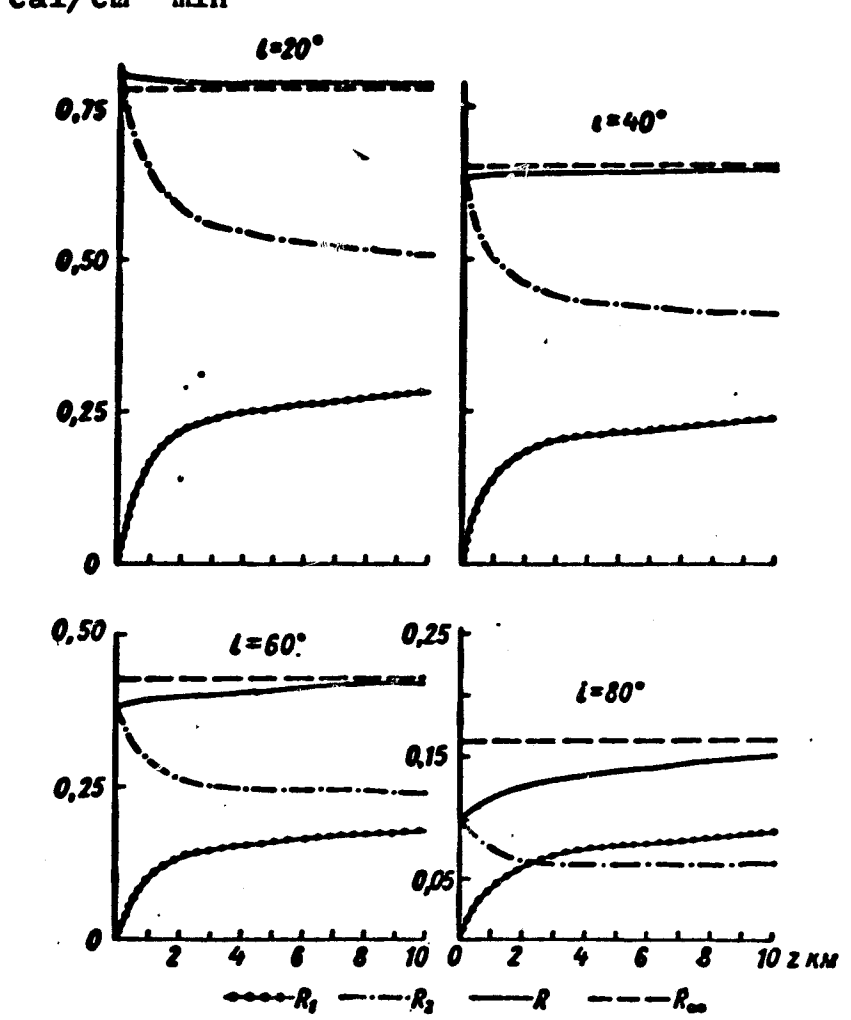

Fig. 14. Integral ascending flux of shortwave radiation versus altitude for snow.

Table 7

Flux of direct solar radiation at various levels striking a horizontal surface (cal/cm² min).

h км	$l = 20°$	$l = 40°$	$l = 60°$	$l = 80°$
0,0	1,116	0,853	0,468	0,0742
0,5	1,200	0,930	0,531	0,0992
1,0	1,247	0,972	0,565	0,118
2,0	1,318	1,040	0,621	0,145
3,0	1,370	1,083	0,651	0,160
5,0	1,430	1,141	0,702	0,187
10,0	1,551	1,253	0,798	0,249

Table 8

Flux of scattered radiation at various levels over typical underlying surfaces (cal/cm^2 min).

z km	$i = 20°$			$i = 40°$			$i = 60°$			$i = 80°$		
	water	grass	snow	water	grass	snow	water	grass	snow	water	grass	snow
0.0	0,203	0,210	0,282	0,173	0,179	0,235	0,142	0,144	0,174	0,0694	0,0667	0,0722
0,5	0,163	0,167	0,216	0,141	0,145	0,182	0,121	0,122	0,141	0,0643	0,0616	0,0644
1,0	0,138	0,140	0,179	0,115	0,113	0,146	0,101	0,102	0,117	0,0597	0,0575	0,0586
2,0	0,0927	0,0963	0,123	0,0805	0,0837	0,103	0,0747	0,0747	0,0810	0,0488	0,0484	0,0462
3,0	0,0697	0,0714	0,0914	0,0611	0,0625	0,0772	0,0575	0,0578	0,0651	0,0417	0,0405	0,0395
5,0	0,0484	0,0507	0,0642	0,0445	0,0445	0,0553	0,0417	0,0420	0,0467	0,0326	0,0317	0,0308
10,0	0,0275	0,0284	0,0362	0,0249	0,0256	0,0313	0,0242	0,0243	0,0283	0,0215	0,0198	0,0190

The albedos for various z were calculated from the data of Tables 6-8. Fig. 15 shows the variation of the albedo with the height above water, grass and snow for four i.

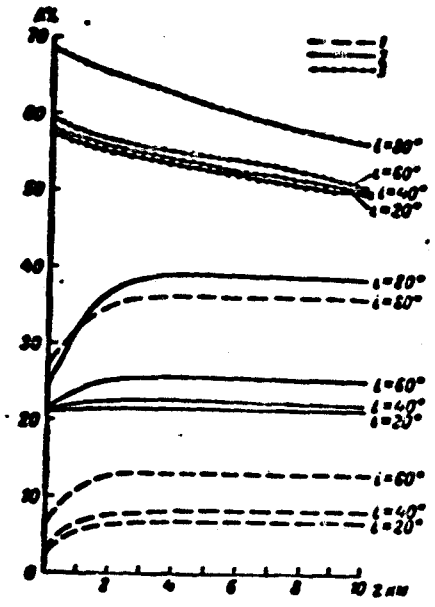

Fig. 15. Change in albedo with altitude over various underlying surfaces.

1 - water; 2 - grass; 3 - snow.

6. Conclusion

The method developed above for calculating the OSR field enabled us to perform a detailed analysis of the angular structure of the field.

The main conclusion to be drawn from this analysis is that as Θ increases, the brightness of the haze $B_1(\Theta)$ increases, and the brightness of the reflected beam $B_2(\Theta)$ usually decreases. The behavior of the resulting function depends on the relation between the absolute values of these brightnesses, and the main factor governing the variability of the

angular structure is the variability of the surface albedo: the optical properties of the atmosphere are more or less standard. A more detailed analysis of this basic fact is given in the second part of Ref. [7].

REFERENCES

1. Shifrin, K. S., Minin, I. N. K teorii negorizontal'noy vidimosti [Theory of Non-horizontal Visibility]. Tr. GGO, vyp. 68, 1957.
2. Shifrin, K. S., Pyatovskaya, N. P. Tablitsy naklonnoy dal'nosti vidimosti i yarkosti bezoblachnogo neba [Tables of Oblique Visibility Range and Brightness of Cloudless Sky]. Gidrometeoizdat, Leningrad, 1961.
3. Shifrin, K. S., Avaste, O. A. Potoki korotkovolnovoy radiatsii v bezoblachnoy atmosfere. Issledovaniya po fizike atmosfery [Fluxes of Shortwave Radiation in the Cloudless Atmosphere. Studies in Atmospheric Physics], No. 2, Tr. IFA AN ESSR, 1960.
4. Krinov, Ye. L. Spektral'naya otrazhatel'naya sposobnost' prirodnykh obrazovaniy [Spectral Reflectivity of Natural Formations]. Izd. AN SSSR, Moscow, 1947.
5. Krasil'shchikov, L. B., Korzov, V. I. Pribor dlya izmereniya indikatris otrazheniya v infrakrasnoy oblasti spektra [Instrument for Measuring Reflection Indicatrixes in the Infrared]. Nauchn. soobshch. In-ta geol. i geogr. AN Lit SSR, t. 13, 1962.
6. Novosel'tsev, Ye. P., Ter-Markaryants, N. Ye. Ob otrazhenii dlinnovolnovoy radiatsii vodnoy poverkhnost'yu [Reflection of Longwave Radiation by Water Surfaces]. Tr. GGO, vyp. 125, 1962.
7. Shifrin, K. S., Kolomiytsov, V. Yu., Pyatovskaya, N. P. Opredeleniye potoka ukhodyashchey korotkovolnovoy radiatsii s pomoshch'yu iskusstvennogo sputnika Zemli [Determination of the Flux of Outgoing Shortwave Radiation by Means of an Artificial Satellite]. See this Collection.
8. Dirmhirn, I. Zur spektralen Verteilung der Reflexion natuerlicher Medien. Wetter und Leben, 9, H. 3--5, 1957.
9. Foitzik, L., Zschaeck, H. Messungen der spektralen Zerstreuungsfunktion bodennaher Luft bei guter Sicht, Dunst und Nebel. Z. f. Meteorolog. 1, 1953.

K. S. Shifrin, V. Yu. Kolomitsov, N. P. Pyatovskaya

DETERMINATION OF THE FLUX OF OUTGOING SHORTWAVE RADIATION BY MEANS OF ARTIFICIAL SATELLITE

1. Introduction. Statement of the Problem.

The problem of determining the flux of outgoing shortwave radiation (OSR) from measurements made by an artificial earth satellite (AES) was formulated in general fashion in [1]. It consists in the development of a method for converting the readings of a narrow-sector receiver (NSR) mounted aboard the AES into values of R - the flux of OSR over the sighted point of the earth's surface. In [1] it was noted that this conversion can be made if the angular structure of the OSR field is known.

NSR gives values of brightnesses I for various areas sighted by the NSR at a given instant. In general, I will depend on a large number of various parameters characterizing the optical properties of the sighted area (albedo A and reflection indicatrix η) and of the atmosphere (distribution of the aerosol, H_2O, optical properties of the aerosol, etc.), on the location of the NSR, and the zenithal distance of the sun i

$$I = I(A, \eta, S_0, \tau_0, w_{H_2O}, w_{CO_2}, \theta, \varphi, i). \qquad (1.1)$$

In accordance with the formulation developed in [1], we included all the optical properties of the atmosphere in the parameters S_0, τ_0, w_{H_2O}, w_{CO_2}. The problem facing us is to find a method of determining the flux of OSR from the sighted area by using the known value of I. This flux R will also depend on a whole series of parameters.

$$R = R(A, \eta, S_0, \tau_0, w_{H_2O}, w_{CO_2}, i). \qquad (1.2)$$

Let us note that the dependence of R on the indicatrix is much less pronounced than that of I.

The problem consists in the determination of R from the known I when θ, φ, i, are given. The knowledge of I makes it possible to determine only one parameter, whereas R actually depends on a set of parameters. It is obvious that a single-valued calculation is not possible in this case. It is necessary to develop a single-parameter method of calculation in which R would be related only to $I(\theta, \varphi, i)$. All other parameters should be fixed at all their typical average values. A correct choice of the model and of the typical values of the parameters will make it possible to determine the most probable value of the flux of OSR corresponding to the given value of $I = I(\theta, \varphi, i)$.

The variability of R may be described by the expression

$$\Delta R = \left(\frac{\partial R}{\partial y}\Delta y + \dots\right)_{I=\text{const}}. \qquad (1.3)$$

The differential ΔR is located on the hypersurface $I(\theta, \varphi, i) = \text{const}$. ΔR depends both on the range of variability of the parameter (Δy) and on the sensitivity of R to the given parameter $\frac{(\partial R)}{(\partial y)}$.

The problem now amounts to the determination of the parameter which has the greatest influence on R; this is the parameter which should be determined from the readings of the instruments aboard the AES.

2. Choice of the Main Parameter

Analysis of the results obtained from calculations of the field structure above typical underlying surfaces, carried out in the first part of [1], shows that I and R are most strongly affected by the albedo of the surface A, the nature of the reflection indicatrix η and the vertical transparency of the atmosphere τ_0.

Vertical transparency of the atmosphere τ_0. All the calculations were carried out for a standard radiation model of a real atmosphere. In this model, the optical thickness of the atmosphere for $\lambda = 0.550\ \mu$ is taken to be constant and equal to $\tau_0 = 0{,}3$. Let us see what actually

happens, i.e., how the transparency of the real atmosphere actually fluctuates in the range of $\lambda = 0.550\ \mu$ around the standard value $\tau_0 = 0.3$ which we have adopted (see [2]). We shall turn to the data obtained by observations of S. I. Sivkov and Ye. P. Barashkova in Karadag for 1942, 1948, and 1949. Using a Michelson actinometer equipped with OG1 and RG2 Schott filters, they obtained data on fluxes of shortwave radiation in the spectral region of 0.509-0.644 μ and calculated the trouble factors T^*.

In [2], 2,591 cases of observations were examined. The mean value of T^* was found to be

$$\overline{T^*} = \frac{\sum T_i^*}{N} = 2{,}77.$$

This value should be referred to the average wavelength of the filter, i.e., to

$$\overline{\lambda} = \frac{0{,}644 + 0{,}509}{2} = 0{,}577\ \mu.$$

The optical thickness of the atmosphere for this $\overline{\lambda}$ will be

$$\tau_{\overline{\lambda}} = 2{,}77 \cdot 0{,}0906 = 0{,}251$$

(0.0906 is the Rayleigh thickness for $\overline{\lambda}$). For this wavelength, τ will be $\tau_{\overline{\lambda}} = 0{,}267$ in our model. We see that the figures are fairly close to each other. It is significant that for Karadag, which is a region of very high transparency, the mean optical thickness based on 2,591 cases turned out to be 6% lower than the standard optical thickness which we adopted for the atmosphere as a whole.

In [2], curves of the probability distribution of the various values of τ were plotted on the basis of observational data. The average curve is shown in Fig. 1. It was found that about 65% of all the observations were within $\pm$20% of the average value of τ.

Let us now see how the variability of the transparency affects the brightness of the OSR.

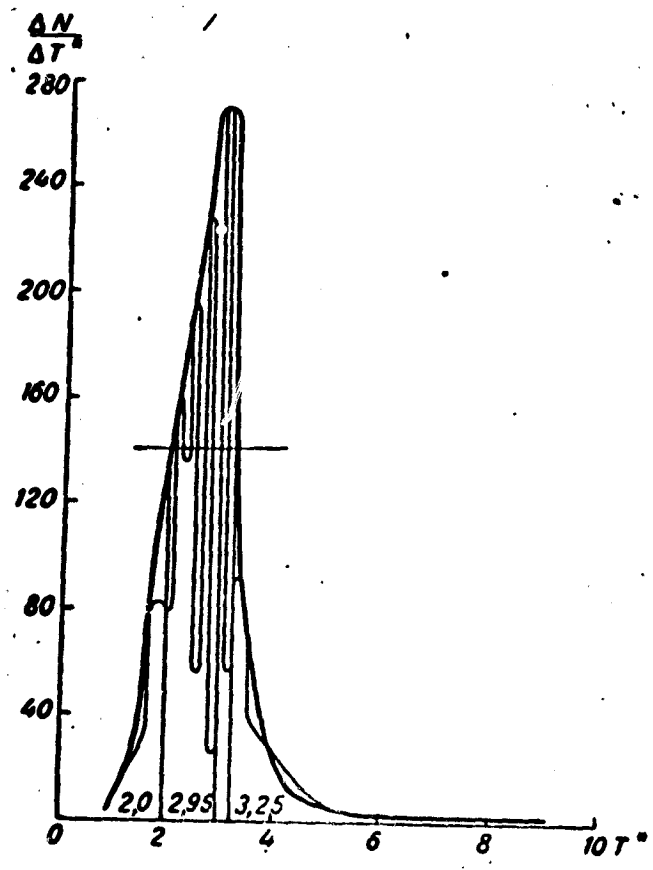

Fig. 1. Statistical structure of vertical transparency.

From formulas (4.1) and (4.2) of [1], we find

$$\frac{\partial I}{\partial \tau_0} = \frac{I_0}{\pi}\left[\frac{\partial D}{\partial \tau_0} + A\frac{\partial}{\partial \tau_0}(B^*T)\right]. \qquad (2.1)$$

Since $\frac{\partial B^*}{\partial \tau_0} \approx 0$ (except for states with a low sun), we have

$$\frac{\partial I}{\partial \tau_0} = \frac{I_0}{\pi}\left[\frac{\partial D}{\partial \tau_0} - \sec\theta AB^*T\right]. \qquad (2.2)$$

It is obvious that the right-hand member will have its highest value when A = 0, i.e., that

$$\frac{1}{I}\frac{\partial I}{\partial \tau_0} = \frac{1}{D}\frac{\partial D}{\partial \tau_0}.$$

Assuming, in accordance with the above, that $\left|\frac{\Delta\tau_0}{\tau_0}\right| = 0{,}2$ and using the results of [3] and [4], we obtain about 10-15% for $\frac{\Delta I}{I}$, associated with fluctuations of τ_0 based on formula (2.2), and 5% for $\frac{\Delta R}{R}$. These estimates show the magnitude of the error which may arise when a standard value of τ_0 is used.

Reflection indicatrix and albedo of the underlying surface. Of these two factors characterizing the reflection of the earth's surface, the one

having the greater importance is the magnitude of the albedo A. The albedo changes very appreciably, and as is evident from Table 1, the brightness of the OSR reacts directly to the value of A. For example, when i = 40° and θ = 45° for changes of A from 0.1 to 0.3, $\bar{I}$ changes from 5 x 10^{-2} to 12 x 10^{-2} cal/cm^2 min ster.

Hence, we are obliged to examine the standard reflection indicatrix.

It is known that on the average, 55% of the earth's surface is covered with clouds. Of the remaining 45%, 15% consists of land. This means that in 70% of the cases the instrument aboard the AES will sight sections with a Lambert reflection indicatrix. For this reason, we have adopted this indicatrix as our standard.

Thus, the readings of the NSR aboard the AES should be used to determine the unknown albedo A of the sighted section. To a given value of A there corresponds a certain structure of the OSR flux and hence, a certain value of the OSR flux.

Generally speaking, the albedo of a surface depends on the wavelength, and it should not be defined by a single number. However, the signal measured by a black receiver generally does not depend very strongly on the form of the function A (λ), but is determined by the average, or more accurately, the effective value of the albedo A_{ef}. This is an albedo with a constant spectrum giving the same value of the integral intensity as the real underlying surface. It is obvious that a given surface will have different values of A_{ef} for different combinations of θ and φ for a given i. Nevertheless, if this spread in A_{ef} leads to slight deviations in the values of R (i, A_{ef}) (OSR fluxes calculated for a constant-spectrum albedo) from the true values of R for a given underlying surface, then any A_{ef} may be used to determine the OSR fluxes.

We carried out calculations for two "poor" cases:

$$\text{a)}\ A(\lambda)=\begin{cases}0 & 0{,}4\leqslant\lambda\leqslant 0{,}75\ \mu\\ 1 & 0{,}75<\lambda\leqslant 2{,}5\ \mu\end{cases}$$

$$\text{б)}\ A(\lambda)=\begin{cases}1 & 0{,}4\leqslant\lambda\leqslant 0{,}75\ \mu\\ 0 & 0{,}75<\lambda\leqslant 2{,}5\ \mu\end{cases}$$

It was found that in both cases the error did not exceed 5% for $\theta \leq 60^\circ$ for any i and φ. Since under actual conditions the albedo has a smoother variation than in the examples which we considered, we can use the effective albedo in our calculations and characterize the real surface by this single number.

3. Calculation of the Brightness Allowing for Absorption

The purpose of our calculations was to obtain data on the radiation balance of the system earth--atmosphere (E--A). For this reason, a correct allowance for the absorption is very important.

Earlier in [1], in calculating the atmospheric haze, we assumed that only pure scattering takes place in the atmosphere. This assumption was justified for the visible portion of the spectrum, but in the infrared portion, it is necessary to allow for absorption. We shall indicate a method of calculating the brightness by introducing absorption functions for water vapor and carbon dioxide. In the calculation, the atmosphere will be divided into eight layers, as was done in [5]. Since in the infrared region of the spectrum the optical thickness is quite small [6], we shall confine ourselves to an analysis of the scattering of the first order. In this case, the OSR field is made up of five components (Fig. 2):

1 - Direct radiation immediately scattered backward;

2 - Direct radiation which passed through the atmosphere, was reflected by the earth's surface and traversed the atmosphere again;

3 - Radiation which was scattered forward, was reflected by the

earth's surface and sent back through the atmosphere;

4 - Radiation which was reflected and scattered forward;

5 - Radiation which was reflected, scattered back, then reflected again and which passed through the atmosphere.

The first and fourth component give a field of atmospheric haze, while the second, third and fifth give a field of reflected radiation at the upper boundary of the atmosphere.

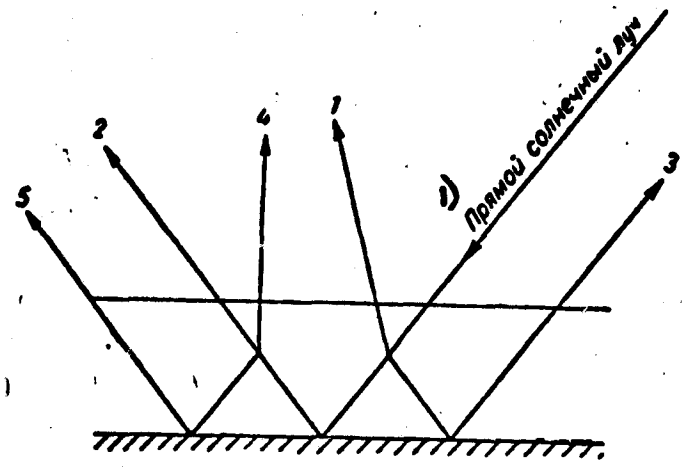

Fig. 2. Diagram of the formation of an OSR beam (single scattering).
Legend: 1) Direct solar ray.

We obtained the formulas for the calculation of all these quantities by numerical integration in accordance with [5].

The spectral brightness of the haze $I_D^0(\lambda, i, \theta, \varphi)$ for an albedo A = 0 (first component) is calculated from the formula

$$I_D^0(\lambda, i, \theta, \varphi) = I_0(\lambda)\frac{\varkappa_\lambda(\gamma)}{4\pi}\sec\theta\sum_{k=1}^{8}T(\lambda, i)\Big|_k^\infty T(\lambda, \theta)\Big|_k^\infty \tau_{k-1}^k(\lambda), \qquad (3.1)$$

where γ is the scattering angle given by the relation

$$\cos\gamma = -\cos\theta\cos i + \sin\theta\sin i\cos\varphi; \qquad (3.2)$$

$\varkappa_\lambda(\gamma)$ is the spectral indicatrix of scattering calculated in [1]: $\tau_k^{k-1}(\lambda)$ are the optical thicknesses of the layers Z_k^{k-1} over which the summation is made (the boundaries of the layers Z_k are shown in Table 9 of [5], and the optical thicknesses are given in [6]; $I_0(\lambda)$ is the flux density of solar radiation striking the upper boundary of the atmosphere, and its values are given in [4]. $T(\lambda, i)\Big|_k^\infty$ and $T(\lambda, \theta)\Big|_k^\infty$ are the transmission

functions in the atmosphere from level k to the upper boundary. They are calculated in accordance with the method given in [5].

For the fourth component $I_D^{refl}(\lambda, i, \Theta, A)$, we obtain:

$$I_D^{refl}(\lambda, i, \theta, A) = \frac{AE_{dir}(\lambda, i)}{2\pi^2} \sec\theta \sum_{k=1}^{8} \varkappa_{k-1}(\lambda) T(\lambda, \theta) \Big|_k^{\infty} \times$$

$$\times \sum_{p=1}^{6} T(\lambda, \theta_p') \Big|_0^k f_p(\lambda, \theta), \qquad (3.3)$$

$$f_p(\lambda, \theta) \equiv [\varkappa_\lambda(\gamma_p) + \varkappa_\lambda(\gamma_p')]\,\Delta\omega_p, \qquad (3.4)$$

where

$$\left.\begin{aligned} \cos\gamma_p &= \cos\theta_p' \cos\theta + \sin\theta_p' \sin\theta \cos 45^\circ \\ \cos\gamma_p' &= \cos\theta_p' \cos\theta - \sin\theta_p' \sin\theta \cos 45^\circ \end{aligned}\right\} \qquad (3.5)$$

$$\Delta\omega_p = \int_0^{\frac{\pi}{2}} d\varphi \int_{\theta_p}^{\theta_{p+1}} \sin t\, dt = \frac{\pi}{2} [\cos\theta_p - \cos\theta_{p+1}], \qquad (3.6)$$

θ_p is equal to 0, 15, 30, 45, 60, 75, 90°. It is obvious that $\sum_{p=1}^{6} \Delta\omega_p = \frac{\pi}{2}$. The values of the quantity θ_p' are 7.5, 22.5, 37.5, 52.5, 67.5 and 82.5°.

$$E_{dir}(\lambda, i) = I_0(\lambda) T(\lambda, i) \Big|_0^{\infty} \cos i \qquad (3.7)$$

is the spectral illumination of the earth's surface by direct rays; $T(\lambda, \theta_p') \Big|_0^k$ is the transmission function of the atmosphere from the ground level to level k.

Combining expressions (3.1) and (3.3), we obtain the intensity of the haze at the upper boundary of the atmosphere

$$I_D(\lambda, i, \theta, \varphi, A) = I_D^{1}(\lambda, i, \theta, \varphi) + I_D^{refl.}(\lambda, i, \theta, A). \qquad (3.8)$$

After integrating with respect to λ, we find the integral intensity of the haze $I_D(i, \theta, \varphi, A)$ in the infrared region

$$I_D^{ir}(i, \theta, \varphi, A) = \sum_n I_D(\lambda_n, i, \theta, \varphi, A)\,\Delta\lambda_n, \qquad (3.9)$$

where the summation integrals $\Delta\lambda_n$ were borrowed from [5].

For the integral intensity of reflected radiation $I_{refl}(i, \theta, A)$ (second, third and fifth component) at the upper boundary of the atmosphere in the infrared region, we obtain

$$I^{ir}_{refl}(l, \theta, A) = \frac{A}{\pi} \sum_{n} E(\lambda, i, A) T(\lambda, \theta) \int_{0}^{\infty} \Delta\lambda_n, \tag{3.10}$$

where $T(\lambda, \theta)\int_0^\infty$ is the transmission function of the atmosphere from the earth's surface to the upper boundary;

$$E(\lambda, l, A) = E_{dir}(\lambda, l) + E_s(\lambda, l, A) \tag{3.11}$$

is the total illumination of the earth's surface by direct light E_{dir} and scattered light E_s.

The first component pertains to the second beam, and the second component to the third and fifth beams

$$E_s(\lambda, l, A) = \int_0^{\frac{\pi}{2}} \int_0^{2\pi} B_H(\lambda, l, \theta, \varphi, A) \cos\theta \sin\theta \, d\theta \, d\varphi, \tag{3.12}$$

$$B_H(\lambda, l, \theta, \varphi, A) = B^0(\lambda, l, \theta, \varphi) + B^*(\lambda, l, \theta, A) \tag{3.13}$$

is the sky luminance, where

$$B^0_H(\lambda, l, \theta, \varphi) = I_0(\lambda) \frac{\varkappa_\lambda(\gamma)}{4\pi} \sec\theta \sum_{k=1}^{\infty} T(\lambda, l) \int_0^k \times$$

$$\times T(\lambda, \theta) \int_0^k \tau^k_{k-1}(\lambda), \tag{3.14}$$

$$\cos\gamma = \cos\theta\cos l + \sin\theta \sin l \cos\varphi, \tag{3.15}$$

$$B^*_H(\lambda, l, \theta, A) = \frac{A E_{dir}(\lambda, l)}{2\pi^2} \sec\theta \sum_{k=1}^{k} \tau^k_{k-1}(\lambda) T(\lambda, \theta) \int_0^k \times$$

$$\times \sum_{p=1}^{6} T(\lambda, \theta'_p) \int_0^k F_p(\lambda, \theta), \tag{3.16}$$

$$F_p(\lambda, \theta) \equiv [\varkappa_\lambda(\gamma_p) + \varkappa_\lambda(\gamma'_p)] \, \Delta\omega_p. \tag{3.17}$$

The brightness B^o_H pertains to the third beam. B^*_H pertains to the fifth beam. For each $\Delta\omega_p$ there are two different scattering angles, γ_p and $\gamma_p{}'$:

$$\left.\begin{aligned} \cos\gamma_p &= -\cos\theta'_p\cos\theta + \sin\theta'_p \sin\theta \cos 45^\circ \\ \cos\gamma'_p &= -\cos\theta'_p\cos\theta - \sin\theta'_p \sin\theta \cos 45^\circ \end{aligned}\right\} \tag{3.18}$$

Table 1

OSR Field ($1 \cdot 10^2$ cal/cm^2 min.ster.)

$\lambda°$	$\varphi°$	$\theta°$																											
		0	15	30	45	60	75	0	15	30	45	60	75	0	15	30	45	60	75	0	15	30	45	60	75	0	15	30	45	60	75
		$A = 0$						$A = 0,2$						$A = 0,5$						$A = 0,75$						$A = 1,0$					
20	0	1,72	1,63	1,67	1,90	2,49	3,95	9,54	9,31	9,21	9,17	9,25	9,54	21,7	21,5	21,1	21,0	19,8	18,5	32,4	32,2	31,6	30,9	29,2	27,0	43,9	43,5	42,8	41,7	39,2	34,7
	45		1,65	1,66	1,92	2,50	4,02		9,33	9,19	9,19	9,25	9,63		21,6	21,1	21,0	20,0	18,5		32,2	31,6	30,9	29,2	27,1		43,6	42,8	41,7	39,2	34,7
	90		1,73	1,80	2,03	2,56	3,90		9,42	9,35	9,30	9,30	9,50		21,6	21,2	21,1	20,0	18,4		32,3	31,8	31,0	29,2	27,0		43,6	42,9	41,8	39,3	34,5
	135		1,82	1,97	2,21	2,74	4,01		9,51	9,50	9,48	9,49	9,61		21,7	21,4	21,3	20,2	18,5		32,4	32,0	31,2	29,4	27,0		43,7	43,1	42,0	39,4	34,7
	180		1,90	2,08	2,32	2,83	4,10		9,58	9,61	9,57	9,58	9,70		21,8	21,5	21,4	20,3	18,6		32,4	32,1	31,3	29,5	27,2		43,8	43,2	42,1	39,6	34,8
40	0	1,49	1,44	1,51	1,83	2,80	5,84	7,62	7,63	7,48	7,61	8,20	10,3	17,2	17,1	16,9	16,6	16,0	15,7	25,8	25,7	25,2	24,3	24,0	21,9	35,0	34,6	34,1	33,2	30,6	29,5
	45		1,46	1,53	1,80	2,54	4,74		7,65	7,51	7,58	7,94	9,18		17,1	16,8	16,6	15,8	14,3		25,7	25,2	24,3	23,8	20,8		34,7	34,1	33,2	30,4	28,4
	90		1,54	1,64	1,88	2,47	3,83		7,72	7,62	7,66	7,85	8,29		17,2	16,9	16,6	15,7	13,6		25,7	25,4	24,4	23,7	19,9		34,7	34,2	33,3	30,3	27,5
	135		1,65	1,86	2,18	2,77	4,15		7,83	7,84	7,96	8,17	8,58		17,3	17,1	17,0	16,0	13,9		25,9	25,6	24,7	24,0	20,1		34,9	34,4	33,6	30,6	27,8
	180		1,70	2,02	2,44	3,10	4,50		7,87	7,73	8,22	8,55	8,94		17,3	17,0	17,2	16,3	14,3		25,9	25,1	24,6	24,1	20,3		34,9	34,6	33,9	30,9	28,2
60	0	1,27	1,29	1,48	2,12	3,80	9,34	5,13	4,94	5,07	5,59	6,98	12,0	11,4	10,6	10,6	11,0	11,6	16,2	16,5	16,3	16,2	16,2	17,1	20,5	21,7	21,5	21,4	21,3	21,6	
	45		1,29	1,43	1,85	2,86	5,80		4,95	5,03	5,32	6,06	8,41		10,6	10,6	10,7	10,7	12,6		16,3	16,2	16,0	16,2	17,1		21,5	21,3	21,0	20,6	
	90		1,32	1,44	1,71	2,26	3,60		4,98	5,04	5,17	5,45	6,21		10,7	10,6	10,6	10,1	10,4		16,3	16,2	15,8	15,6	14,9		21,5	21,3	20,9	20,1	
	135		1,38	1,59	1,94	2,57	3,95		5,04	5,18	5,41	5,76	6,56		10,7	10,8	10,8	10,4	10,8		16,4	16,3	16,0	15,9	15,3		21,6	21,4	21,1	20,4	
	180		1,42	1,73	2,21	3,09	4,66		5,08	5,32	5,69	6,27	7,27		10,8	10,9	11,1	10,9	11,6		16,4	16,5	16,4	16,4	16,0		21,6	21,6	21,4	20,9	
80	0	0,764	0,867	1,18	2,04	3,79	13,0	1,74	1,83	2,12	2,83	4,63	13,8	3,29	3,35	3,62	4,40	6,16	14,8	4,61	4,70	4,95	5,54	7,16	15,7	6,04	6,12	6,33	7,00	8,40	16,1
	90		0,795	0,883	1,07	1,31	2,37		1,75	1,83	1,86	2,16	3,09		3,28	3,34	3,44	3,67	4,21		4,63	4,64	4,58	4,67	5,20		6,04	6,02	6,04	5,92	5,27
	180		0,816	0,951	1,24	1,63	3,13		1,77	1,89	2,03	2,48	3,84		3,30	3,41	3,60	3,99	4,68		4,66	4,72	4,75	5,00	5,89		6,06	6,09	6,22	6,23	6,04

4. OSR field for a cloudless atmosphere

We carried out the calculations of the OSR field for the following values of the parameters: i (zenithal distance of the sun) [20, 40, 60, 80°], θ (sighting angle [0, 15, 30, 45, 60, 75°], φ (azimuth) [0, 45, 90, 135, 180°] A [0, 0.2, 0.5, 0.75, 1] for the standard radiation model of the atmosphere. Tables 1-3 give the values of the functions $I=I(\theta, \varphi, i, A)$, $R=R(i, A)$ and of the total illumination of the earth E, respectively. Fig. 3 illustrates the function $I(\theta)$ for A = 0 and φ, equal to 0 and 180° for four i values. When A = 0, the OSR field is formed only by the haze. The brightness $I(\theta)$ increases considerably with θ. When φ = 0 the curves $I(\theta)$ in the region $\theta \approx 45°$ show that the dependence on i changes to the opposite dependence: the curves intersect. This is readily explained by the fact that at small θ, larger i values correspond to smaller values of the indicatrix, and the reverse is true at larger θ. The dependence on θ is very strong at large θ and is practically nil for $\theta \leqslant 30°$. This is understandable, since large θ correspond to the stretched front portion of the scattering indicatrix and to large scattering thicknesses. Small θ, however, correspond to the rear portion of the indicatrix. The dependence of I on φ increases with rising θ and i, since at large θ and i the scattering angle changes considerably from φ = 0 to φ = 180°.

As the albedo increases, both the values of the haze and those of the field of reflected radiation increase, and therefore the brightnesses and the flux of the OSR field increase on the average by one order of magnitude as the albedo changes from 0 to 1. This is illustrated in Figs. 4 and 5.

Table 2

OSR Flux (cal/cm^2 min)

i°	λ				
	0	0,2	0,5	0,75	1,0
20	0,0718	0,289	0,633	0,936	1,254
40	0,0723	0,253	0,501	0,741	0,994
60	0,0728	0,176	0,334	0,497	0,628
80	0,0544	0,0807	0,126	0,162	0,199

Fig. 4 shows the dependence of the intensity of the outgoing radiation on the albedo of the earth's surface for four values of i and two extreme values of θ : 0 and 75°; the vertical dashes represent the limits of change in I with ω for $\theta = 75°$ (it is known that for $\theta = 0°$ the intensity of I is the same for φ).

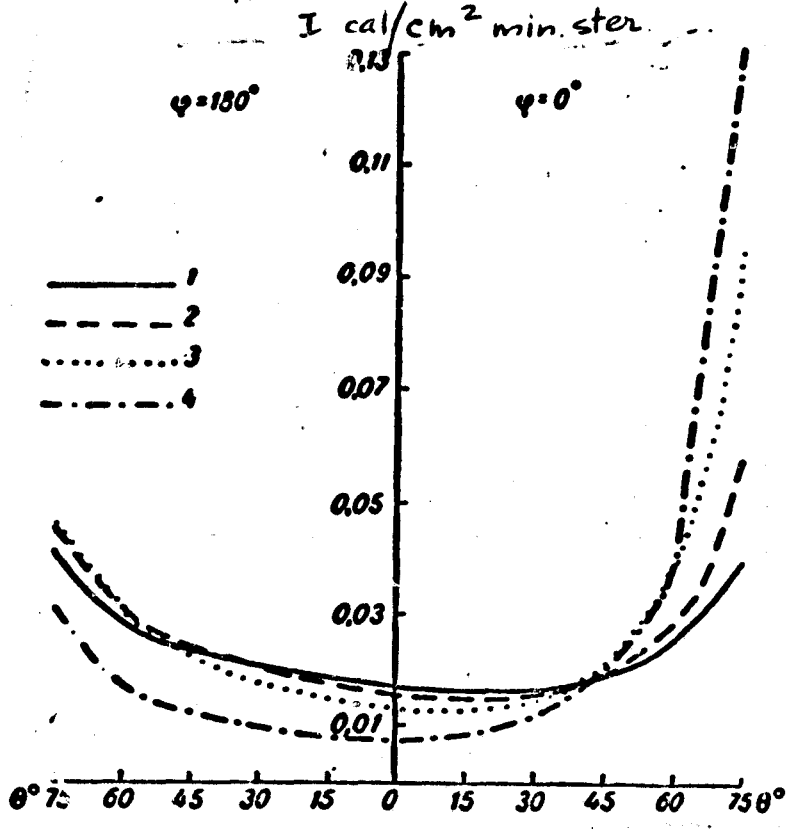

Fig. 3. Intensity of outgoing radiation versus $\theta°$.
1 - i=20°, 2 - i=40°, 3 - i=60°, 4 - i=80°.

Fig. 5 shows the dependence of the flux of outgoing radiation on the albedo of the underlying surface for all four i values.

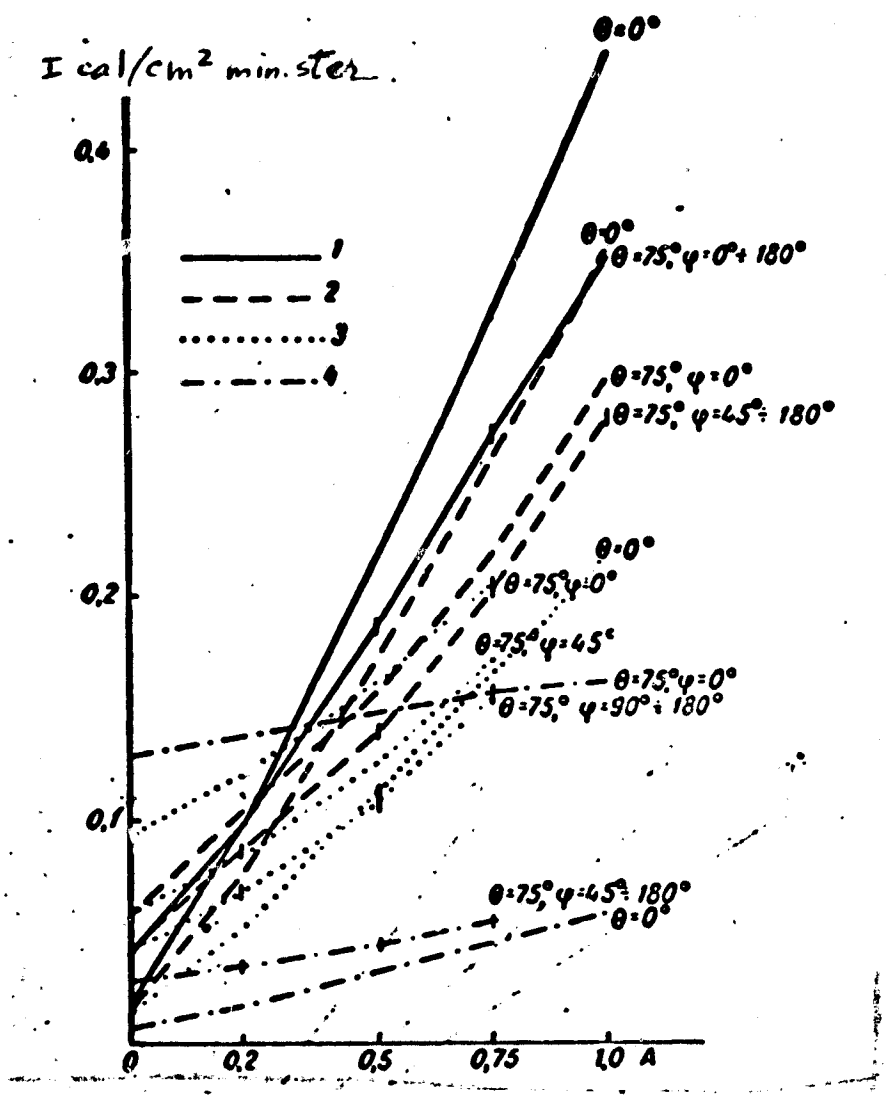

Fig. 4. Intensity of outgoing radiation versus albedo of earth's surface (cloudless atmosphere) Arb. designations, see Fig. 3.

From Figs. 4 and 5 it is obvious that the dependences of I and R on the albedo are almost linear, and that the higher i, the slower is the increase of the OSR field with a rise in A. This is explained by an increase in the relative contribution of the haze to the OSR with a rise in i.

The intensity of reflected radiation decreases with an increase in θ, i.e., it has a course which is opposite to that of the haze. For this reason, when $A \neq 0$, the relation of I to θ depends on the relation between the brightness of the haze and the reflected radiation.

Table 3

Total illumination of the Earth's Surface by Shortwave Radiation (cal/cm^2 min)

i°	A				
	0	0.2	0.5	0.75	1.0
20	1.358	1.376	1.408	1.432	1.461
40	1.084	1.098	1.119	1.141	1.163
60	0.658	0.666	0.682	0.693	0.706
80	0.156	0.160	0.164	0.167	0.170

As the albedo increases, so does the contribution of the reflected radiation, particularly for small i, and the dependence of I on θ characteristic of the haze smoothes out.

This is illustrated in Figs. 6 and 7, which show the indicatrixes of the brightness of the OSR field for two i values (30 and 80°), four azimuths φ (0.90, 180 and 270°) and three albedos A (0, 0.5 and 1).

Let us analyze the relationship between the brightnesses in the various directions and the total fluxes.

To this end, we first have to determine A from the known value $I=I(\theta, \varphi, i, A)$ for given θ, φ, i. Introducing this value of A into Table 2, we find the flux R.

Thus, we compiled special tables relating I, A and R for given i, θ, φ. They are given in the appendix (Tables I-IV) (I in cal · $10^2/cm^2$ min ster, R in cal · $10^2/cm^2$ min). We shall note that on this scale, the brightness does not exceed 50 units, and the fluxes, 150 units. These tables make it possible to determine R from the known NSR signal coming from the AES and the given i, θ, φ.

Analysis of the relation between I and R makes it possible to evaluate the degree of Lambert character of the system E—A. Let us turn to Fig. 8, which shows the functions R = R(I) for θ equal to 0 and 75° for different i values averaged over φ. The same figure shows the Lambert

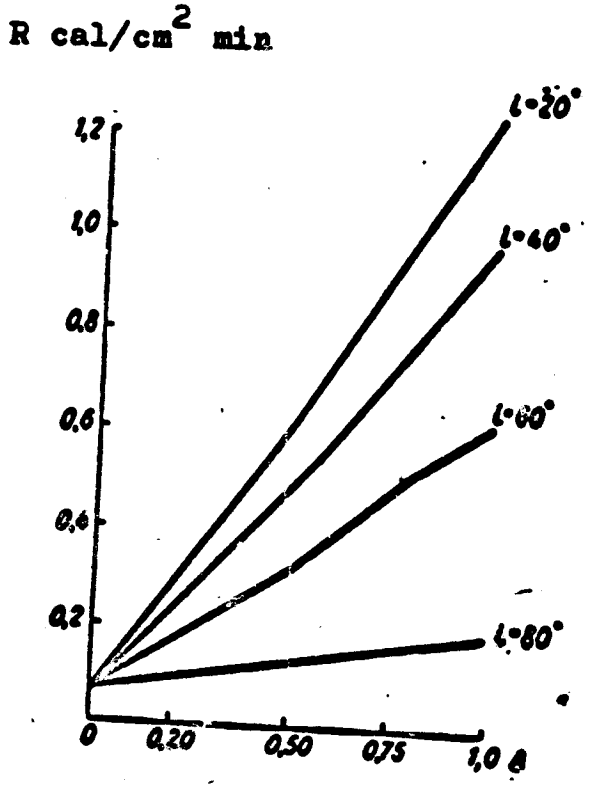

Fig. 5. Flux of outgoing radiation versus albedo of earth's surface (cloudless atmosphere).

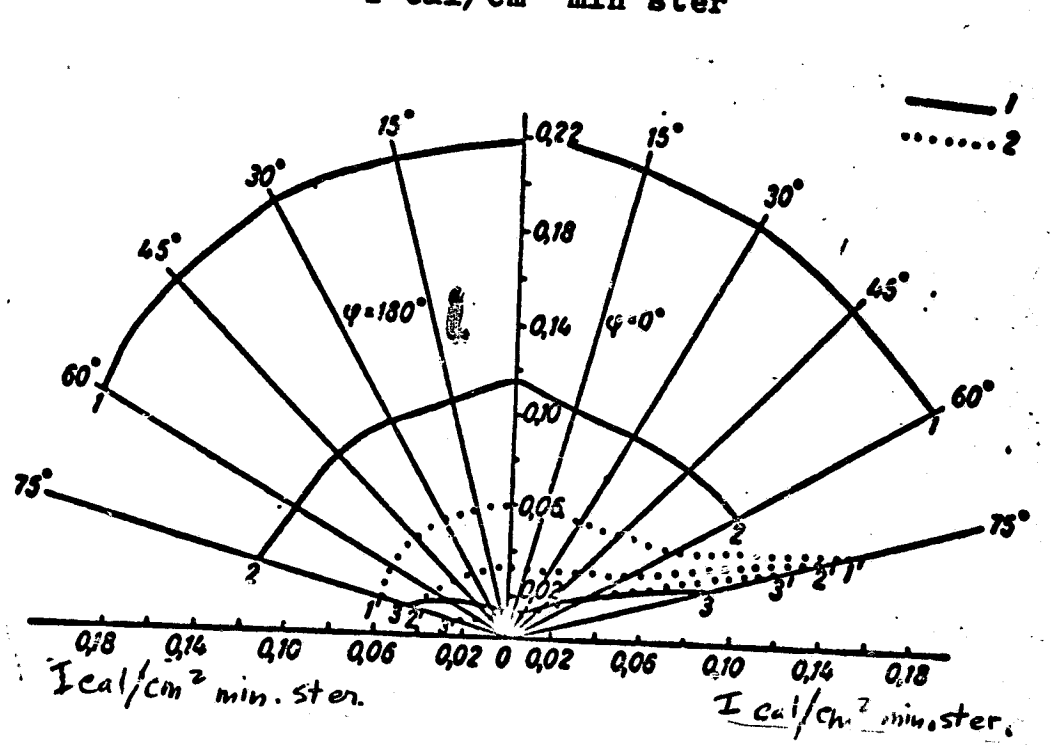

Fig. 6. Indicatrixes of brightness of OSR field (cloudless atmosphere).

1 - i = 60°; 2 - i = 80°; 1 and 1' - A = 1; 2 and 2' - A = 0.5; 3 and 3' - A = 0.

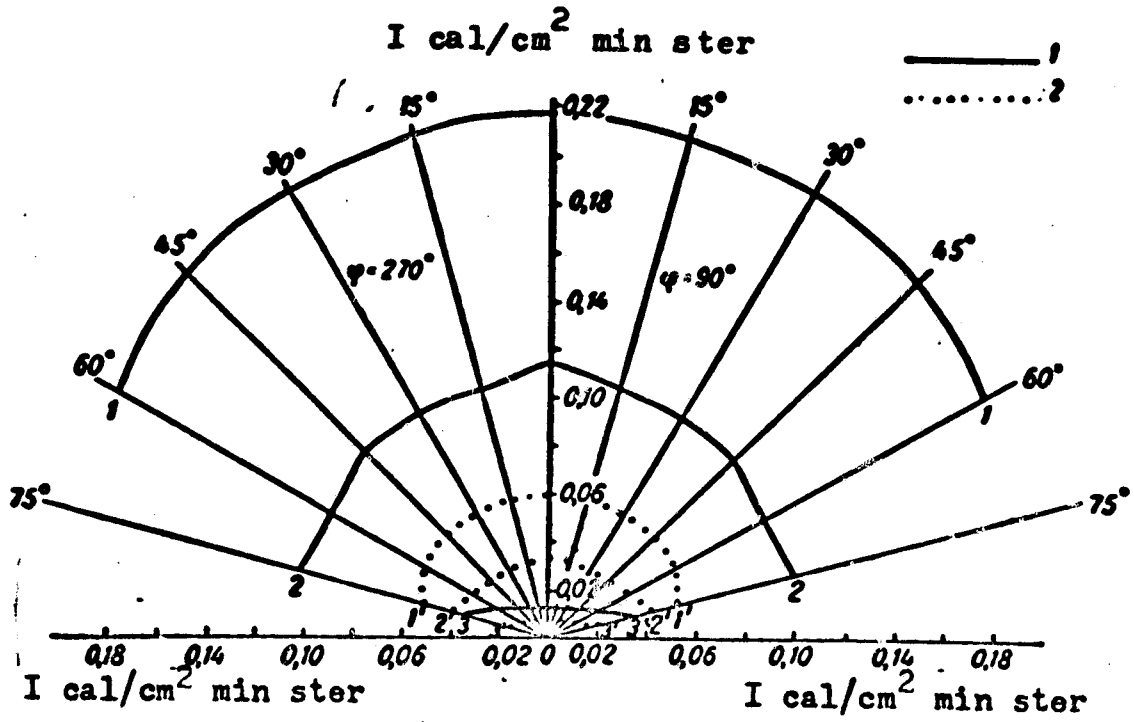

Fig. 7. Indicatrixes of brightness of OSR Field (cloudless atmosphere)
Arb. designations, see Fig. 6.

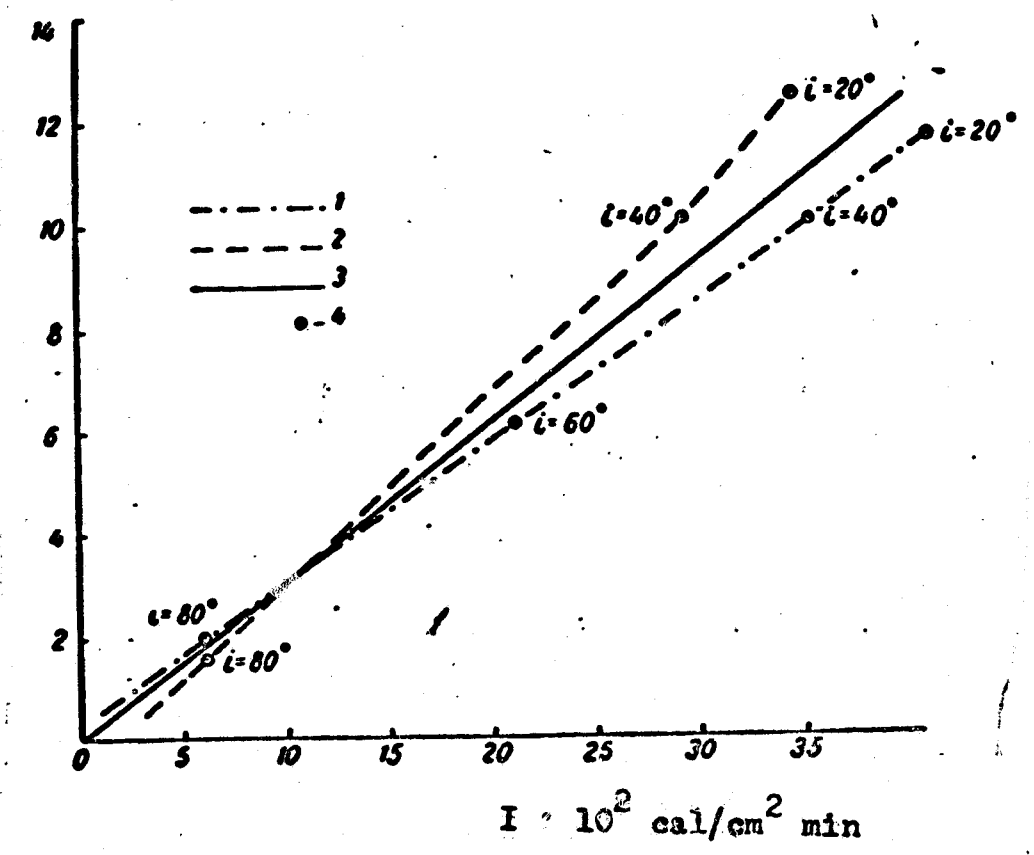

Fig. 8. Relation between flux and intensity of outgoing radiation (cloudless atmosphere).
1 - $\theta = 0°$, 2 - $\theta = 75°$, 3 - Lambert straight line, 4 - limit point.

Table 4

OSR Field ($1' \cdot 10^2$ cal/cm^2 min ster.)

$l°$	$\varphi°$	$\theta°$ 0	15	30	45	60	75	0	15	30	45	60	75	0	15	30	45	60	75	0	15	30	45	60	75	0	15	30	45	60	75
		$A = 0$						$A = 0,2$						$A = 0,5$						$A = 0,75$						$A = 1,0$					
20	0	0,636	0,608	0,616	0,690	0,920	1,68	10,2	10,2	10,1	10,0	10,0	10,2	24,5	24,6	24,4	24,3	23,9	23,0	37,1	37,0	36,8	36,4	35,6	34,0	49,4	49,2	49,1	48,3	47,5	45,0
	90				0,759	0,962	1,66				10,1	10,1	10,2				24,3	23,9	23,0				36,4	35,8	34,0				48,5	47,5	44,9
	180				0,878	1,10	1,79				10,2	10,2	10,3				24,5	24,1	23,2				36,5	35,9	34,1				48,6	47,6	45,1
40	0	0,564	0,522	0,542	0,664	1,05	2,55	8,30	8,25	8,23	8,25	8,44	9,40	20,0	20,0	19,9	19,7	19,6	19,8	30,0	29,9	29,8	29,6	29,2	28,8	40,1	39,9	39,7	39,3	38,8	37,7
	90				0,703	0,924	1,60				8,29	8,31	8,47				19,8	19,5	19,0				29,6	29,1	27,8				39,3	38,7	36,7
	180				0,924	1,22	1,98				8,51	8,61	8,84				20,0	19,9	19,3				29,8	29,4	28,2				39,6	39,0	37,1
60	0	0,448	0,438	0,504	0,776	1,53	4,38	5,38	5,44	5,48	5,68	6,32	8,86	13,0	13,0	13,0	13,1	13,5	15,6	19,4	19,4	19,4	19,3	19,7	21,3	25,9	25,9	25,7	25,7	25,8	27,1
	90				0,608	0,836	1,50				5,52	5,64	6,00				12,9	12,8	12,7				19,2	19,0	18,4				25,5	25,1	24,1
	180				0,836	1,20	2,06				5,75	6,00	6,55				13,1	13,2	13,2				19,4	19,3	19,0				25,7	25,4	24,8
80	0	0,388	0,438	0,612	1,16	2,47	8,32	1,89	1,93	2,11	2,63	3,90	9,64	4,17	4,20	4,36	4,85	6,07	11,7	6,12	6,13	6,29	6,76	7,92	13,4	8,06	8,04	8,21	8,65	9,77	15,1
	90				0,584	0,752	1,35				2,05	2,18	2,68				4,28	4,36	4,70				6,18	6,20	6,41				8,07	8,05	8,14
	180				0,707	0,990	1,84				2,17	2,42	3,18				4,39	4,66	5,20				6,30	6,44	6,9i				8,19	8,29	8,63

straight line. It is apparent from Fig. 8 that in almost all the cases the points do not lie on the straight line. At small I values (albedo of about 0.1), if the averaging over φ is not performed, the deviations reach 35% and about 10% at large I values (albedo of 0.8-1).

The degree of deviation from Lambert character depends only slightly on the sun's altitude in the range i = 20-60°. The deviation is small for a surface with a large albedo, since in this case the light of the haze plays a minor part as compared to the reflected flux.

For the Lambert straight line,

$$R = \pi I. \qquad (4.1)$$

Values of R deviating from πI by more than ±10% for $\theta \leqslant 60°$ are printed in bold face in Tables I-IV.

5. Cloudy Atmosphere. General Case

In the case of a cloudy atmosphere, the OSR field should be calculated for a continuous cloud cover located at an altitude of 4,000 m (this is the average altitude of the clouds for the entire globe). The calculations were made by using the same method and for the same parameter values as in the case of a cloudless atmosphere. For λ = 0.55 μ, the optical thickness of the above-cloud layer $\tau_1^\infty = 0{,}108$. In order to distinguish this case from the cloudless atmosphere, we shall designate the intensities and fluxes by I' and R'. The results of the calculations are shown in Tables 4 and 5.

All that has been stated in section 4 concerning the OSR field for a cloudless atmosphere also applies to a cloudy atmosphere. However, since the above-cloud layer is more transparent than the entire atmosphere, the OSR field in the case of a continuous cloud cover will be closer to an isotropic field.

We shall now consider the relation between brightnesses in the various directions and the field fluxes. Tables were compiled (analogous to the case of the cloudless atmosphere) relating I', A' and R' for given i values, θ, φ. They are given in the appendix (Tables V-VIII). The data for the angles θ 0 and 75° (averaged over φ) for all angles i are shown in Fig. 9.

Table 5

OSR Flux (R' cal/cm^2 min)

i°	A				
	0	0,2	0,5	0,75	1,0
20	0,0277	0,312	0,742	1,109	1,483
40	0,0280	0,258	0,607	0,899	1,201
60	0,0290	0,178	0,402	0,589	0,784
80	0,0335	0,0784	0,146	0,203	0,283

As is evident from Fig. 9, deviations from the Lambert line in the presence of clouds are smaller than in the case of a cloudless atmosphere. At all $i \leq 60^\circ$, the data fit satisfactorily on the Lambert straight line, while at $i = 80^\circ$ the deviation is considerably greater. We shall compare the observations of the OSR field for a cloudy and a cloudless case under identical conditions. At albedos close to 0,

$$I > I', \quad R > R'. \tag{5.1}$$

When the albedo increases, the inequalities are reversed. As in the case of the cloudless atmosphere, the dependence of I' and R' on the albedo are approximately linear. The data of Tables 4 and 5 together with the data of Tables 1 and 2 make it possible to calculate the OSR field for the case where the reflecting surface (cloud) is located at any intermediate height between z = 0 km and z = 4 km. For an intermediate height the data can be determined by interpolation.

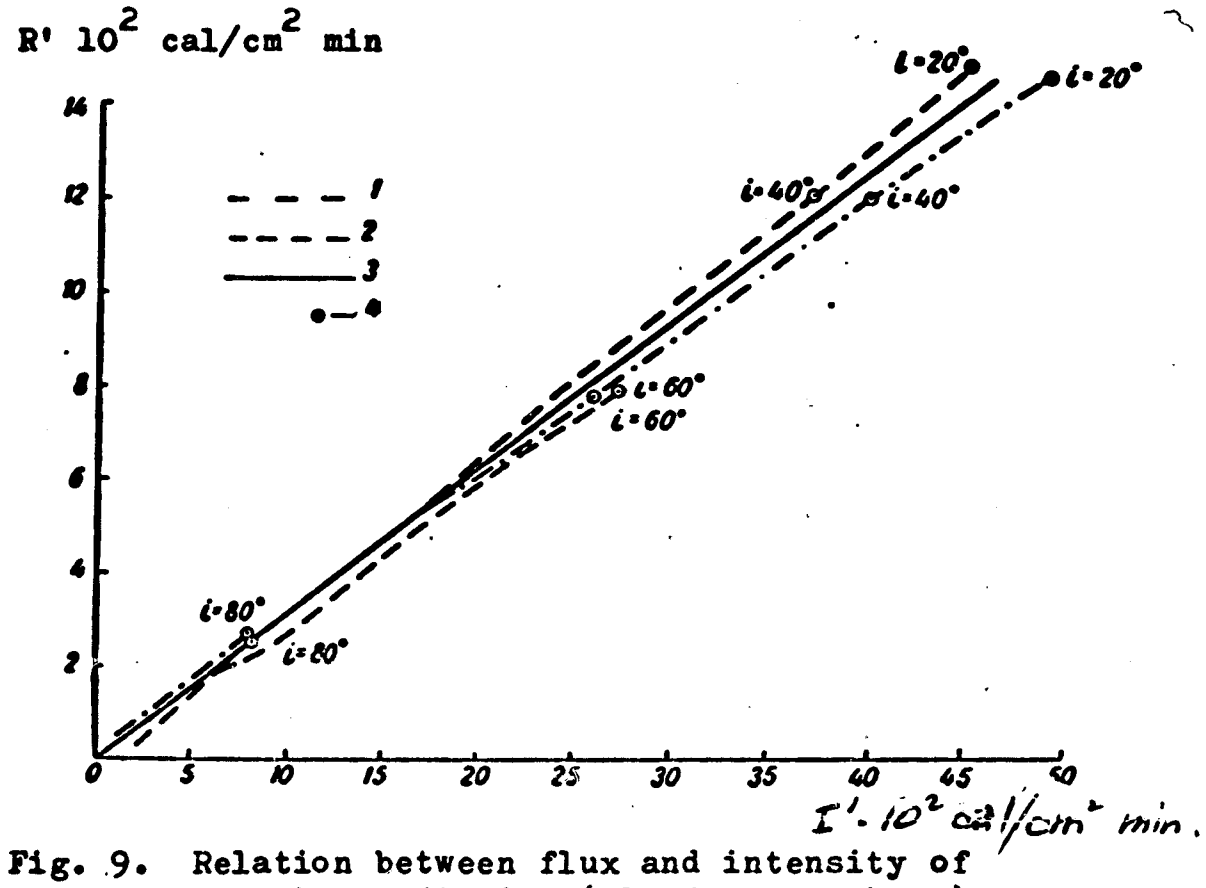

Fig. 9. Relation between flux and intensity of outgoing radiation (cloudy atmosphere). Arb. designations, see Fig. 8

In the presence of a continuous cloud, the conversion from the readings of the NSR to the fluxes may be accomplished by using tables relating I' and R' (see Tables V-VIII). These tables were based on the fact that the principal factor determining the fluxes in the case of cloudiness is the cloud thickness, or more accurately, the albedo of the cloud layer. The brightness of the above-cloud haze which is determined by the height of the upper boundary of the clouds and above-cloud aerosol is usually less than the reflected brightness. A correspondingly minor part is played by an exact knowledge of the height of the upper cloud boundary. For this reason, the calculations for the cloudy case were carried out for the climatological average of this parameter, 4 km, and for the above-cloud haze corresponding to the standard radiation model of the atmosphere.

Let us examine a general case where the earth's surface and a partly cloudy layer are sufficiently visible in the field of vision of the NSR.

Let η be the fraction of the field of vision occupied by the clouds; $\eta = 1$ corresponds to the case of complete masking, and $\eta = 0$ to the case of a cloudless sky. It is readily seen that in a stratified cloud which usually extends without breaks over great distances, the parameter η assumes mainly two values, 0 or 1. This is immediately apparent when one compares the area of a strip of width d (d being the diameter of the sighted spot) and of width $2\pi l$ (l is the radius of the zone occupied by the cloud) with a zone area (πl^2). The fraction of intermediate cases is obviously of the order of magnitude

$$\varepsilon = \frac{2\pi l d}{\pi l^2} = \frac{2d}{l}. \qquad (5.2)$$

When $l \sim 500$ km, ε will be about 15%. In this case, the two methods discussed above will make it possible to solve the problem. If the information available to us is insufficient for the choice of one or the other method, this may be done by using the data on the magnitude of the signal.

As a rule, the albedo of ground covers, A, satisfies the inequality $A \leq 30$, and usually for clouds, $A \geq 40$.

Using the table relating I and R, we arrive at the following values of the critical signals of the NSR (Table 6).

Table 6

i°	20	40	60
I_{cr}	13	10	7
I'_{cr}	19	16	11

If the measured signal satisfies one of the inequalities

$$I \leq I_{cr}, \qquad (5.3)$$

$$I \geq I'_{cr}, \qquad (5.4)$$

we can confidently conclude that the case (5.3) involves sighting a ground cover and case (5.4) involves clouds or snow. If the signal is

intermediate

$$I_{cr} < I < I'_{cr} \qquad (5.5)$$

this may be either dirty snow or ice, or a case where $\eta \neq 1$. If the available information is insufficient, it is impossible to distinguish these signals (by the magnitude of the signal alone).

It is significant, however, that in the solution of the problem with which we are faced, the impossibility of differentiating these cases does not affect the conversion method. In the range of angles which we have examined, the Lambert character of the OSR field for a cloudless and a cloudy atmosphere at moderate and high albedos is approximately the same. For this reason, the conversion from the signal to the flux may be accomplished by any method. We shall illustrate this with Table 7, which shows the OSR fluxes corresponding to NSR signals obtained from a treatment by the cloudless method, R, and the cloudy method, R', as well as the values of the albedo A and A'.

Table 7

$i = 60^\circ$, $\varphi = 90^\circ$

$I - I'$	$\theta = 45^\circ$				$\theta = 60^\circ$			
	A	A'	R	R'	A	A'	R	R'
4	13	13	14,4	12,5	10,5	13	13	12,5
10	45,5	37,5	31,8	31,0	49,0	38	32,8	31,5
18	86	70	56	58	87	71	55,4	56,0

We see that with the exception of the case involving small albedos, the fluxes obtained by the two methods agree within 3%. Hence, the treatments should be carried out by using the cloudless method (Tables I-IV), which thus insures an accuracy of the order of 3% for any A. It is significant that we do not have to know the value of the filling parameter η.

6. Use of the data of a wide-sector receiver

In [1] we used the structure of a WSR signal and showed that it is formed by averaging over a large surface and a wide range of angles θ and φ. Therefore, the system earth-atmosphere may be considered a Lambertian system without much error, and the average (based on the sighted region) albedo of the E—A system may be calculated from the formula

$$A_{E-A} = \frac{\pi \Phi^*}{S_0} \frac{1}{\int_{\omega} \cos i \cos \gamma \, d\omega}. \tag{6.1}$$

Here Φ^* is the system measured by the WSR (see [ ]). In order to calculate the integral in the denominator of (6.1), it is sufficient to know the sun's altitude i_0 relative to an oriented satellite (sun's altitude at the point below the satellite on earth). The sun's altitude i for the section of the earth's surface visible from the satellite at angles γ and μ will be

$$\cos i = \frac{-l \sin i_0 \sin \gamma \cos \mu + (R - l \cos \gamma) \cos i_0}{r}. \tag{6.2}$$

The integral in (6.1)

$$\int_0^{2\pi} d\mu \int_0^{\gamma_0} \cos i \cos \gamma \sin \gamma \, d\gamma \tag{6.3}$$

is determined numerically from the geometrical characteristics of the AES.

When $i_0 = 0$ (this variant was discussed in [1]), angle i changed from 0 to 25°, and correspondingly cos i changed from 1 to 0.91. If we assume for approximation that $i \approx i_0$ over the entire region, the integral (6.1) will be ($\gamma_0 = 65°$)

$$\cos i_0 \int \cos \gamma \, d\omega = 2{,}57 \cos i_0 \text{ ster}. \tag{6.4}$$

and

$$A_{E-A} = 1{,}22 \frac{\Phi^*}{S_0 \cos i_0}. \tag{6.5}$$

Let us note that this formula corresponds exactly to the one which results from the assumption that the flux of outgoing radiation (radiation vector) is directed along a radius from the center of the earth. Indeed, in this case the flux R of outgoing radiation at level H_0 (upper boundary of the atmosphere) is obviously related to the flux at level H by the relation

$$\frac{R(H)}{R(H_0)} = \frac{(H_0+r)^2}{(H+r)^2}, \quad R(H) \equiv \Phi^*. \tag{6.6}$$

It is evident that

$$R(H_0) = A_{E-A} E = A_{3-A} S_0 \cos i. \tag{6.7}$$

Hence

$$A_{E-A} = \frac{\Phi^*}{S_0 \cos i_0} \left(\frac{H+r}{H_0+r}\right)^2. \tag{6.8}$$

Substituting H = 700 km and H_0 = 30 km, we find

$$\left(\frac{H+r}{H_0+r}\right)^2 = 1{,}22,$$

i.e., the formula (6.5).

Thus, the data from the WSR make it possible to determine the average value of the OSR field and A_{E-A} for the entire region sighted. These quantities are of interest for a macro description of the brightness field of the earth in connection with the problems of radiation climatology for various problems of physics of the earth as a planet, etc.

The conversion from a WSR reading to R is given by relation (6.6)

$$R = 1{,}22\,\Phi^*. \tag{6.9}$$

It can be calculated more accurately from the formula

$$R = \frac{\pi \cos i}{\int_{\Omega} \cos i \cos \gamma \, d\omega} \Phi^* \equiv c\Phi^*, \tag{6.10}$$

where the integral in the denominator is calculated from the geometry and kinematics of the AES using (6.2). Tables of values of c should be

compiled for specific launchings and situations.

7. Albedo of the earth—atmosphere system. Balance of the short-wave radiation of the atmosphere.

Using Table 2, one can readily obtain the values of the albedo of the earth—atmosphere system for a cloudless atmosphere (Table 8).

Table 8

Albedo of Earth—Atmosphere System

l°	A				
	0	0,2	0,5	∞	1,0
0	0,0414	0,185	0,401	0,582	0,762
20	0,0441	0,187	0,403	0,582	0,762
40	0,0540	0,195	0,403	0,582	0,758
60	0,0828	0,216	0,416	0,583	0,749
80	0,238	0,331	0,470	0,585	0,701

We shall derive the formula for the albedo A_{E-A}. To do so, we shall note that the following simple relation exists between the OSR flux (in the range $0.4 \leq \lambda \leq 2.5\ \mu$), the zenithal distance of the sun i and the albedo of the earth's surface A:

$$R = [0,07 + 1,31\,(\cos l - 0,07)\,A] \quad \text{cal/cm}^2 \text{ min} \tag{7.1}$$

This formula gives R for all $0 \leq i \leq 80^\circ$ within 5%. Hence, we find the formula for the albedo[1] of the system earth—atmosphere

$$A_{3-A} = \frac{0,07}{1,69}\sec l + \frac{1,31}{1,69}(1 - 0,07\sec l)\,A. \tag{7.2}$$

To an approximation, this formula will apply for the albedo of the E—A system over the entire short-wave range

$$A_{3-A} = 0,041\sec l + 0,78(1 - 0,07\sec l)\,A. \tag{7.3}$$

---

1. Let us note that our calculations are restricted by the "pyranometric" range $\lambda = 0,4—2.5\ \mu$. In this range, the solar constant S_0 is equal to 1.69 cal/cm^2 min.

When $i = 60^\circ$ we have, for example,

$$A_{E-A} = 0{,}08 + 0{,}67A. \qquad (7.4)$$

We shall estimate the influence of absorption in the atmosphere on the albedo of the earth—atmosphere system. If the absorption of short-wave radiation in air is not taken into account, we obviously have the following relation for A_{E-A}

$$S_0 \cos i (1 - A_{E-A}) = E(1 - A). \qquad (7.5)$$

Here S_0 is the solar constant. On the left is the quantity of solar radiation absorbed by the earth—atmosphere system, and on the right, the quantity of radiation absorbed by the earth's surface. Thus, it is assumed that the process of absorption takes place only on the earth's surface. From formula (7.5) it follows that

$$A_{E-A} = 1 - \frac{E(1-A)}{S_0 \cos i}. \qquad (7.6)$$

In [4], the following expression was obtained for the illumination on the earth's surface:

$$E = I_0(\lambda) B^*(\tau_0, i, A).$$

Hence, for a standard atmosphere we obtain

$$A_{E-A} = 1 - (1 - A)\frac{B^*}{\cos i}. \qquad (7.7)$$

Let us compare the data of Table 8 with the result given by formula (7.7). We shall consider the case where $i = 40^\circ$.

Table 9

	A			
	0	0,1	0,5	1
Table 8	0,054	0,12	0,41	0,76
Formula (7.7) . .	0,100	0,18	0,52	1,00
Δ %	85	50	27	32

The data of Table 9 show that a disregard of absorption is too rough an approximation: the errors in the calculation of the albedo of the earth—atmosphere system turn out to be very large. For the earth, they are on the average of the order of 45%. The short-wave radiation balance for a cloudless atmosphere is given by the formula

$$B = (F—R) - E(1—A) = F(1—A_{E—A}) - E(1—A). \qquad (7.8)$$

Here $F = 1.69 \cos i$ cal/cm^2 min is the flux of short-wave radiation at the upper boundary of the atmosphere.

As an illustration, we shall assume that at $i=60°, \Theta=45°, \varphi=90°$, the deviation on the NSR scale was found to be 0.052 cal/cm^2 min ster.

Using the appendices of Table III, we find A = 0.2, and from Tables 2 and 3 we get R = 0.18 cal/cm^2 min, E = 0.67 cal/cm^2 min.

Thus, for the balance of short-wave radiation of an atmospheric column 1 cm^2 in cross-section, we have, based on (7.8),

$$B = (0.85—0.18) — 0.67(1—0.2) = 0.134 \text{ cal/cm}^2 \text{ min} = 5.46 \text{ cal/cm}^2 \text{ hr}.$$

This value represents 16% of the incident flux F. This figure agrees with the experimental data on the short-wave radiation balance. For example, according to the measurements of N. P. Pyatovskaya for an atmospheric layer 0—3 km thick, the value of B amounted to an annual average of 0.135 cal/cm^2 min ([7], p. 141). If it assumed that all this heat was used to heat an atmospheric column, then $\frac{dT}{dt} = 0.034$ deg/hr.

In the case of a cloudy atmosphere, we have the same formula (7.8) for the calculation of B. The main difficulty here is the determination of the total radiation on the earth. We can indicate the following method of solving this problem:

1) From the NSR data we find the albedo of the clouds (using Tables V—VIII) and $A_{E—A}$;

2) We find the total radiation on the earth by using the statistical relationships between the albedo of the clouds and E;

3) Based on the albedo charts of the earth's surface, or else in a completely approximate manner by taking A = 8% for the sea and A = 20% for land, we find B from (7.8).

Needless to say, the accuracy of this method is low. However, in the case of a cloudy sky, the data on the albedo which we obtain from an AES constitute utterly insufficient information for a more precise solution of the problem of determining the short-wave radiation balance. It should be added that by using a complete picture of the data from the AES, for example, data on the albedo of a surface in the absence of cloudiness (during the previous orbit), we can eliminate the error involved in the use of albedo charts. Having accumulated material from systematic airplane (or probe) measurements of the albedo and transparency of clouds, one can refine the relations between E and A and hence improve the method of calculating B from the NSR data. The precision of the determination of B can of course be improved if the program of radiation measurements with AES is expanded.

8. Conclusion

The method developed above makes it possible to determine an OSR flux from the readings of an NSR aboard an AES and from the known geometrical characteristics i, ϑ, φ. It is assumed that no other information on the nature of the sighted area is available. The method is very simple and makes it possible to treat a large mass of data in an operative manner. The method may be improved if some specific properties of the sighted area are considered, such as the non-Lambertian character of the earth's surface. This improvement involves a considerable complication of the calculations.

For a cloudless atmosphere, the method which we have developed makes it possible to determine in an operative manner the radiation balance of the atmosphere. For a cloudy atmosphere this cannot be done on the basis of the AES data alone. Simultaneous measurements on the earth's surface are also necessary.

APPENDIX

Table 1

Relation between Brightness of OSR Field and Flux (cloudless atmosphere)

$i = 20^{\circ}$

l	θ°													l
	0	15		30	45	60	75	0	15		30	45	60	75	
	φ°														
	0—180	0—90	135—180	0—180	0—180	0—180	0—180	0—180	0—90	135—180	0—180	0—180	0—180	0—180	
	A %							R							
0	—	—	—	—	—	—	—	—	—	—	—	—	—	—	0
1	—	—	—	—	—	—	—	—	—	—	—	—	—	—	3,14
2	1,0	1,0	0,4	—	—	—	—	8,0	8,0	7,6	—	—	—	—	6,28
3	3,5	3,5	3,0	2,5	2,0	1,0	—	11,0	11,0	10,5	8,8	9,2	7,6	—	9,42
4	6,0	6,2	5,5	5,0	5,0	4,0	—	14,0	14,2	13,2	12,4	12,4	11,6	—	12,56
5	8,5	8,5	8,2	8,0	7,5	7,0	4,0	16,4	16,4	16,0	16,0	15,2	14,8	11,6	15,70
6	11,0	11,2	10,8	10,5	10,5	10,0	7,5	19,1	19,1	19,2	18,6	18,6	18,0	15,2	18,84
7	13,5	14,0	13,0	13,5	13,5	13,0	11,0	22,0	22,4	21,2	22,0	22,0	21,2	19,2	21,98
8	16,0	16,5	16,3	16,0	16,0	16,0	14,0	24,8	25,4	25,2	24,8	24,8	24,8	22,4	25,12
9	19,0	19,2	18,8	18,5	19,0	19,0	18,0	28,0	28,0	29,2	27,6	28,0	28,0	27,0	28,26
10	21,0	21,5	21,2	21,0	21,5	22,0	21,5	30,4	30,8	30,4	30,4	30,8	31,4	30,8	31,40
11	23,5	24,2	23,7	24,0	24,5	25,0	25,0	33,6	33,6	33,6	33,6	34,0	34,8	34,8	34,54
12	26,0	26,8	26,3	26,0	26,5	27,5	28,0	36,0	37,5	36,0	36,0	36,4	37,6	33,0	37,68
13	28,5	29,0	28,4	28,0	29,5	30,0	32,0	39,2	38,2	39,2	38,0	39,6	40,4	42,2	40,82
14	31,0	31,5	31,0	31,0	31,5	33,0	35,0	41,0	42,0	41,0	41,0	42,0	43,8	46,0	43,96
15	33,5	34,0	33,6	34,0	34,0	36,0	38,5	44,8	44,8	44,8	44,8	44,8	47,2	50,0	47,10
16	36,0	36,5	36,0	36,0	36,5	39,0	42,0	47,2	47,8	47,2	47,2	47,6	50,4	54,0	50,24

30
59

17	38,5	38,8	38,4	39,0	39,0	41,5	45,0	50,0	50,4	50,4	50,4	50,4	53,2	59,2	53,38
18	41,0	41,2	40,8	41,5	42,0	44,5	48,5	52,8	52,8	52,8	53,2	54,0	56,8	61,2	55,52
19	43,5	43,6	43,3	44,0	44,5	47,5	51,5	55,6	55,6	54,8	56,0	56,8	60,0	64,8	59,63
20	46,0	46,2	45,8	46,5	46,5	50,0	54,5	58,4	58,4	58,4	58,8	59,8	63,0	68,2	62,60
21	48,5	48,7	48,2	49,0	49,0	52,5	57,5	61,2	62,0	62,0	62,0	62,0	66,0	72,2	65,94
22	50,5	51,3	50,8	51,5	52,0	55,0	60,0	63,6	64,8	64,0	64,8	65,2	68,2	73,2	69,08
23	53,0	53,2	53,0	53,5	54,5	58,0	63,0	66,8	66,8	66,8	67,2	68,4	72,8	78,8	72,22
24	55,0	56,0	56,5	56,0	57,0	60,5	66,0	68,2	70,4	70,0	70,4	71,6	76,0	82,4	75,36
25	57,5	58,3	57,8	58,5	60,0	63,0	69,0	72,2	73,2	73,0	73,2	73,2	78,8	87,6	78,50
26	60,0	60,5	60,0	61,0	62,0	66,0	71,5	73,2	78,0	73,2	76,4	79,6	82,4	89,2	81,64
27	62,5	63,0	62,6	63,0	65,0	68,5	75,0	77,0	78,8	76,6	78,8	81,5	85,6	94,0	84,78
28	65,0	65,5	64,5	65,5	67,0	71,5	78,0	81,5	82,0	80,4	82,0	84,0	89,2	98,0	87,92
29	67,0	67,9	67,3	68,0	69,5	74,0	82,0	84,0	85,2	84,0	85,2	86,0	90,0	102,0	91,56
30	69,5	70,0	69,5	70,0	72,0	76,5	85,0	86,0	88,6	86,0	88,6	88,8	94,8	107,2	94,20
31	72,0	72,5	71,8	72,5	74,5	79,0	88,5	88,8	90,6	90,6	90,6	93,2	99,2	112,0	97,34
32	74,0	75,0	74,3	75,0	77,0	81,5	92,0	90,0	94,0	92,8	94,0	98,4	102,8	115,6	100,48
33	76,5	77,0	76,4	77,5	79,0	84,0	95,0	94,8	98,4	96,0	98,8	99,2	105,0	120,0	103,62
34	78,5	79,0	78,6	79,5	81,5	86,5	98,5	98,4	99,2	99,2	100,0	102,8	109,2	124,2	106,76
35	80,5	81,4	80,6	82,0	84,0	89,0	—	101,2	102,8	101,2	102,0	106,0	112,4	—	109,90
36	83,0	83,8	83,0	84,0	86,0	91,5	—	104,4	106,0	104,4	106,0	108,4	114,6	—	113,04
37	85,0	85,8	85,4	86,0	88,5	94,0	—	107,2	108,4	108,0	108,4	112,0	116,0	—	116,18
38	87,5	88,0	87,5	88,5	91,0	96,5	—	110,4	111,2	110,4	112,0	116,4	120,6	—	119,32
39	89,5	90,3	90,0	91,0	93,0	99,0	—	113,0	114,0	113,4	116,4	117,0	125,0	—	122,46
40	91,2	92,6	92,0	93,0	95,5	—	—	114,6	117,2	115,6	117,0	120,0	—	—	125,60
41	94,0	94,9	94,0	95,5	98,0	—	—	116,0	120,0	116,0	120,0	124,0	—	—	128,74
42	96,0	97,1	96,3	100,0	100,0	—	—	120,6	121,6	120,6	125,8	125,8	—	—	131,88
43	98,0	99,0	98,6	—	—	—	—	124,0	125,0	125,0	—	—	—	—	135,02
44	100,0	—	—	—	—	—	—	125,8	—	—	—	—	—	—	138,16

Table II

Relation between Brightness of OSR Field, Albedo, and Flux (cloudless atmosphere)

$i = 40^\circ$

I	θ°																					
	0	15	30	45		60	75					0	15	30	45		60	75				
	p°																					
	0—180	0—180	0—180	0—90	135—180	0—180	0	45	90	135	180	0—180	0—180	0—180	0—90	135—180	0—180	0	45	90	135	180
	A %											R										
0	—	—	—	—	—	—	—	—	—	—	—	—	—	—	—	—	—	—	—	—	—	—
1	—	—	—	—	—	—	—	—	—	—	—	—	—	—	—	—	—	—	—	—	—	—
2	1,5	1,2	0,5	0,5	—	—	—	—	—	—	—	8,5	8,0	7,0	7,0	—	—	—	—	—	—	—
3	5,0	4,5	4	4,0	1,0	0,5	—	—	—	—	—	11,8	11,0	10,8	10,8	8,0	7,0	—	—	—	—	—
4	8,5	8,0	7,5	7,5	5,0	4,5	—	—	1,0	—	—	14,4	14,0	13,8	13,8	11,8	11,0	—	—	8,0	—	—
5	11,5	11,0	10,5	10,5	9,0	8,0	—	1,5	6,5	5,0	3,0	17,0	16,8	16,4	16,4	15,0	14,0	—	8,5	12,6	11,6	10,0
6	15,0	14,0	14,0	14,5	12,0	12,0	0,5	7,0	12,5	10,0	9,0	20,0	19,0	19,0	19,4	17,6	17,6	7,0	13,0	18,0	16,0	15,0
7	18,0	17,5	17,5	17,5	15,5	15,5	6,5	12,5	17,5	16,0	14,5	22,4	22,0	22,0	22,0	20,4	20,4	12,6	18,0	22,0	21,0	19,4
8	21,5	20,8	21,0	21,0	19,0	19,5	12,5	18,5	23,5	21,0	20,0	25,0	24,4	24,4	24,4	23,0	23,4	18,0	23,0	27,4	24,4	24,0
9	24,5	24,0	24,0	24,5	22,5	23,0	14,5	23,5	28,5	26,5	25,5	28,0	27,4	27,4	28,0	26,4	26,8	19,4	27,4	31,6	30,0	29,0
10	27,5	27,0	27,5	27,5	26,0	27,0	23,5	28,5	33,0	31,5	30,0	30,8	30,4	30,8	30,8	29,0	30,4	27,4	31,6	35,8	34,0	32,8
11	30,5	30,3	31,0	31,0	28,0	30,5	29,0	33,5	37,5	36,0	35,0	33,4	32,8	34,0	34,0	31,0	33,4	32,0	36,4	39,4	38,0	37,6
12	33,5	33,4	34,0	34,5	32,5	34,5	33,5	38,5	42,5	41,0	39,0	36,0	36,0	36,4	36,8	34,8	36,8	36,0	40,4	44,0	42,4	40,8
13	37,0	36,8	37,0	37,5	36,0	36,0	37,5	43,5	48,0	46,0	43,5	38,8	38,8	38,8	39,4	38,0	38,0	39,4	44,4	48,4	46,4	44,4

14	40,0	39,8	40,0	41,0	39,0	42,5	42,5	48,5	52,0	50,0	48,5	41,8	41,8	41,8	42,4	40,8	44,0	44,0	48,8	52,4	50,0	46,8
15	43,0	43,0	41,0	44,5	42,5	46,0	47,0	52,5	56,0	54,5	52,5	44,4	44,4	42,4	45,4	44,0	46,4	47,8	52,8	55,0	54,4	52,8
16	45,5	46,0	47,0	47,5	46,0	50,0	51,0	56,5	60,0	59,0	57,0	46,8	46,4	47,8	48,0	46,4	50,0	51,0	56,4	59,5	59,0	56,8
17	49,5	49,4	50,0	51,0	48,0	53,0	55,0	60,5	64,0	62,5	61,5	49,8	49,6	50,0	51,0	48,8	53,0	55,0	60,0	63,0	62,0	61,0
18	52,5	52,3	53,0	54,5	52,5	56,5	59,0	64,0	67,5	66,5	65,5	52,8	52,4	53,0	54,4	52,8	56,4	59,0	63,0	66,8	66,5	64,8
19	55,5	55,2	56,0	57,5	55,5	60,0	63,0	68,0	72,0	70,5	70,0	55,6	55,0	56,0	57,0	55,6	59,5	62,4	67,8	71,4	69,6	69,0
20	58,0	57,9	58,5	61,0	59,0	63,0	67,0	72,0	76,0	75,0	73,5	58,0	58,0	58,4	60,8	59,0	62,4	67,4	71,4	74,8	74,0	72,6
21	61,0	61,2	61,5	64,0	62,5	66,0	71,0	75,5	79,0	77,5	77,0	60,8	60,8	61,0	63,0	62,0	65,4	70,0	74,4	78,0	78,4	76,0
22	64,0	63,7	64,0	67,5	65,5	69,0	75,0	79,0	82,5	81,0	80,0	63,0	63,0	63,0	66,8	64,8	68,4	74,0	78,0	81,8	80,0	79,4
23	66,5	66,7	65,0	70,5	68,0	72,5	78,5	82,0	85,5	84,5	83,5	66,5	67,4	64,0	69,6	67,8	71,8	77,6	81,0	84,4	83,8	82,8
24	69,5	69,6	70,5	74,0	72,5	76,0	82,0	85,5	89,0	87,5	85,5	68,8	69,0	69,6	73,4	71,8	74,8	81,0	84,4	88,4	87,6	84,4
25	72,0	72,5	73,5	77,0	75,0	79,5	85,0	89,0	92,0	91,0	90,0	71,4	71,8	72,6	76,0	74,0	78,6	84,0	88,4	91,6	90,4	89,0
26	75,0	76,7	76,0	80,0	78,0	83,0	88,5	92,0	95,5	94,5	93,5	74,0	76,0	74,8	79,4	77,4	82,4	88,0	91,6	94,8	94,0	92,8
27	78,0	78,5	78,5	82,5	81,0	87,0	92,0	95,5	98,5	97,0	96,5	77,4	77,6	77,6	81,8	80,0	87,0	91,6	94,8	98,4	96,8	95,8
28	80,5	81,4	81,5	85,5	84,0	90,5	95,0	98,5	—	—	100,0	79,6	80,0	80,8	84,4	83,6	90,0	94,6	98,4	—	—	99,0
29	83,5	84,1	84,5	89,0	86,5	94,0	98,5	—	—	—	—	82,8	83,6	83,8	88,4	85,8	93,4	98,4	—	—	—	—
30	86,0	86,7	87,5	91,0	89,5	97,5	—	—	—	—	—	85,0	87,0	87,6	90,4	88,8	97,6	—	—	—	—	—
31	89,0	89,5	90,0	93,5	92,0	—	—	—	—	—	—	88,4	88,8	89,0	92,8	91,6	—	—	—	—	—	—
32	92,0	92,3	93,0	96,5	95,0	—	—	—	—	—	—	91,6	91,6	92,4	95,8	94,6	—	—	—	—	—	—
33	94,5	95,1	96,0	99,5	97,5	—	—	—	—	—	—	94,0	94,6	95,4	98,8	97,6	—	—	—	—	—	—
34	97,0	97,8	98,5	—	100,0	—	—	—	—	—	—	96,8	98,0	98,4	—	99,0	—	—	—	—	—	—
35	100,0	—	—	—	—	—	—	—	—	—	—	99,0	—	—	—	—	—	—	—	—	—	—

Table III

Relation between Brightness of OSR Field, Albedo, and Flux (cloudless atmosphere)

$i = 60^\circ$

I	Θ°																			
	0	15	30	45		60					0	15	30	45		60				
	φ°																			
	0—180	0—180	0—180	0,180	45,90, 135	0	45	90	135	180	0—180	0—180	0—180	0,180	45,90, 135	0	45	90	135	180
	A %										R									
0	—	—	—	—	—	—	—	—	—	—	—	—	—	—	—	—	—	—	—	—
1	—	—	—	—	—	—	—	—	—	—	—	—	—	—	—	—	—	—	—	—
2	4,0	3,5	2,5	—	2,0	—	—	—	—	—	—	—	—	—	—	—	—	—	—	—
3	9,0	9,0	8,0	4,5	7,5	—	1,0	4,5	2,5	—	9,4	9,4	9,0	—	8,8	—	—	—	—	—
4	14,5	14,5	14,0	10,0	13,0	1,0	7,0	10,5	9,0	5,5	12,0	12,0	11,6	9,8	11,4	—	8,4	9,8	9,0	—
5	19,5	20,0	19,5	16,0	19,0	7,5	13,5	17,0	15,0	12,0	15,4	15,4	15,0	12,8	14,4	8,4	11,0	13,0	12,0	10,0
6	24,0	25,0	25,0	21,5	24,5	13,5	20,0	23,5	21,5	18,0	18,0	18,0	18,0	16,0	17,6	11,4	14,8	16,6	15,8	13,8
7	29,0	30,5	30,0	27,0	30,0	20,0	26,0	30,0	26,5	25,0	20,0	20,8	20,8	18,8	20,4	14,8	18,4	19,6	18,8	17,0
8	34,0	35,5	35,0	32,5	35,5	26,5	32,5	36,5	34,5	31,0	22,4	23,4	23,0	21,4	23,0	18,4	21,0	23,0	21,4	20,3
9	38,5	41,0	40,5	35,0	41,0	33,0	39,0	42,5	41,0	38,0	25,0	26,0	25,8	24,0	26,0	21,4	24,0	26,4	25,4	23,6
10	43,5	46,0	46,0	40,5	46,5	39,0	45,5	49,0	47,5	44,0	27,6	28,8	28,4	25,6	28,8	24,4	27,6	29,4	28,8	27,0
11	48,0	51,0	51,0	43,5	52,0	46,0	51,5	54,5	53,0	50,5	30,0	31,4	31,4	28,4	31,8	27,6	30,8	32,8	32,0	29,0
12	53,0	56,0	55,0	49,0	56,5	52,0	57,0	60,0	58,0	55,5	32,0	34,0	34,0	30,2	34,6	31,4	34,4	36,0	35,4	33,6
13	58,0	60,0	60,0	54,0	61,5	57,0	62,0	64,5	63,0	60,5	35,4	36,8	36,4	32,8	37,0	34,6	38,0	39,8	38,4	35,8
14	63,0	65,0	64,5	59,0	66,5	61,5	66,0	69,0	67,5	65,0	38,4	39,8	39,8	35,8	40,8	38,0	41,0	42,8	41,6	40,0
15	67,5	69,0	69,0	63,5	71,0	66,0	70,0	72,5	71,0	69,0	41,6	43,0	42,8	39,0	44,0	40,4	43,8	46,0	44,8	43,0
16	72,5	73,5	73,5	68,5	76,0	70,5	74,0	76,5	75,0	73,0	44,8	46,0	46,0	42,0	47,0	43,8	46,4	48,0	47,0	46,0
17	77,5	78,5	78,0	73,0	81,0	75,0	79,0	81,5	80,0	78,0	48,0	48,8	48,8	45,0	50,4	46,6	49,0	50,8	50,0	48,4
18	82,0	83,0	83,0	78,0	86,0	79,0	84,5	87,0	85,5	83,0	51,2	52,0	51,6	48,0	53,0	50,0	52,2	53,4	52,8	51,6
19	87,0	88,0	88,0	83,0	91,0	84,5	89,5	92,5	90,5	88,0	53,8	54,4	54,4	50,0	56,0	52,2	55,0	56,4	55,8	54,4
20	92,0	92,5	93,0	87,5	96,0	90,0	95,0	98,0	96,5	93,5	56,4	56,8	56,8	53,0	58,2	55,0	57,8	59,0	58,0	56,8
21	96,5	97,5	97,5	92,5	100	96,0	—	—	—	100	58,8	59,0	59,6	56,0	60,8	58,0	60,4	62,0	61,0	59,8
22	—	—	—	97,5		—					61,0	61,8	61,8	58,0	63,0	60,8	—	—	—	63,0
23				100							—	—	—	61,8	—	—				
														63,0						

34
63

Table IV

Relation between Brightness of OSR Field, Albedo, and Flux (cloudless atmosphere)

$i = 80^\circ$

I	θ°													θ°											
	0	15	30		45			60			75			0	15	30		45			60			75		
	φ°													φ°											
	0—180	0—180	0	90—180	0	90	180	0	90	180	0	90	180	0—180	0—180	0	90—180	0	90	180	0	90	180	0	90	180
	A %													R											
0	—	—	—	—	—	—	—	—	—	—	—	—	—	—												
1	7,5	4,0	—	2,0	—	—	—	—	—	—	—	—	—	6,4	6,1	—	5,8	—								
2	30	24,0	17,5	22,5	—	23,0	18,5	—	17,5	8,0	—	—	—	9,6	8,8	7,6	8,5	—	8,6	7,8	—	7,6	6,6	—	—	—
3	45,5	44,0	37,5	42,5	23,5	43,0	39,5	—	38,0	30,0	—	18,5	—	11,9	11,6	10,8	11,4	8,8	11,4	11,0	—	10,9	9,6	—	7,8	—
4	63	63,0	57,0	61,0	43,5	62,5	59,0	5,0	59,0	52,5	—	44,0	25,0	14,4	14,4	13,6	14,2	11,6	14,3	13,9	6,1	13,9	12,8	—	11,6	8,9
5	82	81,0	76,5	80,5	63,0	81,5	78,5	27,0	81,0	73,0	—	69,0	52,5	17,3	17,2	16,6	17,1	14,4	17,2	16,8	9,2	17,2	15,0	—	15,5	12,8
6	100	98,0	94,0	98,0	82,5	99,0	96,0	48,0	100	90	—	—	82,5	19,9	19,6	19,2	19,6	17,4	19,8	19,4	12,2	19,9	18,5	—	—	17,4
7	—	—	—	—	100	—	—	70	—	—	—	—	—	—	—	—	—	19,9	—	—	15,6	—	—	—	—	—
8	—	—	—	—	—	—	—	91,5	—	—	—	—	—	—	—	—	—	—	—	—	18,7	—	—	—	—	—
9	—	—	—	—	—	—	—	—	—	—	—	—	—	—	—	—	—	—	—	—	—	—	—	—	—	—
10	—	—	—	—	—	—	—	—	—	—	—	—	—	—	—	—	—	—	—	—	—	—	—	—	—	—
11											75,0													16,2		

Table V

Relation between Brightness of OSR Field, Albedo, and Flux
(cloudy atmosphere)

$i = 20^\circ$

I'	θ°											
	0	15	30	45	60	75	0	15	30	45	60	75
	φ°											
	0—180						0—180					
	A' %						R'					
0	—	—	—	—	—	—	—	—	—	—	—	—
1	0,9	1,0	1,0	0,5	—	—	3,5	3,5	3,5	3,0	—	—
2	3,0	3,0	3,1	2,5	2,1	0,7	6,5	6,5	6,5	6,0	5,0	3,5
3	5,0	5,1	5,2	5,0	4,3	3,0	9,5	9,5	9,5	9,5	8,0	6,5
4	7,1	7,1	7,3	7,0	6,4	5,3	12,5	12,5	12,5	12,5	12,0	9,5
5	9,1	9,2	9,4	9,0	8,6	7,6	15,0	15,0	16,0	15,0	14,5	13,0
6	11,2	11,2	11,5	12,0	10,7	10,0	18,0	18,0	19,0	19,5	18,0	17,0
7	13,2	13,3	13,6	13,5	12,9	12,2	21,0	21,0	21,5	21,5	21,0	19,5
8	15,3	15,4	15,8	15,5	15,0	14,8	24,0	24,5	25,0	24,5	24,0	24,0
9	17,4	17,5	17,9	17,5	17,2	17,2	27,5	27,5	28,0	27,5	27,0	27,0
10	19,5	19,6	20,0	20,0	19,3	19,5	30,0	30,0	31,5	31,5	29,5	30,0
11	21,6	21,7	22,1	22,0	21,5	21,8	32,0	32,0	32,5	32,5	32,0	32,5
12	23,0	23,8	24,2	24,0	23,6	24,1	36,0	36,5	36,5	36,5	36,0	36,5
13	25,7	25,8	26,3	26,0	25,3	26,4	40,0	40,0	40,0	40,0	40,0	40,0
14	27,8	27,9	28,4	28,0	27,9	28,7	42,5	42,5	42,5	42,5	42,5	44,0
15	29,9	30,0	30,5	30,0	30,1	31,0	45,5	45,5	46,0	45,5	45,5	47,0
16	31,0	32,1	32,6	32,5	32,2	33,4	47,0	48,0	50,0	49,0	48,0	50,0
17	34,2	34,2	34,7	34,5	34,4	35,8	51,5	51,5	52,5	52,0	51,5	54,0
18	36,3	36,3	36,8	36,5	36,5	38,2	54,0	54,0	55,5	55,0	55,0	57,0
19	38,4	38,4	38,9	38,5	38,7	40,6	57,0	57,0	58,5	57,5	58,5	61,0
20	40,5	40,5	41,0	41,0	40,8	43,0	60,5	60,5	61,0	61,0	61,0	64,0
21	42,6	42,5	43,1	43,0	43,0	45,3	64,0	63,5	64,0	64,0	64,0	67,0
22	44,7	44,6	45,2	45,0	45,1	47,7	67,0	67,0	67,0	67,0	67,0	71,0
23	46,8	46,6	47,3	47,0	47,3	50,0	69,5	69,5	69,5	69,5	69,5	74,0
24	48,9	48,7	49,4	49,0	49,4	52,4	73,0	73,0	73,0	73,0	73,0	77,0
25	51,0	50,7	51,5	51,5	51,6	54,7	75,5	75,5	76,5	76,5	76,5	82,0
26	53,1	52,8	53,5	53,5	53,7	57,0	78,5	78,5	79,5	79,5	80,0	84,5
27	55,1	54,8	55,5	55,5	55,9	59,3	81,5	81,5	82,0	82,0	83,0	87,5
28	57,2	56,9	57,5	57,5	58,0	61,5	84,5	84,5	85,5	85,5	86,0	91,0
29	59,2	58,9	59,5	59,5	60,2	63,8	87,5	87,5	88,0	88,0	89,0	92,5
30	61,3	61,0	61,5	61,5	62,3	66,0	90,0	90,0	91,0	91,0	91,5	97,5
31	63,0	63,0	63,5	63,5	64,5	68,3	93,0	93,0	94,0	94,0	95,5	101
32	65,0	65,0	65,5	65,5	66,6	70,5	96,0	96,0	97,0	97,0	99,0	104
33	67,0	67,0	67,5	67,5	68,8	72,8	99,0	99,0	100	100	102,5	108
34	69,0	69,0	69,5	69,5	71,0	75,0	102,5	102,5	103	103	105	111
35	71,0	71,0	71,5	71,5	73,1	77,2	105	105	106	106	108	114
36	73,0	73,1	73,5	74,0	75,3	79,5	108	108	109	109,5	111	117,5
37	75,0	75,2	75,5	76,0	77,4	81,8	111	111	111,5	112	114	121
38	77,0	77,3	77,5	78,0	79,6	84,0	114	114	114,5	115,5	118	124
39	79,0	79,4	79,5	80,0	81,7	86,3	117	117	117,5	118	121	127,5
40	81,0	81,5	81,5	82,5	83,9	88,5	119,5	120,5	120,5	122	124	130
41	83,0	83,5	83,5	84,5	86,0	90,7	122,5	123,5	123,5	125	127,5	135
42	85,0	85,5	85,5	86,5	88,2	93,0	125,5	126,5	126,5	128	130	138
43	87,0	87,5	87,5	88,5	90,3	95,4	128	129,5	129,5	130	133	141
44	89,0	89,5	89,5	90,5	92,5	97,7	132	132,5	132,5	132	134,5	145
45	91,0	91,5	91,5	92,5	94,6	100	135	135,5	135,5	134,5	141	148
46	93,5	93,5	93,6	95,0	96,8	—	138	138,0	139	141	143,5	—
47	95,0	95,5	95,7	97,0	98,9	—	141	141,5	142	143,5	146,5	—
48	96,5	97,5	97,8	99,0	—	—	142,5	141,5	145	146,5	—	—
49	98,0	100	100	—	—	—	145	148,0	148	—	—	—

Table VI

Relation between Brightness of OSR Field, Albedo, and Flux (cloudy atmosphere)

$i = 40^\circ$

f'	θ°											
	0	15	30	45	60	75	0	15	30	45	60	75
	φ°											
	0—180						0—180					
	A' %						R'					
0	—	—	—	—	—	—	—	—	—	—	—	—
1	1,5	1,2	1,5	0,5	—	—	4	3,5	4	3	—	—
2	3,1	4,0	4,0	3,5	2,5	—	6	7,5	7,5	7	5	—
3	6,5	6,5	6,6	6,0	5,0	4,5	10	10	10	9,5	8,5	7,5
4	8,9	9,0	9,1	8,5	7,8	5,5	13	13	13	12,5	12	9
5	11,5	11,6	11,7	11,0	10,4	9,0	16	16	16	15,5	15	13
6	14,1	14,1	14,2	14,0	13,0	11,5	19	19	19	19	17,5	16
7	16,7	16,7	16,8	16,5	16,0	14,5	22,5	22,5	22,5	22	21	19,5
8	19,4	19,3	19,4	19,0	19,0	17,5	25	24,5	25	24,5	24,5	23,0
9	22,0	21,9	22,0	22,0	21,5	20,5	28	28	28	28	27,5	26,5
10	24,5	24,5	24,6	24,5	24,0	23,0	31	31	31	31	30,5	29,5
11	27,0	27,0	27,0	27,0	26,5	26,5	34	34	34	34	33	33
12	29,5	29,5	29,5	29,5	29,5	29,0	37	37	37	37	37	36,5
13	32,0	32,0	32,0	32,0	32,0	32,0	39,5	39,5	39,5	39,5	39,5	39,5
14	34,5	34,5	34,5	34,5	35,0	35,0	42,5	42,5	42,5	42,5	43,5	43,5
15	37,2	37,2	37,2	37,0	37,5	37,5	45,5	45,5	45,5	45,5	46	46
16	40,0	40,0	40,0	40,0	40,0	40,5	49	49	49	49	49	49,5
17	42,5	42,5	42,5	42,5	42,5	43,5	52	52	52	52	52	53
18	45,0	45,0	45,0	45,0	45,5	46,0	55	55	55	55	55,5	56
19	47,5	47,5	47,5	47,5	48,0	49,0	57,5	57,5	57,5	57,5	58,5	49,5
20	50,0	50,0	50,0	50,0	50,8	52,0	60,5	60,5	60,5	60,5	61,5	63
21	52,5	52,5	52,5	52,5	53,5	55,0	63,5	63,5	63,5	63,5	64,5	66,5
22	55,0	55,0	55,0	55,0	56,0	57,5	66,5	66,5	66,5	66,5	67,5	69
23	57,5	57,5	57,5	57,5	53,5	60,5	69,0	69,0	69,0	69,0	70,5	73
24	60,0	60,0	60,0	60,0	61,5	63,0	72,5	72,5	72,5	72,5	74	75,5
25	62,5	62,5	63,0	63,5	64,0	66,0	75	75	75,5	75,5	77	79
26	65,0	65,0	65,5	65,5	66,5	68,5	78	78	78,5	78,5	80	82,5
27	67,5	67,5	68,0	68,0	69,0	72,0	82	82	82,5	82,5	83	86,5
28	70,0	70,0	70,5	70,5	72,0	75,0	84	84	84,5	84,5	86,5	90
29	72,5	72,5	73,0	73,0	74,5	77,5	87	87	87,5	87,5	89	92,5
30	75,0	75,0	76,0	76,0	77,0	80,0	90	90	91	91	92	96
31	77,5	77,5	78,5	78,5	79,5	82,5	92,5	92,5	94	94	95	99
32	80,0	80,0	81,0	81,0	82,0	85,5	96	96	97	97	98	102,5
33	82,5	82,5	83,5	83,5	85,0	88,0	99	99	100	100	102	105,5
34	85,0	85,0	86,5	86,5	87,5	91,0	102	102	103,5	103,5	105	108
35	87,5	87,5	89,0	89,0	90,0	93,5	105	105	106,5	106,5	108	112
36	90,0	90,0	91,5	91,5	93,0	97,0	108	108	109,5	109,5	111,5	116,5
37	92,5	92,5	94,0	94,0	95,5	100	111	111	112,5	112,5	114,5	120
38	95,0	95,0	96,5	96,5	98,0	—	114	114	115,5	115,5	117,5	—
39	97,5	97,5	99,0	99,0	—	—	118	118	119	119	—	—
40	100	100	—	—	—	—	120	120	—	—	—	—

4°

Table VII

Relation between Brightness of OSR Field, Albedo, and Flux (cloudy atmosphere)

$i = 60^\circ$

I'	θ°																				
	0	15	30	45	60		75			0	15	30	45	60		75					
	φ°																				
	0—180				0	90	180	0	90	180	0—180				0	90	180	0	90	180	
	A' %										R'										
0	—	—	—	—	—	—	—	—	—	—	—	—	—	—	—	—	—	—	—	—	—
1	2,5	2,5	2,5	0,5	—	0,5	—	—	—	—	4,5	4,5	—	—	—	—	—	—	—	—	—
2	6,5	6,5	6,5	5,0	1,0	5,0	3,0	—	—	—	7,5	7,5	4,5	3,0	—	3,0	—	—	—	—	—
3	10,5	10,5	10,5	9,0	6,0	9,0	7,5	—	1,5	—	10,5	10,5	7,5	6,5	3,5	6,5	5,0	—	4,0	—	6,5
4	14,5	14,5	14,5	13,0	10,0	13,0	11,5	—	7,0	4,0	14	14	10,5	9,5	7,5	9,5	12,0	—	8,0	—	6,0
5	18,5	18,5	18,5	17,5	14,5	17,5	15,5	1,5	15,5	13,0	16,5	16,5	14	12,5	10,5	12,5	11,5	—	11,0	—	9,5
6	22,5	22,5	22,5	21,5	18,5	21,5	20,0	7,0	20,0	17,5	19,5	19,5	19,5	19	16,5	15	14,5	4	14,5	14	
7	26,5	26,5	26,5	25,5	22,5	25,5	24,0	11,5	24,5	22,0	22,5	22,5	22,5	22	19,5	19,5	17,5	8	18	15	
8	30,0	30,0	30,0	29,5	26,5	30,0	28,5	16,0	29,0	26,0	25	25	25	24,5	22,5	22	21	11,5	21	19	
9	34,5	34,5	34,5	33,5	31,0	34,0	32,5	20,5	33,0	30,5	28,5	28,5	28,5	28	26	25	24	15	24,5	22,5	
10	38,0	38,0	38,0	37,5	35,0	38,0	36,5	25,0	37,5	35,0	31,5	31,5	31,5	31	29	28,5	27	18	27,5	25,5	
11	42,0	42,0	42,0	41,5	39,0	44,0	41,0	29,0	42,0	40,0	34,5	34,5	34,5	33,5	32	31,5	30	21,5	31	25	
12	46,0	46,0	46,0	45,5	43,5	46,5	45,0	33,5	46,5	44,0	37,5	37,5	37,5	37	35,5	36	33,5	24,5	34,5	32,5	
13	50,0	50,0	50,0	50,0	47,5	50,5	49,0	38,0	51,0	48,5	40	40	40	40	38,5	37,5	36,5	28	37,5	35,5	
14	54,0	54,0	54,0	53,5	52,0	54,5	53,5	42,5	55,0	52,5	43,5	43,5	43,5	42,5	41,5	40,5	39,5	31,5	41	39	
15	58,0	58,0	58,0	58,0	56,0	58,5	57,5	47,0	60,0	57,0	46	46	46	46	44,5	43,5	42,5	35	44	42	
16	62,0	62,0	62,0	62,0	60,0	62,5	61,5	51,0	64,5	62,0	49	49	49	49	47,5	47	46	38	47,5	45,5	
17	66,0	66,0	66,0	66,0	64,0	67,0	66,0	56,0	69,0	66,5	52	52	52	52	50,5	49,5	48,5	41	51	49	
18	70,0	70,0	70,0	70,0	68,0	71,0	70,0	60,0	73,0	70,5	55	55	55	55	53,5	52,5	52	44,5	54	48,5	
19	73,5	73,5	73,5	73,5	72,5	75,0	74,0	64,5	77,5	75,0	58	58	58	58	57	56	55	47,5	57,5	55,5	
20	77,5	77,5	77,5	78,0	76,0	79,5	78,5	69,0	82,0	79,5	61	61	61	61,5	59,5	62,5	62	51	61	59	
21	81,5	81,5	81,5	82,5	80,5	83,5	82,5	73,5	86,5	83,5	64	64	64	64,5	63	65	64,5	54	64	62,5	
22	85,0	85,0	85,0	86,2	84,5	87,5	86,0	78,0	91,0	88,0	66,5	66,5	66,5	67,5	66	68,5	67,5	58,0	67,5	65	
23	89,0	89,0	89,0	90,0	88,5	91,5	90,0	82,0	95,5	92,5	69,5	69,5	69,5	70,5	73	71,5	70,5	68,0	71	68	
24	93,0	93,0	93,0	94,0	92,5	96,0	94,5	86,5	100	96,0	72,5	72,5	72,5	73,5	72,5	75	74	64	75	72,5	
25	97,0	97,0	97,0	98,0	97,0	100	98,0	91,0	—	—	76	76	76	77	76	78,5	77	67,5	78,5	75	
26	100,0	100	100	—	—	—	—	95,5	—	—	78,5	78,5	78,5	—	—	—	—	71	—	—	
27	—	—	—	—	—	—	—	100	—	—	—	—	—	—	—	—	—	70,5	—	—	
																		78,5			

Table VIII

Relation between Brightness of OSR Field, Albedo, and Flux (cloudy atmosphere)

$i = 80^\circ$

l'	θ°																					
	0	15	30	45		60		75		0	15	30	45		60		75					
	φ°																					
	0—180			0	90	180	0	90	180	0	90	180	0—180		0	90	180	0	90	180	0	90	180
	A' %												R'										
0	—			—			—			—			—										
1	9	8,5	8,5	—			—			—			5										
2	22	21	21	11,5			5,5			3,5			8,2		4,8			4,8					
3	35	35	35	25,0			19,0			17,5			11		8			8					
4	48	48	48	38,0			32,5			31,0			14		11			11					
5	61	61	61	52,5			46,0			44,0			17		14			14					
6	74	74	74	65,0			59,5			57,5			20		17			17					
7	87	87	87	78,0			72,5			71,0			24		20			20					
8	100	100	100	91,5			85,5			84,0			27,5		24			24					
9				—			99,0			97,5					27,5			27,5					
10							—			—					—			—					
11																							
12																							
13																							
14																							
15																							
16																							

θ°																						
0	15	30	45		60		75		0	15	30	45		60		75						
φ°																						
0—180			0	90	180	0	90	180	0	90	180	0—180		0	90	180	0	90	180	0	90	180
A' %												R'										
—			—			—			—			—										
8,5	8,5		—			—			—			3,5										
21	21		11,5			5,5			3,5			7		4,8			4,8					
35	35		25,0			19,0			17,5			10		8			8					
48	48		38,0			32,5			31,0			13,5		11			11					
61	61		52,5			46,0			44,0			16,5		14			14					
74	74		65,0			59,5			57,5			19,5		17			17					
87	87		78,0			72,5			71,0			23,5		20			20					
100	100		91,5			85,5			84,0			28		24			24					
			—			99,0			97,5					27,5			27,5					
						—			—					—			—					

θ°																						
0	15	30	45		60		75		0	15	30	45		60		75						
φ°																						
0—180			0	90	180	0	90	180	0	90	180	0—180		0	90	180	0	90	180	0	90	180
A' %												R'										
—			—			—			—			—										
—			—			—			—			4,5										
3,5			—			—			—			7,5		3,5			3,5					
17,5			—			—			—			10,5		7			7					
31,0			7,5			0,5			—			13,5		10			10					
44,5			21,0			14,0			—			17		13			13,5					
58,0			35,0			27,5			—			20		16			16,5					
72,0			49,0			41,0			—			24		19			19,5					
85,5			62,5			55,0			—			28		23			23,5					
99,5			76,0			68,5			—			—		27,5			28					
—			89,5			82,0			—					—			—					
			—			96,0			—													
						—			—													
									10,0													
									25,0													
									39,5													
									54,0													
									66,8													
									83,5													
									98,5													
									—													

θ°																						
0	15	30	45		60		75		0	15	30	45		60		75						
φ°																						
0—180			0	90	180	0	90	180	0	90	180	0—180		0	90	180	0	90	180	0	90	180
A' %												R'										
—			—			—			—			—										
—			—			—			1			2,0										
—			—			—			10,0			16,0		3,5			3,5					
—			—			—			24,0			31,0		6,5			6,5					
—			—			—			38,5			46,0		10			10					
—			—			—			53,5			61,0		13,5			13,5					
—			—			—			68,0			76,0		17,5			17,5					
—			—			—			82,5			89,0		20,5			20,5					
—			—			—			97,0			—		24,5			24,5					
									—					—			—					

89
36

REFERENCES

1. Shifrin, K. S., Pyatovskaya, N. P. Pole korotkovolnovoy radiatsii nad podstilayushchimi poverkhnostyami [Field of Short-wave Radiation Above Underlying Surfaces]. See this collection.
2. Shifrin, K. S., Shubova, G. L. Statisticheskaya izmenchivost' vertikal'noy prozrachnosti [Statistical Variability of Vertical Transparency]. Izv. AN SSSR, ser. geofiz., no. 2, 1964.
3. Shifrin, K. S., Minin, I. N. K teorii negorizontal'noy vidimosti [Contribution to the Theory of Non-horizontal Visibility]. Tr. GGO, part 68, 1957.
4. Shifrin, K. S., Pyatovskaya, N. P. Tablitsy naklonnoy dal'nosti vidimosti i yarkosti dnevnogo neba [Tables of Oblique Visibility Range and Brightness of the Diurnal Sky]. Gidrometeoizdat, Leningrad, 1959.
5. Shifrin, K. S., Avaste, O. A. Potoki korotkovolnovoy radiatsii v bezoblachnoy atmosfere. Issledovaniya po fizike atmosfery [Fluxes of Short-wave Radiation in the Cloudless Atmosphere. Studies on Physics of the Atmosphere]. No. 2, Tr. IFA AN ESSR, 1960.
6. Avaste, O. A., Moldau, Kh., Shifrin, K. S. Spektral'noye raspredeleniye pryamoy i rasseyanoy radiatsii. Issledovaniya po fizike atmosfery [Spectral Distribution of Direct and Scattered Radiation. Studies on Physics of the Atmosphere], No. 3. Tr. IFA AN ESSR, 1962.
7. Pyatovskaya, N. P. Potoki korotkovolnovoy radiatsii v svobodnoy atmosfere [Fluxes of Short-wave Radiation in the Free Atmosphere]. Tr. GGO, part 109, 1961.

L. R. Rakipova

CALCULATION OF OUTGOING RADIATION FLUXES OF THE EARTH—ATMOSPHERE SYSTEM BY MEANS OF MEASUREMENTS OF LONG-WAVE RADIATION WITH ARTIFICIAL EARTH SATELLITES

The first problem to be solved in approaching the derivation of formulas for the conversion from fluxes of long-wave radiation at the level of the AES to the fluxes of outgoing radiation is the accuracy with which the long-wave radiation must be measured by the AES. In determining the permissible error in the measurement of long-wave radiation by the AES, it is necessary to use the quantitative characteristics of the time and space variability of the fluxes of outgoing radiation. To this end, F. N. Shekhter's radiation diagram was used to calculate the outgoing radiation for the Voyeykovo station for four months (January, June and July 1957, December 1958) and for the Tashkent station for two months (December 1959 and July 1960). The average absolute and relative deviations of the outgoing radiation for each period from its mean monthly value $\overline{E}$ in cal/cm^2 min are given in Table 1.

The average diurnal anomalies and interdiurnal variabilities of the outgoing radiation for each month have values of the same order (Table 2).

The characteristics of the spatial dispersion of the fluxes E are given below (Table 3).

The following conclusion may be drawn from the estimates cited. In order to be able to use the data on outgoing radiation obtained from AES, both as climatological characteristics and for the analysis of the space-time interrelationship of fluxes of outgoing radiation with fields of meteorological elements, particularly for quantitative weather forecasting,

the theoretical error of the long-wave radiation measurements made by the AES should be less than the average estimates obtained for the time and space variability of the outgoing radiation. We can now begin the solution of the following two basic problems:

1. To obtain formulas for converting the measured radiation into fluxes of outgoing radiation for a wide-sector instrument with an unlimited viewing angle and for a scanning narrow-sector instrument. The magnitude of the permissible measurement error will make it possible to determine the order of magnitude of the various factors affecting the long-wave radiation so that they can be considered in the conversion formulas.

2. To determine the feasibility of conversion from asynchronous fluxes of outgoing radiation to values pertaining to a single physical moment or time interval. Without such a conversion, the charting and physical analysis of the outgoing radiation are impossible.

1a. In solving the first problem for a wide-sector instrument, one must evaluate the effects of the horizontal inhomogeneity and anisotropy of the field of outgoing radiation. The flux of long-wave radiation E_h incident on a horizontal area at point A (Fig. 1) is represented as follows:

$$E_h = \int_0^{2\pi} \int_0^{\gamma_0} \frac{I(z)}{r^2} \cos z \cos \gamma R^2 \sin \delta \, d\delta \, d\beta. \qquad (1)$$

It may be assumed that $I(z) = I(0)\psi(z)$. Here $I(z)$ is the intensity of the long-wave radiation in the direction of the nadir angle γ; z is the zenithal angle of point M on the emitting surface corresponding to angle γ; R is the distance from the center of the earth to the radiating surface located at height h_0 above sea level (above the surface, the

Table 1

Average absolute and relative deviations of E for individual cases

	Period				Period			
	1 (1 hr.)	2 (7 hr.)	3 (13 hr.)	4 (19 hr.)	1 (1 hr.)	2 (7 hr.)	3 (13 hr.)	4 (19 hr.)
	Voyeykovo January 1957				Dec. 1958			
$\bar{E}$	0,319	0,324	0,319		0,325	0,322	0,326	0,325
$\Delta\bar{E}$	0,016	0,016	0,012		0,013	0,014	0,012	0,015
$\frac{\Delta\bar{E}}{\bar{E}}$ %	5,0	4,9	3,7		4,0	4,3	3,7	4,6
	June 1957				Tashkent Dec. 1959			
$\bar{E}$	0,351	0,354	0,350	0,354	0,298	0,301	0,300	0,301
$\Delta\bar{E}$	0,017	0,020	0,023	0,020	0,016	0,014	0,020	0,016
$\frac{\Delta\bar{E}}{\bar{E}}$ %	4,8	5,6	6,6	5,6	5,3	4,6	6,6	5,3
	July 1957				July 1960			
$\bar{E}$	0,378	0,378	0,375	0,375	0,414	0,454	0,460	0,419
$\Delta\bar{E}$	0,015	0,017	0,016	0,018	0,024	0,031	0,023	0,021
$\frac{\Delta\bar{E}}{\bar{E}}$ %	4,0	4,5	4,3	4,8	5,8	6,8	6,0	5,0

Table 2

	Voyeykovo				Tashkent	
	Jan 1957	June 1957	July 1957	Dec 1957	Dec 1959	July 1960
Average daily sum (cal/cm^2 day)	464	505	542	465	433	610
Average absolute anomaly	20	21	15	18	21	28
Average relative anomaly (%)	4.3	4.2	2.8	3.9	4.9	4.6
Average absolute interdiurnal variability	17	20	15	15	17	27
Average relative interdiurnal variability (%)	3.7	4.0	2.8	3.2	3.9	4.4

fluxes of ascending long-wave radiation are subjected to a geometrical attenuation only); δ_0 is the central angle defining the segment of spherical surface visible to the instrument; the function $\varphi(z)$ characterizes the angular distribution of the intensity of the outgoing radiation.

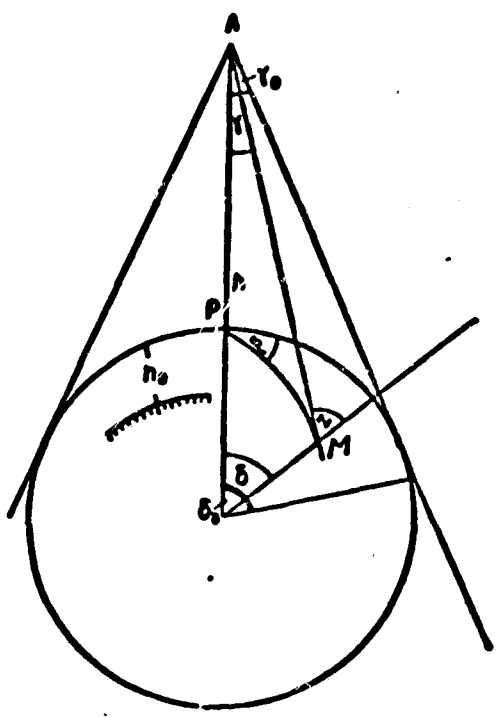

Fig. 1. Geometrical diagram of the calculation of outgoing radiation measured by a wide-sector instrument

Generally speaking, because of the horizontal inhomogeneity of the real radiation fields at the upper boundary of the atmosphere, in formula (1), one should not take out from under the surface integration sign the magnitude of the intensity of outgoing radiation I(0) in the direction perpendicular to the elementary radiating areas (or the isotropic radiation fluxes corresponding to this area). For this reason, even for conditions of isotropic radiation, the instrument will generally give some average weighted characteristic of the radiation field which has no direct meteorological meaning.

In order to elucidate the degree of horizontal inhomogeneity of the type of radiation in which we are interested, i.e., radiation leaving the atmosphere, some statistical treatments have been undertaken. Mean square deviations from average territorial values were determined at 27 points of the territory of the Soviet Union for each of four periods for

August 15, 1960 (Table 3).

The relative values of the deviations turned out to be comparable to the proposed actual measurement error of the long-wave radiation aboard the AES. This fact will make it possible to consider the flux of outgoing radiation constant for large areas of averaging, and to obtain a simple relation between the ascending flux of long-wave radiation at the height of the AES, E_h, and the flux of outgoing radiation E_{h_o}, for the existing wide-sector instruments both with a limited and unlimited viewing angle in the case of isotropic radiation.

$$E_h = k(\gamma) E_{h_o}.$$

Table 3

Characteristics of the horizontal inhomogeneity of the field of outgoing radiation E for the territory of the Soviet Union for 15 August 1960.

	Period			
	1	2	3	4
$\bar{E}_\infty$	0,352	0,374	0,367	0,364
σ	0,022	0,023	0,029	0,024
$\frac{\sigma}{\bar{E}_\infty}$ %	6,2	6,2	7,9	6,6

It is obvious that this will determine only the climatological characteristics E_{h_o} in their dependence on the seasons and the climatological zones. The coefficient $k(\gamma)$ for a given limited viewing angle of the instrument of the height of the AES. For the limiting case, i.e., an unlimited viewing angle, k depends on the height of the AES.

$$k = k_0 = \frac{R^2}{(R+h)^2}. \qquad (2)$$

Let us note that instruments viewing angles of less than 20° make it possible to determine values of radiation fluxes having a moderate area and any degree of horizontal inhomogeneity (both outgoing and

reflected), since in this case it is possible to take out the weight function $f(\gamma) = \frac{\cos\gamma \cos z}{r^2} c$ from under the integration sign in formula (1) with a maximum error of 2% (if the height of the AES is no more than 800 km).

In order to take into account the effect of anisotropicity of the field of outgoing radiation, use was made of data on the angular distribution of the intensity of outgoing radiation obtained for the family of models of the atmosphere given by K. Ya. Kondrat'yev and K. Ye. Yakushevskaya [1]. Based on standard data on the temperature stratification and distribution of humidity in the atmosphere up to an altitude of 39 km (data of London [2] and Murgatroyd [3]), the angular distributions of the outgoing radiation were calculated for a spherical atmosphere:

(1) For winter and summer conditions at a latitude of 65° N.L., for a clear sky and for the case of continuous cloudiness with an upper boundary at an altitude of 3 km.

(2) For summer conditions at the equator, for a clear sky and cases of continuous cloudiness with an upper boundary at altitudes of 3 and 9 km.

Thus, we have models of a very warm and humid atmosphere (equator), a very cold and dry one (65° N.L., winter), and an intermediate one (65° N.L., summer).

It may therefore be assumed that the real stratifications will be situated between the two extreme models.

Having integrated equation (1) for a given $\psi(\gamma)$, we shall get the relation between E_h and the isotropic radiation flux E_{h_0} in the form

$$E_h = ak_0 E_{h_0}. \qquad (3)$$

Coefficient a appears in (3) because of the introduction of the function $\psi(\gamma)$ into (1). The relation between the anisotropic flux E_{ah_o} and the isotropic flux E_h will be obtained from the known formula for the calculation of radiation fluxes

$$E_{ah_o} = 2\pi \int_0^{\frac{\pi}{2}} I(z)\cos z \sin z dz = 2\pi I(0) \int_0^{\frac{\pi}{2}} \psi(z)\cos z \sin z dz = bE_h . \tag{4}$$

where $b = 2\int_0^{\frac{\pi}{2}} \psi(z)\cos z \sin z dz.$

Substituting (4) into (3), we obtain the desired relation between E_h and E_{ah_o}

$$E_h = k_a E_{ah_o} . \tag{5}$$

Here $k_a = \frac{a}{b} k_0$ is the conversion factor used for converting the anisotropic flux of outgoing radiation into a measured flux.

For the families of models of the atmosphere under consideration, the mean value of the ratio $\frac{a}{b}$ was found to be 0.988. Thus, the correction for anisotropy for a wide-sector instrument was found to be considerably less than the determination error E_a related to the horizontal inhomogeneity of the field of outgoing radiation. Obviously, the same kind of relation is preserved for real stratifications between these quantities. Therefore, one should not introduce a correction for the anisotropy into coefficient k_0.

1b. In solving the problem involving the conversion of measured radiation into fluxes of outgoing radiation in the case of narrow-sector instruments, one should evaluate only the effect of anisotropicity. To this end, the following corrections

$$E_h = \gamma_0^2 \frac{\psi(\alpha)}{b} E_{ah_o} , \tag{6}$$

where α is the scanning angle, should be introduced into the conversion

factor for a narrow-sector instrument in the case of isotropic radiation $k = \gamma_0^2$ (γ_0 is one-half of the viewing angle of the instrument).

In general, for different stratifications of the atmosphere, the quantities $\psi(\alpha)$ and b have their own values. However, treatment of the data by means of the angular distribution of the intensity of outgoing radiation for the family of typical models of the atmosphere discussed above has shown that for scanning angles of practical interest ($\alpha \leq 60^\circ$), the angular intensity distribution of outgoing radiation for all models may be represented by a single average function $\overline{\psi}(\alpha)$ which is very close to the corresponding curve obtained by Iamomoto et al. [4] by averaging $\psi(\alpha)$ for 106 real stratifications (Table 4). The mean square deviation for individual models does not exceed 2%, and the maximum error, 3%. The quantity $\overline{b} = 0.98$.

Therefore, the formula $E_h = \frac{\gamma_0^2}{0,98}\overline{\psi}(\alpha)E_{sh}$ should be valid for a large group of real stratifications.

Table 4

Average functions of the angular distribution of outgoing radiation.

α	$\overline{\psi}(\alpha)$	$\frac{\varepsilon}{\overline{\psi}(\alpha)}$ %	Maximum relative error (%)	$\overline{\psi}(\alpha)$ (according to the data of Iamomoto et al)
0	1,00	0	0	1,00
28°02′	0,99	0	0	0,99
46°18′	0,97	1	2	0,97
54°47′	0,94	2	3	0,93
62°30′	0,88	4	6	0,86

Note. The values of angle α are given for an altitude of the AES equal to 700 km.

2a. In order to determine the possibility of obtaining some synchronous characteristics with the aid of asynchronous measurements of fluxes of outgoing radiation, calculations of diurnal sums of outgoing

radiation were made, since such sums are of direct interest for numerical weather forecasting. The diurnal sums were calculated from the total number of diurnal periods (four periods) of aerological observations (exact diurnal sums) and from one and two periods (approximate diurnal sums). To this end, use was made of data obtained from calculations for four months at the Voyeykovo station (two winter ones and two summer ones), for two months at the Tashkent station, and also for 27 points on the territory of the Soviet Union for 15 August 1960. The ratio of the mean square deviations of the approximate sums to the mean value of the exact sum for each of the samples under consideration did not exceed 6% (Table 5).

Table 5

Relative determination errors of daily sums of outgoing radiation based on values of E for one and two periods

Month and year	Period					
	1	2	3	4	1—3	2—4
			Voyeykovo			
January 1957	3	2	3	-	2	-
July 1957	4	3	5	3	3	2
July 1957	2	4	4	3	2	2
December 1958	2	2	2	2	1	1
			Tashkent			
July 1960	4	4	4	4	1	2
December 1959	3	2	3	3	4.3	0.4
			Territory of the Soviet Union			
15 August 1960	6	5	6	3	4	1

Consequently, the diurnal sums of outgoing radiation may be obtained within the accuracy with which the instruments will operate even if a single measurement of long-wave radiation per day is made by the AES, while two measurements per day make this result more accurate to within an error comparable to the theoretically permissible one for measuring long-wave radiation.

REFERENCES

1. Kondrat'yev, K. Ya. and Yakushevskaya, K. Ye. Uglovoye raspredeleniye ukhodyashchego izlucheniya v razlichnykh oblastyakh spektra [Angular Distribution of Outgoing Radiation in Various Regions of the Spectrum]. Iskusstvennyye sputniki Zemli, vyp. 14, 1962.
2. London, I. Issledovaniya teplovogo balansa atmosfery [Studies of the Thermal Balance of the Atmosphere]. Contract N.A.F. 19 (122), 165, 1957.
3. Murgatroyd, R. I. Winds and temperatures between 20 km and 100 km — A review. Quart. Journ. Roy. Met. Soc. v. 83, N 358, 1957.
4. Wark, D., Iamamoto, G., Lienesch, I. Metody otsenok potoka infraktashoy radiatsii i temperatury podstilyushchey poverkhnosti s meteorologicheskikh sputnikov [Methods of Determining the Infrared Radiation Flux and the Temperature of an Underlying Surface from Meteorological Satellites]. Journal of the Atmospheric Sciences, 19, No. 15, 1962.

K. Ya. Kondrat'yev, Kh. Yu. Niylisk

SOME RESULTS OF THEORETICAL CALCULATIONS OF THE ANGULAR DISTRIBUTION OF THERMAL RADIATION OF THE EARTH AS A PLANET UNDER ACTUAL CONDITIONS

Metereological investigations of the upper layers of the atmosphere by means of rockets and satellites have been vastly expanded in the last few years. The main purpose of these investigations is to study the structure and composition of the atmosphere and also to determine the radiation field therein. It should be noted that in treating measurement data and interpreting them scientifically, it is necessary in many cases to have a preliminary theoretical solution of the problem under consideration. However, many problems connected with the determination of metereological and radiation characteristics in the atmosphere have thus far been insufficiently studied. For instance, most of the investigations devoted to the problem of the radiation balance of the earth—atmosphere system give only an idea of the averaged values of the radiation fluxes (see Refs. [1-12]). Only in the work of F. Moeller [14] were calculations undertaken of the geographical distribution of the radiation balance of the troposphere for various synoptic situations. This study is limited, however, by the analysis of only one of the components of the radiation balance. A very small number of papers have been devoted to the theoretical study of the outgoing radiation of the earth—atmosphere system under conditions of concrete synoptic situations. In Refs. [14, 15] calculations of the intensity of outgoing thermal radiation were made within certain spectral intervals by using concrete data on the stratification of the atmosphere above the territory of the U.S.A. It should be noted that the angular distribution of the intensity of outgoing thermal radiation was calculated

only for the case of a "model" atmosphere [11, 16].

The authors of Ref. [16] carried out theoretical calculations for the purpose of studying the laws of the angular distribution of the intensity of outgoing radiation of the earth—atmosphere system in various regions of the spectrum. Since in this work the angular distribution of outgoing radiation was obtained for the mean latitudinal and mean seasonal stratification of the atmosphere, the results given there are important in the elucidation of general rules of the distribution of outgoing radiation in the atmosphere and for the determination of the climatic characteristics of the latitudinal zone considered. The present work continues this study for real atmosphere conditions. We have calculated the angular intensity distribution of outgoing radiation for a point located at an altitude H = 300 km for certain specific synoptic situations. The initial meteorological data used were the results of aerological soundings at several points on the territory of the U.S.S.R. for three dates: 20 July 1956, 25 February and 30 March 1960 (all soundings were made at night). Calculations of the outgoing radiation intensity were made for zenithal angles equal to 0, ± 30, ± 50, ± 60, ± 65, $\pm 70^\circ$, $\pm 72^\circ 45'$, $\pm 72^\circ 52' 30''$, $\pm 73^\circ$, $\pm 73^\circ 07' 30''$, $\pm 73^\circ 15'$ within the confines of six vertical sections of the atmosphere. It should be stated that in the case under consideration, $72^\circ 45' 10''$ is the "critical value" of the zenithal angle (at $\alpha > 72^\circ 45' 10''$ the sighting ray traverses the atmosphere without touching the earth's surface).

In the present work, the radiation intensity was calculated by means of the graphical method (from a radiation nomogram) proposed in Ref. [18]. This method is based on the following relation:

$$I = \int P_\lambda dE_\lambda , \qquad (1)$$

where I is the intensity of outgoing radiation over the spectral interval Δ, P_Δ is the transmission function of the atmosphere for the spectral region Δ, E_Δ is the radiation intensity of an absolute black body in this interval; E_Δ is defined by the formula

$$E_\Delta(T) = f_\Delta(T) E(T). \tag{2}$$

Here $f_\Delta(T)$ is the proportion of the radiation intensity of the absolute black body corresponding to the spectral interval Δ, and E(T) is the integral radiation intensity of the absolute black body. As we know, E, E_Δ and f_Δ are functions of the temperature of the radiator.

In order to simplify the calculations, the following relation is proposed in Ref. [18].

$$E_\Delta(T) = \bar{f}_\Delta E(T), \tag{3}$$

where $\bar{f}_\Delta$ is some average value of the function $f_\Delta(T)$. In other words, the temperature dependence of f_Δ is not taken into consideration. The accuracy of expression (3) depends on the temperature contrasts in the atmosphere and on the location in the spectrum of the interval Δ under consideration. For spectral regions where the relation $f_\Delta = f_\Delta(T)$ is strongly expressed, the use of $\bar{f}_\Delta$ in many cases provides only tentative results (for example, in summer for partial cloudiness, when the temperature of the earth's surface differs considerably from the temperature of the upper cloud boundary. In the present work, the values of I were determined from formulas (1) and (2), and comparisons were made between these results and the corresponding intensity values obtained from (1) and (3). The outgoing radiation intensity was calculated for spectral intervals of 4.88-8.70, 10.55-11.01, 12-18, and 2.27-250 μ. Values of the transmission function of the atmosphere borrowed from Ref. [18] were used for these spectral regions.

It is known that the principal sources of thermal radiation in the atmosphere are the earth, the clouds, water vapor, carbon dioxide and ozone. In the present work, the earth and clouds were assumed to be an absolutely black body, and the effective absorbing masses of H_2O, CO_2 and O_3 were calculated by means of the following formulas (see Refs. [17, 19]):

$$\left.\begin{aligned} w_s^* &= \int \rho_w \left(\frac{p}{p_0}\right)^{0.8} ds \\ u_s^* &= \int \rho_u \left(\frac{p}{p_0}\right)^{0.8} ds \\ m_s^* &= \int \rho_m \left(\frac{p}{p_0}\right)^{0.8} ds \end{aligned}\right\} \qquad (4)$$

Here w_s^*, u_s^*, m_s^* are the effective absorbing masses of water vapor, carbon dioxide and ozone in the path of the rays; ρ_u-, ρ_u and ρ_m are the densities of H_2O, CO_2 and O_3 in the atmosphere, p is the air pressure, and p_0 is some standard value.

The values of the humidity, temperature and pressure in the path of the ray in the atmosphere were determined by using graphs of isolines of these quantities. Such graphs were plotted on the basis of the above-mentioned aerological data within the confines of six vertical sections of the atmosphere (see Table 1)[1)]. Let us note that for cases 1, 2, and 3, the graphs of the vertical sections of the atmosphere were plotted up to a height of 25 km, and for cases 1a, 2a, and 3a, up to 20 km. The path of the ray through the atmosphere is given on these graphs as a function of the zenithal angle, allowing for the spherical shape of the earth and atmosphere.

The program of aerological soundings does not include measurements of the total content and vertical distribution of carbon dioxide and

1) In Table 1, q designates the specific humidity in the atmosphere.

ozone in the atmosphere. Therefore, in order to determine ρ_u and ρ_m, it is necessary to use some average values of these quantities, making use of the results of special studies of the distribution of CO_2 and O_3 in the atmosphere. For carbon dioxide, use was made of the generally adopted average value of its volume concentration in air, 0.03%. The values of the density of ozone in the atmosphere were taken from Ref. [21], where the vertical distribution of O_3 was given as a function of the time of year and geographical latitude.

It should be noted that the data of aerological soundings usually do not exceed an altitude of 15-25 km, and in many cases the values of the humidity above 10-15 km must be considered unreliable (in most cases, such data are completely lacking for the upper part of the troposphere and for the stratosphere). The absence of necessary data on the stratification of the atmosphere at sufficiently high altitudes makes it impossible to calculate the true outgoing radiation. In Ref. [3], the outgoing radiation was identified with the ascending flux of thermal radiation at the level of the tropopause, and it was shown that this assumption introduces an error of no more than 6%. Similar conclusions were obtained in other investigations (for example, in Ref. [5]). It may be assumed, however, that the intensity of the outgoing radiation propagating at large zenith angles is substantially affected by the atmospheric layers in the upper troposphere and stratosphere as well. This is due to the fact that the path length of the ray in such a case is many times greater than the corresponding length of a vertical ray, so that the effective absorbing masses of water vapor, carbon dioxide and ozone have very large values. It should be noted that a particularly important part is played by the upper layers of the atmosphere in the creation of the ascending thermal

Table 1

General characteristics of vertical sections of the atmosphere under consideration

Date	Direction	Section Designation	Characteristics of the vertical sections of the atmosphere under consideration
30 Aug 1960	Odessa-Pechora-Yakutsk	1	Partial cloudiness. Low tropopause ($\sim$8-10 km). At altitude of tropopause, relative minimum of temperature and specific humidity (-65° at $\sim$0.03 g/kg). At altitude of 12 km, temperature inversion (-57°), stratosphere nearly isothermal (-67, -71°). Above the tropopause, a slight increase in specific humidity (up to $\sim$0.05 g/kg at 25 km altitude at the center of the section and up to $\sim$ 0.3 g/kg at its edges). At ground level, dry ($q \approx 1.5$-3.0 g/kg).
	Odessa-Tobol'sk-Borzya	1a	Almost total cloudiness. Low tropopause ($\sim$8-10 km). Above the clouds at altitude of about 11 km, relative minimum of temperature and specific humidity ($\sim$ -65° and $\sim$ 0.01-0.02 g/kg). In the stratosphere, cold and warm regions alternate along the section. Above the tropopause increase in specific humidity which is small at the center of the section (0.1 g/kg at 20 km altitude), but increases appreciably at its edges (up to $\sim$ 0.2-0.4 g/kg at 20 km altitude). At ground level, $q \approx 1$-4 g/kg.
25 Feb 1960	Kaliningrad -Salekhard -Borzya	2	Slight cloudiness. Low tropopause ($\sim$8-10 km). Relative minimum of temperature and specific humidity around the tropopause ($\sim$-55, -65° and $\sim$0.003-0.04 g/kg). At 15-25 km altitude, cold ($\sim$-65°) and warm ($\sim$-45°) regions combine. At ($\alpha \approx 30$-70°, inversion of specific humidity with a maximum at 2-3 km altitude. For negative zenith angles, a very dry atmosphere; for positive α, increase of q above the tropopause ($\sim$ 0.5-0.9 g/kg at 20 km altitude). At ground level, dry ($q \approx 0.2$-1.0 g/kg).
	Odessa-Tobol'sk-Borzya	2a	Complete cloudiness. Low tropopause ($\sim$8-10 km). At altitude of tropopause, relative minimum of temperature, and specific humidity ($\sim$-65° and $\sim$0.1 g/kg). In the stratosphere along the section, cold and warm regions are found and a slight increase in temperature with increasing altitude is observed. Above the tropopause, increase in specific humidity, faster for positive zenith angles (up to $\sim$ 0.55 g/kg at 20 km altitude for $+\alpha$ and up to $\sim$ 0.25 g/kg for $-\alpha$).

20 Jul 1956	Yerevan-Tobol'sk-Yakutsk	3	Partial cloudiness. High tropopause (~11-17 km). Around the tropopause, relative minimum of temperature and specific humidity (~-50° and ~0.02-0.04 g/kg). In the stratosphere, increase in temperature and specific humidity (up to -40° and ~1.5 g/kg at 25 km altitude). At ground level, q ≈ 10-12 g/kg.
20 Jul 1956	Odessa-Tobol'sk-Borzya	3a	Partial cloudiness. Tropopause at moderate altitude (11-12 km). At the altitude of the tropopause, relative minimum of temperature and specific humidity (-50, -55° and ~0.04-0.05 g/kg). In the stratosphere along the section, cold (-50, -56°) and warm (-43, -44°) combine. Above the tropopause, increase in specific humidity (up to ~0.3-0.4 g/kg at 20 km altitude). At $\alpha \approx 72^\circ$ at 12-14 km altitude, relative humidity maximum (~0.25 g/kg). At ground level, q ≈ 6-11 g/kg.

radiation in cases where the source of radiation is only the atmosphere itself (zenith angle $\alpha > 72^\circ 45' 10''$ in cloudless weather.

For want of aerological data for atmospheric layers above 20-25 km, we were able to calculate the true values of the intensity of ascending thermal radiation only up to this level. For this reason, for all the cases considered in the present work, the values of I were calculated assuming that z' = 20 km (z' is the upper boundary of the "radiation" atmosphere). In order to evaluate the role of the atmospheric layer from 20 to 40 km in the creation of outgoing long-wave radiation, values of the intensity of outgoing radiation for cases 1, 2 and 3 were also calculated with the assumption that z' = 40 km. The values of the pressure and temperature in the 30-40 km layer were borrowed from Refs. [20] and [8], respectively. Data on the water content of the stratosphere are fairly contradictory at the present time [5, 6, 9, 10, 22-26]. According to Ref. [24], the average values of the specific humidity at an altitude of 30 km fluctuate between 0.002 and 0.2 g/kg. In the present work, the value q = 0.006 g/kg, taken from Ref. [10], was used for the 30-40 km

layer. In the 25-30 km layer, the values of q, T and p were obtained by interpolating between their values at 25 and 30 km.

Results of calculations of the intensity of outgoing thermal radiation based on formulas (1) and (2) are given in Appendices 1-6. Here I_1, I_2, I_3 and I_4 designate respectively the values of the intensity in the spectral regions of 2.27-250 μ (integral radiation), 10.55-11.01, 4.88-8.70 and 12-18 μ. Appendices 1-6 also list data on the total effective content of water vapor in the path of the ray (w_s^*) and on the height and temperature of the radiating black surface (i.e., the surface of the earth or clouds). (The angular intensity distribution of the integral outgoing radiation is also shown in Fig. 1).

The results given for the calculation of I show a strong dependence of the values of the intensity of outgoing thermal radiation on the cloudiness conditions. The presence of clouds in the atmosphere strongly decreases the intensity of outgoing thermal radiation, particularly in summer, when considerable contrasts are observed between the temperatures of the earth's surface and of the surface of the clouds. For instance, in case 3a, the difference $I_1(\alpha = +30^\circ) - I_1(\alpha = -30^\circ)$ reaches 0.057 cal/cm^{-2} min^{-1} ster^{-1}, which amounts to 46% of $I_1(\alpha = +30^\circ)$. The difference $I_3(\alpha = +30^\circ) - I_3(\alpha = -30^\circ)$ is equal to 0.0093 in this case ($\sim$ 70% of the value of $I_3(\alpha = -30^\circ)$. However, even in winter, the intensity of outgoing radiation in the regions of cloudy weather differs appreciably from the intensity for a clear sky. In case 2, $I_1(\alpha = -70^\circ) - I_1(\alpha = -65^\circ) =$ = 0.024 cal cm^{-2} min^{-1} ster^{-1}, and in case 1a, $I_1(\alpha = +70^\circ) - I_1(\alpha = +72^\circ 45')$ = 0.042 cal cm^{-2} min^{-1} ster^{-1}. Such results are in good agreement with the results of Ref. [16], according to which at 65° N.L. $I_1(\alpha = 0^\circ)$ under conditions of a clear sky exceeds the value of $I_1(\alpha = 0^\circ)$ by 0.045

cal cm^{-2} min^{-1} $ster^{-1}$ in cloudy weather, and the value of $I_3(\alpha = 0^\circ)$ in the presence of clouds decreases by 0.0077 cal cm^{-2} min^{-1} $ster^{-1}$. The physical cause of the decrease in the intensity of outgoing thermal radiation in the cloudy regions is the low temperature of the upper boundary of the clouds and of the above-cloud atmosphere (the clouds absorb practically all of the ascending thermal radiation, screening the upper atmosphere from the effect of the atmosphere under the clouds and from that of the earth).

In a horizontally homogeneous atmosphere, as the zenith angle increases from zero to its critical value ($\alpha = 72^\circ 45'$), a slight decrease in I takes place, and when $\alpha > 72^\circ 45'$, the intensity values decrease sharply [11, 16]. This is the so-called "infrared darkening towards the limb of the earth" and the "infrared darkening towards the limb of the atmosphere." As already mentic ed in Ref. [16], under partial overcast conditions, the infrared darkening towards the limb of the earth and atmosphere may be masked by a change in intensity in passing from a clear sky to cloudy zones. This is also confirmed by the results of the present work (Appendices 1-6 and Figs. 1 and 2). However, the nature of the angular intensity distribution of the outgoing radiation also depends on the distribution of the temperature and that of the substances absorbing the radiation in the atmosphere. As already mentioned, if the atmosphere is horizontally homogeneous and its temperature drops with increasing altitude, there takes place an infrared darkening towards the limb of the earth and atmosphere. However, if the temperature increases with the altitude, the intensity of the outgoing radiation increases in the direction of the zenith angle (assuming that $0 \leq |\alpha| \leq 72^\circ 45'$). In this case there takes place an "infrared lightening towards the limb of the earth."

For $|\alpha| \leq 72^{\circ}45'$ under clear weather conditions, an increase in temperature with the altitude is offset to some extent by a decrease in the content of the radiation-absorbing substances. Therefore, the angular distribution of the outgoing radiation may vary considerably in this case depending upon the vertical distribution of the radiation-absorbing substances in the atmosphere and on the values of its temperature. It is evident, however, that the infrared darkening towards the limb of the atmosphere slows down in the case of temperature inversion, so that in the actual atmosphere the magnitude of the infrared darkening depends on a set of many meteorological factors.

It follows from the above that the infrared lightening towards the limb of the earth is observed in the following cases: 1) when the temperature of the radiating surface and of the atmosphere rises with increasing $|\alpha|$, 2) when the total absorbing mass of the atmosphere increases with increasing $|\alpha|$, 3) when the temperature inversion in the atmosphere is fairly pronounced. The infrared lightening towards the limb of the atmosphere (in cloudless weather) is an indication of temperature inversion and of an increase in the content of the radiation-absorbing substances with increasing altitude. For instance, in case 1 $I(\alpha = \pm 70^{\circ}) > I(\alpha = \pm 65^{\circ}) > I(\alpha = \pm 60^{\circ})$, which is due to a rise in the temperature of the earth's surface with increasing α. In case 1a, $I(\alpha = 72^{\circ}45') \approx \approx I(\alpha = 72^{\circ}52'30'') \approx I(\alpha = 73^{\circ})$. Here, the infrared lightening towards the limb of the atmosphere is masked by the clouds, the temperature of the upper boundary of which is equal to -59°, and above the clouds the temperature inversion takes place. In case 2, the cause of the increase in intensity associated with a change in α from -50 to -65° is a rise in the temperature of the atmosphere in a horizontal direction. In case 2a,

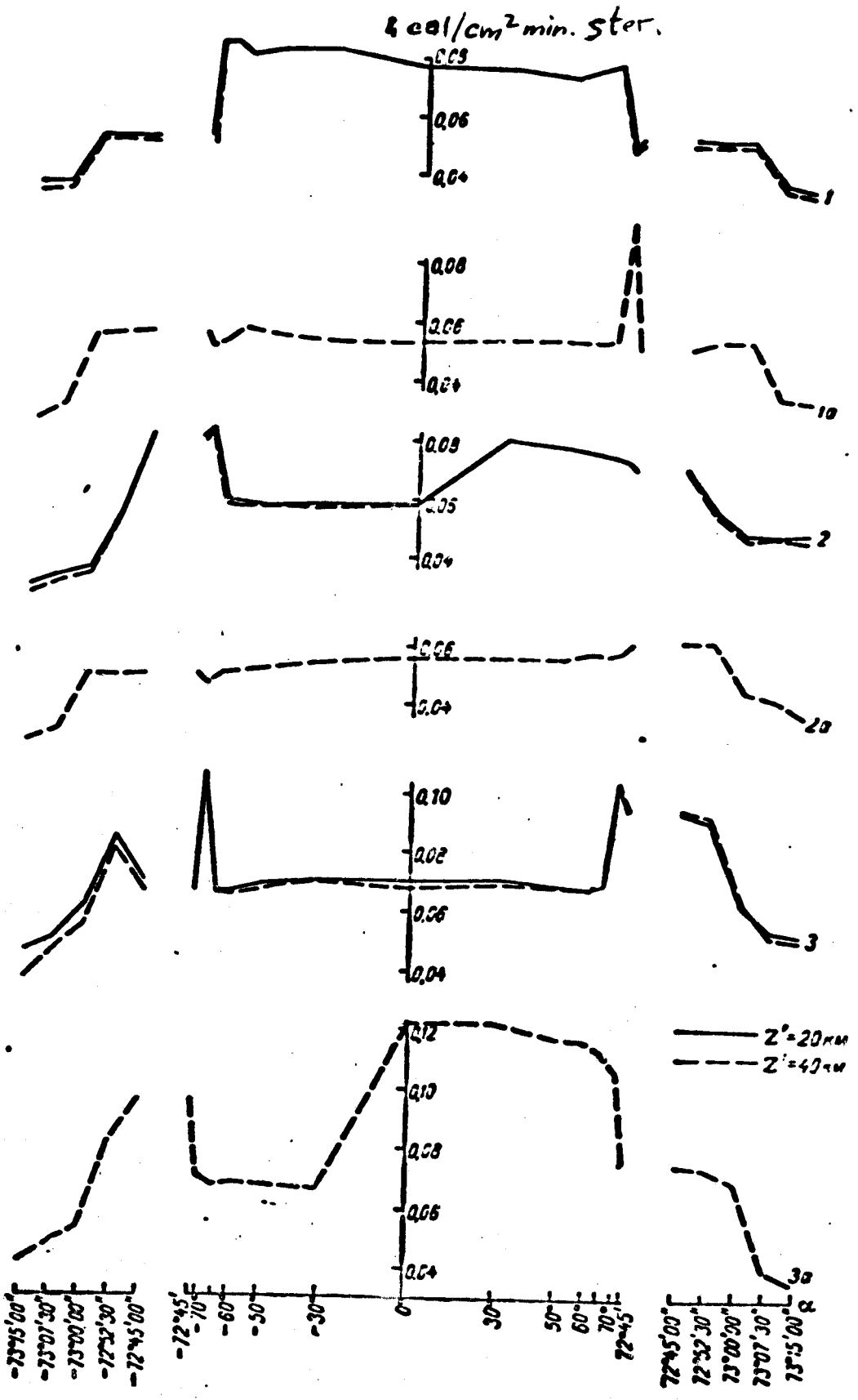

Fig. 1. Integral outgoing radiation of the earth and atmosphere versus zenith angle α.

the temperature inversion begins at 10-11 km. For positive α values, the intensity increases here with increasing α (the temperature of the upper boundary of the clouds remains almost unchanged), and for negative α values, I decreases slightly toward larger values of α (the temperature of the upper boundary of the clouds also decreases with increasing α). In case 3a, $I(\alpha = -70^\circ) > I(\alpha = -65^\circ)$ since t_{zo} $(\alpha = -70^\circ) > t_{zo}$ $(\alpha = -65^\circ)$, which is associated with a temperature inversion in the atmosphere above the clouds.

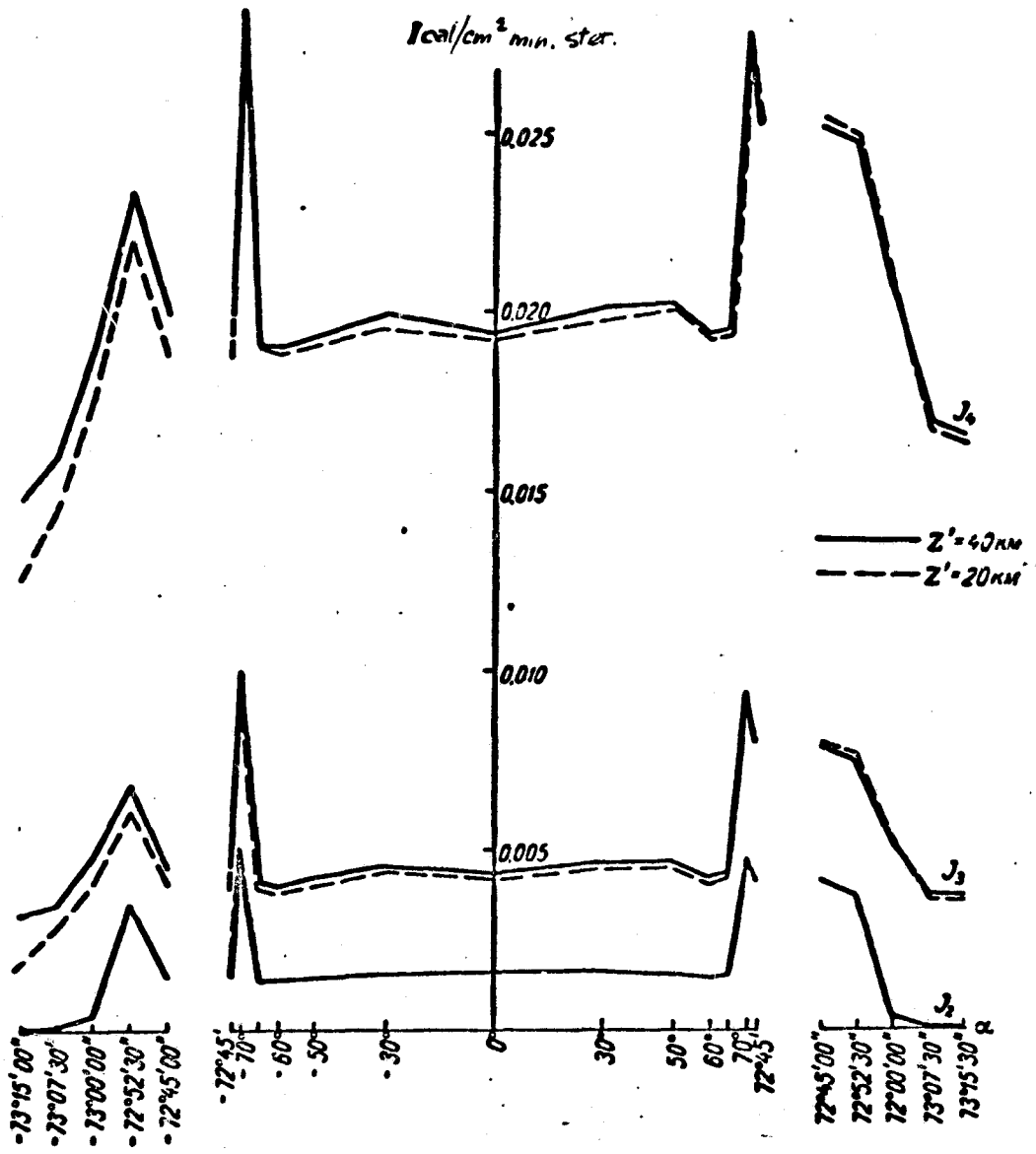

Fig. 2. Angular distribution of outgoing radiation in the spectral intervals of 10.55-11.01 μ (I_2), 4.88-8.70 μ (I_3), and 12-18 μ (I_4) for case 3.

The characteristics of the temperature and humidity distribution in the atmosphere also account for the relatively slight variations of I associated with the change in $|\alpha|$ from 73° to $73^\circ 15'$. The synoptic situations under consideration are in most cases characterized by temperature and humidity inversions above the tropopause (see Table 1). For this reason, the values of the factors determining the outgoing radiation may be approximately the same for all of the above-indicated directions. For instance, in case 2, $I(\alpha = 73^\circ) \approx I(\alpha = 73^\circ 07' 30'') \approx I(\alpha = 73^\circ 15')$. Here the decrease in the total absorbing mass with an increase in α is offset by a temperature and humidity inversion of the tropopause, as a result of which the part played by the upper atmosphere in the creation of I is relatively important. Let us note that similar results were obtained in Ref. [16], where it was shown that a pronounced infrared darkening towards the limb of the atmosphere slows down appreciably beginning at values of the zenith angle of 73°-$73^\circ 10'$.

As an example of a more detailed analysis of the influence of the horizontal inhomogeneity of the atmosphere on the values of the intensity of outgoing thermal radiation, let us examine the angular distribution of I in case 3 (see Fig. 1 and 2 and Appendix 3).

In the central portion of this section ($\alpha = 0 \div \pm 65^\circ$), a continuous cloudiness is observed, the height of the upper boundary of which is equal to about 10-12 km. At $\alpha = 0^\circ$ for all the spectral intervals under consideration, there is a relative minimum in the intensity of the outgoing radiation. The cause of this minimum is the low temperature of the surface of the clouds (-47.4°) and of the above-cloud atmosphere (starting from the upper boundary of the clouds up to a height of 20 km, the temperature fluctuates between -50 and -45°). As the values of $|\alpha|$

increase from 0 to 65°, the atmosphere becomes gradually warmer in the horizontal direction (up to ~ -42°). For zenithal angles of -30, 30 and 50°, the temperature of the upper boundary of the clouds is respectively equal to -45.5, -45 and -45°. Consequently, $I(\alpha = +50^\circ) \approx I(\alpha = \pm 30^\circ) > I(\alpha = 0^\circ)$. Subsequently, as the zenith angle increases, so does the height of the upper boundary of the clouds, and its temperature (see Appendix 3). As a result, $I(\alpha = -60^\circ) < I(\alpha = -50^\circ) < I(\alpha = -30^\circ)$ and $I(\alpha = 60^\circ) < I(\alpha = +50^\circ)$. In this case, the change in the horizontal distribution of the humidity in the atmosphere is not reflected by the results of the calculations of the intensity, and the determining factor in this case is the temperature of the radiating surface and of the atmosphere. A comparison of the I values of zenithal angles of $\pm$ 60 and $\pm$ 65° shows a slight increase in intensity in passing from $|\alpha| = 60^\circ$ to $|\alpha| = 65^\circ$, despite the fact that the temperature of the surface of the clouds remains unchanged. As in the preceding case, the increase in intensity is due to a warming of the atmosphere toward larger $|\alpha|$. It should be noted that in both of the indicated cases, an exception is the spectral region of 10.55-11.01 μ, where $I_2(\alpha = +30^\circ) \approx \approx I_2(\alpha = +50^\circ)$ and $I_2(\alpha = \pm 60^\circ) = I_2(\alpha = \pm 65^\circ)$. This is explained by a considerable transparency of the atmosphere in the spectral interval under consideration, as a result of which I_2 for small absorbing masses of water vapor practically depends only on the temperature of the radiation surface.

At a zenith angle of $\pm$ 70°, there are no clouds, and the radiating surface is the earth, with a temperature of about 19°. As a result, in all of the spectral regions under consideration there takes place a sharp increase in the values of the intensity of outgoing radiation.

Furthermore, the values of the intensity at $\alpha = -70^\circ$ slightly exceed its values at $\alpha = 70^\circ$. Apparently, this is caused by the fact that the water content of the atmosphere is greater at $\alpha = 70^\circ$.

The absorption of the ascending radiation of the earth in the atmosphere has a considerably greater effect on the results of calculations of the intensity of outgoing radiation at $\alpha = 72^\circ 45'$. In this case, in passing from $\alpha = 70^\circ$ to $\alpha = 72^\circ 45'$, the slope of the path of the ray through the atmosphere increases considerably, as a result of which $M_s^*(\alpha = 72^\circ 45') \gg M_s^*(\alpha = 70^\circ)$. ($M_s^*$ is the total absorbing mass of the atmosphere along the path of the ray). Thus, a small temperature rise (from 19 to 20.5°) is offset by an increase in the effective absorbing mass, and consequently $I(\alpha = 72^\circ 45') < I(\alpha = 70^\circ)$.

When $\alpha = 72^\circ 45'$, high cold clouds are observed, and therefore the curve of the intensity of outgoing thermal radiation has a sharp minimum in this case. Beginning with $\alpha = -72^\circ 52' 30''$, a typical picture of infrared darkening towards the limb of the atmosphere takes place (see Figs. 1 and 2). It should be mentioned that at zenith angles $\alpha = -72^\circ 45'$, $-73^\circ 15'$, the sighting ray crosses a dry and cold region of the atmosphere (at heights of 15 to 20 km, a temperature of the order of -55 to -50° is observed). In the stratosphere at heights $z > 24$ km, a considerable warming of the atmosphere takes place. For this reason, the values of $I(z' = 20)$ are considerably smaller than the values of $I(z' = 40)$, and the drop of the curve $I(z' = 20)$ at $\alpha > 73^\circ$ fails to slow down almost completely.

The case of $\alpha = 72^\circ 52' 30''$ is of particular interest because of the exceptional position of the clouds along the path of the ray. In this case, the sighting ray traverses the atmosphere at the lowest point of the ray's path (4.2 km), then continues to a height of 7 km, where it

meets the clouds. In other words, the main sources of radiation in this case are the surface of the clouds (with a temperature of -14°) and the warm layers of the lower troposphere at heights of about 4-5 km (with a temperature of the order of 0°). Since the path of the ray in the vicinity of its lowest point is practically parallel to the earth's surface, the mass of the atmosphere in the interval of 5-4.2-5 km is very large. As a result of this value, the intensities of the outgoing thermal radiation for $\alpha = 72^{\circ}52'30''$ are very high compared to the values of I in the case of $z_0 = 0$. It should be noted that an analysis of the stratification of the atmosphere based on the data of a determination of outgoing radiation intensity is rather difficult in this case.

When $\alpha \geq 73^{\circ}$ a typical picture of infrared darkening towards the limb of the atmosphere is observed. It should be mentioned that in this case, relatively high temperatures (of the order of -45, -40°) prevail in the lower stratosphere (15 - 25 km) and that the temperature and specific humidity rise very quickly with the altitude (q increases from 0.1 g/kg at an altitude of 15 km to 1.2 g/kg at 25 km). For this reason, the values $I(\alpha = 73^{\circ}07'30'')$ and $I(\alpha = 73^{\circ}15')$ are exceptionally high, while the values of the intensity at $z' = 20$ km differ little from the corresponding values at $z' = 40$ km.

From a practical standpoint, the angular distribution of the intensity of outgoing radiation in case 1, when $\alpha = 65\text{-}73^{\circ}$, is of particular interest (see Fig. 1 and Appendix 1). Since in passing from $\alpha = 65^{\circ}$ to $\alpha = 70^{\circ}$ there is a sharp drop in the intensity curve, then by measuring this intensity one might erroneously assume that an infrared darkening towards the limb of the atmosphere is observed and that the limb of the earth's disk has already been passed. Actually, when $\alpha = 65^{\circ}$ there are

no clouds, and when $\alpha = 70^\circ$, high cold clouds appear ($t_{z_o} = -65^\circ$), as a result of which the values of the radiation intensity decrease sharply. When $\alpha = 70\text{-}73^\circ$, the values of I undergo almost no change. The infrared darkening towards the limb of the atmosphere is masked by the presence of the high cold clouds of the atmosphere. Hence, it follows that in this case one should not determine the limb of the earth's disk solely by means of the data obtained by measuring the outgoing thermal radiation.

Taking into consideration the limited scope of this article, we shall not analyze in detail the angular distribution of the outgoing radiation for other sections of the atmosphere. It is clear, however, that the laws and principles of the analysis are similar for all the cases under consideration.

As we know from the general theory of the transfer of thermal radiation in the atmosphere, the effect of any atmospheric layer on ascending thermal radiation depends on the temperature of the radiating surface, distribution of temperature in the atmosphere and content and distribution of the substances absorbing (radiating) thermal radiation in the atmosphere. For $\alpha > 72^\circ 45'$ in clear weather, as a rule $I(z' = 40) > I(z' = 20)$, since the only radiator in this case is the atmosphere itself, and the absorbing mass for the case of $z' = 40$ km is always greater than for the case of $z' = 20$ km. If the outgoing radiation consists of radiation of the earth's surface (or clouds) and of atmospheric radiation, and the temperature of the atmosphere decreases with increasing altitude, then $I(z' = 40) < I(z' = 20)$. In the case of temperature inversion, the effect of the 20-40 km layer may be considerably diversified [$I(z' = 40) \begin{matrix} \leq \\ \geq \end{matrix} I(z' = 20)$]. This is also reflected by the results of the present work (Appendices 1-6 and Figs. 1 and 2). It turns out that the 20-40 km layer

of the atmosphere appreciably affects the value of the outgoing radiation intensity only when $\alpha > 72^{\circ}45'$, and for smaller zenith angles, the differences $I(z' = 40) - I(z' = 20)$ are within the limits of error of the determination of I. For example, when $|\alpha| < 72^{\circ}45'$, the ratios $\frac{I_1(z' = 40) - I_1(z' = 20)}{I_1(z' = 40)}$ do not exceed $\sim$2%, and the ratios $\frac{I_3(z' = 40) - I_3(z' = 20)}{I_3(z' = 40)}$ - $\sim$4%. When $|\alpha| > 72^{\circ}45'$ in clear weather, these ratios are quite variable ($\sim$1-40%) depending upon the specific stratification of the atmosphere. The insignificant role of the 20-40 km layer of the atmosphere in the creation of outgoing radiation of the earth and atmosphere is chiefly explained by the low pressures in the upper atmosphere, as a result of which the effective absorbing masses are very small there. For instance, even assuming that q = 0.2 g/kg ("humid stratosphere") the effective water vapor content in the 30-40 km layer is only 0.000035 cm when $\alpha = 0^{\circ}$ and 0.000348 cm when $\alpha = 72^{\circ}45'$. However, as was mentioned above, the role of the upper atmosphere in the creation of I is considerably greater for $\alpha = 72^{\circ}45'$ in clear weather, when the source of the outgoing thermal radiation is only the atmosphere itself. Therefore, an accurate calculation of the intensity of outgoing radiation for $\alpha > 72^{\circ}45'$ requires the knowledge of the stratification of the atmosphere up to altitudes of $\sim$40-50 km.

Appendices 7-9 contain values of the ratios $\frac{I_2}{I_1}$, $\frac{I_3}{I_1}$, and $\frac{I_4}{I_1}$ (in %). This makes it possible to evaluate the intensities of the radiation in the spectral regions under consideration as compared to the integral intensity I_1. The thermal radiation in the interval of 10.55-11.01 μ does not exceed about 5% of the integral radiation, and in the intervals of 4.88-8.70 μ and 12-18 μ, it amounts to 4-10% and 27-36% of I_1, respectively. The ratio $\frac{I_2}{I_1}$ depends strongly on the temperature t_{z_o}. In cloudy

weather, $\frac{I_2}{I_1}$ is approximately one-half its value in clear weather, when $\alpha < 72^\circ 45'$. In the case of absence of a radiating surface ($\alpha > 72^\circ 45'$), I_2 for a cloudless sky is only 0.02-0.2% of the values of I_1.

In the absence of clouds for $\alpha < 72^\circ 45'$, the values of $\frac{I_3}{I_1}$ for winter soundings are 7-8% and 9-10% in summer. For a "cold radiator" (cloudy sky for all α values, and also in the case where the radiator is only the atmosphere above 10 km), the values of $\frac{I_3}{I_1}$ amount to 4-5%. One can assume that the ratio $\frac{I_3}{I_1}$ depends not only on the temperature of the radiating surface but also on the temperature distribution of the atmosphere.

The ratio $\frac{I_4}{I_1}$ is practically independent of the temperature of the radiating surface and atmosphere; the cloudiness conditions are also very weakly reflected by its values (see Appendices 9 and 1-6). In the case where $\alpha < 72^\circ 45'$, $\frac{I_4}{I_1}$ undergoes little change and varies between 26 and 29%. In cloudy weather, it is somewhat greater than in clear weather. In the case where $\alpha > 72^\circ 45'$, the values of $\frac{I_4}{I_1}$ increase with an increase in the zenith angle. Hence it follows that the relative part played by carbon dioxide in the upper atmosphere is greater than in the vicinity of the earth's surface.

In order to evaluate the relative part played by the content of water vapor in the atmosphere and by the temperature of the radiating surface in the creation of outgoing thermal radiation, let us examine the correlation between I and w_s^* and between I and t_{z_o}. Typical examples of such correlations are given in Figs. 3-5. It turns out that the correlation between I and w_s^* for all of the spectral intervals considered is relatively weak. The scatter of the points is particularly great for large values of w_s^*. This is apparently a manifestation of

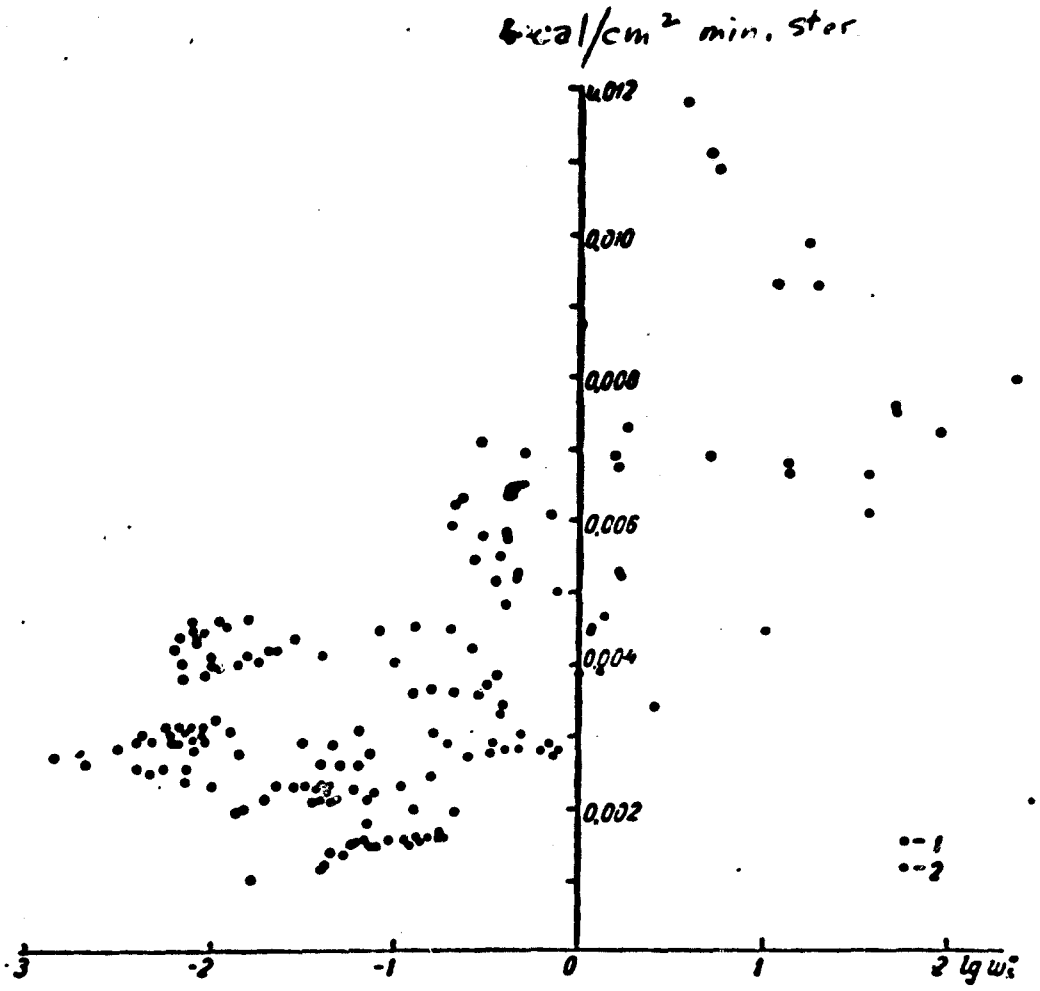

Fig. 3. Correlation between the effective content of water vapor in the atmosphere and the outgoing radiation within the spectral interval of 4.88-8.70μ.

1 - in clear weather for $\alpha > 72^{\circ}45'$, 2 - in the presence of a radiating surface in the atmosphere.

the vertical distribution of temperature in the atmosphere, on which the contribution of individual layers of the atmosphere to the creation of I is substantially dependent. In cloudless weather, there is a somewhat better correlation between I and w_s^* for $\alpha > 72^{\circ}45'$. This is explained by the absence of a radiating surface in this case, the radiation of such a surface playing an important part in the creation of outgoing radiation. Indeed, as is apparent from Fig. 4 and 5, there is a fairly good correlation between I and t_{z_o}, particularly for the interval of 10.55-11.01 μ, where the absorption (radiation) by the atmosphere is slight. The dependence of I on t_{z_o} is somewhat less pronounced in the case of summer

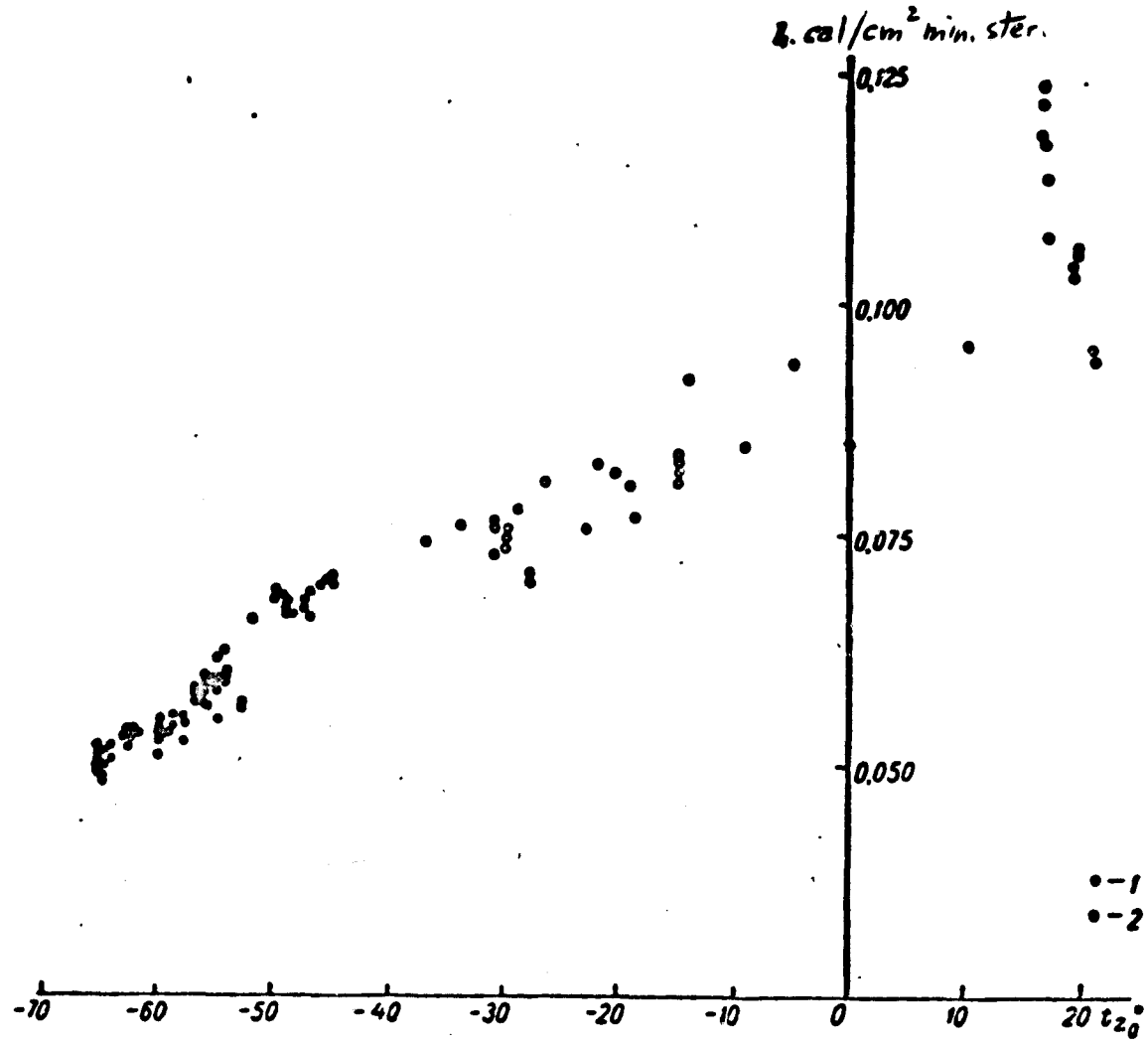

Fig. 4. Correlation between the temperature of the radiating surface and the integral outgoing radiation.

1 - for cases where $z_o \neq 0$; 2 - for cases where $z_o = 0$.

soundings during clear weather, when the relative part played by the humid and warm atmosphere in the creation of I is very important.

As already mentioned, additional calculations of the outgoing radiation with the use of $\bar{f}_\Delta$ were carried out in the present article in order to estimate the accuracy of such a determination of I for various spectral intervals (Fig. 6). Results of these calculations show that for spectral regions of 12-18 and 10.55 and 11.01 μ, the use of average values of f_Δ gives satisfactory results whose deviations from the exact values of I do not exceed about 0.001 cal $cm^{-2}min^{-1}ster^{-1}$ (in most cases, they were within 0.0001-0.0003 cal $cm^{-2}min^{-1}ster^{-1}$). However, for the interval

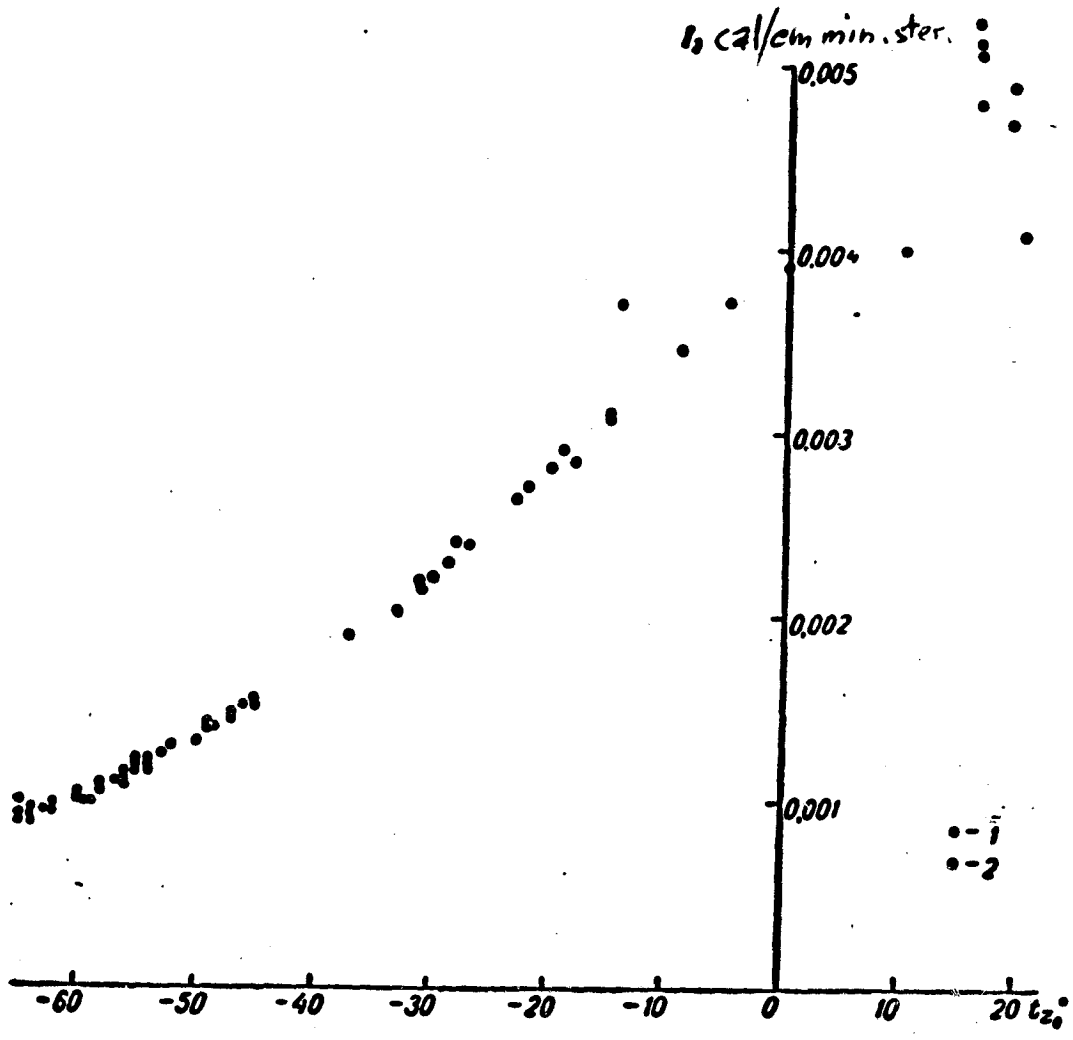

Fig. 5. Correlation between the temperature of the radiating surface and the outgoing radiation within the spectral interval of 10.55-11.01 μ.

1 - for cases where $z_o \neq 0$; 2 - for cases where $z_o = 0$.

4.88-8.70 μ, the use of $\bar{f}$ involves fairly large errors. In this case, the values of $\bar{f}_\Delta$ which were determined for clear weather should not be used in the presence of clouds, and vice versa. Because of the rapid variability of the function $f_\Delta(T)$ with the temperature in the interval of 4.88-8.70 μ, the use of $\bar{f}_\Delta$ should be considered inadvisable here.

Table 2 lists the main seasonal values of the intensity of outgoing radiation for the latitude 65° N.L. taken from Ref. [16]. Since the calculations of the present work were based on meteorological data in temperate latitudes (45-65° N.L.), the mean seasonal values of I for 65°

N.L. may be to some extent characteristic of the cases considered in the present work as well.

Comparison of the data in Table 2 with our results (Appendices 1-6) permits an approximate estimate of the deviation of specific values of the outgoing radiation intensity from its main climatological values. Thus, it is possible to account in some measure for the influence of the horizontal inhomogeneities of the atmosphere and of the characteristics of a specific, real stratification of the atmosphere on the intensity of outgoing thermal radiation. For example, in case 1a, the differences $I_{1,av}-I_1$, $I_{2,av}-I_2$, $I_{3,av}-I_3$, and $I_{4,av}-I_4$ are respectively equal to 0.020, 0.0006, 0.0021, and 0.006 cal $cm^{-2}min^{-1}ster^{-1}$ (27, 35, 44 and 29% of the value of I_{av}). The differences $I_{av}-I$ at $\alpha > 72^{\circ}45'$ are very variable; they amount to over 50% of I_{av} in some cases (cf. Table 2 and Appendices 1-6). Thus, the deviations from the mean climatological values of the intensity of outgoing thermal radiation may be very large in certain synoptic situations.

Summarizing all of the above, we shall note that the horizontal inhomogeneity of the atmosphere has an appreciable effect on the angular intensity distribution of outgoing radiation. Whereas in the "model atmosphere" the angular distribution of I is characterized by a relatively smooth curve, for the case of a real atmosphere the dependence of the intensity of outgoing radiation on the zenith angle and azimuth is very variable and has sharp maxima and minima. Hence, in calculating fluxes of outgoing radiation under actual conditions, it is necessary to take into account as accurately as possible the change in intensity of the zenith angle and azimuth.

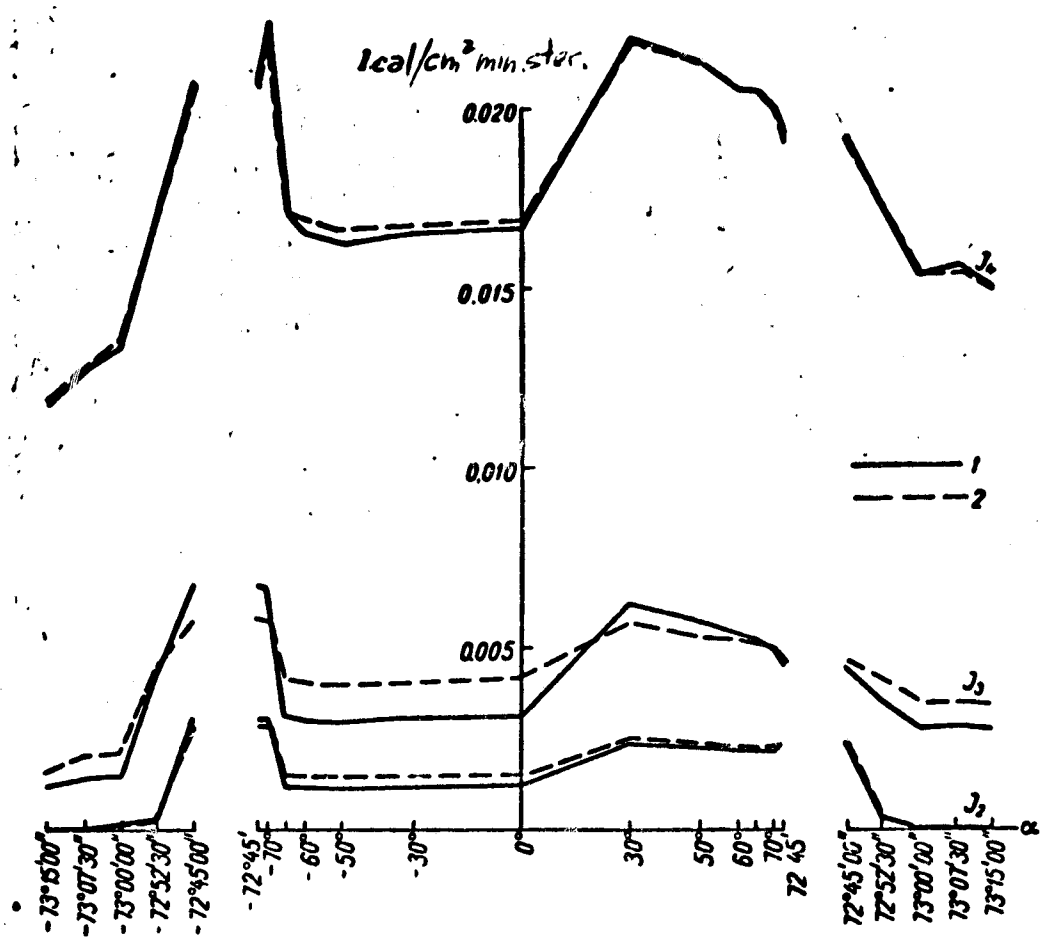

Fig. 6. Angular distribution of outgoing radiation within spectral intervals of 10.55-11.01 μ (I_2), 4.88-8.70 μ (I_3), and 12-18 μ (I_4) for case 2, assuming that $z' = 40$ km.

1 - from formulas (1) and (2); 2 - from formulas (1) and (3), where $\bar{f}_A$ for the above indicated spectral intervals is equal to 0.026, 0.070 and 0.28, respectively.

Table 2

Mean seasonal values of the intensity of outgoing thermal radiation in the case where $\varphi = 65°$ N.L. (cal $cm^{-2} min^{-1} ste.^{-1}$)

	$\alpha = 0°$		$\alpha = 72°45'$		$\alpha = 72°54'$	
	$z_0 = 0$	$z_0 = 9$ км	$z_0 = 0$	$z_0 = 9$ км	$z_0 = 0$	$z_0 = 9$ км
I_1	0,118	0,073	0,092	0,072	0,075	0,074
I_2	0,0048	0,0017	0,0037	0,0017	0,0015	0,0017
I_3	0,0125	0,0048	0,0070	0,0048	0,0058	0,0048
I_4	0,032	0,021	0,027	0,021	0,025	0,022

The authors express their thanks to V. I. Yegorova, who analyzed and prepared the meteorological material for this work.

REFERENCES

1. Kondrat'yev, K. Ya. Luchistyy teploobmen v atmosfere [Radiant Heat Transfer in the Atmosphere]. Gidrometeoizdat, Leningrad, 1956.
2. Kondrat'yev, K. Ya. Meteorologicheskiye issledovaniya s pomoshch'yu raket i sputnikov [Meteorological Research by Means of Rockets and Satellites]. Gidrometeoizdat, Leningrad, 1962.
3. Kondrat'yev, K. Ya., Filippovich, O. P. Ob ukhodyashchem izluchenii [On Outgoing Radiation]. Vestn. LGU, No. 6, 1952.
4. Hales, I. V., Zdunkowski, W. G. The long wave flux density the Earth under various meteorological conditions. AFCRC-TN-59-212. Cambridge, 1959.
5. Hales, I. V., Williams, T. L., Henderson, D. Calculation of infrared radiative flux emission of the Earth plus atmosphere at various levels high above the Earth. Final Report, AFCRL-TR-60-405, Aug. 1960.
6. London, J. A. Study of atmospheric heat balance. Final Report. Contr. No. AF 19 (122) - 165, 1957.
7. Houghton, H. G. On the annual heat balance of the Northern Hemisphere. J. Met., 11, No. 1, 1954.
8. Ohring, G. J. Met., 15, No. 5, 1958.
9. Manabe, S., Moeller, F. Month. Weath. Rev., 89, No. 12, 1961.
10. Davis, P. A. A reexamination of the heat budget of the troposphere and lower stratosphere. Sci. Rep., No. 3, AF 19 (604) - 6146, New York University. Oct. 1961.
11. McGee, R. A. Applied Optics, 1, No. 5, 1962.
12. Hanel, R. A., Bandeen, W. R., Conrath, B. I. The infrared horizon of the planet Earth. Goddard Space Flight Center, MD., 1962.
13. Greenfield, S. M., Kellog, W. W. Calculations of atmospheric infrared radiation as seen from a meteorological satellite. J. Met., v. 17, No. 3, 1960.
14. Moeller, F. Der Strahlungchaushalt der Troposphare. Met. Rund., Bd. 13, H. 3, 1960.
15. Wexler, R. Satellite observations of infrared radiation Second Semi-Annual Technical Summary Report. Contr. No. AF 19 (604) - 5968, 1960.
16. Kondrat'yev, K. Ya., Yakushevskaya, K. Ye. Uglovoye raspredeleniye ukhodyashchego teplogo izlucheniya v razlichnykh oblastyakh spektra [Angular Distribution of Outgoing Thermal Radiation in Various Regions of the Spectrum]. Isk. sputniki Zemli, vyp. 14, 1962.
17. Niylisk, Kh. Yu. Issledovaniya po fizike atmosfery [Studies in Atmospheric Physics], No. 2. Trudy IFA AN ESSR, 1960.
18. Idem. Ibid., No. 3, 1962.
19. Idem. K voprosu o teplovom izluchenii atmosfery. Avtoreferat diss. [On the Problem of Thermal Radiation of the Atmosphere. Author's summary of dissertation], Tartu, 1962.
20. Arkhangel'skiy, V. N., Sukhotskiy, Ye. I. Meteorolgiya i gidrologiya [Meteorology and Hydrology], No. 5, 1958.
21. Ramanathan, K. R., Kulkarni, R. N. Quart. J. Roy. Met. Soc. v. 86, No. 368, 1960
22. Murcray, D. G., Murcray, F. H., Williams, W. I., Leslie, F. E. J. Geophys. Res., v. 65, No. 11, 1960.

23. Mastenbrook, H. I., Dinger, I. E. J. Geophys. Res., v. 66, No. 5, 1961.
24. Gutnick, M. How dry is the sky? J. Geophys. Res., v. 66, No. 9, 1961.
25. Barclay, F. R., Elliot, M. J. W., Coldsmith, P., Jelley, J. V. A. A direct measurement of the humidity in the stratosphere using a cooledvapour trap. Quart. J. Roy. Met. Soc., v. 86, No. 368, 1960.
26. Houghton, J. T., Seeley, J. S. Quart. J. Roy. Met. Sos., v. 86, No. 369, 1960.
27. Moeller, F. J. Met., v. 17, No. 5, 1960.
28. Moeller, F. Atmospheric water vapour measurements at 6.7 microns from a satellite. Planet. Space Sci., v. 5, No. 3, 1961.

Appendix 1

Values of the intensity of outgoing radiation of the earth and atmosphere for case 1

φ	z_0 km	$t^\circ_{z_0}$	w^*_z cm		I_1		I_2		I_3		I_4	
					cal/cm^{-2} min^{-1} ster^{-1}							
			$z' = 20$	$z' = 40$	$z' = 20$	$z' = 40$	$z' = 20$	$z' = 40$	$z' = 20$	$z' = 40$	$z' = 20$	$z' = 40$
−73°15′00″	—	—	0,144	0,171	0,0342	0,0370	0,00001	0,00002	0,00157	0,00161	0,0109	0,0124
−73 07 30	—	—	0,152	0,172	0,0347	0,0372	0,00001	0,00002	0,00161	0,00166	0,0115	0,0128
−73 00 00	11,0	−62,8	0,039	0,045	0,0516	0,0532	0,00095	0,00095	0,00229	0,00233	0,0143	0,0155
−72 52 30	11,0	−62,5	0,028	0,034	0,0519	0,0535	0,00096	0,00096	0,00229	0,00231	0,0143	0,0153
−72 45 00	11,0	−62,8	0,023	0,028	0,0512	0,0532	0,00095	0,00095	0,00230	0,00232	0,0141	0,0153
−70°	0,0	0,0	5,07	5,08	0,0847	0,0847	0,00390	0,00390	0,00688	0,00688	0,0216	0,0220
−65	0,0	−9,0	1,76	1,76	0,0850	0,0850	0,00344	0,00344	0,00730	0,00730	0,0219	0,0222
−60	0,0	−19,2	1,53	1,53	0,0808	0,0805	0,00292	0,00292	0,00692	0,00692	0,0209	0,0213
−50	0,0	−20,4	0,518	0,518	0,0818	0,0818	0,00283	0,00283	0,00696	0,00696	0,0209	0,0212
−30	0,0	−22,0	0,296	0,296	0,0826	0,0826	0,00273	0,00273	0,00713	0,00713	0,0212	0,0213
0	0,0	−31,0	0,212	0,212	0,0770	0,0770	0,00220	0,00220	0,00620	0,00620	0,0198	0,0200
30	0,0	−31,0	0,206	0,206	0,0758	0,0758	0,00218	0,00218	0,00590	0,00590	0,0195	0,0197
50	0,0	−31,0	0,272	0,272	0,0732	0,0732	0,00220	0,00220	0,00543	0,00543	0,0191	0,0194
60	0,0	−23,0	0,400	0,400	0,0760	0,0760	0,00266	0,00266	0,00579	0,00579	0,0197	0,0201
65	0,0	−18,5	0,686	0,687	0,0770	0,0770	0,00287	0,00287	0,00607	0,00607	0,0198	0,0204
70	9,0	−65,0	0,014	0,015	0,0481	0,0493	0,00089	0,00089	0,00199	0,00199	0,0130	0,0138
72°45′00″	8,9	−65,0	0,036	0,040	0,0500	0,0519	0,00100	0,00100	0,00210	0,00212	0,0134	0,0148
72 52 30	8,9	−65,0	0,045	0,049	0,0498	0,0514	0,00089	0,00089	0,00212	0,00214	0,0138	0,0149
73 00 00	8,9	−65,0	0,073	0,078	0,0506	0,0522	0,00089	0,00089	0,00216	0,00221	0,0140	0,0150
73 07 30	—	—	0,124	0,138	0,0347	0,0366	0,00001	0,00002	0,00153	0,00157	0,0115	0,0126
73 15 00	—	—	0,076	0,094	0,0331	0,0353	0,00001	0,00001	0,00149	0,00155	0,0113	0,0124

Appendix 2

Values of the intensity of outgoing radiation of the earth and atmosphere for case 2

φ	z_0 km	i'_{z_0}	w'_s cm		I_1		I_2		I_3		I_4	
					cal/cm^{-2} min.$^{-1}$ ster.$^{-1}$							
			$z' = 20$	$z' = 40$	$z' = 20$	$z' = 40$	$z' = 20$	$z' = 40$	$z' = 20$	$z' = 40$	$z' = 20$	$z' = 40$
−73°15′00″	—	—	0,017	0,040	0,0277	0,0310	0,00001	0,00001	0,00102	0,00115	0,0107	0,0108
−73 07 30	—	—	0,045	0,052	0,0328	0,0342	0,00001	0,00001	0,00140	0,00140	0,0117	0,0128
−73 00 00	—	—	0,060	0,068	0,0337	0,0363	0,00001	0,00002	0,00151	0,00153	0,0124	0,0134
−72 52 30	—	—	1,18	1,18	0,0548	0,0563	0,00025	0,00027	0,00445	0,00446	0,0166	0,0173
−72 45 00	0,0	−15,0	13,6	13,6	0,0810	0,0818	0,00308	0,00308	0,00679	0,00683	0,0201	0,0208
−70°	0,0	−15,0	1,61	1,61	0,0837	0,0840	0,00310	0,00310	0,00675	0,00678	0,0221	0,0225
−65	9,9	−54,4	0,0090	0,0105	0,0592	0,0602	0,00118	0,00118	0,00314	0,00318	0,0165	0,0171
−60	9,1	−55,4	0,0060	0,0074	0,0582	0,0595	0,00118	0,00118	0,00301	0,00306	0,0163	0,0166
−50	9,1	−56,2	0,0080	0,0091	0,0575	0,0582	0,00116	0,00116	0,00297	0,00297	0,0161	0,0163
−30	9,8	−54,9	0,0066	0,0075	0,0576	0,0592	0,00120	0,00120	0,00310	0,00310	0,0164	0,0166
0	10,0	−54,4	0,0059	0,0067	0,0592	0,0595	0,00122	0,00122	0,00314	0,00314	0,0166	0,0167
30	0,0	−27,0	0,234	0,236	0,0805	0,0808	0,00241	0,00241	0,00628	0,00628	0,0218	0,0220
50	0,0	−28,8	0,291	0,293	0,0777	0,0777	0,00230	0,00230	0,00577	0,00581	0,0211	0,0213
60	0,0	−30,0	0,372	0,376	0,0764	0,0764	0,00223	0,00223	0,00552	0,00552	0,0204	0,0206
65	0,0	−30,0	0,458	0,468	0,0751	0,0751	0,00223	0,00223	0,00526	0,00530	0,0202	0,0205
70	0,0	−30,0	0,754	0,761	0,0729	0,0735	0,00224	0,00224	0,00501	0,00501	0,0195	0,0201
72°45′00″	0,0	−28,2	9,74	9,76	0,0703	0,0713	0,00243	0,00243	0,00446	0,00448	0,0188	0,0193
72 52 30	—	—	2,47	2,52	0,0546	0,0557	0,00036	0,00037	0,00344	0,00348	0,0168	0,0173
73 00 00	—	—	0,760	0,814	0,0470	0,0483	0,00008	0,00010	0,00276	0,00280	0,0148	0,0155
73 07 30	—	—	0,651	0,710	0,0475	0,0485	0,00009	0,00011	0,00279	0,00289	0,0152	0,0158
73 15 00	—	—	0,400	0,479	0,0462	0,0481	0,00005	0,00007	0,00282	0,00284	0,0145	0,0150

Appendix 3

Values of the intensity of outgoing radiation of the earth and atmosphere for case 3

φ	z_0 km	$t^\circ_{z_0}$	w°_z cm		I_1		I_2		I_3		I_4	
					cal/cm^{-2} min.$^{-1}$ ster.$^{-1}$							
			$z' = 20$	$z' = 40$	$z' = 20$	$z' = 40$	$z' = 20$	$z' = 40$	$z' = 20$	$z' = 40$	$z' = 20$	$z' = 40$
—73°15′00″	—	—	0,070	0,165	0,0360	0,0458	0,00001	0,00002	0,00178	0,00306	0,0125	0,0147
—73 07 30	—	—	0,331	0,385	0,0455	0,0503	0,00005	0,00005	0,00276	0,00340	0,0145	0,0159
—73 00 00	—	—	1,34	1,39	0,0544	0,0606	0,00026	0,00027	0,00399	0,00467	0,0176	0,0190
—72 52 30	—	—	35,5	35,5	0,0799	0,0837	0,00344	0,00344	0,00611	0,00666	0,0219	0,0233
—72 45 00	10,6	—47,0	0,098	0,125	0,0655	0,0694	0,00148	0,00148	0,00463	0,00450	0,0187	0,0199
—70°	0,0	19,3	16,6	16,6	0,1057	0,1054	0,00188	0,00186	0,00989	0,00989	0,0282	0,0280
—65	12,0	—52,0	0,0091	0,014	0,0659	0,0665	0,00129	0,00129	0,00386	0,00403	0,0190	0,0190
—60	12,0	—52,0	0,0069	0,011	0,0656	0,0662	0,00129	0,00129	0,00382	0,00395	0,0188	0,0190
—50	11,2	—49,0	0,0069	0,010	0,0672	0,0678	0,00139	0,00139	0,00403	0,00414	0,0190	0,0192
—30	10,2	—45,5	0,0068	0,0090	0,0700	0,0703	0,00155	0,00155	0,00437	0,00446	0,0195	0,0199
0	10,0	—47,4	0,0062	0,0084	0,0678	0,0688	0,00147	0,00147	0,00420	0,00429	0,0192	0,0194
30	10,0	—45,0	0,0079	0,011	0,0703	0,0710	0,00156	0,00156	0,00446	0,00458	0,0198	0,0201
50	10,4	—45,0	0,012	0,016	0,0707	0,0713	0,00153	0,00153	0,00454	0,00463	0,0201	0,0202
60	11,2	—50,0	0,016	0,023	0,0678	0,0681	0,00136	0,00136	0,00414	0,00424	0,0192	0,0194
65	11,3	—50,0	0,021	0,029	0,0688	0,0694	0,00136	0,00136	0,00420	0,00437	0,0194	0,0195
70	0,0	19,0	19,0	19,0	0,1038	0,1028	0,00472	0,00472	0,00929	0,00929	0,0278	0,0276
72°45′00″	0,0	20,5	221	221	0,0949	0,0936	0,00407	0,00407	0,00798	0,00794	0,0256	0,0252
72 52 30	7,0	—14,0	50,4	50,4	0,0920	0,0907	0,00373	0,00373	0,00760	0,00751	0,0250	0,0248
73 00 00	—	—	1,63	1,70	0,0649	0,0643	0,00034	0,00034	0,00530	0,00526	0,0205	0,0204
73 07 30	—	—	0,291	0,375	0,0516	0,0525	0,00005	0,00006	0,00361	0,00386	0,0167	0,0169
73 15 00	—	—	0,206	0,319	0,0512	0,0516	0,00004	0,00005	0,00361	0,00373	0,0164	0,0166

Appendix 4

Values of the intensity of outgoing radiation of the earth and atmosphere for case 1a

φ	z_0 km	$t^\circ_{z_0}$	w°_s cm	I_1	I_2	I_3	I_4
				cal/cm^{-2} min.$^{-1}$ ster.$^{-1}$			
—73°15′00″	—	—	0,043	0,0256	0,00001	0,00123	0,0092
—73 07 30	—	—	0,186	0,0313	0,00002	0,00161	0,0108
—73 00 00	9,7	—54,9	0,074	0,0549	0,00119	0,00276	0,0153
—72 52 30	9,2	—53,0	0,047	0,0564	0,00126	0,00293	0,0154
—72 45 00	9,0	—53,0	0,032	0,0566	0,00126	0,00293	0,0155
—70°	10,0	—64,5	0,014	0,0516	0,00091	0,00225	0,0142
—65	9,9	—58,8	0,0082	0,0542	0,00107	0,00276	0,0155
—60	9,8	—56,5	0,0063	0,0577	0,00116	0,00289	0,0157
—50	9,2	—56,0	0,0048	0,0565	0,00116	0,00293	0,0158
—30	9,0	—57,9	0,0019	0,0544	0,00110	0,00276	0,0153
0	9,0	—58,0	0,0014	0,0526	0,00110	0,00272	0,0151
30	9,2	—59,0	0,0021	0,0536	0,00107	0,00259	0,0148
50	9,4	—59,3	0,0041	0,0536	0,00107	0,00255	0,0148
60	9,6	—60,0	0,0055	0,0527	0,00104	0,00250	0,0147
65	9,7	—60,0	0,0073	0,0536	0,00104	0,00255	0,0148
70	0,0	—5,0	1,03	0,0935	0,00372	0,00862	0,0232
72°45′00″	10,0	—60,0	0,039	0,0511	0,00104	0,00263	0,0153
72 52 30	10,2	—60,0	0,049	0,0541	0,00104	0,00263	0,0152
73 00 00	10,0	—60,0	0,065	0,0544	0,00104	0,00263	0,0153
73 07 30	—	—	0,207	0,0343	0,00002	0,00197	0,0116
73 15 00	—	—	0,130	0,0333	0,00002	0,00199	0,0107

Appendix 5

Values of the intensity of outgoing radiation of the earth and atmosphere for case 2a

φ	z_0 km	$t^\circ_{z_0}$	w°_s cm	I_1	I_2	I_3	I_4
				cal/cm^{-2} min.$^{-1}$ ster.$^{-1}$			
—73°15′00″	—	—	0,064	0,0281	0,00001	0,00153	0,0099
—73 07 30	—	—	0,115	0,0307	0,00001	0,00155	0,0106
—73 00 00	11,1	—65,0	0,060	0,0503	0,00090	0,00225	0,0140
—72 52 30	11,0	—65,0	0,044	0,0500	0,00090	0,00225	0,0141
—72 45 00	10,7	—64,2	0,038	0,0505	0,00097	0,00229	0,0141
—70°	10,0	—65,0	0,020	0,0485	0,00091	0,00214	0,0138
—65	10,0	—65,0	0,0098	0,0513	0,00094	0,00228	0,0145
—60	10,0	—64,1	0,0073	0,0524	0,00097	0,00236	0,0147
—50	9,8	—62,0	0,0047	0,0532	0,00099	0,00246	0,0152
—30	9,4	—58,6	0,0032	0,0551	0,00110	0,00280	0,0159
0	9,0	—56,4	0,0043	0,0575	0 00115	0,00301	0,0164
30	9,0	—56,5	0,0039	0,0574	0,00114	0,00293	0,0162
50	9,0	—56,1	0,0068	0,0572	0,00113	0,00293	0,0162
60	9,0	—56,0	0,0089	0,0586	0,00112	0,00300	0,0166
65	9,0	—56,6	0,013	0,0582	0,00111	0,00304	0,0164
70	8,8	—56,0	0,062	0,0594	0,00115	0,00311	0,0170
72°45′00″	8,0	—54,8	0,129	0,0624	0,00118	0,00364	0,0173
72 52 30	8,0	—55,0	0,171	0,0620	0,00120	0,00365	0,0179
73 00 00	—	—	0,492	0,0457	0,00006	0,00301	0,0155
73 07 30	—	—	0,344	0,0429	0,00005	0,00289	0,0143
73 15 00	—	—	0,163	0,0368	0,00002	0,00246	0,0119

Appendix 6

Values of the intensity of outgoing radiation of the earth and atmosphere for case 3a

φ	z_0 km	$t^\circ_{z_0}$ km	w°_s cm	I_1	I_2	I_3	I_4
				cal/cm^{-2} min.$^{-1}$ ster.$^{-1}$			
—73°15′00″	—	—	0,200	0,0401	0,00003	0,00293	0,0131
—73 07 30	—	—	0,378	0,0465	0,00004	0,00331	0,0153
—73 00 00	—	—	1,02	0,0516	0,00016	0,00395	0,0183
—72 52 30	—	—	13,6	0,0808	0,00230	0,00662	0,0231
—72 45 00	0,0	10,0	89,1	0,0955	0,00400	0,00717	0,0240
—70°	10,2	—45,5	0,083	0,0698	0,00153	0,00447	0,0201
—65	10,7	—48,6	0,041	0,0665	0,00139	0,00412	0,0192
—60	11,0	—49,0	0,018	0,0678	0,00140	0,00403	0,0190
—50	11,0	—49,0	0,010	0,0671	0,00139	0,00399	0,0189
—30	11,0	—49,0	0,0070	0,0665	0,00139	0,00399	0,0190
0	0,0	16,2	2,18	0,1219	0,00524	0,0132	0,0331
30	0,0	16,2	2,65	0,1232	0,00525	0,0133	0,0327
50	0,0	16,2	3,81	0,1179	0,00521	0,0124	0,0314
60	0,0	16,2	5,10	0,1171	0,00513	0,0114	0,0305
65	0,0	16,3	5,56	0,1135	0,00507	0,0109	0,0297
70	0,0	16,4	11,6	0,1074	0,00482	0,00934	0,0274
72°45′00″	8,3	—34,0	0,352	0,0762	0,00204	0,00514	0,0211
72 52 30	8,5	—37,0	0,392	0,0749	0,00191	0,00484	0,0207
73 00 00	9,8	—46,0	0,271	0,0698	0,00152	0,00424	0,0194
73 07 30	—	—	0,248	0,0409	0,00003	0,00270	0,0139
73 15 00	—	—	0,108	0,0358	0,00001	0,00229	0,0117

Appendix 7

Value of the ratio $\frac{I_2}{I_1}$ (%)

φ	z'=20 km	z'=40 km	z'=20 km	z'=40 km	z'=20 km	z'=40 km	z'=20 km		
	1		2		3		1a	2a	3a
—73°15′00″	0,02	0,05	0,04	0,03	0,03	0,04	0,04	0,03	0,07
—73 07 30	0,03	0,05	0,03	0,02	0,01	0,10	0,06	0,03	0,08
—73 00 00	0,18	0,18	0,03	0,06	0,48	0,44	2,17	1,79	0,31
—72 52 30	0,19	0,18	0,46	0,48	4,31	4,11	2,23	1,80	2,85
—72 45 00	0,19	0,19	3,80	3,77	2,26	2,13	2,23	1,92	4,19
—70°	4,60	4,60	3,70	3,69	4,62	4,61	1,76	1,88	2,19
—65	4,05	4,05	1,99	1,96	1,96	1,94	1,97	1,83	2,09
—60	3,61	3,63	2,03	1,98	1,97	1,95	2,01	1,85	2,06
—50	3,46	3,46	2,02	1,99	2,07	2,05	2,05	1,86	2,07
—30	3,31	3,31	2,08	2,03	2,21	2,20	2,02	2,00	2,09
0	2,86	2,86	2,06	2,05	2,17	2,14	2,09	2,00	4,30
30	2,83	2,88	2,99	2,98	2,22	2,20	2,00	1,99	4,26
50	3,01	3,01	2,96	2,96	2,16	2,15	2,00	1,98	4,42
60	3,50	3,50	2,92	2,92	2,01	2,00	1,97	1,91	4,38
65	3,73	3,73	2,97	2,97	1,98	1,96	1,94	1,91	4,47
70	1,85	1,81	3,07	3,05	4,55	4,59	3,98	1,94	4,49
72°45′00″	2,00	1,93	3,46	3,41	4,29	2,00	2,04	1,89	2,68
72 52 30	1,79	1,73	0,66	0,66	4,05	1,79	1,92	1,94	2,55
73 00 00	1,76	1,70	0,17	0,20	0,52	1,76	1,91	0,13	2,18
73 07 30	0,02	0,05	0,18	0,22	0,10	0,03	0,06	0,01	0,07
73 15 00	0,03	0,03	0,10	0,14	0,08	0,03	0,06	0,05	0,03

Appendix 8

Value of the ratio $\frac{I_3}{I_1}$ (%)

α	z'=20км	z'=40км	z'=20км	z'=40км	z' 20км	z'=40км	z'=20 км		
	1		2		3		1a	2a	3a
—73°15'00"	4,59	4,35	3,68	3,71	4,94	6,68	4,80	5,39	7,31
—73 07 30	4,64	4,46	4,27	4,09	6,07	6,76	5,14	5,65	7,12
—73 00 00	4,44	4,38	4,48	4,21	7,33	7,71	5,03	4,47	7,66
—72 52 30	4,41	4,32	8,12	7,92	7,65	7,96	5,20	4,50	8,19
—72 45 00	4,49	4,36	8,38	8,35	6,15	6,48	5,18	4,53	7,51
—70°	8,12	8,12	8,06	8,07	9,36	9,38	4,36	4,41	6,40
—65	8,59	8,59	5,30	5,28	5,86	6,06	5,09	4,44	6,20
—60	8,56	8,60	5,17	5,14	5,82	5,97	5,01	4,50	5,94
—50	8,51	8,51	5,17	5,10	6,00	6,11	5,19	4,62	5,95
—30	8,63	8,63	5,38	5,24	6,24	6,34	5,07	5,08	6,00
0	8,05	8,05	5,30	5,28	6,19	6,24	5,17	5,23	10,8
30	7,78	7,78	7,80	7,77	6,34	6,45	4,83	5,10	10,8
50	7,42	7,42	7,43	7,48	6,42	6,49	4,76	5,12	10,5
60	7,62	7,62	7,23	7,23	6,11	6,23	4,74	5,12	9,74
65	7,88	7,83	7,00	7,06	6,10	6,30	4,76	5,22	9,60
70	4,14	4,04	6,87	6,82	8,95	9,04	9,22	5,24	8,70
72°45'00"	4,20	4,08	6,34	6,28	8,41	8,48	5,15	5,83	6,75
72 52 30	4,26	4,16	6,30	6,25	8,26	8,28	4,86	5,89	6,46
73 00 00	4,27	4,23	5,87	5,80	8,17	8,18	4,83	6,59	6,07
73 07 30	4,41	4,29	5,87	5,96	7,00	7,35	5,74	6,74	6,60
73 15 00	4,46	4,39	6,10	5,90	7,05	7,23	5,98	6,68	6,40

Appendix 9

Value of the ratio $\frac{I_4}{I_1}$ (%)

α	z'=20км	z'=40км	z'=20км	z'=40км	z' 20км	z'=40км	z'=20 км		
	1		2		3		1a	2a	3a
—73°15'00"	31,9	33,5	38,6	38,1	34,7	32,1	35,9	34,9	32,7
—73 07 30	33,1	34,4	35,7	37,4	31,9	31,6	34,5	34,5	32,9
—73 00 00	27,7	29,1	36,8	36,9	32,4	31,4	27,9	27,8	35,5
—72 52 30	27,6	28,6	30,3	30,7	27,4	27,8	27,3	28,2	28,6
—72 45 00	27,5	28,8	24,8	25,4	28,5	28,7	27,4	27,9	25,1
—70°	25,5	26,0	26,4	26,8	26,7	26,6	27,5	28,5	28,8
—65	25,8	26,1	27,9	28,4	28,8	28,6	28,6	28,3	28,9
—60	25,9	26,5	28,0	27,9	28,7	28,7	27,2	28,1	28,0
—50	25,6	25,9	28,0	28,0	28,3	28,3	28,0	28,6	28,2
—30	25,7	25,8	28,5	28,0	27,9	28,3	28,1	28,9	28,6
0	25,7	26,0	28,0	28,1	28,3	28,2	28,7	28,5	27,2
30	25,7	26,0	27,1	27,2	28,2	28,3	27,6	28,2	26,5
50	26,1	26,5	27,2	27,4	28,4	28,3	27,6	28,3	26,6
60	25,9	26,4	26,7	27,0	28,3	28,5	27,9	28,3	26,0
65	25,7	26,5	26,9	27,3	28,2	28,1	27,6	28,2	26,2
70	27,0	28,0	26,7	27,3	26,8	26,8	24,8	28,6	25,5
72°45'00"	26,8	28,5	26,7	27,1	27,0	26,9	29,9	28,5	27,7
72 52 30	27,7	29,0	30,8	31,1	27,2	27,3	28,1	28,9	27,6
73 00 00	27,7	28,7	31,5	32,1	31,6	31,7	28,1	33,9	27,8
73 07 30	33,1	34,4	32,0	32,6	32,4	32,2	33,8	33,3	34,0
73 15 00	33,8	35,1	31,4	31,2	32,0	32,2	32,1	32,3	32,7

K. Ya. Kondrat'yev, K. Ye. Yakushevskaya

ANGULAR DISTRIBUTION OF THE THERMAL RADIATION OF THE EARTH—ATMOSPHERE SYSTEM IN VARIOUS REGIONS OF THE SPECTRUM

Quantitative data on the angular distribution of outgoing thermal radiation in various portions of the spectrum have been lacking in the literature until very recently. Only in 1962 were studies published which were devoted to this problem [1-3].

The present work is a continuation of theoretical calculations whose results are given in Ref. [1]. The calculation of the angular dependence of outgoing radiation has now been extended to the far infrared (wavelength $\lambda > 18$ μ) and to the still unstudied regions of the atmospheric window of 8.70-12.00 μ (see Table 1, Portions 10-13). In addition, for all of the selected portions of the spectrum, the outgoing radiation intensity was calculated for the winter atmosphere at a latitude of 65° N.L. (earlier, the summer atmosphere at 0 and 65° N.L. was examined).

As before, the outgoing radiation intensity was calculated graphically by means of radiation nomograms. The absorption characteristics of longwave radiation used in calculations for spectral regions 1-9 are given in Ref. [1].

The transmission function for the far infrared region, 18-40 μ, was determined as follows:

$$P_{18-40}=\sum_{j=1}^{16} p_j P_j, \qquad (1)$$

where P_{18-40} is the transmission function in the spectral interval of 18-40 μ, P_j is the transmission function in portion j of the spectral region of 18-40 μ, p_j is the fraction of radiation of the absolute

Table 1

Spectral Intervals Considered

Number of spectral portion	Spectral interval considered	Limits of spectral interval, μ	Principal radiation-absorbing gases
1	Integrated radiation	0-∞	H_2O, CO_2
2	Portion in the atmospheric window	10.55-11.01	H_2O
3	Absorption band of water vapor, 6.3 μ	4.88-8.70	H_2O
4	Absorption band of carbon dioxide, 15 μ	12-18	CO_2, H_2O
5	Absorption band of ozone, 9.6 μ	9.01-10.29	O_3, H_2O
6	Portion of very strong absorption	6.494 - 6.579	H_2O
7	Portion of very strong absorption	41.67-45.45	H_2O
8	Portion of weak absorption	5.00-5.05	H_2O
9	Portion of weak absorption	17.86-18.52	H_2O
10	Region of the absorption band of water vapor, 80 μ	18-40	H_2O
11	Region of the absorption band of water vapor, 80 μ	40-120	H_2O
12	Portion in the atmospheric window	8.70-9.01	H_2O
13	Portion in the atmospheric window	10.29-12.00	H_2O

black body corresponding to portion j (relative to the total radiation energy in the interval of 18-40 μ).

The transmission function P_j was calculated from the formula

$$P_j = 1 - \Phi\left(\sqrt{\frac{l_j w}{2}}\right), \qquad (2)$$

where $\Phi(y) = \frac{2}{\sqrt{\pi}}\int_0^y e^{-v^2}dy$ is the error probability integral, l_j is the generalized absorption coefficient in portion j, and w is the effective content of water vapor in centimeters of precipitated water.

The transmission function in the still farther infrared region of the spectrum, 40-120 μ, was calculated with a formula similar to (1) (the summation was carried out over eight spectral intervals).

The values of γ_j were taken in accordance with the data of G. Yamamoto and G. Onishi [4] and pertain to a temperature of 260° K (average temperature for the temperature range existing in the atmosphere). An exact comparison of the values of γ_j employed with the generalized absorption coefficients given in the recent paper of D. York, G. Yamamoto and D. Lienesh [5] which are in agreement with the latest investigations of K. Palmer [6] is fairly difficult, since the values of γ in Refs. [4] and [5] are given for different spectral intervals. It may be stated however, that the discrepancy between the data of Refs. [4] and [5] is not large enough to have any substantial influence on the value of the transmission function in the spectral regions under consideration.

In the portions of the atmospheric window of 8.70-9.01 and 10.29-12.00 μ, use was made of the exponential transmission law with an absorption coefficient K = 0.15 cm^2/g, based on the average values of the absorption coefficients of water vapor obtained in Ref. [7].

As before, the effective content of water vapor w, carbon dioxide u and ozone m along the path of the ray s in a spherical atmosphere was calculated by means of the following formula:

$$w = \int_0^s \rho_w(s) \frac{p(s)}{p_0} ds, \tag{3}$$

$$u = \int_0^s \rho_u(s) \frac{p(s)}{p_0} ds, \tag{4}$$

$$m = \int_0^s \rho_m(\,) \left(\frac{p(s)}{p_0}\right)^{0,2} ds. \tag{5}$$

Here ρ_w, ρ_u, ρ_m are the density of water vapor, carbon dioxide and ozone, respectively, p is the pressure and p_0 is the normal pressure (1013 mb). In the case of absorption by water vapor and carbon dioxide, the upper boundary of the radiating atmosphere was considered to be at

an altitude of about 39 km, and in the case of absorption by ozone, at an altitude of 50 km. Numerical integration in formulas (3)—(5) was performed by the trapezoidal method for a 27- and 88 layer atmosphere, respectively.

In order to obtain the angular dependence of the intensity of outgoing radiation for the case of a dry and cold atmosphere (winter, $\varphi = 65^\circ$ N.L.), use was made of average (for the given latitude and season) vertical distributions of the temperature and humidity in the troposphere taken from the work of D. London [8]. In the stratosphere, the average temperatures were taken from the work of R. Murgatroyd [9]. However, the mean seasonal and mean latitudinal distributions of the characteristics of the water content of air in the stratosphere are lacking in the literature, as a result of the scarcity and indeterminacy of the data on the humidity in the upper layers. In the calculations for $\varphi = 65^\circ$ N.L. (winter), the same linear profile log q was used in stratosphere (q is the specific humidity) as in the case where $\varphi = 65^\circ$ N.L. (summer),

$$\lg q = -2{,}667 + 0{,}05556z, \qquad (6)$$

if $12 \leq z \leq 39$ km. In formula (6), the quantity q is expressed in g/kg, and the height z in km.

The adopted profile of the specific humidity is close to the vertical distribution q obtained by E. Barret, L. Herndon and H. Carter (see Ref. [10]) by means of two summer balloon flights, and reflects an increase in specific humidity with increasing altitude in the stratosphere. As was shown by one flight made by these investigators, in winter, the tendency of q to increase does not occur. However, in all three cases (summer and winter), the specific humidity in the 10-30 km layer was between 0.01 and 0.1 g/kg. For this reason, we thought it possible not to change the stratospheric profile of q in passing from summer to winter,

particularly since according to the latest data [11], the increase in specific humidity with increasing altitude in the stratosphere may be observed not only during summer but also during winter. It should be noted that the vertical distribution of specific humidity at altitudes of $12 < z < 31$ km adopted in calculations for 65° N.L. was found to be comparatively close to the first standard mean annual profile of the specific humidity recently plotted by M. Gutnick [12] for middle latitudes ($\varphi = 45°$ N.L.).

In calculations for 65° N.L. (winter), the volume concentration of carbon dioxide, as in the case of other stratifications of the atmosphere (see Ref. [1]), is equal to 0.03%. The ozone concentration in the winter atmosphere at a latitude of 65° N.L. was determined from the winter-spring data of K. Ramanthan and R. Kulkarni [13] (during that time of year, the atmosphere is richer in ozone than during the other seasons).

The angular distributions of the outgoing radiation intensity $U(\vartheta)$ given in the present work were obtained for a point located at an altitude of 300 km.

The conversion to the angular distribution $U(\vartheta_h)$ at a point located at the same latitude but at a different level h may be achieved by means of the relation

$$U(\vartheta) = U(\vartheta_h) \tag{7}$$

with

$$\sin \vartheta_h = \frac{(R + 300) \sin \vartheta}{R + h}, \tag{8}$$

where R is the radius of the earth (R = 6,371 km).

Strictly speaking, such a conversion is valid only when the angular distribution of the outgoing radiation is independent of the azimuth. Since our calculations were made for a spherically quasi-symmetrical

atmosphere (see Ref. [1]), the conversion from $U(\vartheta)$ to $U(\vartheta_h)$ is possible.

Table 2 lists values of the outgoing radiation intensity in the vertical direction for the winter atmosphere at 65° N.L. for nine portions of the spectrum[1] (in the case of a cloudless atmosphere, in order to obtain the absolute intensities for other zenithal angles, it is necessary to turn to relative intensities of the outgoing radiation, given in Figs. 3 and 4). The curves $U(\vartheta)$ in these portions of the spectrum for two other stratifications of the atmosphere have been examined earlier (see Ref. [1]). Figs. 1 and 2 show the angular distributions $U(\vartheta)$ for the new spectral intervals 10-14 for three stratifications of the atmosphere. A supplement to Table 2 and the figures are Tables 3-7, which make it possible to characterize clearly the variability of the outgoing radiation as a function of the conditions of cloudiness and stratification of the atmosphere.

Table 2

Intensity of outgoing radiation (w/cm^2 ster) in the vertical direction for the winter atmosphere at latitude 65° N.L.

Number of spectral portion	Clear sky	h_t = 3 km	h_t = 9 km
1	$6{,}43 \cdot 10^{-3}$	$6{,}22 \cdot 10^{-3}$	$4{,}20 \cdot 10^{-3}$
2	$1{,}99 \cdot 10^{-4}$	$1{,}84 \cdot 10^{-4}$	$3{,}85 \cdot 10^{-5}$
3	$5{,}42 \cdot 10^{-4}$	$5{,}04 \cdot 10^{-4}$	$2{,}23 \cdot 10^{-4}$
4	$1{,}64 \cdot 10^{-3}$	$1{,}58 \cdot 10^{-3}$	$1{,}14 \cdot 10^{-3}$
5	$4{,}16 \cdot 10^{-4}$	$3{,}84 \cdot 10^{-4}$	$1{,}93 \cdot 10^{-4}$
6	$4{,}15 \cdot 10^{-6}$	$4{,}15 \cdot 10^{-6}$	$3{,}43 \cdot 10^{-6}$
7	$8{,}30 \cdot 10^{-5}$	$8{,}30 \cdot 10^{-5}$	$8{,}08 \cdot 10^{-5}$
8	$2{,}05 \cdot 10^{-6}$	$1{,}80 \cdot 10^{-6}$	$4{,}33 \cdot 10^{-7}$
9	$1{,}75 \cdot 10^{-4}$	$1{,}68 \cdot 10^{-4}$	$1{,}12 \cdot 10^{-4}$

1. The numbering of the spectral portions in the text and figures corresponds to that used in the tables. Asterisks in the tables designate portions in which the radiation intensity was not calculated directly but by summing up the intensities in the spectral intervals comprising the wavelength interval considered.

Tables 3-4 show the values of $A = \frac{U_0 - U_\vartheta}{(U_\vartheta)_{\vartheta=0}}$ for two zenith angles: 0 and 70°. Here U_0 and U_9 are the intensities of outgoing radiation for a clear sky and continuous cloudiness with a height of the upper boundary h_t = 9 km. The intensity of the outgoing radiation of a cloudy sky with h_i = 9 km for ϑ = 0 is considered equivalent to the value of the infrared darkening towards the limb of the atmosphere for a high cloudiness. It is obvious that the smaller A as compared to unity, the more homogeneous is the angular distribution of outgoing radiation under conditions of partial cloudiness, and the less important is the masking of the infrared darkening towards the limb of the atmosphere within the confines of the planet's disk. Tables 3-4 are a continuation of Table 1, taken from Ref. [1].

Table 3

Values of $A = \frac{U_0 - U_\vartheta}{(U_\vartheta)_{\vartheta=0}}$ for winter atmosphere at latitude 65° N.L.

Number of spectral portion	$\vartheta = 0°$	$\vartheta = 70°$	Number of spectral portion	$\vartheta = 0°$	$\vartheta = 70°$
1	0,529	0,400	9	0,560	0,444
2	1,25	1,07	10	0,278	0,171
3	1,43	1,05	11	0,0244	0,0101
4	0,350	0,313	12	1,68	1,65
5	1,10	0,754	13	1,20	1,18
6	0,210	0,0111	14*	1,30	1,13
7	0,0277	0,002	15*	0,543	0,399
8	3,73	2,80	16*	0,486	0,358

Note. The limits of spectral intervals 14, 15 and 16 are the following: 8.70-12.0; 4.88-40.0; 4.88-120 μ.

Table 4

Values of $A = \frac{U_0 - U_\vartheta}{(U_\vartheta)_{\vartheta=0}}$ in spectral portions 10-16 for summer atmosphere at latitudes 0 and 65° N.L.

Number of spectral portion	$\vartheta = 0°$		$\vartheta = 70°$	
	$\varphi = 0°$	$\varphi = 65°$ N.L.	$\varphi = 0°$	$\varphi = 65°$ N.L.
10	0,149	0,245	0,058	0,123
11	0,0009	0,008	0	0,0002
12	2,08	2,47	1,48	2,12
13	1,44	1,72	1,03	1,50
14*	1,56	1,73	0,939	1,33
15*	0,628	0,698	0,340	0,451
16*	0,578	0,631	0,313	0,407

Table 5 gives values of $B=\frac{U^0-U^{65}}{U^0}$ for summer at two zenith angles, 0 and 70°. Here U_0 is the intensity of the outgoing radiation at the equatorial latitude, U^{65} is the intensity of the outgoing radiation at the latitude of 65° N.L. Ratio B characterizes the latitudinal variability of the outgoing radiation. Table 5 supplements Table 2, borrowed from Ref. [1].

The calculations of $U(\vartheta)$ which were carried out make it possible to calculate B only for summer conditions. However, if it is assumed that the angular distribution of the outgoing radiation calculated for the summer equatorial atmosphere remains the same in the course of the year (the annual fluctuations of the temperature and humidity at the equatorial latitude are small), an approximate value of the latitudinal variations of $U(\vartheta)$ can also be obtained for the winter (see Table 6). As was shown by Table 6, in most portions of the spectrum this value exceeds the corresponding variation of $U(\vartheta)$ in summer by a factor of 2 or more. The differences U^0-U^{65} for winter conditions are commensurate with the decrease in the outgoing radiation intensity caused by the appearance of high cloudiness, or even surpass it.

Table 5

Values of $B=\frac{U^0-U^{65}}{U^0}$ for the summer in spectral portions 10-16

Number of spectral portion	$\vartheta=0°$			$\vartheta=70°$		
	Clear sky	$h_t=3$ км	$h_t=9$ км	Clear sky	$h_t=3$ км	$h_t=9$ км
10	0,012	0,024	0,087	—0,038	—0,033	0,020
11	—0,082	—0,082	—0,074	—0,152	—0,152	—0,152
12	0,245	0,265	0,329	0,154	0,230	0,328
13	0,197	0,218	0,280	0,111	0,179	0,277
14*	0,228	0,236	0,270	0,124	0,181	0,224
15*	0,108	0,121	0,144	0,015	0,040	0,069
16*	0,098	0,110	0,127	0,005	0,029	0,051

Table 6

Values of $B = \frac{U^0 - U^{65}}{U^0}$ for winter

Number of spectral portion	$\vartheta = 0°$			$\vartheta = 70°$		
	Clear sky	$h_t = 3$ km	$h_t = 9$ km	Clear sky	$h_t = 3$ km	$h_t = 9$ km
1	0,298	0,266	0,309	0,233	0,224	0,267
2	0,536	0,462	0,470	0,460	0,442	0,470
3	0,476	0,468	0,551	0,340	0,370	0,493
4	0,296	0,285	0,269	0,191	0,208	0,225
5	0,600	0,538	0,505	0,533	0,513	0,489
6	0,165	0,165	0,307	0,019	0,019	0,028
7	0,025	0,025	0,051	−0,012	−0,012	−0,009
8	0,583	0,605	0,719	0,436	0,477	0,695
9	0,201	0,222	0,282	0,125	0,141	0,274
10	0,120	0,132	0,211	0,066	0,070	0,154
11	0,011	0,011	0,032	−0,016	−0,016	−0,005
12	0,592	0,521	0,530	0,493	0,490	0,529
13	0,513	0,444	0,456	0,413	0,419	0,455
14*	0,554	0,485	0,477	0,461	0,452	0,477
15*	0,351	0,316	0,316	0,253	0,253	0,274
16*	0,334	0,299	0,293	0,237	0,237	0,252

Table 7 shows the values of $C = \frac{U_s - U_w}{U_s}$ for 65° N.L. (U_s is the intensity of outgoing radiation in summer and U_w is the intensity of outgoing radiation in winter). Ratio C serves as a measure of the seasonal variability of the outgoing radiation at the latitude of 65° N.L.

In studying Tables 5-7, however, we should remember that in the absense of latitudinal and seasonal distributions of humidity in the stratosphere, the quantities B and C characterize the latitudinal and seasonal variability $U(\vartheta)$ in a somewhat arbitrary manner. This applies particularly to portions of intense absorption and also all the portions if $U(\vartheta)$ is examined at large zenith angles. The arbitrariness of the characteristics of the seasonal and latitudinal variability obtained for the angular distributions of the outgoing radiation also follows from the fact that the quantities B and C were calculated for a clear sky and model conditions of continuous cloudiness, and not for the mean seasonal distributions of cloudiness at the latitudes considered. For this reason, the data given in Tables 5-7 are in many cases merely indicate a possible stratificational variability $U(\vartheta)$.

Table 7

Values of $C = \frac{U_s - U_w}{U_s}$ for 65° N.L.

Number of spectral portion	$\theta = 0°$			$\theta = 70°$		
	Clear sky	$h_t = 3$ км	$h_t = 9$ км	Clear sky	$h_t = 3$ км	$h_t = 9$ км
1	0,219	0,176	0,175	0,197	0,172	0,180
2	0,404	0,300	0,260	0,369	0,296	0,260
3	0,379	0,333	0,336	0,319	0,325	0,352
4	0,261	0,225	0,208	0,238	0,234	0,246
5	0,461	0,374	0,336	0,459	0,418	0,432
6	0,350	0,350	0,434	0,509	0,509	0,514
7	0,080	0,080	0,095	0,124	0,124	0,126
8	0,516	0,470	0,452	0,328	0,362	0,448
9	0,171	0,160	0,164	0,100	0,107	0,165
10	0,112	0,111	0,136	0,099	0,100	0,137
11	0,0853	0,0853	0,0995	0,118	0,118	0,127
12	0,460	0,351	0,299	0,406	0,339	0,299
13	0,391	0,294	0,246	0,344	0,284	0,246
14*	0,467	0,363	0,338	0,526	0,463	0,425
15*	0,273	0,222	0,200	0,242	0,222	0,221
16*	0,262	0,213	0,190	0,233	0,214	0,212

The combination of Tables 3-7 and 1-2, taken from Ref. [1], shows that within the confines of the planet's disk in the far infrared, 18-40 μ, the variability of the outgoing radiation as a function of the conditions of cloudiness and stratification of the atmosphere is much less than the corresponding variability of the outgoing radiation in the broad absorption bands located in the range of $\lambda < 18$ μ, particularly in the portions of weak absorption. Even in its radiation sensitivity to clouds and the stratification of the atmosphere, the 15 μ absorption band of carbon dioxide (12-18 μ) considerably exceeds the spectral interval of 18-40 μ. In the wavelength range of 18-40 μ, the quantity

$$A_1 < 0{,}28 \quad \left(A_1 = \frac{(U_0 - U_9)_{\theta=0}}{(U_9)_{\theta=0}}\right),$$

and

$$A_2 \leqslant 0{,}17 \quad \left(A_2 = \frac{(U_0 - U_9)_{\theta=70°}}{(U_9)_{\theta=0}}\right),$$

whereas in the spectral interval of 12-18 μ, $A_1 \leq 0.55$, $A_2 \leq 0.30$. The stratification changes of the outgoing radiation in the 18-40 μ interval amount to no more than 20%. Thus, in the far infrared, 18-40 μ, the

possible inhomogeneities of the angular distribution of outgoing radiation within the confines of the planet's disk, caused by a partial cloudiness and by inhomogeneities in the stratification of the atmosphere, cannot mask the infrared darkening towards the limb of the atmosphere.

The result obtained is a consequence of an intense absorption in the spectral region $\lambda > 18$ μ (a strong rotational band of water vapor is located here, with an absorption maximum in the vicinity of 80 μ) and of the weak temperature dependence of the radiation energy of the absolute black body in this wavelength interval. The role of these factors has been clearly identified earlier (see Refs. [1,14], and an examination of the spectral regions of identical absorption but located at different ends of the infrared spectrum (regions 6 and 7, 8 and 9) stimulated the calculation of the angular distributions of the outgoing radiation in the intervals of 18-40 and 40-120 μ.

The radiation of the earth—atmosphere system in the spectral region of 40-120 μ is still less sensitive to clouds and stratifications of the atmosphere than in the range of 18-40 μ. In this region, the outgoing radiation practically no longer reacts to the appearance of high cloudiness. The indicated properties of the far infrared region of the spectrum are particularly manifest against a background of strong dependence of $U(\vartheta)$ on the conditions of the cloudiness and stratification of the atmosphere in the regions of the atmospheric window (Figs. 1 and 2).

At large zenith angles in intervals 10 and 11, the variability of the outgoing radiation as a function of the cloudiness conditions is also small. As regards the dependence of $U(\vartheta)$ on the stratification of the atmosphere in this region, it is much less in the range of the angles $72^\circ 40' - 73^\circ$ than in many other spectral intervals (these include regions

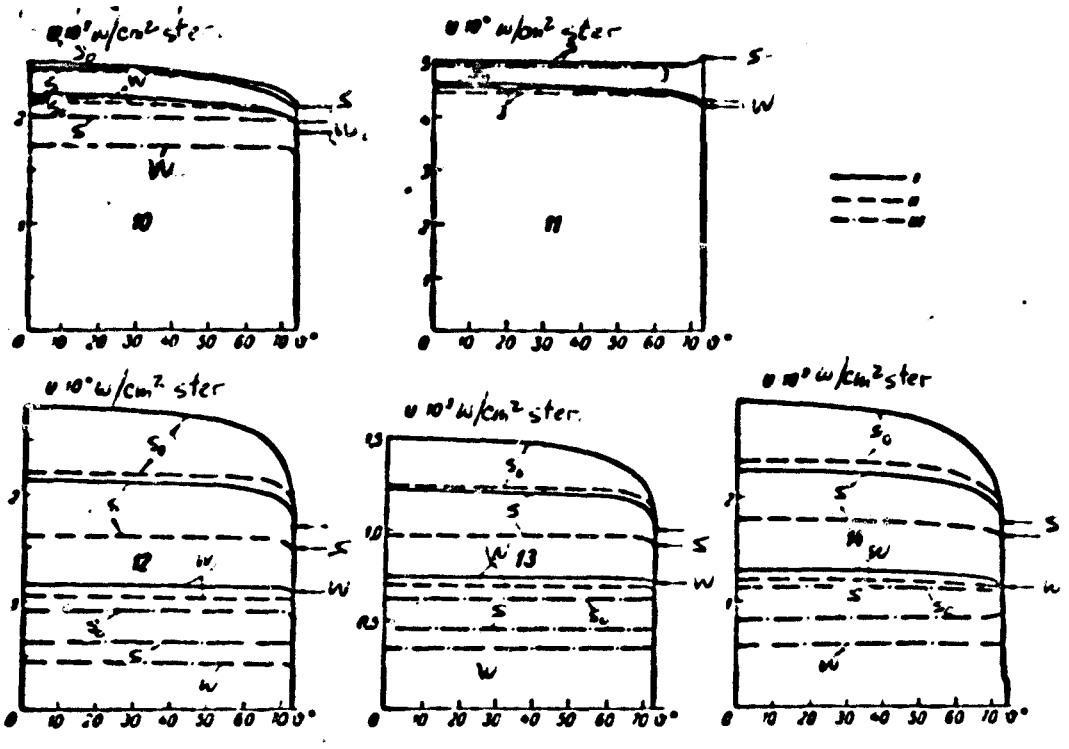

Fig. 1. Comparison of the angular distributions of outgoing radiation intensity in spectral portions 10-14 for three stratifications of the atmosphere.

s_0 - summer, 0°; s - summer, 65° N.L.; w - winter, 65° N.L.

I - clear sky; continuous cloudiness; II - upper boundary h_t = 3 km; III - h_t = 9 km. Arrows on the right indicate the intensity of outgoing radiation for a cloudless atmosphere at angle $\vartheta = 72°45'$ at which the limb of the earth is seen from an altitude of 300 km.

of weak absorption 2, 8, 12-14, absorption bands 3-5, and the region of strong absorption 6). However, at $\vartheta > 73°$ the far infrared region of the spectrum is very sensitive to the stratification of the atmosphere.

In order to further compare the results pertaining to different portions of the spectrum, we shall turn to the relative intensity of the outgoing radiation $\frac{U(\vartheta)}{U(0)}$. Here $U(\vartheta)$ is the radiation intensity at a zenith angle ϑ, $U(0)$ is the radiation intensity at $\vartheta = 0$. It is evident from Fig. 3 that in the case of winter at a latitude of 65° N.L., an infrared darkening toward the limb of the earth is observed in all portions of the spectrum, but that this darkening is much smaller in magnitude than the corresponding darkening in the case of summer atmosphere

at latitudes of 0 and 65° N.L. (cf. Fig. 3 and Figs. 2 and 3 of Ref. [1]). At large zenith angles, the relative angular distributions of the outgoing radiation for summer and winter conditions at a latitude of 65° N.L. differ little from one another, with the exception of regions 6 and 8, located in the near infrared region of the spectrum (cf. Fig. 4 with Fig. 6 of Ref. [1]).

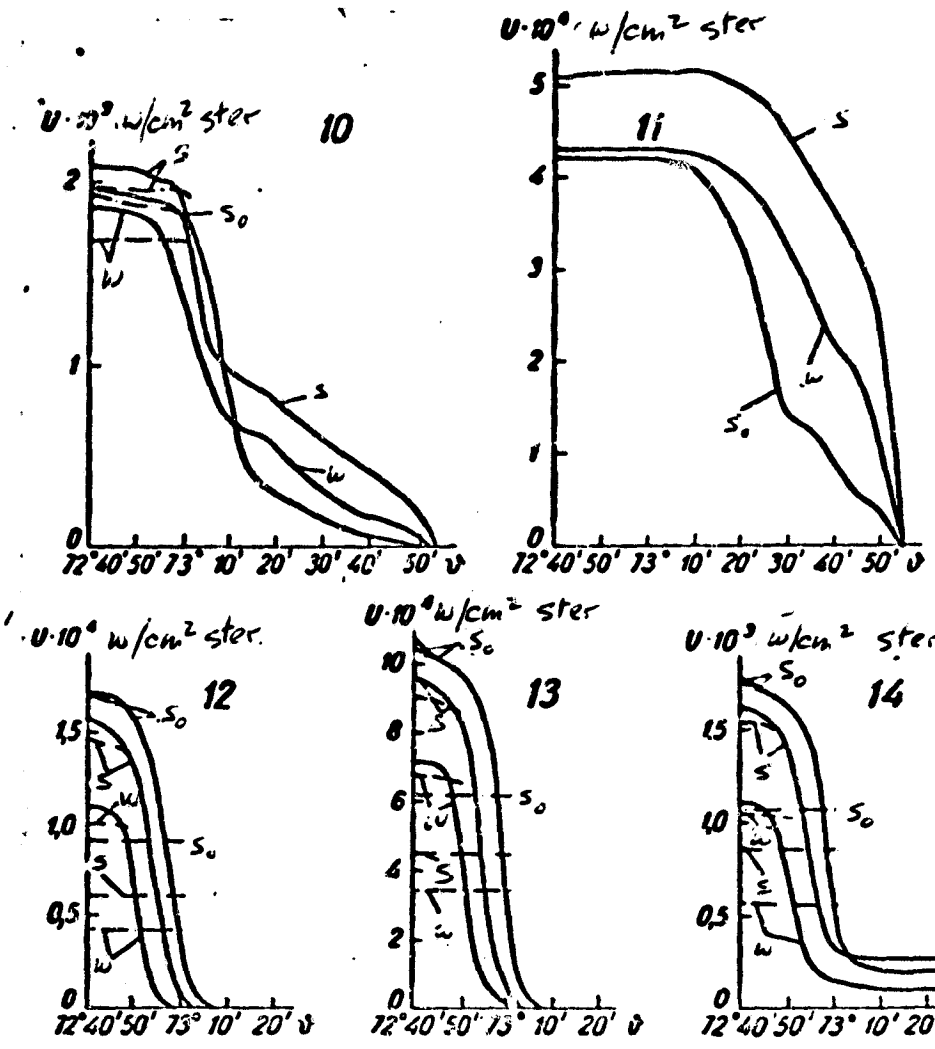

Fig. 2. Comparison of the angular distributions of outgoing radiation intensity in spectral portions 10-14 for three stratifications of the atmosphere in the region of large zenith angles. For designations of the curves, see Fig. 1.

In the spectral region of 18-40 μ, the course of the curve $\frac{U(\vartheta)}{U(0)}$ is close to the relative angular distribution in the absorption band of carbon dioxide 15 μ (12-18 μ). It is true that the slope of the steep drop of $\frac{U(\vartheta)}{U(0)}$, beginning at $\vartheta > 72°55'$ in interval 10 is somewhat greater than in the absorption band 4. In the spectral region of 40-120 μ, the

relative angular distribution of the outgoing radiation almost coincides with the curve $\frac{U(\vartheta)}{U(0)}$ in the region of intense absorption 7.

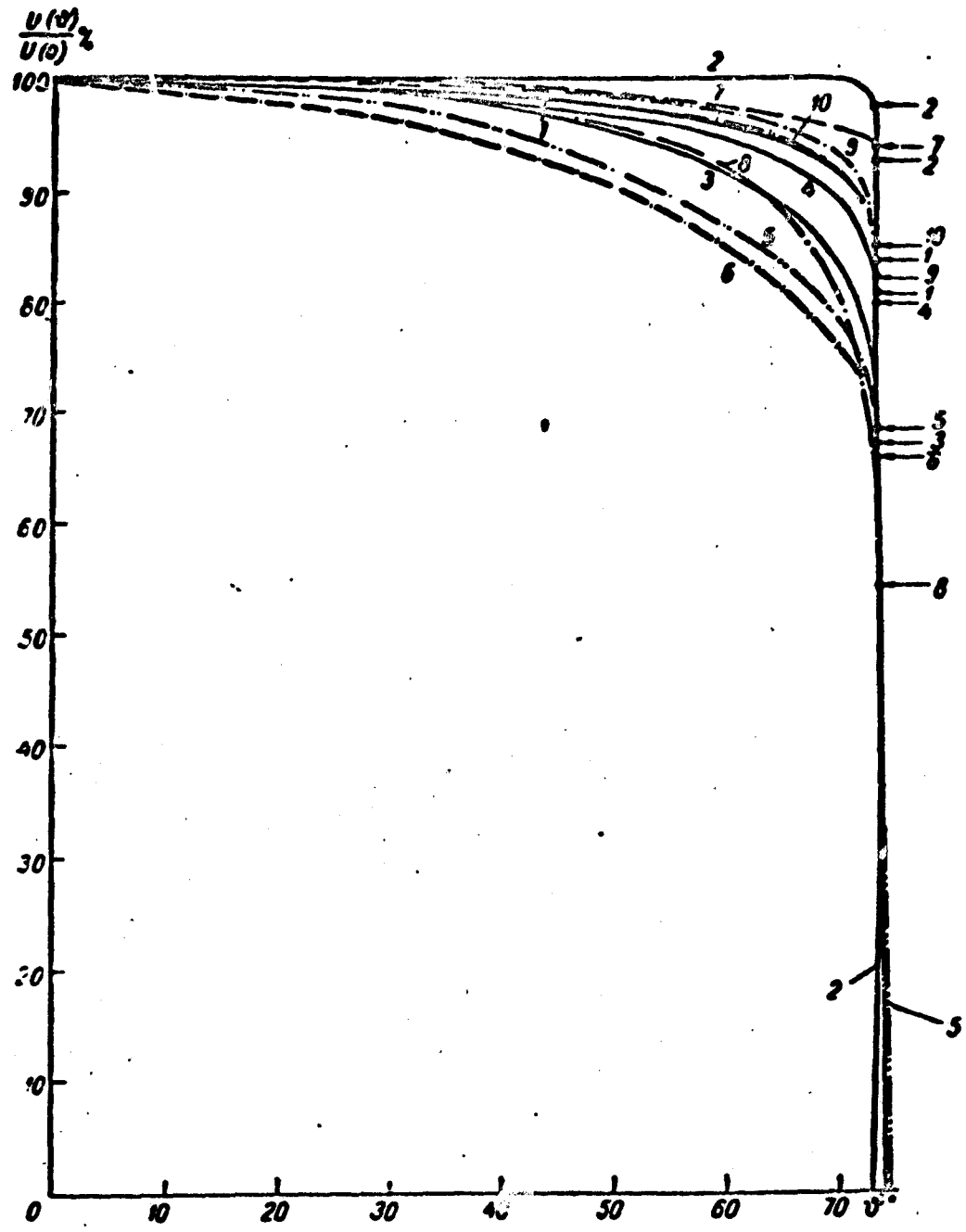

Fig. 3. Comparison of the relative intensities of outgoing radiation in various portions of the spectrum, $\varphi = 65^{\circ}$ N.L., winter, clear sky. Horizontal arrows on the right indicate the intensity at $\vartheta = 72^{\circ}45'$.

The relative intensities of the outgoing radiation in portions 12 and 14 of the atmospheric window are shown in Figs. 5 and 6. From Figs. 5 and 6 it is evident that in the atmospheric window of 8.70-12.00 μ, the radiation of ozone contributes to an increase in the infrared darkening towards the limb of the earth and slows down the direct darkening

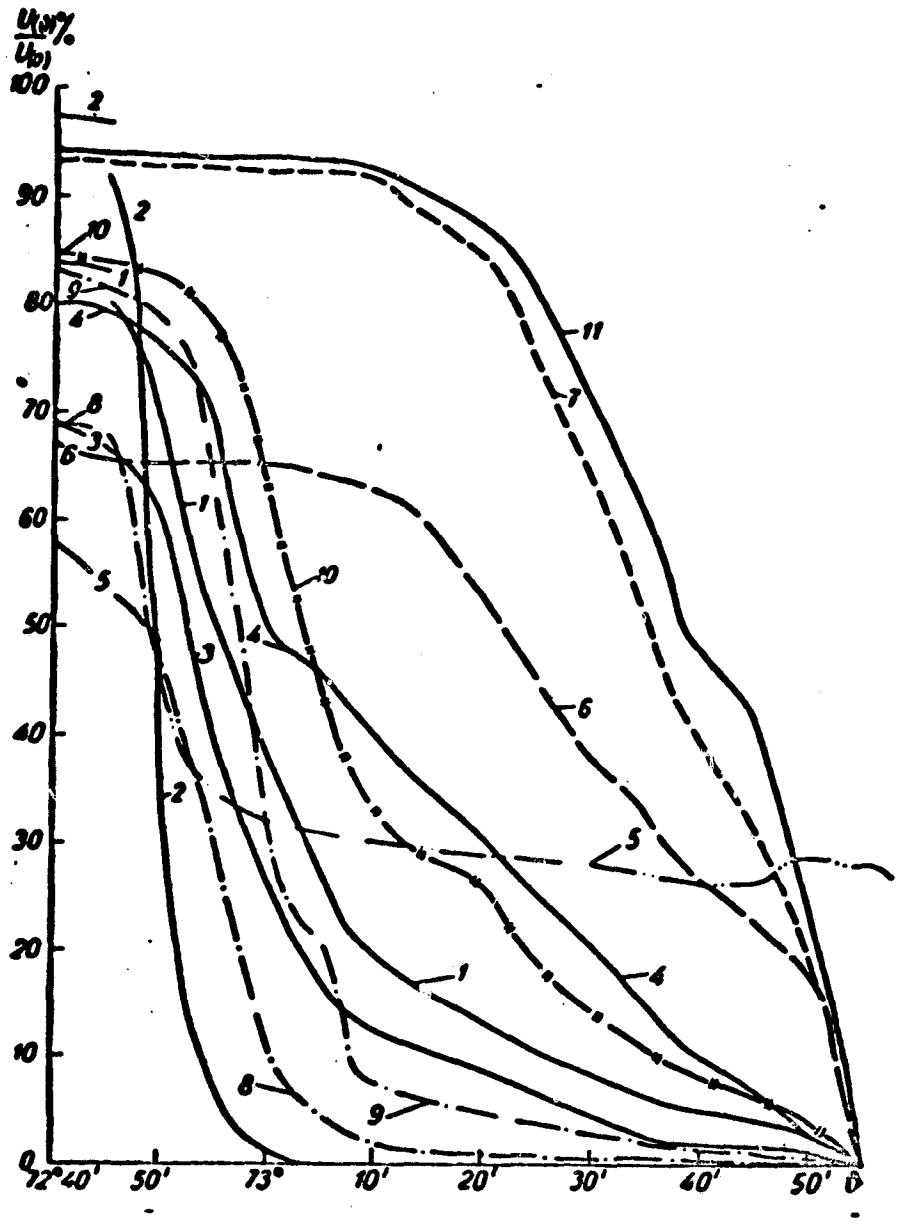

Fig. 4. Comparison of relative intensities of outgoing radiation in various portions of the spectrum in the range of large zenith angles, $\varphi = 65^\circ$ N.L., winter, clear sky.

towards the limb of the atmosphere. In the interval of 8.70-12.00 μ as well as in the region of the 9.6 absorption band of O_3, a slight, broad peak in the outgoing radiation intensity is observed at large zenith angles. However, in the absorption band of ozone, this peak is sharper and occurs at higher values of $\frac{U(\vartheta)}{U(0)}$. The maxima in portions 5 and 14 coincide. In summer at latitude 65° N.L., the relative maximum of radiation intensity is observed at $\vartheta = 73^\circ 34'$. The given zenith angle corresponds to the ray traversing the greatest distance (as compared to the rays in the other directions) in the layer of maximum ozone concentration

(h_0 = 27.3 km)[1]. In summer at a latitude of 0° and in winter at 65° N.L., the peak of $\frac{U(\vartheta)}{U(0)}$ is more pronounced and occurs at $\vartheta = 73°49'$ (h_0 = 36 km). The latter i. due to the vertical distribution of the temperature: the relative maximum of the radiation intensity is caused by a layer with a smaller ozone concentration, but with a higher temperature.

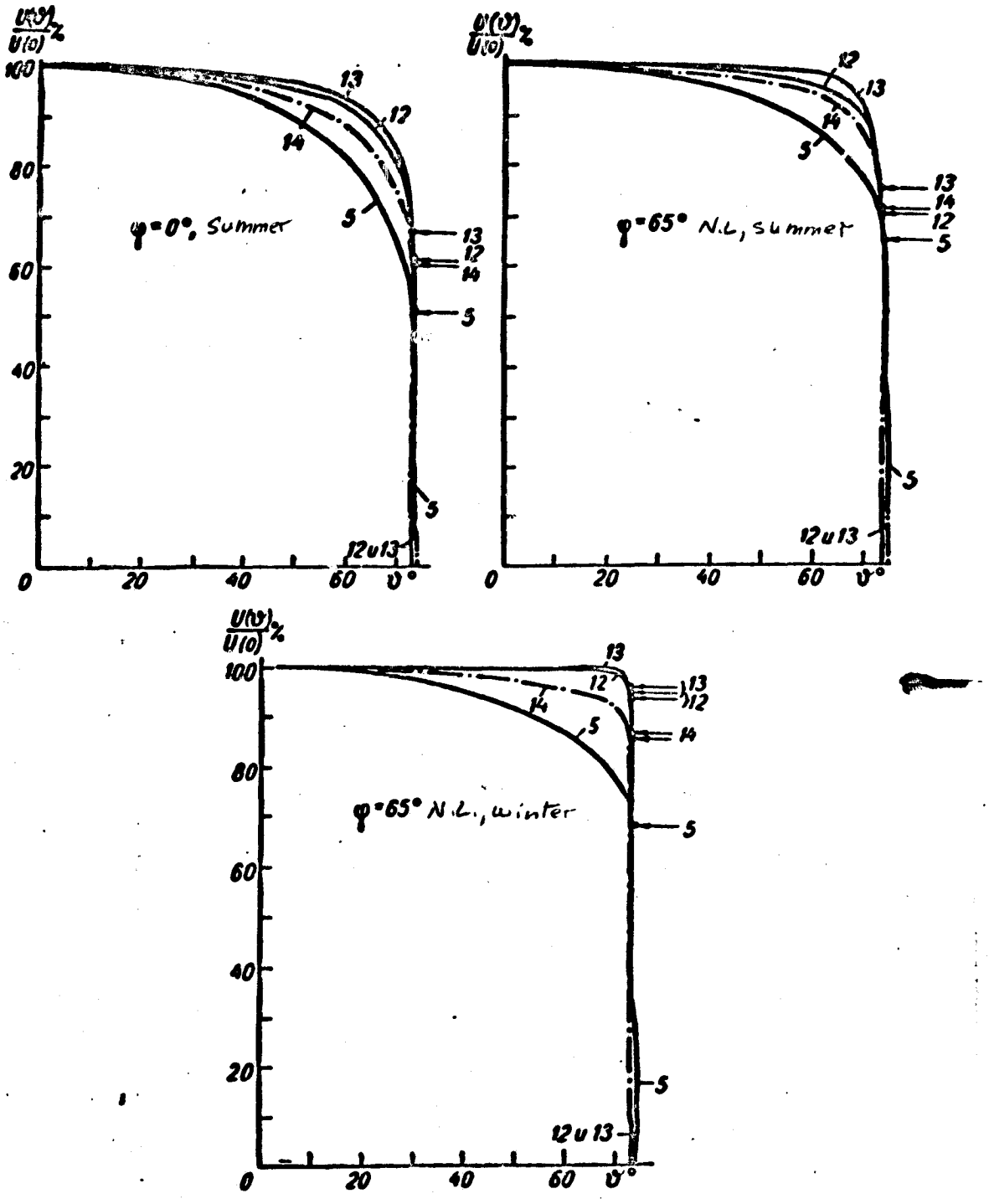

Fig. 5. Comparison of relative angular distributions of outgoing radiation intensity in portions of the spectrum comprising the window of 8.70-12.00 μ, clear sky.

1. h_0 is the shortest distance from the direction of the ray to the earth's surface.

We shall now examine the problem of the feasibility of using the transmission radiation function P_{sh} plotted by F. N. Shekhter [15] for calculations of the intensity of the integrated outgoing radiation. This function does not take into account the absorption of radiation by ozone. In addition, in plotting P_{sh}, as was indicated by the author himself, use was made of the average dependence between the effective content of water vapor w and carbon dioxide U by measuring w and U from the earth's surface, whereas the calculation of the outgoing radiation requires that w and U be measured from the upper boundary of the atmosphere. It should also be expected that in the spherical atmosphere at large zenith angles, the functional relationship between w and U depends not only on the origin of the measurement, but also on the direction in which the measurement is performed (in Ref. [15], the dependence U(w) was established for the vertical direction). Finally, the use of the transmission function obtained by F. N. Shekhter presupposes the use of a different correction for the pressure in formulas (3) and (4) $\left(\sqrt{\frac{p}{p_0}} \text{ not } \frac{p}{p_0}\right)$.

In order to elucidate the problem of the significance of the enumerated inaccuracies, it is necessary to compare the integrated outgoing radiation calculated on the basis of the function P_{sh} with the integrated radiation calculated in a more rigorous manner. For the latter radiation, we shall use the intensity of the outgoing radiation in the spectral region of 4.88-120 μ, obtained by summing up the radiation intensities in portions 3, 12, 5, 13, 4, 10, 11. In the spectral range of 4.88-120 μ, the overwhelming proportion of the radiation energy of the absolute black body (about 99%) lies within the range of atmospheric temperatures, so that a comparison of Curves 1 and 2 (Figs. 7 and 8) achieves the stated purpose.

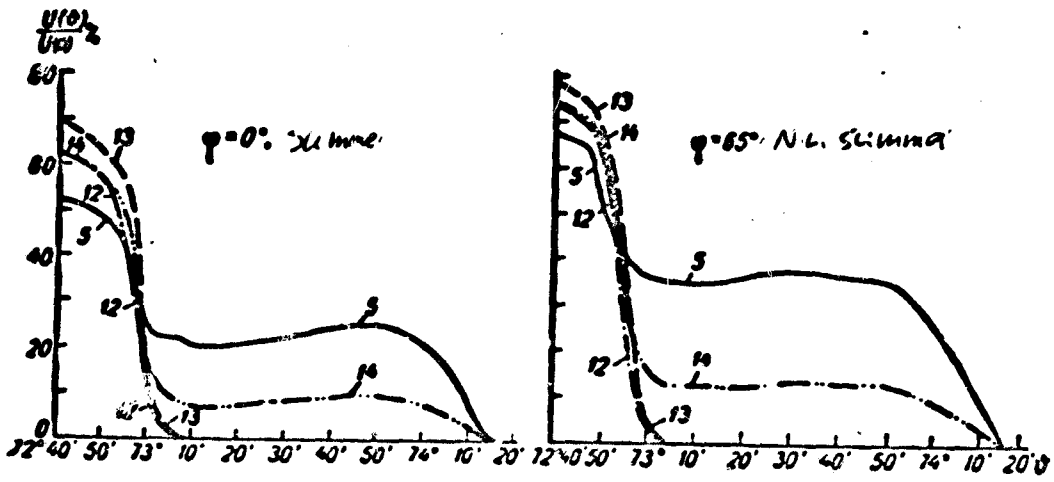

Fig. 6. Comparison of relative angular distributions of outgoing radiation intensity in portions of the spectrum comprising the window of 8.70-12.00 μ, in the range of large zenith angles, clear sky.

As is shown by Figs. 7 and 8, the discrepancy between Curves 1 and 2 in the angular interval of 0—73° is insignificant. Beginning with 73° ($h_0 \approx 9$ km), the difference between the data of curves $U(\vartheta)$ becomes appreciable, the difference in radiation intensities being several times greater than the radiation in the absorption band 9.6 of O_3. This is true up to a zenith angle $\vartheta = 73°55'$, and at $\vartheta > 73°55'$ the integral radiation is determined by the radiation of ozone in accordance with the upper boundary of the radiating atmosphere (39 km) adopted for water vapor. Thus, from this comparison it follows that when $h_0 = 9$ km, the transmission function obtained by F. N. Shekhter can be used for calculating the intensity of the integral outgoing radiation.

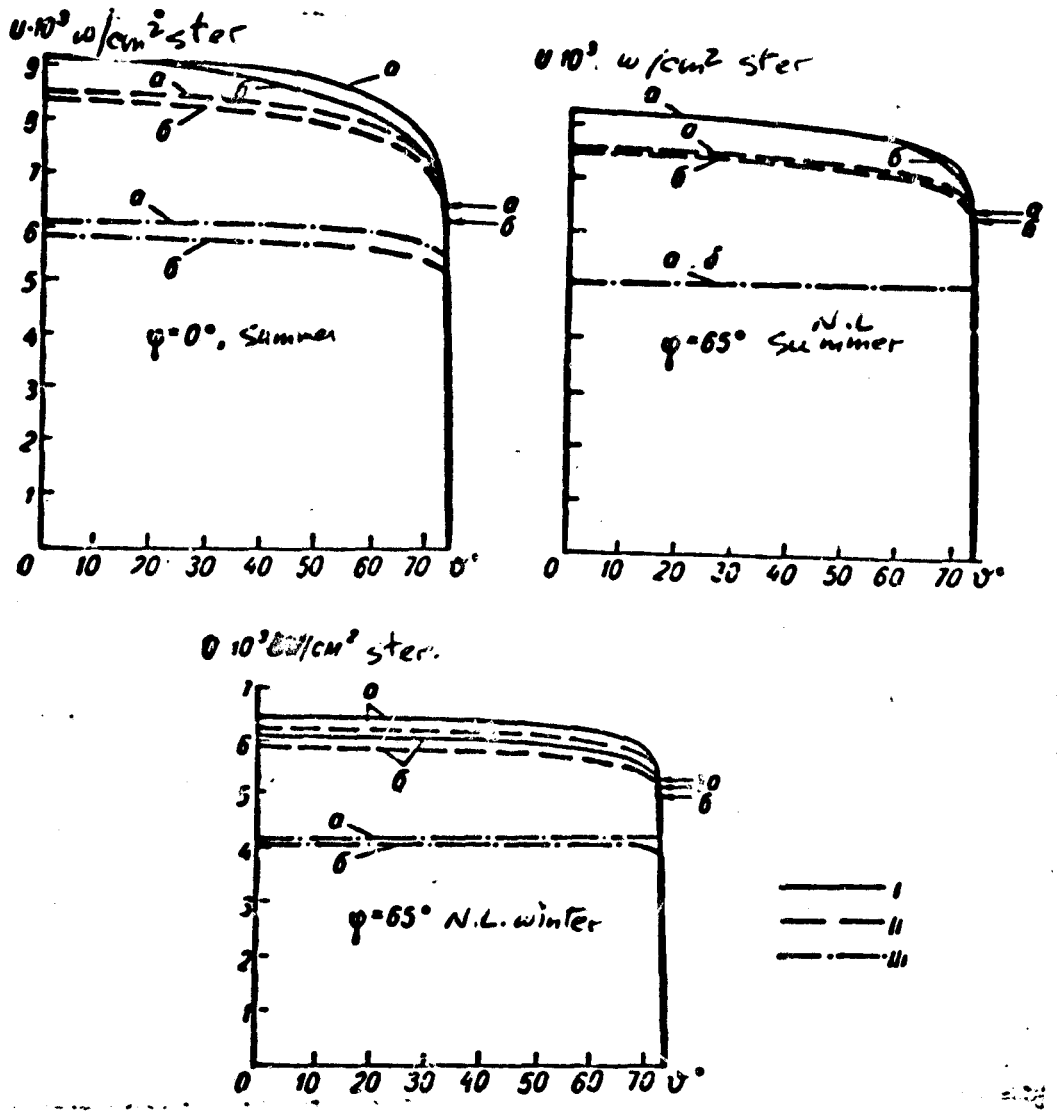

Fig. 7. Comparison of the intensity of integral outgoing radiation calculated by using the transmission function $P_{sh}(a)$ with the intensity of outgoing radiation in the spectral region 4.88-120 μ (b). For designations of I, II, III, see Fig. 1.

It should be noted that the transmission function P_{sh} is calculated on the basis of different absorption characteristics of water vapor and carbon dioxide than those used in our calculations of $U(\vartheta)$. This fact may also be one of the causes of the discrepancy between Curves 1 and 2. For this reason, the above comparison does not reveal the exact magnitude of the errors caused by neglecting the influence of ozone and by the inaccurately established functional dependence U(w). Moreover, it is natural to assume that a compensation of the latter error by the use of various absorption characteristics is possible. In any event, the

surprixingly good agreement in the interval of 0—73° between the angular distributions of the integrated outgoing radiation, which were calculated by two different methods, indicates that the use of P_{sh} in calculations of the intensity of the integrated outgoing radiation at $h_0 < 9$ km results in inaccuracies which are within the limits of error defined by the discrepancy of the various data on the absorption of longwave radiation.

In conclusion, we shall examine the results of calculations of $U(\vartheta)$ obtained in Refs. [2] and [3].

Fig. 8. Comparison of the intensity of integral outgoing radiation calculated by using the transmission function $P_{sh}(a)$ with the intensity of outgoing radiation in the spectral region 4.88-120 μ (b) at large zenith angles. For arbitrary designations I, II, III, see Fig. 1.

In the work of R. McGee [2], calculations of the intensity of outgoing radiation were made for a large number of narrow spectral portions in the wavelength interval of 2.7-13.6 μ. The calculations were made for five stratifications of the atmosphere for a clear sky and various altitudes of the upper boundary of continuous cloudiness: 2, 6, 10, and 12.5 km. The calculations were based on a nine-layer model of the

atmosphere. Of all the results obtained in Ref. [2], only the spectral[1] and angular distributions of outgoing radiation are given in the spectral region of 7.1-13.6 μ for the model of a standard atmosphere ARDC-1959. The cited data show a strong dependence of $U(\vartheta)$ on the conditions of the cloudiness and also a rapid and pronounced infrared darkening toward the limb of the atmosphere, which is in agreement with the results of our calculations in the atmospheric window.

The calculations of R. Hanel, W. Bandeen and B. Conrath [3] were performed for the following five spectral intervals: 6.33-6.85, 8.9-10.1, 10.75-11.75, 14-16 and 21-125 μ. The authors of Ref. [3] used five models of the atmosphere. In addition to clear-sky conditions, conditions of continuous cloudiness were introduced into all the models, except the atmosphere of the desert. The adopted altitude of the upper cloud boundary was the level of the tropopause, i.e., an altitude of 16.5 km in the case of tropical atmosphere, 12 km for the model of the standard atmosphere ARDC-1959, 9 km for the summer arctic atmosphere, and 8.5 km for the winter arctic atmosphere. Integration in the calculation of the effective content of absorbing substances was performed beginning at an altitude of 70 km, and the altitude increment was 0.05 km. The calculation of the intensity of outgoing radiation was done graphically from radiation nomograms of the same type as ours.

The character of the angular distribution of outgoing radiations obtained by R. Hanel, W. Bandeen and B. Conrath in the spectral intervals of 6.33-6.85, 8.9-10.1 and 10.75-11.75 μ is similar to the character of $U(\vartheta)$ which we calculated for portions 6, 5 and 2, respectively. The

1. The spectral distributions are given for three sighting directions: in the direction of the nadir, of the earth's horizon, and in the direction above the line of the horizon.

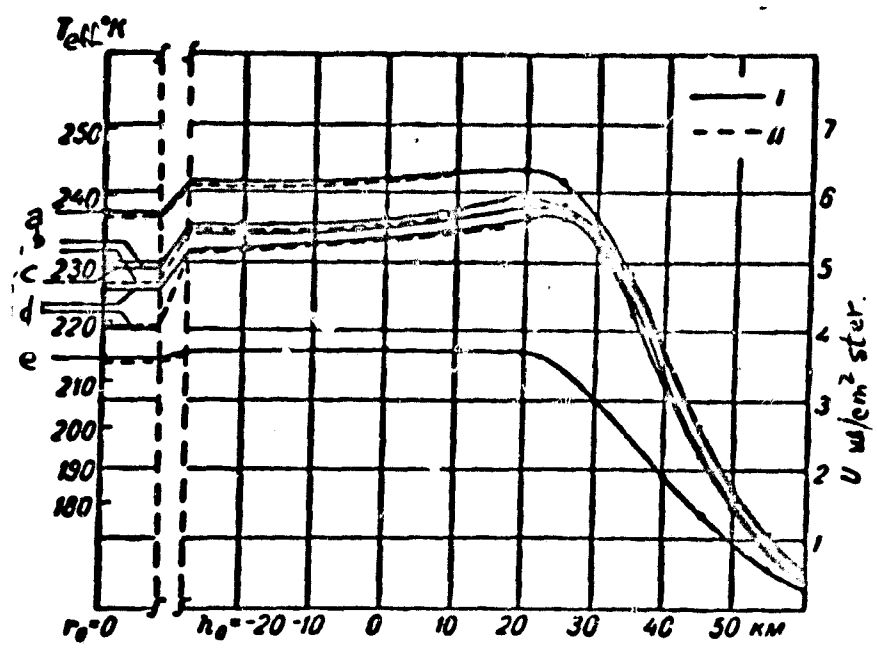

Fig. 9. Angular distribution of the intensity of outgoing radiation in the spectral region of 14-16 μ according to the calculation of R. Hanel, W. Bandeen, and B. Conrath [3].

I - clear sky, II - continuous cloudiness with the upper boundary at the level of the tropopause, a - arctic summer, b - ARDC-1959, c - desert, d - tropics, e - arctic winter.

magnitude of the variability of $U(\vartheta)$ as a function of the conditions of cloudiness and stratification of the atmosphere in the compared portions is approximately of the same order.

The angular distribution of outgoing radiation in the central portion of the absorption band, 15 μ of CO_2, is absent from our calculations, and for this reason the data of R. Hanel, W. Bandeen and B. Conrath for the 14-16 μ interval are of particular interest and are given in full in Fig. 9. Here T_{ef} is the effective temperature of the outgoing radiation; $\vartheta = 0$ corresponds to the direction of the radius vector, i.e., $r_0 = 0$. It is evident from Fig. 9 that in the spectral interval of 14-16 μ, the sensitivity of the outgoing radiation to clouds is negligibly small (this cannot be said of the 12-18 μ interval studied in the present work). However, the general character of the angular distribution of outgoing radiation is closer to the course of the curve $U(\vartheta)$ in the portions of intense absorption by water vapor 6 and 7 than to $U(\vartheta)$ in the spectral

region of 12-18 μ (an abrupt decrease in the radiation intensity begins fairly late beginning at h_0 = 20 km and is preceded by a slight infrared lightening).

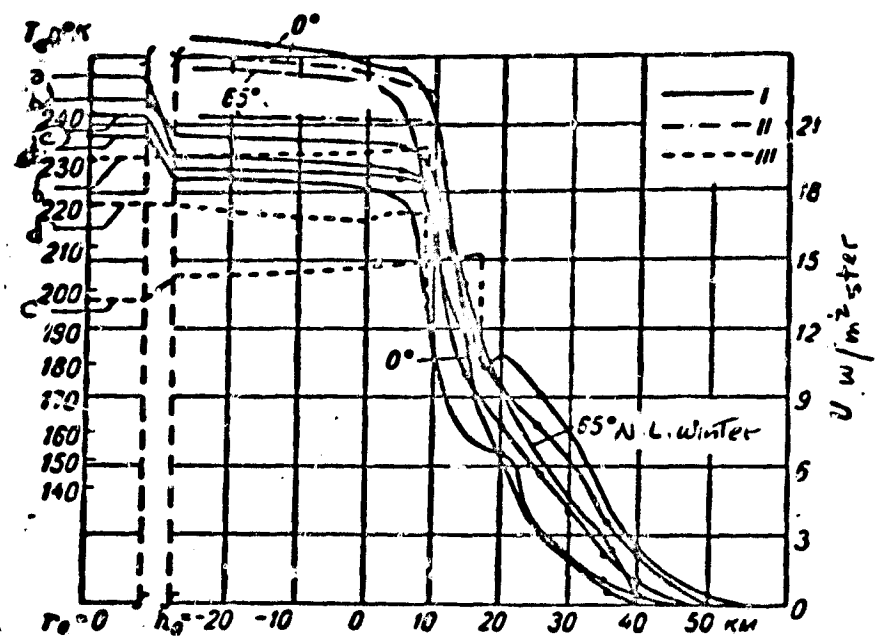

Fig. 10. Angular distribution of outgoing radiation intensity with the spectral region 21-125 μ based on calculations of R. Hanel, W. Bandeen and B. Conrath [3]. For comparison, the curves $U(h_0)$ for $\varphi_0 = 0^\circ$ and $\varphi = 65^\circ$ (winter) are also shown in the spectral interval 18-120 μ, obtained in the present work.

I - clear skies; II - continuous cloudiness with upper boundary at the level of 9 km; III - continuous cloudiness with upper boundary at the level of the tropopause; a - desert, b- arctic summer, c - tropics, d - arctic winter.

The angular distributions of the radiation of the earth—atmosphere system obtained in Ref. [3] for the far infrared, 21-125 μ, are shown in Fig. 10. Also shown are curves of $U(h_0)$ in the interval of 18-120 μ which we calculated for $\varphi = 0^\circ$ and $\varphi = 65^\circ$ N.L. (winter). The radiation intensity in the spectral region of 18-120 μ was calculated by summing up the radiation intensities in spectral portions 10 and 11. Despite somewhat different spectral intervals and models of the atmosphere, Fig. 10 shows a good agreement between the data of Ref. [3] and our calculations. The conclusion that the outgoing radiation is weakly sensitive to clouds and to the stratification of the atmosphere in the far

infrared is fully confirmed.

The authors express their gratitude to A. D. Poddubik and other collaborators who carried out the various calculations for the present work.

Note. We calculated the radiation intensity for the following zenith angles: 0, 30, 50, 60, 70, 71, 72°, 72°20', 72°40', 72°45'. When $\vartheta > 72°45'$, the calculations were made on the average with $\Delta\vartheta = 4'$.

REFERENCES

1. Kondrat'yev, K. Ya., Yakushevskaya, K. Ye. Uglovoye raspredeleniye ukhodyashchego teplovogo izlucheniya v razlichnykh oblastyakh spektra [Angular Distribution of Outgoing Thermal Radiation in Various Regions of the Spectrum]. Iskusstevennyye sputniki zemli, vyp. 14, 1962.
2. McGee, R. A.. An analytical infrared radiation model of the Earth. Applied Optics, v. 1, No. 5, p. 649, 1962.
3. Hanel, R. A., Bandeen, W. R., Conrath, B. J. The infrared horizon of the planet Earth. X-650-62-164 (preprint). Goddard Space Flight Center, Greenbelt, Md, August 1962.
4. Jamamoto, G. and Onishi, G. Absorption coefficient of water vapour in the far infrared region. Science Reports of the Tohoku University, ser. 5, v. 1, No. 1, p. 5, 1949.
5. Wark, D. Q., Jamamoto, G., Lienesch, J. H. Methods of estimating infrared flux and surface temperature from meteorological Satellites. Journ. of the Atmospheric Sciences, v. 19, No. 5, p. 369, 1962.
6. Palmer, C. H. Experimental transmission functions for the pure rotation band of water vapor. Journal of the Optical Society of America, v. 50, p. 1232, 1960.
7. Niylisk, Kh. Yu. Novaya radiatsionnaya nomogramma [New Radiation Nomogram]. Izv. AN ESSR, ser. fiz.-mat. i tekhn. nauk, Vol. 10, No. 4, p. 329, 1961.
8. London, J. A study of the atmospheric heat balance. Contract, No. AF 19-(122)-165, 1957.
9. Murgatroyd, R. J. Winds and temperatures between 20 km and 100 km — a review. Quart. Journ. Roy. Met. Soc., v. 83, No. 358, p. 417, 1957.
10. Barclay, F. R., Elliot, M. J., Goldsmith, P. and Jelley, J. V. A direct measurement of the humidity in the stratosphere using a cooled - vapour trap. Quart. Journ. Roy. Met. Soc., v. 86, No. 368, p. 368, 1960.
11. Gutnick, M. How dry is the sky? Journ. of Geophys. Res. v. 66, No. 9, p. 2867, 1961.
12. Gutnick, M. Mean moisture profiles to 31 km for middle latitudes. Applied Optics, v. 1, No. 5, p. 670, 1962.

13. Ramanathan, K. R. and Kulkarni, R. N.. Mean meridional distributions of ozone in different seasons calculated from umkehr observations and probable vertical transport mechanisms. Quart. Journ. Roy. Met. Soc., v. 86, No. 368, p. 144, 1960.
14. Yakushevskaya, K. E. Ob odnom pribilizhenii v raschetakh teplovoy radiatsii atmosfery. Problemy fiziki atmosfery [An Approximation in Calculations of the Thermal Radiation of the Atmosphere. Problems of Atmospheric Physics]. Izd. LGU, 1963.
15. Shekhter, F. N. K vychisleniyu luchistykh potokov tepla v atmosfere [Calculation of Radiant Thermal Fluxes in the Atmosphere]. Tr. GGO, vyp. 22, p. 38, 1950.

M. S. Malkevich

SOME PROBLEMS OF THE INTERPRETATION OF THE FIELD OF OUTGOING RADIATION OF THE EARTH I. DETERMINATION OF THE TEMPERATURE OF THE UNDERLYING SURFACE AND ALTITUDE OF THE UPPER BOUNDARY OF CLOUDS

1. Introduction

The field of outgoing radiation reflected and radiated by the earth into space in various portions of the spectrum contains some information on the thermodynamic state of the atmosphere and its structure. By studying the radiation field characteristics measured by means of artificial earth satellites or high altitude rockets, one can obtain information:

1) On the thermal behavior of the atmosphere and underlying surface, including clouds;

2) On the energy balance of the earth and the space-time distribution of the sources and outlets of heat;

3) On the nature of the synoptic processes in the atmosphere and the type of cloud formations;

4) On the distribution in the atmosphere of substances active from the standpoint of radiation, in particular, on the content of water vapor, carbon dioxide, ozone and aerosol in the atmosphere.

The extraction of this information involves serious difficulties, chief of which consist in the following:

1. The earth's radiation field is generated under the influence of various factors, for example, the state of the earth's surface, the content in the atmosphere of substances absorbing and scattering the radiation, the nature of the clouds, the temperature distribution, etc. For this reason, in order to determine the parameter which is of interest to us, we must have data on the other factors, or we must choose those

characteristics of the radiation field in which the major part is played by the given factor and where the influence of the others is minor. In this connection, in elaborating programs for radiation investigations, it is extremely important to choose correctly a set of the most informative characteristics of the radiation field and the spectral intervals providing for the most reliable interpretation of the observational results.

2. Changes in sum of these factors are sufficiently regular in character and follow a more or less reliable pattern which can be taken into consideration (for example, the radiation properties of continents, oceans and of the plant cover, the content of oxygen and carbon dioxide in the atmosphere). Many factors, however, vary strongly in time and space (for example, clouds, water vapor, aerosol, temperature of the atmosphere), and these variations are random in character, so that when they are taken into consideration in the interpretation of radiation measurements, it is necessary to use statistical methods.

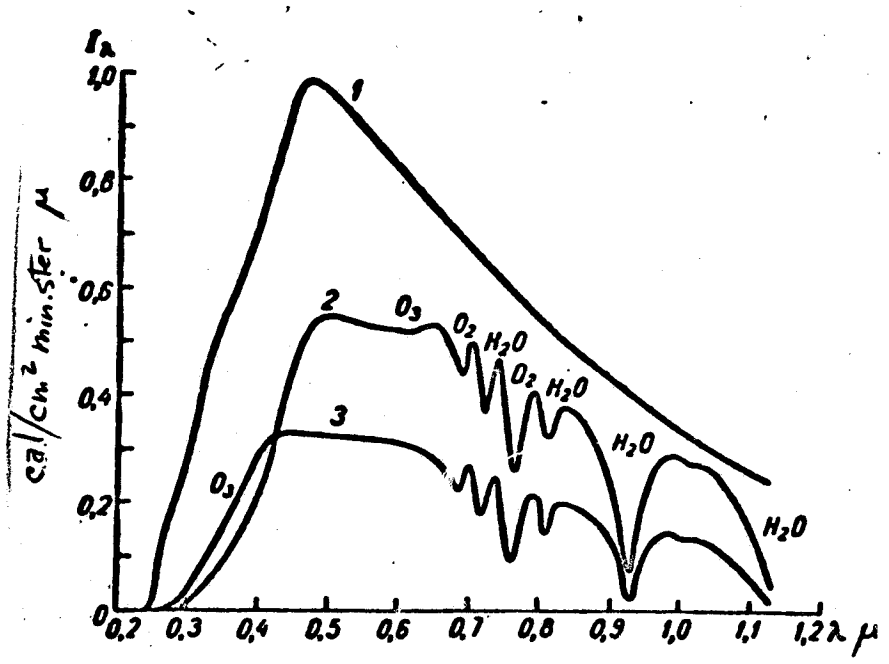

Fig. 1. Spectral variation of the intensity of solar radiation (cal/cm^2 min ster μ)

1 - exoatmospheric solar radiation; 2 - solar radiation at sea level ($\xi = 60^\circ$); 3 - solar radiation leaving the upper boundary of the atmosphere ($\xi = 60^\circ$; $\theta = 0$; $q = 0.8$).

In developing a method for the interpretation of radiation measurements, it is obviously advisable to simulate radiation fields, taking as the basis models of the atmosphere and of the underlying surface which are close to the actual conditions. By using the apparatus of the theory of radiation transfer in a turbid and thermally stratified atmosphere, whose model is specified by the vertical distribution of the absorbing and scattering substances, by the temperature, and other parameters, it is not difficult to calculate the characteristics of the field of outgoing radiation in the various portions of the specturm (direct problem). On the basis of the calculated data, the same parameters of the atmosphere may be found by solving the reverse problem, then they can be compared with the initial data. This allows the following: a) to calculate the main possibilities of extracting the necessary information; b) to elaborate methods of interpretation of the measurement data; c) to estimate the errors made in the determination of the desired quantities, due to the error of the measurements themselves and to the insufficiency of information on the other factors.

Some results of the solution of direct problems applicable to investigations of the earth's radiation field from satellites were obtained in several works [1-5]. Examples of the spectral variation in the intensity of radiation leaving the upper boundary of the atmosphere are given in Figs. 1 and 2 (see also [2-5]). In addition, results of direct radiation measurements have already appeared [6-9] which make it possible on the one hand to check the calculated data, and on the other, to estimate the effectiveness of the methods of interpretation.

In the present work, consideration is given to some possibilities of obtaining geophysical information from the results of measurements of radiation reflected and radiated by the earth into space in various portions

of the spectrum. The first part of the paper suggests methods for determining the temperature of the underlying surface and the altitude of clouds from radiation measurements. The second presents a method of solving the problem of discrimination of clouds and natural surfaces (snow, ice and desert) having the same reflective or radiative characteristics and therefore indistinguishable in certain spectral intervals.

2. Temperature of the underlying surface

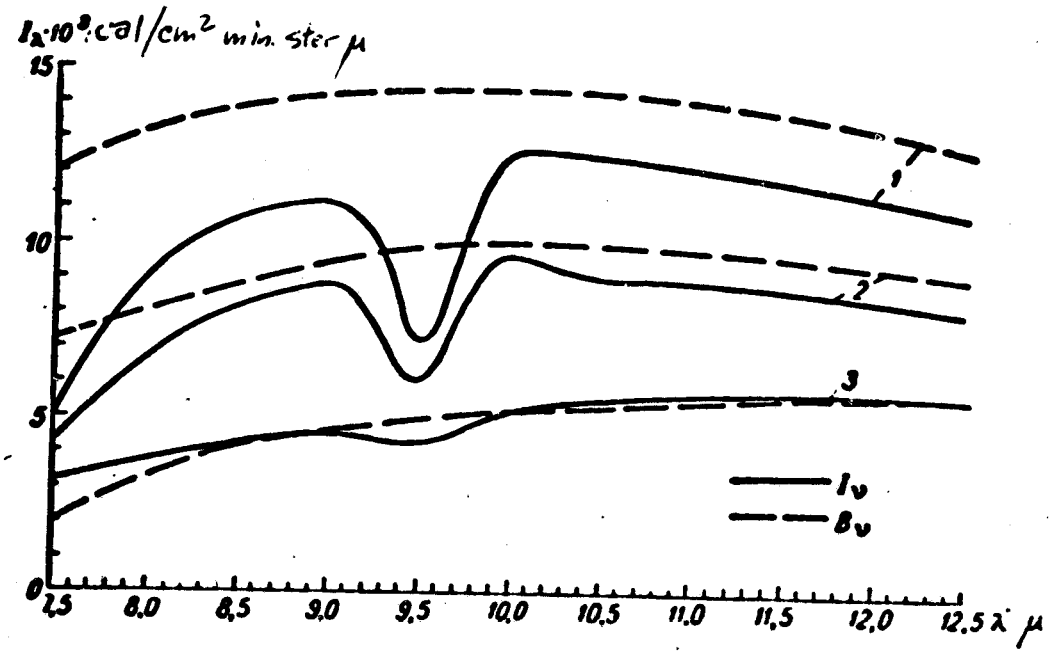

Fig. 2. Spectral variation of the intensities of the radiation of a black body and of the outgoing radiation in the "transparency window" of the atmosphere ($\theta = 0$) for for some latitudinal belts (10^3 cal/cm^2 min ster μ).

1 - tropics; 2 - temperate latitudes; 3 - polar latitudes.

From Fig. 2 it follows directly that the temperature of an underlying surface may be obtained most reliably by using radiation in the spectral interval of 8-12 μ or in its parts. In this interval of the spectrum, called the "transparency window" of the atmosphere, the outgoing radiation is closest to the radiation of the surface. This is due to the fact that the latter radiation is only slightly distorted in the atmosphere, since the 8-12 μ region contains only weak absorption bands of water vapor and carbon dioxide, which are chiefly

responsible for the formation of the field of thermal radiation in the atmosphere. The 9.6 absorption band of ozone, which is located in this interval, is relatively narrow and cannot appreciably attenuate the emission of the underlying surface.

The intensity of the radiation $I_\nu(w^*, \theta)$ (ν is the frequency) leaving the upper boundary of the atmosphere as defined by the following relation:

$$I_\nu(w^*,\theta) = B_\nu(T_0) P_\nu(w^* \sec\theta) \bar{P}_\nu(m^* \sec\theta) + \int_0^{w^*} B_\nu[T(z)]\, d\{P_\nu[(w^* - w)\sec\theta]\, \bar{P}_\nu[(m^* - m)\sec\theta]\}. \quad (1)$$

Here T_0 is the temperature of the underlying surface; T(z), w(z), and m(z) are the vertical distributions of the temperature and of the masses of water vapor and ozone contained in a vertical column of air starting from the underlying surface (z = w = m = 0) up to level z; $w^* = w(\infty)$, $m^* = m(\infty)$ are the masses in the entire column of air; $B_\nu(T)$ is Planck's function, and P_ν and $\bar{P}_\nu$ are transmission functions of water vapor and ozone; θ is the angle between the sighting direction and the nadir direction ($\theta = 0$). Let us note that in considering the sphericity of the atmosphere, the dependence on angle θ intervenes in a more complex manner, although the form of expression (1) is retained. The first term in (1) describes the attenuation of atmospheric radiation by the underlying surface, which is assumed to emit as a black body at temperature T_0[1]. The second term characterizes the contribution to the outgoing radiation of the self-radiation of the atmosphere, which in some degree compensates for the attenuation of the radiation of the underlying surface.

1. Taking the coefficient of the emissivity of the underlying surface does not present any difficulty and does not appreciably change the form of formula (1) as long as this parameter is known. Unfortunately, such data for natural surfaces are either almost completely lacking or are unreliable.

Thus, owing to the absorption of radiation by water vapor and ozone, and also because of the self-radiation of these gases in a thermally stratified atmosphere, the outgoing radiation intensity I_ν will differ from the radiation intensity of the underlying surface $B_\nu(T_0)$. Hence, the so-called equivalent radiation temperature, i.e., the temperature of a black body whose intensity is $I_\nu(w^*, \theta)$, will differ from T_0. However, for reasons indicated above, this difference in the region of 8-12 μ will be small, and in any event smaller than in the other spectral intervals. The outgoing radiation itself is rather appreciable in this spectral interval and can be reliably recorded with radiometers (let us recall that the "transparency window" corresponds to the region of maximum emission at earth temperatures).

The determination of T_0 is further facilitated by the fact that water vapor and ozone are separated in space. Actually, the bulk of water vapor is concentrated in the troposphere (up to 10-12 km), where small vertical temperature gradients are also observed, whereas the bulk of ozone is concentrated in the stratosphere (10-30 km), where the temperature itself and its gradient are low. For this reason, the contribution to the outgoing radiation of the self-radiation of the atmosphere, the allowance for which causes the greatest difficulty in (1), is accomplished only by the radiation of water vapor. The contribution of the self-radiation of the ozoneosphere will be small for understandable reasons, and it is sufficient to take into consideration only the total attenuation of the radiation of the underlying surface by ozone. However, at very low temperatures of the underlying surface, particularly in the case of high clouds, this contribution will be substantial and will cause the outgoing radiation to surpass the emission of the underlying surface (see below). Concrete calculations of the outgoing

radiation intensity $I_\nu(w^*, \theta)$ were carried out for various models of the atmosphere characterized by averaged latitudinal distributions of the vertical profiles of temperature and water vapor density. In each latitudinal belt, the entire actual range of variations in the mass of ozone in the atmosphere was considered. The transmission functions $P_\nu(w)$ were calculated from the data of [10, 21] on the absorption coefficients of water vapor, and $P_\nu(m)$ was calculated from the data of [11] on the absorption of ozone. The results of calculations of I_ν in the spectral interval of 7.5-12.5 μ for the tropical, temperate and polar zones are given in Fig. 2. It is interesting to note that for the polar zone, the values of I_ν obtained in the transparency interval were greater than the corresponding values of $B_\nu(T_0)$. This is explained by a fairly deep temperature inversion of the atmosphere existing in the polar regions up to altitudes of 3-4 km. For this reason, the emission of the warmer atmosphere layer is sufficient to not only offset the attenuation of radiation by the cool underlying surface, but also to raise somewhat the general level of the outgoing radiation. A colder atmospheric layer located above the inversion emits effectively at the wings of the absorption bands of water vapor (7-8 μ) and carbon dioxide (12-13 μ), and this compensation does not take place. The results shown in Fig. 2 were obtained without taking into account the radiation of the mesosphere. However, even when the moisture content of the mesosphere, where a deep temperature inversion also exists, is moderate, a certain contribution to the outgoing radiation will also be made by the 30-50 km layer.

In this case, when the underlying surface has a very low temperature (for instance, the upper boundary of high clouds), the contribution of the emission of the mesosphere will cause the intensity of the outgoing

radiation in the absorption bands of water, carbon dioxide, and ozone to be higher than the radiation intensity of the surface itself. In the transparency window, however, this effect naturally will not be observed. In other words, an inversion variation of the radiation level in the spectrum should be observed: a maximum in the absorption bands and a minimum in the transparent intervals (see also the second part of this article). It should be noted that under actual conditions, high clouds are usually insufficiently dense and can transmit the radiation of a warmer atmosphere located underneath. For this reason, this effect will apparently be observed only in exceptional cases, for example in the case of heavy thunder clouds with a high upper boundary. It would be interesting to check this conclusion experimentally, since it may serve as a criterion for detecting thunderstorm clouds.

Thus, differences between I_ν and $B_\nu(T_0)$ will vary considerably depending upon the variation in the mass of water vapor and the temperature profile (the actual variations in the mass of ozone are practically not manifested in the variations of I_ν. This is clearly demonstrated in Ref. [4], in which similar calculations were made for 106 models of the atmosphere. This fact makes the determination of T_0 from the data of radiation measurements in the "transparency window" very difficult. These difficulties are compounded by the inadequacy of the instruments. For example, the spectral characteristics of the radiometer used to measure the radiation in the "transparency window" from the "Tiros" satellites was such that an appreciable part of the radiation corresponding to the wings of the neighboring bands of strong absorption of water vapor and carbon dioxide was recorded.

If k_ν is the spectral sensitivity of the radiometer, the intensity of the measured radiation is given by the formula:

$$I_{\Delta\nu}(w^*, \theta) = \int_{\nu_1}^{\nu_2} k_\nu I_\nu(w^*, \theta) d\nu \qquad (2)$$

($k_\nu \cong 0$ outside the interval $\nu_1 < \nu < \nu_2$), and ν_1 and ν_2 may differ appreciably from the limits of the transparency interval. For example, for the radiometer of "Tiros", ν_1 = 700 cm (λ_1 = 14.3 μ), ν_2 = 1400 cm (λ_2 = 7.2 μ), the values of k_ν being very small in the vicinity of these limits.

Having determined $I_{\Delta\nu}$ from the calculations of I_ν for various models of the atmosphere, we can, as was done in Ref. [4], derive the relation between $I_{\Delta\nu}$ and

$$I'_{\Delta\nu} = \int_{\nu'_1}^{\nu'_2} I_\nu d\nu, \qquad (3)$$

where ν'_1 and ν'_2 are some effective limits of the spectral interval selected so that the linear dependence

$$I_{\Delta\nu} = k' I'_{\Delta\nu} \qquad (4)$$

exists between $I_{\Delta\nu}$ and $I'_{\Delta\nu}$ (k' may be treated as the average transmission of the instrument). This dependence makes it possible to make the conversion from the measured intensity $I_{\Delta\nu}$ to the quantity $I'_{\Delta\nu}$, which is independent of the spectral sensitivity of the radiometer, and the latter value can be used to determine the temperature of the underlying surface. In order to solve this problem, in Ref. [4] corrections were calculated which should be introduced into $I'_{\Delta\nu}$ because of the attenuation of the radiation of the underlying surface by water vapor and ozone, and also because of the self-radiation of the atmosphere.

It was found that the scatter of the corrections was very high. For this reason, the temperature T_0 is obtained with a high degree of

indeterminacy. This indeterminacy was not eliminated by the fact that the authors of Ref. [4] used two different relations for the conversion of $I'_{\Delta v}$ to T_0 for high and low humidity, since the latter remains unknown in the "Tiros" experiment. This situation may be improved somewhat, however, if use is made of the climatic data of the geographical and seasonal distribution of the vertical profiles of temperature and water vapor, and also data on the deviations of these profiles. In any event, the mean square deviation from the average profiles will make it possible to obtain the corresponding error in the determination of T_0. In addition, the interpretation of directly measured values of $I_{\Delta v}$ may be simplified; namely, relations between $I_{\Delta v}$ and T_0 may be derived (examples of such a relation for the radiometer of "Tiros" and for filters indicated in Ref. [12] are given in Fig. 3).

Since our calculations of $I_{\Delta v}$ were based on average profiles T(z) and w(z), the relations between $I_{\Delta v}$ and T_0 were found to be completely regular, but strongly dependent on the spectral sensitivity of the instrument. It is interesting to note that the differences between the radiation temperature and T_0 (Fig. 3) may attain 20-25° for large masses of water vapor, and the correction for ozone absorption, 5°. This is also confirmed by direct measurement [7].

In using individual temperature and humidity profiles, a scatter of curves similar to those shown in Fig. 4 is obtained. This scatter is mainly due to a difference in T_0 for the same w^*, or conversely, to a difference in w^* for the same value of T_0. Much of the scatter may be eliminated by introducing the transmission function

$$\tilde{P}_{\Delta\nu}(w^*, \theta) = \frac{I_{\Delta\nu}(w^*, \theta)}{B_{\Delta\nu}(T_0)}, \qquad (5)$$

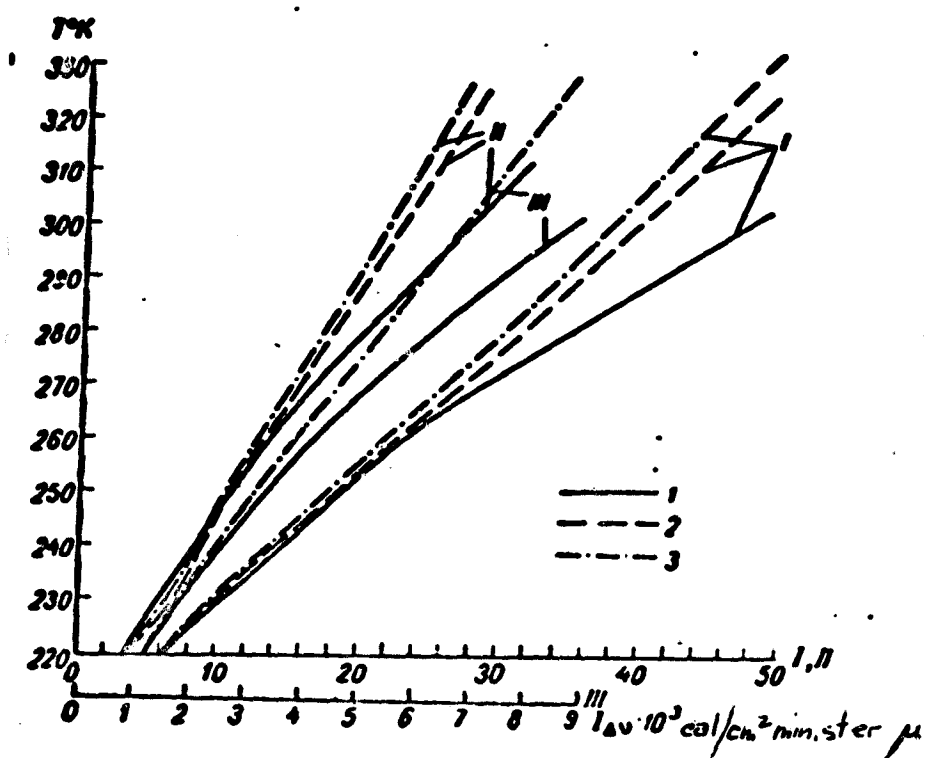

Fig. 3. Dependence between the temperature of the underlying surface and the outgoing radiation intensity in the atmospheric "transparency window" for the radiometer of "Tiros" [4]; (I); and for the radiometers of Ref. [12] (II, III).

1 - equivalent radiation temperature; 2 - true temperature allowing for absorption by water vapor (without ozone); 3 - same, but taking into account the absorption by both gases.

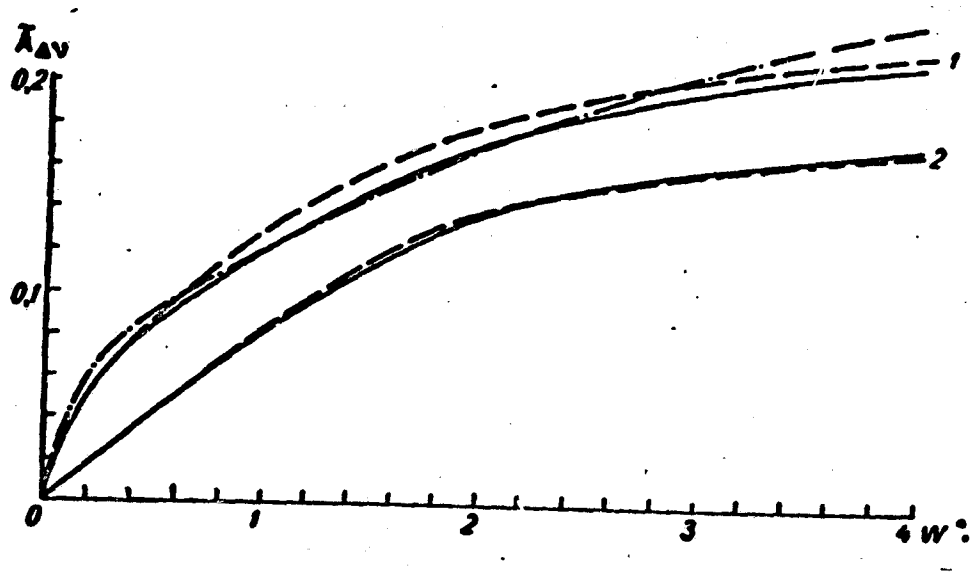

Fig. 4. Effective absorption function $\tilde{A}_{\Delta\nu}$ on the mass of water vapor.

1 - considering the absorption by water vapor and ozone; 2 - considering the absorption by water vapor alone.

which characterizes the transformation of the emission of the underlying surface, allowing for the transmission and self-radiation of the atmosphere. It is easy to understand that this function depends weakly on the spectral sensitivity of the instrument k_v and on the temperature of the underlying surface T_0, since in relation (5), both the numerator and the denominator depend on these parameters. This is immediately apparent from Fig. 4, which shows the function $\tilde{A}_{\Delta v} = 1 - \tilde{P}_{\Delta v}$, plotted for the above-indicated radiometers and for average profiles of T(z) and w(z) as a function of the main argument (mass of water vapor w*) and for $\theta = 0$ (the functions $\tilde{A}_{\Delta v}$ or $\tilde{P}_{\Delta v}$ also depend on m* and on the vertical temperature gradient $\frac{\partial T}{\partial z}$, which may also be treated as parameters).

The use of functions $\tilde{A}_{\Delta v}$ or $\tilde{P}_{\Delta v}$ for the determination of T_0 has a certain advantage over the relation represented by Fig. 3, since these functions vary slightly with the variability of such parameters as the spectral sensitivity of the instrument and the temperature of the underlying surface. Furthermore, since the humidity of the atmosphere correlates with the temperature, the increase in the mass of water vapor w*, which results in an increased attenuation of the radiation of the underlying surface, will be accompanied by an increase in the contribution of the self-radiation of the atmosphere, which offsets this attenuation to a considerable extent. Therefore, it may be expected that the transmission function will be fairly stable in a statistical sense in relation to variations of T and w.

One can also find the correction to the "transmission" function $\tilde{A}_{\Delta v}$ obtained for averaged $\bar{T}(z)$ and $\bar{w}(z)$ by expressing it through the pulsations $T'(z) = T(z) - \bar{T}(z)$ and $w'(z) = w(z) - \bar{w}(z)$.

Actually, writing (1) for T'(z) and w'(z) and averaging over all the realizations, we obtain

$$\tilde{I}'_{\Delta\nu} = \left(\frac{\partial B_\nu}{\partial T}\right)_{\bar{T}_0} \frac{\partial P_\nu(\bar{w}^*)}{\partial w} \overline{w^{*\prime} T'_0} + \int_0^{\bar{w}^*} \frac{\partial B_\nu(\bar{T})}{\partial T} \frac{\partial^2 P_\nu(\bar{w}^* - \bar{w})}{\partial(w^* - w)^2} \overline{(w^{*\prime} - w')T'} dw \qquad (1')$$

(for simplicity, we set $\theta = 0$ and $\bar{P}_\nu \equiv 1$, i.e., ν is outside the band of ozone).

Thus, the correction for the "transmission" function $\tilde{P}'_{\Delta\nu} = \frac{\tilde{I}'_{\Delta\nu}}{B_{\Delta\nu}(\bar{T}_0)}$ may be expressed by a mutual correlation function $k_{wT} = \overline{w'T'}$. If $k_{wT} > 0$, the first term in equation (1') is less than zero, the second is greater than zero, and depending upon their relation, $\tilde{P}'_{\Delta\nu}$ will be greater or smaller than zero. Having determined k_{wT} for a given geographical point and time interval (day, month, season), one can allow for the pulsations of temperatures and humidity in the transmission function.

Thus, using the functions $\tilde{A}_{\Delta\nu}$ plotted for the averaged profile T(z) and w(z) and their pulsations, we can determine T_0 and the corresponding error. As is shown by the calculations, the error involved in the use of average profiles alone may be appreciable and exceed 5°. If one specifies a set of radiation measurements which would permit the determination of the mass of water vapor w* and ozone m* (this may be done by measuring the reflected solar radiation in the absorption bands of water vapor in the near infrared and of ozone in the ultraviolet), the error in the determination of T_0 will be substantially decreased. A still more reliable determination of T_0 may be achieved by determining the temperature profile by means of independent spectral measurements of the outgoing radiation in the absorption band of carbon dioxide at 15 μ, as was suggested in Ref. [13].

3. Altitude of the Upper Boundary of Clouds

In the case where the underlying surface is a sufficiently dense

cloud optically, the above-described method makes it possible to determine the temperature of the upper boundary of this cloud[1]. If the vertical temperature distribution is known, the altitude of the upper cloud boundary will thus also be determined. It is quite evident that to the above-described errors in the determination of T_0 will be added the error due to the lack of information on the actual (and not average) correspondence of the determined temperature to a certain altitude z. It should be remembered that the vertical temperature profiles may be substantially different both under cloudy and cloudless conditions and for various realizations of cloud formations.

Attempts to determine the altitude of the upper cloud boundary by means of data on the outgoing radiation in the "transparency window" obtained with the satellite "Tiros-II" and data on the stratification of the atmosphere in the corresponding regions were undertaken in Refs. [6, 14]. A comparison with the altitudes of clouds obtained by means of aerological data on the vertical distribution of humidity showed [14] that the differences between the altitudes determined by the two methods amount to an average of 1 km, but in some cases exceed this value considerably.

The results given in Refs. [6, 14] do not provide a reliable estimate of the error in the determination of the altitude of the upper cloud boundary, since actual data on the cloud level are lacking. However, it is quite clear that the necessity of using information on the temperature profile is a serious disadvantage of the proposed method, and one which cannot be easily eliminated. At the same time, this method has a definite advantage, since it can be used on the dark side of the earth, and

1. The concept of the upper cloud boundary may be treated only in an arbitrary sense, since the upper boundary of most cloud systems has a complex structure and it can be identified with a horizontal plane only in certain cases of stratified clouds.

when information on only one field of outgoing radiation is available, it is the only possible method. However, on the illuminated side of the earth, the altitude at the upper cloud boundary may be determined by other methods (a brief description of these methods is given in Ref. [2]) based on a measurement of the solar radiation reflected off the earth, in various portions of the spectrum, including the absorption bands of atmospheric gases, whose concentration varies slightly in time and space (such gases are oxygen and carbon dioxide, for example).

The method involving the use of the absorption bands of gases of constant concentration consists in the following: if one measures the radiation reflected from a cloud for a given position of the sun and a given sighting direction, within and without the absorption band of such a gas, one can determine the transmission of the atmosphere in this band as a function of the mass of the absorbing substance contained in a column of the atmosphere between the cloud and the observer (it is assumed that the dependence between the transmission and the mass is known). Since the concentration of the absorbing substance in the atmosphere is constant, the mass will be a single-valued function of the altitude of the cloud.

The use of the absorption bands of CO_2, centered in the infrared region of the spectrum, is complicated by the fact that they overlap with the strong absorption bands of water vapor located in the same region, the concentration of water vapor being subject to considerable variations. Furthermore, this spectral region corresponds to fairly small values of solar energy, which complicates the measurements and results in large errors.

More favorable conditions for the determination of the altitude of the upper cloud boundary are offered by the absorption band of molecular

oxygen, 0.762 μ (7590-7650 Å). The main advantage is the fact that this band does not overlap with the absorption bands of the other gases. In this spectral region, there is still much solar energy, and very sensitive receivers exist which make it possible to measure this radiation with a high degree of accuracy. Unfortunately, the dependence of the transmission of oxygen in this band on its mass has been insufficiently studied. For small masses, the absorption coefficient of oxygen at the center of this band is given in Ref. [15]; it is 0.012-0.018 cm^2/g for an oxygen mass of the order of 2 g/cm^2. If use is made of the solar spectrograms given in Ref. [16] for five positions of the sun, one can determine the absorption coefficient for masses of oxygen varying from 200-1000 g/cm^2. In the central portion of the 7590-7650 Å band, the absorption coefficient of oxygen changes from 0.0012 to 0.0010 cm^2/g, and for the center of the band, from 0.0011 to 0.0013 cm^2/g, i.e., one order of magnitude less than the above-mentioned coefficient for small masses. A value of the same order is obtained if use is made of the transmission function o oxygen averaged over the entire band and given in Ref. [17].

Thus, the absorption coefficient of oxygen obtained on the basis of measurements by spectroscopic instruments of low resolving power are found to be dependent on the mass u. When the mass increases by two orders of magnitude, the absorption coefficients decrease by one order, i.e.,

$$a(u) \sim u^{-1/2}. \tag{6}$$

Hence, for absorption functions for masses of the same order, the square root law is valid:

$$A(u) \sim \sqrt{u}, \tag{7}$$

which also holds for the absorption bands of water vapor[1]. Let us note that for large oxygen masses contained in inclined columns of air (large θ's and zenithal distances of the sun ξ), formulas (6) and (7) will no longer apply. However, for preliminary evaluations of the possibility of determining the altitude of clouds by this method, it is not necessary to use these formulas.

Below we shall see how the altitude of the upper cloud boundary z_0 shall be determined if the corresponding measurements of the outgoing radiation intensity are made in the centers of the absorption band of oxygen and of the neighboring transparent interval (7350-7450 Å). The intensities in the first and second regions of the spectrum are given respectively by the following formulas:

$$I_1(u, m; \theta, \xi) = I_1^0 q_1 \exp[-(\sigma u + \sigma_1 m)(\sec\xi + \sec\theta)] + \bar{I}_1, \quad (8)$$

$$I_2(u, m; \theta, \xi) = I_2^0 q_2 \exp[-\sigma_2 m(\sec\xi + \sec\theta)] + \bar{I}_2, \quad (9)$$

where I_i^0 are the values of the solar constant in the corresponding portions of the spectrum (i = 1, 2), $\bar{I}_i$ are the intensities of multiple scattered radiation in a layer of air located above the reflective surface; q_i is the albedo of the surface; σ_i is the mass scattering coefficient; m is the mass of air in the vertical column above the cloud.

Since both spectral intervals lie in a region of fairly weak scattering of solar radiation in the atmosphere, and are located close to each other, it may be assumed with a high degree of accuracy that $\sigma_1 = \sigma_2 = \sigma$ and $I_1^{(0)} = I_2^{(0)}$. As far as the values of $\bar{I}_i$ and q_i are concerned, it follows from Ref. [18-20] that they may differ strongly within and without the absorption bands. These differences depend on the ratio

1. V. I. Dianov-Klokov drew the author's attention to the existence of relations (6) and (7)

$r = \frac{\sigma}{\sigma + \alpha\beta}$ ($\beta = 0.23$ is the relative oxygen concentration in air). For air, $\sigma \approx 1 \times 10^{-4}$ cm^2/g, i.e., $r = 0.3$. Hence, $\bar{I}_1$ is approximately one order of magnitude smaller than $\bar{I}_2$. For clouds, $\sigma = 1{,}000$ cm^2/g and the ratio $r = 0.9994$, so that the ratio of the values of the albedo $\frac{q_1}{q_2}$ will be close to unity (see Ref. [18]), although according to other data, (for example, Ref. [20]), q_1 may be less than q_2.

If the cloud reflects the radiation strongly (large q), the sun is located relatively high above the horizon (small ξ), and the sighting direction does not deviate from the nadir too much, the values of $\bar{I}_i$ will be small compared to the intensity of the direct solar radiation reflected from the cloud and described by the first terms in (8) and (9). For example, for ground level at $q = 0.8$ and for θ and ξ smaller than 60°, the value of $\bar{I}_i$ does not exceed 15% of the first terms and is considerably smaller for intermediate and high cloudiness.

When these terms are neglected in (8) and (9), an error results in the relation

$$P(u, m; \xi, \theta) = \frac{I_1}{I_2} \tag{10}$$

of the order of 5-7% in the direction of an increase in the transmission function. If the difference in albedo in this and the other portion of the spectrum is neglected, this may also result in approximately the same error, also in the direction of an increase in P. If the dependence of the transmission function P on the mass of oxygen u and also the dependence of the latter on the altitude of the upper cloud boundary z_0 are known, a relation between P and z_0 may be derived from which z_0 is readily determined for given values of θ and ξ (Fig. 5). The transmission function may also be approximated by the exponential function

$$P(u) = e^{-au(z_0)}, \tag{11}$$

where $\alpha = \sec \xi + \sec \theta$ is the air mass; α is the absorption coefficient averaged over the portion of the band, and which in the range of oxygen masses under consideration (100-1,000 g/cm^2) is practically independent of the mass. Hence,

$$u(z_0) = \frac{1}{a\alpha} \ln \frac{1}{p}. \tag{12}$$

For the earth's atmosphere, the dependence of the oxygen mass on z_0 may be represented by the exponential function

$$u(z_0) = u^* e^{-\gamma z_0}, \tag{13}$$

where u^* is the total mass of oxygen in a vertical column of the atmosphere, equal to the standard atmosphere, 230 g/cm^2, γ is a parameter equal to 0.134 km^{-1} for a standard atmosphere and 0.125 km^{-1} for an isothermal atmosphere.

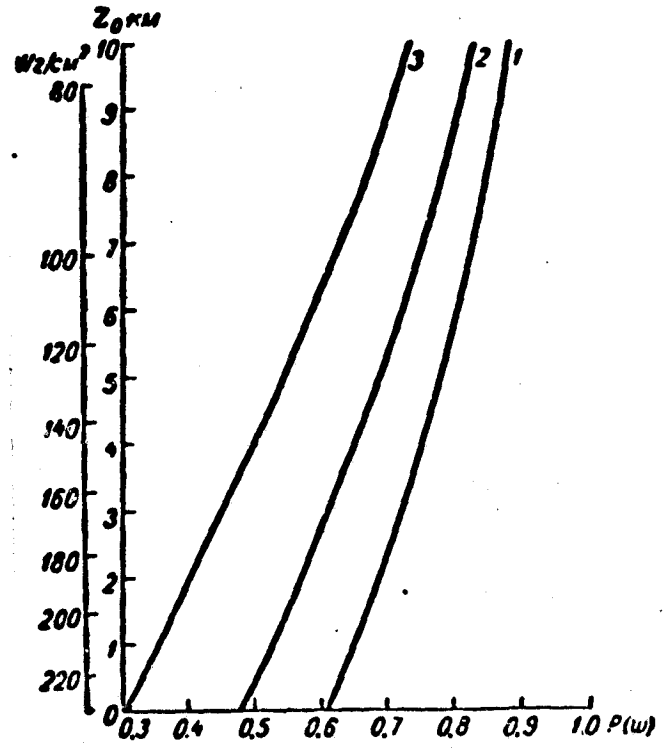

Fig. 5. Dependence of the transmission function of the atmosphere in the oxygen band (7590-7650 Å) on the altitude of the upper cloud boundary at $\theta = 0$.

1 - $\xi = 0$; 2 - $\xi = 60^\circ$; 3 - $\xi = 75^\circ$.

In this case

$$z_0 = -\frac{1}{\gamma} \ln \left[\frac{1}{a\alpha^\circ} \ln \frac{1}{p} \right], \tag{14}$$

where $\tau^* = \alpha u^*$ is the optical thickness of the atmosphere in the region of the absorption band of oxygen ($\tau^* = 0.25$). Formula (14) makes it possible to determine the error in the determination of z_0 if the transmission function P is measured with an error ΔP, or the error due to the above-mentioned approximation is taken into account. We shall also note that the oxygen masses may also vary somewhat as a function of the latitude and season, as follows from the data of aerological soundings (Table 1).

It is easy to see that

$$\Delta z_0 = \frac{1}{a\gamma}\left[\frac{\Delta\tau^*}{(\tau^*)^2}|\ln P| + \frac{1}{\tau^*|\ln P|}\frac{\Delta P}{P}\right]. \qquad (15)$$

In particular, when $\gamma = 0.125$ km^{-1} and a = 3, the errors in the determination of z_0 will be as follows: for $\frac{\Delta P}{P} = \frac{\Delta\tau^*}{\tau^*} = 5\%$ in the range of altitudes of $0 \leq z_0 = 5$ km $\Delta z_0 = 0.5 \div 1$ km, and when $\frac{\Delta P}{P}$ increases by a factor of two, the error also increases by a factor of almost two. As the altitude z_0 increases, the altitude Δz_0 also increases.

Table 1

Vertical distribution and variability of the oxygen mass

Station	Date	Height of cloud, km													
		0	0,5	1,0	1,5	2,0	2,5	3	4	5	6	7	8	9	10
ARDC-1959		239	220	211	199	187	176	165	145	127	111	97	84	72	62
Dolgo-prudnaya	6 XII 1958	239	234	203	189	179	168	156	135	117	107	86	74	63	53
	17 VI	235	226	216	201	187	175	163	135	114	98	86	79	72	64
Colombo	22 I	234	226	216	201	169	154	145	128	116	100	89	81	75	68
	22 VII	236	222	210	198	189	179	168	135	113	99	89	82	75	68
Mirnyy	12 II	229	219	203	189	177	166	156	138	120	105	89	76	67	56
	1 VII	229	217	198	187	175	163	152	132	117	99	82	71	61	51
Lake Kheysa[?]	5 VII	235	226	212	198	182	170	154	121	105	97	91	81	69	58
	18 XII	241	228	210	198	184	170	161	141	126	111	97	81	65	57

As a increases, i.e., the zenithal distance of the sun or the sighting angle θ increases, the error calculated from formula (15) decreases. However, one should bear in mind that this will be associated with a considerable increase in errors due to the disregard of the intensity of the radiation scattered in the atmospheric layer located above the cloud. Indeed, as ξ and θ increase, the first terms in (8) and (9) will decrease and the second one will increase. Differences in the albedo q_1 and q_2 will also increase [20]. For this reason, the use of formulas (11) or (14) may lead to large errors in the determination of z_0. In these cases, a more rigorous consideration of the intensity of scattered radiation is necessary. This may be done by solving the radiation transfer equation within and without the absorption band for some range of changes in all parameters of the problem that is encountered under actual conditions: q, ξ, θ and the aerosol scattering coefficient of the atmosphere. On the basis of this solution, one can derive a relation between the mass of oxygen u (or z_0) and the transmission function (10), which takes into account the effect of multiple scattering and the difference in albedo.

The determination of the altitude of the upper cloud boundary by the method considered has a definite advantage over the method based on the use of the outgoing radiation in the "transparency window," since no additional data are necessary on the other strongly varying parameters of the atmosphere. However, it is applicable only on the illuminated side of the earth. When highly sensitive radiation detectors are available, it may be hoped that this method will be successfully applied when the clouds are illuminated on the night side by the moon or by an artificial light source carried by a satellite.

4. Conclusion

The above results should be regarded only as an illustration of the proposed methods of determining the temperature of an underlying surface and the altitude of the upper cloud boundary by means of measurements of outgoing radiation made from a satellite in selected portions of the spectrum. In order to develop a method, in the full sense of this word, which would permit its operative use for the indicated purposes, it is necessary to carry out the described calculations for actual atmospheric conditions and to check the results of these calculations experimentally. However, it is possible to reach several conclusions even at this stage; these conclusions should be regarded as a substantiation of the necessity of such work.

1. The temperature of the underlying surface and clouds and the average error may be determined from the outgoing radiation in the "transparency window" with a sufficient degree of reliability if use is made of climatic data on the vertical profiles of humidity and temperature and if deviations from these profiles are used. The error in the determination of the temperature may exceed 5%.

2. If additional information is obtained on the content of water vapor in the atmosphere, which may be accomplished by means of independent radiation measurements from a satellite, this error will be considerably reduced.

3. The altitude of the upper cloud boundary based on the outgoing radiation in the "transparency window" and in the absorption band of oxygen is determined with an error of the order of 1 km.

The latter method is obviously not reliable, since it does not require any additional information. In any event, the combination of this and the other method makes it possible to raise the reliability of the

determination of the cloud altitude and probably decrease the error.

In conclusion, the author expresses his gratitude to G. V. Rozenberg, who suggested the use of the absorption band of oxygen for the determination of the altitude of the upper cloud boundary before the publication of such suggestions in the foreign literature, and who contributed many comments during the execution of this work.

The author thanks V. I. Dianov-Klokov for reviewing many of the results given in this work, and also K. S. Glazov and B. A. Stoyushchev, who performed a considerable part of the calculations.

REFERENCES

1. Kondrat'yev, K. Ya., Yakushevskaya, K. Ye. Uglovoye raspredeleniye ukhodyashchego teplovogo izlucheniya v razlichnykh oblastyakh spektra [Angular Distribution of Outgoing Thermal Radiation in Various Regions of the Spectrum]. Iskusstvennyye sputniki Zemli, vyp. 14, 1962.
2. Malkevich, M. S. Uglovoye i spektral'noye raspredeleniye radiatsii otrazhennoy Zemley v mirovoye prostranstvo [Angular and Spectral Distribution of Radiation Reflected off the Earth into Space]. Iskusstvennyye sputniki Zemli, vyp. 14, 1962.
3. Hanel, R. A., Bandeen, W. R., Conrath, B. J. The Infrared Horizon of the Planet Earth. J. of the Atmospheric Sci., v. 20, No. 2, 1963.
4. Wark, D. Q., Yamamoto, G., Lienesh, J. H. Methods of estimating infrared flux and surface temperature from meteorological satellites. J. of the Atmosph. Sci., v. 19, No. 5, 1962.
5. McGee, R. A. An analytical infrared radiation model of the Earth. Applied Optics, v. 1, No. 5, 1962.
6. Fritz, S., Winston, J. S. Synoptic use of radiation measurements from satellite Tiros II. Month. Weather Rev., v. 90, No. 1, 1962.
7. Nordberg, W., Bandeen, W. R., Conrath, B. J., Kunde, V., Persano, I. Preliminary results of a radiation measurements from the Tiros III meteorological satellite. J. of the Atmosp. Sci., v. 19, No. 1, 1962.
8. Aver'yanov, I. P., Kasatkin, A. M., Liventsov, A. V., Markov, M. I., Merson, Ya. I., Shamilev, N. R., Shervinskiy, V. Ye. Izmereniye s vysotnoy geofizicheskoy avtomaticheskoy stantsii teplovogo izlucheniya Zemli v kosmicheskom prostranstve vo vremya polnogo solnechnogo zatmeniya 15 fevralya 1961 g. [Measurement of Thermal Radiation of Earth in Space from an Automatic Geophysical Space Station during the Complete Solar Eclipse of 15 February 1961]. Iskusstvennyye sputniki Zemli, vyp. 14, 1962.
9. Murcray, D. G., Brooks, J. N., Sible, N. J., Westdal, H. C. Optical measurements from high altitude balloons. Applied Optics, v. 1, No. 2, 1962.

10. Yamamoto, G., Onishi, G. Absorption coefficient of water vapour in the far infrared region. Sci. Reports of the Tohoku University. Ser. 5, v. 1, No. 1, 1949.
11. Walshaw, C. D. Integrated absorption by the 9.6 band of ozone. Quart. J. of the Roy. Meteorol. Soc., v. 83, No. 357, 1957.
12. Gayevskiy, V. L., Rabinovich, Yu. I. See this collection.
13. Kaplan, L. Inference of atmospheric structure from remote radiation measurements. J. Opt. Soc. Amer. v. 49, No. 10, 1959.
14. Boldyrev, V. G. Ob ispol'zovanii radiatsionnykh izmereniy so sputnikov v sinopticheskom analize [Use of Radiation Measurements from Satellites in Synoptic Analysis]. Meteorol. i gidrol., No. 10, 1962.
15. Dianov-Klokov, V. I. K voprosu o proiskhozhdenii spektra zhidkogo i szhatogo kisloroda (12600-3000 Å) [On the Origin of the Spectrum of Liquid and Compressed Oxygen]. Optika i spektroskopiya, t. 6, vyp. 4, 1959.
16. Handbook of Geophysics. Ch. 16 Thermal radiation. The MacMillan Company, New York, 1960.
17. Yamamoto, G. Direct absorption of Solar Radiation by atmospheric water vapour, carbon dioxide and Molecular Oxygen. J. of Atm. Sci., v. 19, v. 2, 1962.
18. Romanova, L. M. Pole izlucheniya v ploskikh sloyakh mutnoy sredy s sil'nym anizotropnym rasseyaniyem [Radiation Field in Plane Layers of a Turbid Medium with strong Anisotropic Scattering]. Optika i spektroskopiya, t. 14, vyp. 2, 1963.
19. Rozenberg, G. V. Svetovyye kharakteristiki tolstykh sloyev rasseivayushchey sredy s malym udel'nym pogloshcheniyem [Luminous Characteristics of Thick Layers of a Scattering Medium with a Low Specific Absorption]. DAN SSSR, t. 145, No. 4, 1962.
20. Feygel'son, Ye. M. See this collection.
21. Roach, W. T., Goody, R. M. Absorption and emission in the atmospheric window from 770 to 1250 cm^{-1}. Quart. J. Roy. Met., Soc., v. 84, No. 362, 1958.

M. S. Malkevich

SOME ASPECTS OF THE INTERPRETATION OF THE FIELD OF THE EARTH'S OUTGOING RADIATION. II. DISTINCTION OF CLOUDS AGAINST A BACKGROUND OF NATURAL SURFACES

1. Statement of the Problem

In order to study the nature of cloud formations on a planetary scale and their relation to the thermodynamic processes in the atmosphere, use is made at the present time of television pictures of clouds in the visible region of the spectrum, obtained by means of artificial satellites on the illuminated side of the earth (see, for example, Refs. [1, 2]). These investigations show that the outlines of clouds can be readily detected when the pictures are made against a background of areas of the earth's surface whose reflecting properties differ sharply from those of the upper boundary of the cloud cover (ocean, wooded areas). If, however, the characteristics of the reflection by the clouds and by the background are similar (for example, when the background is a snow cover, ice or a desert), the problem of tracking cloud systems becomes complicated. In the case of pictures of clouds in the visible region of the spectrum, the distinction between the cloud formations and the background may be accomplished by geographical referencing of the pictures to the area. The detection of characteristic features of the earth's surface on the picture (outlines of oceans, seas, lakes and rivers) obviously makes it possible to distinguish a cloud from the background, since in the case of cloudiness these outlines will not be visible on television pictures. This method was used by Fritz [3], who analyzed the television pictures obtained in April 1960 by the satellite "Tiros-I" over the Alps, the peaks of which were covered with snow during that period. However, this

approach does not permit the detection of a cloud above a homogeneous background.

The same problem arises for pictures of the earth obtained in the infrared region of the spectrum, for example, in the "transparency window" of the atmosphere (8-12 μ). Such measurements must be employed in order to track cloud formations on the dark side of the earth.

Geographical referencing and the tracking of outlines of characteristic earth features (coastline, river beds, islands) on infrared pictures make it possible, as in the visible region of the spectrum, to distinguish clouds by means of their thermal contrast against a background of natural surfaces which radiate like the clouds. However, if the background is homogeneous, the detection of clouds is difficult as before.

The problem of distinguishing clouds against a background of natural surfaces reflecting or radiating the same radiation as the cloud can be solved by means of additional information on the field of outgoing radiation in the pictured portions of the spectrum, radiation obtained simultaneously with television pictures. In Ref. [4], mention was made of the possibility of using in this problem measurements of the intensity of outgoing radiation in the ultraviolet and infrared portions of the shortwave region of the spectrum (0.35-1 μ) outside the absorption bands of atmospheric gases. This method, which was recommended by Caulson for use in determining the altitude of clouds (see Ref [4]) is based on the fact that the ratio of the intensities of the radiation in the two indicated portions of the spectrum will vary with the altitude of the reflecting surface. In particular, for high-altitude clouds reflecting nonselectively, this ratio will be close to the ratio of the intensities of the extraterrestrial radiation of the sun in the corresponding portions of the

spectrum, whereas for an underlying surface with the same reflectivity it may be substantially different, since the atmosphere scatters ultraviolet radiation more strongly than infrared radiation. As was shown in Ref. [4], under actual conditions, this ratio can be scarcely used for the determination of cloud altitudes, but it can probably be employed for distinguishing clouds from the background in qualitative estimates.

We present below still another method of solving the problem under consideration, applicable to both the illuminated and the dark side of the earth.

2. Description of the Method

The method is based on a difference in the absorption of radiation of the clouds and background in an atmospheric layer located at a higher altitude. This difference is due to the fact that the upper cloud boundary always (perhaps with the exception of mountainous conditions) lies considerably above ground level, and the density of the absorbing substances decreases rapidly with altitude. Hence, the masses of these substances, present in a column of air between the upper cloud boundary and an extraterrestrial observer, will be considerably smaller than above the earth's surface. For this reason, the solar radiation reflected by the cloud (or the self-radiation of the cloud) will be absorbed along its path toward the observer to a lesser extent than the radiation reflected (or radiated) by the earth's surface.

In short, the contrasts between radiation in the transparent intervals of the spectrum and in the absorption bands above the cloud will not be as pronounced as above a background reflecting or radiating the same radiation as the clouds in the "transparency windows". This is the fact on which the proposed method of distinction is based. When this method is used, two situations may arise: 1) The size of the clouds is

not very large, so that in the course of a brief flight of the satellite, the instruments record the radiation from both the background and the clouds (the problem of distinction consists in finding the boundaries of the cloudiness); 2) The instruments record the radiation from vast homogeneous areas, and the problem of distinction consists in determining the nature of the underlying surface.

We shall treat the first of these situations as the simpler one.

Let the background and the object generate the same outgoing radiation in the "transparency windows" of the atmosphere (it is advisable to get television pictures precisely in these portions of the spectrum). In other words, the values of the albedo (in the "window" of the shortwave region) or of the radiation-equivalent temperatures (in the "window" of the longwave region) of the cloud and background are equal.

If the outgoing radiation is then measured in the absorption bands adjoining the transparency intervals or in some parts of these bands, one of the following two cases will arise:

1. The outgoing radiation in the band above the background and object is the same. This will mean that either there is no cloud, or that it is located so low that the selected portion of the band is not sufficiently sensitive to differences in the absorbing masses contained in the atmospheric column between the objects and the observer. Such a portion, for example, is the central part of the band in which the transmission of the atmosphere changes little with moderate changes of fairly large masses, but does react strongly to changes in small masses (see the transmission functions in the central parts of the bands in Fig. 1).

A second possibility also exists in this case: both objects are such high clouds that the selected portion of the band does not react to small

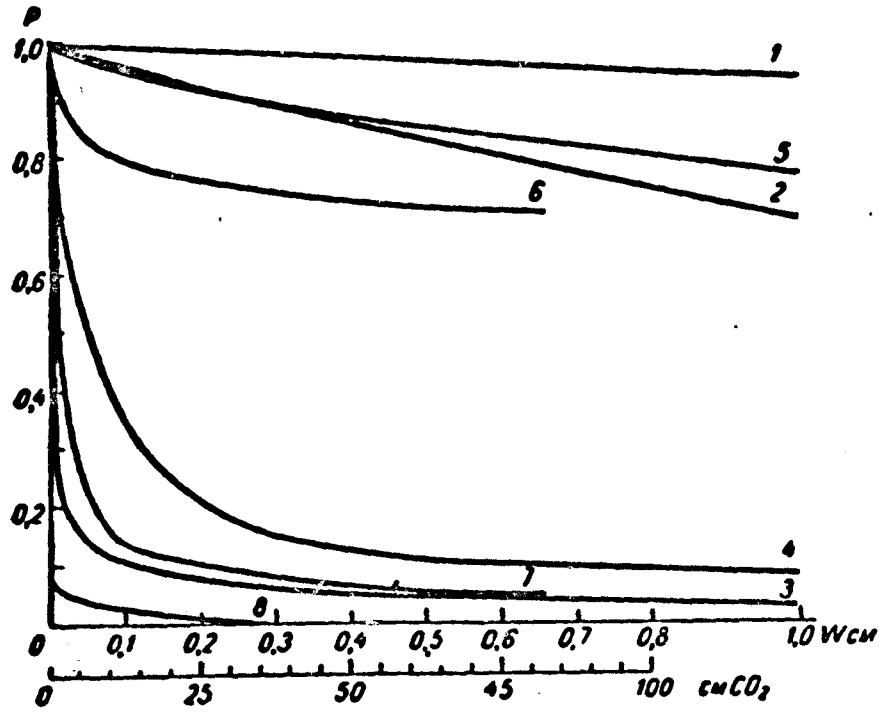

Fig. 1. Transmission functions of water vapor and carbon dioxide in various portions of the spectrum:

H_2O: 1 - 0.81 μ; 2 - 0.93 μ; 3 - 6-7 μ; 4 - 7-8 μ; 5 - 8-9 μ;

CO_2: 6 - 12-13 μ; 7 - 13-14 μ; 8 - 14-15 μ.

differences of the absorbing masses contained between these clouds and the observer. This may occur if the peripheral parts of the bands or their wings are chosen, since the transmission of the atmosphere in these portions undergoes little change with a change in small masses, but depends strongly on changes of large masses (Fig. 1). This permits one to draw the following conclusion, which is important for the practical application of the proposed method: in order to achieve a reliable distinction between the background and different cloud levels, one must combine the measurements of outgoing radiation in several portions of the absorption bands, since the central parts of the bands permit the identification of high level clouds, and the peripheral parts, that of low level clouds.

2. The outgoing radiation in the absorption bands above the background and the cloud is different. Then, the object above which this

radiation, and consequently the albedo in the shortwave region of the spectrum or the equivalent-radiation temperature in the longwave region will be closer to the corresponding characteristics in the "transparency windows", will be identified as a cloud or at least as a cloud of higher level.

In order to establish the true levels of the surfaces being studied, which is particularly important when the second situation arises, it is necessary to know the relationships between the transmission of the atmosphere in the selected portion of the spectrum and the mass of the absorbing substance, and also between the mass and the altitude of the reflecting or radiating surface. The first of these relations are known, although not reliably enough, but the second ones may be found only for absorbing substances of constant concentration (for example, for carbon dioxide and oxygen). For water vapor, however, which varies strongly in time and space, the dependence of the mass on the altitude cannot be single-valued, and thus, in order to solve the problem under consideration, it is advisable to use the absorption bands of gases whose concentration undergoes little change in the atmosphere.

We shall make two additional remarks:

1. The method described is applicable to the case of dense clouds radiating like black bodies.

2. The scattering of shortwave radiation in the atmosphere and the self-radiation of the atmosphere will offset the contrasts between the radiation in the "windows" and in the bands, decreasing the effectiveness of the proposed method. Sometimes, for example, in the case of temperature inversions, an opposite variation of the contrast can even be observed. A certain role can also be played here by the inversion layer

of the mesosphere at 25-50 km [5], particularly in the case of high and cold clouds (see below).

3. Use of Reflected Radiation

The method, considered in Ref. [6], of determining the altitude of the upper cloud boundary from the data on outgoing radiation in the 0.76 μ absorption band of molecular oxygen also solves the problem of distinguishing the background from the cloud on the illuminated side of the earth. Since this method permits the determination of the altitude of the reflecting surface, it makes it possible to solve the problem in its entirety, i.e., not only to identify the cloud, but also to determine its level and hence, to distinguish it from the earth's surface. We shall not dwell on this method, since it has been discussed in sufficient detail in Ref. [6]. We shall only note that in the case of very low cloudiness, the use of this method apparently will not permit a reliable distinction between a cloud and the background, for the masses of oxygen will not be markedly different because of the comparatively slow decrease in the density of oxygen with the altitude. In this case, it is desirable to use the outgoing radiation in the weak absorption band of water vapor, located in the near infrared. The density of water vapor decreases rapidly enough with the altitude, so that the first two kilometers contain about 70% of its entire mass. Fig. 2 shows the outgoing radiation in the absorption bands of oxygen (0.76 μ) and water vapor (0.72, 0.81, 0.93 μ) for clouds reflecting nonselectively and identically and located at different levels. The data of Fig. 2 and Table 1, which lists the values of the contrast r of the effective albedo (i.e., the total albedo of the cloud and atmosphere) in band q_2 and outside band q_1 ($r = \frac{q_1 - q_2}{q_1}$) provide a graphical illustration of the above-described method and indicate the

possible limits of its applicability. Indeed, it is easy to see that low cloudiness can be distinguished more reliably by means of weak absorption bands, and high cloudiness, by strong ones.

Table 1

Contrast r of the effective albedo of the underlying surface and clouds at the upper boundary of the atmosphere

$\Delta\lambda$ μ	z km				
	0	1	3	6	9
0,72—0,74	0,31	0,22	0,03	0	0
0,74—0,76	0,58	0,53	0,45	0,31	0,20
0,79—0,81	0,30	0,20	0	0	0
0,85—0,93	0,86	0,75	0,40	0,25	0,18

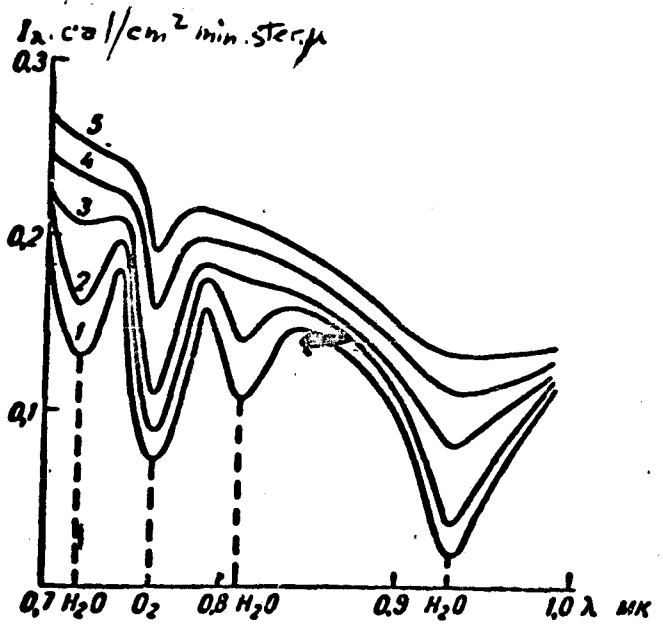

Fig. 2. Spectral variation of the outgoing radiation intensity in the near infrared for various cloud altitudes ($\xi = 60^\circ$; $\theta = 0$; $q = 0.8$).

1 - $z_o = 0$; 2 - $z_o = 1$ km; 3 - $z_o = 3$ km; 4 - $z_o = 6$ km; 5 - $z_o = 9$ km.

The possibility of distinguishing the levels of reflecting surfaces on the basis of the contrast in albedo in the "transparency window" and in the spectral interval including the absorption bands of atmospheric gases is also confirmed by the data of direct measurements of outgoing

radiation made by "Tiros-III" [7] in two spectral intervals: in the region of 0.50-0.75 μ, which may be regarded as the "transparency window" (although it contains both weak and fairly narrow bands of water vapor) and in the entire shortwave region of 0.2-7 μ, which includes strong and broad bands of water vapor and carbon dioxide (Table 2). Let us note that the contrast in albedo in any region will be minimized because the

Table 2

Results of measurements of outgoing radiation from the Satellite "Tiros III"

	Radiation Temperature			Temperature contrast				Spectral interval μ		Albedo contrast
	Spectral interval μ							0.5–0.75	0.2–7	
	7.5–13.5	7–32	5.5–6.7	T_1-T_2	T_1-T_3	$\frac{T_1-T_2}{T_1}$	$\frac{T_1-T_3}{T_1}$	albedo		
	T_1	T_2	T_3					q_1	q_2	$\frac{q_1-q_2}{q_1}$
Ocean (tropics), T_o = 300° K										
No clouds	281	264	244	17	37	0.06	0.13	6	3	0.5
Clouds (low)	270	255	240	15	30	0.06	0.11	20	14	0.3
Clouds (high)	249	235	229	14	20	0.06	0.08	20	16	0.2
Dry land (eastern USA), T_o = 290° K										
No clouds	283	266	236	17	30	0.06	0.06	16	10	0.38
Clouds (low)	257	244	229	13	28	0.05	0.11	56	35	0.37
Clouds (high)	239	235	229	6	10	0.025	0.04	57	40	0.3
Desert (North Africa), T_o = 315° K										
Low humidity	310	287	258	23	52	0.07	0.17	30	26	0.13
High humidity	284	264	235	20	49	0.07	0.17	23	16	0.3
Clouds (low)	268	261	236	7	32	0.026	0.12	29	24	0.17
Snow on peaks	268	257	228	11	40	0.04	0.15	28	28	0
Clouds (high)	242	240	227	2	15	0.008	0.06	33	30	0.09
Same at various levels	242	231	218	11	24	0.045	0.10	43	32	0.26

region of 0.2-7 μ also includes a spectral interval where the atmosphere located above the reflecting surface scatters radiation very strongly. Therefore, in the problem under consideration, the use of radiation in

such broad spectral intervals as were used in the radiometers of "Tiros" considerably decreases the effectiveness of the proposed method. However, the data of "Tiros" illustrate the fundamental principle of the method and in addition, may be used for the practical distinction of levels of reflecting surfaces. Let us consider some special cases. For example, in the area of the Atlantic Ocean, above which the albedo is q_1 = 6% and q_2 = 3% in the respective spectral intervals, strongly reflecting surfaces were observed which, judging from the radiation temperatures T_1 in the "transparency window" (270 and 240° K), are clouds of two levels. Their albedo in the spectral region of 0.5-0.75 μ is identical and equal to 20%. Hence, neither the television pictures of the clouds, which incidentally were taken by this satellite, nor the measurements of the albedo in the shortwave "transparency window" will permit a distinction of their levels. However, the use of even such a broad portion of the spectrum as 0.2-7 μ immediately detects a contrast (0.2-0.3), which indicates that one of these clouds lies above the other. This is also confirmed by the data of measurements in the thermal region of the spectrum, which will be discussed below. The same conclusion is obtained from an examination of the values of the albedo in two cases of cloudiness above dry land (U.S.A.), having an albedo q_1 = 56-57% in the first interval, and an albedo of 35 and 40% in the second, q_2.

It is interesting to mention another case of measurements over Africa, including measurements over the desert, which, as can be seen from Table 2, can indeed have the same albedo as a cloud. Let us note that it is difficult to distinguish a cloud from a desert by comparing the albedo in two shortwave spectral intervals. This is accomplished much more reliably by comparing the radiation temperatures in the "transparency

window" of 7.5-13.5 μ. In this case, two objects were observed whose albedo q_1 was 29 and 28%, and the radiation temperatures in the "window" of 7.5-13.5 μ were also the same ($T_1 = 268^\circ$ K). In the case of Africa, such temperatures signify that these objects are other clouds or snow-covered mountain peaks[1] present in this area. If the albedo in the broad band of 0.2-7 μ is compared (q_2 is equal to 24 and 28%), then for one of the objects the contrast will turn out to be zero (i.e., this is clearly a cloud above which the water vapor is present in small quantity), and for the second one, 0.17 (i.e., there is a certain quantity of water vapor present above it) and hence, this object will be found to lie below the first.

The same also occurs in the other observed case of high cloudiness ($T_1 = 242^\circ$) with different values of the albedo q_1 in the "window" of 0.5-0.75 μ (43 and 33%) and fairly close values of q_2 (32 and 30% respectively). However, when the radiation temperatures in these two cases are carefully analyzed, in the case of $T_1 = 268^\circ$ one can easily find a contradiction between the contrast of the albedo and the contrast of the radiation temperatures. In particular, according to the contrast of the albedo (0.17) the first object with $T_1 = 268^\circ$ K is located below the second, and on the basis of the contrast of temperatures $T_1 - T_2$ (or $T_1 - T_3$), it is located above. Hence it may be concluded that in the two indicated shortwave portions of the spectrum, the data on the albedo alone do not permit a reliable distinction between the levels of the reflecting surfaces. Let us note that this contradiction may be attributed to the possibility of the existence of a horizontal humidity gradient, since the cited data obtained from "Tiros-III" correspond to points separated by 1. In Table 2, this case is arbitrarily termed "Snow on Peaks."

distances of 300-500 km from one another. When more detailed information becomes available, this indeterminacy will be eliminated. However, even in this case, a greater reliability will require additional information on the outgoing radiation above the objects being studied. As is evident from the above-cited examples, such information is given by the characteristics of the field of self-radiation of clouds and background.

4. Use of Data on Self-Radiation

Data on the field of outgoing radiation in the thermal region of the spectrum are used not only to improve the reliability of the solution of the problem of distinction on the illuminated side of the earth, but, in the framework of radiation investigations, they also constitute the only possible method of solving this problem under nocturnal conditions.

By using direct calculations of outgoing radiation in the "transparency window" of the atmosphere (8-12 μ) and in the absorption band of water vapor (5-8 μ) and carbon dioxide (12-18 μ), it is easy to show that as the altitude of the radiating surface increases, the contrast of the radiation temperatures corresponding to these spectral intervals will decrease. This follows, for example, from Fig. 3, which shows the intensity of the outgoing radiation for an underlying surface and three levels of clouds radiating like black bodies at the air temperature at these levels, and from Table 3, which lists the corresponding radiation temperatures. The designations of the radiation temperatures remain the same for portions of the "transparency window", 8-9 and 11-12 μ (T_1 and $\tilde{T}_1$), for portions of medium transparency 7-8 and 12-13 μ (T_2 and $\tilde{T}_2$), and for the central absorption bands of 6-7 and 13-14 μ (T_3 and $\tilde{T}_3$).

As had been postulated, the difference between the radiation temperatures for the "transparency window" and the centers of bands decreases

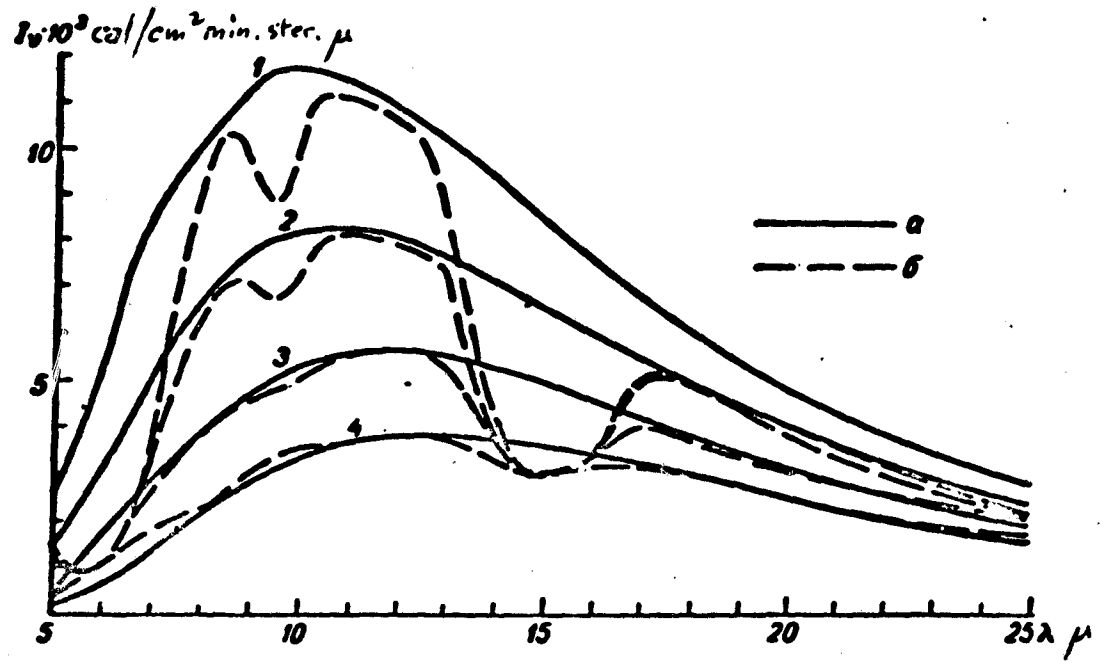

Fig. 3. Spectral variation of the intensity of radiation of a black body at the surface temperature of the cloud (a) and of the outgoing radiation in the thermal region of the spectrum (7-32 μ) for various cloud altitudes z_o (standard atmosphere) (b).

Table 3

Calculation of radiation temperatures

Surface type	Temperature T_0 °K	Spectral interval, μ									
		6–7	7–8	8–9	11–12	12–13	13–14	Contrasts			
		T_3	T_2	T_1	$\tilde{T}_1$	$\tilde{T}_2$	$\tilde{T}_3$	$\frac{T_3}{T_1}$	$\frac{T_2}{T_1}$	$\frac{\tilde{T}_2}{\tilde{T}_1}$	$\frac{\tilde{T}_3}{\tilde{T}_1}$
1. Earth's surface	288	250	274	286	284	274	251	38	12	10	33
2. Clouds (low)	273	250	266	273	273	265	249	23	7	8	24
3. Clouds (medium)	250	242	247	247	248	248	238	5	0	0	10
4. Clouds (high)	223	226	226	223	223	218	217	–3	–3	5	6
5. Snow	260	238		258				20			
Cloud	258	244		258				14			

when the altitude of the cloud increases. Furthermore, this difference changes sign for a high and cold cloudiness, i.e., the atmosphere becomes warmer in the centers of the bands in this case. A similar inversion was observed in the radiation measurements made by Tiros II in the "transparency window" of 7.5-13 μ and in the central portion of the absorption

band of water vapor at 6-6.5 μ (see Ref. [2]). For example, in measurements over the U.S.A. on 23 November 1960, it was found that above a dense cloudiness with a fairly high boundary, the radiation temperature corresponding to the interval of 7.5-13 μ reached 207-212° K, whereas the radiation temperature corresponding to the interval of 6-6.5 μ was equal to 232° K above these points, i.e., the "inversion" reached -25°. This inversion is apparently due to the appreciable contribution (against a background of a cold cloud) of the warm layer of the mesosphere. Since the optical density of high clouds is usually low, the inversion effect will apparently be observed infrequently, since the radiation of the warmer layer below the cloud will be propagated upward. However, in the case of heavy thunder clouds, the upper boundary of which usually reaches high altitudes, this effect should be appreciable. Hence, the inversion effect of outgoing radiation will be used to locate heavy cumulus and thunder clouds.

A similar calculation was made for a cloud located at a level of 3 km and for a snow cover, the actual temperature of which were close to each other, and the radiation temperatures in the "transparency window" were the same (this case arises in deep inversions near the ground under polar conditions). It is easy to see from Table 3, (case 5) that despite the temperature inversion, which reduces the effectiveness of the proposed method, the difference in the radiation temperatures in the "transparency window" and in the band center for the cloud is found to be considerably smaller than for snow (by 6°).

Thus, the following recommendations may be given for distinguishing a cloud from a background whose radiation temperatures in the "transparency window" are the same:

1. If the difference in the radiation temperatures in the "window" and in the absorption band is different for two objects, the cloud will be that object for which this difference is less. However, as was indicated above, one should not exclude the possibility that both objects may be clouds of different levels.

2. If the difference in the indicated radiation temperatures is found to be the same, this will mean that the radiating boundaries of both objects are located at the same level. If in addition this difference is small and, most importantly, undergoes little change when different portions of the absorption bands are used, the objects are clouds. In the opposite case, they are the background, or very low clouds. In order to illustrate this criterion, we shall turn to Table 2, which lists the radiation temperatures obtained from observations of outgoing radiation made by "Tiros III" in the "transparency window" of 7.5-13.5 μ and in the spectral interval of 5.9-6.7 μ (central portion of the absorption band of water vapor) and 7-32 μ (interval which contains almost all of the energy of the earth's thermal radiation; this interval may be regarded as the region of medium transparency of the atmosphere). In the first interval, the outgoing radiation characterized the temperature of the atmospheric layer near the ground; in the second case, of fairly high layers; in the third, of medium layers. Table 2 also gives the values of the temperature of the underlying surface T_0.

Let us examine some specific cases of cloudiness which have already been analyzed from the standpoint of variations in albedo.

1. Low and high cloudiness above the ocean (T_1 equal to 270 and 249° K respectively) is identified both by means of the albedo and by means of the difference in radiation temperatures $T_1 - T_3$, which for

high cloudiness, in accordance with the criterion formulated above, was found to be less (20°) than for low cloudiness (30°).

2. The same applies to cloudiness of two levels above dry land (T_1 = = 257 and 239° K). It is interesting to note that T_3 above both types of cloudiness was the same (T_3 = 229° K), although the corresponding values of the albedo indicate that above a low cloud there is more water vapor than above a high cloud. The identical value of T_3 apparently means that above the high cloud as well, the mass of the vapor is sufficiently high to make the transmission in the central portion of the band fairly insensitive to changes in mass. At the same time, in the more transparent region of 7-32 μ, the transmission reacts to the difference in the masses of water vapor above this and the other cloud.

3. Let us note that in analyzing the cloudiness (T_1 = 268° K) above Africa, based on variations in albedo and in the radiation temperatures, a contradiction was observed: T_3 was found to be greater when the difference in albedo (29 and 24%) indicated the presence of a certain mass of water vapor above the cloud, and, conversely, smaller when the albedos coincided (28%), i.e., there is more water vapor above the cloud. If this is not an error, such differences in T_3 (236 and 228° K) above the clouds (and also differences in q, although less pronounced) are due to a difference in the vertical temperature profiles. In particular, an inversion may exist above the first of these objects (T_3 = 236° K, T_2 = = 261° K).

The second case of cloudiness above Africa with the same temperature of T_1 = 242° K provides a fairly good confirmation of the cloud levels established above on the basis of the difference in the albedos q_1 and q_2. The cloud for which q_1 = 0.33, q_2 = 0.30 was considered to be higher

than the neighboring cloud ($q_1 = 0.43$, $q_2 = 0.32$). This also follows from a comparison of the temperature difference $T_1 - T_3$ (or $T_1 - T_2$), which for the first cloud was 15° (respectively, 2°) and for the second, 24° (respectively, 11°). The large differences in radiation temperature and the lower radiation temperature $T_3 = 218^\circ$ of the second cloud indicate that the large mass of water vapor is located above it, and hence, that the cloud itself is situated underneath[1].

5. Conclusions

Some conclusions may be drawn from the above discussion:

1. If the first situation prevailed (broken clouds above a homogeneous earth's surface), which can be detected from the variegation of the field of outgoing radiation of the cloudiness in the absorption bands, then by comparing the outgoing radiation in the "transparency windows" and in the absorption bands, one can determine the boundary of the clouds and also detect clouds of different levels and distinguish them from the earth's surface; for the latter, the contrast of the albedo or of the radiation temperatures in the "windows" and in the bands should be a maximum.

2. On the illuminated side of the earth, the indicated problem admits of a reliable solution owing to the combination of data on the outgoing radiation in the shortwave and longwave regions of the spectrum.

3. When use is made of the field of outgoing radiation in the absorption bands of atmospheric gases of constant concentration, the problem of distinguishing and determining the cloud levels can also be solved in the second situation (the variegation of the field of outgoing radiation

1. Let us note that this conclusion will be inaccurate if an appreciable horizontal humidity gradient exists in the region under consideration.

is weakly expressed). To this end, on the illuminated side of the earth, use should be made of data on the contrast of outgoing radiation in the absorption bands of oxygen (0.76 μ) and the closest "window" (0.74 μ). On the dark side, use may be made of the earth's radiation in different portions of the absorption band of carbon dioxide (12-15 μ). However, in the latter case, the problem of distinction is intimately related to the problem of determining the vertical temperature profile from the outgoing radiation in this band.

REFERENCES

1. Kondrat'yev, K. Ya. Meteorologicheskiye sputniki [Meteorological Satellites]. Gidrometeoizdat, Leningrad, 1963.
2. Rakety i iskusstvennyye sputniki v meteorologii [Rockets and Artificial Satellites in Meteorology]. IL, Moscow, 1963.
3. Fritz, S. Pictures of the Snow-Covered Alps during April 1960. Archiv fuer Meteorologie, Geophysik und Bioklimatol. Ser. A, B. 12, H. 2, 1962.
4. Malkevich, M. S. Uglovoye i spektral'noye raspredeleniye radiatsii otrazhennoy Zemley v mirovoye prostranstvo [Angular and Spectral Distribution of Radiation Reflected by Earth into Space]. Iskusstvennyye sputniki Zemli, No. 14, 1962.
5. Koprova, L. I. and Malkevich, M. S. Teplovoye izlucheniye sfericheskoy atmosfery. II. Uglovaya i spektral'naya struktura ukhodyashchey radiatsii [Thermal Radiation of the Spherical Atmosphere. II. Angular and Spectral Structure of Outgoing Radiation]. Kosmicheskiye Issledovaniya [Cosmic Research], Vol. II, 1963.
6. Malkevich, M. S. Nekotoryye voprosy interpretatsii polya ukhodyashchey radiatsii. I. Opredeleniye temperatury podstilayushchey poverkhnosti i vysota verkhney granitsy oblakov [Some aspects of the Interpretation of the Field of Outgoing Radiation. I. Determination of the Temperature of the Underlying Surface and Altitude of Upper Cloud Boundary]. See this Collection.
7. Nordberg, W., Bandeen, W. R., Courath, B. J., Kunde, V., Persano, I. Preliminary results of radiation measurements from the Tiros II. J. of Atmosph. Sci., v. 19, No. 1, 1962.

SPECTRAL REFLECTION OF RADIATION BY CLOUDS

Ye. M. Feygel'son

1. Introduction

In order to interpret the optical measurements made by satellites, particularly to determine the upper boundary of a cloud and to distinguish clouds of various levels and snow clouds, one needs to know the laws governing the behavior of radiation reflected and emitted by clouds.

Below is given some information on the ascending radiation at the upper boundary of a cloud layer, obtained by the author by solving a mathematical problem on radiation transfer in the absorbing, emitting and scattering medium constituted by a cloud [1].

In the relation to a horizontal cloud layer, the equation of radiation transfer may be written as follows:

$$\cos\theta\frac{\partial I_\lambda(\tau, r)}{\partial\tau} = [1-\varphi_\lambda(\tau)]B_\lambda(T) + \frac{\varphi_\lambda(\tau)}{4\pi}\times$$
$$\times\int I_\lambda(\tau, r')\gamma_\lambda(\tau, r, r')d\omega' - I_\lambda(\tau, r). \quad (1)$$

Here $I_\lambda(\tau, r)$ is the intensity of radiant energy at level z, is associated with an optical thickness τ; r is the direction of propagation of the radiant energy, making an angle θ with the vertical; ψ is the azimuth of the ray r; $\gamma_\lambda(\tau, r, r')$ is the indicatrix of scattering; $\varphi_\lambda(\tau)$ is given by the formula

$$\varphi_\lambda(\tau) = \frac{\tilde{\sigma}_{v,\lambda}(\tau)}{\tilde{\sigma}_{v,\lambda}(\tau) + \tilde{\alpha}_{v,\lambda}(\tau) + \tilde{\alpha}_{w,\lambda}(\tau)}, \quad (2)$$

where $\tilde{\sigma}_{v,\lambda}$ and $\tilde{\alpha}_{v,\lambda}$ are the coefficients of scattering and absorption of water drops, calculated per unit volume; $\tilde{\alpha}_{w,\lambda}$ is the volume coefficient of absorption of water vapor. If $\rho_w(\tau)$ and $\rho_v(\tau)$ are the densities of water vapor and water in the cloud, then

$$\tilde{\alpha}_{\omega,\lambda}(\tau)=\alpha_{\omega,\lambda}\rho_{\omega}(\tau);\quad \tilde{\alpha}_{\nu,\lambda}(\tau)=\alpha_{\nu,\lambda}\rho_{\nu}(\tau);\quad \tilde{\sigma}_{\nu,\lambda}(\tau)=\sigma_{\nu,\lambda}\rho_{\nu}(\tau),$$

where $\alpha_{\nu,\lambda}$, $\alpha_{\omega,\lambda}$ and $\sigma_{\nu,\lambda}$ — are coefficients calculated per unit mass.

The optical thickness of the cloud τ_λ is related to the quantities $\tilde{\alpha}_{\nu,\lambda}$; $\tilde{\alpha}_{\omega,\lambda}$ and $\sigma_{\omega,\lambda}$ as follows:

$$\tau_\lambda=\int_0^z\left[\tilde{\alpha}_{\nu,\lambda}+\tilde{\alpha}_{\omega,\lambda}+\tilde{\sigma}_{\nu,\lambda}\right]dz. \tag{3}$$

The height is measured from the lower boundary of the cloud.

The total optical thickness of the cloud corresponding to $z = \infty$ is designated below by $\tau_{0,\lambda}$.

The transfer of radiant energy in the cloud is accomplished in different ways in the visible, ($0.4 \leq \lambda\mu \leq 0.72$), near infrared (in $0.72 \leq \lambda\mu \leq 3$) and long-wave ($3 \leq \lambda\mu \leq 40$) spectral intervals. Thus, in the first, the major part is played by scattering; in the second, a relatively weak absorption is added in the bands of water vapor and water; finally, in the third, one has to take into account the scattering, adsorption and self-radiation of the cloud.

The author has developed methods of approximate solution of equation (1) for each of the indicated spectral intervals; these methods are described in [1]. Only a few results of the calculations made by each of these methods are given below.

3. Reflection of light from the upper boundary of a cloud

The angular distribution of the brightness I_λ of light reflected by clouds was calculated in [1] with an error of the order of 10%. Independently, a calculation was made of the flux of reflected light F_λ, equal to

$$F_\lambda=\int_0^{2\pi}\int_0^{\frac{\pi}{2}} I_\lambda(r)\sin\theta d\theta d\psi, \tag{4}$$

with an error of 1%, and of the albedo of the cloud A_λ, given by the formula

$$A_\lambda = \frac{F_\lambda}{F_{0,\lambda}} \tag{5}$$

$F_{0,\lambda}$, the light flux striking the cloud, is represented by

$$F_{0,\lambda} = \pi S_\lambda \cos\zeta e^{-\tau_{2,\lambda}\sec\zeta} + F_{0,\lambda,d}. \tag{6}$$

Here πS_λ is the spectral solar constant; ζ is the zenithal solar angle; $\tau_{2,\lambda}$ is the optical thickness of the above-cloud layer; $F_{0,\lambda,d}$ is the flux of scattered light striking the cloud.

Table 1 gives the average albedo of stratiform clouds St, Sc, systems Ns—As and individual As layers as a function of the position of the sun. In calculating these values, use was made of cloud characteristics given in Table 2 (see [1]).

Table 1

Albedo of Stratified Clouds A%

Cloud Type	ζ°		
	30	50	70
St	59	63	69
Sc	63	72	76
Ns—As	85	88	90
As	63	68	73

Table 2

Some Parameters of Stratified Clouds

Cloud Type	Thickness of cloud layer H km	Altitude of upper boundary z_2 km	Scattering coefficient $\tilde{\sigma}$, 1/km	Optical thickness τ_0
St	0,5	1	28	14
Sc	0,5	1,5	40	20
Ns—As	2,5	3	26	65
As	0,9	4—5	19	17

The change in the albedo as a function of the optical thickness of the cloud is illustrated in Fig. 1, which shows that the reflectivity of moderately dense clouds ($\tau_0 < 20$) increases quickly with increasing τ_0; the albedo of dense clouds ($\tau_0 > 20$) is characterized by a reflectivity which

changes only slightly and does not reach 100% for an actually observed cloudiness ($\tau_0 \leqslant 60-70$).

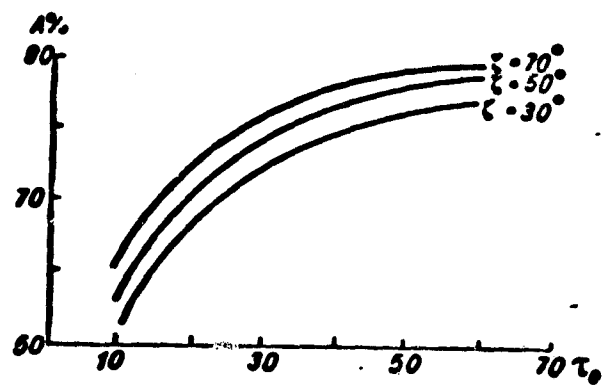

Fig. 1. Change of albedo with increasing thickness of cloud.

Fig. 1 and Table 1 also show a slight increase of the albedo accompanying the descent of the sun.

One should add that in the range of short-waves ($\lambda < 2\ \mu$) outside the absorption bands, the albedo is independent of the wavelength as a result of the non-selectivity of scattering of light by drops.

Thus, the reflectivity of real clouds (with the exception of optically thin ones) is found to undergo little change. The behavior of light fluxes reflected by the cloud, F_λ, is more complex and variable. This complexity is created by the interaction of the following factors determining the quantity F_λ:

1) Different reflectivity of individual clouds;

2) Spectral variation of the attenuation of light in the above-cloud atmosphere;

3) Changes in the solar energy spectrum;

4) Different attenuation of light along the path leading to clouds located at different altitudes;

5) Changes in the brightness of the scattered light reaching the cloud as a function of the thickness of the above-cloud layer.

The fluxes of reflected light forming under the influence of the above factors are shown in Table 3 and Fig. 2.

In calculating the values of F_λ shown in Table 3, use was made of the

data on the fluxes of directed and scattered solar radiation $F_{0,\lambda}$ striking the cloud, borrowed from [2](see Table IV and the appendices of [2] pt. 1).

The spectral optical thickness of the above-cloud atmosphere $\tau_{2,\lambda}$ was determined on the basis of the experimental data of Yu. I. Rabinovich [3,4]. The values of $\tau_{2,\lambda}$ corresponding to the heights of the upper boundaries z_2 of various forms of clouds indicated in Table 2 are given in Table 4.

Table 3

Flux of Light Reflected by Cloud (w/cm^2)

Cloud Type	λ μ							
	0,4	0,475	0,55	0,70	0,4	0,475	0,55	0,70
	ζ = 30°				ζ = 75°			
St	0,0654	0,0966	0,0894	0,0687	0,0130	0,0208	0,0192	0,0148
Sc	0,0757	0,1128	0,1042	0,0802	0,0149	0,0233	0,0213	0,0170
Ns — As	0,0969	0,1459	0,1338	0,1010	0,0189	0,0284	0,0260	0,0210
As	0,0741	0,1099	0,1007	0,0767	0,0159	0,0232	0,0221	0,0214

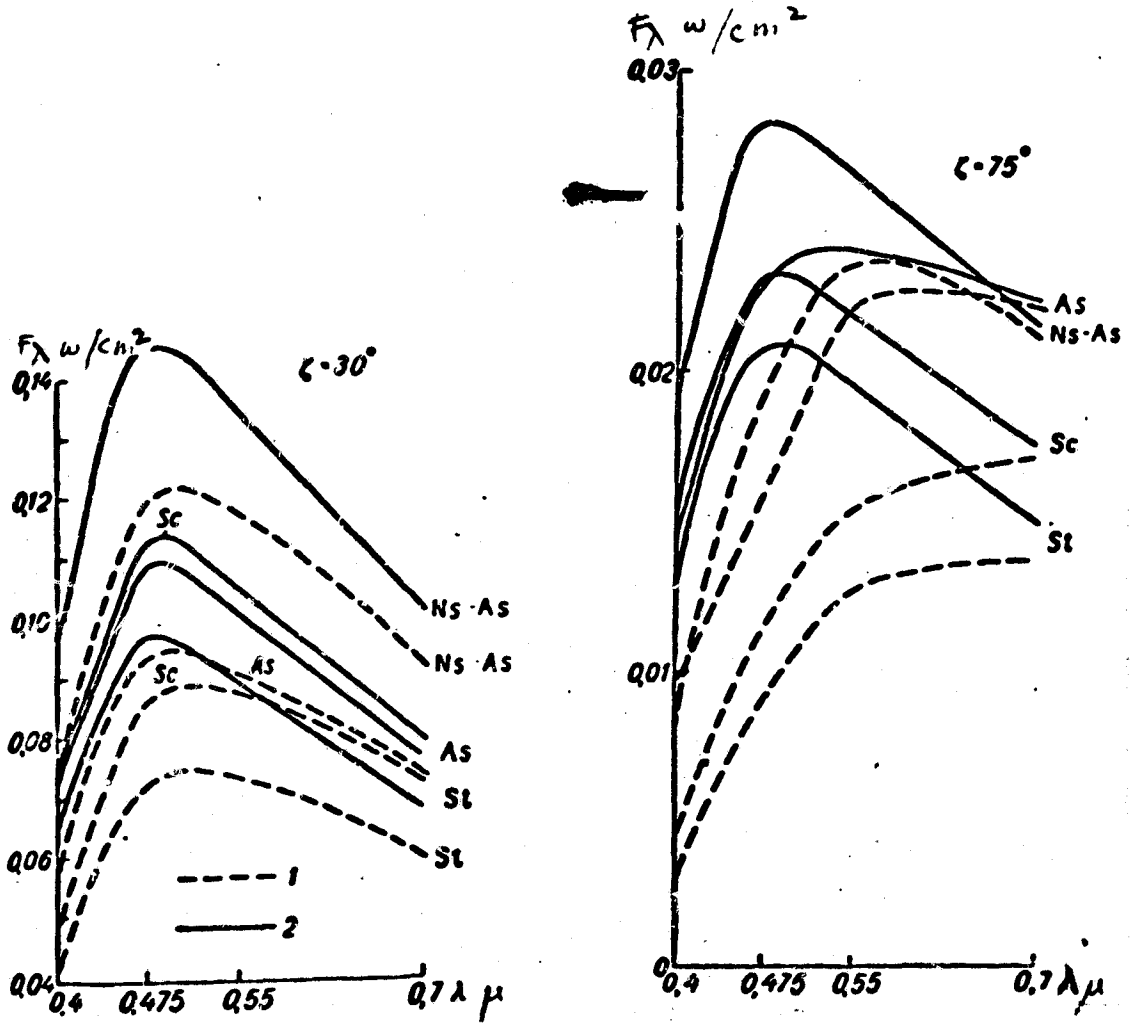

Fig. 2. Spectra of Fluxes of light reflected by cloud.
1 - reflection without taking into account scattered radiation striking cloud; 2 - reflection with the latter taken into account.

Fig. 2 shows the fluxes of reflected light F'_λ without allowance for the scattered radiation striking the cloud, as calculated from the formula

$$F'_\lambda = A\pi S_\lambda \cos\zeta e^{-\sec\zeta\tau_{2,\lambda}}. \quad (7)$$

Curves 2 are the total reflected fluxes calculated from formulas (5) and (6). The figures show the essential part played by the scattered light in the formation of the fluxes reflected off the cloud, particularly in the range of short waves at low positions of the sun. Under these conditions, the reflected light "turns blue" because of the scattered atmospheric light striking the cloud. The figures also show that the light fluxes coming from clouds of different forms do not correspond to the order of their arrangement in space. Thus, the clouds Ns—As are brighter than clouds located higher (As). Light fluxes coming from clouds at a lower level (Sc) and intermediate level (As) are approximately the same.

Table 4

Spectral Optical Thickness of Above-cloud Atmosphere $\tau_{2,\lambda}$

z_2	Cloud Type	λ μ			
		0,4	0,475	0,55	0,7
1	St	0,56	0,38	0,26	0,7
1,5	Sc	0,51	0,34	0,23	0,13
3	Ns — As	0,39	0,25	0,17	0,10
5	As	0,30	0,21	0,13	0,06

Table 5

Light Fluxes $F_{\lambda,d}$ w/cm^2 mi: at Boundary of Atmosphere

Cloud Type	λ μ							
	0,4	0,475	0,55	0,7	0,4	0,475	0,55	0,4
	$\zeta = 30°$				$\zeta = 75°$			
St	0,064	0,089	0,079	0,059	0,025	0,037	0,033	0,025
Sc	0,068	0,096	0,085	0,063	0,027	0,039	0,036	0,027
Ns — As	0,077	0,107	0,095	0,071	0,030	0,046	0,042	0,031
As	0,066	0,093	0,082	0,061	0,027	0,039	0,035	0,027

Along its path through the atmosphere, the light reflected off a cloud is transformed by the scattering.

Table 5 shows the spectral fluxes coming from clouds of various forms at the upper boundary of the atmosphere $F_{\lambda,d}$.

By comparing the corresponding data of Tables 3 and 5, one can evaluate the influence of the haze — the above-cloud layer. It turns out to be appreciable, even at small zenithal distances of the sun and in the long-wave range. The haze may cause the light flux to increase ($\zeta \approx 75^\circ$) or decrease ($\zeta \approx 30^\circ$) as a result of the interaction of the increase and decrease in the intensity of the scattered light in the turbid layer with an increase in its turbidity [2,5]. The difference between the spectral dependence of radiation which has been directly reflected off the cloud and radiation which has passed through the haze layer is best manifested by the relative fluxes $\frac{1}{S_\lambda} F_\lambda$ and $\frac{1}{S_\lambda} F_{\lambda,d}$ (Fig. 3). When the sun is high, the following relation is valid within a small margin of error

$$\frac{1}{S_\lambda} F_\lambda \sim e^{-\tau_{2,\lambda} \sec \zeta},$$

which expresses the behavior of the dotted curves in Fig. 3 ($\zeta = 30^\circ$). The quantity $\frac{1}{S_\lambda} F_{\lambda,d}$ does not vary with the wavelength because of the combination of scattered and reflected radiation. The balancing effect of the intensity of scattered light in the atmosphere for a high degree of reflection from the underlying layer and $\zeta \leq 75^\circ$ has been analyzed in detail in [2] and [5].

Thus, within the range of the visible portion of the spectrum, light traveling from a cloud to high altitudes will change little with the wavelength, either because of the neutrality of the reflecting properties of the cloud (in the case of high clouds) or as a result of the influence of the haze (if the cloud is located at a moderate altitude). At l

positions of the sun, a more appreciable spectral variation of the radiation coming from the cloud is observed, but here as well it is impossible to establish any characteristic properties which would make it possible to differentiate between clouds of different levels.

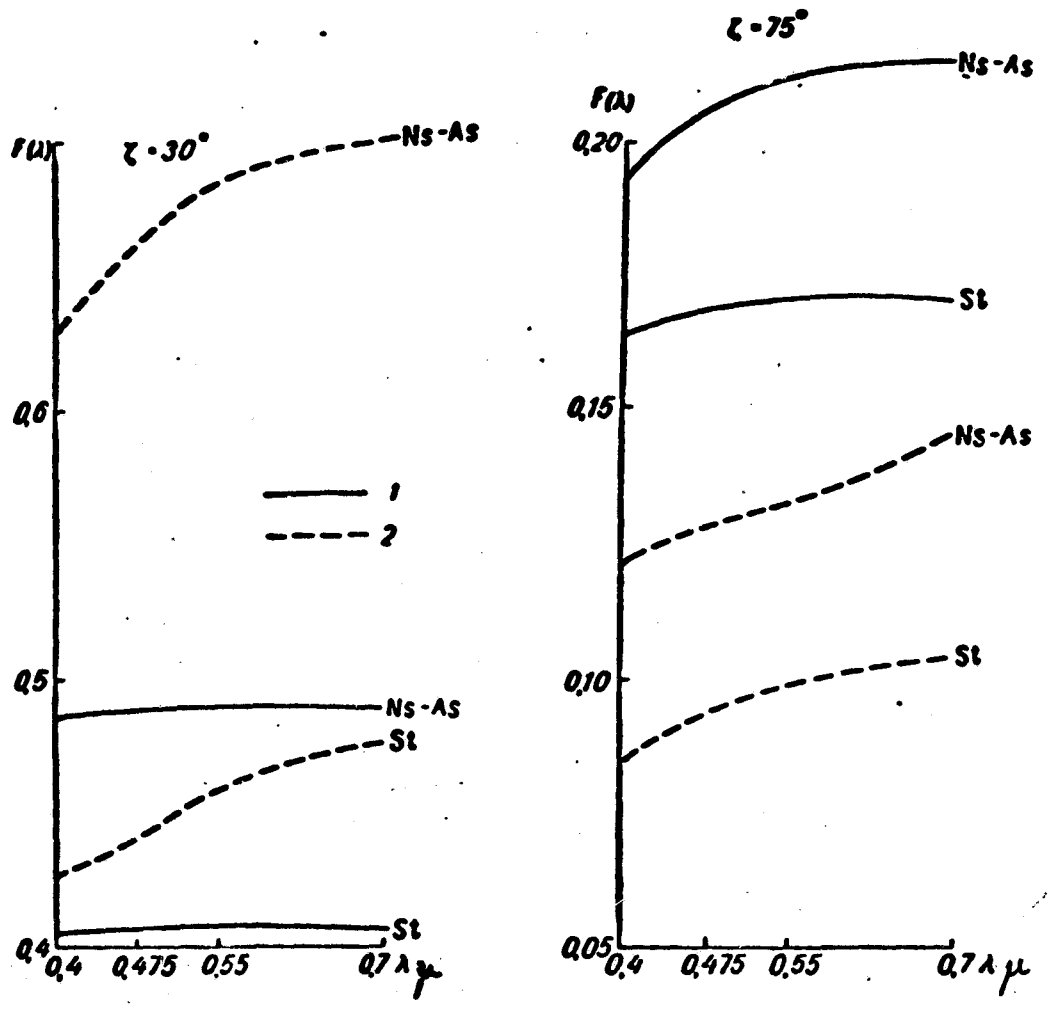

Fig. 3. Reflected Flux next to the upper boundary of cloud (2) and at the upper boundary of atmosphere (1).

The angular distribution of the light reflected off a cloud or the brightness of a cloud observed in the immediate vicinity of its upper boundary is shown in Fig. 4. The direction of the sighting is taken with reference to the solar vertical, and the azimuth $\psi = 0$ is attributed to rays directed toward the sun (with the sun behind the observer).

When this reading system is used, small scattering angles φ are achieved at the azimuth $\psi = 180^\circ$ with sighting directed at the horizon and low positions of the sun. Because of the stretched character of the cloud indicatrixes of scattering, small angles are associated with large

quantities of scattered energy, and this explains the character of the curves of Fig. 4: a rapid increase in brightness at $\psi = 180^\circ$ with growing θ, manifested particularly when $\zeta = 70^\circ$. Something reminiscent of the specular effect is observed - a maximum brightness of the reflected light in the plane of incidence, but not at a reflection angle equal to the incident angle but in the sighting directions close to the horizon. At high positions of the sun and also at low positions in the range of $\psi \leq 135^\circ$, the brightness of the reflected light changes little with the direction of the sighting, so that to a rough approximation it may be considered isotropic and related to the flux as follows:

$$I_\lambda(\theta; \psi) \approx \frac{1}{\pi} F_\lambda.$$

It is also useful to note that the brightness of the reflected light depends only slightly on the optical thickness of the cloud, as is evident, for example, from Fig. 5.

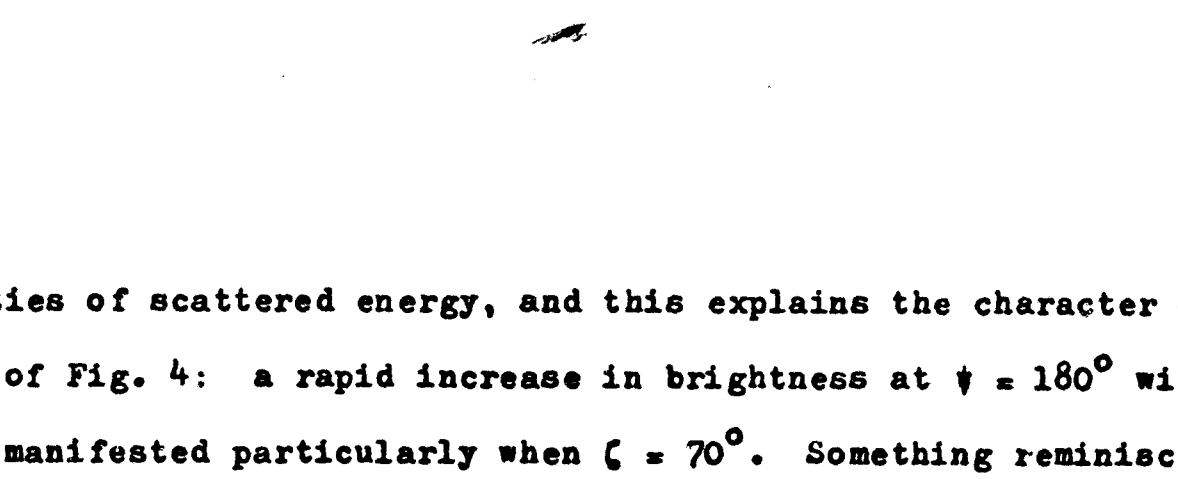

Fig. 4. Angular distribution of light reflected by cloud.

It is interesting to elucidate two points: first, to what extent the characteristics of the angular distribution of the cloud brightness are altered by the superposition of haze; second, whether the angular distributions of the brightness of the light reflected off the cloud and snow cover differ appreciably.

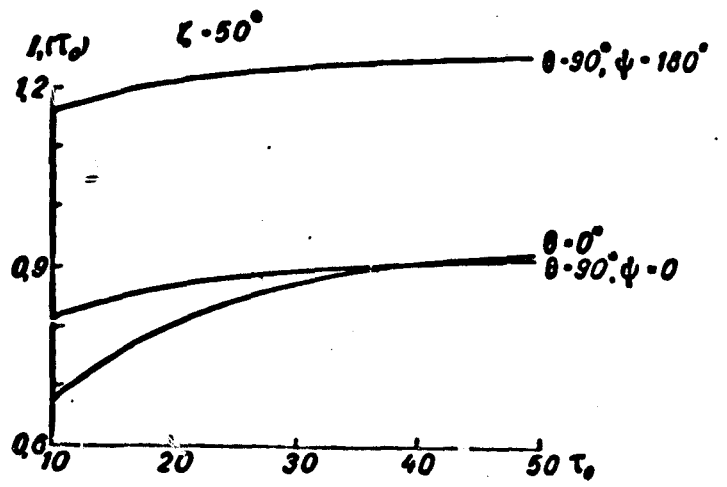

Fig. 5. Brightness of reflected light versus optical thickness of cloud.

In order to answer the first question, we shall represent the brightness of some surface observed through a layer of haze in the form

$$I_d(\theta, \psi) = I(\theta, \psi)\, e^{-\sec\theta\tau_2} + I_{1,d}(\theta, \psi) + I_{2,d}(\theta, \psi). \qquad (8)$$

The first term in the right-hand member of (8) is the brightness of the direct light reflected by the surface, allowing for the attenuation in the haze layer; $I_{1,d}$ is the scattered light coming from the underlying surface; $I_{2,d}$ is the brightness of the haze in the absence of a surface.

[2] contains data on the quantity I_d and each of the terms of the sum (8) for the case of an orthotropic[1)] underlying surface.

Table 6

Angular Distribution of Brightness of Orthotropic Surface Observed through a layer of Haze

φ°	$I(\theta,\psi)e^{-\sec\theta\tau_2}$	$I_{1,d}$	$I_{2,d}$	$Ie^{-\sec\theta\tau_2}+I_{2,d}$	$\frac{I_{1,d}}{Ie^{-\sec\theta\tau_2}+I_{2,d}}$
0	0,19	0,13	0,05	0,24	0,54
30	0,18	0,12	0,07	0,25	0,48
60	0,15	0,13	0,19	0,34	0,38
75	0,11	0,14	0,46	0,57	0,25

Table 6 illustrates these values for $\tau_2=0{,}2$; $\zeta=75°$, $\psi=180$, $A=0{,}8$. It takes into account the illumination of the surface by direct solar light and scattered sky light. If the orthotropic surface is replaced by a

1) The light reflected by an orthotropic surface has a uniform directional distribution.

cloud, it is easy to calculate the first term in formula (8); the third term remains unchanged, and only the second term will cause some difficulty, since its determination will require a solution of the transport equation for a non-orthotropic underlying surface. Such a solution has not yet been obtained, and for this reason in the case of the cloud we shall use the values of $I_{1,d}$ borrowed from [2], assuming that the error is smaller than the values shown in the last column of Table 6.

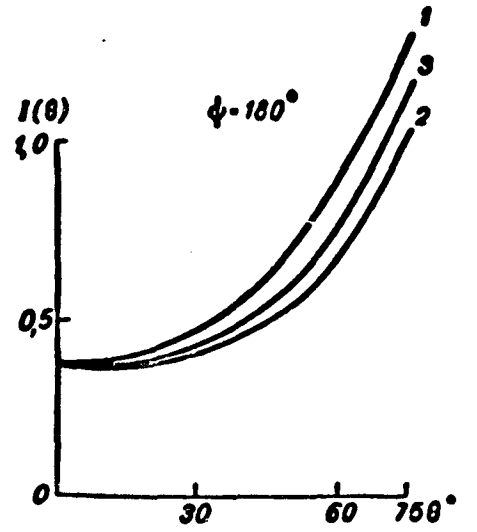

Fig. 6. Angular variation of brightness.
1 - next to the upper boundary of cloud; 2 - at the upper boundary of atmosphere with $\tau_2 = 0.2$; 3 - same, with $\tau_2 = 0.6$.

The brightness of the cloud observed through a haze and calculated within this margin of error, $I_d(\theta, \psi)$, is shown in Fig. 6 for two values of the optical thickness of the above-cloud layer τ_2 : 0.2(2) and 0.6(3). The figure also shows the distribution of the true brightness of the cloud (1). The figure shows a slight variation of the angular distribution of the brightness due to the haze, a fact which can be readily accounted for.

Actually, in the case of the haze, the same indicatrix effect is operative as the one which causes a rapid increase in the brightness of the cloud with angle θ when $\psi = 180^\circ$ and $\zeta = 75^\circ$. The difference between the slightly stretched indicatrix of the above-cloud layers of the atmosphere and the highly stretched indicatrix of the cloud turns out to be small because of the more pronounced multiple scattering in the cloud. When $\tau_2^* = 0{,}2$, the brightness increases more slowly than when $\tau_2 = 0.6$, since in the first case a more important part is played by the quantity $I_{1,d}$, which has a uniform angular distribution.

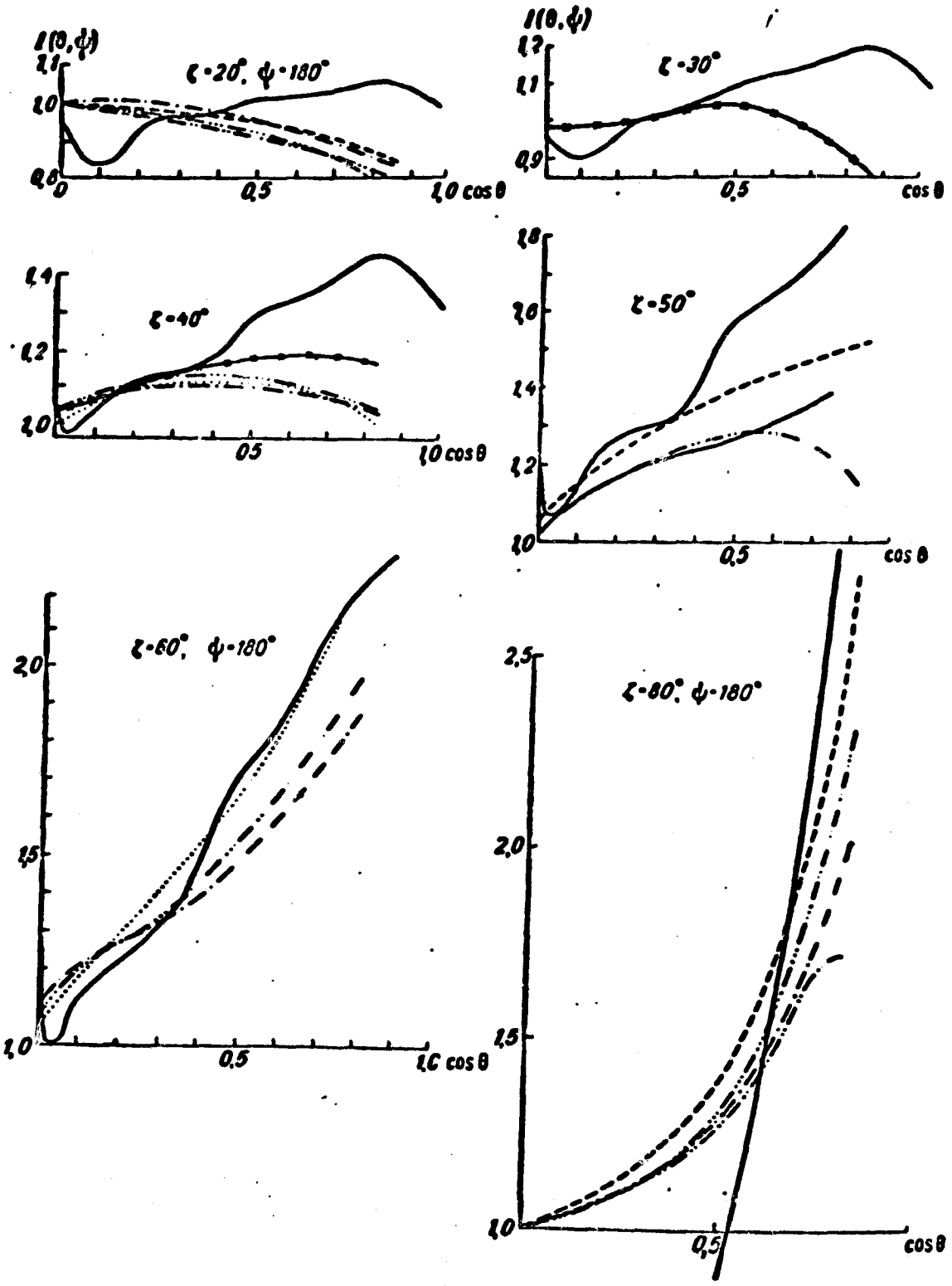

Fig. 7. Comparison of cloud brightness and snow brightness.

In order to compare the brightness of a cloud and that of snow, use is made below of snow brightness measurements made by I. P. Malkov at the Institute of Atmospheric Physics. In Fig. 7, the solid curves represent the calculated angular distribution of light reflected off a cloud at $\varphi = 180^\circ$ with an increasing angle of incidence of the parallel beam of light, while all the remaining curves represent the measured brightness

of snow under these conditions. The figures show a qualitatively identical behavior of the brightness — a rotation of the curves with increasing ζ, i.e., an acceleration of the angular variation of brightness at $\psi = 180^\circ$.

3. Fluxes of infrared radiation reflected by a cloud

The method used in [1] for the calculation of the solar radiation reflected by a cloud in the range of absorption bands of $0.7 \leq \lambda\mu \leq 2.5$ does not permit the determination of the brightness, but gives only the fluxes and albedo of the clouds within an error of the order of 10%.

When the absorption is taken into account, the main parameter of the problem is the quantity

$$k_\lambda = \frac{\tilde{\sigma}_{\lambda,0}}{\tilde{\sigma}_{\lambda,0} + \tilde{\varepsilon}_{\lambda,0} + \tilde{\varepsilon}_{\lambda,0}},$$

which in the present work is assumed to be constant.

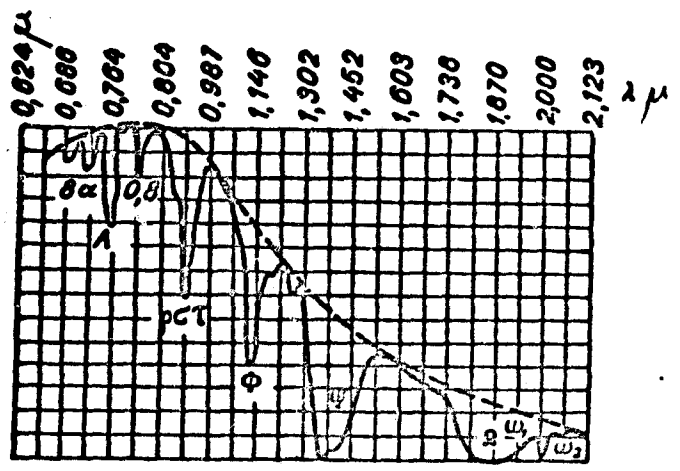

Fig. 8. Principal absorption bands of atmospheric gases in the near infrared.

Fig. 8 (see [6]) shows the absorption bands of the earth's atmosphere in the near infrared region. Band A belongs to oxygen, ω_1 and ω_2 to carbon dioxide, and the remaining ones to water vapor. Liquid water also absorbs in the cloud, and the spectrum of this absorption is shown in Fig. 9, borrowed from [6].

The scattering in the spectral range under consideration is much greater than the absorption, and the parameter k_λ is close to unity. An

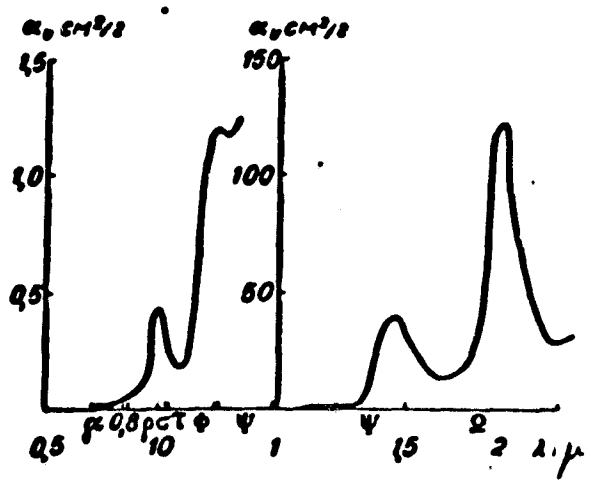

Fig. 9. Absorption spectrum of liquid water.

idea of the variation of k_λ with the wavelength may be obtained from Table 7, which takes into account only the absorption by water and water vapor. The table shows the central parts of the water vapor bands, their wings, and the gaps between the bands (see [1]).

Table 7

Spectral Dependence of k_λ parameter

		$\Delta\lambda$ μ	k_λ			$\Delta\lambda$ μ	k_λ
α	1	0,700—0,719	0,999684	Φ	13	1,030—1,112	0,999333
	2	0,719—0,721	0,995649		14	1,112—1,148	0,981700
	3	0,721—0,740	0,999674		15	1,148—1,230	0,998464
	4	0,740—0,790	0,999967		16	1,230—1,240	0,998852
0,8 μ	5	0,790—0,814	0,999645				
	6	0,814—0,816	0,992209	Ψ	17	1,240—1,321	0,998124
	7	0,816—0,840	0,999644		18	1,321—1,449	0,940141
	8	0,840—0,860	0,999962		19	1,449—1,530	0,963792
ρστ	9	0,860—0,915	0,999314				
	10	0,915—0,935	0,981380	Ω	20	1,530—1,755	0,984811
	11	0,935—0,990	0,998990		21	1,755—1,965	0,897819
	12	0,990—1,030	0,999664		22	1,965—2,190	0,962316

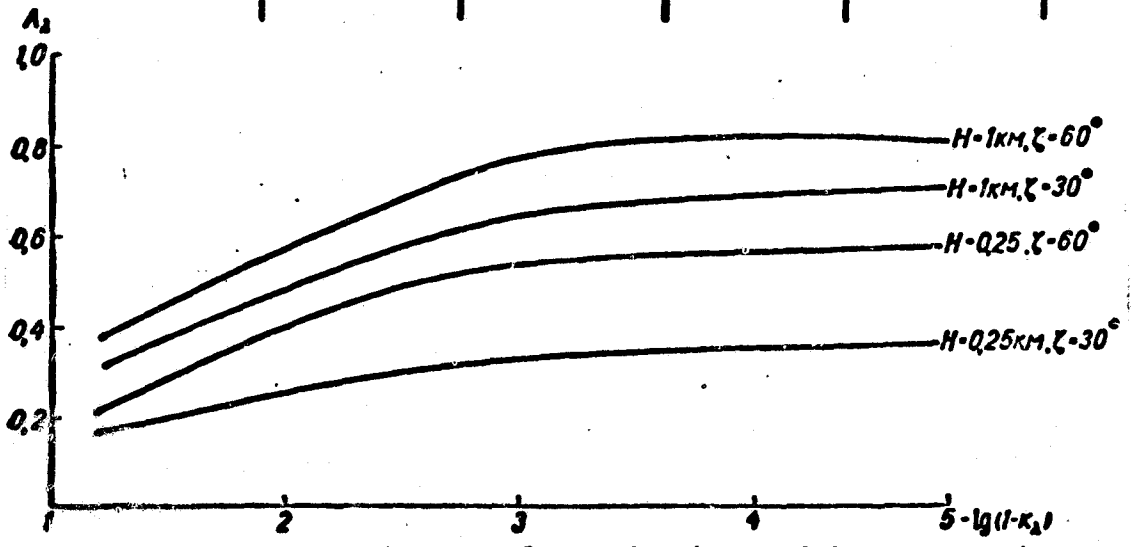

Fig. 10. Spectral variation of k_λ parameter

Fig. 10 shows the manner in which the albedo of a cloud changes with k_λ for different thicknesses of the cloud H in km and at a zenithal solar distance of ζ°. The curves of Fig. 10 obviously make it possible to determine the spectral albedo of a thick or thin cloud for a high or low position of the sun, independently of the nature of the absorbing substance. For example, one can evaluate the albedo in the bands of CO_2 and O_2.

It is known [7,8] that the measurement from satellites of the cloud brightness at the center I_1 and at the wing I_2 of the absorption band of one of these substances is considered to be a promising method of determining the altitude of clouds because of the stability of the oxygen and carbon dioxide content of the atmosphere.

The idea of the method is simple and enables one to obtain an elementary formula for the optical thickness at the center of the absorption band of the respective substance.

$$\tau = \frac{1}{\sec\theta + \sec\zeta} \ln \frac{I_2}{I_1} \qquad (9)$$

with two assumptions: (a) that the brightness of the haze can be neglected, and (b) that the albedo of the cloud at the center and at the wing of the band is the same. Fig. 10 can be used to determine the validity of the second assumption.

Let us consider the most interesting oxygen band (see [8]) with its center at $\lambda = 0.762\mu$. Unfortunately, this band has been little studied thus far, and there are only some relatively unreliable data on its properties [8], according to which one can write

$$a = a_0 \sqrt{\frac{m_0}{m}} . \qquad (10)$$

where $m_0 = 200$ g/cm^2 is the oxygen content of the entire thickness of the atmosphere, $\alpha_0 = 0.001$ cm^2/g is the absorption coefficient at $\lambda = 0.762\ \mu$ and $m = m_0$. If the cloud is homogeneous and the scattering coefficient is 30 1/km, when $\alpha = 0.001 \div 0.002$ cm^2/g we obtain the relations between the albedo at the center of band A_1 and at the wing A_2 shown in Table 8.

Table 8

Albedo of Cloud in the Absorption Band of Oxygen

		$H = 1$ км		$H = 0{,}25$ км	
		$\zeta = 30°$	$\zeta = 60°$	$\zeta = 30°$	$\zeta = 60°$
$\alpha = 0{,}001$ см^2/g	A_1	0,65	0,78	0,34	0,55
	A_2	0,70	0,81	0,38	0,58
	A_1/A_2	0,92	0,96	0,89	0,95
	$\delta\tau$ %	14	7	19	8
$\alpha = 0{,}002$ см^2/g	A_1	0,58	0,68	0,31	0,50
	A_2	0,70	0,81	0,38	0,58
	A_1/A_2	0,83	0,84	0,82	0,86
	$\delta\tau$ %	15	14	16	12

The values of $\delta\tau$% constitute the error in the determination of the optical thickness of oxygen in the above-cloud atmosphere, assuming that $A_1 = A_2$. The error is calculated from the formula

$$\delta\tau = \frac{\tau - \tau'}{\tau^*} = -\frac{\ln \frac{A_1}{A_2}}{M\tau^*}, \tag{11}$$

where τ is the optical thickness provided that $A_1 = A_2$; τ' is the optical thickness allowing for a difference between A_1 and A_2; τ^* is the optical thickness of the entire atmosphere, equal to

$$\tau^* = \alpha_0 m_0,$$
$$M = \sec\vartheta + \sec\zeta. \tag{12}$$

It is apparent from formula (11) that the error decreases with increasing M, but M should not be increased much because this causes an increase in the haze. When M = 3, the values of $\delta\tau$ shown in Table 8 are obtained; they show a very appreciable error in the determination of τ due

to the neglect of the difference in the reflecting properties of the cloud at the center and wing of the band.

Fig. 11 shows the spectral variation of the albedo of the cloud, account being taken of the absorption bands of water vapor and water droplets.

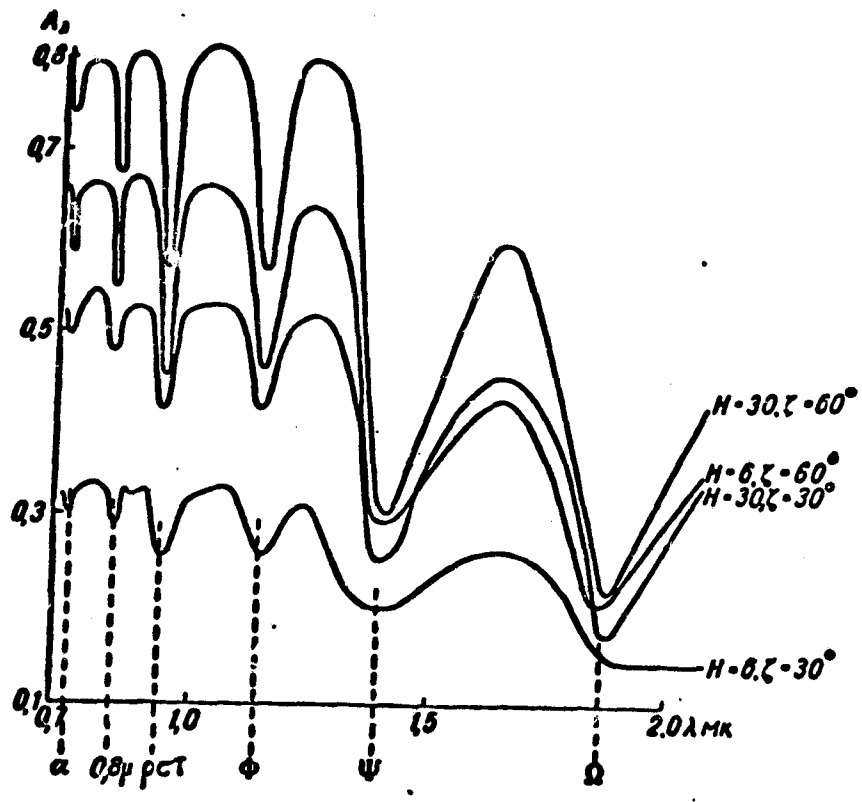

Fig. 11. Spectral variation of albedo of clouds.

4. Reflection and self-radiation of clouds in the far infrared.

In [1] simple expressions were found for the fluxes of long-wave radiation ($4 \leq \lambda\mu \leq 40$) passing through a cloud layer, allowance being made for absorption by water and water vapor, scattering by water droplets and the self-radiation of the cloud. On the basis of a comparison with a solution of this problem obtained earlier by K. S. Shifrin [9,10], a more sound choice of parameters and allowance for the scattering indicatrix were made in [1].

Unfortunately, thus far no accurate solution has been obtained for the indicated problem, and it is impossible to determine the error of our calculations or those of K. S. Shifrin.

For fluxes of outgoing radiation at the upper boundary of a cloud of moderate thickness[1)], the following expression was obtained in [1]:

$$F_\lambda = A_\lambda F_{0,\lambda} + \pi(1-A_\lambda)P_\lambda \int_0^\infty B_\lambda(t) e^{-P_\lambda(t-t)} dt. \qquad (13)$$

Here A_λ is the albedo of the cloud, expressed by the formula

$$A_\lambda = \frac{\frac{1}{2}P_\lambda - (1-k_\lambda)}{\frac{1}{2}P_\lambda + (1-k_\lambda)}, \qquad (14)$$

k_λ retains its former meaning - ratio of scattering to attenuation; P_λ is the parameter of the problem

$$P_\lambda = \sqrt{(1-k_\lambda)(4-k_\lambda C_1)}, \qquad (15)$$

C_1 is the parameter related to the form of the scattering indicatrix

$$C_1 = \int_0^{\frac{\pi}{2}} \gamma(\varphi)\cos\varphi\sin\varphi\, d\varphi - \int_{\frac{\pi}{2}}^{\pi} \gamma(\varphi)\cos\varphi\sin\varphi\, d\varphi. \qquad (16)$$

In its physical meaning, C_1 is the resultant flux of scattered radiation arising from a single scattering event, $B_\lambda(t)$ is Planck's function of temperature T(t) in the cloud at the level having an optical thickness t, $F_{0,\lambda}$ is the flux of radiation striking the cloud from above. If in the vicinity of the upper boundary of the cloud the water content exceeds 0.1 g/m^3, and the temperature gradient does not exceed 10°/100 m (see [1]), relation (13) may be given the form

$$F_\lambda = A_\lambda F_{0,\lambda} + (1-A_\lambda)\pi B_\lambda(T_0). \qquad (17)$$

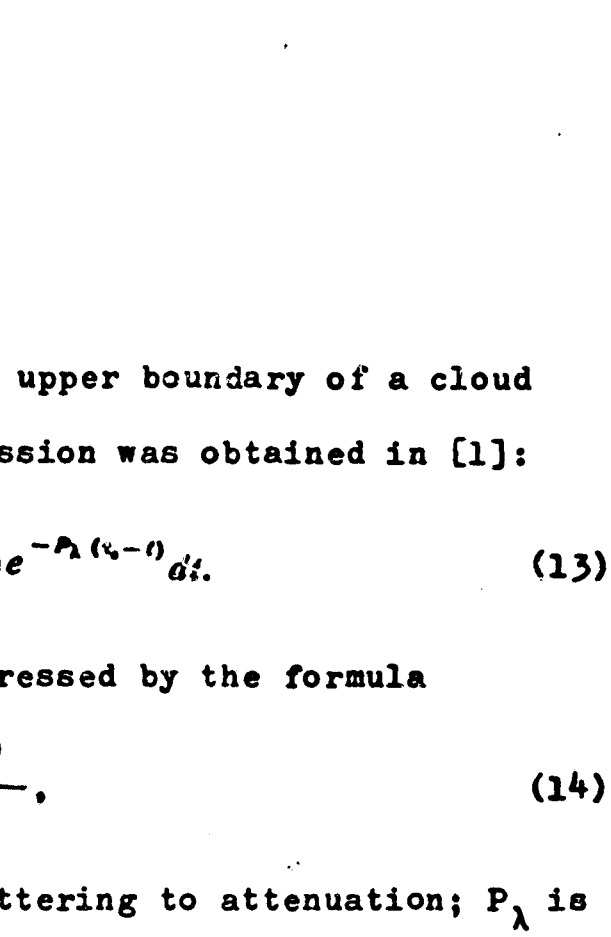

Fig. 12. Long-wave spectral albedo of clouds.

1) A cloud which is not too thin, i.e., whose thickness is not translucent in the visible.

where T_0 is the temperature of the upper boundary of the cloud.

It is easy to see that expression (13) assumes the same form if the temperature inside the cloud remains constant.

In the long-wave range of the spectrum, the cloud (Fig. 12) is often treated as a black body radiating in accordance with the law

$$F_\lambda = \pi B_\lambda(T_0). \tag{18}$$

Since a scattering of the long-wave radiation in the clouds should not be neglected, equality (18) is fundamentally impossible and should be replaced by relation (17), which shows the fulfillment of Kirchhoff's law (with the adopted assumptions) in the vicinity of the upper boundary of the cloud. The deviation of the actual radiation of the cloud from the black body radiation depends on the magnitude of the albedo A_λ.

We shall show first of all that the albedo calculated from formula (14) depends on the water content and temperature of the cloud because of the quantity k_λ, equal to

$$k_\lambda = \frac{\tilde{\varepsilon}_{v.\lambda}}{\tilde{\varepsilon}_{v.\lambda} + \tilde{\varepsilon}_{v.\lambda} + \tilde{\varepsilon}_{w.\lambda}} = \frac{\varepsilon_{v.\lambda}\rho_v}{\varepsilon_{v.\lambda}\rho_v + \varepsilon_{v.\lambda}\rho_v + \varepsilon_{w.\lambda}\rho_w}. \tag{19}$$

The coefficients of scattering and absorption in the middle member of the above equality are calculated per unit volume, and those in the right-hand portion, per unit mass; ρ_v is the water content of the cloud, and ρ_w its humidity. The latter is assumed to be saturated and hence, dependent on the temperature. From (19) it is apparent that when $\alpha_w = 0$

$$k_\lambda = \frac{\varepsilon_{v.\lambda}}{\varepsilon_{v.\lambda} + \varepsilon_{v.\lambda}} = \text{const} \tag{20}$$

and thus, in the "windows of transparency" of water vapor, for example, in the range of 8-12 μ, the dependence of the albedo on the water content and temperature will be slight.

In [1], calculations were made of the average albedo of a cloud in the wavelength intervals of 4-8, 8-12, ..., 24-28 μ, and in the range of

temperatures of 0 to -10°, humidity of 0.1-0.5 g/m^3, and parameter C_1 of 0.5-3. An example of the values of A_λ obtained is given in Fig. 12 for the case ρ_v = 0.2 g/m^3 and t = 0°. The albedo increases with increasing water content, a decrease in temperature and a decrease in C_1; this corresponds to a decrease in the average radius of the drops or an increase in the wavelength. Within the above-indicated limits of variation in parameters outside the transparent interval (8-12 μ), the albedo does not exceed 15%, and the cloud may be considered to be a black body within this margin of error. In the transparent interval, the albedo increases appreciably, since the absorptive capacity of water vapor and water droplets decreases sharply. Depending upon the value of C_1, the change in A_λ is confined within the following limits:

$$15\% \leqslant A_\lambda \leqslant 27\%.$$

The distribution of the drops according to size in real clouds leads to the values $C_1 \approx 2$-2.4. The values of A_λ for C_1 = 2 are shown in Table 9.

Table 9

Long-Wave Albedo of Clouds
C_1 = 2

t°	ρ_v g/m^3 0,1	0,2	0,5	0,1	0,2	0,5
	4—8 μ			16—20 μ		
0	0,06	0,09	0,14	0,05	0,06	0,07
—5	0,07	0,11	0,15	0,06	0,07	0,08
—10	0,09	0,13	0,17	0,06	0,07	0,08
	8—12 μ			20—24 μ		
0	0,19	0,19	0,19	0,03	0,05	0,06
—5	0,19	0,19	0,19	0,04	0,05	0,07
—10	0,19	0,19	0,19	0,05	0,06	0,08
	12—16 μ			24—28 μ		
0	0,07	0,07	0,07	0,02	0,03	0,05
—5	0,07	0,07	0,07	0,03	0,04	0,06
—10	0,07	0,07	0,07	0,03	0,05	0,06

In order to describe thin clouds, it is interesting to determine the free path of radiation R_λ, i.e., the depth to which the flux penetrating into the cloud is attenuated by a factor of ℓ times. We obtained the following expression for this quantity:

$$R_\lambda = \frac{1}{P_\lambda\left(\tilde{\sigma}_{\omega,\lambda} + \tilde{\sigma}_{\omega,\lambda} + \tilde{\sigma}_{\omega,\lambda}\right)} = \frac{k_\lambda}{\tilde{\sigma}_{\omega,\lambda}\sqrt{(1-k_\lambda)(1-k_\lambda C_\lambda)}}. \qquad (21)$$

5. Conclusion

In conclusion, it is interesting to formulate the results obtained and to determine the place occupied by the present work among the investigations designed to find methods of interpretation of radiation measurements carried out with satellites.

The work does not offer any methods of interpretation. Nevertheless, the collected data on the radiation properties of clouds may be useful in developing such methods and make it possible to determine various kinds of errors and to carry out methodical calculations. They may also be used in designing apparatus. However, one should allow for a certain conventionality of the data, due to the difference between the actual atmosphere and the models used for the calculation, and also to the insufficiency of data on the optical properties of clouds - their scattering and absorbing capacity.

The main conclusions, most of them unfortunately negative, are enumerated below.

1. In the visible portion of the spectrum, even for high positions of the sun and red rays, the scattered light of the haze appreciably alters the light coming from a cloud.

2. The light of the haze above the clouds is neutral relative to wavelength, just as is the albedo of clouds. Therefore, one should not try to distinguish clouds located at different levels by means of their spectral brightness alone.

3. Clouds located at low levels may be brighter than higher ones because of the greater scattering capacity of the former. Therefore, the possibility of distinguishing cloud levels on the basis of differences in their brightness is also doubtful.

4. The angular distribution of light reflected off a cloud is relatively uniform, with the exception of the range of azimuthal angles $135^\circ \leq \varphi \leq 180^\circ$. In this case, a rapid increase in brightness along the direction of the horizon is observed at low positions of the sun. This characteristic of the angular distribution can hardly be used for purposes of interpretation, since it is characteristic of snow and atmospheric haze.

5. The difference in the albedo at the center and at the wing of the absorption band may introduce an error of the order of 10-20% into the determination of the optical thickness of the atmosphere above the cloud.

6. Opaque clouds may be considered black bodies within an error of 5-10% in the spectral intervals $4 \leq \lambda\mu \leq 8$ and $12 \leq \lambda\mu \leq 40$. In the atmospheric window of transparency ($8 \leq \lambda\mu \leq 12$), this error amounts to 15-25%.

REFERENCES

1. Feygel'son, Ye. M. Radiatsionnyye protsessy v sloistoobraznykh oblakakh. Monografiya. [Radiation Processes in Stratified Clouds. Monograph]. Izd. AN SSSR, Moscow, 1963.
2. Feygel'son, Ye. M., Malkevich, M. S., et al. Raschet yarkosti sveta v atmosfere pri anizotropnom rasseyanii [Calculation of the Luminosity in the Atmosphere in Anisotropic Scattering]. Monografiya, ch. I. Tr. IFA AN SSR, No. 1, 1958. ch. II. Tr. IFA AN SSR, No. 3, 1962.
3. Rabinovich, Yu. I. Tr. GGO, Vyp. 108, 1961.
4. Feygel'son, Ye. M. Tr. AFI AN KazSSR, t. III, 74, 1962.
5. Fowle, F. E. Astrophys. Journ. 35, 401, 1912.
6. Aschkinss Ann d. Phys., 35, 401, 1895.
7. Mal'kevich, M. S. Nekotoryye voprosy interpretatsii polya ukhodyashchey radiatsii Zemli [Certain Aspects of the Interpretation of the Earth's Outgoing Radiation]. See this collection.
8. Jamamoto, G., Wark, D. O. Journ. Geophys. Res. V. 66, 3596, 1961.
9. Shifrin, K. S. O vychislenii radiatsionnykh svoystv oblakov [Calculation of the Radiative Properties of Clouds]. Tr. GGO, vyp. 46, 1955.
10. Shifrin, K. S. Ibid., p. 34.

O. A. Avaste

METHOD OF CALCULATING THE INTENSITIES AND FLUXES OF OUTGOING RADIATION IN THE VICINITY OF A SPHERICAL EARTH IN THE INFRARED REGION OF THE SPECTRUM

1. Introduction. Statement of the Problem

At the present time, the measurement of outgoing radiation fluxes of the earth—atmosphere system by means of meteorological satellites is a very pressing problem. Of great importance for the interpretation of such measurements is the development of simple methods of calculation of the radiation fluxes.

The purpose of the present work is to derive formulas for the calculation of outgoing radiation (intensities and fluxes) in the near infrared, taking the curvature of the earth's surface into account.

We shall consider a scattering and absorbing atmosphere illuminated by parallel rays of direct solar radiation. The satellite is located at point P_0 at altitude H above the earth's surface (Fig. 1), at which the angle of incidence of the direct solar radiation will be designated by i_0 (measured from the outer normal). The change in the position of P is defined by angular coordinates (α,β), where α is the angle between P_0P and the inner normal at point P_0, β is the azimuth measured from the plane defined by the normal and the incident solar ray at point P_0 (against the sun, $\beta = 0$; with the sun $\beta = \pi$). At point P, the angle of incidence of direct solar radiation will be designated by i and the zenithal angle by θ. The earth's radius will be designated by R, and the central angle by $P_0OP = \delta$.

The scattering and absorption of shortwave radiation ($\lambda = 0.29 \div 5$ μ) takes place mainly in a relatively thin layer. In the estimation of

Fritz [1], only 1% of solar energy is absorbed in the layers of the earth's atmosphere above 30 km. Direct measurements of Miley, et al [2,3] showed that the intensity of the light scattered at 30 km altitude amounts to only 2-3% of the intensity on the earth's surface. It follows from the above that practically all the processes of conversion of solar heat in the earth's atmosphere are concentrated in the 0-30 km layer. All of the atmosphere located higher may be considered optically void (diathermal) with respect to the conversion of the fluxes in the near infrared. Since the satellite is generally located at an altitude $H \gg 30$ km, the following problems may be examined to a first approximation: 1) Calculation of the intensity of outgoing radiation at altitude $z = 30$ km; 2) Consideration of the so-called dilution (rarefaction) effect of radiation for the calculation of the ascending flux at the level of the satellite, i.e., consideration of a purely geometrical effect due to a decrease in the solid angle defined by the area of the earth's surface visible from the satellite with an increase in the altitude H.

Under average conditions in the atmosphere, in the infrared region of the spectrum, the spectral optical thickness of the atmosphere $\tau_\lambda < 0.1$ (see Ref. [4]); this means that if we confine ourselves to the consideration of absorption and single scattering, we shall still have a sufficient accuracy.

Absorption by water vapor and carbon dioxide is determined by means of absorption functions obtained from experimental data of Howard, Burch and Williams [5] and Fowle [6]. The effect of pressure on the absorption is considered (for more detail, see Ref. [4]).

The concentration of water vapor decreases with the altitude in accordance with an exponential law (Yamamoto's formula [7]). The volume

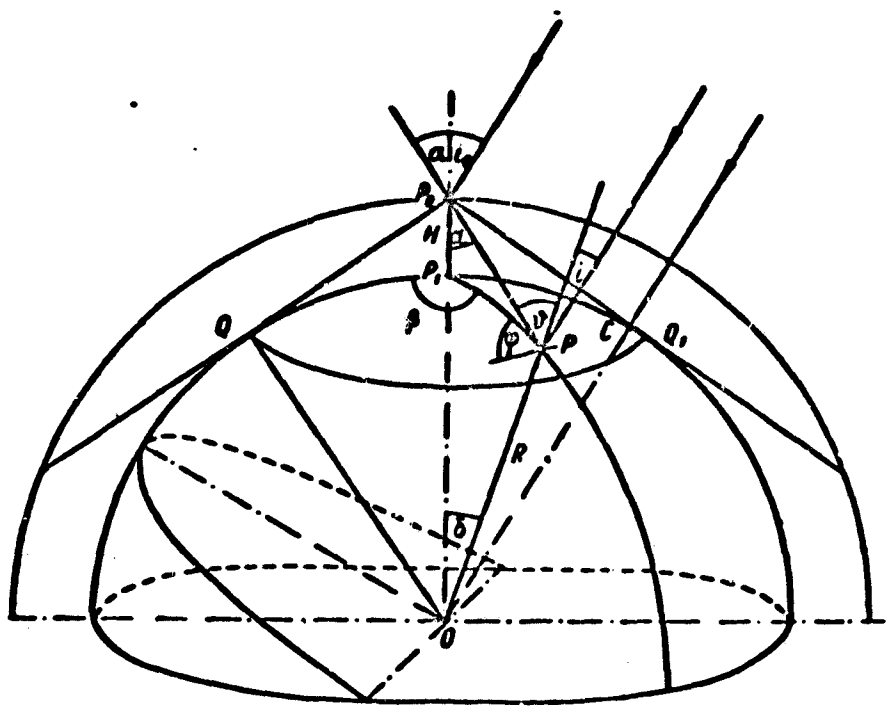

Fig. 1. Geometrical parameters of the problem of radiation transfer for a spherical earth.

concentration of carbon dioxide is constant (0.033%). The virtual temperature decreases linearly with the altitude. The scattering is due to molecules of air and aerosol. Aerosol and molecular scattering is calculated by the scheme developed by K. S. Shifrin and I. N. Ninin [8].

2. Formulas for the Intensity of Ascending Radiation

In approximating the atmosphere by an eight-layer model, we assume that the scattering events occur only at the centers of mass of the layers. The thickness of the layers is selected so that the masses of the individual layers are the same in the standard radiation model of the atmosphere which we are using. The boundaries and centers of the layers are taken from Ref. [4] (Table 1).

The intensity of direct solar radiation at level $C_{m,k}$ (we shall henceforth designate it by the index k) is

$$I_0 e^{-\tau_2 m_l} T\left(\bar{x}_l \cdot m \int_{\infty}^{h}\right) T\left(\bar{x}_l \cdot \mathrm{co}_2 \int_{\infty}^{h}\right). \qquad (1)$$

Table 1

Boundaries z_k and centers $c_{m,k}$ of layers in the calculation of single scattering.

k	1	2	3	4	5	6	7	8
z_k km	1,12	2,37	3,82	5,52	7,63	10,4	14,8	48,2
$c_{m,k}$ km	0,55	1,74	3,08	4,65	6,55	8,96	12,4	19,3

where $\tau_\lambda = \int_z^\infty \sigma_\lambda(z)dz$ will be obtained in accordance with Ref. [8]. Here I_0 is the spectral intensity of extra-atmospheric solar radiation according to Ref. [9], $\sigma_\lambda(z)$ is the spectral scattering coefficient, $T\left(\bar{x}_{i,w}\Big|_z^\infty\right)$ and $T\left(\bar{x}_{i,CO_2}\Big|_z^\infty\right)$ are, respectively, the transmission functions of water vapor and carbon dioxide from the boundary of the atmosphere to level k at an angle of incidence i of the direct solar radiation [4], and m_i is the mass of the atmosphere, which takes into account the length of the path of the oblique rays

$$m_i = \sec i, \quad \text{if} \quad i < 60°. \tag{2}$$

From simple geometrical relations we find that for $i > 60°$

$$m_i = \frac{1}{z}\int_0^z \frac{dx}{\sqrt{1-\left(\frac{R}{R+x}\right)^2 \sin^2 i}} = \frac{1}{z}\left[\sqrt{(R+z)^2 - R^2\sin^2 i} - R\cos i\right], \tag{3}$$

where z is the thickness of the scattering layer (z = 30 km) and R is the earth's radius.

We obtain similar formulas for masses of the atmosphere in the direction ϑ. The transmission functions may be obtained from formulas (9) and (10) of Ref. [4], which also gives expressions for the weighted parameters $\bar{x}_{i,w}$ and $\bar{x}_{i,CO_2}$.

If we consider a unit volume at level k, then in the direction defined by angle i for single scattering, the energy

$$I_0 e^{-\tau_k m_i} T\left(\bar{x}_{i,w}\Big|_z^\infty\right) T\left(\bar{x}_{i,CO_2}\Big|_z^\infty\right) \frac{\varkappa(\gamma)}{4\pi}, \tag{4}$$

is radiated, where $\varkappa(\gamma)$ is the normalized scattering indicatrix, i.e.,

$$\int \varkappa(\gamma) \frac{d\omega}{4\pi} = 1. \tag{5}$$

The energy of scattering from a unit volume at level k after attenuation along the path leading to the satellite is represented by the expression

$$I_0 e^{-\tau_k m_l} T\left(\bar{x}_{l,\omega} \int_{-\infty}^{h}\right) T\left(\bar{x}_{l,\infty} \int_{-\infty}^{h}\right) \frac{\varkappa(\gamma)}{4\pi} e^{-\tau_k m_0} \times$$
$$\times T\left(\bar{x}_{0,\omega} \int_{h}^{\infty}\right) T\left(\bar{x}_{0,\infty} \int_{h}^{\infty}\right). \tag{6}$$

We can represent the transmission function by the formula

$$T\left(\bar{x}_{l,\omega} \int_{-\infty}^{h}\right) T\left(\bar{x}_{0,\omega} \int_{h}^{\infty}\right) = T\left(\bar{x}^{(k)}_{l,0,\omega}\right), \tag{7}$$

where

$$\bar{x}^{(k)}_{l,0,\omega} = \sqrt{w_k (m_l + m_0)} \quad \overline{(P_k + e_k)^n}. \tag{8}$$

Here w_k is the content of water vapor in a vertical column above level k; P_k and e_k are respectively the total and partial pressure at level k; n is a constant (for water vapor $n \approx 0.3$); $\overline{(P_k+e_k)^n}$ is a weighted value obtained from Ref. [4]. From formula (8), we obtain

$$\bar{x}^{(k)}_{l,0,\omega} = \bar{x}^{(k)}_{\omega} \sqrt{m_l + m_0}, \tag{9}$$

where $\bar{x}^{(k)}_{\omega}$ is a weighted parameter; if the ray travels in a vertical direction from infinity to level k,

$$\bar{x}^{(k)}_{\omega} = \sqrt{w_k} \quad \overline{(P_k + e_k)^n}. \tag{10}$$

We obtain similar formulas for carbon dioxide, but in this case $n \approx 0.4$. Considering the above, we can write instead of expression (4),

$$\frac{\varkappa(\gamma)}{4\pi} I_0 e^{-\tau_k (m_l + m_0)} T\left(\bar{x}^{(k)}_{l,0,\omega}\right) T\left(\bar{x}^{(k)}_{l,0,\infty}\right). \tag{11}$$

Since we postulate that the scattering events occurred at the centers of mass of the selected layers, it is necessary to multiply expression (11) by the optical thickness of the layer for the direction ϑ, i.e., by

$$\Delta\tau_k m_\vartheta = (\tau_k - \tau_{k-1}) m_\vartheta. \tag{12}$$

The intensity of singly scattered radiation in the direction ϑ at altitude z = 30 (i.e., above the scattering and absorption layer) is expressed by

$$I_1(\tau, \vartheta, i, \varphi) = I_0 \frac{\varkappa(\gamma)}{4\pi} \sum_{k=1}^{n} e^{-\tau_k (m_\vartheta + m_i)} T\left(\bar{x}^{(k)}_{i,\vartheta,w}\right) \times \\ \times T\left(\bar{x}^{(k)}_{i,\vartheta,\varphi_0}\right) \Delta\tau_k m_\vartheta. \tag{13}$$

Let us consider the albedo of the underlying surface. Assuming that the surface is orthotropic, we have

$$I(\tau, \vartheta, i, \varphi, A) = I_1(\tau, \tau_0, \vartheta, i, \varphi) + I_A e^{-\tau_0 m_\vartheta} T\left(\bar{x}_{\vartheta,w}\int_0^\infty\right) \times \\ \times T\left(\bar{x}_{\vartheta,\varphi_0}\int_0^\infty\right), \tag{14}$$

where

$$I_A = \frac{A}{\pi} E. \tag{15}$$

In order to calculate the illumination in the non-absorbing plane-parallel atmosphere with a finite optical thickness, V. V. Sobolev [12] proposed the formula

$$E = 2I_0 \frac{R(\tau_0, i)\cos i}{4 + (3 - \varkappa_1)\tau_0 (1 - A_A)}. \tag{16}$$

Substituting m_i for sec i in Sobolev's formula in the expression for $R(\tau_0$ i), we obtain

$$R(\tau_0, i) = 1 + \frac{3}{2}\frac{1}{m_i} + \left(1 - \frac{3}{2}\frac{1}{m_i}\right) e^{-\tau_0 m_i}, \tag{17}$$

where we calculate m_i from formulas (2) and (3). We obtain constant $\varkappa_1$ of formula (16), characterizing the elongation of the scattering

indicatrix, by means of formula

$$x_1 = \frac{3}{2}\int_0^{\pi} x(\gamma)\sin\gamma\cos\gamma d\gamma . \qquad (18)$$

If we bear in mind that the role of the scattered radiation in the near infrared is small in the creation of the total illumination on the earth's surface, we can assume that in the presence of absorption, the illumination E decreases in proportion to the attenuation of direct solar radiation by the absorption.

We then obtain, instead of formula (16), the formula

$$E = 2T\left(\bar{x}_{i,w}\int_0^{\infty}\right) T\left(\bar{x}_{i,CO_2}\int_0^{\infty}\right) I_0 \frac{R(\tau_0, i)\cos i}{4 + (3 - x_1)\tau_0(1 - A)}, \qquad (19)$$

where $T(\bar{x}_{i,w}\int_0^{\infty})$ and $T(\bar{x}_{i,CO_2}\int_0^{\infty})$ are the transmission functions of water vapor and carbon dioxide in a layer extending from the upper boundary of the atmosphere to the earth's surface in the direction i. Taking formulas (14) and (15) into account, we obtain the formula

$$I(\tau, \tau_0, \vartheta, i, \varphi, A) = I_1(\tau, \vartheta, i, \varphi) + \\ + \frac{2A}{\pi} I_0 T(\bar{x}_{i,\vartheta,w}^{(h=0)}) T(\bar{x}_{i,\vartheta,CO_2}^{(h=0)}) \frac{R(\tau_0, i)\cos i}{4 + (3 - x_1)\tau_0(1 - A)} e^{-\tau_0 m_\vartheta}, \qquad (20)$$

for the outgoing intensity in direction ϑ, where the functions $T(\bar{x}_{i,\vartheta,w}^{(h=0)})$ and $T(\bar{x}_{i,\vartheta,CO_2}^{(h=0)})$ are defined by formulas (7) and (8). The value of I_i is obtained from formula (13).

The dependence of the scattering indicatrix on the wavelength is obtained from Ref. [8] in the form

$$\frac{p_\lambda}{p_0}(1)\varkappa_p(\gamma) + \frac{q_\lambda}{q_0}(1)\varkappa_a(\gamma) = (1)\varkappa \qquad (21)$$

where $\frac{p}{p_0}$ and $\frac{q}{q_0}$ are respectively the Rayleigh and aerosol "weights," which depend on the wavelength, and $\varkappa_p(\gamma)$ and $\varkappa_a(\gamma)$ are, respectively, the Rayleigh and aerosol scattering indicatrices for wavelength λ. For

wavelength λ_0

$$p_{\lambda_0} + q_{\lambda_0} = \tau_0(\lambda_0), \tag{22}$$

and for wavelength λ

$$p_{\lambda_0}\left(\frac{\lambda_0}{\lambda}\right)^4 + q_{\lambda_0}\frac{\lambda_0}{\lambda} = \tau_0(\lambda). \tag{23}$$

We see that as λ increases, the fraction of the aerosol component increases appreciably, and the elongation of the indicatrix increases correspondingly [10].

For parameter $\varkappa_1$, which characterizes the elongation of the indicatrix [see formula (18)], we obtain the expression

$$\varkappa_1(\lambda) = \frac{3}{2}\int_0^\pi \varkappa_0(\gamma)\frac{q_{\lambda_0}\frac{\lambda_0}{\lambda}}{p_{\lambda_0}\left(\frac{\lambda_0}{\lambda}\right)^4 + q_{\lambda_0}\frac{\lambda_0}{\lambda}}\sin\gamma\cos\gamma\,d\gamma \tag{24}$$

and, considering the elongation of the aerosol indicatrix at wavelength λ_0, expressed by the formula

$$\varkappa_{1,0} = \frac{3}{2}\int_0^\pi \varkappa_0(\gamma)\sin\gamma\cos\gamma\,d\gamma, \tag{25}$$

we obtain, from formula (24)

$$\varkappa_1(\lambda) = \varkappa_{1,0}\frac{1}{\frac{p_{\lambda_0}}{q_{\lambda_0}}\left(\frac{\lambda_0}{\lambda}\right)^3 + 1}. \tag{26}$$

Let us note that in the case of a spherical earth, the straight line P_0Q is defined by the angle

$$\alpha_{max} = \arcsin\frac{R}{R+H}. \tag{27}$$

As H increases, the area of the earth's surface visible from the satellite increases rapidly. On this area, we should consider the change of the angle of incidence of direct solar radiation. The following relations exists between the angular coordinates:

$$\cos i = \cos i_0\cos\delta + \sin i_0\sin\delta\cos\beta, \tag{28}$$

$$\alpha = \vartheta - \delta, \tag{29}$$

$$\frac{R}{\sin\alpha} = \frac{R+H}{\sin(\pi-\vartheta)}. \tag{30}$$

In addition, as is evident from Fig. 1, instead of the usual relation

$$\cos\gamma = -\cos\vartheta\cos i + \sin\vartheta\sin i\cos\beta \tag{31}$$

we can use the relation

$$\cos\gamma = -\cos\alpha\cos i_0 + \sin\alpha\sin i_0\cos\beta, \tag{32}$$

which relates the angle of scattering γ to the angles ϑ, i_0, φ.

3. Formula for Ascending Radiation Flux at Level of Satellite

We shall derive a formula for the ascending radiation flux at altitude H. A horizontal surface at point P_0 is traversed by a flux from an element of solid angle

$$dF_\uparrow = I\cos\alpha d\omega, \tag{34}[sic]$$

where $d_w = \sin\alpha\, d\alpha\, d\beta$. The flux of ascending radiation received by a wide-angle receiver at level H is given by the formula

$$F_\uparrow = 2\int_0^{\pi} d\beta \int_0^{\alpha_{max}} I(\alpha, \beta)\cos\alpha\sin\alpha\, d\alpha. \tag{34}$$

Here the intensity $I(\alpha,\beta)$ is calculated from formula (20), and the relations between the angular parameters are calculated from formulas (28)-(32). Taking the form of the function $I(\alpha,\beta)$ into account, one can obtain the fluxes F by numerical integration alone, for example by using Simpson's formula [11].

In solving certain problems, it is more convenient to perform the integration with respect to the coordinates (δ,β). In this case, d_w will be defined by an area element dS on the surface of a sphere with radius R + z, i.e.,

$$d\omega = \frac{\vec{n}\cdot\vec{L}}{|\vec{L}|^3}dS, \tag{35}$$

where $\vec{n}$ is the unit vector of the normal of the area element dS and $\vec{L} = \vec{PP}_0$ (see Fig. 1). Considering

$$\vec{n} \cdot \vec{L} = |\vec{L}| \cos \delta \tag{36}$$

and

$$dS = (R+z)^2 \sin \delta d\delta d\beta, \tag{37}$$

we obtain from (33)

$$dF_1 = I\left(\frac{R+z}{L}\right)^2 \cos\alpha \cos(\alpha+\delta) \sin\delta d\delta d\beta. \tag{38}$$

Introducing the variable

$$\xi = \cos\delta; \quad d\xi = -\sin\delta d\delta, \tag{39}$$

we obtain

$$L^2 = (R+H)^2 + (R+z)^2 - 2(R+H)(R+z)\xi. \tag{40}$$

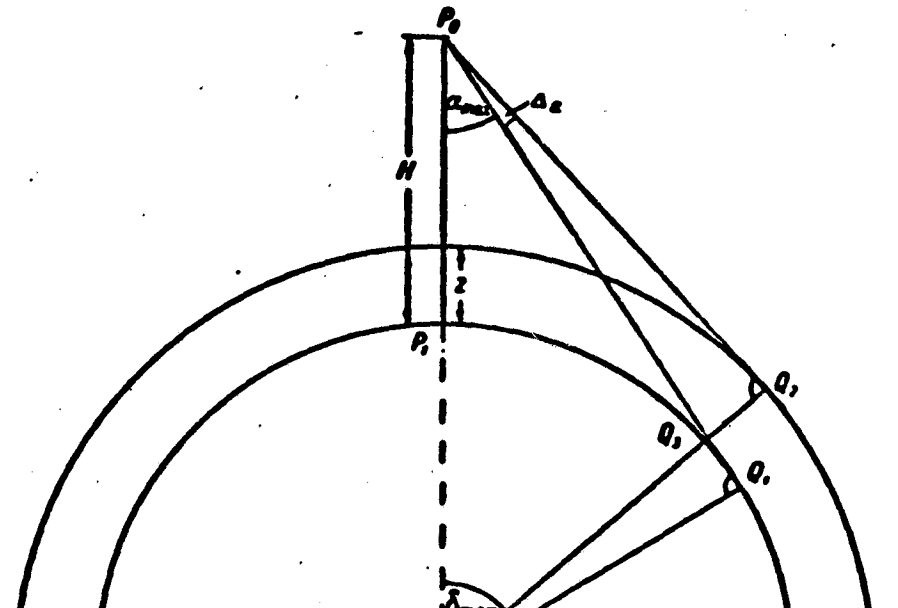

Fig. 2. Geometrical parameters of the problem of radiation transfer with the consideration of the altitude of the scattering layer z.

Since

$$\cos(\alpha+\delta) = \cos\alpha\cos\delta - \sin\alpha\sin\delta \tag{41}$$

and (from Fig. 1)

$$\left.\begin{aligned}\cos\alpha &= \frac{R+H-(R+z)\cos\delta}{L}\\ \sin\alpha &= \frac{(R+z)\sin\delta}{L}\end{aligned}\right\} \tag{42}$$

we can rewrite formula (38) in the form

$$dF_1 = -\frac{I(R+z)^2|R+H-(R+z)\xi|\,|(R+H)\xi-(R+z)|\,d\xi d\beta}{|(R+H)^2+(R+z)^2-2(R+H)(R+z)\xi|^2}. \tag{43}$$

Furthermore, for the upper limit of the integration with respect to ξ we take the value

$$\xi_m = \cos\tilde{\delta}_{max} = \frac{R+z}{R+H}. \tag{44}$$

Let us note that $\tilde{\delta}_{max}$ determines the position of point Q_2, i.e., the point of tangency of the straight line P_0Q_2 to the sphere of radius R + z (Fig. 2).

The formula for the ascending flux at the point of the satellite assumes the form

$$F_1 = -2(R+z)^2\int_0^{\pi} d\beta \int_1^{\frac{R+z}{R+H}} I\,\frac{|R+H-(R+z)\xi|\,|(R+H)\xi-(R+z)|}{|(R+H)^2+(R+z)^2-2(R+H)(R+z)\xi|^2}\,d\xi. \tag{45}$$

4. Parameters and the Method of Calculation

We shall note in conclusion that the following physical parameters are included in the proposed method of calculation:

1) Scattering function $\varkappa_\lambda(\gamma)$ which generally depends on the height above the earth's surface and on the wavelength (see Ref. [10]). We shall use the indicatrix weighted for the entire layer of the atmosphere and borrowed from [8]. The values of $\varkappa_\lambda(\gamma)$ are cited in tabulated form;

2) Optical thicknesses $\tau_k(\lambda)$, determined in accordance with Ref. [8];

3) Transmission functions $T(\bar{x})$ for the absorption bands of water

vapor and carbon dioxide, determined in accordance with Ref. [4];

4) Total content of water vapor in the atmosphere determined from several characteristic cases;

5) Content of carbon dioxide, determined by the model of the atmosphere adopted in this work and by the condition that the volume concentration of CO_2 is constant (0.033%);

6) Average value of the spectral albedo A_λ of the underlying surface, taken from the experiment.

In addition, the following geometrical parameters are included in the proposed method of calculation:

1) Altitude of the satellite H,

2) Earth's radius R,

3) Altitude of the scattering and absorbing layer of air z,

4) Coordinates of the satellite relative to the sun, defined by the angle of incidence of the direct solar radiation i_0,

5) Sighting direction determined by one of the pairs of angles (α,β), (δ,β), or (ϑ,φ). The relations between these angular coordinates are given by formulas (28)-(32).

REFERENCES

1. Fritz, S. Proc. Nat. Acad. Sci., Wash., 43, 95, 1957.
2. Miley, A. H., Cullington, E. H., Bedinger, J. F. Trans. Am. Geophys. Union, v. 34, 680, 1953.
3. Morozov, V. M. UFN, 53, 142, 1954.
4. Shifrin, K. S., Avaste, O. IFA AN ESSR, No. 2, 23, 1960.
5. Howard, J. N., Burch, D. E., Williams, D. JOSA, 46, 186, 237, 334, 452, 1956; Geophys. Res. Papers No. 40, Nov., 1955 (AF CRC-TR-55-213).
6. Fowle, F. E. Smiths Misc. Collect., v. 68, No. 8, 1917.
7. Yamamoto, G. Sci. Rep. Tohoku Univ., Ser. 5, v. 1, 76, 1949.
8. Shifrin, K. S., Minin, I. N. Tr. GGO, vyp. 68, 5, 1957.
9. Johnson, F. S. Journ. Meteorol., 11, 431, 1954.
10. Avaste, O., Moldau, Kh., Shifrin, K. S. Issledovaniya po fizike atmosfery. IFA AN ESSR, No. 3, 23, 1962.
11. Berezin, I. S., Zhidkov, N. P. Metody vychisleniy [Computational Methods]. Fizmatgiz, Moscow, 1959.
12. Sobolev, V. V. Uch. zap. LGU, ser. mat. nauk, 18, 17, 1949.

O. A. Avaste

RESULTS OF CALCULATIONS OF THE INTENSITY AND FLUXES OF OUTGOING RADIATION FOR A SPHERICAL EARTH IN THE NEAR INFRARED

1. Introduction. Concrete problem

The article cites the results of calculations made by using the method presented in Ref. [1]. The symbols used in the latter are employed.

We shall consider a concrete problem in which the point of observation above the earth's surface is located at an altitude of 300 km (earth's radius R = 6,371 km). From formula (27.1)[1], we shall obtain the angle defining a cone whose base will be the visible surface of the earth. In our case, this angle is equal to $72^{\circ}45'$.

Furthermore (see Fig. 2 of Ref. [1]), we get, for example,

$$P_0Q=(H+R)\cos\alpha_{max}=1980 \text{ km} \tag{1}$$

and

$$P_1Q=R\delta_{max}=R\left(\frac{\pi}{2}-\alpha_{max}\right)=1908 \text{ km}. \tag{2}$$

Let us recall that scattering takes place mainly in the 0-30 km layer. In the method of calculation which we are using, the layer above the horizon defined by the angle

$$\Delta\alpha=\operatorname{arc\,tg}\frac{z}{P_0Q}=52'. \tag{3}$$

is not considered.

In calculating the ascending flux at the level of the satellite, this omission is obviously acceptable.

Formula (34.1) for the calculation of the ascending flux at point P_0 does not take into account the radiation coming from the solid angle defined by the rotation of angle $Q_3\hat{O}Q_1$ above axis P_0O. For the concrete

1. References to formulas of Ref. [1] will be designated by the numeral 1 following the number of the formula.

case above ($Q_3OQ_1=\delta_{max}-\delta_{max}=53'$, $Q_1Q_3=98$ км), the intensity $I(Q_3)\approx$ $\approx I(Q_1)$, i.e., we shall take the intensity at point Q_1 instead of the intensity at point Q_3 in an interpretation in accordance with formula (34.1).

We shall briefly discuss the parameters of the concrete problem. Appendix 1 gives values of the parameters $\bar{X}_w^{(k)}$ and $\bar{X}_{CO_2}^{(k)}$ for various layers (see Ref. [1]) and various contents of water vapor w. In the calculation of $\bar{X}_{CO_2}$, the volume concentration of carbon dioxide was 0.033%. The parameters $\bar{X}_w^{(k)}$ and $\bar{X}_{CO_2}^{(k)}$ are used for calculating the transmission function from formulas (13.1) and (20.1). The method of calculating the transmission function is given in Ref. [2], where the following was obtained:

$$T(\bar{x}_w^{(k)};\ \bar{x}_{CO_2}^{(k)})=T(\bar{x}_w^{(k)})\,T(\bar{x}_{CO_2}^{(k)}) \tag{4}$$

and

$$T(\bar{x}^{(k)})=1-\frac{\bar{x}^{(k)}}{a\bar{x}^{(k)}+b}. \tag{5}$$

Table 1 gives the parameters a_w, b_w, a_{CO_2}, b_{CO_2}, based on the data of Ref. [2] and the spectral intensities of extra-atmospheric solar radiation given by Johnson [3].

We see from this table that the calculations were carried out in weak bands of water vapor (0.7; 0.8 μ), in the strong band of water vapor Y outside the bands (0.762, 0.85, 1.68 μ), and also in the bands of carbon dioxide (1.4, 1.6, 2.7 μ). We shall note that the 1.4 and 2.7 bands of CO_2 overlap, respectively, with the strong bands of water vapor Y and X.

The remaining parameters of the method of calculation are given in the tables of the appendix.

Table 1

Extra-atmospheric spectral intensities of direct solar radiation in mcal $cm^{-2} min^{-1} \mu^{-1}$ and parameters a_w, b_w, a_{CO_2}, b_{CO_2} of formula (5)

λ μ	Δλ	Name of band	$J_{0,\lambda}$	a_w	b_w	a_{CO_2}	b_{CO_2}
0,74	0,735—0,745	H_2O (0,7 μ)	1864	0	160,5	1	∞
0,762	0,759—0,765		1764	1	∞	1	∞
0,82	0,79 —0,84	H_2O (0,8 μ)	1537	0	142,8	1	∞
0,85	0,84 —0,86		1438	1	∞	1	∞
1,31	1,25 —1,38	H_2O (Ψ)	567	0,878	7,15	1	∞
1,44	1,38 —1,50	H_2O (Ψ) CO_2 (1,4 μ)	437	0,878	7,15		$9,8 \cdot 10^3$
1,60	1,54 —1,67	CO_2 (1,6 μ)	316	1	∞	0	$9,5 \cdot 10^3$
1,68	1,67 —1,70		270	1	∞	1	∞
2,75	2,63 —2,87	H_2O (X) CO_2 (2,7 μ)	53	0,927	3,00	0,940	80

Remarks:

1. The interval 0.735-0.745 μ constitutes the 0.7 μ wing of the water vapor band. According to Fowle [4], the limits of this band are 0.70-0.74 μ.

2. The interval 1.25-1.38 μ constitutes the wing of the Ψ band of water vapor. In Ref. [5], the limits of the Ψ band are 1.25-1.54 μ.

3. In the portion of the 1.6 CO_2 band, there is no absorption by water vapor. The limits of the 1.6 CO_2 band are 1.53-1.67 μ according to Ref. [5].

Appendix 2 gives normalized scattering indicatrixes $\varkappa_\lambda(\gamma)$ calculated from formula (21.1) using data of Ref. [6]. The values of $\varkappa_a(\gamma)$ were taken in accordance with the parameters:

$\tau_0(\lambda_0) = 0,2$; $V = 50$ км,
$\tau_0(\lambda_0) = 0,3$; $V = 20$ км,
$\tau_0(\lambda_0) = 0,5$; $V = 10$ км.

Here V is the horizontal visibility range. The values of $\varkappa_\lambda(\gamma)$ for any scattering angle $\gamma = \gamma(i_0, \alpha, \beta)$ were determined by the root-mean-square interpolation of the data of Appendix 2 with the "Ural-1" electronic computer.

Appendix 3 gives the relative spectral optical thicknesses of the Rayleigh and aerosol components for the value $\tau_0(\lambda) = 0.2; 0.3; 0.5$, calculated from formula (23.1).

Appendix 4 gives the values of the parameter $\varkappa_1$ calculated from formulas (18.1), (25.1), and the optical thicknesses $\tau_\lambda(z)$ at altitudes z equal to 0, 5.52, 7.63, and 10.4 km, calculated from the data of Ref. [6]

$$\tau_\lambda = \tau_\lambda(z) = pe^{-\tilde{\alpha} z_k} + qe^{-\tilde{\beta} z_k}. \qquad (6)$$

Here $\alpha = 0.125$ km^{-1}, and from Ref. [6], we obtain

$\tilde{\beta} = 0{,}633$ км$^{-1}$ where $\tau_0(\lambda) = 0{,}2$; $V = 50$ км,
$\tilde{\beta} = 0{,}898$ км$^{-1}$ where $\tau_0(\lambda) = 0{,}3$; $V = 20$ км,
$\tilde{\beta} = 0{,}936$ км$^{-1}$ where $\tau_0(\lambda) = 0{,}5$; $V = 10$ км.

The values of p and q are given in Appendix 3. Appendix 4 gives values of $\tau_\lambda(z)$ corresponding to the selected altitude of the upper cloud boundary. The altitudes z, equal to 5.52, 7.63 and 10.4 km, are the boundaries of the atmospheric model employed [1]. Let us note that according to various authors [7], the upper boundary of fleece clouds (Cu, cong.) at middle latitudes are located in most cases at altitudes exceeding 3.5 km. The upper boundary of cumulolimbus clouds (Cb) reaches an altitude of 9-11 km [7]. According to the data of A. N. Baranov [8], the upper boundary of frontal clouds on the European territory of the USSR has an annual variation z = 10.2-11.2 km, and, according to the many measurements of E. G. Zak [9], the altitude of the upper cloud boundary varies between 6.5 and 14 km. The highest recurrence (23%) corresponds to the 9.0-9.9 interval, and 63% of the 8,179 cases considered are distributed at altitudes of 8.0-10.9 km. Thus, the selected altitudes z (5.52, 7.63, 10.4 km) characterize the possible locations of the upper cloud boundary.

2. Ratio of Scattered to Reflected Radiation

The role of scattered atmospheric radiation in the ascending flux of the visible region of the spectrum (0.40-0.80 μ) is discussed in

detail in Ref. [10]. In this work it was found that even in the visible region of the spectrum, the variability of the albedo of the reflecting surfaces has a much lesser influence on the variations of the angular and spatial distribution of the outgoing radiation than the variability of the optical properties of the atmosphere. In the near infrared, at $A_\lambda \geq 0.1$, we find that in formula (20.1)

$$I_1 \ll I_A \tag{7}$$

for angles α not too close to the horizon. Here

$$I_A = \frac{2A}{\pi} I_0 T\left(\bar{x}_1^{(h=0)}, \theta, w\right) T\left(\bar{x}_1^{(h=0)}, \theta, CO_2\right) \frac{R(\tau_0, l)\cos l}{4 + (3 - \varkappa_1)\tau_0(1 - A)} e^{-\tau_0 m\theta}. \tag{8}$$

Table 2 gives ratios of the fraction of singly scattered radiation I_1 to the reflected radiation I_A for $\tau_0(\lambda_0) = 0.3$, w = 2.0 cm, $\lambda = 0.82\ \mu$. As λ increases, the role of scattered radiation diminishes rapidly, since the optical thickness decreases in accordance with formula (23.1).

The increase in the ratio $\frac{I_1}{I_A}$ when $\alpha \to 72^\circ 45'$ is due mainly to a decrease in I_A. The scattered radiation I_A in the infrared region of the spectrum has, when compared to I_A at $A \geq 0.1$, appreciable values only in the case where the whole atmospheric layer at the horizon scatters ($\alpha > 60^\circ$). We see from Table 2 that the scattering can be neglected in the above-cloud layer ($I_1 \leq 0.016 I_A$).

To a first approximation, expression (7) is proportional to the albedo. For this reason, it is very important to know representative values of the spectral albedo for average conditions. A survey and analysis of the available data on the spectral albedo in the near infrared is given in Ref. [11], which also provides average values of A_λ for the plant cover, snow, clouds and sea. These values of A_λ were used in the present work (see Appendix 5). It should be noted at this point that the values of A_λ borrowed from Ref. [11] are only tentative: they

Table 2

Ratio of singly scattered radiation I_1 to reflected radiation I_A calculated from formulas (20.1) and (8) for $\tau_0(\lambda_0) = 0.3$; w = 2.0 cm; $\lambda = 0.82\ \mu$; $i_0 = 0°$ and $i_0 = 30°$

z	$i_0 = 0°$	$i_0 = 30°$						
	β							
	0—180°	0°	30°	60°	90°	120°	150°	180°
Grass, z=0, A_λ=0,46								
0°	0,043	0,045	0,045	0,045	0,045	0,045	0,045	0,045
30°	0,047	0,047	0,047	0,048	0,050	0,054	0,057	0,059
60°	0,000	0,113	0,119	0,110	0,105	0,106	0,112	0,116
70°	0,224	0,393	0,439	0,362	0,319	0,304	0,310	0,315
Clouds, z=5,52 km, A_λ=0,55								
0°	0,002	0,002	0,002	0,002	0,002	0,002	0,002	0,002
30°	0,002	0,002	0,002	0,003	0,003	0,003	0,003	0,003
60°	0,001	0,005	0,005	0,005	0,005	0,005	0,005	0,005
70°	0,011	0,014	0,016	0,013	0,011	0,011	0,011	0,011
Clouds, z=7,63 km, A_λ=0,55								
0°	0,002	0,002	0,002	0,002	0,002	0,002	0,002	0,002
30°	0,002	0,002	0,002	0,002	0,002	0,002	0,002	0,002
60°	0,003	0,004	0,004	0,004	0,004	0,003	0,004	0,004
70°	0,007	0,010	0,011	0,009	0,008	0,008	0,008	0,008
Clouds, z=10,4 km, A_λ=0,55								
0°	0,001	0,001	0,001	0,001	0,001	0,001	0,001	0,001
30°	0,001	0,001	0,001	0,001	0,001	0,001	0,001	0,002
60°	0,002	0,003	0,003	0,003	0,003	0,003	0,003	0,003
70°	0,005	0,007	0,008	0,006	0,005	0,005	0,005	0,005

do not allow for the non-orthotropic nature of real surfaces, do not take into account the seasonal changes in spectral albedo, etc. Furthermore, because of the lack of data, Ref. [11] does not give any values for the spectral albedo of desert areas, which are important in the calculation of the radiation regime of the earth—atmosphere system. Hence, a further refinement of data on the spectral albedo becomes an unavoidable problem. Its solution requires direct spectral measurements above natural surfaces (under field conditions) in various climatic zones.

3. Angular Distribution of the Intensities of Outgoing Radiation

The angular distribution of intensities for $A_\lambda = 0$ is determined by the zenithal angle of the sum, the scattering indicatrix, the optical thickness of the atmosphere, and the absorption in the bands of water vapor and carbon dioxide. Whereas in the near infrared $A_\lambda > 0.1$, the angular distribution of the intensity of outgoing radiation is mainly determined by the zenithal angle of the sum i_0, the spectral albedo A_λ, and the absorption in the bands of water vapor and CO_2.

A general idea of the distribution of the intensity of the outgoing radiation can be obtained from Figs. 1-6, which show the isophotes of the relative intensities at $i_0 = 30^\circ$; $\tau_0(\lambda_0) = 0.3$; $w = 2.0$ cm for $\lambda =$ $= 1.31\ \mu$ (the band Ψ of water vapor) and $\lambda = 1.68\ \mu$ (outside the band). We shall note that the intensities are distributed symmetrically relative to the solar vertical. For this reason, Figs. 1-6 show only the region $0 < \alpha_{max} < 72^\circ 45'$, $0 < \beta < \pi$. We shall recall that the azimuth against the sun is $\beta = 0$, and with the sun, $\beta = \pi$.

As is evident from Figs. 1-6, the absorption not only decreases the intensities but also causes a qualitative change in the distribution of the isophotes of the relative intensities. Absolute values of the intensities are given in Figs. 1-6 for the point at the nadir I_N in mcal. $cm^{-2}\ min^{-1}\ \mu^{-1}\ ster^{-1}$. The dependence on the sighting angle α is illustrated more graphically in Fig. 7, which shows cases of $\lambda = 0.74$-$9.68\ \mu$ for various underlying surfaces at $i_0 = 0$; $_0(\lambda_0) = 0.3$; $w = 2.0$ cm. Values of $I(\alpha)$ are given in relative units in the figure. Absolute values of the intensities will be obtained by multiplying the values of I by the ratios $\frac{I_{0,\lambda}}{I_H}$ (see Tables 1 and 3). From Fig. 7 it is evident that in the absorption bands, as the sighting angle α increases, the

intensity decreases faster than in the portions outside the bands. A decrease in intensity outside the bands occurs only close to the horizon, i.e., at $\alpha \to 72^{\circ}45'$. Furthermore, it is clear that when $A_\lambda = 0$ (curve 6 of Fig. 7), the intensities I increase with rising α, so that the optical thickness along the path of the ray increases as the horizon is approached.

The following conclusions can be reached on the basis of Figs. 1-7:

1. When $A_\lambda = 0$, the increase in intensity at the horizon (due to the increase in the optical thickness along the path of the ray) is greater without than within the absorption bands.

2. The distribution of intensities for an albedo of the underlying surface $A_\lambda = 0$ is determined by the angle of incidence of solar ray i_0, the scattering indicatrix, and the increase in optical thickness in the direction of the horizon. For example, for $i_0 = 30^{\circ}$ and $A_\lambda = 0$ in the region of $\alpha = 20 \div 40^{\circ}$ and $\beta = 0^{\circ}$, a weak minimum is observed for all the wavelengths which we studied. This minimum is preserved at $A_\lambda = 0.027$ (see Fig. 3).

3. When $z = 0$ and $A_\lambda \geq 0.1$, the distribution of the intensities of ascending radiation in the near infrared is determined by the radiation reflected off the earth's surface. At a sufficiently high A_λ, the brightness in the direction of the horizon decreases (darkening of the edge of the visible disk of the earth).

4. When $i_0 = 30^{\circ}$ and $A_\lambda \geq 0.1$, for all of the wavelengths which we studied, the maximum in the intensity distribution was observed around the angles $\alpha = 20 \div 30^{\circ}$, $\beta = 180^{\circ}$. At $i_0 = 60^{\circ}$, such a maximum is observed at $\alpha = 60^{\circ}$, $\beta = 180^{\circ}$. Obviously, the reason for this is the fact that in these regions (α, β) the conditions of illumination of the

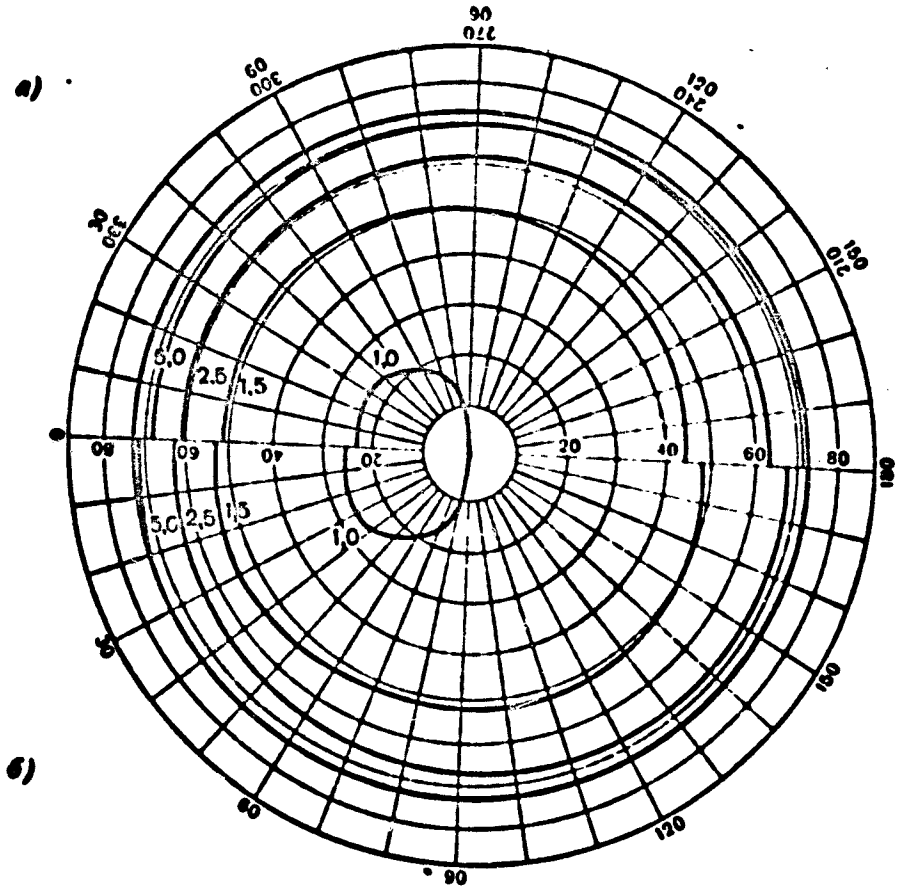

Fig. 1. Isophotes of relative intensities in the absorption band of water vapor ψ and outside the band λ = 1.68 μ for an albedo of the underlying surface A_λ = 0 at H = 300 km.

$i=30°$, $\tau_0(\lambda_0)=0.3$, $w=2.0$ см, $A_\lambda=0$, $z=0$. а — $\lambda=1.68$ μ; $I_\mu=0.465$; б — $\lambda=1.31$ μ, $I_N=0.504$.

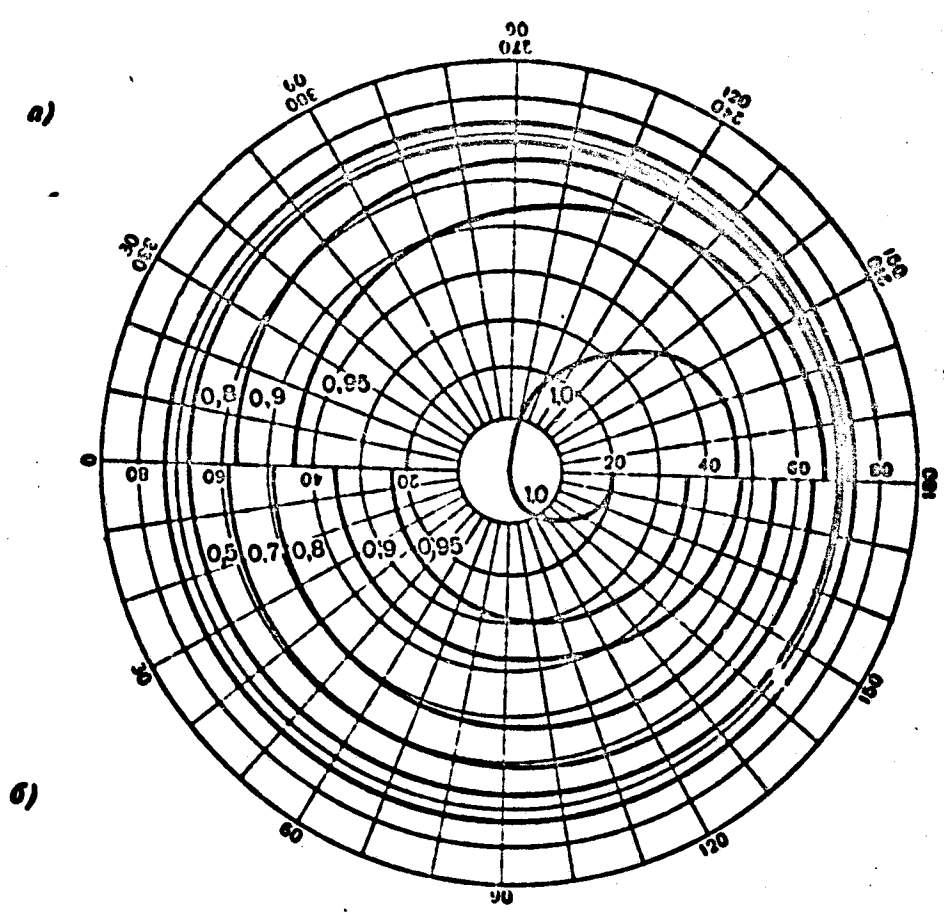

Fig. 2. Isophotes of relative intensities in the absorption band of water vapor ψ and outside the band λ = 1.68 μ above a grass cover at H = 300 km.

$i_0=30°$, $\tau_0(\lambda_0)=0.3$, $w=2.0$ см, grass. а — $\lambda=1.68$ μ $A_\lambda=0.35$, $I_N=24.7$, б — $\lambda=1.31$ μ, $A_\lambda=0.44$, $I_N=17.3$.

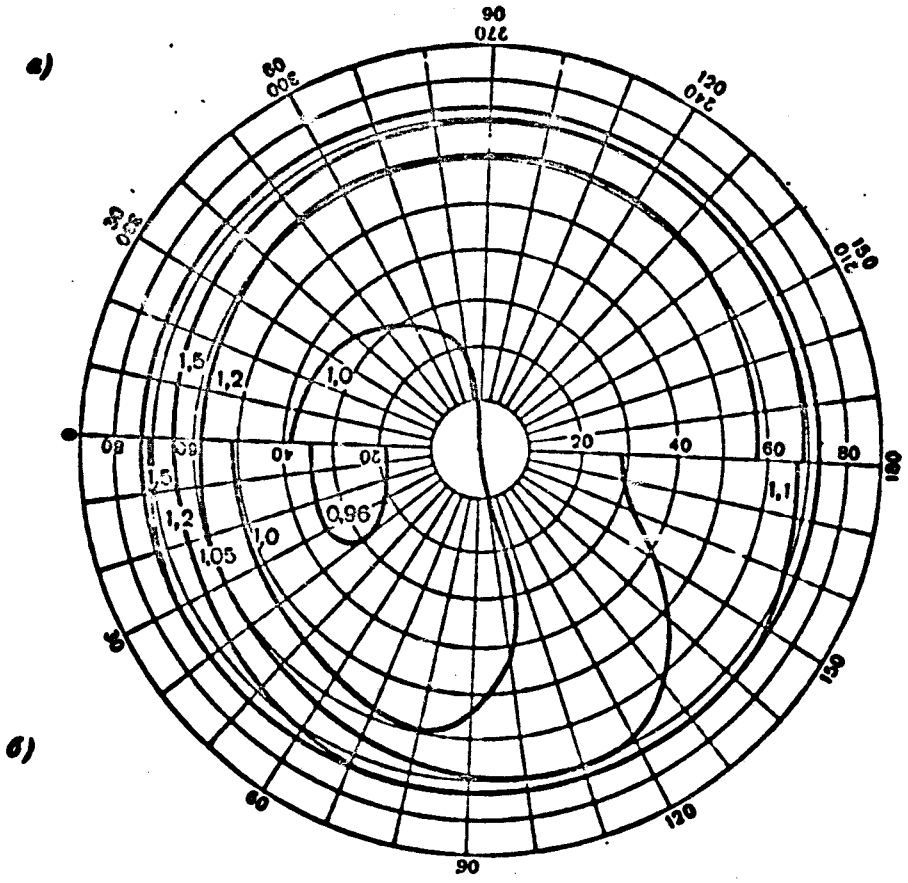

Fig. 3. Isophotes of relative intensities in the absorption band of water vapor ϒ and outside the band λ = 1.68 μ above the sea at H = 300 km.

$\mu_0 = 30°$, $\tau_0(\lambda_0) = 0.3$, $w = 3.0$ cm, sea. а – $\lambda = 1.68$ μ, $A_\lambda = 0.026$, $I_N = 2.26$; б – $\lambda = 1.31$ μ, $A_\lambda = 0.027$, $I_N = 1.38$

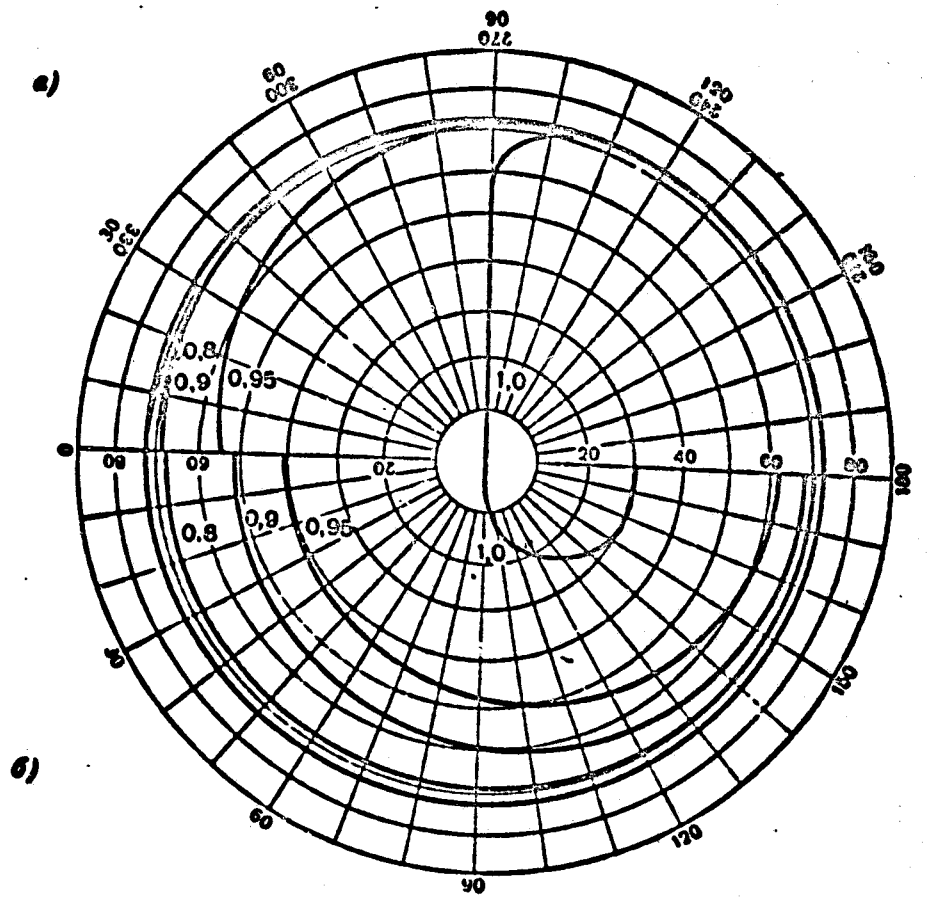

Fig. 4. Isophotes of relative intensities in the absorption band of water vapor ϒ and outside the band λ = 1.68 μ above clouds at H = 300 km.
Altitude of upper cloud boundary z = 5.5 km.

$\mu_0 = 30°$, $\tau_0(\lambda_0) = 0.3$, $w = 2.0$ cm, clouds z = 5.5 km, а – $\lambda = 1.68$ μ, $A_\lambda = 0.34$, $I_N = 25.3$; б – $\lambda = 1.31$ μ, $A_\lambda = 0.51$, $I_N = 56.9$

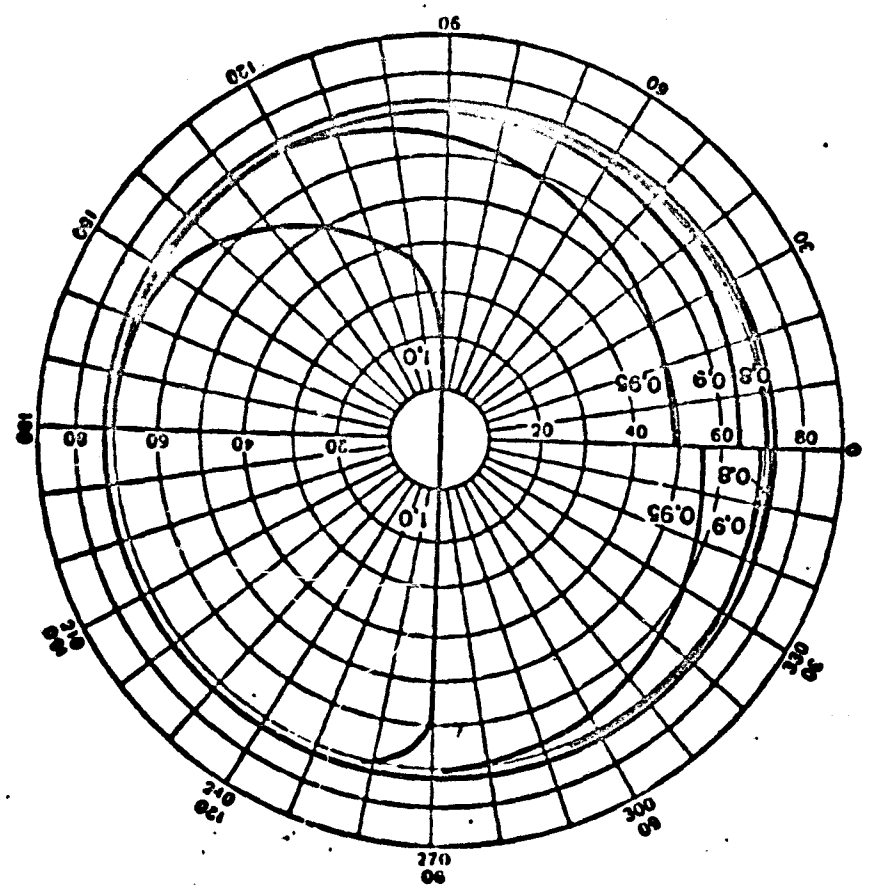

Fig. 5. Isophotes of relative intensities in the absorption band of water vapor Ψ and outside the band λ = 1.68 μ above clouds at H = 300 km.
Altitude of the upper cloud boundary z = 7.6 km.

$\theta_0=30°$, $\tau_0(\lambda_0)=0.3$, $w=2.0$ cm, clouds, $z=7.6$ km, $\theta-\lambda=1.68\ \mu$, $A_\lambda=0.34$, $I_N=25.3$; $\theta-\lambda=1.31\ \mu$, $A_\lambda=0.51$, $I_N=63.6$.

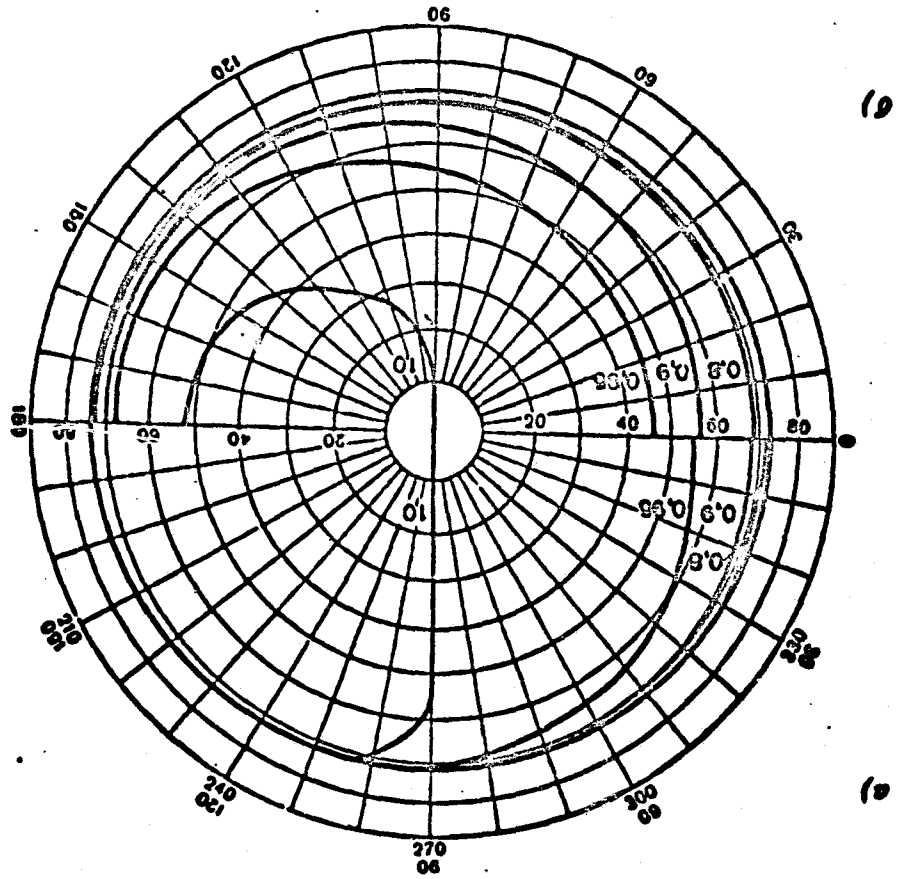

Fig. 6. Isophotes of relative intensities in the absorption band of water vapor Ψ and outside the band λ = 1.68 μ above clouds at H = 300 km
Altitude of upper cloud boundary z = 10.4 km

$\theta_0=30°$, $\tau_0(\lambda_0)=0.3$, $w=2.0$ cm, clouds, $z=10.4$ km, $\theta-\lambda=1.68\ \mu$, $A_\lambda=0.34$, $I_N=25.3$; $\theta-\lambda=1.31\ \mu$, $A_\lambda=0.51$, $I_N=71.5$.

underlying surface will be best and the greatest contribution is made by the scattered radiation.

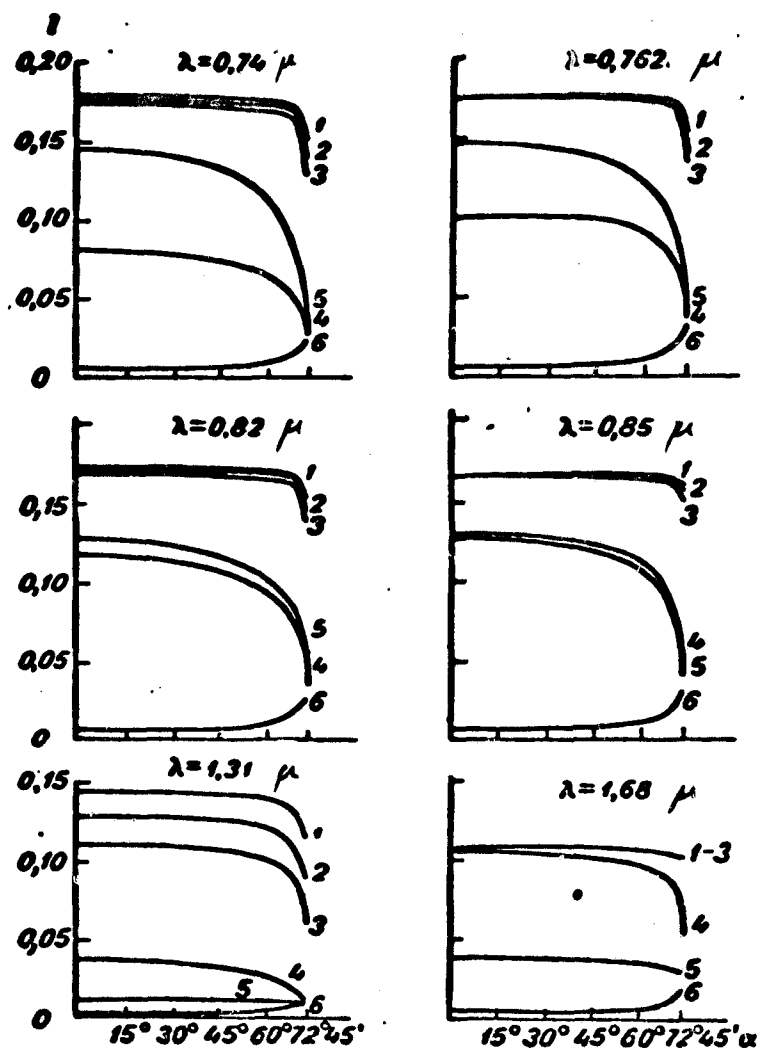

Fig. 7. Variation of the intensity of ascending radiation (relative units) as a function of the sighting angle α at $i_0 = 0^\circ$, H = 300 km.

1 - Upper cloud boundary z = 10.4; 2 - clouds, z = 7.6 km; 3 - clouds, z = 5.5 km; 4 - underlying surface is grass; 5 - underlying surface is snow; 6 - albedo of the underlying surface $A_\lambda = 0$ at z = 0.

As i_0 increases, the map of the distribution of the intensity isophotes changes because of a change in the scattering angles γ and in the ratios $\frac{I_1}{I_A}$. For example, at $i_0 = 60^\circ$, on the side opposite the sun ($\beta = 0^\circ$), a small intensity maximum is sometimes observed for large α's. At $i_0 > 72^\circ 45'$, a portion of the earth not illuminated by direct solar

radiation is observed in the field of view of the wide-angle receiver. The decrease in intensity at the nadir associated with the increase of the zenithal angle of the sun i_0 is given in Table 3.

Table 3

Intensity of outgoing radiation I_H mcal cm^{-2} min^{-1} μ^{-1} $ster^{-1}$ at the nadir at various zenithal angles of the sun i_0

i_0°	Grass	Snow	Sea	Clouds			$A_\lambda = 0$; $z = 0$
				$z = 5{,}52$ км	$z = 7{,}63$ км	$z = 10{,}4$ км	
			$\lambda = 0{,}82$ μ				
			$\tau_0(\lambda_0) = 0{,}2$; $w = 0{,}5$ см				
0	205	222		265	266	268	9,40
30	175	190		229	230	232	6,76
60	98	106		131	133	133	5,16
90	2,48	2,48		0,66	0,47	0,32	2,48
			$\tau_0(\lambda_0)$ 0,3; $w = 2{,}0$ см				
0	182	198		262	265	267	7,56
30	156	169		226	229	231	6,74
60	85,1	92,2		130	132	133	5,42
90	2,04	2,04		0,46	0,34	0,24	2,04
			$\tau_0(\lambda_0) = 0{,}5$; $w = 3{,}0$ см				
0	159		15,5	260	264	266	6,84
30	134		13,4	225	228	230	6,14
60	70,8		8,86	129	131	133	5,13
90	1,52		1,52	0,34	0,24	0,17	1,52
			$\lambda = 0{,}85$ μ				
			$\tau_0(\lambda_0) = 0{,}2$				
0	210	197		255	255	256	8,53
30	180	169		220	221	221	6,11
60	102	95,5		127	127	128	4,70
90	2,45	2,45		0,57	0,39	0,26	2,45
			$\tau_0(\lambda_0) = 0{,}3$				
0	191	186	17,6	255	255	256	7,10
30	170	159	15,3	220	221	221	6,36
60	94,5	88,8	10,1	127	127	128	5,20
90	2,23	2,23	2,23	0,46	0,29	0,20	2,23
			$\tau_0(\lambda_0) = 0{,}5$				
0	177	166	15,8	254	255	255	6,56
30	150	141	13,8	220	221	221	5,93
60	80,9	76,0	9,22	127	127	127	5,07
90	1,63	1,63	1,63	0,29	0,20	0,14	1,63
			$\lambda = 1{,}31$ μ				
			$\tau_0(\lambda_0) = 0{,}2$; $w = 0{,}5$ см				
0	37,6	11,0		75,9	82,1	87,3	1,07
30	31,6	9,08		65,3	70,8	75,4	0,71
60	16,3	4,82		36,4	40,0	43,1	0,55
90	0,12	0,12		0,048	0,030	0,018	0,12

i_0°	Grass	Snow	Sea	Clouds			$A_\lambda = 0$, $z = 0$
				$z = 5{,}52$ км	$z = 7{,}63$ км	$z = 10{,}4$ км	
			$\tau_0(\lambda_0) = 0{,}3$; $w = 2{,}0$ см				
0	21,1	6,13		64,1	74,0	82,9	0,57
30	17,6	5,12		54,9	63,6	71,5	0,50
60	8,45	2,57		29,9	35,4	40,5	0,40
90	0,08	0,08		0,024	0,017	0,013	0,08
			$\tau_0(\lambda_0) = 0{,}5$; $w = 3{,}0$ см				
0	16,5		1,43	60,0	71,0	81,1	0,47
30	13,6		1,21	51,1	61,0	70,0	0,41
60	6,25		0,70	27,6	33,6	39,5	0,35
90	0,07		0,07	0,018	0,012	0,009	0,07
			$\lambda = 1{,}68\ \mu$ $\tau_0(\lambda_0) = 0{,}2$				
0	29,6	10,5		29,2	29,2	29,2	0,63
30	25,5	8,99		25,3	25,3	25,4	0,41
60	14,6	5,21		14,6	14,6	14,6	0,34
90	0,27	0,27		0,017	0,007	0,004	0,27
			$\tau_0(\lambda_0) = 0{,}3$				
0	28,7	10,1	2,59	29,2	29,2	29,2	0,51
30	24,7	8,75	2,26	25,3	25,3	25,3	0,46
60	14,1	5,07	1,42	14,6	14,6	14,6	0,42
90	0,31	0,31	0,31	0,009	0,004	0,002	0,31
			$\tau_0(\lambda_0) = 0{,}5$				
0	27,1	9,56	2,46	29,2	29,2	29,2	0,50
30	23,3	8,24	2,14	25,3	25,3	25,3	0,46
60	13,0	4,72	1,38	14,6	14,6	14,6	0,46
90	0,27	0,27	0,27	0,007	0,003	0,002	0,27

It is apparent from Table 3 that as $\tau_0(\lambda_0)$ changes from 0.2 to 0.5, the value of I_H above the clouds ($z \geq 5.5$ km) changes relatively little, since the role of scattered radiation in the above cloud layer is a minor one. At $A_\lambda = 0$; $z = 0$; $i_0 = 0$; $\lambda = 0.85\ \mu$ and I_H decreases by 23% as $\tau_0(\lambda_0)$ increases from 0.2 to 0.5. This effect is explained by the interaction of two factors acting in opposite directions.

1. As $\tau_0(\lambda_0)$ increases, the indicatrix $\chi_\lambda(\gamma)$ is more elongated, and the back-scattered energy decreases. From Appendix 2 we find when $\lambda = 0.85\ \mu$, the value of $\chi(180^\circ)$ decreases 2.7 times (from 0.960 to 0.262), with an increase in $\tau_0(\lambda_0)$ from 0.2 to 0.5.

2. As the amount of the scattering substance, i.e., the optical thickness $\tau_0(\lambda_0)$ increases, the scattered radiation increases. As is evident from the above example, the effect of an increase in the elongation of the scattering indicatrix surpasses the effect of an increase in the amount of the scattering substance.

In the presence of a reflecting surface, the value of I also decreases with increasing $\tau_0(\lambda_0)$, since the attenuation of solar radiation in the atmosphere increases before and after reflection.

4. Albedo of the Earth—Atmosphere System

The effect of an atmospheric layer on the albedo may be evaluated as follows. We calculate the albedo $\bar{A}_\lambda$ of an orthotropic surface located outside the atmosphere and designate by I_N the intensity of the radiation reflected in the direction $\alpha = \beta = 0$ by the earth—atmosphere system. We then obtain

$$I_N = \frac{\bar{A}_\lambda}{\pi} E_0, \tag{9}$$

where E_0 is the extra-atmospheric illumination

$$E_0 = I_{0,\lambda} \cos i_0. \tag{10}$$

For the albedo of the earth—atmosphere system, we obtain

$$\bar{A}_\lambda = \frac{I_N}{I_{0,\lambda}} - \frac{\pi}{\cos i_0}; \tag{11}$$

the results of the calculations are given in Table 4.

$\bar{A}_\lambda$ depends only slightly on i_0 Comparing the values of $\bar{A}_\lambda$ and A_λ (Appendix 5), we see that outside the absorption bands, the influence of the atmosphere on the albedo of the underlying surface will be insignificant. In the absorption bands, the atmosphere decreases the albedo substantially. In the spectral region under consideration, the

Table 4

Albedo of the earth—atmosphere system $\bar{A}_\lambda$ for various underlying surfaces

λ	Grass	Snow	Sea	Clouds			$A_\lambda = 0$, $z = 0$
				$z = 5{,}52$ км	$z = 7{,}63$ км	$z = 10{,}4$ км	
$l_0 = 0°$, $\tau_0(\lambda_0) = 0{,}2$; $w = 0{,}5$ см							
0,82	0,42	0,45		0,54	0,54	0,55	0,019
0,85	0,46	0,43		0,56	0,56	0,56	0,019
1,31	0,21	0,06		0,42	0,45	0,48	0,006
1,68	0,35	0,12		0,34	0,34	0,34	0,007
$l_0 = 0°$; $\tau_0(\lambda_0) = 0{,}3$; $w = 2{,}0$ см							
0,82	0,37	0,41	0,035	0,54	0,54	0,55	0,015
0,85	0,43	0,41	0,038	0,56	0,56	0,55	0,016
1,31	0,12	0,03	0,008	0,35	0,41	0,46	0,003
1,68	0,35	0,12	0,030	0,34	0,34	0,34	0,006
$l_0 = 30°$; $\tau_0(\lambda_0) = 0{,}3$; $w = 2{,}0$ см							
0,82	0,37	0,40	0,035	0,54	0,54	0,55	0,018
0,85	0,43	0,40	0,038	0,56	0,56	0,56	0,016
1,31	0,11	0,03	0,008	0,35	0,41	0,46	0,003
1,68	0,35	0,12	0,030	0,34	0,34	0,34	0,006
$l_0 = 60°$; $\tau_0(\lambda_0) = 0{,}3$; $w = 2{,}0$ см							
0,82	0,35	0,40	0,040	0,53	0,54	0,54	0,022
0,85	0,41	0,39	0,044	0,56	0,56	0,56	0,023
1,31	0,09	0,03	0,008	0,33	0,39	0,45	0,004
1,68	0,35	0,12	0,033	0,34	0,34	0,34	0,009
$l_0 = 0°$; $\tau_0(\lambda_0) = 0{,}5$; $w = 3{,}0$ см							
0,82	0,33	0,36	0,032	0,53	0,54	0,55	0,014
0,85	0,39	0,36	0,035	0,55	0,56	0,56	0,014
1,31	0,09	0,03	0,008	0,33	0,39	0,45	0,003
1,68	0,35	0,12	0,029	0,34	0,34	0,34	0,006

atmosphere itself reflects back less than 2% of the incident flux.

5. Spectral Fluxes Reflected off the Earth—Atmosphere System

For a plane-parallel model of the atmosphere, the flux of ascending radiation is obtained from the formula

$$F_\uparrow = 2\int_0^{2\pi} d\beta \int_0^{\pi/2} I \cos\alpha \sin\alpha \, d\alpha, \qquad (12)$$

and for a spherical model, the flux is calculated from formula (45.1). Comparing formulas (12) and (34.1), we see that a consideration of the dilution (rarefaction) of the radiation leads to a change from the upper limit of integration $\pi/2$ to the quantity α_{max} [see formulas (27.1)]. At values $\alpha < 60^{\circ}$, the intensities $I(\alpha, \beta)$ differ only slightly from the intensities for the plane-parallel model of the atmosphere. Allowance for the curvature of the atmosphere leads to considerable changes in the field of the intensities at the horizon only, and this confirms the conclusion arrived at in Ref. [10]. At moderately low positions of the sun and sighting directions distant from the horizontal one, at $H <$ $< 1{,}000$ km, one can make use with sufficient accuracy, of the results of calculations made for the plane-parallel model of the atmosphere.

However, a calculation of the flux of outgoing radiation received by the wide-angle receiver at the altitude of the satellite makes it necessary to take into account the curvature of the atmosphere, particularly for an inhomogeneous underlying surface, since the albedo depends on the angular coordinates (α, β).

Table 5 gives several data from the calculation of fluxes of outgoing radiation received by the wide-angle receiver at altitude $H = 300$ km. The angular aperture of the radiation receiver should be equal to $2\alpha_{max} = 145^{\circ}35'$. The calculation of $F_{\uparrow}$ by means of formula (45.1) were made with a certain error due to the inaccuracy involved in taking into account the scattering layer z. In changing from the parameter ξ to angle α, considering formulas (29.1), (30.1), (39.1), we shall obtain $g(\alpha, H)$ instead of $\sin\alpha\cos\alpha$ in formula (45.1). The function $g(\alpha, H)$ is given in Fig. 8. Possible errors due to the inaccuracy of the function $g(\alpha, H)$ do not exceed the accuracy of the numerical integration

Table 5

Spectral fluxes (mcal cm^{-2} min^{-1} μ^{-1}) reflected by the earth—atmosphere system at distance H = 300 km from the earth's surface for $o(\lambda_0) = 0.3$; w = 2.0 cm, w_{CO_2} = 264 atm cm (volume concentration of CO_2, 0.033%) for various underlying surfaces.

λ	Grass	Snow	Clouds			A = 0, z = 0
			z = 5,52 km	z = 7,63 km	z = 10,4 km	
			$l_0 = 0°$			
0,82	466	506	738	752	760	29,8
0,85	497	485	724	725	729	28,7
1,31	50,2	15,1	174	204	233	2,12
1,68	75,0	28,2	83,4	83,5	83,5	2,18
			$l_0 = 30°$			
0,82	402	436	639	650	657	30,1
0,85	443	418	625	629	630	29,2
1,31	42,4	13,0	149	176	201	2,13
1,44 $(CO_2)^1$	145	56,7	308	311	312	14,2
1,44 (CO_2, w)	23,3	8,87	127	154	179	2,03
1,60	63,3	23,9	105	106	106	2,87
1,68	67,8	24,8	72,3	72,3	72,3	2,45
2,75	0,0880	0,0401	0,0606	0,0948	0,149	0,0082
			$l_0 = 60°$			
0,82	232	250	277	292	360	33,3
0,85	261	246	272	285	347	32,9
1,31	21,6	7,11	81,8	98,3	108	2,30
1,68	39,8	15,6	37,9	38,0	40,2	3,05
			$l_0 = 90°$			
0,82	5,20	5,35	6,68	6,81	6,93	3,44
0,85	6,04	5,85	6,70	6,68	6,66	3,68
1,31	0,255	0,199	1,07	1,41	1,83	0,179
1,68	1,02	0,588	0,808	0,748	0,754	0,423

1. Only the absorption by carbon dioxide is considered.

performed (2-5%).

In the calculations made in Table 5, the spectral albedos were taken from Appendix 5. Considering that at altitudes $z \geq 5.5$ km the role of scattered radiation is minor and that the radiation I_A reflected by the clouds—atmosphere system is proportional to A_λ to a first approximation [see formula (8)], we can, for any albedo of the clouds $\tilde{A}_\lambda$, readily calculate $F_\uparrow$ from the approximate formula

$$F_{\uparrow}(\tilde{A}_{\lambda}) = \frac{\tilde{A}_{\lambda}}{A_{\lambda}} F_{\uparrow}(A_{\lambda}), \tag{13}$$

where A_λ are the values of the cloud albedo taken from Appendix 5, and $F_\uparrow(A_\lambda)$ are the ascending fluxes of the clouds—atmosphere system at altitude H = 300 km based on Table 5.

The fluxes determined by means of receivers with a small angular aperture (for example, $\varepsilon = \Delta\alpha = \Delta\beta = 1 \div 2^\circ = 0.017453 \div 0.034906$ rad.) can be calculated from the formula

$$\Delta F = I(\alpha, \beta)\Delta\omega, \tag{14}$$

where

$$\Delta\omega \approx \pi\varepsilon^2. \tag{15}$$

Here ε is in radians, for $\Delta\alpha = 1^\circ$ $\Delta\omega = 9.5695 \times 10^{-4}$ ster.

6. Determination of the Altitude of the Upper Cloud Boundary

A very important problem is the determination of the altitude of the upper boundary of the clouds observed from the satellite. In solving this problem, use can obviously be made of measurements of the intensity of outgoing radiation in the ultraviolet and near infrared [14]. It is assumed that in the ultraviolet, because of the quasi-Rayleigh scattering of the atmospheric layer above the clouds, the intensity of the outgoing radiation will depend substantially on the thickness of this layer, and hence on the location of the upper cloud boundary. M. S. Malkevich [10] showed that the turbidity of the atmosphere affects not only the dependence of the optical thickness on the altitude, but also the scattering indicatrix. For this reason, an interpretation of the measurements in the ultraviolet for the purpose of determining the altitude of the upper cloud boundary involves serious difficulties.

We shall discuss the possibility of determining the altitude of the upper cloud boundary from the outgoing intensities in the absorption

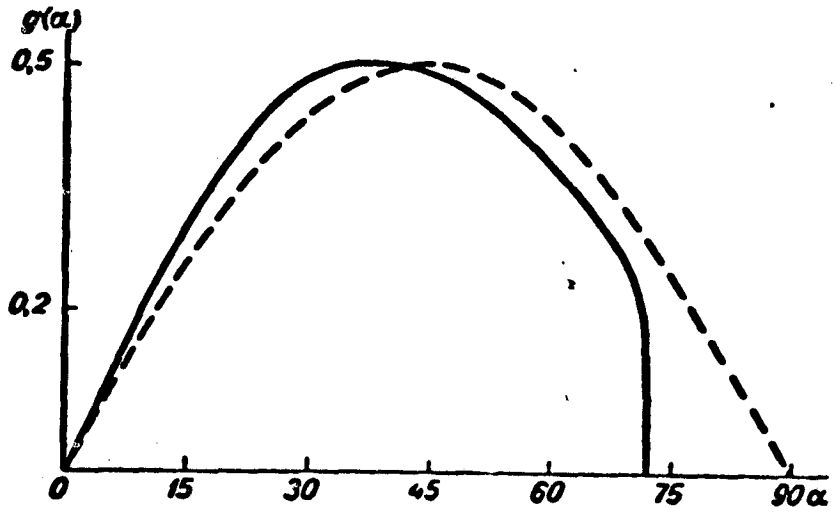

Fig. 8. The function $g(\alpha, H)$ at H = 300 km. The dashed line is a plot of $g_1(\alpha) = \sin \alpha \cdot \cos \alpha$.

bands of the near infrared. Hanel [15] recommends that the absorption intensity of CO_2 be measured in the 2.0 μ band and outside this band. The volume concentration of CO_2 may be considered constant. The radiation absorbed in the above-cloud layer determines unequivocally the altitude of the upper cloud boundary. Measurements outside the band are used to eliminate the nonselective attenuation (by scattering). Yamamoto and Wark [16] did not consider the use of the 2.0 μ band advisable, since it overlaps with the Ω band of water vapor and furthermore, the intensity of the extra-atmospheric solar radiation is low in this band. According to Johnson [3], $I_{0,\lambda}$ equals 155 mcal cm^{-2} min^{-1} μ^{-1} at λ = = 2.0 μ. The authors of Ref. [16, 17] suggest that in the determination of the upper cloud boundary, the 0.76 O_2 band should be used for the following reasons:

1. The 0.76 O_2 band is stronger than the above-discussed CO_2 band.

2. The 0.76 O_2 does not overlap with other bands, and the reference region, i.e., the region without absorption, is located next to somewhat smaller λ values.

3. The intensity of the spectral extra-atmospheric solar radiation is sufficiently high for this band.

4. Photoelectric receivers of high sensitivity are available for this spectral region.

5. The O_2 content of the atmosphere remains unchanged. However, the 0.76 O_2 band has been insufficiently studied, and the determination of the altitude of the upper cloud boundary by using the absorption bands of CO_2 is of some interest. It is more convenient to use the 1.6 CO_2 band, since in this case $I_{0,\lambda}$ is greater than in the 2.0 CO_2 band, and the 1.6 CO_2 band in the portion $\lambda = 1.54 \div 1.67\ \mu$ does not overlap with the bands of water vapor. The reference portion, i.e., the portion without absorption, is located next to $\lambda = 1.67 \div 1.70\ \mu$.

As was mentioned above, there are as yet no sufficiently reliable data on the spectral albedo of the clouds in the near infrared. In order to eliminate the effect of the albedo, we shall consider the quantity $f = \frac{I_{\lambda_1}}{I_{\lambda_2}} \frac{A_{\lambda_2}}{A_{\lambda_1}}$, where $\lambda_1 = 1.60\ \mu$, $\lambda_2 = 1.68\ \mu$ (see Fig. 9). We find that for the point at the nadir, $\alpha = \beta = 0$ at $i_0 = 0$; f depends slightly on z. The use of the curve $i_0 = 90^\circ$ is not advisable, because the intensities are weak and the measurement errors substantial.

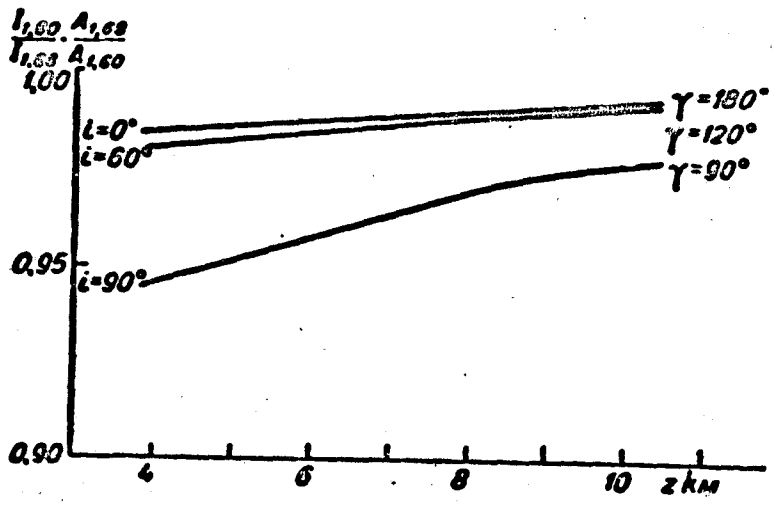

Fig. 9. Dependence of f on the altitude of the upper cloud boundary z for a zenithal angle of the sun i_0 equal to 0, 60 and 90° (A_λ is the spectral albedo of the clouds, I_λ is the intensity of outgoing radiation, γ is the scattering angle).

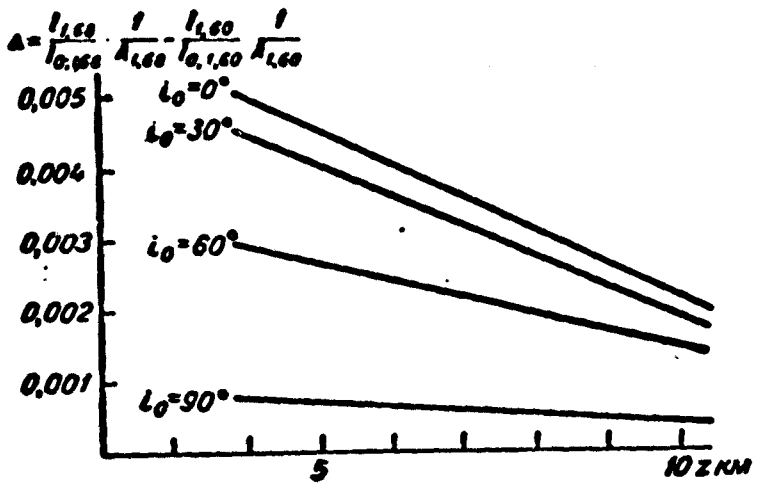

Fig. 10. Dependence of Δ on the altitude of the upper cloud boundary at a zenithal angle of the sun i_0 equal to 0, 30, 60 and 90°.

The dependence of the quantity

$$\Delta = \frac{I_{\lambda_2}}{I_{0,\lambda_2}} \frac{1}{A_{\lambda_2}} - \frac{I_{\lambda_1}}{I_{0,\lambda_1}} \frac{1}{A_{\lambda_1}} \quad (\lambda_1 = 1{,}60\ \mu\ ;\ \lambda_2 = 1{,}68\ \mu) \tag{16}$$

on the altitude of the upper cloud boundary is more pronounced (see Fig. 10), where $I_{0,\lambda}$ is the spectral intensity of the extra-atmospheric solar radiation. From Fig. 10 we see that to a first approximation Δ depends linearly on z. It is more convenient to perform the measurements at $i_0 = 0°$.

It follows from the above that by using measurements within and without the 1.6 CO_2 band, it is possible to determine the altitude of the upper cloud boundary completely if the spectral albedos of the cloud are known.

7. Conclusion

Results of measurements of intensities of outgoing shortwave radiation by "Tiros-II" and "Tiros-III" satellites [18-23] and balloons [24-25] give more variegated pictures of the distribution of isophotes than the calculated data. A preliminary comparison was found to be particularly qualitative, since the intensities measured by "Tiros-II" and "Tiros-III" were distributed over relatively wide regions of the spectrum:

0.55-0.75 μ (spectral region of the "Vidicon" television camera) and 0.2-6 μ (shortwave radiation). The measurements [24, 25] were made in the spectral regions of 1-2, 2-3 and 3-5 μ. In comparing the results for 300 km altitude with balloon measurements at 26 km altitude, it is necessary to bear in mind that the sighting angles of a given point on the earth's surface are different (except the point $\alpha = 0$). For example, when H = 26 km, at the horizon $\alpha_{max} = 84^{\circ}48'$, and when H = 300 km, $\alpha_{max} = 72^{\circ}45'$. The general laws governing the distribution of the intensities of outgoing radiation, obtained in the present work, are confirmed by experimental investigations [18-25]. The variegation of the experimentally obtained maps of intensity isophotes is explained by the variability of the albedo of the underlying surface. In addition, in Refs. [21, 22] it was shown that the observational data of "Tiros-II" did not always provide sufficiently reliable values of the albedo of the system earth's surface—atmosphere in the 2-3 and 3-5 μ regions, the measured intensities were too low, and for this reason no definite conclusions could be drawn concerning their distribution.

The author is deeply indebted to K. Ya. Kondrat'yev and K. S. Shifrin for many important suggestions offered during the execution of this work.

REFERENCES

1. Avaste, O. A. See this Collection.
2. Shifrin, K. S., Avaste, O. A. Issledovaniya po fizike atmosfery [Studies in Atmospheric Physics]. IFA AN ESSR, No. 2, 1960.
3. Johnson, F. S. J. Met., v. 11, 431, 1954.
4. Fowle, F. E. Smiths. Misc. Collect., v. 68, No. 8, 1917.
5. Howard, J. N., Burch, D. E., Williams, D. J. Opt. Soc. Amer., v. 46, 186, 237, 334, 452, 1956; Geophys. Res. Papers, No. 40, Nov., 1955 (AF CRC-TR-55-213).
6. Shifrin, K. S., Minin, I. N. Tr. GGO, vyp. 68, 5, 1957.
7. Fizika oblakov [Physics of Clouds]. Pod red. Khrgiana, A. Kh. Gidrometeoizdat, Leningrad, 1961.
8. Baranov, A. M. Izv. AN SSSR, ser. geofiz., No. 3, 438, 1962.
9. Zak, E. G. Tr. TsAO, vyp. 39, 13, 1962.

10. Malkevich, M. S. Iskusstvennyye sputniki Zemli, vyp. 14, 30, 1962.
11. Avaste, O. Issledovaniya po fizike atmosfery, Tr. IFA AN ESSR, No. 4, 1963.
12. Dimhirn, I. Wetter und Leben, v. 9, 41, 1957.
13. Fritz, S. J. Met., v. 15, 51, 1958.
14. Coulson, K. L. Planet. and Space Sci., v. 1, No. 4, 1959.
15. Hanel, R. A. J. Geophys. Res., v. 66, 1300, 1961.
16. Yamamoto, G., Wark, D. Q. J. Geophys. Res., v. 66, 3596, 1961.
17. Chapman, R. M. Planet. and Space Sci., v. 9, 70, 1962.
18. Hanel, R. A., Wark, D. Q. J. Opt. Soc. Amer., v. 51, 1394, 1961.
19. Bandeen, W. R., Hanel, R. A., Licht, J., Stampfl, R. A., Stroud, W. G. J. Geophys. Res., v. 66, 3169, 1961.
20. Hanel, R. A., Stroud, W. G. Tellus, v. 13, 486, 1961.
21. Kondrat'yev, K. Ya., Fedorova, M. P. Iskusstvennyye sputniki Zemli, vyp. 14, 95, 1962.
22. Moeller, F. Arch. Met. Geophys. Biokl., Ser. B, v. 12, 78, 1962.
23. Nordberg, W., Bandeen, W. R., Conrath, B. J., Kunde, V., Persano, I. Atm. Sci., v. 19, 20, 1962.
24. Murcray, D. G., Brooks, J. N., Sible, N. J., Westdal Ch. Contract AF 33 (616)-5199, Special Report, No. 1. Denver Res. Inst., Univ. Denver, 1959.
25. Murcray, D. G., Brooks, J. N., Sible, N. J., Westdal, H. C. Appl. Opt., v. 1, 121, 1962.

APPENDIX 1

σ см	z км											
	0	0.55	1.74	3.08	4.65	5.52	6.55	7.63	8.96	10.4	12.4	19.8
	Parameter $\bar{x}_{\sigma}^{(z)}$											
0.5	4.79	4.12	2.97	2.05	1.32	1.04	0.75	0.60	0.40	0.27	0.15	0.016
2.0	9.59	8.24	5.93	4.10	2.65	2.05	1.56	1.19	0.79	0.55	0.30	0.032
3.0	11.74	10.09	7.26	5.02	3.24	2.54	1.91	1.46	0.97	0.67	0.36	0.040
	Parameter $\bar{x}_{CO_2}^{(z)}$											
264 атм. см	164.5	155.6	136.6	117.6	95.0	58.4	75.0	65.4	57.6	47.5	35.2	11.0

APPENDIX 2

Spectral scattering indicatrixes $\gamma_{\lambda}(\gamma)$ for various optical thicknesses $\tau_0(\lambda_0)$

γ	λ μ							
	0,74	0.762	0.52	0.55	1.31	1.60	1.68	2.75
	$\tau_0(\lambda_0) = 0.2$; $V = 50$ км							
0	7.91	8.06	8.47	8.59	9.73	9.98	10.0	10.2
10	5.66	5.76	6.03	6.11	6.86	7.01	7.06	7.16
20	3.51	3.56	3.70	3.74	4.12	4.20	4.22	4.27
30	2.39	2.42	2.49	2.52	2.71	2.75	2.76	2.78
40	1.66	1.67	1.70	1.70	1.79	1.81	1.81	1.82
50	1.23	1.23	1.24	1.25	1.28	1.28	1.28	1.29
60	0.946	0.947	0.947	0.948	0.949	0.949	0.949	0.949
70	0.767	0.766	0.761	0.759	0.747	0.744	0.743	0.742
80	0.645	0.645	0.637	0.634	0.612	0.607	0.606	0.603
90	0.561	0.557	0.545	0.542	0.507	0.500	0.498	0.494
100	0.550	0.546	0.531	0.527	0.487	0.479	0.477	0.471
110	0.560	0.554	0.535	0.530	0.480	0.470	0.466	0.459
120	0.587	0.579	0.557	0.550	0.487	0.474	0.470	0.461
130	0.618	0.608	0.580	0.572	0.492	0.476	0.471	0.460
140	0.664	0.652	0.619	0.609	0.514	0.495	0.489	0.476
150	0.742	0.739	0.702	0.692	0.589	0.570	0.565	0.550
160	0.848	0.835	0.799	0.788	0.686	0.666	0.660	0.646
170	0.941	0.928	0.893	0.883	0.786	0.767	0.760	0.748
180	1.01	1.00	0.969	0.960	0.872	0.854	0.849	0.837
	$\tau_0(\lambda_0) = 0.3$; $V = 20$ км							
0	11.5	11.6	12.0	12.1	13.0	13.2	13.2	13.4
10	8.12	8.21	8.44	8.51	9.12	9.24	9.26	9.35
20	5.15	5.20	5.33	5.37	5.71	5.78	5.79	5.84
30	3.07	3.09	3.15	3.17	3.33	3.36	3.37	3.39
40	1.98	1.99	2.02	2.03	2.10	2.11	2.12	2.13
50	1.33	1.34	1.34	1.34	1.37	1.37	1.38	1.38
60	0.926	0.926	0.926	0.925	0.925	0.924	0.924	0.924
70	0.667	0.664	0.659	0.656	0.641	0.638	0.637	0.634
80	0.524	0.520	0.511	0.509	0.485	0.481	0.481	0.477
90	0.438	0.434	0.423	0.419	0.391	0.386	0.384	0.380

ϑ	λ μ							
	0,74	0,762	0,82	0,85	1,31	1,60	1,68	2,75
100	0,408	0,402	0,390	0,386	0,352	0,346	0,345	0,340
110	0,400	0,394	0,379	0,374	0,335	0,326	0,325	0,319
120	0,405	0,397	0,379	0,373	0,324	0,315	0,312	0,306
130	0,425	0,415	0,393	0,387	0,328	0,317	0,314	0,306
140	0,450	0,440	0,415	0,407	0,339	0,325	0,323	0,314
150	0,482	0,470	0,441	0,432	0,356	0,342	0,339	0,328
160	0,504	0,491	0,460	0,450	0,367	0,350	0,347	0,336
170	0,526	0,513	0,480	0,469	0,383	0,366	0,362	0,350
180	0,536	0,522	0,488	0,476	0,390	0,373	0,369	0,357
	$\tau_0(\lambda_0) = 0{,}5$; $V = 10$ км							
0	14,9	15,0	15,3	15,3	16,0	16,1	16,1	16,2
10	11,1	11,2	11,4	11,5	11,9	12,0	12,0	12,1
20	6,33	6,37	6,46	6,49	6,72	6,76	6,77	6,80
30	3,72	3,74	3,78	3,79	3,90	3,92	3,93	3,94
40	2,08	2,08	2,10	2,10	2,14	2,15	2,15	2,16
50	1,24	1,25	1,25	1,25	1,26	1,26	1,26	1,26
60	0,782	0,782	0,779	0,778	0,771	0,770	0,769	0,768
70	0,511	0,508	0,502	0,500	0,485	0,483	0,482	0,480
80	0,380	0,377	0,369	0,368	0,349	0,346	0,345	0,343
90	0,309	0,305	0,297	0,294	0,274	0,271	0,270	0,267
100	0,276	0,273	0,262	0,261	0,237	0,233	0,232	0,230
110	0,256	0,252	0,241	0,237	0,211	0,206	0,205	0,202
120	0,250	0,244	0,231	0,227	0,196	0,191	0,189	0,185
130	0,248	0,242	0,227	0,222	0,185	0,179	0,167	0,172
140	0,262	0,254	0,237	0,232	0,189	0,182	0,181	0,174
150	0,274	0,266	0,247	0,241	0,192	0,185	0,183	0,177
160	0,286	0,278	0,257	0,250	0,199	0,190	0,188	0,181
170	0,296	0,287	0,264	0,258	0,204	0,195	0,193	0,185
180	0,301	0,292	0,269	0,262	0,208	0,198	0,196	0,188

APPENDIX 3

Rayleigh $\frac{p}{\tau_0}$ and aerosol $\frac{q}{\tau_0}$ spectral relative optical thicknesses.

λ μ	$\tau_0(\lambda_0) = 0{,}2$		$\tau_0(\lambda_0) = 0{,}3$		$\tau_0(\lambda_0) = 0{,}5$	
	$\frac{p}{\tau_0}$	$\frac{q}{\tau_0}$	$\frac{p}{\tau_0}$	$\frac{q}{\tau_0}$	$\frac{p}{\tau_0}$	$\frac{q}{\tau_0}$
0,55	0,476	0,524	0,317	0,683	0,190	0,810
0,74	0,272	0,728	0,160	0,840	0,088	0,912
0,762	0,255	0,745	0,148	0,852	0,081	0,919
0,82	0,208	0,792	0,119	0,881	0,064	0,936
0,85	0,191	0,806	0,110	0,890	0,059	0,941
1,31	0,062	0,938	0,033	0,967	0,017	0,983
1,60	0,036	0,964	0,018	0,982	0,010	0,990
1,68	0,028	0,972	0,015	0,985	0,008	0,992
2,75	0,010	0,990	0,004	0,996	0,002	0,998

APPENDIX 4

Parameters $\varkappa_1$ and optical thicknesses τ_λ^z for various turbidities

λ μ	$\varkappa_1$	τ_λ^z			
		$z = 0$	$z = 5.52$ км	$z = 7.63$ км	$z = 10.4$ км
		$\tau_0(\lambda_0) = 0.2$, $V = 50$ км			
0.74	0.93	0.1069	0.0109	0.01151	0.00802
0.762	0.95	0.1015	0.0153	0.01057	0.00715
0.82	1.00	0.0858	0.0114	0.00769	0.00514
0.85	1.02	0.0841	0.0103	0.00652	0.00454
1.31	1.19	0.0469	0.00279	0.00147	0.00084
1.60	1.22	0.0374	0.00176	0.00080	0.00041
1.68	1.23	0.0353	0.00156	0.00068	0.00033
		$\tau_0(\lambda_0) = 0.3$, $V = 20$ км			
0.74	1.48	0.1812	0.0156	0.01136	0.00793
0.762	1.50	0.1736	0.0140	0.01012	0.00705
0.82	1.54	0.1555	0.0103	0.00728	0.00505
0.85	1.56	0.1483	0.00911	0.00643	0.00445
1.31	1.70	0.0889	0.00206	0.00122	0.00080
1.60	1.73	0.0717	0.00116	0.00059	0.00037
1.68	1.73	0.0680	0.00099	0.00047	0.00029
		$\tau_0(\lambda_0) = 0.5$, $V = 10$ км			
0.74	1.91	0.3298	0.01634	0.01143	0.00792
0.762	1.92	0.3180	0.01463	0.01019	0.00705
0.82	1.93	0.2905	0.01083	0.00733	0.00506
0.85	1.96	0.2783	0.00967	0.00649	0.00446
1.31	2.05	0.1729	0.00242	0.00125	0.00080
1.60	2.07	0.1405	0.00146	0.00062	0.00037
1.68	2.07	0.1330	0.00127	0.00051	0.00029

APPENDIX 5

Spectral albedo of vegetation (for Ref. [12]), snow (Ref. [12]), clouds (Ref. [13]) and reflection coefficients of water r_λ in the near infrared

λ μ	A_λ plant leaves	A_λ old snow	A_λ clouds	r_λ water at $i_0 = 45°$	λ μ	A_λ plant leaves	A_λ old snow	A_λ clouds	r_λ water at $i_0 = 45°$
0.72	0.20	0.62	0.59	0.027	1.51	0.27	0.08	0.31	0.027
0.76	0.35	0.55	0.56	0.027	1.53	0.28	0.09	0.35	0.026
0.82	0.46	0.50	0.55	0.027	1.60	0.31	0.10	0.33	0.026
0.85	0.48	0.45	0.56	0.027	1.68	0.35	0.12	0.34	0.026
0.93	0.51	0.36	0.42	0.027	1.81	0.30	0.11	0.07	0.025
1.01	0.52	0.28	0.58	0.027	1.98	0.15	0.07	0.08	0.025
1.14	0.52	0.23	0.31	0.027	2.09	0.17	0.08	0.19	0.024
1.24	0.48	0.16	0.57	0.027	2.19	0.20	0.09	0.27	0.024
1.31	0.44	0.12	0.51	0.027	2.45	0.16	0.06	0.07	0.022
1.44	0.31	0.10	0.13	0.027	2.75	0.10	0.04	0.01	0.013

M. E. Shvets, B. E. Shneyerov, L. F. Kolosskova

USE OF RESULTS OF RADIATION MEASUREMENTS FROM SATELLITES IN THE MODEL OF LARGE-SCALE ATMOSPHERIC MOTIONS

Radiative heating or cooling involving the influx of heat due to turbulent heat conduction and the materialization of the latent heat of condensation plays an important part in the development of atmospheric movements. Calculations by D. E. Martin [8] have shown that a further improvement of the methods of weather forecasting unquestionably requires the consideration of nonadiabatic effects in the prediction methods. To this end, however, it is necessary to have detailed information on the space-time distribution of the sources and sinks of heat. Because of the extreme complexity of this problem, it is desirable first of all to study the influence of the influx of heat averaged over the entire thickness of the atmosphere on large scale motions. Data obtained by means of weather satellites [7, 9] make it possible to find the value of this influx directly.

As the initial system of equations for the problem, we shall choose the equation of transfer of the velocity vortex, taking into account the forces of turbulent friction

$$\frac{d_h(\Omega+l)}{dt} - \frac{g^2}{p_0^2}\frac{\partial}{\partial z}\left(K\rho^2\frac{\partial\Omega}{\partial z}\right) = l\frac{\partial\omega}{\partial z} \qquad (1)$$

and the equation of the influx of heat

$$\frac{d_h T}{dt} - \frac{c^2}{R}\frac{\omega}{z} = -\frac{g}{c_p p_0}\frac{\partial Q}{\partial z} + \frac{\sigma}{c_p}. \qquad (2)$$

Here Ω is the vertical component of the relative velocity vortex, l is the coriolis parameter, g is the acceleration due to gravity, K is the coefficient of turbulent viscosity, ρ is the density of air, T is the absolute temperature, R is the gas constant, $c^2 = \frac{(\gamma_a - \gamma)R^2T}{g}$,

γ and γ_a are the actual and dry-adiabatic vertical temperature gradients, c_p is the specific heat capacity of air at constant pressure, p is the pressure, p_0 is the standard pressure at sea level, and $\zeta = \frac{p}{p_0}$.

In both equations, the symbol $\frac{d_n}{dt}$ designates the individual time derivative on a horizontal plane, and $\omega = \frac{d\zeta}{dt}$ is the analog of vertical velocity in the system of coordinates x, y, ζ, t.

The first term on the right side of equation (2) describes the influx of heat into a unit mass of air due to turbulent and radiant heat exchange, and $\frac{\sigma}{c_p}$ is the influx of heat due to the latent heat of condensation. If D designates the turbulent heat flux, B and A the thermal radiation fluxes directed upward and downward, respectively, and $F^{(1)}$ and $F^{(2)}$ the ascending and descending fluxes of shortwave radiation, then

$$Q = D + A - B + F^{(2)} - F^{(1)}. \tag{3}$$

For the boundary conditions along the vertical, we shall assume that

$$\omega = 0 \text{ at } \zeta = 0 \text{ and } \zeta = 1 \tag{4}$$

In order to pass from heat influxes to fluxes in the given model, we take into consideration a system of equations averaged vertically. Thus, by integrating equation (1) with respect to ζ from 0 to 1 and performing an approximate calculation of the friction near the ground in accordance with A. F. Dubuque [2], we obtain, assuming (4)

$$\overline{\frac{d_n(\Omega + l)}{dt}} + K^* \Omega_g = 0. \tag{5}$$

Here $K^* \approx \frac{\varepsilon p_0}{p_0}\sqrt{\frac{K_h l}{2}}$, K_h is the value of the coefficient of turbulent viscosity at the upper boundary of the lowest sublayer, Ωg is the geostrophic vortex at sea level, and $\overline{(\quad)} = \int_0^1 (\quad)\, d\zeta$. [sic]

The vertical velocity ω is determined from equation (1)

$$\omega = \frac{1}{l}\left\{\int_0^\zeta \frac{d_n(\Omega + l)}{dt}\, d\zeta - \frac{\varepsilon^2}{p_0^2}\left(K p^2 \frac{\partial \Omega}{\partial \zeta}\right)\right\}. \tag{6}$$

Substituting (6) into (2), averaging the equation obtained over the entire thickness of the atmosphere, and combining with equation (6), we obtain

$$\overline{\frac{d_a T}{dt}} + \frac{c^2}{R\bar{l}}\left\{\overline{\varphi \frac{d_a(\Omega + l)}{dt}} - K^*\Omega_g + \overline{\frac{g^2}{p_0^2}\frac{K\rho^2}{\zeta}\frac{\partial\Omega}{\partial\zeta}}\right\} = \frac{R}{c_p p_0}(Q_0 - Q_1) + \frac{RLr}{c_p p_0}. \qquad (7)$$

Here $\varphi = 1 + \ln\zeta$, L is the latent heat of condensation, and r is the amount of precipitation.

As is shown by the calculations, the quantity $\frac{g^2}{p_0^2}\overline{\frac{K\rho^2}{\zeta}\frac{\partial\Omega}{\partial\zeta}}$ may be neglected as compared to $K^*\Omega g$.

The integral is

$$\overline{\frac{K\rho^2}{\zeta}\frac{\partial\Omega}{\partial\zeta}} = \frac{K\rho^2}{\zeta}\Omega\Big|_0^1 - \overline{\Omega\frac{d}{d\zeta}\left(\frac{K\rho^2}{\zeta}\right)}.$$

But $\frac{K\rho^2}{\zeta}\Omega\Big|_0^1 = 0$, and since $\rho^2 = \left(\frac{p_0}{RT}\right)^2\zeta^2$, we have

$$\overline{\frac{K\rho^2}{\zeta}\frac{\partial\Omega}{\partial\zeta}} = -\left(\frac{p_0}{RT}\right)^2\overline{\Omega\left(K + \zeta\frac{dK}{d\zeta}\right)}.$$

We shall assume that above the lowest sublayer h, the turbulence coefficient has a constant value equal to K_h; then

$$\overline{\frac{K\rho^2}{\zeta}\frac{\partial\Omega}{\partial\zeta}} = -\left(\frac{p}{RT}\right)^2 K_h\left[\left(\overline{\Omega} + \Omega(1)\right)\right].$$

Hence,

$$\frac{g^2}{p_0^2}\frac{K\rho^2}{\zeta}\frac{\partial\Omega}{\partial\zeta} \sim 10^3 K_h\overline{\Omega}.$$

Setting $K_h \approx 10$ m^2/sec, we find that

$$K^*\Omega_g(1) \gg \frac{g^2}{p_0^2}\overline{\frac{K\rho^2}{\zeta}\frac{\partial\Omega}{\partial\zeta}}.$$

We now adopt the condition of thermotropicity of the atmosphere [10] (although this is not mandatory in this method)

$$\nabla T(x, y, \zeta, t) = F(\zeta)\nabla\overline{T}(x, y, t), \qquad (8)$$

where ∇ is the gradient operator on the plane. The function $F(\zeta)$ may be determined by a statistical treatment of the observational material.

According to L. Berkofsky [6], we can write approximately $F(\zeta) = 2\zeta$.

By using the equation of statics

$$T = -\frac{g\zeta}{R}\frac{\partial H}{\partial \zeta}, \tag{9}$$

it is easy to obtain the following relations by means of (8):

$$(H)_{\zeta=1} = \overline{H} - \frac{R}{g}\overline{T} \quad \text{и} \quad \nabla H = \nabla\overline{H} + \frac{R\Phi}{g}\nabla\overline{T}, \tag{10}$$

where $\Phi = 1 - \int_{\zeta}^{1}\frac{F(\zeta)}{\zeta}d\zeta$. We note that $\overline{F} = 1$ and $\overline{\Phi} = \overline{\varphi} = 0$.

If we assume the motion to be quasi-geostrophic, then on the basis of the above we obtain

$$\overline{\frac{d_a T}{dt}} = \frac{\partial\overline{T}}{\partial t} + \frac{g}{l}(\overline{H}, \overline{T});$$

$$\overline{\frac{d_a(\Omega + l)}{dt}} = \frac{g}{l}\left\{\Delta\frac{\partial\overline{H}}{\partial t} + \left(\overline{H}, \frac{g}{l}\Delta H + l\right) + \frac{R^2\overline{\Phi^2}}{g^2}\left(\overline{T}, \frac{g}{l}\Delta\overline{T}\right)\right\};$$

$$\overline{\varphi\frac{d_a(\Omega + l)}{dt}} = \frac{g}{l}\left\{\frac{R^2\overline{\varphi\Phi^2}}{g^2}\left(T, \frac{g}{l}\Delta\overline{T}\right) - \frac{R\overline{\varphi\Phi}}{g}\left[\Delta\frac{\partial T}{\partial t} + \left(\overline{T}, \frac{g}{l}\Delta\overline{H}\right) + \left(\overline{H}, \frac{g}{l}\Delta\overline{T}\right) + (\overline{T}, l)\right]\right\}.$$

The symbols Δ and (a, b) designate as usual the Laplace operator on the plane and the Jacobian.

Collecting the results obtained, we finally arrive at the following system of equations of the model:

$$\Delta\frac{\partial\overline{H}}{\partial t} + \left(\overline{H}, \frac{g}{l}\Delta\overline{H} + l\right) + \frac{R^2\overline{\Phi^2}}{g^2}\left(\overline{T}, \frac{g}{l}\Delta\overline{T}\right) + K^*\left(\Delta\overline{H} - \frac{R}{g}\Delta\overline{T}\right) = 0, \tag{11}$$

$$(\Delta - \mu^2)\frac{\partial\overline{T}}{\partial t} - \frac{R}{g}\frac{\overline{\varphi\Phi^2}}{\overline{\varphi\Phi}}\left(\overline{T}, \frac{g}{l}\Delta\overline{T}\right) + \left(\overline{T}, \frac{g}{l}\Delta\overline{H} + l\right) + \left(\overline{H}, \frac{g}{l}\Delta\overline{T}\right) - \frac{g\mu^2}{l}(\overline{H}, \overline{T}) - \frac{gK^*}{R\overline{\varphi\Phi}}\left(\Delta\overline{H} - \frac{R}{g}\Delta\overline{T}\right) = \frac{\mu^2 g}{c_p p_0}(Q_0 - Q_1) + \frac{\mu^2 g l r}{c_p p_0}. \tag{12}$$

The methods for solving this system of equations are known (see Ref. [2]).

We shall now discuss the right side of equation (12).

The quantity Q_0 represents the radiation balance of the system earth's surface—atmosphere, which can be calculated directly from the

measurement data of the satellite.

For forecasting purposes, this quantity is calculated from the known formula

$$Q_0 = S_0(1 - \Gamma) - B_0, \tag{13}$$

where S_0 is the flux of solar radiation reaching the upper boundary of the atmosphere, Γ is the albedo of the system earth's surface—atmosphere, and B_0 is the outgoing thermal radiation of the earth and atmosphere. According to (3), the following expression may be obtained for Q_1:

$$Q_1 = (1 - \alpha)S - E_{eff} - D. \tag{14}$$

Here α is the albedo of the underlying surface, S is the flux of total radiation, E_{eff} is the effective radiation of the earth's surface, and D is the turbulent heat flux on the earth's surface.

The first two terms on the right side of (14) as well as B_0 and Γ in formula (13) are calculated from the data of vertical sounding of the atmosphere, which in principle may be accomplished by means of weather satellites. The calculation of the turbulent heat flux involves the temperature of the underlying surface, for which, in the case of ocean regions, one can use the mean monthly temperatures of the ocean's surface recorded over many years. In calculating Q_1 for dry land conditions, it is desirable to use the equation for the heat balance of the underlying surface

$$-D + (1 - \alpha)S - E_{eff} = G + LE, \tag{15}$$

where G is the heat flux into the ground and E is the evaporation rate. We thus obtain, instead of (14),

$$Q_1 = G + LE. \tag{16}$$

If we use data on the radiation temperature of the surface of the ground T_g obtained from the satellite measurements, the heat flux into

the ground may be calculated from the following formula [3]:

$$G = \sqrt{\frac{c\rho\varkappa}{\pi}} \int_{-\infty}^{t} \frac{dT_g}{d\tau} \frac{d\tau}{\sqrt{t-\tau}}. \qquad (17)$$

Here c, ρ, and $\varkappa$ are, respectively, the specific heat capacity, density and coefficient of thermal conductivity of the ground. For winter conditions and in regions where the evaporation is slight, we obtain $Q_1 \approx G$. For these regions, the flux G may be found by means of equation (15) if data on the temperature of the ground are lacking. As we know, the turbulent heat flux is a function of the wind velocity u and temperature difference $T - T_g$ [4]. In turn T_g is determined via the flux G, according to (17), as follows:

$$T_g = \sqrt{\frac{1}{\pi c\rho\varkappa}} \int_{-\infty}^{t} \frac{G\,dt}{\sqrt{t-\tau}}. \qquad (18)$$

Substituting (18) into (15), we obtain an integral equation which gives the heat flux into the ground for a given radiation balance and air temperature

$$D\left(T - \sqrt{\frac{1}{\pi c\rho\varkappa}} \int_{-\infty}^{t} \frac{G\,dt}{\sqrt{t-\tau}}, u\right) + G = (1-a)S - E_{eff} \qquad (19)$$

Finally, in calculations of the condensation influxes of heat, one must first use factual data on the amount of precipitation.

The proposed method may be used for forecasting purposes if it is made to include a moisture transfer equation for precalculating fields of humidity, cloudiness and precipitation.

As an illustration of the proposed method, three daily forecasts for the middle of January 1960 were calculated with a digital computer. The problem was solved for a rectangular grid area of 23 x 17 nodes with 300 km spacings along the horizontal. N. I. Buleyev's method [1] was

used to solve equations (11) and (12) for the quantities $\frac{\partial \bar{H}}{\partial t}$ and $\frac{\partial \bar{T}}{\partial t}$. The time interval chosen for finding $\bar{H}$ and $\bar{T}$ was 1.5 hours. $\bar{H}$ was taken as the altitude of the isobaric surface of 500 mb, and $\bar{T}$ was identified as the average temperature at the 500-1,000 mb layer.

The quantity Q_1 entering into the right-hand side of equation (12) [see (16)] was assumed to be equal to zero in view of the relatively low values of the heat fluxes into the ground and of the evaporation in winter. The condensation influxes of heat were not considered either. The fields of the radiation fluxes Q_0 were calculated beforehand from factual data for 03 and 15 hr Moscow time, and were introduced into the operative memory every eight time intervals, which corresponded to the replacement of the time-continuous function Q_0 by a step function. The technique of the calculations of Q_0 is described in Ref. [5].

The results of one of the forecasts of $\bar{H}$ and $\bar{T}$ are shown in Fig. 1a, 1b, 1c and 2a, 2b, and 2c. For comparison, a forecast without consideration of Q_0 was made in all three cases. The data obtained are collected in the following table:

Forecast	Model	$\bar{H}$		$\bar{T}$	
		r	ε	r	ε
From 1-13 to 1-14	Nonadiabatic	0.87	0.61	0.72	0.68
	Adiabatic	0.87	0.61	0.71	0.86
From 1-14 to 1-15	Nonadiabatic	0.64	1.20	0.62	0.90
	Adiabatic	0.64	1.19	0.62	1.00
From 1-15 to 1-16	Nonadiabatic	0.92	0.42	0.83	0.54
	Adiabatic	0.90	0.43	0.80	0.69

In this table, r is the correlation coefficient and ε is the relative error pertaining to the region marked on the figures. The estimates given on the line marked "Nonadiabatic" for each of the cases correspond to the allowance for Q_0 in the computational method, and those

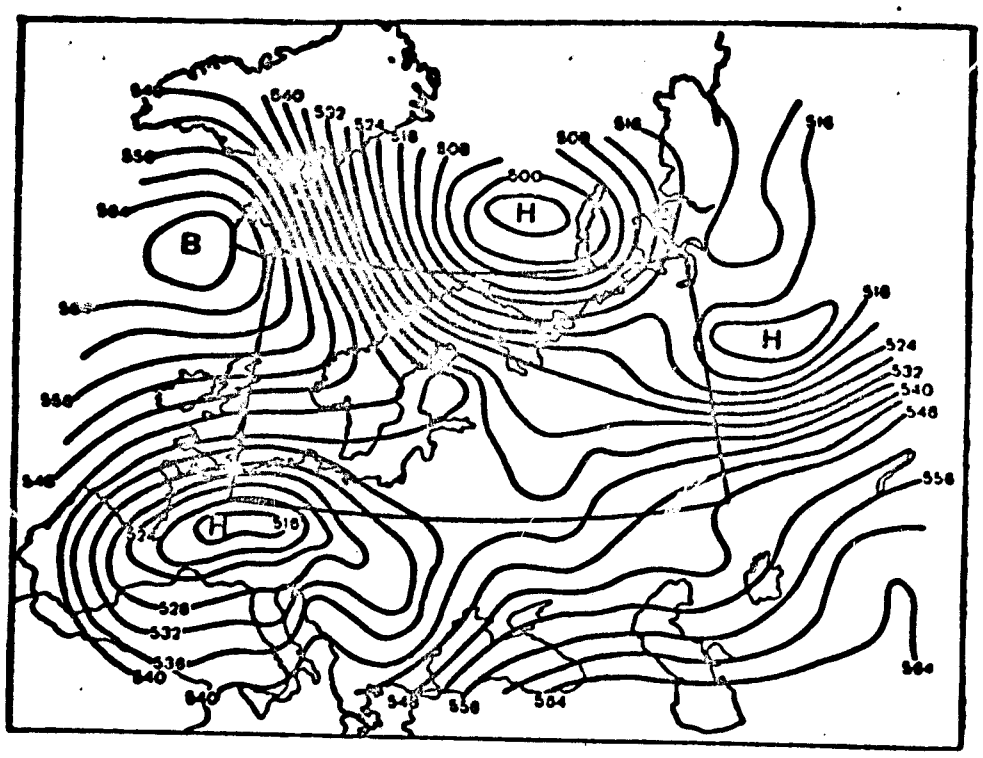

Fig. 1a. Initial field $\overline{H}$ at 03 hours on 15 January 1960.

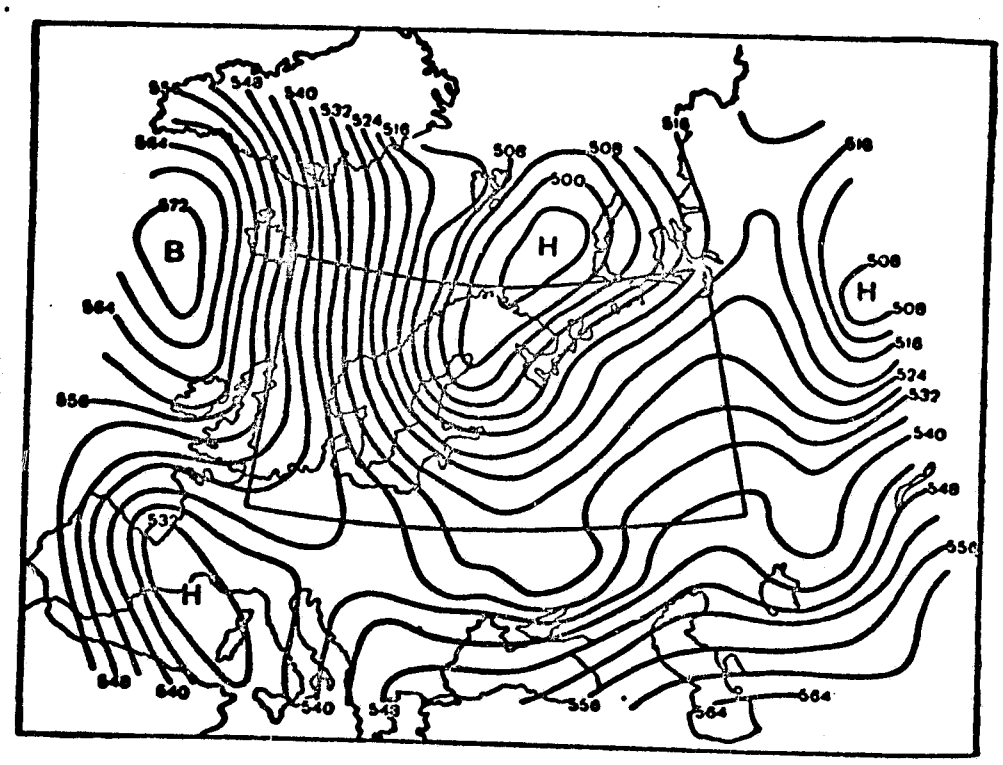

Fig. 1b. Actual field $\overline{H}$ at 03 hours on 16 January 1960.

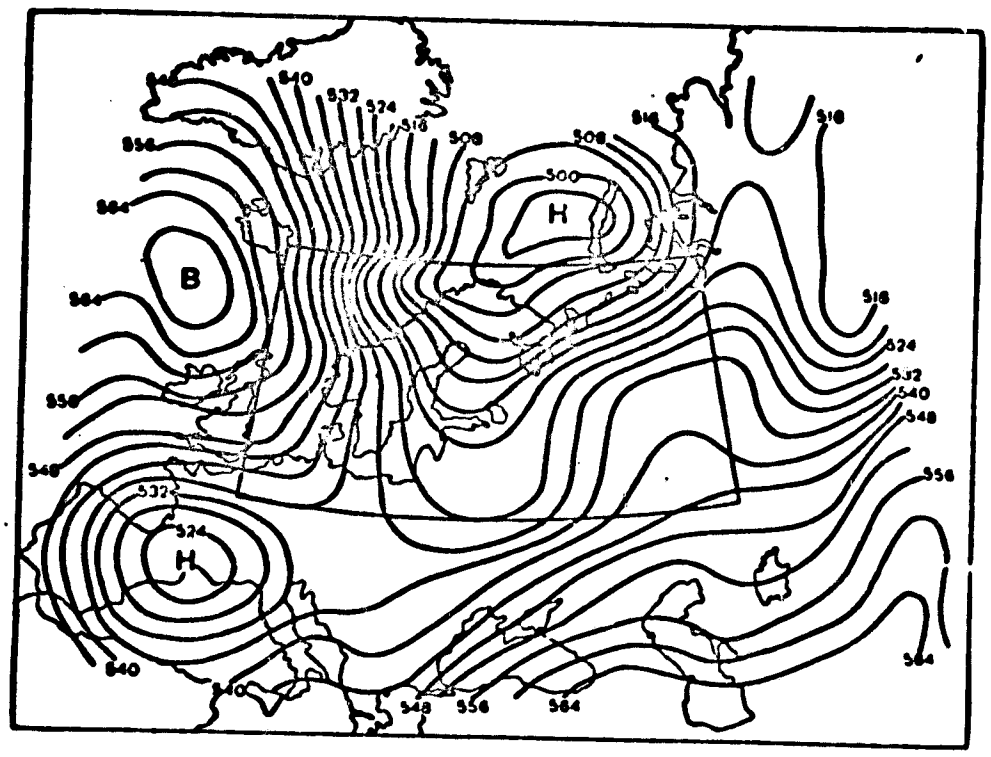

Fig. 1c. Predicted field $\bar{H}$ at 03 hours on 16 January 1960.

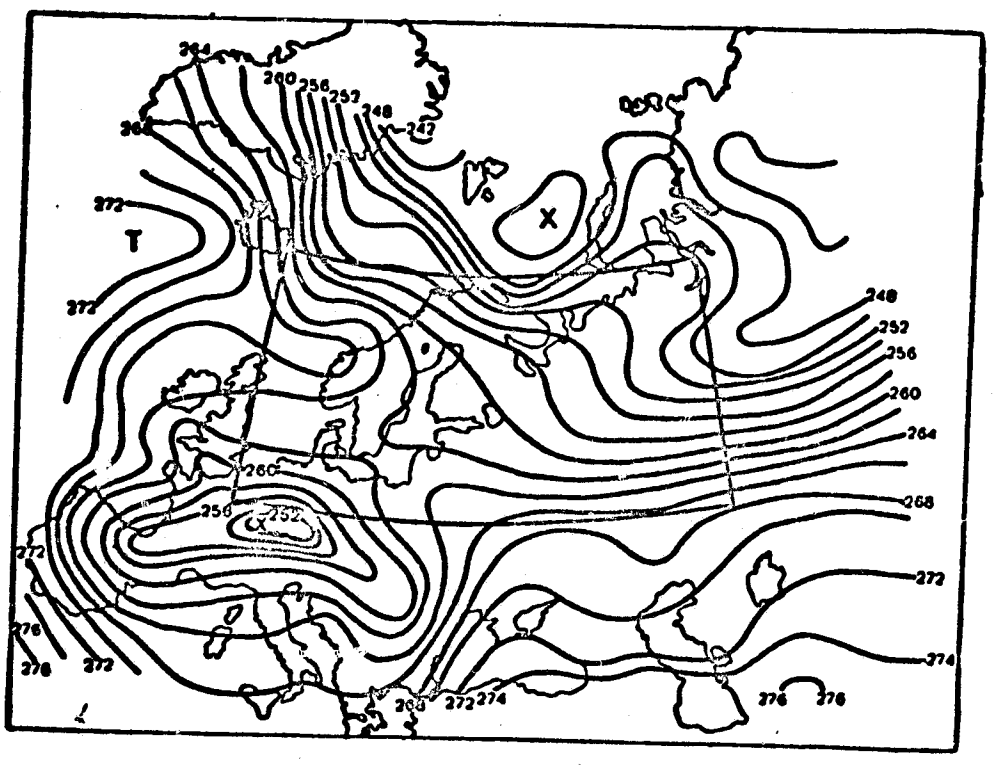

Fig. 2a. Initial field $\bar{T}$ at 03 hours on 15 January 1960.

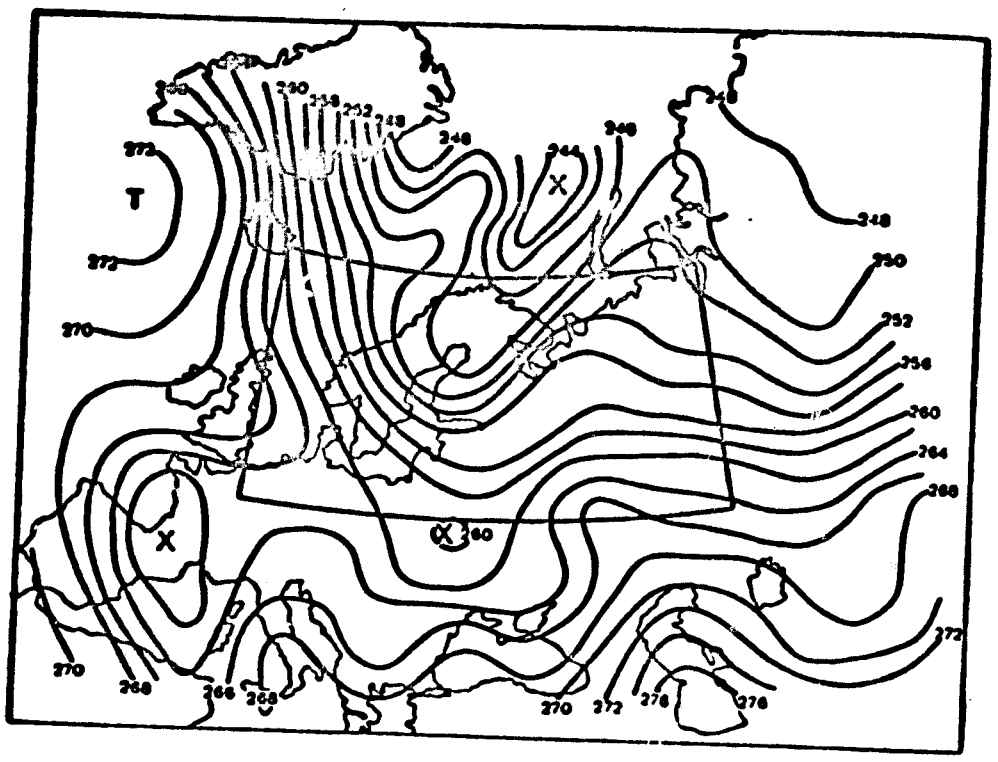

Fig. 2b. Actual field $\bar{T}$ at 03 hours on 16 January 1960.

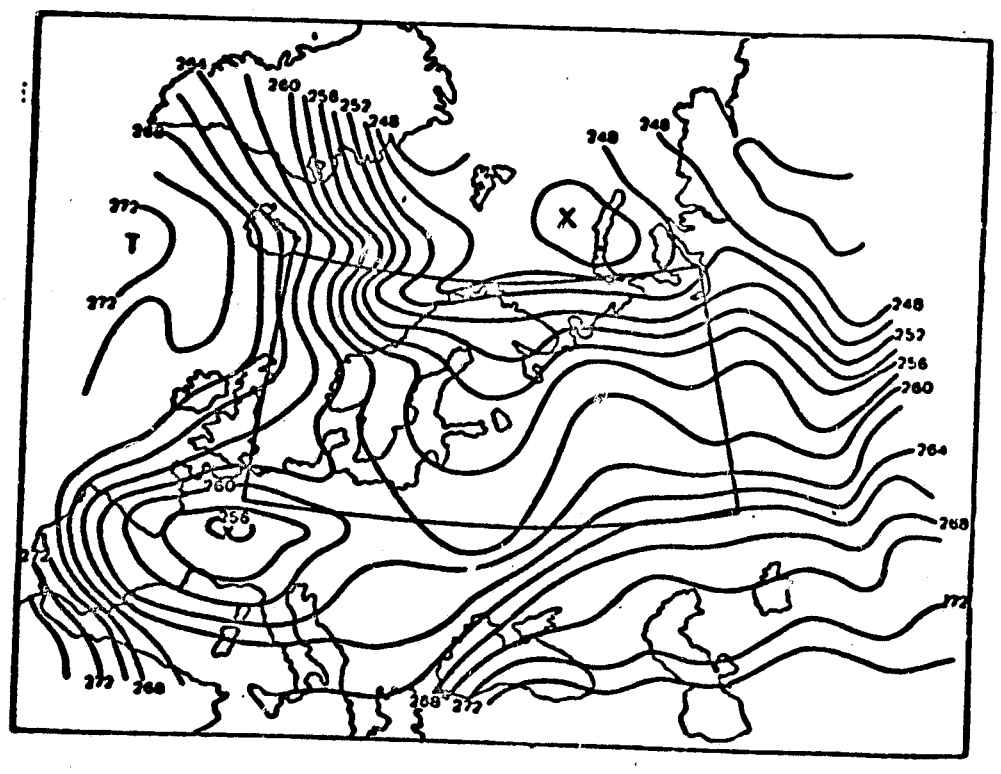

Fig. 2c. Predicted field $\bar{T}$ at 03 hours on 16 January 1960.

given on the line marked "Adiabatic" correspond to the forecast made without taking Q_0 into account. The data obtained show that the allowance for nonadiabatic factors improves the prediction of the temperature $\bar{T}$ (this has a particularly pronounced effect on the decrease of the relative error); as far as the contribution of these factors to the change of the average altitudes per day is concerned, it is a minor one. There is no doubt, however, that this contribution increases appreciably when the forecast period is increased to 2-3 days or more.

In conclusion, the authors express their deep appreciation to N. P. Shchukina for her participation in setting up the program and carrying out the calculations on the digital computer.

REFERENCES

1. Buleyev, N. I., Marchuk, G. I. O chislennom reshenii uravneniy dinamiki atmosfery. Nekotoryye problemy meteorologii. Mezhduvedomstv. komitet po provedeniyu MGG [Numerical Solution of Equations of Atmospheric Dynamics. Problems of Meteorology. Interdepartmental Executive Committee on the IGY]. Izd. AN SSSR, M., 1960.
2. Kibel', I. A. Vvedeniye v gidrodinamicheskiye metody kratkosrochnogo prognoza pogody [Introduction Into Hydrodynamic Methods of Short-Range Weather Forecasting]. GITTL, Moscow, 1957.
3. Landau, L. D. and Lifshits, Ye. M. Mekhanika slozhnykh sred [Mechanics of Complex Media]. GITTL, Moscow, 1953.
4. Monin, A. S., Obukhov, A. M. Osnovnyye zakonomernosti turbulentnogo peremeshivaniya v prizemnom sloye atmosfery [Fundamental Principles of Turbulent Mixing in the Lowest Atmospheric Layer]. Tr. Geofiz. in-ta AN SSSR, No. 24 (151), 1954.
5. Shneyerov, B. Ye. Raschet radiatsionnogo balansa sistemy zemnaya poverkhnost'-atmosfera i ego sostavlyayushchikh [Calculation of the Radiation Balance of the System Earth's Surface—Atmosphere and its Components]. Meteorologiya i gidrologiya, No. 7, 1963.
6. Berkofsky, L., Seager, G. B. Forecast height changes at various levels computed from the thermotropic model. Bulletin of Americ. Met. Soc., v. 37, N 5, 1956.
7. Hanel, R. A., Stroud, W. G. The Tiros II radiation experiment. Tellus, v. 13, No. 4, 1961.
8. Martin, D. E. The relation between Non-adiabatic Heating and the Errors of Numerical Forecasts. Proceedings of the Intern. Simposium on numerical Weather Pred in Tokyo. Met. Soc. of Japan, 1962.

9. Nordberg, W., Bandeen, W. R., Courath, B. T., Kunde, V., Persanol, T. Preliminary results of radiation measurements from Tiros III meteorological satellite. Journ. Atm. Sci. v. 19, No. 1, 1962.
10. Thompson, P. D. and Gates, W. L. A test of numerical prediction methods based on the barotropic and two-parameter baroclinic models. Journ. of Met. v. 13, No. 2, 1956.

M. I. Yudin, N. P. Yesakova, V. B. Afanas'yeva

PRELIMINARY EVALUATION OF THE PROGNOSTIC SIGNIFICANCE OF INFORMATION OBTAINED FROM WEATHER SATELLITES

1. It is known that the main purpose of weather satellites is to obtain information on the distribution of clouds and radiation fluxes over the entire globe. Also of great importance is the possibility of using satellites for observations of glaciation and boundaries of the snow cover. At the present time, data on these hydrometeorological elements are practically not used at all for purposes of long-range weather forecasting. As a rule, in synoptic, statistical and hydrometeorological forecasting methods, the initial data used are merely certain characteristics of atmospheric circulation.

In our opinion, a successful development of long-range forecasts makes it absolutely necessary to consider the global characteristics of the state of the underlying surface and cloud distribution. Sufficiently complete data on these hydrometeorological elements can be obtained only by means of a system of weather satellites. However, it is possible even now to obtain some characteristics of the distribution of these elements on territory covered by regular hydrometeorological observations. We undertook the task of developing first of all the methods of describing anomalies of the cloud cover, radiation balance of the underlying surface, boundaries of the snow cover, and glaciation for the purpose of subsequently using these characteristics in long-range forecasting.

The prognostic value of the above characteristics may be verified by statistical methods. To this end, statistical relations were established between anomalies of the cloud cover, radiation balance, boundaries of the snow cover, glaciation, and the characteristics of future

weather (temperature and precipitation). At the same time, the relations between certain direct characteristics of atmospheric circulation[1] and future weather were subjected to the same type of analysis.

The method and main conclusions of the performed investigation are described below.

2. In order to characterize the anomalies of cloudiness, boundaries of the snow cover, glaciation and radiation balance, we used the mean ten-day values of these quantities for the period of September-November 1948-1957. These values were charted, and the parameters characterizing the fields of the individual elements were then determined.

We shall dwell very briefly on the technique of plotting the charts and on the description of the anomalies.

Snow boundaries. In order to plot the maps of the snow cover, about 300 stations over the territory of the USSR were selected. On the basis of data from these station, the number of days during which a snow cover was present in each of the ten-day periods included in these months was calculated for the months of September, October, November and December. The data from each of the selected stations were then plotted on blanks, and maps of the number of days with the presence of a snow cover for each ten-day period were thus plotted. Isolines showing the number of days with snow within a given ten-day period were drawn on these maps. The isoline 0 bounds the territory free of snow cover, and the isoline 10 is the boundary of a stable snow cover. The plotted maps indicate with sufficient clarity the successive displacements of the boundary of the stable snow cover (isoline 10), generally in a direction from the northeast to

1. The contrasting of circulatory and noncirculatory characteristics of the state of the atmosphere is very arbitrary. For instance, the cloudiness is closely related to the characteristics of cyclonicity, i.e., to circulatory factors. The term "direct circulatory characteristics" as used here refers to those characteristics which can be calculated directly from the field of isohypses.

the southwest from October to December. After a series of methodical treatments, the parameter characterizing the boundaries of the snow cover which was selected was the latitude φ_c of the isoline 5 (five days with snow) as a function of the longitude λ and of time. Subsequent values of $\varphi_c(\lambda, t)$ during a given calendar ten-day period were averaged over the nine-year period, and deviations of the snow-cover boundary from the averages thus obtained were considered.

Radiation balance of the underlying surface. In the last few years, some definite results have been obtained at the Main Geophysical Observatory in the development of climatological methods of calculating the components of the radiation balance.

The technique of the calculation of average monthly values of the radiation balance is described in the articles of M. I. Budyko, T. G. Berlyand, L. I. Zubenok [3], M. I. Budyko and N. A. Yefimova, and V. V. Mukhenberg, and L. A. Strokina [4]. We attempted to use the same technique to calculate the values of the radiation balance for shorter time intervals. To this end, ten-day values of a series of points in the USSR were compared with data of actual observations during the period of the IGY.

The relative error constituted by the error of calculation and observational errors was found to be of the order of 15%. To a first approximation, this makes it possible to use the method of calculation of M. I. Budyko and other authors for determining the values of the radiation balance and their deviations (radiosonde) from climatic averages (in practice, averages for the nine years were used). The values of the anomalies of the radiation balance were determined for each nodal point of the grid shown in Fig. 1. The latitude spacing of the grid is equal to 3°, and the longitude spacing, to 5°.

Glaciation. Ten-day maps of the glaciation for the navigational period were plotted at the Arctic and Antarctic Institute. We made use of these maps in our calculations. The average spatial values of the ice cover were calculated in points for northern seas (Barents and Karsk) and their deviations (L) from averages for the nine-year period were calculated.

Cloudiness. In order to bring out the fundamental relationships in the distribution of the ten-day values of the total cloudiness, we plotted maps of its mean ten-day values for the fall months of 1948-1957. For comparison of the cloudiness maps, use was made of tables TM-1 for the 300 stations in the USSR. The mean ten-day values of the total cloudiness were calculated in points and were then plotted on maps and used for the determination of cloudiness anomalies (Cl) at individual nodal points of the grid of Fig. 1.

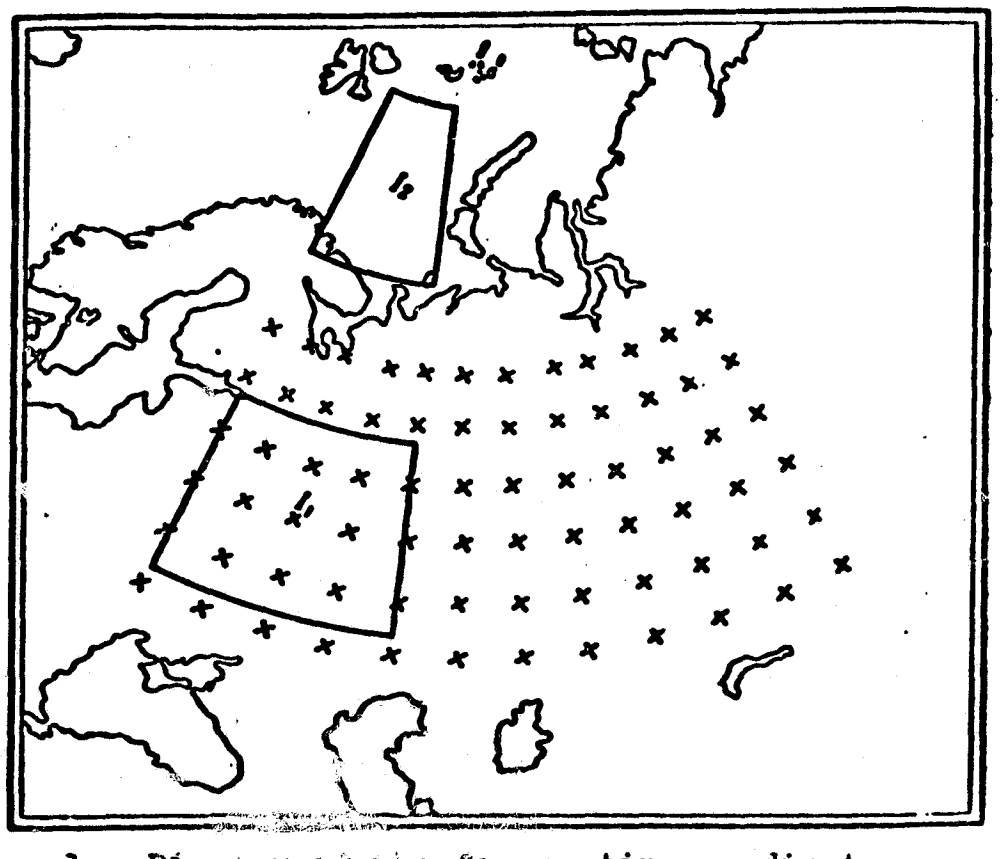

Fig. 1. Diagram of the forecasting gradient.

3. To describe the state of the atmospheric circulation, the parameters which had been studied earlier were chosen: zonal index I_z used in the work of Ye. N. Blinova [1], the meridional index I_m contributed by M. I. Yudin and A. A. Rozhdestvenskiy [6], the hydrodynamic indices I_1 and I_2 [6], proportional to the circulation of the velocity along the two closed circuits shown in Fig. 1. Among these parameters, only the values of the zonal index were taken from Ref. [2], while the remaining three indices were calculated in the Department of Dynamic Meteorology of the Main Geophysical Observatory. Further averaging over ten-day periods and determination of the anomalies were carried out in the same manner as for the characteristics indicated in section 2.

The system of parameters discussed is supplemented by mean ten-day values of the temperature T and precipitation r. These values were determined from ten-day maps plotted in the Department of Long-Range Forecasting of the Central Forecasting Institute for each nodal point of the grid shown in Fig. 1.

4. The next stage of the work consisted in establishing synchronous statistical relations between the ten parameters considered above, and also asynchronous "prognostic" relations. In the derivation of the latter, the ten parameters considered were correlated with the temperature and precipitation of the following ten-day period.

The computations of the correlation coefficients were made with the "Ural-1" electronic computer. To this end, a special program was set up which allowed for the fact that the various parameters are expressed in different ways. Some of them (I_z, I_m, I_1, I_2, L) are characterized by one number for each ten-day period, the values of φ_c depend on the longitude, and the remaining parameters are different at every nodal point.

In cases where we were dealing with such variable parameters, they were taken in the same nodes of the grid (while φ_c was taken on the meridian passing through the nodal point under consideration). Most of the results of the calculation were presented in the form of maps on which the values of the correlation coefficients were plotted. In all, 66 such maps were plotted.

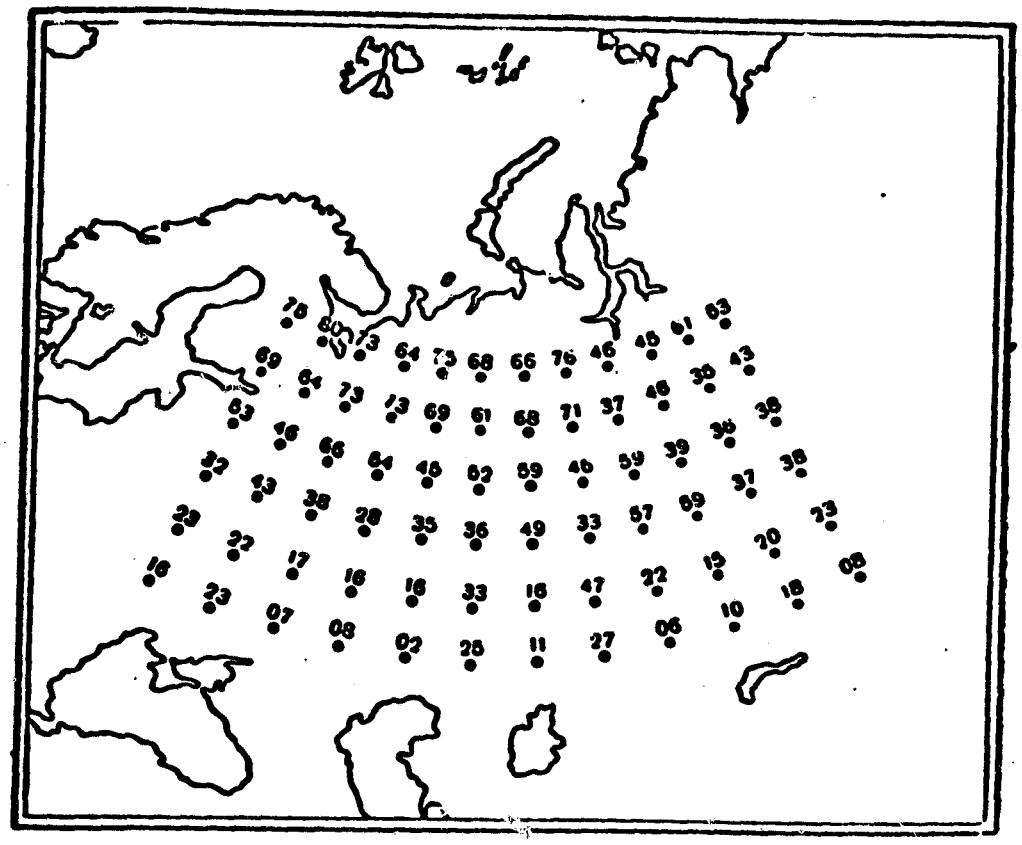

Fig. 2. Map of correlation between snow cover boundary and future temperature.

In a whole series of cases, relationships were observed which were characterized by fairly high correlation coefficients and had the same unchanging sign over the entire territory considered.

We shall dwell briefly on a few prognostic relations. We note first of all that the selected parameters generally give more information for predicting the temperature than does the precipitation. Thus, there are fairly close relations between the indices φ_c, I_l, L, I_m, I_z and the future temperature. As an example, we present the maps for the correlation of the quantities φ_c — T with a shift of one ten-day period (Fig. 2).

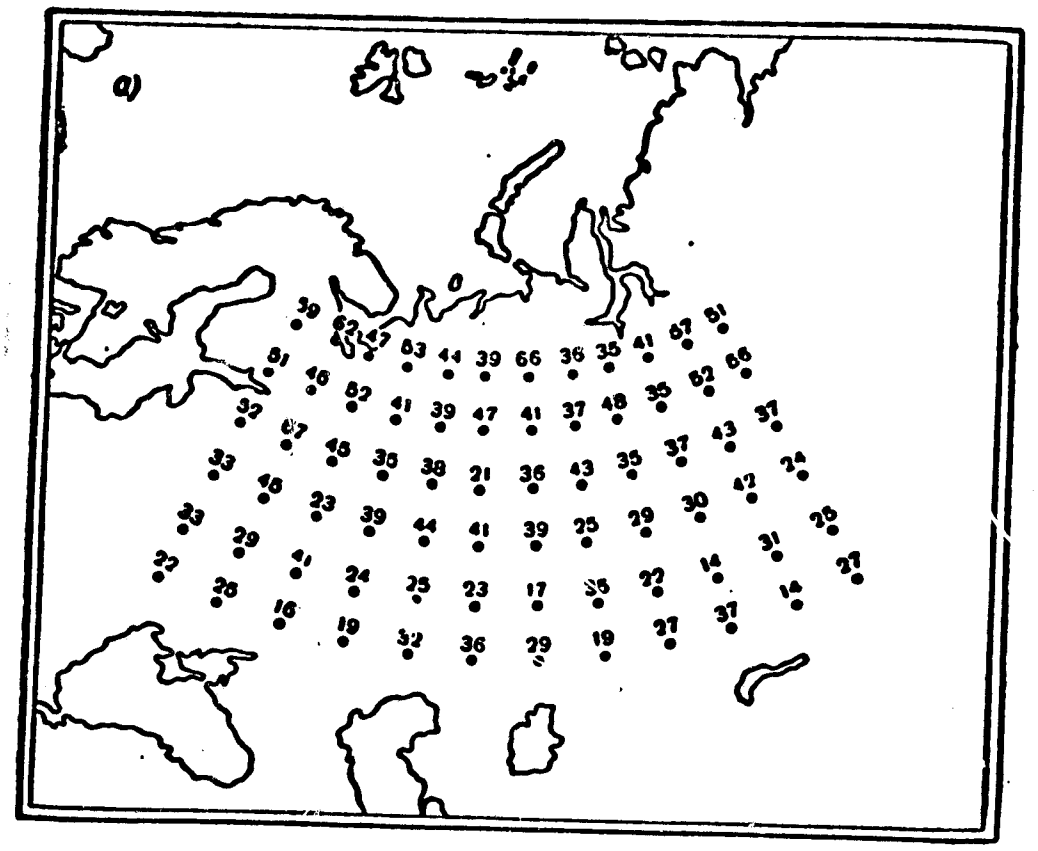

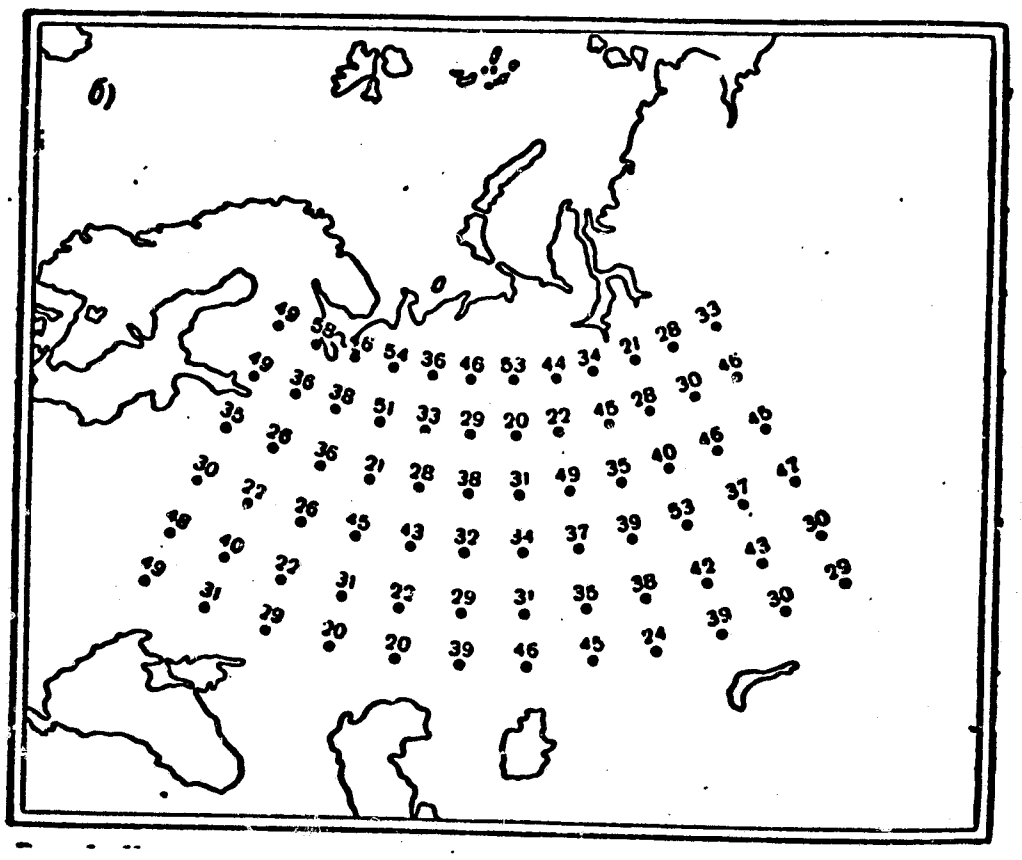

Fig. 3. Map of correlation of cloudiness (a) and radiation balance (b) with temperature.

The values of the coefficients of the correlation of temperature with cloudiness (Fig. 3a) and radiation bounds (Fig. 3b) were found to be relatively small, but fairly stable over the entire territory. Therefore, it is not very improbable that these relations were obtained as a result of random coincidences.

The absence of prognostic relations in a number of cases is fairly apparent from the plotted maps. As an example, we give a map of the correlation between I_2 and the future temperature (Fig. 4).

Relatively close relations with the future precipitation was given by three prognostics - Cl, I_z and I_1 (Fig. 5).

If we proceed from the simplest estimate of the root-mean-square error of the correlation coefficient based on the formula

$$\varepsilon_R = \sqrt{\frac{1-R^2}{n}}$$

and assume that the coefficients exceeding $3\varepsilon_R$ are sufficiently reliable, then for n = 56 we shall obtain the condition that the correlation may be

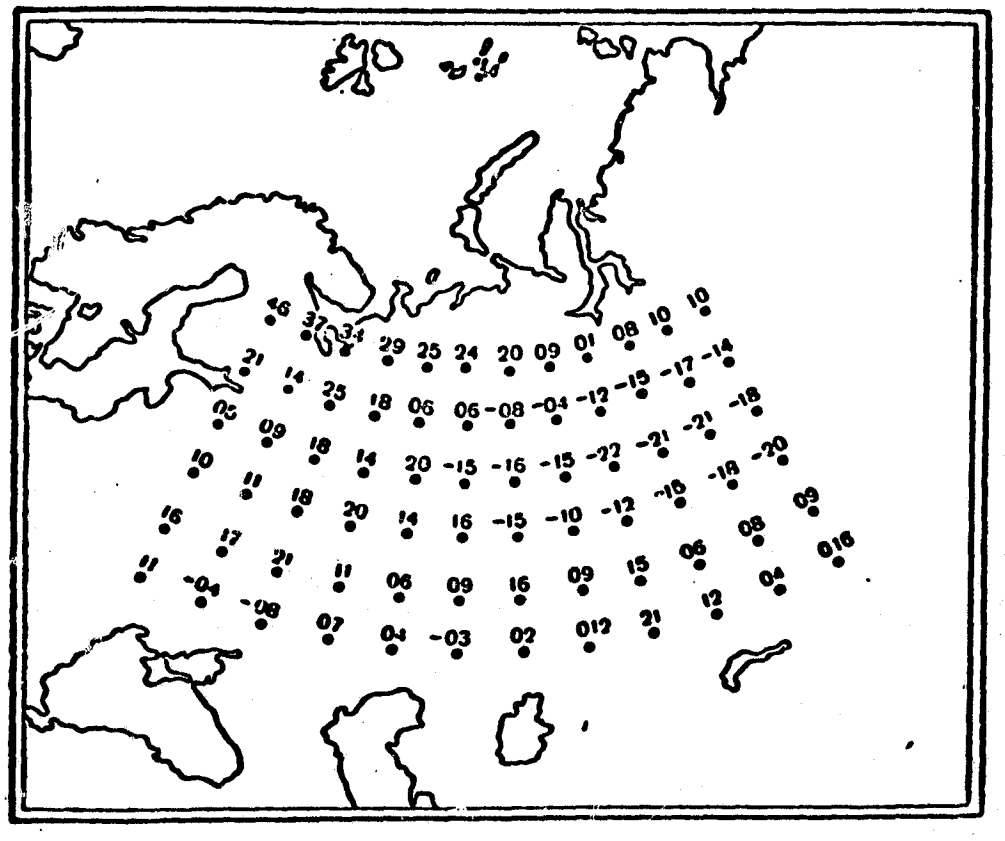

Fig. 4. Map of correlation between circulatory velocity I_2 and future temperatures.

considered to be not random in the form

$$R \geqslant \frac{3}{8} \approx 0{,}4.$$

On this basis, we selected only those prognostics which give sufficiently reliable correlations. Curves of the distribution of the correlation coefficient were determined for these prognostics. In other words, the recurrence periods of the values of the correlation coefficients exceeding certain values were determined for this territory. These periods are listed in Table 1.

An inspection of Table 1 leads to two basic conclusions:

1. The proposed method made it possible to establish a series of parameters for the state of the atmosphere and of the underlying surface which are related fairly closely to the characteristics of the future weather ten days in advance.

2. Most of the parameters pertain to those elements which cannot be determined globally without observations from weather satellites. This emphasizes the great importance of satellite observations for purposes of long-range forecasting.

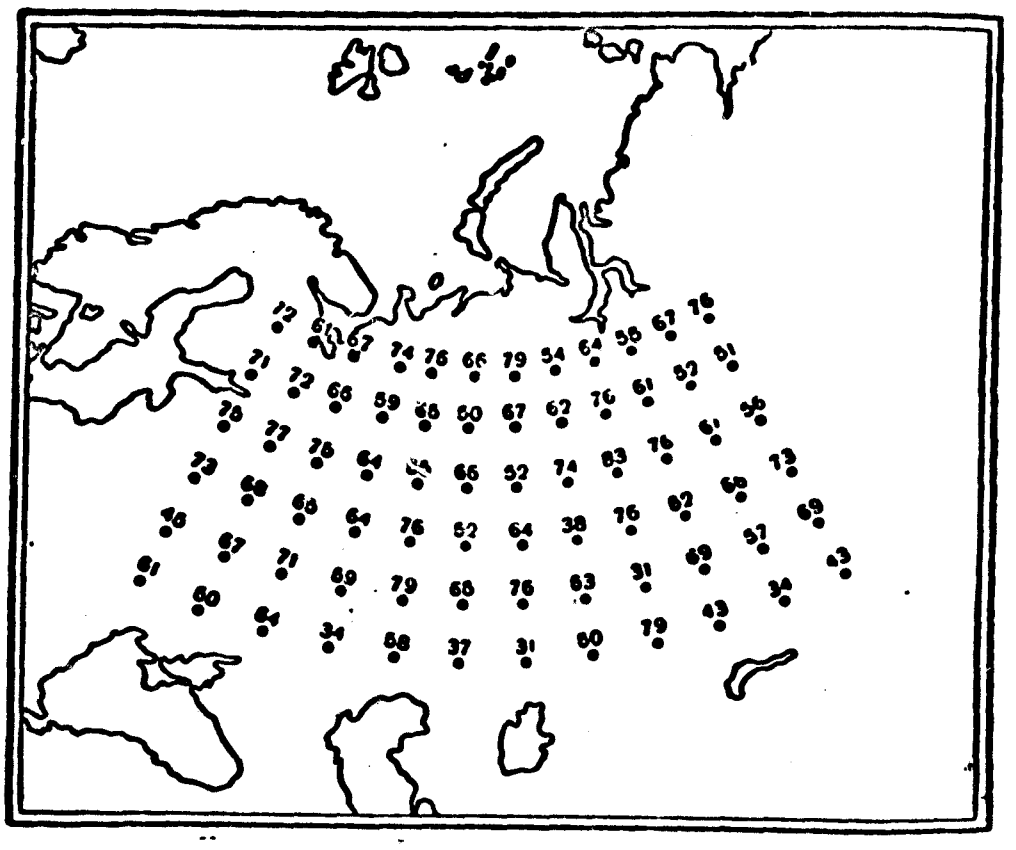

Fig. 5. Map of correlation between cloudiness and future precipitation.

Table 1

	$R > 0.4$	$R > 0.5$	$R > 0.6$	$R > 0.7$
$\varphi_c - T$	0,50	0,36	0,25	0,11
$J_1 - T$	0,38	0,24	0,12	0,04
$J_2 - T$	0,27	0,15	0,08	0,01
$Об - T$	0,39	0,17	0,04	0
$J_z - T$	0,35	0,07	0	0
$J_м - T$	0,34	0,10	0	0
$R.З. - T$	0,33	0,07	0	0
$J_1 - r$	0,29	0,12	0,06	0
$J_2 - r$	0,46	0,25	0,1	0,01
$Об - r$	0,94	0,88	0,63	0,26

REFERENCES

1. Blinova, Ye. N. Gidrodinamicheskaya teoriya voln davleniya, temperaturnykh voln i tsentrov deystviya atmosfery [Hydrodynamic Theory of Pressure Waves, Temperature Waves, and Action Centers of the Atmosphere]. DAN SSSR, Vol. 39, No. 7, 1943.
2. Bogdanova, N. P. Izucheniye bariko-tsirkulyatsionnogo rezhima Everopeyskoy territorii SSSR dlya osennego perioda [Study of the Barometric Circulation Regime of the European Territory of the USSR for the Autumn Period]. Tr. GGO, vyp. 14, 1960.
3. Budyko, M. I., Berlyand, T. G., and Zubenok, L. I. Metodika klimatologicheskikh raschetov sostavlyayushchikh teplovogo balansa [Method of Climatological Calculations of the Components of the Thermal Balance]. Tr. GGO, vyp. 48, 1954.

4. Budyko, M. I., Yefimova, N. A., Mukhenberg, V. V., Strokina, L. A. Radiatsionnyy balans severnogo polushariya [Radiation Balance of the Northern Hemisphere]. Izv. AN SSSR, ser. Geogr., No. 1, 1961.
5. Mashkovich, S. A., Dobryshman, Ye. M., Kheyfets, Ya. M. Kharakteristiki zonal'noy tsirkulyatsii [Characteristics of Zonal Circulation]. Gidrometeoizdat, Leningrad, 1958.
6. Rozhdestvenskiy, A. A. Issledovaniye sinopticheskikh protsessov svyazannykh s osushchestvleniyem karskikh vozdeystviy na osnove izucheniya indeksov tsirkulyatsii [Study of Synoptic Processes Involved In Karsk Modifications Based on a Study of the Circulation Indices]. Tr. GGO, vyp. 55, 1955.

Sh. A. Musayelyan, A. Z. Chekidra

NUMERICAL INTERPRETATION OF INFORMATION ON CLOUDINESS RECEIVED FROM WEATHER SATELLITES

The nature of atmospheric processes is such that a change in one of the characteristics of the condition of the atmosphere causes a change in all the others. This property is particularly reflected in a closed system of differential equations - equations of hydrothermodynamics, transfer of radiant energy, and state and turbulent diffusion. The close interrelationship of the characteristics of the condition of the atmosphere and their interdependence determine the nature of the development of atmospheric processes, in particular the process of formation, development and breakdown of cloudiness. If only because the formation of a cloud is the result of changes in the fields of vertical currents, temperature, humidity, pressure and other meteorological elements, it may be regarded as a very complex hydrothermodynamic process. Changes in all of these fields have of course different effects on the process of cloud formation.

In the present work, it is assumed that the most important role in the process of cloud formation is played by ascending vertical currents, and that in descending motions, no new cloud is formed, and those clouds which are already present must disappear. It should be noted that the process of cloud formation, like many other meteorological phenomena, is to some extent characterized by the property "inertia." Actually, this assumption is used by all researchers who correlate the calculated or predicted fields of vertical motions with the fields of cloudiness or precipitation.

Whereas up to the present time the long-existing problem has been to determine the field of cloudiness from the field of vertical motions, the

opposite problem has now arisen - the determination of the field of vertical currents from the field of cloudiness. This new problem has arisen because of the appearance of weather satellites, whose principal information, in addition to information on the radiation characteristics, is information on the state of the cloud cover of the earth, which must be applied in practice and with maximum benefit in the meteorologist's work.

Photographs of cloud systems made by satellites make it possible to determine the structure and size of various cloud formations and their characteristic features in various synoptic situations. Such information is particularly valuable when obtained for regions where meteorological observations are very rare.

Many meteorologists are concerned with the synoptic interpretation of information on cloud systems which is obtained from satellites. In the final analysis, this interpretation amounts to a visual inspection of the field of cloudiness and to the introduction of corrections (which are sometimes essential) into the weather map, particularly in those regions where the ground information is insignificant or completely lacking.

From numerical forecasts, it is necessary to obtain a quantitative, not qualitative, interpretation of the information pertaining to cloudiness. The present work offers a method of determining the fields of vertical currents from the distribution of cloudiness.

Let us assume that the fields of the total amount of cloudiness and vertical currents are given over the northern hemisphere, respectively, by functions $S(\varphi, \lambda, t)$ and $W(\varphi, \lambda, t)$ (φ is the latitude of the location, λ is the longitude, and t is the time) Generally speaking, all these functions depend strongly on the latitude. However, we shall consider a case in which the field of the vertical currents is given at a certain

standard level (for example, 500 mb), and the function $S(\varphi, \lambda, t)$ describes the total amount of cloudiness, i.e., represents the function "integrated over the altitude." It is assumed that all functions satisfy the Dirichlet conditions.

We shall further consider the discreet values of the functions $S(\varphi, \lambda, t)$ and $W(\varphi, \lambda, t)$ with respect to φ and t, i.e., the functions $S(\varphi_i, \lambda, t_j)$ and $W(\varphi_i, \lambda, t_j)$, where $i = 1, 2, \ldots, n$; $j = 1, 2, \ldots, k$, which means that these functions are given at certain definite latitudes and instants of time.

To simplify the notation, we introduce the following symbols:

$$S(\varphi_i, \lambda, t_j) = S_i^j(\lambda), \quad W(\varphi_i, \lambda, t_j) = W_i^j(\lambda). \tag{1}$$

We represent the functions $S_i^j(\lambda)$ and $W_i^j(\lambda)$ in the form of a Fourier series:

$$S_i^j(\lambda) = \frac{S_{i0}^j}{2} + \sum_{m=1}^{p} (S_{im}^j \cos m\lambda + S_{im}^{'j} \sin m\lambda); \tag{2a}$$

$$W_i^j(\lambda) = \frac{W_{i0}^j}{2} + \sum (W_{im}^j \cos m\lambda + W_{im}^{'j} \sin m\lambda), \tag{2b}$$

where

$$\left.\begin{aligned} S_{i0}^j &= \frac{1}{\pi} \int_{-\pi}^{\pi} S_i^j(\lambda)\, d\lambda \\ S_{im}^j &= \frac{1}{\pi} \int_{-\pi}^{\pi} S_i^j(\lambda) \cos m\lambda\, d\lambda \\ S_{im}^{'j} &= \frac{1}{\pi} \int_{-\pi}^{\pi} S_i^j(\lambda) \sin m\lambda\, d\lambda \end{aligned}\right\} \tag{3a}$$

$$\left.\begin{aligned} W_{i0}^j &= \frac{1}{\pi} \int_{-\pi}^{\pi} W_i^j(\lambda)\, d\lambda \\ W_{im}^j &= \frac{1}{\pi} \int_{-\pi}^{\pi} W_i^j(\lambda) \cos m\lambda\, d\lambda \\ W_{im}^{'j} &= \frac{1}{\pi} \int_{-\pi}^{\pi} W_i^j(\lambda) \sin m\lambda\, d\lambda \end{aligned}\right\} \tag{3b}$$

According to the adopted assumption on the relation between the fields of cloudiness and the vertical currents, we shall assume that the Fourier coefficients W_{im}^{j} and S_{im}^{j} and also $W_{im}^{\prime j}$ and $S_{im}^{\prime j}$ are related by a linear dependence of the form

$$\begin{aligned} W_{im}^{\prime} &= a_{im}^{\prime} S_{im}^{\prime} + b_{im}^{\prime}, \\ W_{im}^{\prime\prime} &= a_{im}^{\prime\prime} S_{im}^{\prime\prime} + b_{im}^{\prime\prime}. \end{aligned} \tag{4}$$

The numbers a_{im}^{j}, b_{im}^{j}, $a_{im}^{\prime j}$ and $b_{im}^{\prime j}$ will be referred to as the coefficients of linear relation between the Fourier coefficients of the fields of vertical currents and cloudiness.

Since in the case under consideration all the latitudes are equivalent, and both expressions (4) are similar, we shall continue all subsequent arguments with reference to the linear dependence between the Fourier coefficients for cosines at any one latitude. Bearing this in mind, we rewrite the first of relations (4) for each wave number m(m = = 1, 2, ..., P) in the form of the system

$$\left.\begin{aligned} W_m^1 &= a_m^1 S_m^1 + b_m^1 \\ W_m^2 &= a_m^2 S_m^2 + b_m^2 \\ &\cdots\cdots\cdots \\ W_m^k &= a_m^k S_m^k + b_m^k \end{aligned}\right\} \tag{5}$$

Considering that the functions $W_i^j(\lambda)$ and $S_i^j(\lambda)$ and hence the Fourier coefficients as being given, and using the method of least squares, we find the characteristic values of the coefficients of the linear relation a_m and b_m from system (5) for each recorded wave number m. This actually means that a system of the form of (5) for each wave number m is replaced by a single relation:

$$W_m^{\prime j} = a_m S_m^{\prime j} + b_m, \tag{6}$$

where

$$
\left.
\begin{aligned}
a_m &= \frac{\sum_{j=1}^{k} (W'_m - \overline{W}_m)(S'_m - \overline{S}_m)}{\sum_{j=1}^{k} (S'_m - \overline{S}_m)^2} \\
b_m &= \overline{W}_m - a_m \overline{S}_m \\
\overline{W}_m &= \frac{1}{k} \sum_{j=1}^{k} W'_m \\
\overline{S}_m &= \frac{1}{k} \sum_{j=1}^{k} S'_m
\end{aligned}
\right\} \qquad (7)
$$

Applying similar arguments to the second of expressions (4), we find the relations for the Fourier coefficients for sinuses:

$$W'^{j}_{m} = a'_m S'^{j}_{m} + b'_m, \qquad (8)$$

where

$$
\left.
\begin{aligned}
a'_m &= \frac{\sum_{j=1}^{k} (W'^{j}_{m} - \overline{W}'_m)(S'^{j}_{m} - \overline{S}'_m)}{\sum_{j=1}^{k} (S'^{j}_{m} - \overline{S}'_m)^2} \\
b'_m &= \overline{W}'_m - a'_m \overline{S}'_m \\
\overline{W}'_m &= \frac{1}{k} \sum_{j=1}^{k} W'^{j}_{m} \\
\overline{S}'_m &= \frac{1}{k} \sum_{j=1}^{k} S'^{j}_{m}
\end{aligned}
\right\} \qquad (9)
$$

$$m = 1, 2, \ldots, P$$

Having the values of a_m, b_m, a'_m and b'_m, precalculated from formulas (7) and (9) for each latitude φ_i ($i = 1, 2, \ldots, n$), one can calculate the field of vertical currents from a given field. To this end it is necessary to use successively formulas (3a), (6) and (8), and (2b).

The success of the method herein described of determining the field of vertical currents from the field of cloudiness will depend not only on the essence of the method itself but also on the quality and quantity of the initial data from which the characteristic values of the coefficients of the linear relations are calculated.

In the numerical experiment which was carried out, the initial used were calculated fields of diagnostic vertical currents and the amount of total cloudiness in points for July 1962. All of the initial

material pertains to the period of aerological observations of 03 hours.

The fields of vertical currents were calculated at the level AT_{500} by the two-level linear scheme for the entire northern hemisphere elaborated and programmed by G. P. Kurbatkin [1]. In the numerical experiment described, use was made of a grade grid with the dimensions $\Delta\theta = 5^{\circ}$ and $\Delta\lambda = 10^{\circ}$, and, since the values of the vertical velocities were calculated at the nodes of such a grid, no additional treatment of the fields of vertical currents was performed.

Data on the total amount of cloudiness were taken directly from daily meteorological telegrams and were mapped. During the mapping, these data were throughly checked for the purpose of detecting and discarding contradictory data. In order to record data at the nodes of the adopted grade grid, the maps of the total amount of cloudiness were analyzed by drawing isolines of equal quantity of cloudiness at 3-point intervals.

In this part, the analysis of information on cloudiness has a particularly subjective character. Generally, an analysis of the amount of cloudiness is a difficult and complex task, particularly in a numerical experiment.

The necessary information was obtained from maps processed in this fashion and representing the total amount of cloudiness at the nodes of the grid. It should be noted that the dimensions of the adopted grade grid were not able to reflect certain features of the field of cloudiness; certain details may disappear from the field of view: cloud masses whose dimensions are smaller than the spacing of the grid, narrow bands, etc. This of course has a negative effect on the results of the calculations. On the other hand, there are vast uninhabited and water areas for which information on cloudiness as well as other meteorological elements cannot

sufficiently describe the condition of the cloudiness, and hence, the analysis is performed very roughly and its results may turn out to be far removed from the actual conditions.

Fig. 1A. Photograph of cloudiness obtained from satellite on 19 May 1960.

Even over well-illuminated regions, the analysis of the amount of cloudiness suffers considerably from subjectivity. This is evident from an analysis of the cloudiness of an occluded cyclone performed by the prognosticator (Fig. 1B). Only photographs of this cloudiness from a satellite (Fig. 1A) enabled the prognosticator in his analysis to reflect a picture of the field of cloudiness which was more or less similar to the actual one.

We shall note in passing that the spiral structure of the cloudiness has suggested that the isobars in such cyclones should have a peculiar shape reflecting the structure of the cloudiness. Bearing this in mind,

we performed a detailed isobaric analysis of such cyclones (the isobars were drawn every 2 mb), and also an analysis of the cloudiness. We found that the closed isobars in the region of such cyclones contain alternating bands forming troughs and crests. Cloud bands are associated with the troughs, and gaps or bands of minimum cloudiness are associated with the crests (Fig. 1Bb).

A detailed analysis of the combined maps of the total amount of cloudiness showed that broad masses of large horizontal dimensions undergo little change in time and have a more organized character in regions of large mountainous systems. In carrying out the calculations, only the following values of the indices were used: $j = 1, 2, \ldots, 31$; $i = 1, 2, \ldots, 16$; $m = 1, 2, \ldots, 18$. The choice of the values of index j was determined by the number of days in the month. The choice of a monthly interval was desirable in order to reflect the characteristics of a given season. The choice of the values of i (which corresponds to an interval of 5° along the meridian) is sufficient for describing the fields. As far as the choice of the values of m is concerned, the accuracy of representation of fields of total cloudiness was first checked by 18 harmonics. The results of this representation confirm the choice of the number of harmonics, and hence, make it possible to use ready program units, (Fourier series expansions and restoration) set up by G. P. Kurbatkin.

Further, an analysis of the Fourier coefficients was performed for the initial fields of vertical currents and cloudiness in order to check the basic assumption of the method concerning a linear relation between the coefficients of the two fields. The analysis was carried out by plotting the points in the plane $W_m S_m$. As is evident from Fig. 2, the distribution of the points has a tendency to be stretched by a narrow band along a

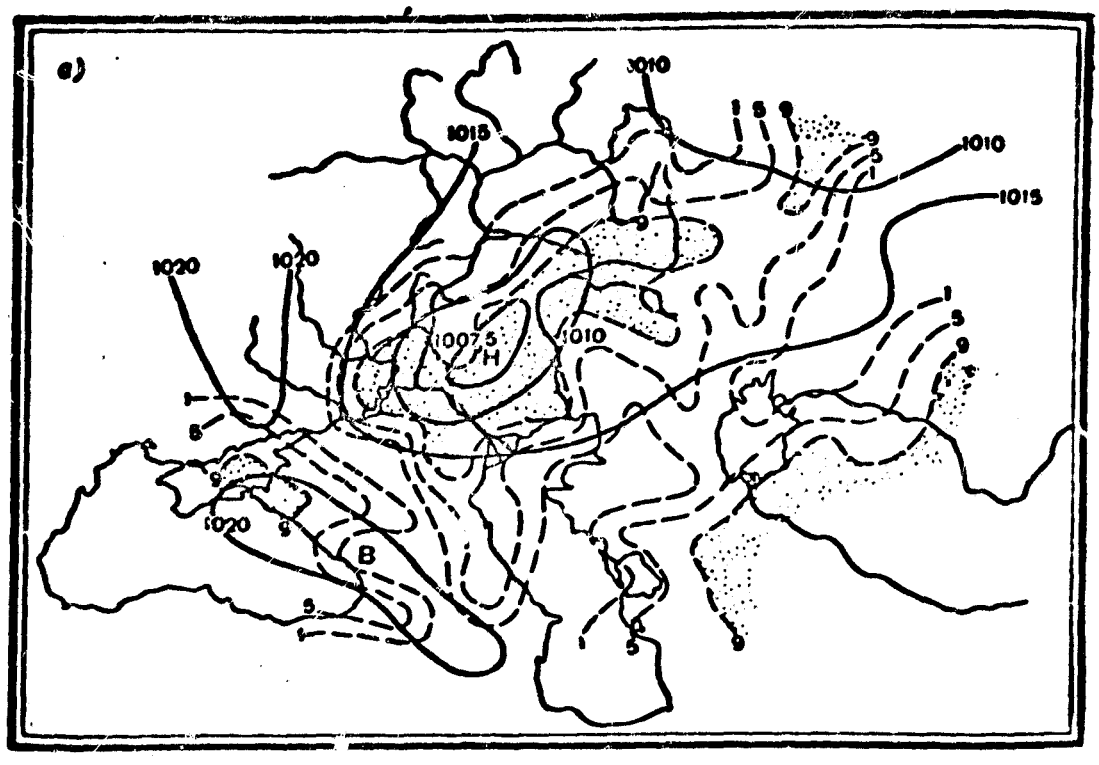

Fig. 1B. Maps of pressure fields and cloudiness at 03 hours on 19 May 1960.

a - analyzed by prognosticator; b - analyzed by using photography (Fig. 1A).

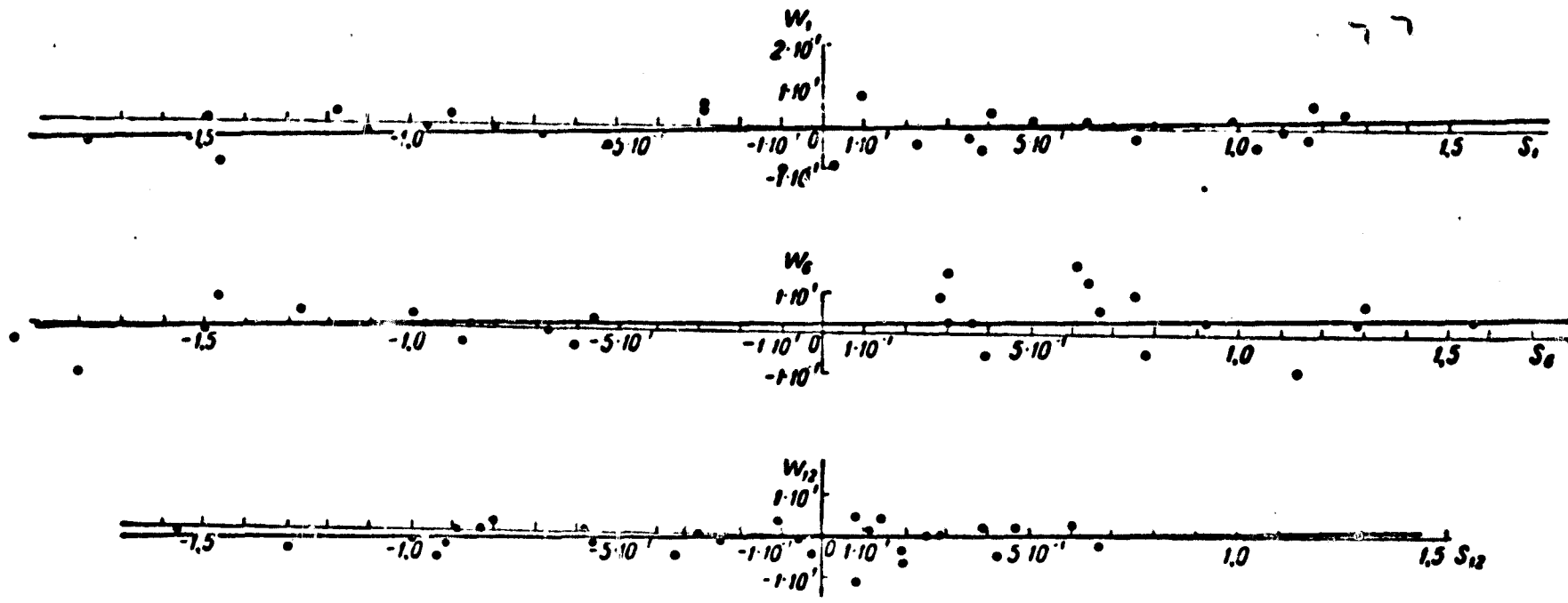

Fig. 2. Graphs of relation between Fourier coefficients for cosines (i = 1, 6, 12) for fields of cloudiness and vertical currents.

straight line, i.e., in general, despite a certain scatter of the points, the linear relation approximately describes the dependence between the Fourier coefficients of the fields of cloudiness and vertical currents.

Thus, in calculating the characteristic values of the coefficients of linear relations, the initial data used were data on the total amount of cloudiness in points, taken from maps at the nodes of a grade grid with the dimensions $\Delta\theta = 5^{\circ}$ and $\Delta\lambda = 10^{\circ}$ for July 1962 at an observational time of 03 hours, and also data on vertical currents calculated at the same nodes of the grid for the corresponding period. Since calculated characteristic values of the coefficients of the relation were available for all the harmonics at all the latitudes, the fields of the vertical currents for July were calculated from the field of cloudiness.

An analysis of the results was performed in order to elucidate the correspondence between the regions of positive vertical currents and the cloud masses, and the correspondence between regions of negative currents and the absence of cloudiness or a limited cloudiness. Most of the

Fig. 3. Maps of total amount of cloudiness (a), vertical currents calculated from the field of cloudiness (b) and from G. P. Kurbatkin's scheme for 03 hours on 1 July 1962 (c) the marked areas correspond to ascending vertical currents and to a cloudiness of over 6 points.

attention was concentrated on well-illuminated regions.

Fig. 3 shows the maps of the total amount of cloudiness at 03 hours on 1 July 1962 and vertical curves calculated from the field of cloudiness. A comparison of these maps indicates a satisfactory reflection of the field of cloudiness in the field of vertical currents. In particular, large cloud masses above the territory of western Europe, a substantial portion of the European territory of the USSR west of the Urals, above the vast territory of Siberia, in the areas of Chukotka and Kamchatka and above the North American continent correspond to areas of ascending fluxes. A lack of correspondence can be observed only in the details. Furthermore, the orientation of cloud systems and cloudless regions is clearly reflected in the field of vertical currents. Such an agreement is characteristic of all the examples for July. This figure also shows a map of vertical currents calculated by the method of G. P. Kurbatkin.

In order to elucidate the possibility of applying the relation coefficients calculated from the data for July to the neighboring months of the summer season, an experiment was performed which involved the calculation of the fields of vertical currents from the cloudiness for individual days of June and August. Results shown in Figs. 4 and 5 indicate the feasibility of a successful application of these coefficients to the neighboring months of the season.

The field of vertical currents calculated from the cloudiness for 03 hours on 10 June 1962 (Fig. 4) corresponds fully to the field of cloudiness. Above the European territory of the Soviet Union, cloud masses of large dimensions were located from which an elongated band of cloud masses extended across the northern Urals and into the region of Novosibirsk. Two more similar bands joined this region from the east and south. All of these, and also the cloud masses located in the form of a band from the Caucasus region across the Caspian and Aral Sea into western Siberia, bounding the cloudless region of southern Urals and western Kazakhstan from the south and southeast, were reflected in the field of vertical currents.

A similar correspondence was also obtained above the North American continent and Greenland. The distribution of the cloud masses for 03 hours on 20 August 1962 was reflected very clearly in the field of vertical currents calculated from the cloudiness (Fig. 5). On the map of cloudiness one can distinguish the principal masses of cloudiness in the form of bands oriented in a more or less meridional direction over the Eurasian continent and in the latitudinal direction over the North American continent. Three such bands can be distinguished over the Eurasian continent: one over the European territory of the USSR; the second in the Yenisei River Basin and

on across the Altai Mountains and the Tibet Highlands to the south, where the cloud masses extend over a vast territory and lose their meridional orientation; the third in the region of the Far East and the Maritime Territory. Two such bands can be distinguished over the North American continent. One runs along the northern shores of the continent, and the second, from the area of New York westward up to the mountain ranges, then on to the northwest and into an area between latitudes of 50 and 55°.

The calculated field of vertical currents corresponds to the distribution of the cloud masses.

On the basis of the analysis of the results obtained, one can conclude that the principal cloud masses are in reliable agreement with the field of vertical currents calculated from the field of cloudiness by means of the method proposed. Fine cloud systems or gaps, narrow bands, etc., are not reflected in basic detail. In order to bring them out, it is necessary to take a finer grade grid, at least along the circle of altitude.

Particular attention should be focused on the fact that the coefficients of linear relation were calculated from the field of cloudiness, information on which was very scarce for vast uninhabited and water spaces, and its analysis suffered a great deal from subjectivity.

Information from satellites will fill this gap to a considerable extent. On the other hand, these data make it possible to define the values of the linear relation; this is a necessity at the present time.

In addition to a series of calculations for the entire northern hemisphere, individual examples of which were demonstrated in checking the applicability of the method, an attempt was also made to perform the calculations for a limited territory. This was dictated by the necessity of using data on cloudiness obtained from satellites. To this end, a sample

Fig. 4. Maps of total amount of cloudiness (a) and vertical currents calculated from the field of cloudiness for 03 hours on 10 June 1962 (b).

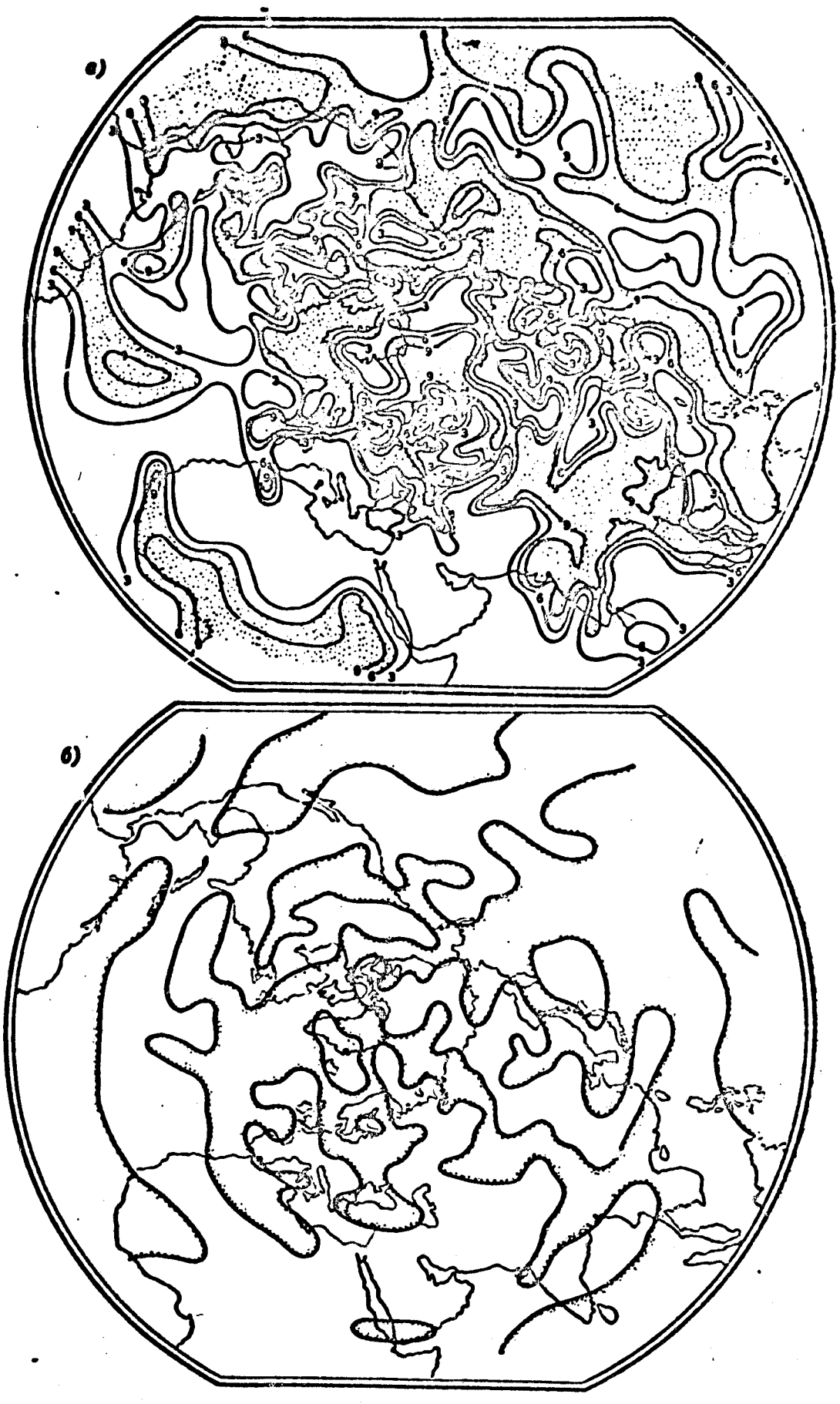

Fig. 5. Maps of total amount of cloudiness (a) and vertical currents calculated from the field of cloudiness for 03 hours on 20 August 1962 (b).
The marked areas correspond to ascending vertical currents and to a cloudiness of over 6 points.

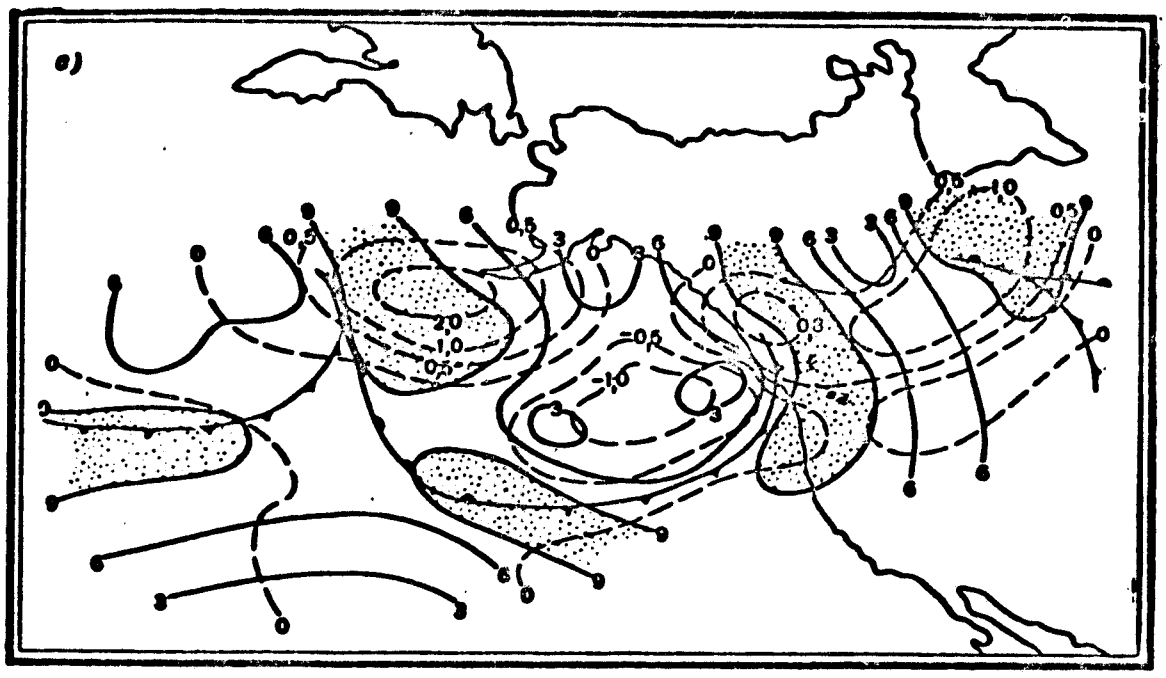

Fig. 6. Maps of interpreted photograph obtained on 20 May 1960, and of vertical currents calculated from cloudiness (a), and of the corresponding field AT_{500} and vertical currents calculated by G. P. Kurbatkin's scheme (b).

photograph from the "Tiros-I" satellite was selected which showed the cloudiness extending over the northern portion of the Pacific Ocean and adjoining the territory of the USA. The photographs of the cloudiness were interpreted (Fig. 6) and a calculation of the vertical velocities was made on the basis of these data. It should be noted that the analysis

of cloudiness in this region based on the data of ground and ship observations differs appreciably from the analysis performed on the basis of the photographs. The results of the calculations are given in Fig. 6; they confirm the possibility of applying the method to a limited territory. In addition, the method has proven applicable to the interpolation of data on cloudiness obtained from satellites.

In conclusion, the authors wish to express their appreciation to the candidate of physical and mathematical sciences G. P. Kurbatkin for supplying individual units of ready programs, D. M. Sonechkin for interpreting the photographs of cloudiness obtained from the satellite, and V. M. Karpov, M. I. Shareyko and R. N. Razorenov for preparing and processing the data.

REFERENCE

1. Kurbatkin, G. P. Prognoz poley davleniya na dvukh urovnyakh dlya severnogo polushariya Zemli [Prognosis of Pressure Fields at Two Levels for the Northern Hemisphere]. Izv. AN SSSR, ser. geofiz., No. 2, 1962.

Sh. A. Musayelyan

CERTAIN PROBLEMS DEALING WITH THE NUMERICAL INTERPRETATION OF CLOUD INFORMATION RECEIVED FROM ARTIFICIAL EARTH SATELLITES

Introduction

Study [1] demonstrated a method of making a quantitative interpretation of cloud information as received from an artificial earth satellite (AEC). It was shown that at each latitude the following relationships held true between the Fourier coefficients of cloud fields and vertical currents:

$$\left.\begin{aligned} W_m(\theta) &= a_m(\theta) S_m(\theta) + b_m(\theta) \\ W'_m(\theta) &= a'_m(\theta) S'_m(\theta) + b'_m(\theta) \end{aligned}\right\} \qquad (1)$$

Here, S_m, S_m' and W_m, W_m' are the Fourier coefficients of the m-th order for cloud fields and vertical currents respectively. In this, the constants a_m, b_m, a_m', and b_m' were computed by the method of least squares in accordance with observation data for the month of July 1962. The computations showed that these constants can be used not only for the month of July, but also for other months during the warm half of the year. At any rate, computations on vertical currents of a cloud field for June and August of 1962, as well as for May of 1960 gave completely satisfying results.

Analysis of a large number of cloud charts demonstrated [1, 2] that large scale cloud fields have a definite conservative property and change very little from day to day, although the cloud cover may undergo considerable changes in specific points for short periods of time.

Since it is possible to compute diagnostic, vertical currents by this method, the question arises about their utilization.

By way of application of this method, let us consider the problem of determining the geopotential field of cloud distribution.

1. Determining the Current Function Field by Cloud Distribution.

The problem of determining the field of vertical currents by a geopotential field has already become a classic. Setting up the problem in this manner was occasioned by the fact that the vertical velocity is not measured by instruments and the meteorologists were therefore forced to compute it by the geopotential, which is measurable. However, because artificial earth satellites can now provide sufficiently representative and detailed information about earth cloud cover with the aid of which it is possible to determine the distribution of vertical currents, we are confronted with the reverse problem -- the problem of finding the geopotential field by the distribution of vertical currents.

Assume that we have given the function $S(\theta, \lambda, z, t)$, which describes the cloud field in space and time, and that it is required to determine the geopotential field $h(\theta, \lambda, z, t)$. Since the function $S(\theta, \lambda, z, t)$ is given, the field of vertical currents is computed in accordance with the above-described method. Thus, the problem boils down to establishing the relationship between the geopotential field and the distribution of vertical currents.[1]

As a basic equation, let us consider the linearized relationship of the zonal flux of the equation of vorticity expressed as follows:

$$\frac{\partial \Delta\psi}{\partial t} + \alpha(z)\frac{\partial \Delta\psi}{\partial \lambda} + 2(\alpha + \omega)\frac{\partial \psi}{\partial \lambda} = \frac{a^2\omega\cos\theta}{\tilde{p}}\frac{\partial \tilde{p}\, w}{\partial z}. \qquad (1.1)$$

Here, $\psi(\theta, \lambda, z, t)$ and $w(\theta, \lambda, z, t)$ are the deviations from the zonal value of the function of current and vertical velocity, respectively, $\alpha(z)$

1. After this article was prepared for publication, there appeared the work by E. N. Blinova, corresponding member of the USSR Academy of Sciences, in which consideration is given to the more general problem of determining the current function field by distribution of vertical movements and temperatures [12].

is the index of circulation of the atmosphere, ω is the angular speed of the earth's rotation, t is the time, λ is the geographic longitude, is the supplement to the latitude, $\tilde{\rho}(z)$ is the density which is a function of the altitude, and a is the mean radius of the earth.

Equation (1.1) will be resolved given the following initial conditions: $t = 0$ $\psi = \psi^{(0)}$ is a predetermined function.

For purposes of simplicity we will designate the right portion of the equation (1.1) as $f(\theta, \lambda, z, t)$ and introduce the time spacing δt such as to fulfill the following approximate relationships [3]:

$$\left.\begin{aligned} \frac{\partial \Delta\psi}{\partial t} &\approx \frac{\Delta\psi^{(1)} - \Delta\psi^{(0)}}{\delta t}; \quad \frac{\partial \Delta\psi}{\partial \lambda} \approx \frac{\partial}{\partial \lambda}\left\{\frac{\Delta\psi^{(1)} + \Delta\psi^{(0)}}{2}\right\} \\ \frac{\partial \psi}{\partial \lambda} &\approx \frac{\partial}{\partial \lambda}\frac{\psi^{(1)} + \psi^{(0)}}{2}; \quad f = \frac{f^{(1)} + f^{(0)}}{2} \end{aligned}\right\} \tag{1.2}$$

in which the sign (0) is used to designate the values of the functions considered at the initial moment, and (1) issued to designate these functions at the end of the first spacing with respect to time.

Taking into account (1.2), equation (1.1) can be rewritten as follows:

$$\Delta\psi^{(1)} + \frac{a\delta t}{2}\frac{\partial \Delta\psi^{(1)}}{\partial \lambda} + \omega\delta t \frac{\partial \psi^{(1)}}{\partial \lambda} = \Delta\psi^{(0)} - \frac{a\delta t}{2}\frac{\partial \Delta\psi^{(0)}}{\partial \lambda} -$$

$$- \omega\delta t \frac{\partial \psi^{(0)}}{\partial \lambda} + \frac{\delta t}{2}\left(f^{(1)} + f^{(0)}\right) \ldots . \tag{1.3}$$

In this equation the value α is negligible in comparison with ω; all functions in the right portion are deemed known, and $\psi^{(1)}$ is the unknown function.

We represent the functions under consideration as follows:

$$\left.\begin{aligned} f^{(0)} &= \mathrm{Re}\sum_{n=1}^{\infty}\sum_{m=1}^{n} \bar{f}_{0n}^{m} e^{-im\lambda} P_n^m(\cos\theta) \\ f^{(1)} &= \mathrm{Re}\sum_{n=1}^{\infty}\sum_{m=1}^{n} \bar{f}_{1n}^{m} e^{-im\lambda} P_n^m(\cos\theta) \\ \psi^{(0)} &= \mathrm{Re}\sum_{n=1}^{\infty}\sum_{m=1}^{n} \bar{\psi}_{0n}^{m} e^{-im\lambda} P_n^m(\cos\theta) \\ \psi^{(1)} &= \mathrm{Re}\sum_{n=1}^{\infty}\sum_{m=1}^{n} \bar{\psi}_{1n}^{m} e^{-im\lambda} P_n^m(\cos\theta) \end{aligned}\right\} \tag{1.4}$$

in which

$$\left.\begin{aligned} \bar{f}^m_{0n} &= f^m_{0n} + i f'^m_{0n}; \quad \bar{f}^m_{1n} = f^m_{1n} + i f'^m_{1n} \\ \bar{\psi}^m_{0n} &= \psi^m_{0n} + i \psi'^m_{0n}; \quad \bar{\psi}^m_{1n} = \psi^m_{1n} + i \psi'^m_{1n} \end{aligned}\right\} \tag{1.5}$$

and P^m_n is added through the Legendre polynomial.

From equation (1.3) it follows, taking into account relationships (1.4) and (1.5), that the unknown coefficients ψ^m_{1n} and ψ'^m_{1n} are determined from the following linear algebraic system:

$$\left.\begin{aligned} n(n+1)\psi^m_{1n} - \left[\tfrac{a}{2} n(n+1) - \omega\right] m\delta t\, \psi'^m_{1n} &= n(n+1)\psi^m_{0n} - \\ - \left[\tfrac{a}{2} n(n+1) - \omega\right] m\delta t\, \psi'^m_{0n} &+ \tfrac{\delta t}{2}\left(f^m_{0n} + f^m_{1n}\right) \\ \left[\tfrac{a}{2} n(n+1) - \omega\right] m\delta t\, \psi^m_{1n} - n(n+1)\psi'^m_{1n} &= -n(n+1)\psi'^m_{0n} - \\ - \left[\tfrac{a}{2} n(n+1) - \omega\right] m\delta t\, \psi^m_{0n} &+ \tfrac{\delta t}{2}\left(f'^m_{0n} + f'^m_{1n}\right) \end{aligned}\right\} \tag{1.6}$$

Whence,

$$\left.\begin{aligned} \psi^m_{1n} = {} & \frac{1 - \left\{\left[\frac{a}{2} - \frac{\omega}{n(n+1)}\right] m\delta t\right\}^2}{1 + \left\{\left[\frac{a}{2} - \frac{\omega}{n(n+1)}\right] m\delta t\right\}^2} \psi^m_{0n} - \\ & - \frac{2\left[\frac{a}{2} - \frac{\omega}{n(n+1)}\right] m\delta t}{1 + \left\{\left[\frac{a}{2} - \frac{\omega}{n(n+1)}\right]^2 m^2 (\delta t)^2\right\}^2} \psi'^m_{0n} - \\ & - \frac{\delta t}{2n(n+1)\left\{1 + \left[\frac{a}{2} - \frac{\omega}{n(n+1)}\right]^2 m^2 (\delta t)^2\right\}^2} \left(f^m_{0n} + f^m_{1n}\right) + \\ & + \frac{\left[\frac{a}{2} - \frac{\omega}{n(n+1)}\right] m \frac{(\delta t)^2}{2}}{n(n+1)\left\{1 + \left[\frac{a}{2} - \frac{\omega}{n(n+1)}\right]^2 m^2 (\delta t)^2\right\}^2} \left(f'^m_{0n} + f'^m_{1n}\right) \end{aligned}\right\} \tag{1.7}$$

$$\left.\begin{aligned} \psi'^m_{1n} = {} & \frac{2\left[\frac{a}{2} - \frac{\omega}{n(n+1)}\right] m\delta t}{1 + \left\{\left[\frac{a}{2} - \frac{\omega}{n(n+1)}\right] m\delta t\right\}^2} \psi^m_{0n} - \\ & - \frac{1 - \left\{\left[\frac{a}{2} - \frac{\omega}{n(n+1)}\right] m\delta t\right\}^2}{1 + \left\{\left[\frac{a}{2} - \frac{\omega}{n(n+1)}\right] m\delta t\right\}^2} \psi'^m_{0n} - \\ & - \frac{\delta t}{2n(n+1)\left\{1 + \left[\frac{a}{2} - \frac{\omega}{n(n+1)}\right]^2 m^2 (\delta t)^2\right\}} \left(f'^m_{0n} + f'^m_{1n}\right) - \\ & - \frac{\left[\frac{a}{2} - \frac{\omega}{n(n+1)}\right] m \frac{(\delta t)^2}{2}}{n(n+1)\left\{1 + \left[\frac{a}{2} - \frac{\omega}{n(n+1)}\right]^2 m^2 (\delta t)^2\right\}} \left(f^m_{0n} + f^m_{1n}\right) \cdots \end{aligned}\right\}$$

These formulas are a solution of the problem posed.

It should be noted that the factors with ψ^{m}_{0n}, ψ'^{m}_{0n}, $(f^{m}_{0n} + f^{m}_{1n})$ and $(f'^{m}_{0n} + f'^{m}_{1n})$ in formulas (1.7) are proper fractions. In order to make computations in accordance with the system proposed, it is essential to have information about the initial distribution of current functions and about the cloud condition at moment t_o, as well as information about the cloud cover at moment $t_o + \delta t$. If such data are available, ψ^{m}_{1n} and ψ'^{m}_{1n} can be determined by formulas (1.7), and the function $\psi^{(1)}$ can be determined by the fourth formula of (1.4).

Now, instead of relationships (1.2) we take into consideration the following:

$$\frac{\partial \Delta\psi}{\partial t} \approx \frac{\Delta\psi^{(2)} - \Delta\psi^{(1)}}{\delta t}; \quad \frac{\partial \Delta\psi}{\partial \lambda} \approx \frac{\partial}{\partial \lambda}\left(\frac{\Delta\psi^{(2)} + \Delta\psi^{(1)}}{2}\right)$$
$$\frac{\partial \psi}{\partial \lambda} \approx \frac{\partial}{\partial \lambda}\frac{\psi^{(2)} + \psi^{(1)}}{2}; \quad f = \frac{f^{(2)} + f^{(1)}}{2} \ldots, \tag{1.8}$$

and get equation

$$\Delta\psi^{(2)} + \frac{2\delta t}{2}\frac{\partial \Delta\psi^{(2)}}{\partial \lambda} + \omega\delta t\frac{\partial \psi^{(2)}}{\partial \lambda} = \Delta\psi^{(1)} - \frac{2\delta t}{2}\frac{\partial \Delta\psi^{(1)}}{\partial \lambda} - \omega\delta t\frac{\partial \psi^{(1)}}{\partial \lambda} +$$
$$+ \frac{2\delta t}{2}(f^{(2)} + f^{(1)}) \ldots. \tag{1.9}$$

The right portion of this equation contains only known functions.

The unknown function $\psi^{(2)}$ is determined in exactly the same manner as $\psi^{(1)}$ from equation (1.3). After determining $\psi^{(2)}$, we find $\psi^{(3)}$, and so on.

2. Determining $\psi^{(o)}$

As a first step we propose the following less strict but simpler method of calculation to determine $\psi^{(o)}$. To be sure, this method of determining the field of the current functions will describe the real picture only in a general way, but as preliminary calculations have demonstrated, it can be used as initial data in resolving equations (1.3).

We have already indicated that large-scale cloud fields have a certain conservative aspect; they change very little over a 24-hour period. If we take into account such large-scale cloud fields and the basic patterns associated with them and disregard the rapidly moving small-scale formations, we can consider the process as approximating a stationary condition.

If this is so, we can propose, by way of a first experiment, that the relationship between the current function and the vertical speed in the initial moment can be given by the equation for vorticity, which is written as follows:

$$a\frac{\partial \Delta\psi^{(0)}}{\partial\lambda}+2(\alpha+\omega)\frac{\partial\psi^{(0)}}{\partial\lambda}-\frac{\nu}{a^2}\Delta\Delta\psi^{(0)}=\frac{2\omega a^2\cos\theta}{\tilde{p}}\frac{\partial\tilde{p}w}{\partial z}. \qquad (2.1)$$

If we introduce the following into the function under consideration

$$\phi=\frac{1}{H}\int_0^H\psi^{(0)}dz,$$

where H is the height of the tropopause, then (2.9) [sic] will appear as follows:

$$a\frac{\partial\Delta\psi}{\partial\lambda}+2(\alpha+\omega)\frac{\partial\psi}{\partial\lambda}-\frac{\nu}{a^2}\Delta\Delta\psi=\frac{2a^2\omega\cos\theta}{H}\int_0^H\frac{\partial\tilde{p}w}{\tilde{p}\partial z}dz\ \ldots \qquad (2.2)$$

Function ψ, which is a mean current function for the entire thickness of the troposphere, is assumed to apply to level AT_{500}.

The relationship to z of function w is given in accordance with the parabolic law:

$$w(\theta,\lambda,z,t)=\left(\frac{2z}{z_{av}}-\frac{z^2}{z^2_{av}}\right)w_{cp}(\theta,\lambda,t). \qquad (2.3)$$

Here, z_{av} is the height of the so-called mean level of the atmosphere, w_{av} is the vertical velocity at this level. From formula (2.3) it follows that the vertical velocity attains its maximum at altitude $z = z_{av}$.

If, in addition, we assume that

$$\tilde{p}=p_0\left(1-\frac{\gamma}{T_0}z\right)^{\frac{g}{\gamma R}-1} \qquad (2.4)$$

(ρ_0 and T are the density and temperature at sea level respectively, γ is the vertical temperature gradient, g is the acceleration of gravity, R is the gas constant), the integral in the right portion of the equation is computed and this equation will appear as follows:

$$a\frac{\partial \Delta\psi}{\partial\lambda}+2(z+\omega)\frac{\partial\psi}{\partial\lambda}-\frac{\nu}{a^2}\Delta\Delta\psi=rw_{av}\cos\theta, \tag{2.5}$$

in which

$$r\approx -1{,}283\frac{2\omega a^2}{H}.$$

In computing the integral referred to, the following values of constants were used: $g = 10\text{m/sec.}$, $\gamma = 5.10^{-3}$ degrees/meter, $H = 10^4$ m, $T_0 = 250^\circ$, $z_{av} = 5.10^3$ m, and $R = 287\ \text{m}^2/\text{sec}^2$ degree.

If the function $w_{av}\cos\theta$ is presented as a series in accordance with Legendre polynomials

$$w_{av}\cos\theta=\sum_{n=1}^{\infty}\sum_{m=1}^{n}\left(w_n^m\cos m\lambda+w_n^{'m}\sin m\lambda\right)P_n^m(\cos\theta) \tag{2.6}$$

and seek a solution of equation (2.5) in the form

$$\psi=\sum_{n=1}^{\infty}\sum_{m=1}^{n}\left(\psi_n^m\cos m\lambda+\psi_n^{'m}\sin m\lambda\right)P_n^m(\cos\theta), \tag{2.7}$$

then

$$\left.\begin{aligned}\psi_n^m&=\frac{r}{\omega}\,\frac{m\left[\frac{a}{\omega}n(n+1)-2\right]w_n^{'m}-\frac{\nu}{a^2\omega}n^2(n+1)^2w_n^m}{m^2\left[\frac{a}{\omega}n(n+1)-2\right]^2+\frac{\nu^2}{a^4\omega^2}n^4(n+1)^4}\\ \psi_n^{'m}&=-\frac{r}{\omega}\,\frac{m\left[\frac{a}{\omega}n(n+1)-2\right]w_n^m+\frac{\nu}{a^2\omega}n^2(n+1)^2w_n^{'m}}{m^2\left[\frac{a}{\omega}n(n+1)-2\right]^2+\frac{\nu^2}{a^4\omega^2}n^4(n+1)^4}\end{aligned}\right\} \tag{2.8}$$

in which

$$\left.\begin{aligned}w_n^m&=2\int_0^{\frac{\pi}{2}}\left[a_m(\theta)S_m(\theta)+b_m(\theta)\right]P_n^m(\cos\theta)\sin\theta\,d\theta\\ w_n^{'m}&=2\int_0^{\frac{\pi}{2}}\left[a'_m(\theta)S'_m(\theta)+b'_m(\theta)\right]P_n^m(\cos\theta)\sin\theta\,d\theta\end{aligned}\right\} \tag{2.9}$$

Formulas (2.7) - (2.9) make it possible to determine by the cloud field the field of the current function $\psi^{(0)}$, and, therefore, the geopotential field, because if $S_m(0)$ and $S'_m(0)$ are known, then we can determine from formulas (1) and (2.8) w_m, w'_m and φ_m^m, $\varphi_m'^m$ respectively, and the field of the current function is computed by (2.7).

3. Samples of Computation.

In accordance with the theory presented in the foregoing, the problem is programmed so that when cloud information in the northern hemisphere is fed into the machine as initial data, one immediately gets the geopotential field for these regions.

We offer two examples computed by stages: first, the distribution of vertical currents was computed by cloud fields on a high-speed computer, and then the geopotential fields were computed on an ordinary arithmometer according to formulas (2.7) - (2.8).

We shall consider each of these examples separately.

Given in Fig. 1 [2] is a picture of cloud vortexes in a family of cyclones located over the Pacific Ocean and North America photographed by satellite Tiros-I on 20 May 1960, and the corresponding chart of ground pressures with the system of atmospheric fronts (the light background corresponds to solid cloud cover).

Shown in Fig. 2a are the deviations from zonal heights of the isobaric surface ΔT_{500} computed from the cloud field.

In computing the geopotential h by the stream function, the following well-known approximation relationship was used:

$$h \approx \frac{l}{g}\psi,$$

where l is the Coriolus parameter as a function of the latitude. In addition, the following values of constants were used: $\nu = 3.10^5$ m^2/sec.,

ω = $7.29.10^{-5}$ sec.$^{-1}$, a = $6.37.10^{6}$ M, $\frac{\alpha}{\omega}$ = 0.021. (The values of $\frac{\alpha}{\omega}$ here and further on are taken from materials available in the long-range forecast section of VMTs GUGMS [Main Administration of the Hydrometeorological Service of the USSR].).

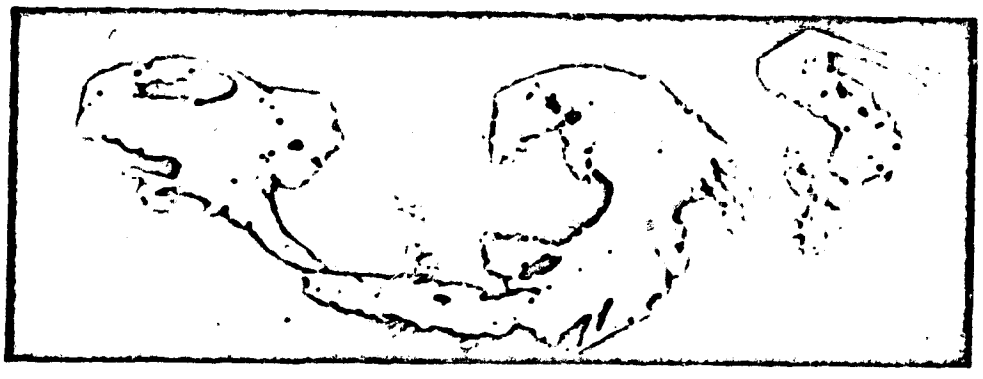

Fig. 1a. Family of cloud vortexes photographed from satellite Tiros-I on 20 May 1960 over the northern part of the Pacific Ocean, Canada, and northwestern United States [8].

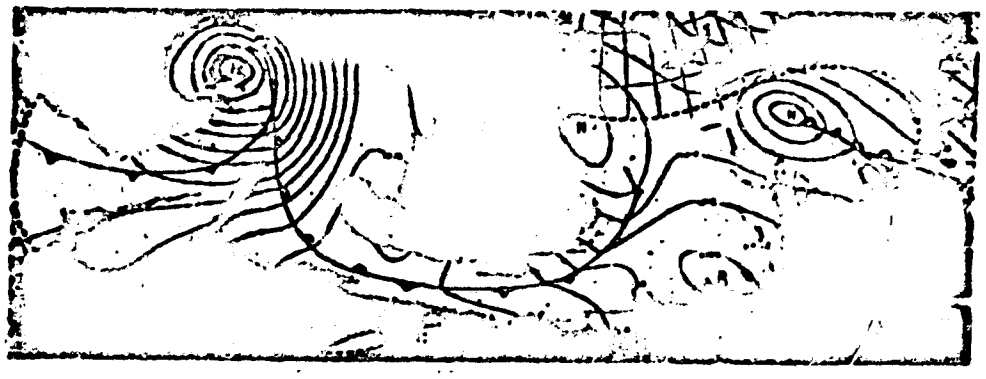

Fig. 1b. Chart of ground pressures on 20 May 1960. Light areas -- solid overcast; dark areas -- no clouds [8]

Since extensive cloud fields have a certain conservative aspect, the computed chart (Fig. 2a) can be compared with the actual chart ΔT_{500} for 0300 hours on 20 May 1960.

Such a comparison shows a definite resemblance between the two charts, the only difference being that the cyclone, whose center on the actual chart is at coordinates 54° Latitude South, 142° Longitude East, appeared to be shifted markedly toward the southeast. This was apparently due to the following. First, from the actual ground chart it is apparent that the information

about the clouds in the area of the cyclone was not complete -- all data for the area north of the cyclone center were missing. Secondly, and this is important, in the high pressure ridge area over the western coast of the USA solid overcast was noted. Together with the solid overcast area located in the forward portion of the cyclone under consideration it constituted a sort of single cloud field.[1]

Thirdly, in the rear of the cyclone there was predominantly good weather with few clouds.

Fig. 2a. Computed field of variations of AT_{500} from zonal values.

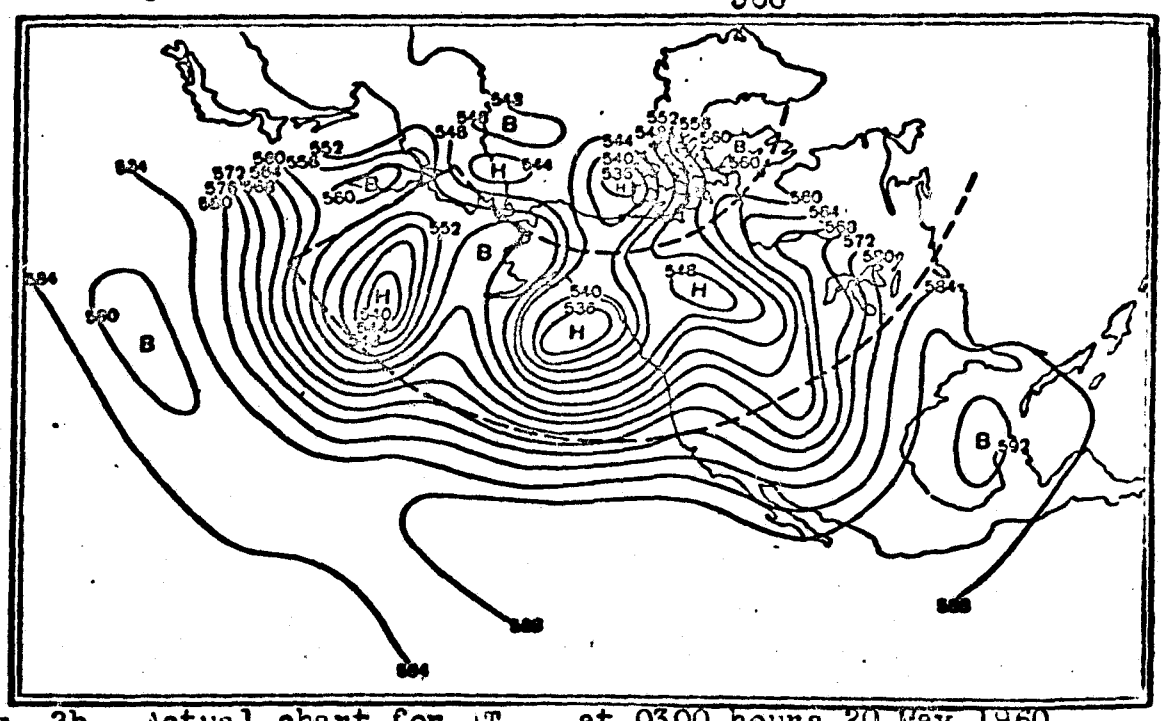

Fig. 2b. Actual chart for AT_{500} at 0300 hours 20 May 1960.

1. In the next 12 hours the cyclone was observed to move southeast at about 40 km/hr.

The second and third causes may be studied in detail after a large number of examples have been computed and thoroughly analyzed.

Using similar reasoning one might explain the fact that the cyclone, whose center on the actual chart AT_{500} has its coordinates at 47° Latitude South and 180° Longitude East, is also shifted toward the east.

We will now consider a second example.

Shown in Fig. 3a is the field of deviation from zonal values of heights of isobaric surface AT_{500}, computed from the actual distribution of cloud cover for 0300 hours 6 July 1962, throughout the entire northern hemisphere. Fig. 3b shows the actual chart of AT_{500} for this same time. In the computations $\frac{\alpha}{\omega} = 0.019$.

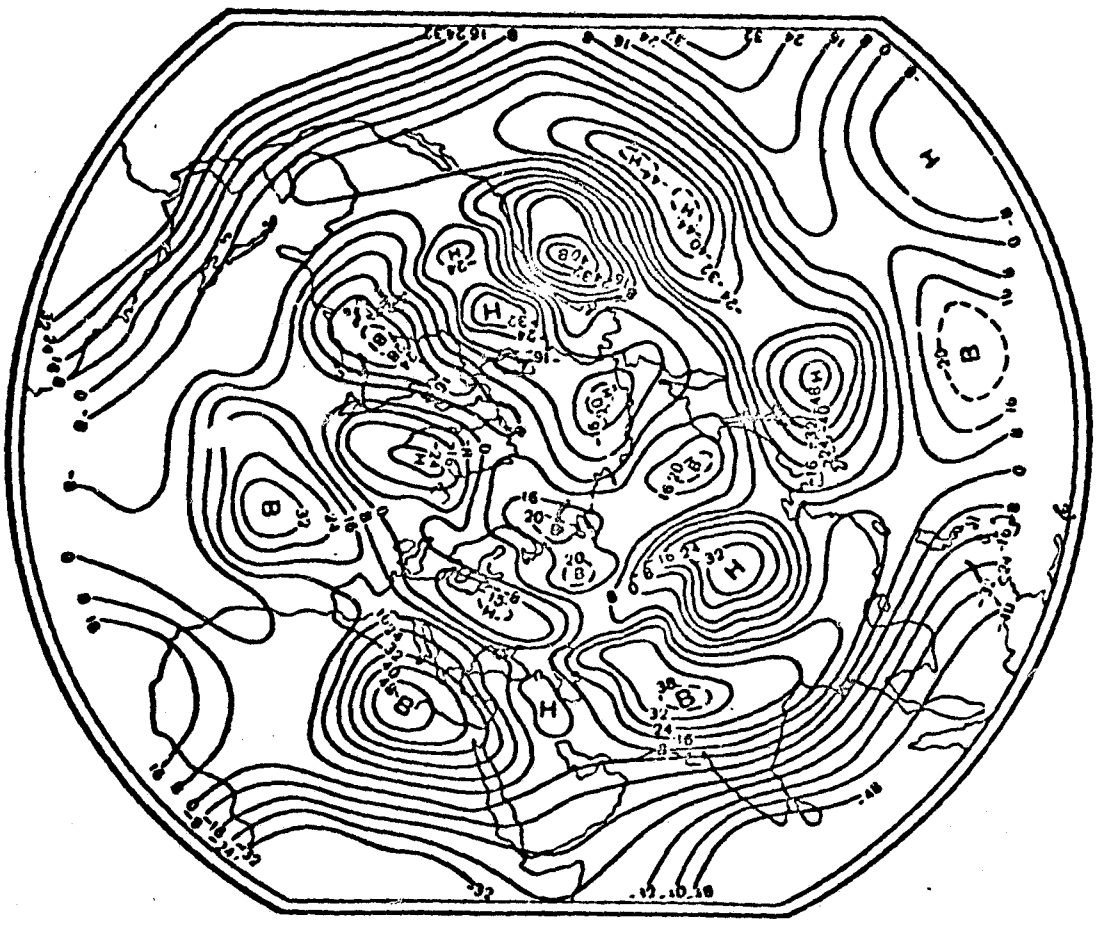

Fig. 3a. Computed field of deviations AT_{500} from the zonal values for 0300 hours on 6 July 1962.

The results of computations for the lower latitudes (south of 30° Latitude South) should be examined rather critically, because these regions had

Fig. 3b. Actual chart AT_{500} for 0300 hours on 6 July 1962.

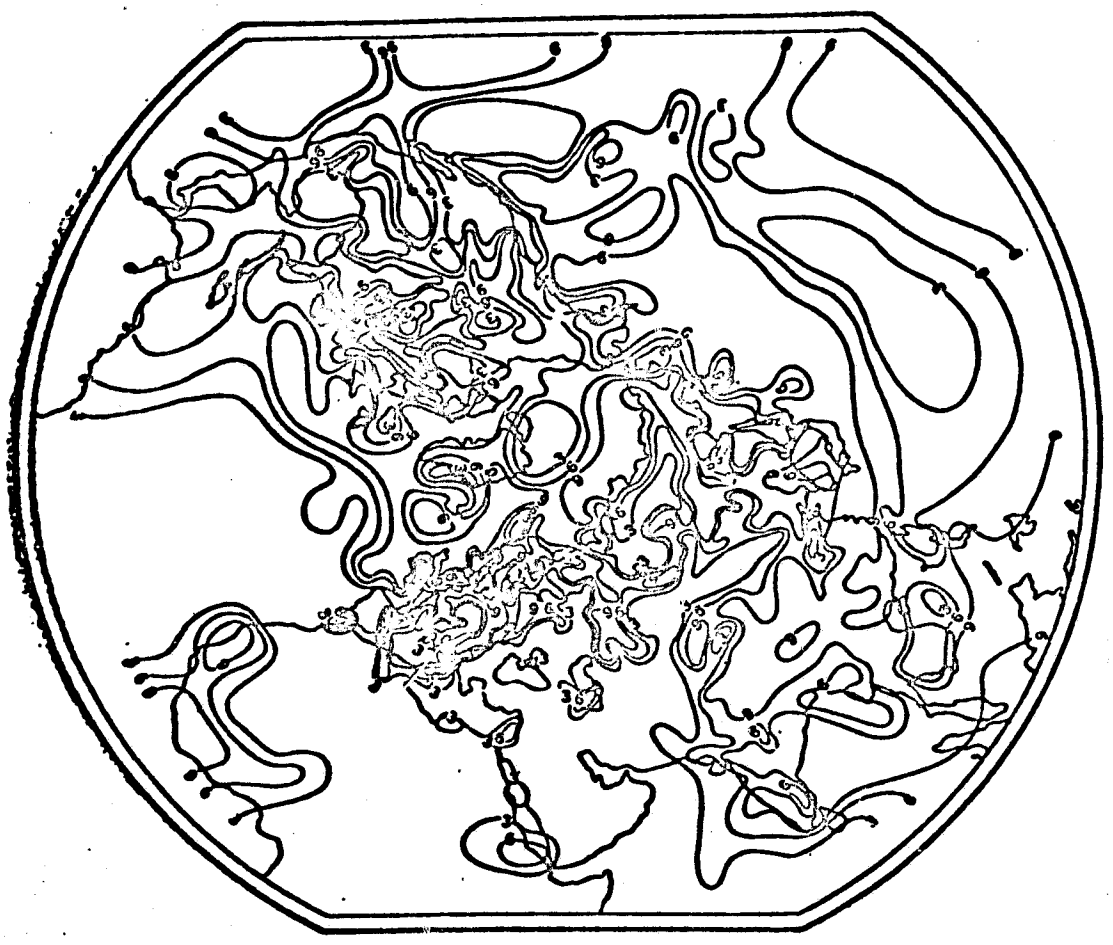

Fig. 3c. Value of cloud cover taken in geographic grid node from chart of total cloud cover for 0300 hours 6 July 1962.

insufficient data on cloud cover. One should be especially critical of the numerical values of the coupling coefficient. All that has been said pertains also to the polar regions.

If we now compare the computed geopotential field with the actual chart, we will find that above the eastern regions of North America the results of computation proved very poor. On the actual chart above these regions there is found a deep cyclone with many closed isohypses, whereas on the computed chart above these areas there was obtained a high pressure region with a north-oriented narrow ridge. Thus, above these regions the results of computation proved directly opposite to the actual picture of the isohypse field. The reason for this will become clear if we refer to Fig. 3c on which are shown the values of the actual cloud conditions photographed on a geographic grid; these are the values on which the computations were made. From this chart it appears that directly over the regions mentioned there is some insignificant cloud cover, the zone of minimum clouds being extended in a northerly direction as a narrow band. We should also take into account the fact that in computing the geopotential field use was made of a different geographic grid whose longitude nodes were spaced 15° (this was dictated by the fact that the geopotential field was computed manually at the NIIAK factory, where similar computations are made on just such a grid).

The computed field of absolute topography over all of Europe agrees generally with the actual chart, although the cyclone with its center over southern Scandinavia was extended in latitude because of the zone of solid clouds over Belorussia, and the depressions over Baykal and Kamchatka are shifted toward the south. Further, if the results of computations were far from realistic on the poorly scanned eastern regions of the Pacific Ocean, the general picture of the areas of the United States and Canada between 130° Longitude and 90° West was grasped.

Thus, an analysis of the computations made demonstrates that the proposed method can be used for computing the initial fields of absolute topography by cloud distribution.

References

1. Musayelyan, Sh. A., Chekirda, A. I. O chislennoy interpretatsii oblachnosti postupayushchey iz meteorologicheskikh sputnikov. See this collection.
2. Boucher, Roland J., Newcomb, Ralph I. Synoptic interpretation of Tiros vortex patterns: A preliminary cyclone model. "J. Appl. Meteorol." 1962, 1, N2, 127-136.
3. Sadokov, V. P. O priblizhennykh resheniyakh nelineynogo oravneniya vikhrya skorosti v sredney troposfere. DAN SSSR, v. 134, No. 3, 1960.
4. Blinova, E. N. Metod resheniya nelineynoy zadachi ob atmosfernykh dvizheniyakh planetarnogo masshtaba, DAN SSSR, V. 110, No. 6, 1956.
5. Buleyev, N. I. and Marchuk, G. I. O dinamike krupnomasshtabnykh atmosfernykh protsesov. Tr. IFA AN SSSR, No. 2, 1958.
6. Musayelyan, Sh. A. Planetarnyye orograficheskiye volny v zapadnom potoke. "Voprosy dinamicheskoy meteorologii." Izd. AN SSSR, M., 1960.
7. Neiburger, M. and Wexler, H. Weather satellites. Scientific American, July, 1961.
8. Annual Report of the World Meteorological Organization, 1961, WMO -- No. 115, RP. 47, pp. 52-53.
9. Mashkovich, S. A. Kuchetu effekta nelineynykh chlenov oravneniy pri reshenii zadachi o prognoze davleniya i temperatury maloy zablagovremmennosti. Tr. TsIP, Vol. 60, 1957.
10. Mashkovich, S. A. K teorii voln davieniya v baroklinnoy atmosfere. Tr. TsIP, vyp. 111, 1961.
11. Blinova, E. N. K teorii godovogo khoda nezonal'noy tsirkulyatsii atmosfery Zemli. Tr. IFA AN SSSR, No. 2, 1959.
12. Blinova, E. N. Ob opredelenii nachal'nykh poley davleniya i vetri po raspredeleniyu temperatury i vertikal'nykh dvizheniy vozdukha. DAN SSSR v. 149, No. 4, 1963.

L. T. Matveyev

METHOD OF COMPUTING THE ALTITUDE OF THE UPPER BOUNDARY OF CLOUDS AND REQUIREMENTS FOR ACCURACY IN DETERMINING INFRARED RADIATION FLUXES WITH SATELLITES

The launching of weather satellites opens up broad possibilities for developing some new methods of diagnosing the predicting individual meteorological elements, phenomena, and, in the final analysis, the weather as a whole. Cloud cover is one of these phenomena. It has a considerably greater effect on the thermic changes of the atmosphere and the earth's surface and, therefore, on the field of winds and pressures because they depend on the distribution of temperature in space and its changes in time.

Cloud cover is an atmospheric element which can be observed with equipment mounted in a satellite in a most complete and reliable manner.

In order to make use of the data which can be obtained from a satellite, it is necessary to develop a theory tying in cloud cover parameters (as well as other atmospheric elements) with those magnitudes about which information is received from satellites.

In this article there has been developed a theory for determining the upper limit of clouds. By means of it we can resolve two basic problems applied to satellites:

a) we can formulate the requirements to be set forth concerning accuracies in measuring infrared radiation fluxes which come from the atmosphere and are registered in the weather satellite;

b) we can develop a method of using one of the most important magnitudes about which information can be obtained only with a satellite -- the integral (total) flux of infrared radiation given off by the earth's surface and atmosphere.

In some previous works by the author [2,3] there was developed a sufficiently

general method of analysis of a system of equations for the transfer of humidity and heat in a turbulent atmosphere. That method allows one to study the process of cloud evolution and formation, trace the distribution of temperature, humidity and water content by altitude, as well as to note changes in the boundary of cloud cover in time in a general (non-stationary) case. However, concrete computations by a complete system of equations is possible only with electronic computers.

In this article the author will restrict himself to a sufficiently detailed review of special, but in practice exceptionally important, instance -- the quasi-stationary distribution of cloud characteristics. Compared with previous studies, this work contains an element of generalization: it takes into account the effect of falling droplets affected by the force of gravity, and, what is especially important from the standpoint of utilization of data received from satellites, it takes into account the influence of radiating heat currents on the formation of clouds (primarily in the upper boundary).

1. Equation for moisture balance in a cloud. Velocity of fall of cloud elements and humidity flow caused thereby.

The transfer and redistribution of moisture in the atmosphere (in all of its phases) is mathematically described by the following differential equation and partial derivates:

$$\rho\frac{\partial s}{\partial t}+\rho\left(u\frac{\partial s}{\partial x}+v\frac{\partial s}{\partial y}\right)+\rho w\frac{\partial s}{\partial z}=\frac{\partial}{\partial z}\rho k\frac{\partial s}{\partial z}-\frac{\partial Q_k}{\partial z}. \qquad (1)$$

Here, s is the specific moisture content of a cloud, i.e., the mass of water vapor, drops of water and drystal ice in a unit mass of air; u, v, and w are the projections of the regulated speed of transfer of air mass on the rectangular axes x, y, and z respectively (the axes x and y are horizontal; axis z is directed vertically upward); t is time; k is the coefficient of turbulence (with dimensionality $cm^2\ sec^{-1}$); ρ is the air density; and Q_k is the flow of water droplets and ice crystals due to the force of gravity (g/cm^2 sec).

In equation (1) all the components in the left portion have the same order of magnitude. However, members $\rho\frac{\partial s}{\partial t}$ and $\rho\left(u\frac{\partial s}{\partial x}+v\frac{\partial s}{\partial y}\right)$ have opposite signs in the overwhelming majority of cases. Actually, from synoptic tests it is well known that in the advection of the more moist air (as a rule, more warm air) when the component $\rho\left(u\frac{\partial s}{\partial x}+v\frac{\partial s}{\partial y}\right)$ is less than zero[1], the moisture content of the air at fixed points in space increases with time $\left(\rho\frac{\partial s}{\partial t}\geqslant 0\right)$. And inversely, in the advection of less moist air (as a rule, more cold air) when the component $\rho\left(u\frac{\partial s}{\partial x}+v\frac{\partial s}{\partial y}\right)$ is greater than zero, the moisture content of the air at points with fixed coordinates decreases with time $\left(\rho\frac{\partial s}{\partial t}<0\right)$. Thus, components $\rho\frac{\partial s}{\partial t}$ and $\rho\left(u\frac{\partial s}{\partial x}+v\frac{\partial s}{\partial y}\right)$, being of the same order of magnitude but opposite in sign, will in summary give a value which is considerably less (at least by one order) than the third component in the left portion of the equation (1). Because of this, in solving the problems we can write down equation (1) in a first approximation as follows:

$$\frac{d}{dz}\left(\rho\frac{ds}{dz}\right)-\rho w\frac{ds}{dz}-\frac{dQ_k}{\partial z}=0. \qquad (2)$$

We shall call this the balance of moisture in the cloud equation.

It should be emphasized that disregarding the advection of moisture in passing over from (1) to (2) does not by any means lessen its role in the process of cloud formation and production of precipitation. It follows from the foregoing considerations that local changes in moisture content are determined to a marked degree by advection (horizontal transfer of moisture); this was demonstrated from the quantitative standpoint for the first time by E. K. Fedorov and E. F. Mamina [1]. However, distribution of moisture vertically, which governs the distribution of water and the position of cloud boundaries, is determined mainly by turbulence exchange regulated by vertical

1. We can become convinced of this most simply if the axis x is directed along the speed of transfer. Then $u > 0$, $v = 0$, $\frac{ds}{dx} < 0$, and, consequently, $\frac{\partial s}{\partial x}+v\frac{\partial s}{\partial y}<0$.

currents and moisture currents under the influence of gravity.

The physical essence of the moisture balance equation is as follows. The first two components take into account the influx of water vapor and cloud elements (droplets of water and ice crystals) to a unit volume of air under the influence of a turbulent exchange and regulated vertical currents. In this, basing ourselves on previous studies, we feel that drops of water and ice crystals are completely evicted by turbulent particles (this was reflected in the fact that the coefficient of turbulence is the same for water vapor and drops of water). However, within the limits of a turbulent particle the droplets have their own speed of motion due to the force of gravity. This effect is described from the quantitative aspect by the 1st component in equation (2).

We shall pause, first of all, to get the relationships for the flow Q_k. If v(r) stands for the speed of fall of drops of radius r, and f(r) is the function of distribution of drops by their dimensions, then, due to the falling of drops of radius r through 1 cm^2 of horizontal area per second there passes a mass of water equal to:

$$n f(r) dz \cdot \frac{4}{3} \pi \rho_k r^3 v(r),$$

where n is the total number of drops and crystals in 1 cm^3 of cloud air; ρ_k is the density of water droplets or crystals of ice. Summating the last expression for all radii, we get a formula for the flow of water droplets and crystals of ice

$$Q_k = -\frac{4}{3} \pi n \rho_k \int_0^\infty r^3 f(r) v(r) dr \qquad (3)$$

(streams directed upward are deemed positive). On the other hand, we can set down the following relationship for the specific water content of a cloud δ (the mass of water droplets and ice crystals in one gram of air):

$$\delta = s - q_m = \frac{n}{\rho} \int_0^\infty \frac{4}{3} \pi \rho_k r^3 f(r)\, dr, \tag{4}$$

in which q_m is the maximum specific humidity; $\frac{n}{\rho}$ is the number of droplets and crystals of ice in 1 gram of air.

From equations (3) and (4) it follows that

$$Q_k = -\rho(s - q_m)\tilde{v}, \tag{5}$$

in which $\tilde{v}$ is the weighted mean velocity of fall of cloud elements.

$$\tilde{v} = \frac{\int_0^\infty r^3 f(r)\, v(r)\, dr}{\int_0^\infty r^3 f(r)\, dr}. \tag{6}$$

Taking into account relationship (5) the equation for moisture balance in a cloud may be rewritten in the following form:

$$\frac{d}{dz}\left(k\rho \frac{ds}{dz}\right) - \frac{d(\rho w s)}{dz} + \frac{d\rho \tilde{v}(s - q_m)}{dz} = 0. \tag{7}$$

2. Suspended mean velocity of fall of cloud elements.

Since velocity $\tilde{v}$ is of interest not only in connection with the solution of the problem under consideration, we shall pause to make a somewhat detailed analysis of it. The velocity of fall of water droplets in the air does not, in contrast with solid particles, increase without limit with increased size; rather, it strives toward a certain finite value because of the flattening of the droplets. An analysis of experimental materials, the most complete of which were the data presented by Gunn and Kinzer [10], showed that the relationship of the velocity of fall of droplets to the radius can be approximated to a satisfactory degree of accuracy by the following formula:

$$v(r) = v_\infty [1 - \exp(-ar)]. \tag{8}$$

The constants v_∞ and a being determined by the method of least squares, were equal to $v_\infty = 995$ cm/sec.; $a = 12 \cdot 10^{-4}\ \mu^{-1}$. Fig. 1 shows to what extent formula (8) agrees with the test data of Gunn and Kinzer. In accordance with this drawing, which was computed with the aid of formula (8), the velocity of fall of droplets is somewhat high (compared with experimental results) for small values of r, and somewhat too low for large radius values of droplets. In computing the suspended mean velocity $\tilde{v}$ the errors in computation v(r) -- since they are of different sign -- will compensate for one another to a certain extent and, therefore, the velocity $\tilde{v}$ computed by formula (6) will be closer to the actual than velocity v(r) determined by formula (8) will be to the experimental.

Formula (6) includes, in addition to v(r), the function for distribution of droplets by dimensions. Best in agreement with test data, as shown by recent studies, is the normal-logarithmic formula proposed by A. N. Kolmogorov. However, in utilizing this formula computation of $\tilde{v}$ by relationship (6) can be made only through numerical integration. Therefore, we took for the function f(r) the formula

$$f(r) = \frac{b^{b+1}}{r_m^{b+1}\,\Gamma(b+1)}\, r^b \exp\left(-\frac{br}{r_m}\right), \qquad (9)$$

which is known as gamma distribution. Here, r_m is the radius of droplets at which f(r) attains a maximum; b is a parameter determined from experimental data; $\Gamma(b+1)$ is the gamma function.

Formula (9) was widely used in recent years by P. V. Diyachenko [4], K. S. Shifrin [6], L. M. Levin [6] and others in studying the microphysical properties of clouds. In a special case (when b = 2)

$$f(r) = \frac{4r^2}{r_m^3} \exp\left(-\frac{2r}{r_m}\right). \qquad (10)$$

A. Kh. Khrgian and I. P. Mazin [7,8] demonstrated that computations by this formula agree satisfactorily with experimental data. Considerable deviations of formula (10) from Kolmogorov's distribution are observed only at small and large values of r where f(r) is extremely insignificant.

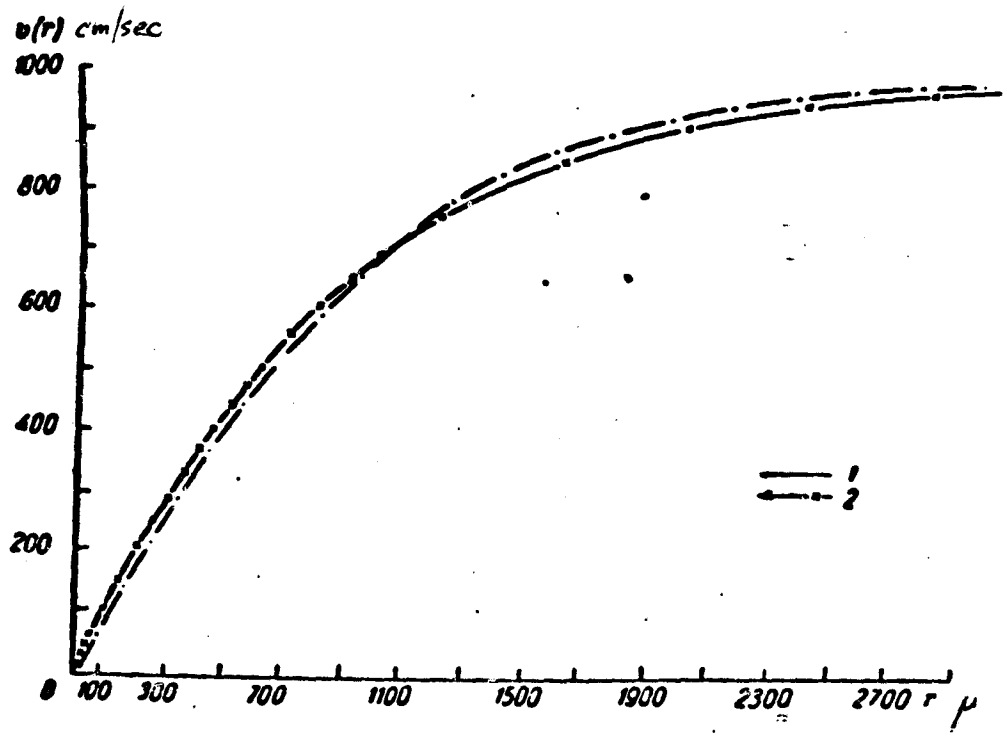

Fig. 1. Relationship of velocity of fall of water droplets to radius.
1. experimental data. 2. computed data

Substituting in (6) the functions f(r) and v(r) determined by formulas (8) and (10) and integrating we get

$$\tilde{v} = v'_\infty \left[1 - \frac{64}{(2 + ar_m)^6}\right]. \qquad (11)$$

The values of the mean suspended velocity for various r_m are as follows:

r_m μ	5	10	15	20	50	100	200	500	1000
$\tilde{v}$ cm/sec	18	34	52	72	161	292	480	790	935

The radius r_m in turn depends on the water content of a cloud or the intensity of precipitation.

3. Distribution of moisture content and cloud water by altitude.

We will solve equation (7) for a layer of atmosphere contained between the lower and upper boundaries of a cloud. Integrating (7) with respect to z we get

$$k\frac{ds}{dz}-(w-\tilde{v})s-\tilde{v}q_m=c_1, \tag{12}$$

in which c_1 is the constant of integration.

To get the second integral we establish, beforehand, the relationship of q_m to z. With this aim in view we make use of a known formula relating q_m to the maximum elasticity E of water vapor,

$$q_m=0{,}622\frac{E}{p} \tag{13}$$

and the Clausius-Clapeyron equation

$$E=E_k\exp\left\{\frac{L}{AR_p}\left(\frac{1}{T_k}-\frac{1}{T}\right)\right\}, \tag{14}$$

in which E_k is the saturation vapor pressure at temperature T_k of the lower boundary of the cloud; L is the specific heat of vaporization; AR_p = 0.111 cal/gram·degree. If we use the barometric formula

$$p=p_k\exp\left(-\frac{gz}{RT_k}\right), \tag{15}$$

and consider the termperature inside the cloud a linear function of the altitude[1]

$$T=T_k-\gamma z, \tag{16}$$

we then arrive at the following relationship of q_m to z:

$$q_m(z)=q_k\exp\left(-\frac{z}{B}\right). \tag{17}$$

In the last formulas γ is the vertical gradient of temperature in the cloud; g is the acceleration of gravity; R is the specific gas constant of the air ($\approx$ 287 m^2/sec^2 degree); q_k is the maximum specific humidity at the lower boundary of the cloud from which, as one can readily see in (16), we can

1. The method developed by the author [2,3] makes it possible to determine the temperature inside the cloud on the basis of solving an equation obtained from equations of heat influx and moisture transfer. However, we get rather cumbersome formulas as a result. Since the basic purpose of this article is to get relationships applicable in practice we shall consider only the simplest case (thoroughly in accord with test data) -- the linear relationship of T to z.

compute altitude z; B is the parameter whose length is related with γ and T_k by the relationship:

$$\frac{1}{B}=\left(\frac{L\gamma}{AR_{\rho}T_k^2}-\frac{g}{RT_k}\right). \tag{18}$$

In all subsequent discussions this parameter plays an exclusively important role. Its values are given in Table 1.

Although, generally speaking, the values k, w and $\tilde{v}$, which are part of the left portion of the differential equation (12), are variables depending on the height, nevertheless, due to the present state of our knowledge of clouds it is not possible to establish this relationship in any concrete form. The simplest and at the same time most sensible assumption which can be made in such cases is the independence of these values to altitude. If we understand k, w, and $\tilde{v}$ to be certain mean values for the entire cloud then, using known methods we find a solution to equation (12), with $q_m(z)$, determined by formula (17), in the following form:

$$s(z)=c_2\exp\left(\frac{w-\tilde{v}}{k}z\right)-\frac{c_1}{(w-\tilde{v})}-Dq_k\exp\left(-\frac{z}{B}\right), \tag{19}$$

Table 1

Values of $2.30 \cdot 10^{-3}$ B(m)

t_k°	γ Degrees/100M								
	0,2	0,3	0,4	0,5	0,6	0,7	0,8	0,9	1,0
—70	20,5	9,11	5,86	4,32	3,42	2,83	2,41	2,10	1,86
—60	25,0	10,5	6,68	4,89	3,86	3,18	2,71	2,36	2,09
—50	30,7	12,2	7,59	5,52	4,33	3,57	3,03	2,63	2,33
—40	38,1	14,1	8,61	6,21	4,85	3,98	3,38	2,93	2,59
—30	48,5	16,3	9,77	6,98	5,43	4,45	3,76	3,26	2,88
—20	62,2	18,9	11,1	7,85	6,08	4,96	4,18	3,62	3,19
—10	85,3	21,8	12,5	8,77	6,75	5,49	4,62	4,00	3,52
0	—	25,2	14,1	9,77	7,48	6,06	5,09	4,39	3,86
10	—	29,2	15,8	10,9	8,26	6,67	5,59	4,81	4,22
20	—	34,0	17,3	12,1	9,13	7,34	6,14	5,27	4,62
30	—	39,7	20,0	13,4	10,1	8,05	6,71	5,76	5,05
40	—	46,1	22,4	14,8	11,0	8,79	7,31	6,26	5,50

in which c_2 is the second constant of integration, and D is a dimensionless parameter related to k, w, $\tilde{v}$ and B by the relationship

$$D=\frac{\tilde{v}}{\left(w-\tilde{v}+\frac{k}{B}\right)}. \tag{20}$$

Together with the cloud, we will consider a layer of the atmosphere inclosed between the upper limit of the cloud (we will designate it as z*) and the tropopause (level of minimal temperature) whose height will be designated H. The humidity balance equation for this layer appears as follows:

$$\frac{d}{dz}\left(k\rho\frac{dq}{dz}\right)-\frac{d(\rho wq)}{dz}=0, \tag{21}$$

where q is the specific humidity of the air. Solution of this equation appears as

$$q(z)=c_4\exp\left[\frac{w'}{k'}(z-z^*)\right]-\frac{c_3}{w'}, \tag{22}$$

where w' and k' are the mean values of the vertical velocity and coefficient of turbulence in the layer between z^* and H; c_3 and c_4 are the constants of integration. The constants c_1, c_2, c_3, and c_4, which are part of (19) and (22), will be determined from the following boundary conditions:

a) on the lower boundary of the cloud there is a known intensity of precipitation. Designating the latter by the letter I, on the basis of (5) we get

$$I=\rho\left(\tilde{v}-w\right)(s-q_m)|_{z=0};$$

in this, we take into account the fact that the droplets fall, with respect to a fixed level (e.g., earth's surface) at a speed of $\tilde{v}$ - w (the velocity w is considered positive when the air moves upward); they fall with a speed of $\tilde{v}$ due to the force of gravity and are raised (or lowered) at a speed of w with the air. Inserting s here according to (19) and q_m according to (17) we find

$$\frac{I}{\rho\left(\tilde{v}-w\right)}=c_2-\frac{c_1}{\left(w-\tilde{v}\right)}-q_k(D+1); \tag{23}$$

b) on the upper boundary of cloud z^* the water equivalence disappears ($\delta = 0$). Since, according to (4) $\delta = s - q_m$, then on the basis of (17) and (19) we get

$$c_3 \exp\left(\frac{w-\tilde{v}}{k} z^*\right) - \frac{c_1}{(w-\tilde{v})} - q_2(D+1)\exp\left(-\frac{z^*}{B}\right) = 0; \qquad (24)$$

c) the specific humidity on the lower boundary of the second layer (between z^* and H) is equal, apparently, to the maximum specific humidity on the level of the upper boundary of the cloud. Making use of (22) and (17) we find

$$c_4 - \frac{c_3}{w'} = q_2 \exp\left(-\frac{z^*}{B}\right); \qquad (25)$$

d) the specific humidity on the tropopause level is, in consequence of the very low temperature, close to zero: $q \approx 0$ at $z = H$. Formula (22) gives

$$c_4 \exp\left[\frac{w'}{R'}(H - z^*)\right] - \frac{c_3}{w'} = 0. \qquad (26)$$

Conditions "a" to "d" and the relationships (23) - (26) resulting from them are sufficient to determine the four constants of integration if we know the height of the upper boundary of cloud cover z^*. However, there is presently no method of determining z^*. One of the problems in this project is to work out a method of computing the height of the upper boundary of cloud cover. With this aim in view, along with conditions "a" - "d", we will formulate conditions which express the balance (preservation) of heat and humidity when the upper boundary of the cloud formation shifts. These latter conditions were widely employed in solving problems of ground freezing, or in the hardening of any other body when we deal with a moveable boundary that divides the hard and liquid phases of a body. Conditions on moveable boundaries applicable to clouds were first formulated by M. E. Shvets [9].

We will designate through v^* the velocity of movement of the upper boundary of a cloud relative to the earth's surface. Since the cloud elements are in motion together with the air (at a speed of w), the upper boundary will

shift vertically with respect to the air a distance equal to $v^* - w$ per unit of time. The vertical column with a transverse section of 1 cm^2 and a height of $v^* - w$ is filled with drops of water the total mass of which is equal to

$$\rho\delta(v^* - w), \tag{27}$$

where, as was true above, δ is the specific water equivalence of the cloud, and ρ is the density of the air. These drops have a dual origin: some of them are formed anew due to the condensation of water vapor whose mass is equal to the difference of the incoming (from the cloud) and departing streams of vapor

$$-\left(\rho k \frac{dq_m}{dz}\right)_{z=z^*-0} - \left(-\rho k \frac{dq}{dz}\right)_{z=z^*+0}, \tag{28}$$

and the other part is brought in by the turbulent flow of droplets from the cloud

$$-\left(\rho k \frac{d\delta}{dz}\right)_{z=z^*-0}. \tag{29}$$

Comparing expression (27) to the sum of (28) and (29) we get an equation for the balance of moisture on the upper boundary of the cloud

$$\rho\delta(v^* - w) = -\left(\rho k \frac{dq_m}{dz}\right)_{z=z^*-0} + \left(\rho k \frac{dq}{dz}\right)_{z=z^*+0} - \left(\rho k \frac{d\delta}{dz}\right)_{z=z^*-0}. \tag{30}$$

The equation for heat balance with $z = z^*$ is obtained on the basis of the following considerations. With the condensation of water vapor, the mass of which is determined by expression (28), there is given off a mass of heat equal to the product

$$L\left[-\left(\rho k \frac{dq_m}{dz}\right)_{z^*-0} + \left(\rho k \frac{dq}{dz}\right)_{z^*+0}\right],$$

where L is the specific heat of vaporization. In addition, a mass of heat equal to $-\left(c_p \rho k \frac{d\theta}{dz}\right)_{z=z^*-0}$ enters from the bottom (from the cloud) under the influence of the turbulent exchange in the volume of air under consideration. The heat loss through the upper boundary of the volume is made up of the

turbulent flow $-\left(c_p\rho k\frac{d\theta}{dz}\right)_{z=z^*+0}$ and the flow of the effective radiation F from the upper boundary of the cloud formation. Comparing the heat coming in with that being given off we get an equation for heat balance on the upper boundary of tne cloud

$$L\left[-\left(\rho k\frac{dq_m}{dz}\right)_{z^*-0}+\left(\rho k\frac{dq}{dz}\right)_{z+0}\right]-\left(c_p\rho_k\frac{d\theta}{dz}\right)_{z^*-0}= \\ =-\left(c_p\rho k\frac{d\theta}{dz}\right)_{z^*-0}+F. \tag{31}$$

In this equation θ is the potential temperature whose gradient, as we know, can be presented in the following form

$$-\frac{d\theta}{dz}=\frac{\theta}{T}(\gamma-\gamma_a)\approx\gamma-\gamma_a \tag{32}$$

(γ_a -- is the dry adiabatic gradient).

Equations (30) and (31) are the mathematical formulation of those missing conditions which are necessary for determining the height of the upper boundary of cloud cover z^* which are part of conditions "a" - "d", as well as the speed of motion of the upper boundary v^* which appears upon their withdrawal.

Equation (31), taking into account relationship (32), can be rewritten as

$$\left(\frac{dq}{dz}\right)_{z^*+0}-\left(\frac{dq_m}{dz}\right)_{z^*-0}=\frac{c_p}{L}(\gamma'-\gamma)+f, \tag{33}$$

where γ' and γ are the vertical gradients of the temperature above the cloud and in the cloud respectively; $f=\frac{F}{L\rho k}$. Equations (30) and (33) are a summation of conditions previously formulated by M. E. Shvets, when he accounted for radiation and the transfer of droplets by a turbulent flow.

Without stopping to determine the constants of integration from relationships (23) - (26) we will cite the final formulas for the distribution of the specific moisture content in a cloud

$$S(z)=\frac{\frac{f}{\rho(\bar{v}-w)}+q_k(D+1)}{1-\exp(\eta z^*)}[\exp(\eta z)-\exp(\eta z^*)]- \\ -\frac{q_k(D+1)\exp\left(-\frac{z^*}{B}\right)}{1-\exp(\eta z^*)}[\exp(\eta z)-1]-q_kD\exp\left(-\frac{z}{B}\right) \tag{34}$$

and the specific humidity in the layer between the cloud and the tropopause

$$q(z)=q_k\exp\left(-\frac{z^*}{B}\right)\frac{\exp[\eta'(z-z^*)]-\exp[\eta'(H-z^*)]}{1-\exp[\eta'(H-z^*)]}, \qquad (35)$$

where the following designations are introduced

$$\eta=\frac{w-\tilde{w}}{k_*};\quad \eta'=\frac{w'}{k'}. \qquad (36)$$

In finding the derivatives of z with respect to q_m from (17) and with respect to q from (35), and inserting them in the heat balance equation (33) we get the following relationship for determining the altitude z^* of the upper boundary of cloud cover:

$$\frac{\eta' H\exp\left(-\frac{z^*}{H}\frac{H}{B}\right)}{1-\exp\left[\eta' H\left(1-\frac{z^*}{H}\right)\right]}+\frac{H}{B}\exp\left(-\frac{z^*}{H}\frac{H}{B}\right)=\frac{c_p H}{Lq_k}(\gamma'-\gamma)+\frac{fH}{q_k}. \qquad (37)$$

Thus, the ratio $\frac{z^*}{H}$ is a function of four dimensionless parameters:

$\eta' H$; $\frac{B}{H}$; $\frac{c_p H}{Lq_k}(\gamma'-\gamma)$ and $\frac{fH}{q_k}$.

We use formula (37) for solving two problems. On the one hand, we will formulate the requirements which must be required for accuracy in the measurement of infrared radiation currents coming from clouds and registered by the satellite. On the other hand, with known values of flow (measured by meteorological satellites) we can use it for determining the height of the upper boundary of clouds.

4. Accuracy in measuring infrared ray (long wave) radiation fluxes with a satellite

In order to get a formula of the value of error in determining the height of the upper boundary of clouds we take the differential from the left and right sides of formula (37), regarding as variables the height of the upper boundary z^* and the radiation flow F. We will note beforehand that the first component in the left portion (37) can be somewhat simplified. Since the index of the exponent $\eta' H\left(1-\frac{z^*}{H}\right)$ is considerably less than unity, we

can expand in a series

$$\exp \eta' H\left(1-\frac{z^*}{H}\right)=1+\eta' H\left(1-\frac{z^*}{H}\right)+\ldots,$$

retaining in it only the first two components. Taking this into account, formula (37) will appear as follows

$$\left(\frac{H}{B}-\frac{1}{1-\frac{z^*}{H}}\right)\exp\left(-\frac{z^*}{B}\right)=\frac{c_p H}{Lq_k}(\gamma'-\gamma)+\frac{HF}{Lpkq_k}. \qquad (38)$$

Having taken the differential from the right and left portions of the last formula we get

$$-\frac{\Delta z^*}{B}\exp\left(-\frac{z^*}{B}\right)\left[\frac{H}{B}-\frac{H}{H-z^*}+\frac{BH}{(H-z^*)^2}\right]=\frac{H}{Lpkq_k}\Delta F, \qquad (39)$$

where ΔF is the error in determining the infrared radiation current which produces a corresponding error Δz^* in computing the altitude of the upper boundary of the cloud cover.

If formula (39) is rewritten as

$$-\frac{HB}{Lka_k}\frac{\Delta F}{\Delta z^*}=\left[\frac{H}{B}-\frac{1}{1-\frac{z^*}{H}}+\frac{\frac{B}{H}}{\left(1-\frac{z^*}{H}\right)^2}\right]\exp\left(-\frac{z^*}{H}\frac{H}{B}\right). \qquad (40)$$

it will become clear that the value of relationship $\frac{\Delta F}{\Delta z^*}$ is a function of four values: $\frac{H}{B}$; $\frac{z^*}{H}$; B; and $\frac{Lka_k}{H}$ (here, $a_k=\rho q_k$ is the absolute humidity of the air at the level of the lower boundary of the cloud, depending only on the temperature at this level).

The result of computing $\frac{\Delta F}{\Delta z^*}$ and then ΔF at a given Δz^* by formula (40) and with the aid of Table 1 are given for several cases in Table 2.

Table 2

Permissible error in determining the integral flow of infrared radiation from the upper boundary of clouds

γ degree/100 m	t_k^o	z^* m	k m^2/sec	H m	$\frac{\Delta F}{\Delta z^*}$ cal/cm^3min	ΔF cal/cm^2min at Δz^* = 250 m
0,6	0	5000	50	9000	$2,16\cdot10^{-7}$	0,0054
0,8	−20	2000	50	4000	$2,20\cdot10^{-7}$	0,0056
0,4	10	1000	50	10000	$1,50\cdot10^{-7}$	0,0038
0,8	−10	9000	50	10000	$4,80\cdot10^{-7}$	0,0120

The cited examples of computation cover practically all possible cases which might be encountered in actual conditions of the atmosphere. Both on the basis of these examples and on a number of others we come to the conclusion that the permissible error in determining the integral flow of infrared radiation from the upper boundary of a cloud should not exceed 0.005 cal/cm^{2}min. (with a given accuracy in determining the height of the upper boundary of 250 meters). The relative error in determining the flux F at different values of the temperature t^* of the upper boundary of cloud cover should not exceed the following values:

t^*	−40°	−20°	0°
$\frac{\Delta F}{F}$ %. . .	2,2	1,6	1,1

We analyzed more common instances when the parameter $\eta' H = \frac{w'}{k'} H$ is not a small value, i.e., when the vertical speed is great. Having taken the differential from the left and right parts of formula (37) we get in this case

$$-\frac{HB}{La_k k}\frac{\Delta F}{\Delta z^*} = \left[\eta' H \frac{1+\left(\eta' H \frac{B}{H}-1\right)\exp \eta' H\left(1-\frac{z^*}{H}\right)}{\left[1-\exp \eta' H\left(1-\frac{z^*}{H}\right)^2\right]} + \frac{H}{B}\right]\exp\left(-\frac{z^*}{H}\frac{H}{B}\right). \quad (41)$$

Analysis and results of computation by this formula demonstrate that an increase in the vertical speed causes an increase in the dimensionless magnitude $-\frac{HB\Delta F}{La_k k \Delta z^*}$. This, in turn, means that on increasing the vertical velocity (more specifically parameter $\eta' H$) the permissible error of measurement of current increases, to be sure, by an insignificant amount. Thus, the above-cited estimates of error in measurement of the current F are suitable also for instances of large values of vertical speed (at considerable vertical speeds with an accepted error in the measurement of the current F, e.g., of 0.005 cal/cm^{2}min., the height of the upper boundary of clouds will be determined with greater accuracy than 250 m). Thus, it can be confirmed that the relative error in determining the current of 1 - 2% will give an error in computing the height of the upper cloud boundary of not over 250 meters under all conditions observed in the atmosphere.

However, formula (37) includes not only the radiation flux F, but also a number of other values. Standard values can be used for certain of them (H,k). Information about the others (primarily, the vertical gradient of temperature γ) should be obtained from satellites or ground means of sounding the atmosphere. Analysis of formula (37) demonstrated that due to the errors in determination of all other parameters the error in computing z^* also amounts to about 250 meters. The overall error in computing the height of the upper cloud boundary by the method proposed, given information about the flow of radiation, is, therefore, about 500 meters.

Thus far, it has been possible to make checks of the method on materials which contained no data about radiation flux. The recurrence Π of errors in computing z^* by data from one excerpt (including 94 instances) is given in Table 3.

Table 3

Recurrence Π of errors in computing the height of the upper cloud boundary

Δz^* м	0—300	300—500	500—1000	1000—2000	>2000
Π	35	17	27	11	10

According to the data in this table the error in computing z^* in the absence of information about the radiation flux from the upper boundary of clouds does not exceed 1000 m in 79% of the cases. The analysis in this article enables us to conclude that the information we used from a satellite enables us to decrease the error in computing the upper boundary of clouds by at least one-half.

5. Method of computing the altitude of the upper cloud boundary using satellite data

Since one of the pressing problems at the present time is determining the complex of measuring equipment to be installed in a meteorological satellite

and working out the requirements for accuracy, we can limit ourselves only to brief remarks about the use of data obtained through a satellite for the purpose of computing the upper cloud boundary. We will first note that equation (1) and similar equations obtained in studies /2,3/ for the function $\Pi = \theta + \frac{L}{c_p} q$, where θ is the potential temperature and q is the specific humidity, can be used effectively for forecasting the cloudy zones. With this aim in view we use the electronic computer to determine, using equation (1), the specific moisture content

$$s = s(x, y, z, t). \tag{42}$$

From the known fields of temperature and pressure we compute the field of maximum specific humidity

$$q_m(T, p) = q_m(x, y, z, t). \tag{43}$$

Comparing fields (43) and (42) enables us to conclude as to the presence or absence of clouds: when $s \geqslant q_m(T,p)$ we get clouds, and when $s < q_m(T,p)$ there is an absence of clouds, or the clouds are breaking up. This system is presently applied in forecasting using computers.

We note that in realizing the method worked out by the author /2,3/, no difficulties associated with the "difference of two large values" arise since the problem is only one of whether clouds are forming or are absent (an answer to this question is given in the systems worked out by other authors). But the method developed in /2,3/ enables us to go one step further compared to all the other methods: it enables us also to forecast the field of a cloud water equivalence

$$\delta = \delta(x, y, z, t). \tag{44}$$

This last question is simply not raised (and it cannot be raised) in studies the basis of which is, for example, the equation of transfer of a deficit dew point.

It goes without saying that the forecast of such a "thin" value like water equivalence is already fraught with a considerably greater number of difficulties than the prognosis of the simple fact of cloud formation.

In this article we have restricted ourselves to a detailed analysis of the profile of water equivalence in a quasi-stationary case, assuming a known temperature distribution. Formula (32) enables us to compute the distribution of the specific moisture content s and the specific water equivalence δ with a height, assuming that the thermodynamic parameters of the cloud and the height of its upper boundary are known. The latter is computed if there are data on the flow of radiation F with formula (35).

REFERENCES

1. Federov, E. K., Mamina, E. F. O vodnom balanse oblachnoy sistemy. Izv. AN SSSR, seriya geofiz., No. 5, 1957.
2. Matveyev, L. T. Usloviya obrazovaniya i evolyutsii oblakov pod vliyaniyem vertikal'nykh tokov i turbulentnogo obmena. Izv. AN SSSR, seriya geofiz., No. 1, 1961.
3. Matveyev, L. T. Nekotoryye voprosy obrazovaniya i evolyutsii sloisto-obraznoy oblachnosti. Tr. AANII, v. 228, No. 1, 1959.
4. D'yachenko, P. V. Opyt primeneniya metodov matematicheskoy statistiki k izucheniyu mikrostruktury tumanov i oblakov. Tr. GGO, No. 101, 1959.
5. Shifrin, K. S. O vychislenii radiatsionnykh svoystv oblakov. Tr. GGO, No. 46/108, 1955.
6. Levin, L. M. O funktsiyakh raspredeleniya oblachnykh kapel' po razmeram. Opticheskaya plotnost' oblaka. Izv. AN SSSR, seriya geofiz., No. 10, 1958.
7. Khrgian, A. Kh., Mazin, I. P. O raspredelenii kapel' po razmeram v oblakakh. Tr. TsAO, No. 7, 1952.
8. Khrgian, A. Kh., Mazin, I. P. Analiz sposobov kharakteristiki spektrov raspredeleniya oblachnykh kapel'. Tr. TsAO, No. 17, 1956.
9. Shvets, M. E. O kondensatsii vodyanogo para v atmosfere. Izv. AN SSSR, seriya geofiz., No. 6, 1955.
10. Gunn, R. and Kinzer, R. D. The terminal velocity of fall for water droplets. Journal of Meteor., 6, p. 2, 1949.

R. L. Kagan and K. Ya. Vinnikov

PROBLEMS OF MAPPING RADIATION MEASUREMENTS OF WEATHER SATELLITES

Maps of radiation fields in the upper boundary of the atmosphere [2-5] can be obtained operationally by working out measurement data obtained from weather satellites on electronic computers along with other materials.

As shown in [2,3] forecasting centers are interested in their operational work, in information about fields of integral, long-wave, outgoing radiation [ukhodyashego izlucheniye] in the "transparency window" region of the atmosphere (8 - 12), as well as reflected solar radiation. Integral long-wave radiation characterizes the thermal state of the tropospheric layer above the clouds.

The temperature of radiation in the "transparancy window" region is close to the temperature of the underlying surface (if dense clouds are present, the upper edge of the clouds serves as the underlying surface). The reflected solar radiation gives some idea about the reflecting capacity of the ground-atmosphere system.

These data may be used for an analysis of cloud systems, for a study of the state of the earth's surface (snow cover, ice conditions, etc.) and for many other purposes.

Compiling operational charts of outgoing radiation for other portions of the spectrum is hardly expedient because the methods of using them in forecasting are not yet clear.

At present, there have been developed methods for the automatic compilation of charts of weather fields using electronic computers [2,4,5]. Modern mapping devices are capable in principle not only of constructing fields of isolines but also of entering the necessary inscriptions and markings.

In this article, consideration is given to certain questions arising in mapping the data of radiation measurements by weather satellites.

Very important in solving the problem at hand is the selection of a suitable mapping basis. A natural requirement in this is a minimal distortion of the fields described and the greatest possible comparability of radiation charts with those of other meteorological elements at the disposal of forecasters. It is apparent that the selection of a mapping base depends, primarily, on which territories of the earth's surface are subject to exposure, and this in turn is determined to a considerable degree by the orbit of the weather satellite. If the orbiting plane of the satellite is inclined to the equatorial plane by not more than 30°, and if it is under 1,000 km above the earth, radiation measurements can be made of an area on both sides of the equator to latitudes of 45-50 degrees. Mercator projection-type charts are most convenient to use in getting the results of measurements over this territory.

If the orbit is inclined at greater angles, data may be obtained from higher latitudes. In the case of polar and quasi-polar orbits it is possible to include polar regions, including both poles. For mapping the results of measurements in these regions, the Mercator projection is not suitable due to the rather marked distortions which such a projection makes of these areas. Here, the most appropriate are polar stereographic projection charts. Two charts of the hemispheres in this projection can represent the results of measurements of the entire world area and they are convenient to use in studying processes occurring in one or the other hemisphere. However, in studying processes that occur in the equatorial region, the use of such charts is difficult because it is then necessary to consider two different charts, which, in addition, give maximum distortions in this area. Therefore, even if there are polar satellites it is desirable, in a study of processes in the equatorial zone, to scan this territory on Mercator charts additionally. One of the advantages of using both types of charts is that all the forecasting stations in

our country make up their baric topographical charts and, in many cases, ground synoptic charts on similar projections. This facilitates making comparisons of radiation fields with fields of other meteorological elements and conducting a joint analysis.

The more important criteria which should be taken into account in selecting chart scales are the requirements for retaining in them the maximum amount of synoptic, meaningful information and convenience in using them. It is apparent that small-scale charts are not suitable because it will eventually become necessary to omit a number of isolines, thereby losing a portion of the information. Charts of very large scale are rather cumbersome and inconvenient. For example, a 1:10,000,000 (scale along the 60th parallel of latitude) of a polar stereographic hemisphere should be printed on a blank sheet approximately 240 cm on a side. Charts of this size are difficult to use operationally.

On the other hand, increasing the scale makes it possible to increase the scope of synoptically significant information only within certain limits. Further increasing the scale with a corresponding increase in detail may result in overloading the chart with small-scale features about the radiation field. These small-scale peculiarities are of little interest in an analysis of the processes taking place over the entire hemisphere. Moreover, they may be without any physical meaning in that they do not describe the real fields of measured elements, but only "noises" in the metering system.

The most convenient charts to use are those of the 1:30,000,000 scale. Such charts are widely used in weather forecasting; this facilitates making comparisons of fields of radiation with the fields of other meteorological elements. A comparatively small format of the blanks is most convenient for mapping work. For example, a polar stereographic chart of the hemisphere (form MPK-6) is placed on a blank with dimensions 80 x 80 cm.

Depending on the possibilities for adapting mapping devices to electronic computers, as well as to apparatus for facsimile communication, charts may be drawn and transmitted either in their entirety or by sections; these are subsequently pasted together by the users.

In the first launchings of meteorological satellites, when it is unnecessary to chart the measurement data of several satellites, it might be desirable to prepare complete charts of the hemisphere. Actually, in such cases a chart 80 x 80 cm will have one-half of a convolution in the form of a band 10-15 cm wide, i.e., the capacity of the recording device will be inefficiently used. At this stage it is more desirable to subject small portions of each convolution to mapping. If the measurement data are entered on a separate chart -- measurements made on one-fourth of a convolution -- it is sufficient to use 40 x 40 cm dimensions in the 1:30,000,000 scale for the plotting boards of the charting device and facsimile apparatus. It is more convenient in practice to lengthen somewhat one of the sides of the plotting board (e.g., up to 50 cm) to insure a certain overlap of charts. Selection of comparatively small dimensions of plotting boards for the mapping device makes it possible considerably to simplify its design and operation.

In the program of the electronic computer, account should be taken of the fact that the coordinates on the plotting board of the charting device are not identically tied in with the geographic coordinates, as would be the case in making charts of entire hemispheres, but depend on the territory scanned. In some instances it may be possible to draw the geographic bases (a coordinate grid, basic contours of continents, etc.) directly by the charting device. In other instances it may be more convenient to use blanks prepared beforehand, blanks which are essentially cut-outs from basic chart blanks. The selection of one kind of blank or another should be determined by the predicted orbit and the area to be scanned. To each such blank in the charting program there

correspond constants in formulas for conversion from geographic coordinates to "plotting board" coordinates.

By way of example let us consider how we can make a system of cutouts for a meteorological satellite traveling in a circular orbit inclined to the equatorial plane at an angle of 65° at a height of 600 km above the earth's surface.

It is easy to get a formula describing the change in geographic coordinates of a subsatellite spot as it travels in orbit:

$$\begin{aligned} \sin\varphi &= \sin\delta \sin\omega t, \\ \operatorname{tg}(\lambda + \Omega t) &= \cos\delta \operatorname{tg}\omega t; \end{aligned} \qquad (1)$$

where φ is the latitude, δ is the angle of inclination of the orbit, ω is the angle speed of rotation of the satellite about the earth, t is the time elapsing after crossing the equator, λ is the longitude, Ω is the angular speed of rotation of the earth about its axis.

As shown by the experience of processing the results of measurements by American meteorological satellites, the data on outgoing radiation at nadir sighting angles in excess of 60° are very inaccurate. Therefore, it is desirable to restrict one's self to measurement data at nadir angles of less than 60°. In such case, when the satellite travels in its orbit the data about a band approximately 2,500 km wide are subject to processing and mapping. This band is described on a chart of the northern hemisphere (Fig. 1). For convenience, selection was made of an orbit with node at 0° meridian (the node is the point of intersection of a projection of the satellite trajectory with the equator).

From the chart of the northern hemisphere there should be prepared 14 blanks of cutouts; 12 of these are used when the lower and temperate latitudes are subjected to scanning. These cutouts are made as follows. The middle line, parallel to the long side of a rectangle (50 cm), is coincided with a meridian that is a multiple of 30°, and one of the short sides (40 cm) is

disposed along a tangent to the equator at the point of intersection with this meridian (Fig. 2).

Fig. 1. Region scanned during the motion of a meteorological satellite over the northern hemisphere in a circular orbit and altitude of 600 km.

Selection of the cutout is determined by the longitude of the angular point (depending on its longitude, selection is made of a cutout which corresponds closest to a multiple of 30°).

Two cutouts from charts of the northern hemisphere are obtained if we place the center of the rectangle at the pole and dispose the long side parallel to the 0 and 90° meridians. They are used for scanning the temperate and high latitudes. In practice, the selection of one of these cutouts is determined by which of the meridians (0 or 90°) is closest to the node point.

If we take the direction of the axes of the plotting board system of coordinates such as described in Fig. 2 and denote through x_0, and y_0 the lengths of the sides of the rectangle, we can readily get formulas for converting geographic coordinates to plotting board coordinates [1]:

$$x = \frac{x_0}{2} + 1{,}866\, RM \operatorname{tg}\left(\frac{\pi}{4} - \frac{\varphi}{2}\right)\sin(\lambda - \lambda_0),$$
$$y = y' - 1{,}866\, RM \operatorname{tg}\left(\frac{\pi}{4} - \frac{\varphi}{2}\right)\cos(\lambda - \lambda_0), \qquad (2)$$

where R is the radius of the earth, M is the main scale (along the 60° parallel), λ_0 and y' are certain constants. For the first twelve blanks of cutouts $\lambda_0 = \frac{\pi}{6}(n-1)$, where n = 1, 2, . . ., 12 is the number of cutout, and y' = 1,866 M. For the 13th and 14th cutouts λ_0 is equal to 0° and 90°, respectively, and $y' = \frac{y_0}{2}$. In a like manner 14 cutouts are prepared and used from a full blank of a chart of the southern hemisphere.

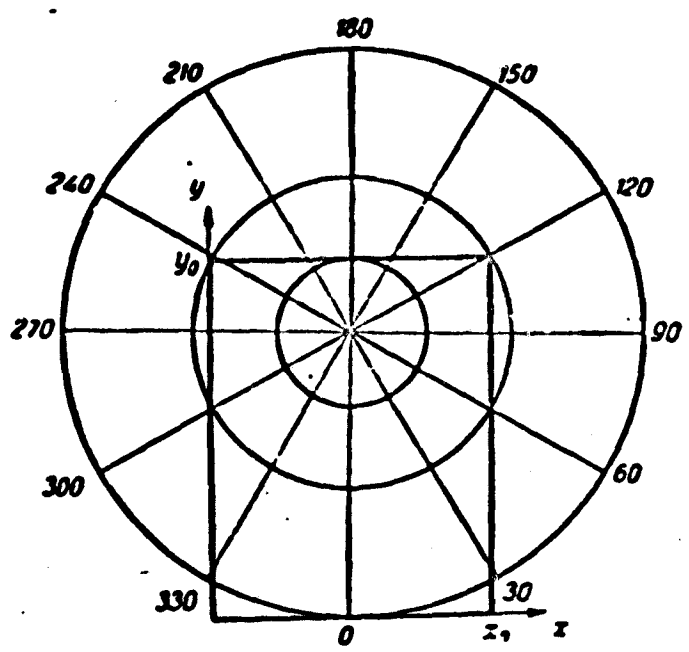

Fig. 2. Diagram for preparing cutouts from a chart of the hemisphere.

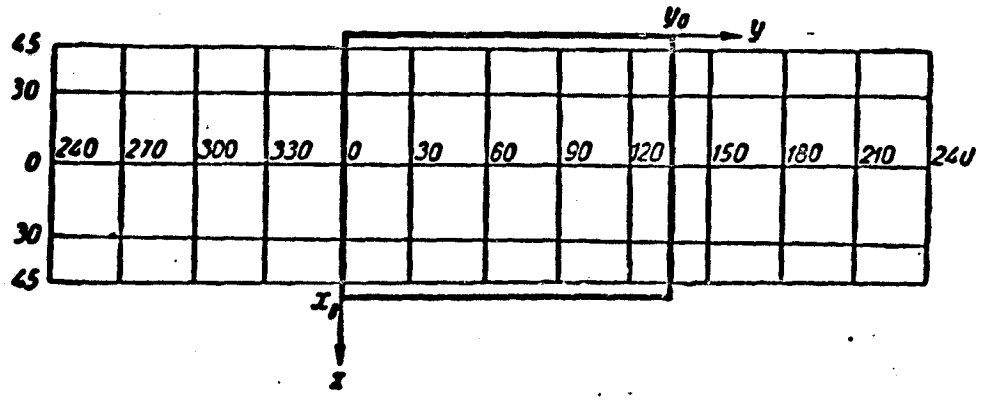

Fig. 3. Diagram for preparing cutouts from a Mercator projection chart.

Eight cutouts are prepared from a Mercator projection. For this purpose the middle line of a rectangle is made to coincide with the equator, and the short side with the meridian of longitude; this is a multiple of 45° (Fig. 3.). The practical selection of one of the eight cutouts obtained is governed by noting to which cutout center the node is disposed the closest. In that case, the formulas for converting from geographic coordinates of a point to plotting board coordinates appear as follows:

$$x = \frac{1}{2} x_0 - \frac{RM \cos \varphi_0}{0{,}43429} \log \operatorname{tg}\left(90^\circ - \frac{\varphi}{2}\right),$$
$$y = \frac{2\pi R \cos \varphi_0 M}{360^\circ} (\lambda - \lambda_0), \qquad (3)$$

where $\varphi_0 = 22^\circ 30'$, $\lambda_0 = \frac{\pi}{4}(m-1)$, $m = 1, 2, 3, \ldots, 8$.

Thus, in the case under consideration, it is possible, in order to show the results of measuring radiation currents on an artificial satellite, to use a system of previously prepared 36 cutouts of basic chart blanks.

The units of value of outgoing radiation, which are entered on the chart, can be different for differing spectral intervals. The values of currents of long-wave radiation may be presented in energy units (e.g. wt/M^2 or cal/cm^2 min) and in effective temperatures of radiation. The energy units are convenient in number forecasts and balanced computations. For mapping purposes, when the greatest clarity is required, it is desirable to use effective temperatures. Maps of effective temperatures for various spectral intervals can give a more or less clear idea about the fields of temperature in the different atmospheric layers.

The results of measurement of reflected solar radiation can best be represented as a chart of albedo values of an earth-atmosphere system rather than as a map of absolute values of radiation currents. The former is computed by the following formula:

$$\Gamma = \frac{R}{I_0 \cos z}, \qquad (4)$$

where Γ is the value of the ground-atmosphere system albedo, R is the flux of short wave outgoing radiation, I_0 is the solar constant, z is the zenith angle of the sun at a given point at the instant of measurement. The albedo value is determined in large measure by the state of the atmosphere and underlying surface and depends little on the latitude of the area and the sun's altitude. This considerably simplifies analysis and interpretation of charts.

Let us consider the question of the discreteness of drawing an isoline.

The maximum interval possible between isolines of a charted magnitude is determined by the probable range of its change. It is apparent that at least four or five isolines should be laid out in this range. Otherwise, the charts will contain a minimum of information and there will be little sense in making them. If the probable range of temperature change in the ground layer is about 100°, the interval between isotherms on the chart should not be over 20-25°. On the other hand, the minimal interval possible is determined by the accuracy of measurement of the equipment used.

It is obviously senseless to draw isolines at intervals less than the mean value of a probable error of measurement. An attempt to plot isolines as densely as this would result in the appearance of a number of fictitious isolines about random emerging measurement data. In tracing isolines on an uneven field of measurement data, even an interval equal to a doubled random error is underestimated. Actually, assuming a normal distribution of errors, we can expect that in 5% of the measurements the value obtained will vary from the real value by more than double the value of the mean square error. Consequently, up to 5% of the points of measurement in this case can be given off by individual and fictitious isolines. This, of course, would make reading the chart very difficult. The great amount of detail shown on the field would be fictitious.

Systematic errors in the measuring system can distort the absolute values of the magnitude charted even in processing, but they have comparatively little effect on the configuration of the isolines on the chart. In this sense it is clear that the possibility of systematic errors occurring is not very great in determining the discreteness of drawing isolines.

It is a known fact that the accuracy with which measurements can be transmitted from a weather satellite to ground points of communications is determined

by the capabilities of the metering and telemetering systems. The latter does not insure the transmission of any data whatever obtained from measurement but only of a limited number of fixed values. As a result, the possible differences between the real measured values and those obtained at the ground points may attain half an interval between adjacent fixed values of the telemetering system. As a rule, these intervals are so computed as to be not less than double the mean square error of measurement. Taking this fact into account, this interval can be accepted as a minimal allowable interval between isolines. This is possible when, in an analysis of a field that is subjected to measurement there is a smoothing out effect, even though minimal.

On the basis of the foregoing, as well as from the experience of analyzing radiation charts [4,5], it seems desirable to draw isolines of the effective temperature in the area of the atmosphere's "transparency window" 8-12 μ every 5°. The isolines of effective temperature for integral radiation are plotted every 2° (this corresponds approximately to 10 v/m^2 in energy units), and isolines on a ground-atmosphere system albedo chart are drawn through tenths of units.

Some difficulties may arise in representing areas of increased gradients and discontinuities of radiation fields in the process of charting. Such areas may occur along the coast, along the boundaries of packed snow fields, as well as on the boundaries of cloud systems. An excessively dense field of isolines may complicate the operation of a charting device (great waste of machine time, merging of isolines, etc.). These difficulties could be avoided if, upon analysis, the isolines are plotted taking into account the gradient of the magnitude charted. If the gradient does not exceed a certain fixed value the isolines are drawn in succession. If the gradients are large a series of isolines may be omitted. It should be borne in mind, however, that thinning out the field in this manner has definite shortcomings. Chief of

them is the ambiguous connection between the density of isolines and the gradient of magnitude measured.

Conclusions

1. 1. By way of a charting base in depicting radiation fields, it is desirable, in the case of satellites with a small orbital inclination, to use Mercator projection charts. For satellites with a greater inclination of the plane of the orbit to the equatorial plane stereographic polar projection charts should be used for the northern and southern hemispheres. Along with this, the measurement data of the equatorial zone to about 45° of latitude can be duplicated on a Mercator chart.

2. The optimum scale for charts of radiation fields is 1:30,000,000.

3. Where a small dimensioned plotting board is employed in a charting device, use a system of blanks, which are cutouts of basic charts, in a manner similar to that shown in the example.

4. Isolines on charts are plotted for the values of charted elements and multiples as follows:

a. 5° for charts of the effective temperature of outgoing radiation /radiatsiya/ in the area of the atmosphere's "window of transparency".

b. 2° for charts of the effective temperature of integral outgoing long wave radiation (which corresponds to an interval of 10 wt/m^2 using energy units).

c. a tenth part of a unit for albedo charts of a ground-atmosphere system.

REFERENCES

1. Graur, A. V. Matematicheskaya kartografiya. Izd. LGU, 1956.
2. Kondrat'yev, K. Ya. Meteorologicheskiye sputniki. Gidrometeoizdat. L., 1963.
3. Fritz, S. Winston, S. Synoptic use of radiation measurements from satellite Tiros II, Monthly Weather Review. Vol. 90, No. 1, 1962.
4. Tiros II radiation data catalogue., Vol. 1, Goddard Space Flight Center, Greenbelt, Maryland, Aug. 15, 1961.

5. Tiros II radiation data. User's Manual. Goddard Space Flight Center, Greenbelt, Maryland, Aug. 15, 1961.

L. S. Gandin and V. P. Boltenkov

METHODS OF AN OBJECTIVE ANALYSIS OF ACTINOMETRIC INFORMATION FROM METEOROLOGICAL SATELLITES

1. General Considerations

Actinometric information coming in from meteorological satellites is very broad in scope. As a result, analysis of spatial distribution of radiation magnitudes and manually entering such data on charts and drawing isolines is extremely difficult if not impossible. Insofar as the processing of actinometric information is concerned we can only speak about fully automated procedures for making up the charts, i.e., an objective analysis.

American investigators [6] have used two methods for an objective analysis of actinometric information from meteorological satellites. The first method is for getting large-scale fields of radiation currents. This method is extraordinarily simple; it consists in averaging out all data for points lying within each node of a square grid with an interval [shag] of about 350 km. From the data of a single orbit with this method, we get values only in a few of the 1977 points which fill the hemisphere. The second method of analysis used by the Americans is for getting small-scale distributions of radiation data. The analysis is made for grid nodes also consisting of 1977 points in a similar grid for the hemisphere but having one-fifth as many intervals. There are several variations for arranging this small grid in accordance with the various kinds of possible satellite orbits.

The method of analysis for this grid differs only slightly from the usual method of analysis of meteorological fields accepted in forecasting work in the USA [4] and is, in effect, a modification of a method proposed by the Swedish scientists, Bergthorsson and Doos [3]. This method consists of the successive introduction of corrections in a certain preliminary field. The results of a linear extrapolation of observation data are the corrections

entered in the node of a regular grid and are introduced with weights that are greater the less is the distance between the point to which the observation is referred and the grid node. By way of a preliminary field in this case we use the results of the application of the first method.

Using the results of an objective analysis of radiation fields we make up their charts with the aid of a digital planetary press [tsifrovaya planetarnaya pechat'] or by plotting the curves automatically. An assembly of such charts constructed on the basis of data from the "Tiros II" satellite is contained in a catalog [5].

In study [2] there was a comparison made of the various methods of interpolation in conformance with the height of the isobaric surfaces (geopotential), and it was shown that the greatest accuracy was insured by the system of so-called optimal interpolation, based on the use of information about the statistical structure of the field analyzed. We can also assume that it is the same way with respect to the majority of usual meteorological elements.

However, the fields of actinometric characteristics measured in weather satellites have a number of peculiarities which should be borne in mind in considering the methods of analyzing them objectively.

The first peculiarity of these fields consists in the fact that they form bands of measurements which are very densely saturated with data. In contrast to usual aerological measurements which have intervals of from 300 to 400 km between adjacent points of observation, even in regions with dense networks of stations, the distance between adjacent points "seen" from a satellite may be 30 km and even less. Also, it is known that with a dense network of data all intelligent methods of interpolation insure approximately the same accuracy [2]. Therefore, the interpolation within zones, e.g., for making charts of isolines of radiation fluxes or radiation temperatures can be performed by any formal method.

A second peculiarity of actinometric data from artificial satellites consists in the fact that, if one or several satellites are functioning near bands filled with data, there are vast intermediate regions which lack this information. Interpolation in such areas according to data obtained from the zones of observation is a considerably more difficult task than interpolation within the zone. To resolve this problem, there is every reason to recommend the method of optimal interpolation.

Finally, the third peculiarity of actinometric information obtained from satellites is the fact that it contains characteristics which are not used directly in numerical forecasts of meteorological fields. Along with this, the information about radiation fluxes may be used in restoring the temperature fields, since it is apparent that between the fields of temperature and radiation currents there should be a close relationship. Along with the actinometric measurements from the satellite it is desirable to utilize temperature data obtained through the usual radio sonde observations.

The problem of reconstructing the temperature fields from actinometric information from a satellite and radiosonde data can best be resolved by using optimal interpolation. For this purpose it is necessary to know the correlation function of temperature, the correlation function of radiation fluxes, and the mutual correlation function which describes the statistical relationship between the temperature and radiation fluxes. Described in the next paragraph is a method of optimal interpretation of several fields, and in parts 3 and 4 there are some data on correlation functions of radiation fluxes from weather satellite data, and information about the mutual correlation function of "radiation fluxes -- temperature". Reference /1/ has information about the spatial correlation functions of temperature.

2. Optimal Interpolation by Data About Several Meteorological Fields

Let it be necessary to find the value of several meteorological elements f^0 at point $\vec{r}_0^{\,0}$ according to known values of elements $f^1, f^2, \ldots f^k, \ldots f^s$ at points r_1^k and element f^1 is known at points $\vec{r}_1^{\,1}, \vec{r}_2^{\,1}, \ldots, \vec{r}_i^{\,1}, \ldots, \vec{r}_{n_1}^{\,1}$; element f^2 is known at points $\vec{r}_1^{\,2}, \vec{r}_2^{\,2}, \ldots, \vec{r}_i^{\,2}, \ldots, \vec{r}_{n_2}^{\,2}$ etc; element f^k is generally known at points $\vec{r}_i^{\,k}$ $(i = 1, 2, \ldots, n_k)$. The value of element f^k at point $\vec{r}_i^{\,k}$ will be designated as f_i^k

$$f_i^k = f^k\left(\vec{r}_i^{\,k}\right). \tag{1}$$

In this, we only know about point $\vec{r}_i^{\,k}$ that with the same k all points $\vec{r}_i^{\,k}$ are different. With different k certain of the points $\vec{r}_i^{\,k}$ may coincide. Element f^0 may differ from all elements f^k $(k = 1, 2, \ldots, s)$, and it may coincide with one of them. Likewise, point $\vec{r}_0^{\,0}$ may coincide with one of the points $\vec{r}_i^{\,k}$.

We will present the unknown value

$$f_0^0 = f^0\left(\vec{r}_0^{\,0}\right) \tag{2}$$

in the form of a linear combination of all known values

$$f_0^0 = \sum_{k=1}^{s} \sum_{i=1}^{n_k} p_i^k f_i^k, \tag{3}$$

where p_i^k are the weight factors which are not yet determined.

The mean square error of representation (3) is equal to

$$E = \overline{\left(f_0^0 - \sum_{k=1}^{s} \sum_{i=1}^{n_k} p_i^k f_i^k\right)^2}, \tag{4}$$

where the line represents averaging understood in the statistical sense. Inasmuch as such an averaging can be presented with summation, formula (4) can be written as

$$E = \overline{(f_0^0)^2} - 2 \sum_{k=1}^{s} \sum_{i=1}^{n_k} p_i^k \overline{f_0^0 f_i^k} + \sum_{k=1}^{s} \sum_{l=1}^{s} \sum_{i=1}^{n_k} \sum_{j=1}^{n_l} p_i^k p_j^l \overline{f_i^k f_j^l}. \tag{5}$$

Without lessening the generality, we can say that the mean values of all the elements considered at all points are equal to zero

$$\overline{f_i^k} = 0. \tag{6}$$

This means that instead of the actual values of magnitudes under consideration, the deviations from the mean value (norm) figure for each given point throughout. In practice, this boils down to the fact that before beginning the interpolation it is necessary to compute the value of the norm from each observed value of a meteorological element, and after making the interpolation to add to the resulting value of deviation from the norm the corresponding value of the norm. It goes without saying that all this presupposes a knowledge of the norms of the meteorological elements under consideration.

On the strength of equation (6) the mean products on the right side of formula (5) are the values of the mutual correlation functions which describe the statistical relationship between the measured values of the meteorological elements at the different points:

$$\overline{f_0^0 f_i^k} = \tilde{m}_{0k}(\vec{r}_0, \vec{r}_i) \equiv \tilde{m}_{0i}^{0k}, \tag{7}$$

$$\overline{f_i^k f_j^l} = \tilde{m}_{kl}(\vec{r}_i, \vec{r}_j) \equiv \tilde{m}_{ij}^{kl}, \tag{8}$$

where $\tilde{m}$ is the correlation function of the measured values. Since measurements are subject to error, the correlation function of the measured values, generally speaking, differs from the correlation function of the actual values. Moreover, if we assume that the errors of measurement of different elements do not correlate with one another nor with the true values of elements, and that the errors of measurement at the various points are also not correlated then we have a simple relationship as

$$\tilde{m}_{ij}^{kl} = m_{ij}^{kl} + \delta_{ij}\delta_{kl}\sigma_{ik}^2, \tag{9}$$

where $\tilde{m}$ is the correlation function of the measured values; m is the correlation function of the real values; σ_{ik} is the mean square error in measuring

element f^k at the point $\vec{r}_i^k$; $\delta_{\alpha\beta}$ is the Kronecker symbol:

$$\delta_{\alpha\beta} = \begin{cases} 1 & \text{when } \alpha = \beta \\ 0 & \text{when } \alpha \neq \beta \end{cases}$$

Substituting (7), (8), and (9) in (5) we get

$$E = m_{00}^{00} - 2\sum_{k=1}^{s}\sum_{i=1}^{n_k} p_i^k m_{0i}^{0k} + \sum_{k=1}^{s}\sum_{i=1}^{s}\sum_{i=1}^{n_k}\sum_{j=1}^{n_l} p_i^k p_j^l m_{ij}^{kl} + \tag{10}$$

$$+ \sum_{k=1}^{s}\sum_{i=1}^{n_k} (p_i^k)^2 \sigma_{ik}^2.$$

We pass over to formula (10) to the dimensionless magnitudes and substitute

$$E = m_{00}^{00}\varepsilon, \tag{11}$$

$$m_{ij}^{kl} = \sqrt{m_{ii}^{kk} m_{jj}^{ll}}\,\mu_{ij}^{kl}, \tag{12}$$

$$\sigma_{ik}^2 = m_{ii}^{kk}\eta_i^k. \tag{13}$$

According to formula (13) the magnitude η_{ik} is the mean square error of measurement of element f^k at point $\vec{r}_i^k$ referred to the dispersion of this element at this point. We shall term the magnitude η_i^k the measure of error of observation. Correspondingly, the quantity ε is a measure of error in interpolation, i.e., the ratio of the mean square error of interpolation to dispersion of the unknown value of element f^0 at point r_0^0. Finally, μ_{ij}^{kl} is the value of the standardized correlation function of elements f^k and f^l for points $\vec{r}_i^k$ and $\vec{r}_j^l$ respectively or, in other words, the coefficient of correlation between the value of element f^k at point $\vec{r}_i^k$ and the value of element f^l at point $\vec{r}_j^l$.

After substituting formulas (11), (12), and (13) in expression (10) it becomes converted into the following:

$$\varepsilon = 1 - 2\sum_{k=1}^{s}\sum_{i=1}^{n_k} p_i^k \sqrt{\frac{m_{ii}^{kk}}{m_{00}^{00}}}\,\mu_{0i}^{0k} + \tag{14}$$

$$+ \sum_{k=1}^{s}\sum_{i=1}^{s}\sum_{i=1}^{n_k}\sum_{j=1}^{n_l} p_i^k p_j^l \frac{\sqrt{m_{ii}^{kk} m_{jj}^{ll}}}{m_{00}^{00}}\mu_{ij}^{kl} + \sum_{k=1}^{s}\sum_{i=1}^{n_k} (p_i^k)^2 \frac{m_{ii}^{kk}}{m_{00}^{00}}\eta_i^k.$$

It is convenient to introduce instead of the weights p_i^k the values

$$q_i^k = \sqrt{\frac{m_{ii}^{kk}}{m_{00}^{00}}}\, p_i^k. \tag{15}$$

because, as a result, expression (14) will be simplified and become

$$\varepsilon = 1 - 2\sum_{k=1}^{s}\sum_{i=1}^{n_k} q_i^k \mu_{0i}^{0k} + \sum_{k=1}^{s}\sum_{i=1}^{s}\sum_{i=1}^{n_k}\sum_{j=1}^{n_i} q_i^k q_j^i \mu_{ij}^{ki} + \sum_{k=1}^{s}\sum_{i=1}^{n_k} (q_i^k)^2 \eta_i^k. \tag{16}$$

We shall now require that the measure of error in interpolation ε be minimal with respect to all values q_i^k. This reduces to a system of linear equations

$$\sum_{i=1}^{s}\sum_{j=1}^{n_i} \mu_{ij}^{ki} q_j^i + \eta_i^k q_i^k = \mu_{0i}^{0k}. \tag{17}$$

It is easy to see that the number of equations (17) and the number of unknown q_i^k coincides, or

$$N = \sum_{k=1}^{s} n_k, \tag{18}$$

i.e., with the total amount of data for interpolation. It can also be shown that the determinant of system (17) differs from zero so that it has a solution -- only one solution. Finally, it can readily be seen that this solution actually corresponds to the minimum of magnitude ε and not to a stationary point of another kind.

After finding value (17) we can then compute the weight p_i^k by formula (15) if we know the fields of dispersion of all elements used in the computation. Following this, we can perform the interpolation by formula (3).

It is more logical, however, to proceed in a different manner, namely, to replace p_i^k in formula (3) by q_i^k with the aid of relationship (15). Then, instead of formula (3) we get

$$\frac{f_0^0}{\sqrt{m_{00}^{00}}} = \sum_{k=1}^{s}\sum_{i=1}^{n_k} q_i^k \frac{f_i^k}{\sqrt{m_{ii}^{kk}}}. \tag{19}$$

Formula (19) shows that the magnitudes q_i^k and p_i^k can be considered as interpolation weights, but in contrast to p_i^k the values of q_i^k represent the weights for interpolation not of absolute values of deviation of elements from norms, but the relative deviations -- in fractions of the mean square variability of each element at each point.

Thus, the solution of the problem boils down to finding the weights q_i^k with the aid of the solution of system N linear algebraic equations.(17) with the subsequent interpolation by formula (19).

3. Correlation Functions of Radiation Fluxes

From a discussion of the preceding paragraph, it follows that, to make an analysis of temperature fields with actinometric information from a satellite, it is necessary to have information about the correlation functions of temperature and radiation fluxes. More correctly, it is necessary to know the auto-correlation function of temperature of radiation fluxes and the mutual correlation function describing the statistical relation between the temperature and radiation fluxes.

The auto-correlation functions of temperature were studied in detail in reference [17]. The information in this study was wholly adequate for our purposes. Therefore, our task consisted only in studying the two remaining kinds of correlation functions.

To get these functions, it is important to have information about the radiation currents. In principle, it does not matter how this information is obtained -- from measurement data of weather satellites or by other means. However, at the present time we do not have data on the comparison of radiation currents obtained by satellites and determined by independent methods using a large amount of materials. Hence, there is no guarantee that the correlation function for values of radiation fluxes computed, say, from data on the vertical temperature sounding of the atmosphere will be close to the correlation function

for values of radiation fluxes based on data from satellites. In addition the amount of information on radiation fluxes computed by indirect methods is still insufficient to make a study of the statistical structure of such fluxes. Therefore, the decision was made to use data from actinometric observations from satellites.

By way of such data at out disposal we simply had the fields of radiation fluxes from observations of the U. S. satellite "Tiros-II", which were listed in the catalog [5]. These data have a number of shortcomings, as far as our task was concerned, and this fact has to be takn into account in analyzing the results obtained.

First, the catalog [5] did not list the original data, but the results of an analysis, i.e., interpolations of values of radiation fluxes in the nodes of square grids [uzel kvadratnoy setki]. Accordingly, in processing the data, we get correlation functions of analyzed values which may be somewhat different than the correlation functions of the original observed values.

Second, the catalog [5] does not contain any data about temperature fields at fixed isobaric surfaces, hence we were forced to derive such data from other sources, to wit, from the observation tables of radio sounding stations. It goes without saying that in this there were no data of observation synchronized with measurements from the satellite. Hence, we had to assume as approximations the synchronized observations which were not over 90-100 minutes apart. The error of this approximation could also have had an effect on the computed correlation functions.

In addition, the need to use values which were only approximations of the synchronized values resulted in a marked decrease of the total amount of information for the study of mutual correlations compared with the total amount of material for studying correlation functions of temperature and radiation fluxes individually.

In order to have comparative data on the different characteristics of a structure, the correlation functions of radiant currents and correlation functions of temperature were computed on the same materials which were used for determining the mutual correlation functions. The total amount of data for computing each of the functions was approximately one-tenth as great as the amount on which was based the information on correlation functions of temperature cited in reference [1].

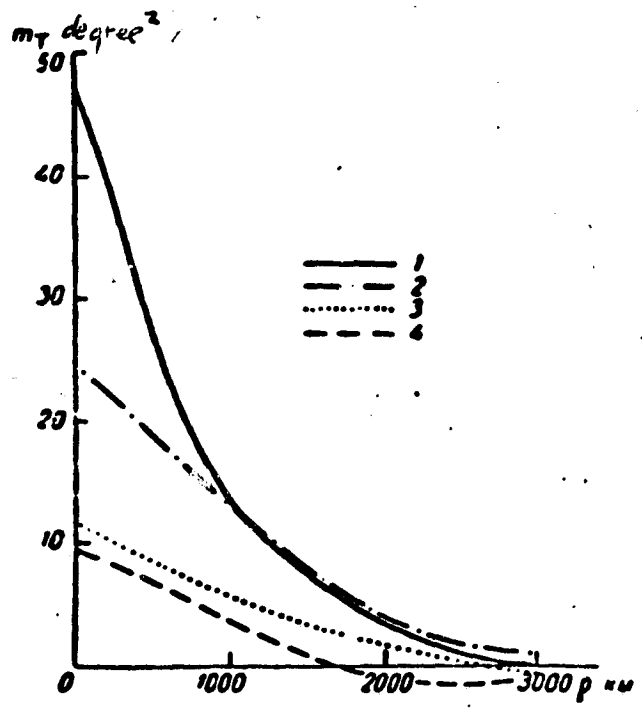

Fig. 1. Auto-correlation functions of air temperature for various levels.

1 -- ground, 2 -- 500 mb, 3 -- 300 mb, 4 -- 100 mb.

Such an amount of initial information cannot be considered adequate and therefore the results listed in the following should be regarded only as preliminary evaluations. Along with this, the comparison of correlation functions of temperature (Fig. 1) with functions obtained in study [1], show that for the lower levels where the data on the temperature are quite accurate and the amount of information not too small the results are close to one another.

Given in Fig. 2 are the auto-correlation functions of radiation currents -- an integral long wave current (8-30 μ) and a current in the interval of waves corresponding to the "window of transparency" of water vapor (8-12 μ),

as well as the mutual correlation function describing the relationship of the integral radiation to the radiation in the window of transparency. This relationship proved very significant -- the coefficient of correlation between the two fluxes is as high as 0.94. It should be emphasized that in the interests of using actinometric information obtained from satellites in an objective analysis of a temperature field this factor plays a negative role. It indicates that when using, say, information about integral radiation the information on radiation in the window of transparency contains virtually no supplemental data.

Characteristic of all curves in Fig. 2 is a sharp "slope" in the area of low values for distance r approximately to a distance of the order of 1000 - 1500 km. These areas of lowered values of correlation functions hardly exist in reality. More probably, they are due to errors in measurements, i.e., to errors of "tying in", that is, in determining the coordinates of points "visible" to the equipment in a satellite.

As we know, the U. S. "Tiros" satellites have no fixed orientation relative to the earth and they maintain a fixed position of the axis in space. The satellite rotates about its axis, and the visual beam of the actinometric apparatus describes an angle of 45° with the axis of rotation. In consequence of this, the visible point describes a complex trajectory, the position of this point for certain moments of measurement being determined by interpolation. Of course, all this leads to errors in tying-in the actinometric data which, according to the American authors, is an average of 300 - 500 km.

It is easy to understand that the errors of tying-in lead not only to random but also to systematic errors in distance values between points. Specifically, the less the mean value of the measured distance compared with the tying-in error, the more probable it is that the actual mean distance substantially exceeds the mean of the measured distances. Therefore, the ordinates

actually correspond, in the case of low values of abscissas in Fig. 2, to the considerably greater values of the abscissas. This does not pertain to the zero abscissa, i.e., to the dispersion of each of the fluxes and to the coefficient of correlation between them since in these cases we are actually dealing, each time, with the same point, i.e., the distance is actually equal to zero, regardless of the tying-in error.

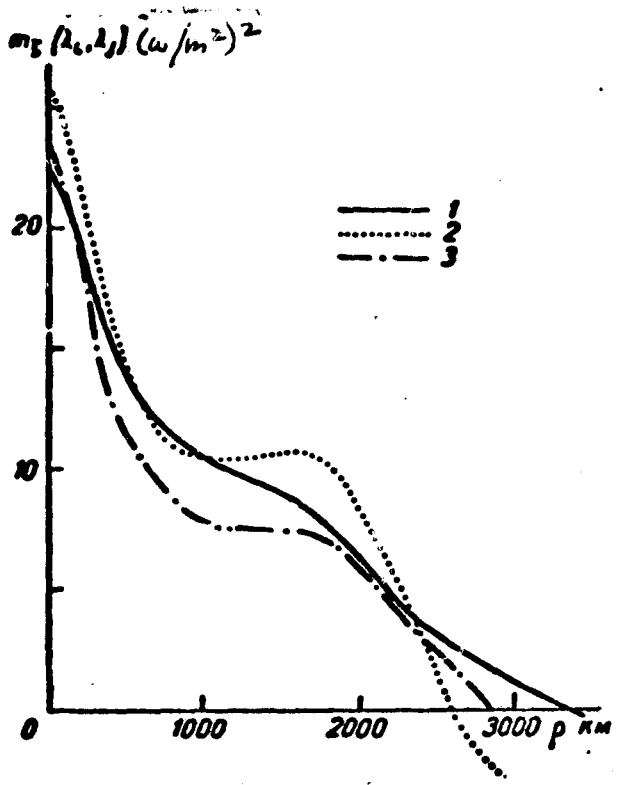

Fig. 2. Auto-correlation and mutual correlation function of fluxes of long wave radiation for various portions of the spectrum.

1 -- 8-30 μ , 2 -- 8-12 μ , 2 -- 8-30-8-12 μ .

The conclusions about the effect of tying-in errors is also supported from a consideration of Fig. 3 on which are given the mutual correlation functions of temperature and radiation fluxes. This figure calls our attention to the low coefficients of correlation between the temperature and each of the radiant fluxes. The smallness of these coefficients can partially be attributed to the effect of non-synchronized observations of the temperature and radiant fluxes. More importantly, the relationship between the temperature and radiant fluxes should be different, depending on the cloud cover. Actually, both the integral radiation and the flux in the transparency window

should, in the case of a cloudless sky, correlate better with the temperature of the underlying surface; and if clouds prevail they should correlate with the temperature on the surface, close to the upper boundary of cloud cover. However, since the amount of initial information was small, we had to refrain from dividing it on the basis of cloud cover. As a result, there was a lessened correlation between the radiation fluxes and the temperature.

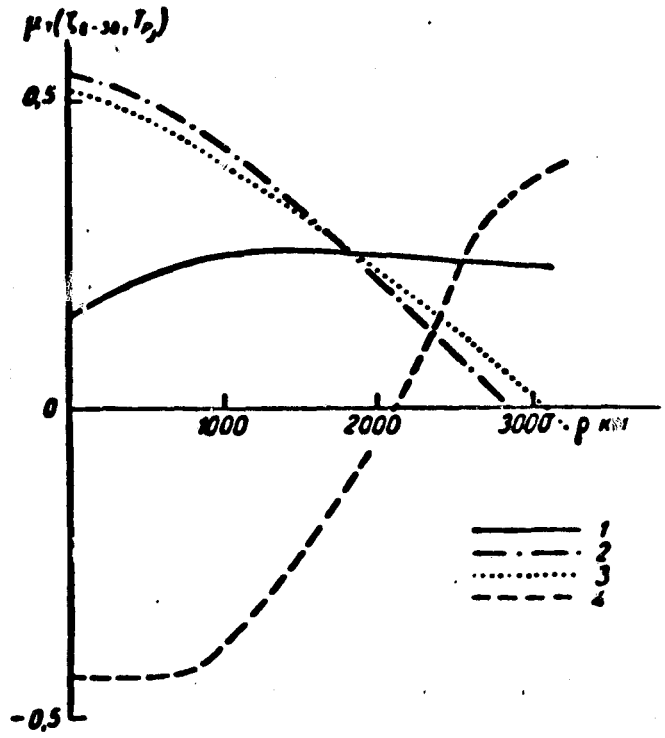

Fig. 3. Standardized mutual correlation functions of radiation fluxes on the 8-30 μ section of the spectrum and air temperatures at different levels.

(See Fig. 1 for conventional markings)

However, even the mutual correlation functions, apart from everything else, are clearly distorted due to tying-in errors. This is seen from the fact that in the case of distances of the order of 1,000 km these functions change the sign of curves, just like the auto-correlation functions do for radiant fluxes.

In the next section, we present an evaluation of the effect of tying-in errors on correlation functions. On the basis of these estimates attempts were made to correct the data received.

4. The Influence of Errors in Determining the Coordinates of Points on the Values of Correlation Functions

In this next problem, let there be two points, the distance between them being a, and let the position of each of the points be known with an error whose probability is subject to the normal law on the plane

$$f(x, y) = \frac{1}{2\pi\sigma^2} e^{-\frac{x^2+y^2}{2\sigma^2}} \tag{20}$$

with the same dispersion σ^2 of errors for the positions of both points. Find the mean square distance A between the points, taking these errors into account.

Assuming for definiteness that the points under consideration without error have the coordinates $(-\frac{a}{2}, 0)$ and $(\frac{a}{2}, 0)$, we get the formula

$$A^2 = \int\int\int\int_{-\infty}^{\infty} [(x-x')^2+(y-y')^2] f\left(x-\frac{a}{2}, y\right) f\left(x'+\right. \tag{21}$$
$$\left. +\frac{a}{2}, y'\right) dx\,dy\,dx'\,dy'$$

or after replacing the variables of integration

$$x = \frac{1}{\sqrt{2}}(u+u'); \quad x' = \frac{1}{\sqrt{2}}(-u+u');$$
$$y = \frac{1}{\sqrt{2}}(v+v'); \quad y' = \frac{1}{\sqrt{2}}(-v+v'); \tag{22}$$

$$A^2 = \int\int\int\int_{-\infty}^{\infty} (u^2+v^2) f\left(u-\frac{a}{\sqrt{2}}, v\right) f(u', v')\,du\,dv\,du'\,dv'. \tag{23}$$

Substituting in this expression f(x,y) from (20) and making the replacement

$$\frac{u}{\sigma\sqrt{2}} = s; \quad \frac{v}{\sigma\sqrt{2}} = t; \quad \frac{u'}{\sigma\sqrt{2}} = q; \quad \frac{v'}{\sigma\sqrt{2}} = q'; \quad \frac{a}{2\sigma} = \beta, \tag{24}$$

we get

$$A^2 = \frac{4\sigma^2}{\pi^2} \int\int\int\int_{-\infty}^{\infty} (s^2+t^2) e^{-(s-\beta)^2} e^{-q^2-q'^2-t^2}\,dq\,dq'\,ds\,dt. \tag{25}$$

The squares in expression (25) are easily replaced on the basis of relationship

$$\int_{-\infty}^{\infty} e^{-q^2} dq = \sqrt{\pi};$$

$$\int_{-\infty}^{\infty} s^2 e^{-(s-\beta)^2} ds = \sqrt{\pi}\left(\frac{1}{2} + \beta^2\right).$$

which results in a simple final formula

$$A^2 = 4\sigma^2(1 + \beta^2)$$

or on the basis of (24)

$$A = \sqrt{a^2 + 4\sigma^2}. \tag{26}$$

In a similar manner we can find the mean square distance when there are errors in determining the position of only one of two points. Then, for A^2 we get expression

$$A^2 = \int_{-\infty}^{\infty}\int (x^2 + y^2) f(x - a, y)\, dx\, dy, \tag{27}$$

from which, after squaring, we get the simple formula

$$A = \sqrt{a^2 + 2\sigma^2}. \tag{28}$$

In accordance with formulas (26) and (28) the mean distance with errors in determining the position of points is greater, and it cannot be less than 2σ with errors in tying-in both points, and $\sqrt{2}\sigma$ when there are errors in tying-in one point.

If the value σ -- the mean square error of tying-in -- is known, the graph of a correlation function can be easily reconstructed using formulas (26) and (28). Formula (26) must be used with respect to the auto-correlation functions of radiation fluxes and mutual correlation functions of the integral current and the current in the transparency window for all distances a, except zero distance. Formula (28) should be used with respect to the mutual correlation functions that tie in the radiation fluxes with the temperature, because a tying-in error is peculiar only to actinometric information, while the tying-in of temperature information may be considered accurate.

The use of formulas (26) and (28) boils down to the fact that the abscissa a of each point of the curve is replaced by the value A with an invariable ordinate. In practice this substitution should be made up to comparatively large distances of a, beginning with which it changes results insignificantly.

A curve corrected in this manner differs from the original one in two respects. First, it is smoother with lesser changes in curvature. Second, the area of short distances appears on it to be completely unscanned [osveshchennoy]. To get some idea about the behavior of the correlation function at these short distances, all we need do is extrapolate or interpolate. For correlation functions of radiation fluxes, there are known values at zero distance and hence interpolation is possible; this gives us some idea about the probable appearance of these functions at short distances. As far as the mutual correlation functions which describe the relationship of radiation fluxes and temperature are concerned, we can merely extrapolate these functions in the direction of the short distances. Of course, such an extrapolation is not very reliable, but nevertheless it can offer us an approximate idea about the order of magnitude of mutual correlation functions of short distances which might arise if there were no tying-in errors.

In actual practice, the matter becomes somewhat complicated by the fact that we have only a rough estimate of the mean square error of tying-in σ. Hence, our computations were made using several values of σ, analyzing the while as to the amount of "improvement" in the curves after inserting the appropriate corrections.

As a result of these corrections, which are essentially an indirect estimate of the value σ, it was established that $\sigma = 500$ km should be accepted.

Shown in Fig. 4 are certain corrected correlation functions using the method indicated. The short distance portions of these functions, obtained

through interpolation or extrapolation, are indicated by broken lines.

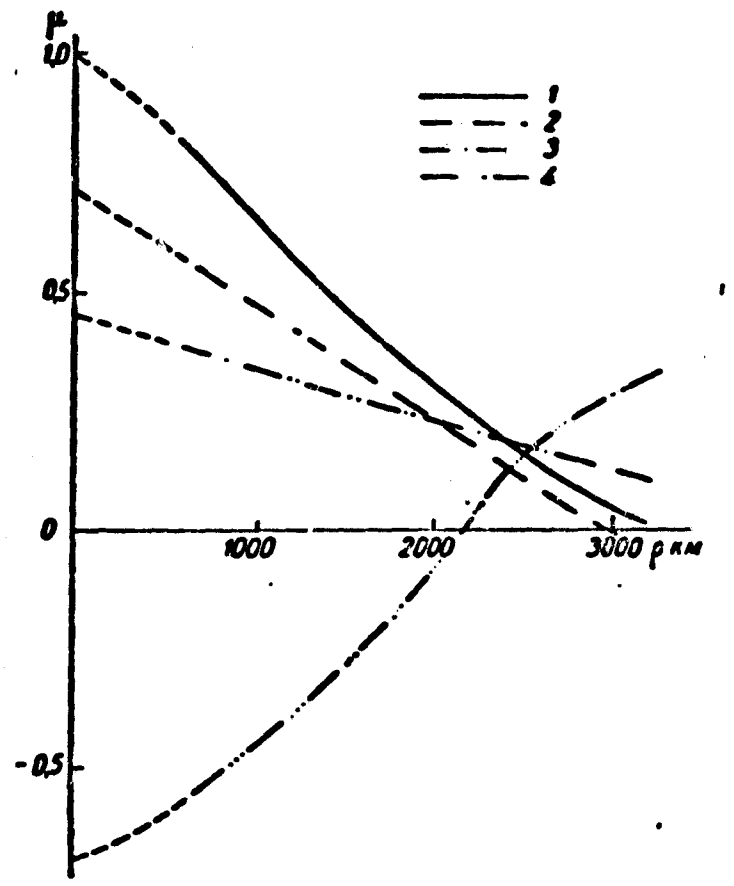

Fig. 4. Corrected standard auto-correlation and mutual correlation functions of radiation fluxes and air temperature.

1 -- $\mu(\zeta\ 8-30,\ \zeta\ 8-30,\ \rho)$; 2 -- $\mu(\zeta\ 8-30,\ T_{500},\ \rho)$; 3 -- $\mu(\zeta\ 8-12,\ T_{ground},\ \rho)$; 4 -- $\mu(\zeta\ 8-30,\ T_{100},\ \rho)$.

As we can see from the graphs of mutual correlation functions, the introduction of corrections results in a marked increase in correlation between the temperature and radiation fluxes. We can therefore assume that if there are no great errors in tying-in, the greatest values of these coefficients would increase approximately from 0.50 to 0.70.

REFERENCES

1. Boltenkov, V. P. Issledovaniye statisticheskoy makrostruktury temperatury voxdukha. Tr. GGO, No. 174, 1964.
2. Gandin, L. S. Fateyev, A. V. Analiz tochnosti raxlichnykh metodov interpolyatsii. Tr. GGO, No. 121, 1961.
3. Bergthorsson P., Doos, B. R. Numerical weather map analysis. Tellus, vol. 7, No. 3, 1955. Translation in "Chislennyye metody prognoza pogody" edited by L. S. Gandin and A. S. Dubova. Gidrometeoizdat, 1960.
4. Cressman, G. P. An operational objective analysis system. Monthly Weather Review, vol. 87, No. 10, 1959.

5. TIROS II radiation data catalog. Vol. 1. Goddard Space Flight Center, 1961.
6. TIROS II radiation data user's manual. Goddard Space Flight Center, 1961.

V. L. Gayevskiy and Yu. I. Rabinovich

CALCULATING THE INFLUENCE OF THE ATMOSPHERE ON THE RESULTS OF MEASUREMENT OF RADIATION TEMPERATURES OF THE EARTH'S SURFACE OBTAINED FROM ARTIFICIAL EARTH SATELLITES

1. Some Data on the State of the Problem.

The main drawback in the method of determining radiation temperatures of the surface according to data obtained from the measurement of its own radiation is the difficulty in making a reliable calculation of the effect of the atmosphere on the transfer of radiation from the earth's surface to the instrument.

As we know, absorption by the atmosphere of the earth's thermal radiation in the 4 to 40 μ sector of the spectrum -- the earth's radiation under natural conditions is practically restricted to this -- and the inherent radiation of the atmosphere have a sharply expressed selectivity. To measure the radiation temperature of the surface, it is very important to select that portion of the spectrum in which the influence of the atmosphere on the transfer of radiation would not be very considerable.

Analysis of spectral transmission by the atmosphere of infrared radiation shows that the best sector of the spectrum for measuring radiation temperatures is one that is about 0.1 μ wide with a wave length of 11 μ in which absorption by the atmosphere is virtually absent, and scatter effect is negligibly small. However, at the present time we still have not designed equipment that operates well on aircraft.

Another sector of the spectrum which is used for measuring radiation temperatures [1, 2, 3, 4] lies within the limits of 8 - 12 μ, in which there is a happy combination of a comparatively slight absorption of water vapor and maximum surface radiation at temperatures from 220 to 320°. At the same time Deirmendjian [5] demonstrated, while studying the influence of radiation scatter by aerosols in the atmosphere in the 8 - 12 μ sector of the spectrum, that this attenuation is less by an order then the influence of absorption and

radiation of water vapor for the wave lengths in question. The presence of narrow and weak CO_2 absorption bands has no marked influence on the overall magnitude of transmission in this range of wave lengths.

In measuring the radiation temperature from a satellite a certain influence on the transfer of radiation may be exerted by a narrow, sufficiently strong ozone band of absorption with a maximum at 9.6 μ . As shown in references [5,7], the maximum error in determining the radiation temperature of the surface which can be introduced, disregarding the influence of ozone, is about 5°; this is approximately one-fifth as great as the maximum error due to disregarding the influence of water vapor. The influence of ozone can be eliminated in practice if we select a spectral range from 10 to 12 μ ; the energy of measurement will hereby be decreased somewhat (about one-half).

If the change in stratification of the ozone layer does not exercise a considerable effect on the absorption of radiation from the surface of the earth, then the change in the distribution of water vapor and temperature in the atmosphere plays an important role in the mechanism of radiation transfer [6 - 10]. According to data provided by Greenfield and Kellog [10], depending on the stratification of the atmosphere in the overall radiation flux entering the boundary of the atmosphere, radiation from earth may be from 2/3 to 1/3 of the total amount. This means that in order to insure the accuracy essential for practical purposes in determining the radiation temperature of the surface, it is necessary reliably to take into account the influence of the temperature on the transfer of radiation.

The influence of atmospheric water vapor and ozone on the transfer of escaping earth radiation in the 8-12 μ sector of the spectrum is considered in studies [6,7] with the object of increasing the accuracy in determining the surface temperature according to measurement data from the satellite.

Wark, Iamamoto and Lienesh [7] considered the transfer of earth surface radiation with 106 samples of atmosphere with various contents and distribution

of water vapor and air temperature, and at different intensities of earth radiation. On the basis of the data they obtained they made a graph of corrections which are to be used in the measurement data from the satellite in order to get the real temperature of the surface. The results of their computations indicate that depending on the stratification of the atmosphere the errors in measuring the temperature from the satellite can attain large values. In order to decrease this error, the authors suggested using corrections based on the amount of water vapor in the atmosphere separately for stratifications with high and low atmospheric water content. The test they made demonstrated that the error of individual measurements is as much as 10°. The error introduced in measuring the surface temperature by a layer of ozone was determined by the authors from computation data based on 40 models of ozone stratification. The maximum error on the influence of the ozone layer in determining the temperature of the surface is about 5°. Unfortunately, in their published work the authors did not indicate the amount of water vapor that pertains to corrections for high and low contents of water vapor, which, as properly pointed out by M. S. Malkevich [6], injects some uncertainty in getting the surface temperature.

In the study of M. S. Malkevich [6] computations were made of escaping radiation for latitudinal distributions of vertical temperature and humidity profiles. On the basis of these computations, they constructed a graph of corrections which should be injected into the measurement data from the satellite to determine the surface temperature. The correction due to the influence of water vapor may amount to 25°. As Malkevich demonstrates, the introduction of these corrections makes it possible to evaluate the temperature of the earth's surface with an error which may exceed 5°. The method of computing corrections proposed by the author may give an accuracy of the order of 5° in determining the mean surface temperature of large territories when mean values

of stratification for a given area. For comparatively small sections the errors in determining surface temperatures should be greater than those indicated by the author because the deviations from mean values of stratification for a given instance may be considerable and their precise determination extremely difficult. Thus, improving the accuracy of a single determination of surface temperature by the radiation method is an extremely difficult task. In addition, the absence of experimental data about the influence of atmospheric stratification on the transfer of the earth's radiation complicates considerably any further work on enhancing the accuracy of determining surface temperatures by this method.

In the A. I. Voykova Main Geophysical Observatory measurements were made in 1961-1962 of the radiation temperature of natural surfaces from an aircraft; the results obtained may be used for a more accurate determination of the influence of the atmosphere.

2. Brief Description of an Instrument for Measuring Radiation Temperatures of the Earth's Surface From an Aircraft

In keeping with the accepted method we developed a mock-up of an instrument for measuring radiation temperatures of various underlying surfaces. The basis of it was a compensating system with registration on paper of measured values. By way of a recording instrument we used an EPP-09 electronic potentiometer. A radiation thermo-element (RTE), type TK x 1.5, serves as the radiation receiver.

The overall block diagram of the apparatus, explaining the compensating method of measurement is shown in Fig. 1. The signal from the thermo-element is fed to the compensating-balancing circuit. Potentiometer R_1 balances the sensitivity of the thermo-element platforms. Resistances R_2 and R_3 make up the divider to feed a constant compensating voltage with hand-set zero point. A similar divider, R_4 - R_5, in the other circuit of the thermo-element serves

as auto-compensation; this is achieved by feeding a compensating voltage from the rheochord of electron potentiometer EPP-09.

The alternating current pre-amplifier with vibrator converter at the input and synchronous detector at the output insure pre-amplification of the radiation thermo-element signal. The amplified and detected signal goes to the input of EPP-09. Since the system of adjustment also includes a pre-amplifier, changing the gain in certain limits does not affect the output value registered by the instrument.

The power unit contains the PO-300 motor alternator (120 v 50 cycles) for feeding the EPP-09 and motor-generator RUN-11 for feeding the tube plates of the pre-amplifier.

Also included in the apparatus set is the power unit for heating and controlling the temperature of the thermo-element, which insures maintaining a constant temperature in the thermo-element housing.

In order to have uninterrupted recording of radiation fluxes and to graduate the instrument in absolute units, it is necessary during the operation to maintain the temperature of the thermo-element constant. This is the most complex problem if we take into account the fact that in making measurements from an aircraft at various heights the temperature of the surrounding air undergoes marked changes. However, temperature variations in the thermo-element housing within the limits of even several tenths of a degree does not insure sufficient stability of operation. It is essential to have a higher uniformity of the temperature field within the thermo-element housing. Completed measurements have shown that discontinuities in the temperature field inside a housing which are less than 0.001°, cause a considerable drift in the zero position of the instrument; this makes it impossible to give prolonged, uninterrupted registrations of radiation fluxes.

To insure uniformity of temperature in the housing and in the temperature

field the thermo-element is placed in a heated housing with good thermal insulation and a large-sized thermal conductor made of red copper ore. The heating is controlled by manually controlling the temperature; the temperature is measured by a resistance thermometer of copper wire.

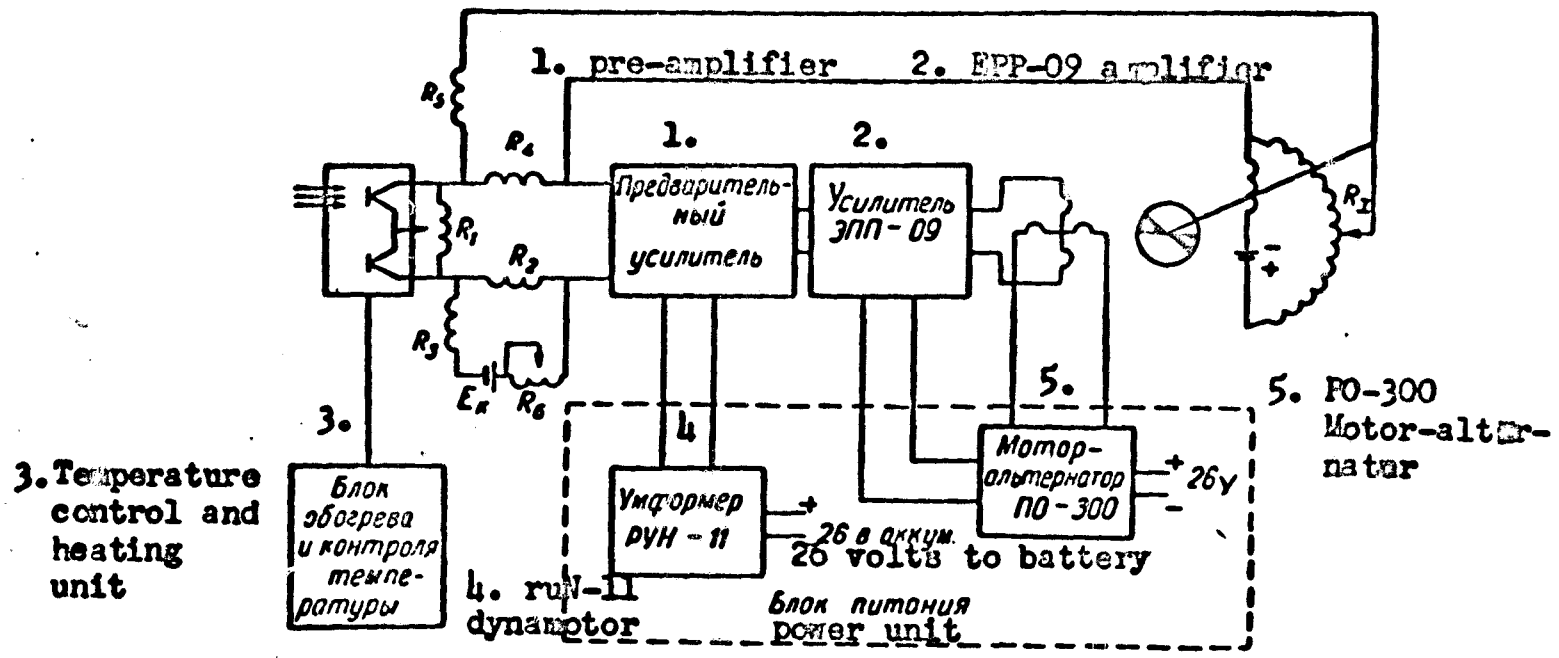

Fig. 1. Block diagram of apparatus.

A schematic diagram of the thermocouple unit system is shown in Fig. 2. Thermocouple II is contained inside a copper heat conductor 4 consisting of two detachable parts secured by threaded collars 6. Sealed into the body of the thermal conductor are two resistance thermometers. The red copper ore adapter 3, inside of which filters 15 and the valve flap are contained, is secured to the thermal conductor on the input opening side of the thermocouple. The combination filter consists of two round plates with a diameter of 10 mm. The internal plate is made of fluorite (CaF_2) 1 mm thick, and the external one is made of indium antimonide (InSb) that is 0.2 mm thick. This combination insures separating out a spectrum from 7.5 to 12.0 μ . The spectral characteristics of a light filter are shown in Fig. 3. Between the output opening of the thermocouple housing and the light filter there is a flap; the zero position of the instrument is set here. The interior surface of the flap that faces the thermocouple is covered with a sooty composition, while the external surface

is meticulously polished. Between the flap and housing there is a good thermal contact on a large surface; this makes it possible to receive a temperature equal to that of the thermocouple.

The thermal conductor with thermo-element and the cap for the flap and filters is placed inside the heater which is made in the form of an aluminum cylinder 12. Placed on the outside of the cylinder is heating coil 14, covered by a layer of asbestos insulation and fiber glass. Inside the heater there is an index 2 and lock ring 7 to lock the thermocouple in position. The heater is set in a tube of polychlorvinyl 5 covered on the ends by glass textolite. Set on the upper flange 7 are two joints: one 9 for cutting in the thermocouple, and the other 10 for cutting in the heater coil, the thermoregulator pickup, and the resistance thermometers.

The thermocouple joint has copper, gold plated contacts. The leads from the thermocouple are weld connected with the joint, and the hose is connected with copper screws. Such a design makes it possible to reduce to a minimum the chance appearance of parasitic thermo emf at the contacts. To improve the thermal insulation, the measuring head is protected from the outside by a cotton quilted hood.

The thermo-element visual field angle for radiation coming in from the measured surface is limited by the opening in the cap for the filters and flap. Since the receiver area of the thermo-element is rectangular in form (3 x 1.5 mm) the visual field of the thermo-element is likewise non-symmetrical. The linear visual field angle on the short side of the platform is 23°. The thermo-element is so constructed that its visual field is not obscured by elements of construction which have a temperature that differs from the temperature of the thermo-element.

The entire apparatus is disposed on two tables which are secured to the decking of the aircraft passenger compartment. The measuring head with thermo-element is installed at the low point of the fuselage. Disposed on the first

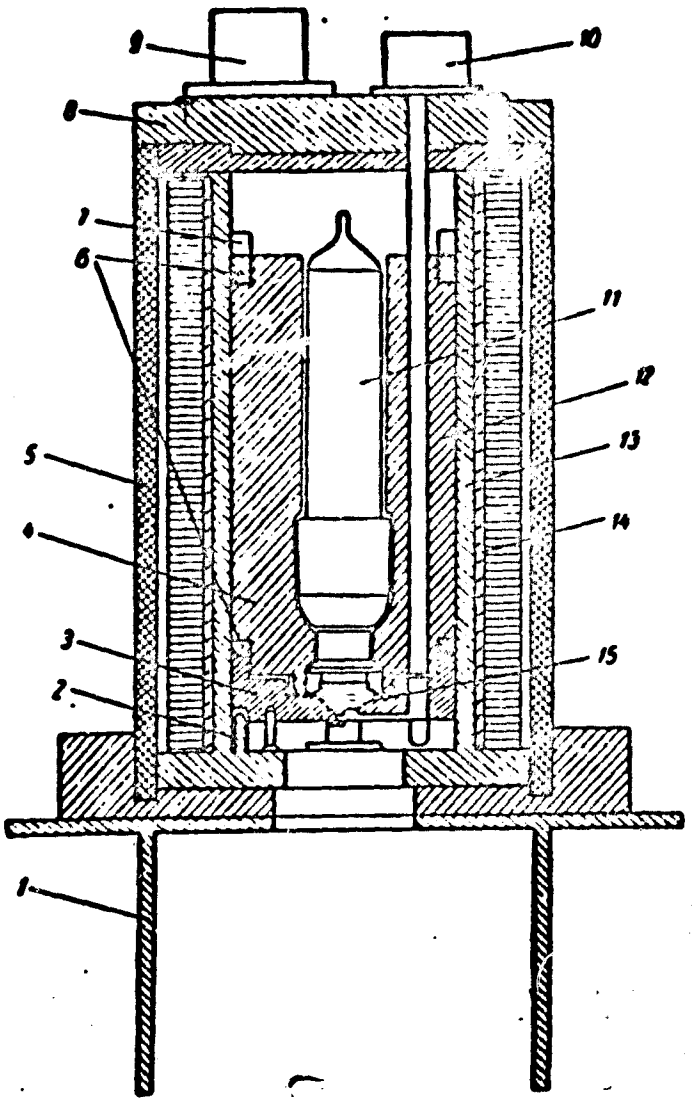

Fig. 2. Block diagram of a thermo-element.

table are the amplifier units, the compensator, and the EPP-09 electronic potentiometer. On the lower shelves of this table are contained the amplifier power unit and the RUN-11 dynamotor, as well as the container with spare parts and tools. On the second table we find the panel with control instruments and fuses for connecting all units that are fed by the aircraft power system.

Here, we find the apparatus for control and measurement of the temperature of the measuring head. On the lower shelf there is PO-300 converter and ferroresonance stabilizer, ST-250, mounted on shock absorbers. The whole set weighs about 250 kg.

Absolute calibration of the instrument can be done according to the density of the radiation flux from the surface or power brightness, as well as

according to the absolute temperatures of this surface. The latter occurs only if the surface that is being measured is a black body. For surfaces whose coefficient of radiation is not equal to unity, this temperature will differ from the actual temperature, and it is usually defined as the "radiation temperature of a measured surface." It should be noted that both kinds of calibration are absolute, and a simple conversion from the one to the other is possible if the coefficient of surface radiation according to which the calibration was made is known, or if this surface is a black body.

The absolute calibration of a radiometer was made on a black body, the scale of the instrument being temperature calibrated. Since the method of measurement, as will be seen in the following, consists of giving a signal at the output of the instrument in the form of a difference between the temperature of the measured surface the inherent temperature of the thermo-element, we select the latter temperature for the zero position of the scale. In this case the reading on the scale of the output instrument (EPP-09) gives the direct radiation temperature of the measured surface or the absolute temperature for the black body.

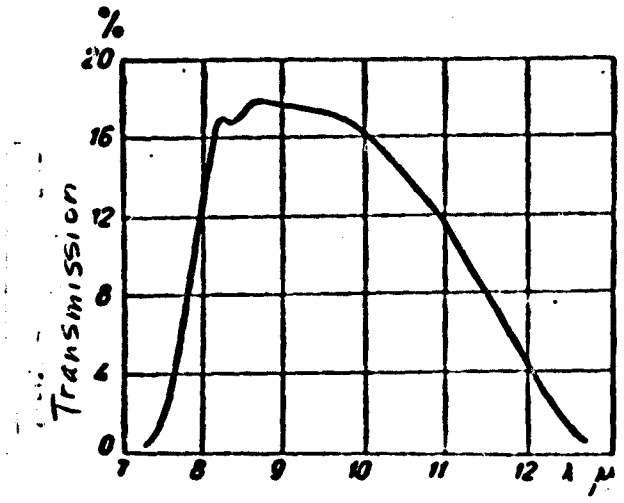

Fig. 3. Spectral characteristics of a light filter.

In calibrating the instrument -- and this is true in other measurements with this instrument -- the assumption was that the temperature of the thermo-element housing, the sealed compensating platform, the flap covering the measured flux, and the light filter remains the same and constant during the calibration

process. This is insured by the construction of the measuring head and is determined by checking the convergence of repeated calibrations.

We will determine the basic relationship which describes the operation of the instrument. When the flap is closed the equation for the heat balance in a measuring head of a radiometer appears as

$$\omega\sigma T_0^4 + w_0 - \varepsilon s\sigma T_0^4 = 0,$$

in which T_0 is the temperature of the thermo-element and flap, ω is the solid angle of the instrument, ε is the coefficient of radiation of the platform, s is the total radiating surface of the platform, w_0 is the energy arriving at the platform from the entire solid angle except the operating angle, σ is the Boltsman's constant.

It is assumed here, that the coefficient of radiation of all sides of the platform is the same. If this assumption is not made the last member of the equation changes. If we now open the flap and direct the instrument toward the black body with temperature T_1, this equation will appear as follows

$$\omega\sigma T_1^4 + w_0 - \varepsilon s\sigma (T_0 + \Delta T)^4 - \varkappa \Delta T = 0,$$

where T_1 is the temperature of the calibrated black body, $\Delta T = T_1 - T_0$ is the overheating or cooling of the platform under the influence of incoming radiation, $\varkappa$ is the coefficient of heat conductivity of the holders on which the receiving platform is suspended.

The first member of the equation determines the flux from the black body in the solid angle ω, the second member determines the flux from the thermo-element housing in all the remaining angles, the third member determines the inherent flux of the platform, and, finally, the last member determines the heat loss of the platform due to the heat conductivity of the holders.

Taking into account the fact that the platform is not excessively overheated during the measuring process, inasmuch as the greatest difference in temperature

of the thermo-element and the measured surface is 20° within the limits of the instrument scale, we get the following after conversion:

$$\Delta T = \frac{\omega\left(T_1^4 - T_0^4\right)}{4\varepsilon\sigma T_0^4 + \varkappa}.$$

This equation enables us to find the amount of overheating of the receiving platform of the thermo-element resulting from the effect of the radiation being measured.

The output value of the instrument is determined by the following expression:

$$u_{out} = k u_{in} = k\eta\,\Delta T,$$

where k is the transmitting characteristic of the system, η is the specific emf of the thermocouple of the thermo-element.

Substituting ΔT in the expression for u_{out} we get

$$u_{out} = k\eta\,\frac{\omega\left(T_1^4 - T_0^4\right)}{4\varepsilon\sigma T_0^4 + \varkappa}.$$

In order further to convert the equation it is necessary to assume that the losses due to radiation in the thermo-element are equal to the losses due to thermal conductivity, i.e.,

$$4\varepsilon\sigma T_0^4 = \varkappa.$$

Ordinarily, in designing thermo-elements this condition is observed. Then, taking into account the previously accepted assumption about the small difference in T_1 and T_0, we get, after conversion

$$u_{out} = k\eta\,\frac{\omega}{2\varepsilon S}\left(T_1 - T_0\right).$$

From the expression derived, we can make two important conclusions:

1. The output value is linearly related to the difference in temperature between the thermo-element and the surface measured.[1]

---

1. The divergence of the scale from the linear due to the light filter is not considered here.

2. The output value depends on the temperature of the thermo-element, i.e., the calibration should be done for each value of the inherent temperature of the measuring head.

It is now necessary to evaluate the discriminating capacity of the apparatus and the accuracy of measurements.

By discriminating capacity, we mean the dimensions of the smallest surface whose temperature differs from that of the surrounding background by the value ΔT. The latter can be recorded by a radiometer with a given precision. The value of the discriminating capacity is a function of many variable parameters. First of all, it will depend on the geometric characteristics of the apparatus: the measuring head of the instrument, the height and air speed of the aircraft, the sighting angle of the radiometer, as well as the time constant of the apparatus, i.e., the speed of measurement and calibration of the flux. Finally, the discriminating capacity depends on the nature of the spatial distribution of the temperature of the underlying surface that is being studied.

The following initial data may be accepted in making computations of the discriminating capacity:

1. Altitude of flight $H = 5{,}000$ meters.
2. Velocity of aircraft $V = 200$ km/hr $= 56$ m/sec.
3. Viewing field angle $\alpha = 20^{\circ}$
4. Time constant of thermo-element $\tau_T = 0.2$ sec.
5. Time for adjusting the entire EPP-09 scale $\tau_p = 1.0$ sec.
6. 20° instrument scale (the difference between the surface temperature and that of the thermo-element.)

The time constant of the entire system is determined by the time constant of the thermo-element since it is the system element having the greatest inertia (without taking into account the time of adjusting EPP-09). In order reliably

to reproduce a signal the time of its action on the system should be not less than 5 τ . In that case the error in reproducing the signal amplitude will be 0.7%. During the time of the non-stationary process t = 1 second, the apparatus will record the mean temperature of the surface with dimensions $a=2H\,\mathrm{tg}\,\frac{\alpha}{2}, b=2H\,\mathrm{tg}\,\frac{\beta}{2}+V$ or 1760 x 2320 m.

On the other hand, during the time of the non-stationary process t = 1 sec the carriage of the potentiometer may run through the entire scale, i.e., it may record a change in temperature equal to 20°. In order that the error in determining the temperature may not contain an additional component due to the discriminating capacity being over 0.7%, the maximum difference between the temperatures of the surface with minimal dimensions s and the surrounding background should not exceed 20°.

It is now necessary to evaluate the greatest theoretical accuracy of measurement in calibrating the instrument according to a black body, whose temperature is known within an accuracy of 0.1°.

Given a mean coefficient of amplification, the threshold of response u_{th} with an error of less than 0.5%, is $0.5 \cdot 10^{-7}$ volts. The input signals $< 0.5 \cdot 10^{-7}$ volts are worked out by the system with an error that increases rapidly in measure as the signal is decreased. The activating threshold of the system is $5 \cdot 10^{-9}$ volts.

In using a calibration with a scale of 20°, the variation of the potentiometer carriage by one graduation is $u_1 = 0.625 \cdot 10^{-7}$ volts/graduation, the variation over the whole scale $u_m = 62.5 \cdot 10^{-7}$ volts or $u_T = 0.625 \cdot 10^{-7} \cdot 5 = 3.125 \times 10^{-7}$ volts/degree.

Taking into account the threshold value of the signal we can determine the least difference in temperature between the thermo-element and the calibrating body which the instrument will register

$$\Delta T_{th} = \frac{0{,}5 \cdot 10^{-7}}{3{,}125 \cdot 10^{-7}} = 0{,}15°.$$

The total absolute error in determining the radiation temperature will still have errors in measuring the temperatures of the black body and the measuring head.

$$\Delta T = \Delta T_{th} + \Delta T_{b.b} + \Delta T_{h.el.} = 0{,}15 + 0{,}1 + 0{,}15 = \pm 0{,}4^{\circ}.$$

The relative error corresponding to it will be equal to

$$\varepsilon_{pr} = \pm \frac{0{,}4 \cdot 100}{20} = \pm 2\%.$$

The relative error of measurement, when the difference in temperature between the thermo-element and the black body is 5°, will be equal to

$$\varepsilon\% = \pm \frac{0{,}4 \cdot 100}{5} = \pm 8\%.$$

Thus, in order to insure a theoretical accuracy of measurement of not over ± 10% it is necessary to have a difference in temperatures between the thermo-element and the measured surface of not less than 4°.

Real errors of measurement in the summer may differ from the computed errors due to possible temperature non-uniformities in the temperatures of the thermo-element housing, the flap, and the filter. The values of the real errors of measurement may be estimated by comparing the data of aircraft measurements and the data of ground measurements of temperature for water surfaces which approximate the black body in their properties.

The measurement of the radiation temperature of a water surface was made over the Caspian Sea in the region of Neftyannyye Kamni a distance of 50 km from the coast, and for comparison we used the water temperature measurement data of the Main Meteorological Station at Neftyannyye Kamni.

Given in Table 1 are the results of water temperature measurements t_{st} and radiation temperature measurements t_{rad}, as well as the absolute errors Δ_t (all in °C). According to the table the greatest value of absolute error does not exceed 2.3°, and the mean error for all 33 cases of measurement is 0.85°. The results of comparison support the correctness of the above-produced estimates of measurement accuracy.

Table 1

$t°_{st}$	$t°_{rad}$	$\Delta t°$	$t°_{st}$	$t°_{rad}$	$\Delta t°$	$t°_{st}$	$t°_{rad}$	$\Delta t°$
15.5	16.2	0.7	21.4	20.2	1.2	16.0	14.6	1.4
16.0	16.3	0.3	22.8	22.0	0.8	16.0	13.7	2.3
16.5	16.1	0.4	22.5	22.9	0.4	16.0	14.7	1.3
15.5	16.0	0.5	23.6	24.0	0.4	16.1	15.5	0.6
16.9	17.9	1.0	23.6	24.4	0.8	16.1	15.8	0.3
17.0	16.4	0.6	22.8	24.5	1.7	16.5	17.7	1.2
17.0	18.0	1.0	22.8	24.4	1.6	16.0	17.0	1.0
17.5	17.8	0.3	23.0	24.5	1.5	16.0	16.4	0.4
21.0	20.8	0.2	24.0	22.3	1.7	16.0	16.2	0.2
21.4	21.8	0.4	24.0	23.7	0.3	16.0	17.0	1.0
21.0	20.7	0.3	24.0	24.3	0.3	16.5	16.9	0.4
22.0	20.4	1.6						

3. Results of Measurements and Practical Recommendations

Measurements of radiation temperatures were conducted above the water surface in the areas of the Caspian Sea, Gulf of Finland, and the White Sea, and over snow surfaces in parts of Leningrad Oblast at altitudes of 100, 200, 400, 600, 800, 1000, 1500, 4000, and 6000 meters. Simultaneously with measurements of radiation temperature recordings were made in the aircraft of the temperature and humidity of the air by aircraft meteorograph, and measurements were made of the temperatures of the water surface and the snow cover. Since the radiating capacities of the water surface and snow cover were close to unity in the 8 - 12 μ section of the spectrum [11, 12], we can compare the radiation temperature measurement data from direct measurements.

A total of 73 series of observations during different seasons of the year and with different stratifications of the atmosphere were made during the period in question. The measurements were carried out with the water vapor content at from 0.2 to 3.6 cm of precipitated water and a surface temperature of from -27 to 26°.

The correction for the influence of stratification in measuring the surface temperature was determined as the difference between the real temperature of the surface and that measured by the radiation method.

Typical profiles of stratification of the atmosphere and radiation temperature are shown in Figs. 4, 5, and 6; we can judge from these as to the influence

of stratification on the accuracy of measuring the radiation temperature. As we can see from the drawings, the profile of changes in the radiation temperature with height depends both on the distribution of water vapor with altitude and on the temperature profile. The maximum difference between the measured temperature and the actual temperature was 15° with a water vapor content of 3.6 cm of precipitated water and a surface temperature of 20°. The corrections we obtained take into account not only the influence of the water vapor and the air temperature, but also other factors like, for example, aerosols, the inaccurracies in computations on the radiation capacity of the surface and others. Hence, the corrections to the computations [7], which were determined mainly by the distribution of water vapor and the temperature, are somewhat high.

Let us consider the effect of the isothermic and inversion types of stratification on the accuracy of measurements of radiation temperatures. With an isothermic profile of air temperature and a normal distribution of water vapor with altitude, the radiation temperature is virtually equal to the temperature of the surface at all levels of the isothermic profile. Changes in the amount of water vapor in the atmosphere in this kind of stratification have no noticeable effect on the transfer of outgoing radiation.

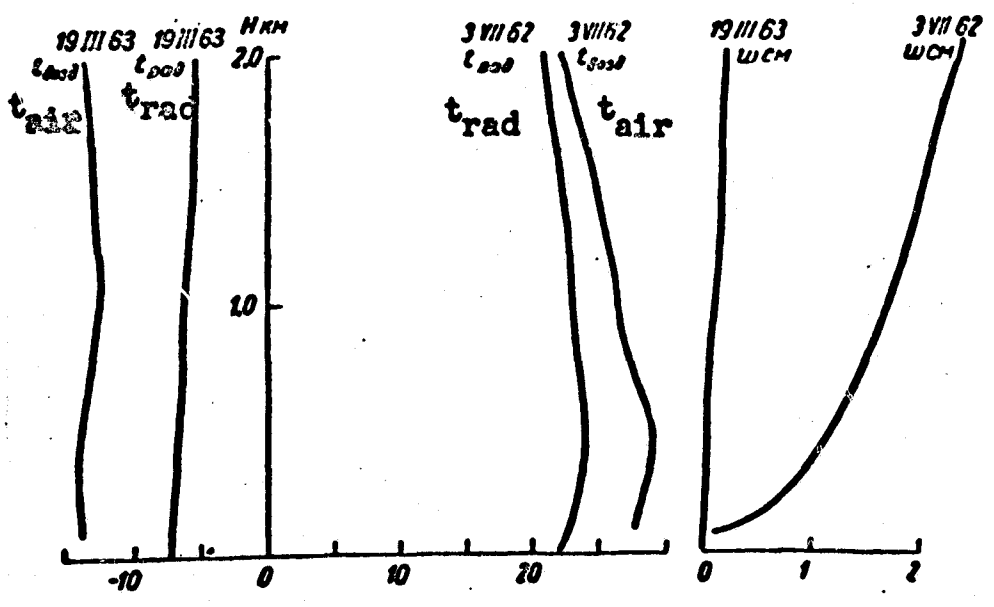

Fig. 4

With an inversion which goes up to 3 km, the correction for the effect of the atmospheric layer between the surface and the instrument changes in sign and the size of the correction is a function of the change in water vapor content. Inversions up to 1 km in altitude decrease the correction but they do not result in changes of sign to the correction.

The negative correction with inversion reached -4°. In the majority of cases this correction is equal to -2°. In winter inversions (with negative ground surface temperatures) it is 1 - 2°.

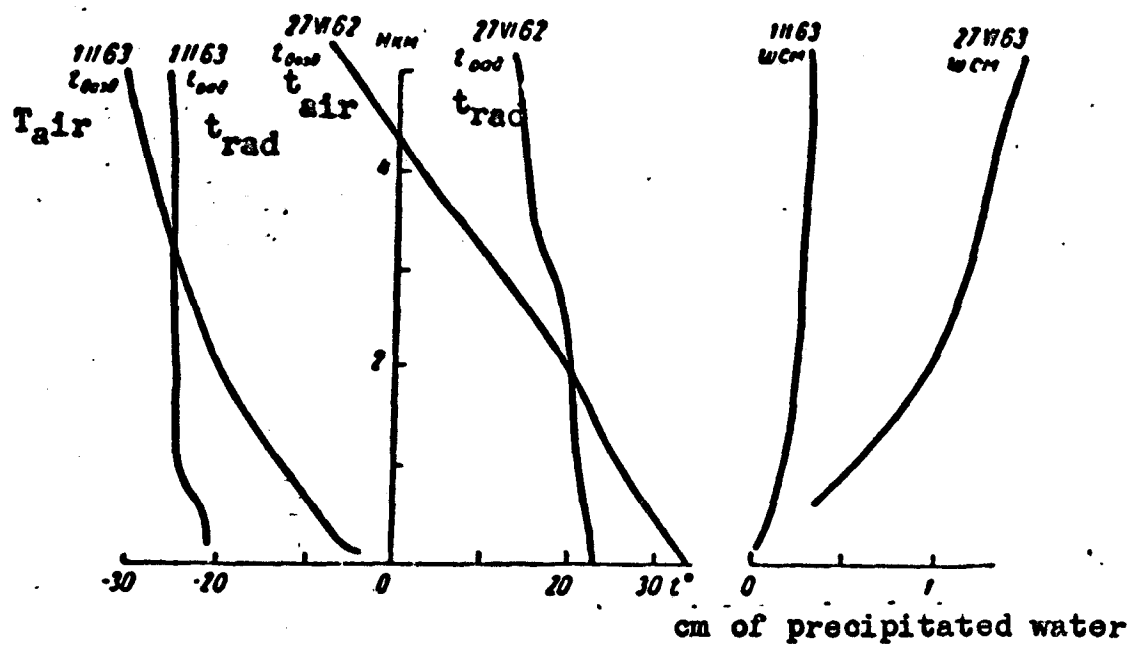

Fig. 5

Shown in Fig. 7 are the differences between radiation temperature and the actual temperature of the surface for all series of observations excepting the inversion types with negative correction. The data presented in the graph make it possible to determine the existing relationship of the size of the correction to the amount of water vapor in the atmosphere. Hence, a change in water vapor content of 1 cm of precipitated water results in a change to the correction by an average 5° with a surface temperature of 26° and by 3° with a surface temperature of 15°.

The lines in Fig. 7 show the mean values of corrections to the following values of water vapor in the atmosphere: 0.5, 1.0, 2.0, and 3.0 cm of precipitated water. Utilizing the corrections for the indicated gradations of

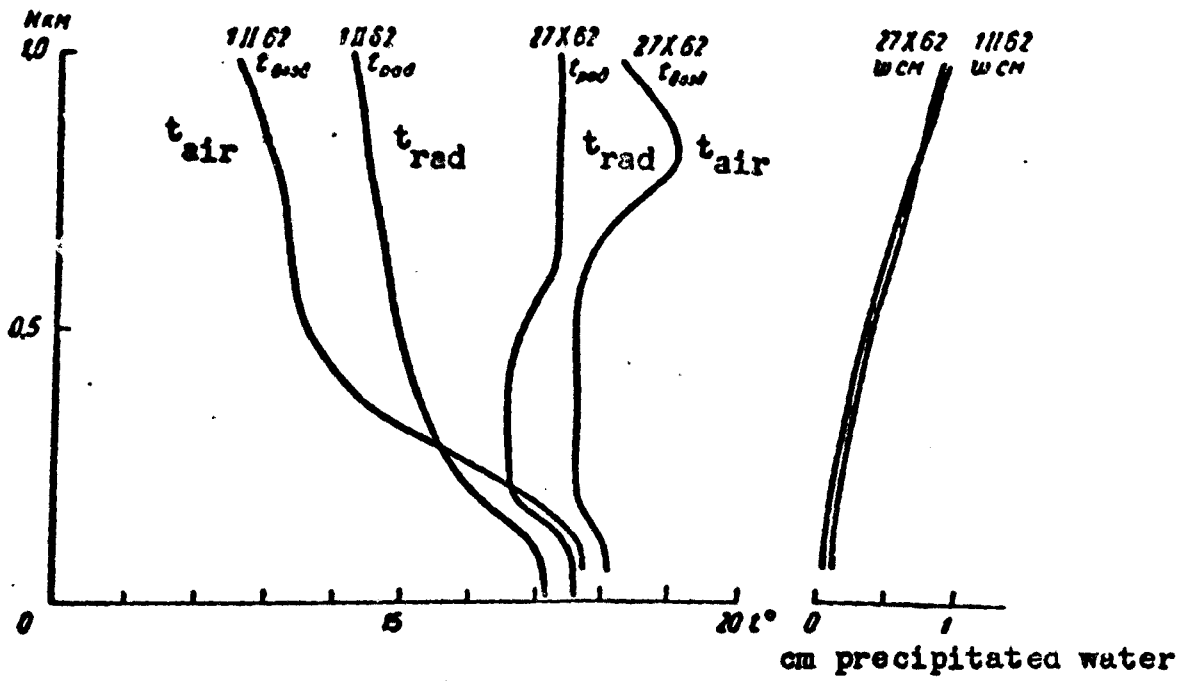

Fig. 6

precipitated water in the atmosphere, the maximum error in determining the real temperature will not exceed $\pm$ 2.5°. Shown here is a curve of corrections which we derived from study [6] computed for an instrument with which we made the present study.

To take into account the influence of the ozone layer on the measurement of the surface radiation temperature we used the corrections cited in references [5,7,8]. Because in the case of small values of ground surface radiation this correction is considerably smaller than the correction caused by the effect of stratification, the correction indicated can be disregarded with negative temperatures of ground surface.

Fig. 8 shows the total correction for the influence of the water vapor and ozone which should be introduced with the measurement data from the satellite to determine the real radiation temperature of the surface.

The amount of water vapor in the atmosphere necessary as an input parameter is determined from the synoptic data on air temperature and humidity or from the data of isobaric surface charts made approximately at the same time as those recorded by a weather satellite. Computations on the amount of precipitated water in the atmosphere are made on the basis of empirical formulas of

Nakorenko. If the reliability in determining the amount of water vapor in the atmosphere is not under 50%, the error of a single temperature determination will not exceed 4°.

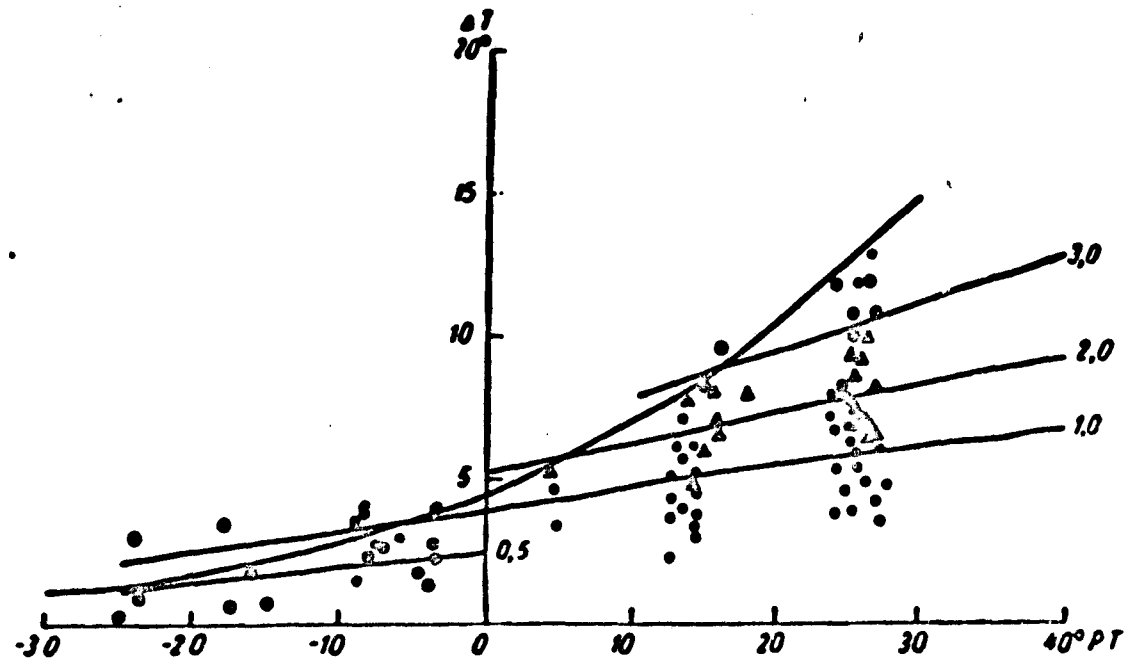

Fig. 7. Differences between the radiation temperature and the surface temperature for all series of observations.

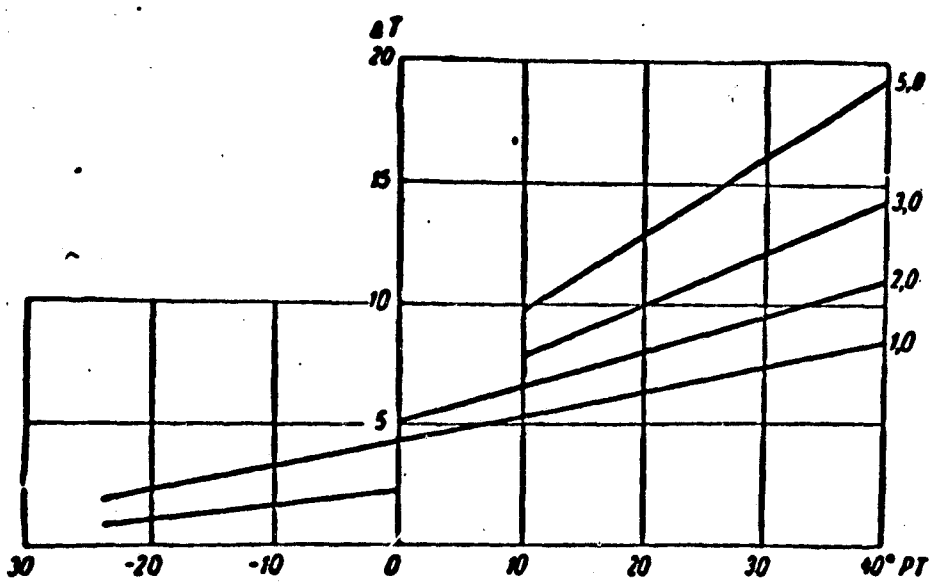

Fig. 8. Graph for determining the actual surface radiation temperature.

In addition to determining the influence of stratification on the accuracy of measuring the radiation temperature, measurements were made of the radiation temperature of certain types of surfaces, and a comparison was made

with surface temperature data obtained at meteorological stations. The results of comparisons are shown in Table 2.

The radiation temperature was determined on an area 200 to 300 km in extent. The mean values of radiation temperature differ from the data of meteorological stations by not over 1.5°. Individual measurements in station areas differ by not more than 7°. These data show that the radiating capacity of the majority of natural surfaces is close to unity. In averaging out for the area the differences between the real and radiation temperature are quite small.

Table 2

October 1962

	t°_{mean}	t°_{max}	t°_{min}	t°_{real}
Coniferous forest. .	12.2	16.2	9.3	--
Alma-Ata - Tashkent.	26.4	28.0	25.2	27.8
Krasnovodsk-Tashauz.	25.1	32.3	20.0	26.0
Gur'yev - Volgograd.	14.3	17.5	11.2	12.0
Moskva - Leningrad .	12.2	13.0	10.5	13.1
Water	21.7	22.3	21.5	22.0

References

1. Gayevskiy, V. L. Temperatura poverkhnostey bol'shikh territoriy. Tr. GGO, No. 26, 1951.
2. Richardson, W. and Wilkins, C. An airborne radiation thermometer -- Deep Sea Res., v. 5, 1958.
3. Hall, F. F. and Stanley, C. V. Infrared satellite radiometry. Appl. Optics, v. 1, No. 2, 1962.
4. Hanel, R. A., Wark, D. Q. TIROS II radiation experiment and its physical significance.
5. Deirmendijian, D. Atmospheric extinction of infrared radiation. Quart. Journ. of the Roy. Met. Soc., v. 86, 1960.
6. Maklevich, M. S. Nekotoryye voprosy interpretatsii ukhodyashchey radiatsii zemli. 1. See this collection.
7. Wark, D., Tamamoto, G. and Lienesh, I. Methods of Estimating Infrared Flux and Surface Temperature from Meteorological Satellites. Journ. of Atmos. Science. v. 19, No. 5, 1962.
8. Moller, F. Correlations between the tropospheric radiation balance and certain meteorological quantities. Journ. of Met., v. 17, No. 5, 1960.
9. Kondrat'yev, K. Ya. Meteorologicheskiye sputniki. Gidrometeoizdat, L., 1963.
10. Greenfield, S. M. and Kellog, W. W. Calculations of atmospheric infrared radiation as seen from a meteorological satellite. Journ. of Met., v. 17, No. 3, 1960.
11. Novosel'tsev, E. P. Ter-Markoryants, N. E. Ob otrazhenii dlinnovolnovoy radiatsii vodnoy poverkhnost'yu. Tr GGO, No. 125, 1962.
12. Kondrat'yev, K. Ya. Luchistyy teploobmen v atmosphere. Gidrometeoizdat. L., 1956.

B. P. Kozyrev

MULTIPLE JUNCTION RADIATION THERMOELEMENTS FOR MEASURING HIGH POWER RADIATIONS FROM HALF SPACE IN THE 0.3 - 2.5 AND 2.5 - 40 MICRON SPECTRAL REGIONS

1. At the present time there are so many projects devoted to the theory and design of radiation thermoelements (r.t.e.) as to give one the idea that the development of some new system is virtually impossible. However, some very complex problems have been created by modern science and technology whose solution is not possible by the already existing thermoelements. In this connection, it is necessary to review all available materials on thermoelements, primarily to consider the basic formulas that characterize r.t.e. parameters and their relationship to the structural and operational data without going into a more detailed analysis of the operation of an r.t.e., for example, as considered in references [1,2].

If we designate as E the power radiance (watt/cm^2) of the receiving platform s; l and q as the length (cm) and cross section (cm^2) of the different wires soldered to s and forming an active ("hot") soldered joint; λ_1, λ_2 as the coefficients of thermal conductivity (wt/cm. degree) of the wires; b as the integral coefficient of absorption of the r.t.e. surface for radiations striking it, then we can use the following formula to indicate the power balance of this r.t.e. in a high vacuum

$$bEs = \left[(O_1 + O_2)s + (\lambda_1 + \lambda_2)\frac{l}{q}\right]\tau, \qquad (1)$$

in which $\tau = T - T_0$ is the so-called excessive temperature of the hot soldered joint, i.e., the excess of its temperature T over the temperature T_0 of the surrounding medium; $O_1 + O_2$ expresses the power loss from 1 cm^2 of surface for back radiation when $\tau = 1^\circ$.

At comparatively small values of τ which are ordinarily found in radiation thermoelements and which do not exceed 5 - 10°, the following is

the accepted assumption in computations dealing with radiation thermoelements

$$O_1 + O_2 = 4T_0^3 C_s(\varepsilon_1 + \varepsilon_2) = 6 \cdot 10^{-4} \text{ watts/cm}^2\text{/degree}$$

if the coefficients of the total radiation of the front and rear sides of the receiving surface give a total of $\varepsilon_1 + \varepsilon_2 \approx 0{,}9 + 0{,}1 = 1$.

However, bearing in mind that the r.t.e. in this study is subjected to powerful irradiation, it is desirable immediately to direct our attention to the magnitude of error occurring in a computation of the r.t.e. sensitivity if we replace the exact value of loss from 1 cm^2

$$\left[C_s(T_0 + \tau)^4 - C_s T_0^4\right](\varepsilon_1 + \varepsilon_2)$$

by an approximate value

$$(O_1 + O_2)\tau = 4T_0^3 C_s(\varepsilon_1 + \varepsilon_2)\tau.$$

Upon representing the error of the approximated expression in the form

$$4T_0^3 C_s(\varepsilon_1 + \varepsilon_2)\tau\left[\frac{3\tau}{2T_0} + \frac{\tau^2}{T_0^2} + \frac{\tau^3}{4T_0^3}\right] = (O_1 + O_2)\tau\alpha,$$

we will readily see that then $\frac{\tau}{T_0} = \frac{10}{300} = 0{,}033$ we have a comparatively small relative error $\alpha = 0.05$ or 5%. However, when $\frac{\tau}{T_0} = \frac{40}{300} = 0{,}132$ we get $\alpha = 0.2$, i.e., by replacing the exact expression of losses $(O_1+O_2)\,\tau\,(1+\alpha)$ by the approximated expression $(O_1+O_2)\tau$, we decrease the losses in the computation for back radiation by 20%. In Gill's study [3] there are given some graphic relationships of α to $\frac{\tau}{T_0}$ and $O_1 + O_2$ to T_0.

Designating the thermo emf in v/degree by P and bearing in mind equation (1) we get an expression for the emf in the circuit of the opened thermoelement

$$\varepsilon = P\tau = \frac{bEsP}{(O_1 + O_2)s + (\lambda_1 + \lambda_2)\frac{l}{q}},$$

whence for the specific sensitivity ε' (v/wt) we find

$$\varepsilon' = \frac{\varepsilon}{Es} = \frac{bP}{(O_1 + O_2)s + (\lambda_1 + \lambda_2)\frac{l}{q}} = \frac{bP}{(O_1 + O_2)s(1 + k)}. \qquad (2)$$

where the coefficient $k = \frac{(\lambda_1 + \lambda_2)\frac{l}{q}}{(O_1 + O_2)s}$ characterizes the relationship between the losses of the thermojunction on the run-off of heat to the cross-arms and to the back radiation of the receiving surface.

The inertness of action by the r.t.e. is determined from the equation for change in excess temperature $d\tau$ during the time interval dt:

$$bEs\,dt = \left[(O_1 + O_2)s + (\lambda_1 + \lambda_2)\frac{l}{q}\right]\tau\,dt + s\Delta c\delta\frac{d\tau}{dt}dt,$$

where Δ is the thickness of the surface s in cm, and c and δ are the thermal capacity (joules/gram degree) and the specific weight (gr/cm^3) of surface material.

From the equation obtained,

$$\frac{d\tau}{dt} + \frac{(O_1 + O_2)s + (\lambda_1 + \lambda_2)\frac{l}{q}}{s\Delta c\delta}\tau - \frac{bEs}{s\Delta c\delta} = 0$$

we find

$$\tau = \frac{bEs}{(O_1 + O_2)s + (\lambda_1 + \lambda_2)\frac{l}{q}}\left[1 - e^{-\frac{(O_1 + O_2)s + (\lambda_1 + \lambda_2)\frac{l}{q}}{s\Delta c\delta}}\right],$$

whence for the time constant $T_{0.63}$ we have

$$T_{0.63} = \frac{s\Delta c\delta}{(O_1 + O_2)s + (\lambda_1 + \lambda_2)\frac{l}{q}} = \frac{s\Delta c\delta}{(O_1 + O_2)s(1 + k)} = \frac{c\delta\Delta}{(O_1 + O_2)(1 + k)}. \qquad (3)$$

Since the specific sensitivity ε' and the time constant $T_{0.63}$ preserve their values for the multiple junction r.t.e. consisting of n series-connected single junction radiation thermoelements, we can write down the set of formulas for the basic parameters of an n-junction r.t.e. as follows:

$$\left.\begin{aligned} \varepsilon_n' = \varepsilon' &= \frac{bP}{(O_1 + O_2)s(1 + k)} \\ T_{0.63} &= \frac{c\delta\Delta}{(O_1 + O_2)(1 + k)} = \frac{c\delta\Delta}{bP}S\varepsilon' \\ \varepsilon_n = nE\varepsilon';\ \tau &= \frac{\varepsilon n}{nP} = \frac{bE}{(O_1 + O_2)(1 + k)} \\ R_n &= n\frac{\rho_1 + \rho_2}{q}l = \frac{n(\rho_1 + \rho_2)(\lambda_1 + \lambda_2)}{k(O_1 + O_2)s} \end{aligned}\right\} \qquad (4)$$

where R_n is the total resistance of all n junctions of the r.t.e., and p_1 and p_2 represent the specific electrical resistances (ohm cm) of the materials in the wires of the r.t.e. For the alloys, chromel and kopel', which are frequently used in constructing r.t.e. we have, in consequence of their good inherent mechanical properties and rather high thermo emf at $T_o = 290^oK$: $p = 65 \cdot 10^{-6}$ v/degree; $\lambda_1+\lambda_2=0,4$ wt/cm degree; $\rho_1+\rho_2=1,19\cdot 10^{-4}$ ohm cm.

By using silver here as a material for the receiving platform we can say that c δ = 2.45 joules/cm^3 degree (for the copper alloy and Dutch gold, oftentimes used c δ = 3.4 joules/cm^3 degree). If, in addition, we assume that b = 0.9 then the formulas (4) for the r.t.e. of chromel and kopel' will appear as follows:

$$\left.\begin{aligned} \varepsilon_n' &= \frac{0,0975}{s(1+k)} \\ T_{0,63} &= 4160\frac{A}{1+k} \\ \varepsilon_n &= nE\frac{0,0975}{1+k} \\ \tau &= 1500\frac{E}{1+k} \\ R_n &= 0,078\frac{n}{ks} \end{aligned}\right\} \qquad (5)$$

It seems that the simple relations (5) thus produced would be adequate to depict the characteristics of multi-junction r.t.e. and to discuss the trends in design. As we can see, the main parameter in all the formulas was the coefficient k, which determines the relationship between the junction losses to heat radiation along wires and for back radiation. Assuming k = 1, i.e., that these losses are equal, we get the optimum effect of the r.t.e. in the outer circuit if the resistance of the latter will be equal to the resistance of the r.t.e. The receiving platfo. s of one junction is a part of values ε' and R_n and has no effect on $T_{0.63}$, ε_n, and τ. Since the effectiveness of an r.t.e. in practical use is expressed by the electromotive force generated by all of its thermocouples, we should direct our attention

to the direct proportionality of $\mathcal{E}_n$ to the number of junctions n and to the independence of $\mathcal{E}_n$ to the receiving surface of one junction. However, upon increasing n to raise $\mathcal{E}_n$, it should be borne in mind that according to (5) the resistance R_n also grows linearly with n.

All the work done thus far on the theory and design of r. t. e. are directed toward producing an r.t.e. for situations in which the incoming radiation flux is small. Therefore, the task of producing an r.t.e. system such as would function from the action upon it of the inherent radiation from the earth's surface or the direct radiation of the sun seems at first glance to be quite simple, but actually it is quite complicated due to the many strict requirements imposed upon such a radiation thermoelement. The following are the basic requirements according to which the r.t.e. was developed.

1. $E = 1$ small calorie/min·cm^2 = 0.07 wt/cm^2; E_0 = 0.14 wt/cm^2
2. $\Omega = 2\pi$.
3. $0.3\mu < \lambda_c < 2.5\mu$; $2.5 < \lambda_3 < 40\mu$
4. $T_0 \neq$ const; ΔT_0 = 100 degree/10 min.
5. $T_{0.63} < 3$ sec.
6. Compensating.
7. Precise calibration.

Each of these requirements appeared complicated either because of its uniqueness in the practical development of an r.t.e. or from the quantitative point of view. Moreover, particularly great difficulties were presented by the need simultaneously to satisfy all the conditions presented. For example, the receiving of radiation by the r.t.e. surface from half space, i.e., from the solid angle $\Omega = 2\pi$ is not of itself unusual, but because of the small diameter of the receiver (diameter of base $<$ 40 mm) and the rather considerable area of all junctions (8 x 8 mm^2), as well as because the crystal KRS-5 was used as a material for the input window, undoubtedly complications

are introduced in the matter or designing an r.t.e. Compensation of the r.t.e. that is, the presence of two oppositely coupled groups of thermo junctions, is also a commonly encountered method of r.t.e. design, but here, only one, the so-called active system, of the junctions is subjected to irradiation, while the other -- the passive -- system remains unirradiated. In connection with the fact that it is impossible to use movable and even fixed reflectors in front of the junctions, the r.t.e. being developed should operate immediately the radiation hits both groups of junctions. The effect on the r.t.e. of a powerfule current of radiation, up to $E_0 = 0.14$ wt/cm^2, called for decreasing the heat for the cold junctions; the small dimensions of the r.t.e. (diameter of base $\simeq$ 40 mm and length L $<$ 130 mm) necessitated the use of a temperature control for the hemispheric input window and a supporting glass plate carrying the r.t.e. assembly. The small time constant ($<$ 3 sec) while counteracting vibrations also could not easily be made to agree with the requirements for a rather high sensitivity 0.6 - 1.0 v/wt. Most unusual in the practice of designing r.t.e. were the above-indicated points about distributing the effects of the r.t.e. by spectral regions and the independence of the zero reading to very marked variations in the surrounding temperature ($\Delta T \approx 100$ degree/10 min). The radiation thermoelement is regarded, because of the thermic principle of its action, as a typical non-selective receiver of radiation; and the division of its effectiveness into two wave zones -- 0.3 - 2.5μ (radiation of the sun) and 2.5 - 40 μ (inherent radiation of the earth) -- made it necessary to do a lot of work in the study and selection of infrared filters for the input windows of the r.t.e., especially in studying the spectral properties of the coverings of its receiving surfaces. This work, still in progress, is the essence of the entire problem and is of great general importance. Stabilizing the zero reading when the surrounding temperature varies 100° in 10 minutes was also not a part of the established idea of insuring

zero stability in the r.t.e. circuit, because in ordinary experiments the temperature surrounding it changes only a few degrees over a very long period of time. Finally, the last requirement in making the r.t.e. was far from simple, namely the accurate calibration of sensitivity of the r.t.e. It should be mentioned that regardless of the long history of development of thermic receivers and the great accomplishments in design in recent times, the problem of calibrating them has not been thoroughly studied. For example, methodological errors in estimating the parameters of r.t.e. even in generally recognized work leads to great divergences in values.

Therefore, thus far in studies specially devoted to questions of calibration of r.t.e. (e.g., [4-7]) the authors are still analyzing methods of calibration. Because much stress was placed in this study on the accuracy of rated data of radiation thermoelements, we devoted much effort to an analysis of existing methods of calibration, improving on such methods and computing the values of errors.

2. In connection with the fact that formulas [5] show the proportionality of the signal e given at the output of the r.t.e. to the number of junctions n of the r.t.e., and since it was evident that we had to get the greatest possible value of $\mathcal{E}$, we selected a multiplex jundtion type of design for the r.t.e. Moreover, having no chance to increase the overall dimensions of the r.t.e., it became necessary to make its receiving platforms comparatively small (2 mm x 2mm) and to increase their number to 16, dividing the surfaces into two groups of eight; these correspond to two groups of series-connected and oppositely-coupled junctions to compensate for the effect of variations in the surrounding temperature.

Selected as thermoelectrical materials, as we have already indicated, were chromel and kopel', which were adaptable for simple drawing through dies and thereby making thin wires that could be soldered. Since the r.t.e. system

should have a certain rigidity and capacity to withstand vibration, we selected a wire 70 μ in diameter and 4 mm long after some calculations and tests. The receiving surfaces were first cut out of silver foil and were 20 μ thick; then we used sheets of a copper alloy of Dutch gold 3 μ thick; and the last time we used a sheet of highly polished silver 2.5 - 3 μ thick. The measurements showed that in order to decrease the losses in back radiation of the rear side of the receiving surface -- and the front side in one of the designs of an r.t.e., as we can see from Fig. 1 -- it is essential to polish the silver surface as highly as possible. Thus, after many experiments and computations the basic element in the thermic sensor unit was made in the form of a short, rigid r.t.e. of chromel and kopel' ($l=0{,}4$ см, $q=\frac{\pi\cdot 0{,}007^2}{4}=3{,}85\cdot 10^{-5}$ см^2, $z=\frac{q}{l}=$ $=9{,}6\cdot 10^{-5}$ см), soldered to the center of the square silver surface 2 mm x 2 mm which was about 3 μ thick. The base for the assembly of all 16 junctions was a circular glass plate (diameter 18 mm, 3 mm thick) with 22 molybdenum wires (diameter 0.5 mm) soldered into it) which, after straightening and tinning became the supports for the 32 ends of the wires of all single junction radiation thermoelements. The supporting points of the polished nickel shield flanging the system of receiver surfaces and protecting the interior zone of the r.t.e. against the strong radiations striking it were soldered to the two molybdenum wires. The glass plate was rigidly secured to four molybdenum crossarms of the base with current leads. To control the temperature of the cold junctions i.e., the temperature of the plate, there was attached to its lower side by means of an epoxy resin a platinum wire 20 μ in diameter and 10.5 cm long with a resistance of 20 ohms at a temperature of 20°, which is cut in during operation into the bridge circuit. After the reflecting and absorbing coatings have been placed on the receiving areas, the support (glas No. 46) with the plate mounted on it was placed in a cylindrical vessel (diameter 20 mm, lenth 80 mm) of No. 46 glass, having at the forward input portion a welded

hemispherical cupola-shaped window of ultraviolet glass, the spectral transparency of which is shown in one of the curves of Fig. 2. Although the thermoelement made thus, with ultraviolet transmitting glass window (hereinafter referred to as uviol for the sake of brevity), has no external bonded sections and is erected on a welded base, nevertheless, due to the large number of internal tinned junction points and BF-4 cement in the coverings of the receiving surfaces it prevents overheating in the furnace during the vacuum pumping process. Hence, this type of r.t.e. was ordinarily heated to a temperature of 120° in two hours during the evacuating process, and toward the end of the vacuum pumping period a tablet of BATO getter was injected to insure a high vacuum. After assembly in a metallic base -- diameter 23.2 mm, length 125 mm -- the prepared thermoelement was subjected to various measurements and calibration. The main test for the uviol r.t.e. was, of course, the action of a powerful radiation flux of the order of $E = 0.07$ wt/cm^2, which corresponds to sunlight. The effects in the different portions and elements of such an r.t.e. are shown in Figs. 1 and 3. As we can see, this compensated thermoelement, having eight blackened and eight white surfaces covered with magnesium oxide, gives off an electromotive force on the output conductors equal to 0.025 volts (25 mv). However, due to the gradual increase in the temperature of the glass plate by 8.5° and that of the dome-shaped uviol window by 12°, the initial indication will drop in about 15 minutes by 3 mv. By experimentation and computation it was found that heating the plate 8.5° should have lowered the emf by 4.8 mv, but the heating of the window by 12° due to the absorption of the radiation passing through it raises the emf generated by the hot junctions by 1.8 mv; as a result, the overall emf is lowered 4.8 - 1.8 = 3 mv. The excess temperature τ of the hot junctions is equal to 41.5° in this, as shown by computation.

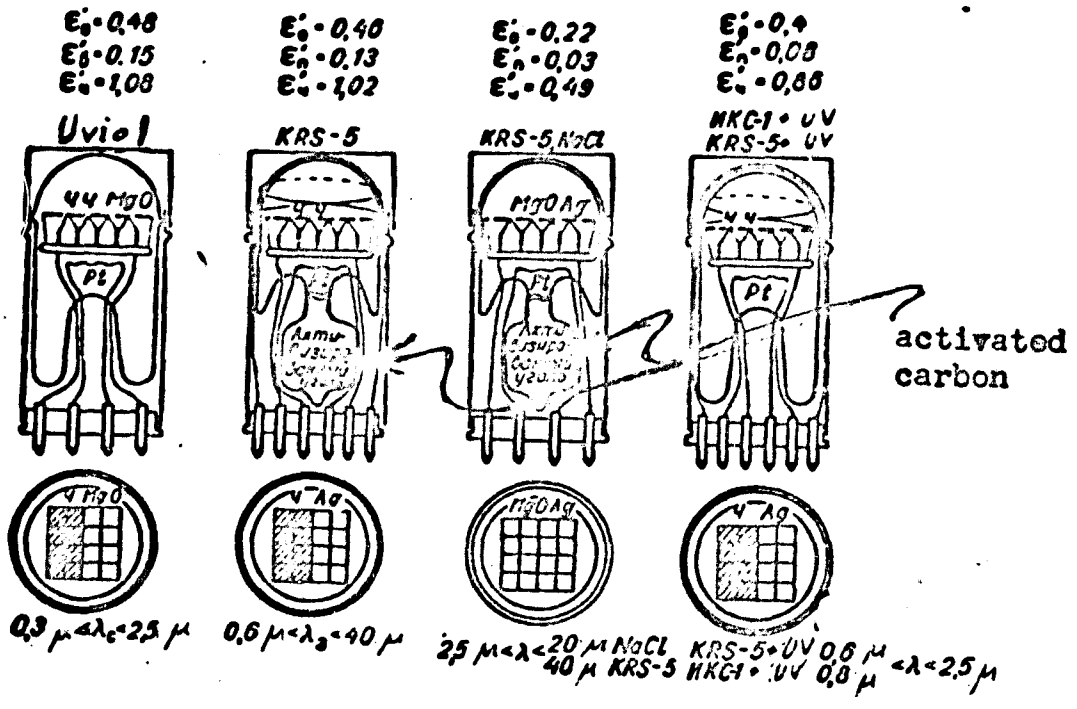

Fig. 1. Diagrams of various types of radiation thermoelements. $S_p = 16 \cdot 0.04$ cm^2; $R_p = 23$ ohms; $T_{0.63} = 2.5$ sec.

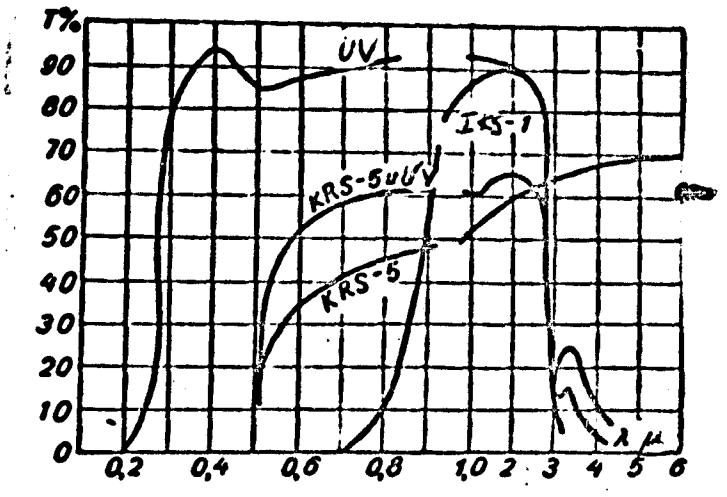

Fig. 2. Transmission of KRS-5, uviol (UV) and KRS-5 with uviol.

The thermoelement designed for recording the inherent radiation of the earth's surface, i.e., for waves up to 40 μ, was equipped with an input hemispherical window of crystalline material which passed infrared waves; usually it was of KRS-5, which consists of a mixture of thallium iodide and bromide (TlI 58.3% and TlBr 41.7%). Since KRS-5 and other crystals known for their transparency in the infrared region cannot be fused directly with glass, it was necessary to bond the hemispheres of KRS-5 to the glass with an epoxy

composition, using an intermediate cylindrical thin-walled rind of dyural (α = $23 \cdot 10^{-6}$ degree) for reducing the great difference in the coefficients of expansion of glass No. 23 (α = $8.9 \cdot 10^{-6}$ degree) and KBS-5 (α = $60 \cdot 10^{-6}$ degree). The use of a bonded window in the system of a vacuum r.t.e.

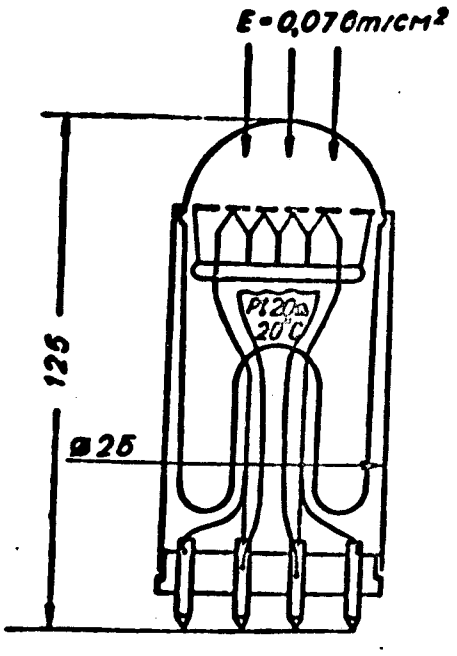

Fig. 3. Thermic and electrical operating characteristics in an r.t.e. with strong flux (0.07 wt/cm^2); s = 0.64 cm^2; R = 23 ohms; $\mathcal{E}$ = 0.025 volts; in 15 minutes $\mathcal{E}$ = 0.022 volts; with ΔT = 100° in 10 min. $\Delta\mathcal{E}$ = 0.45 mv; T_{junct} = 41.5°; ΔT_{plate} = 8.5°; $\Delta T_{filter\ UV}$ = 12°; $\Delta T_{filter\ KBS-5}$ = 10°.

gave rise to the possibility of a certain amount of gas leakage out of the bonding substance with time and called for the introduction into r.t.e. designs of activated carbon a a getter to maintain the high vacuum. Hence, the glass vessel for such a thermoelement was of a more complex non-cylindrical form, and the glass plate with junctions was mounted in a small flask (glass No. 23) with four individual leads of platinum. Shown in Fig. 1 is a schematic of an r.t.e. with a KBS-5 window, as well as the schematic diagram of a uviol r.t.e.; in the description of these thermoelements there are notes about the tupes of waves that affected them, and above the r.t.e. there are given the mean values of the specific sensitivities $\mathcal{E}'$ for the individual systems of junctions (black, white, and glistening), and the overall $\mathcal{E}_0'$ for the r.t.e. as a whole. These values of sensitivity $\mathcal{E}'$, which are in agreement with

formulas (4) insofar as the basic characteristics of the r.t.e. are concerned, were obtained for each type as mean indexes and developed from measurements made on many samples of r.t.e. units developed. Also shown in the caption of Fig. 1 are the receiving surface and the resistance and time constant of the radiation thermoelement. Since the transmission of the window made of KRS-5 described in Fig. 2 begins with 0.6 μ waves, the measurement of inherent radiation from the earth's surface with the simultaneous radiation of the earth by the sun cannot be made by one r.t.e. with a window of KRS-5. We, therefore, developed a so-called combination r.t.e. shown in Fig. 1, having, in contrast to the black-white uviol r.t.e., black and shining surfaces and equipped with another cupola-shaped window of KRS-5 above the uviol window. It is cemented with epoxy not to the glass vessel but to the end of the metallic base. The combination thermoelement with double windows of KRS-5 and uviol has an operating waveband of 0.6 - 2.5 μ . Recently, in order to shift the beginning point of transmission into the area of longer waves there were developed hemispheres of IKS-1 glass for the combination r.t.e. instead of the KRS-5 hemispheres for waves in the 0.8 to 2.5 μ region. Thus, instead of the direct separation of the radiation studied into two bands of waves -- 0.3 - 2.5 μ and 2.5 - 40 μ -- we can use three r.t.e. (the uviol, combination, and one with window of KRS-5), which divide the entire wave band into three sectors: 0.3 - 2.5; 0.6 - 2.5; and 0.6 - 40 μ ; and it is only by a corresponding reading of the last two r.t.e. that we get a reading for the 2.5 - 40 μ interval. Recently, there has been developed the radiation thermoelement shown in Fig. 1 which has white and shining receiving surfaces and a window of KRS-5. An r.t.e. of this type with white and shining receiving surfaces and window of KRS-5 operates in the 2.5 - 40 μ wave region, and to make separate spectral measurements of the solar and earth flux it is sufficient to have a set consisting of only two r.t.e., i.e., it is then unnecessary to have a combination thermoelement. This eliminates the complex process with its

errors from finding differences in readings. Incidentally, the first of the modifications of the new system of r.t.e. shown in Fig. 1, i.e., a thermoelement with black and white surfaces and a uviol window, is similar in operating principle to a pyranometer, very commonly used in meteorological practices; for that reason, it is interesting to compare the parameters of these instruments. Special measurements have shown that with a resistance of 30.7 ohms and an overall receiving surface of 9 cm^2 (3 x 3 cm) i.e., 9/0.64 = 14 times greater than the area of the r.t.e. shown in Fig. 1, the pyranometer gives, from the effects of solar radiation (E = 0.07 wt/cm^2) and emf $\mathcal{E}$ = 8.45 mv from which we get its specific sensitivity of $\mathcal{E}'$ = 0.0132 v/watt.

The uviol r.t.e. (cf. Fig. 1) gives $\mathcal{E}_o$ = 22 mv and has $\mathcal{E}'_o$ = 0.48 v/wt, which is 36 times greater. Also great was the inertness of action of the pyranometer - $T_{0.9}$ = 38 secs. compared with $T_{0.9}$ = 2.3, $T_{0.63}$ = 2.3 • 2.5 = 5.8 secs for the uviol r.t.e.

3. The most difficult task in building an r.t.e., without a doubt, is the requirement for separate action by the r.t.e. in two spectral regions -- 0.3 - 2.5 μ (the sun), and 2.5 - 40 μ (the earth). As we know, there is no standard, established solution of this problem now either in the way of indicators or existing filters. Even if we could name a photoelement such as a germanium photoresistance operating in the band of visible radiations and infrared region to about 2 μ, there is, nevertheless, no photoelectrical indicator that operates only in the 2.5 - 40 μ band. In addition, photoelements, which are in principle selective with respect to their spectral sensitivity, are not suitable for measuring in the case concerned because the spectral composition of the inherent flux of the earth may change, depending on the nature of the underlying surface. Therefore, we must have not only indicators with strictly divided zones of spectral sensitivity: 0.3 - 2.5 and 2.5 - 40 μ, but also with non-selectiveness within the limits of these wave bands. Naturally,

only thermic receivers can satisfy this requirement, but to make demarcations by individual zones we must have supplemental devices in which filters can be used. No special search is necessary for the 0.3 - 2.5 μ band because uviol glass (cf. Fig. 2) is quite adequate. However, for the 2.5 - 40 μ zone there is absolutely nothing, and, as we have already indicated, it was necessary to make a combination r.t.e. to exclude the effects of the 0.6 - 2.5 μ band. Unfortunately, however, we get a low order of accuracy hereby in the final totals of measurement. The point is that solar rays in the 0.6 - 2.5 μ zone have a great amount of power and with this as a background, radiation in the 2.5 - 40 μ zone, which corresponds to the inherent flux of the earth, represents a very insignificant amount.

If we consider the radiation of the sun ($T = 5750^{\circ}$ K) and that of the earth's surface ($T - 300^{\circ}$ K) as coinciding in composition with the radiation of absolutely black bodies corresponding in temperatures, and if we take into account the very great difference in these temperatures, then actually in comparing the radiations in the different regions of the spectrum, shown in Table 2, we need concern ourselves only with the data for $T = 5750^{\circ}$ K, taken from the tables cited in the monograph by Harrison /87. As we can see from Table 2, the power for the 2.5 - 40 μ wave interval is a very small portion of the sun's radiation that is reflected by the earth. Using hemispheres of IKS-1 or IKS-2 filters instead of KRS-5 we can decrease the effect of the solar component, but as we can see from the ratios $\frac{Е-Д}{Д-Б}$ and $\frac{Е-Д}{Д-В}$, we still do not get any considerable increase in accuracy of measurements in this. It is only when we shift the initial point of transmission of the filter to the 1.2 wave or still closer to the 2.5 μ wave that we get any noticeable improvement in precision, because at 1.2 μ in Table 1 we have $\frac{Е-Д}{Д-Г}=15{,}4\%$. As we have already shown, filters with so-called "cutting" initial points of transmission do not exist in the infrared portion of the spectrum, and we can only

try to make them up from some crystallic materials which transmit the visible and infrared rays, and thin coverings which hold up the visible and shortwave infrared wave bands. Recently, successes were achieved in making hemispherical input windows of silver chloride with a deposit on it of tellurium sublimated in a vacuum; as a result, the initial point of transmission was shifted by $\lambda =$ = 1.2 microns, for which data have been computed as shown in Table 1. Shown in Fig. 4 are curves of spectral transparency of various coatings for AgCl.

Table 1

$T = 5750^{\circ}K$

Designation of spectral region	Filters	$\Delta\lambda$ microns	$\frac{w_{0,\lambda}}{w_{0,\infty}}$ %
A_0			100
A		0—0,6	37
$Б$		0—0,8	58
B		0—0,9	65
$Г$		0—1,2	80
$Д$		0—2,5	96,5
E		0—40,0	99,0
$A_0 - A$	KRS-5	0,6—40	61
$Д - A$	KRS-5 + УВ	0,6—2,5	59,5
$Д - Б$	ИКС-1	0,8—2,5	38,5
$Д - B$	ИКС-2	0,9—2,5	31,5
$Д - Г$	AgCl + Te	1,2—2,5	16,5
$E - Д$		2,5—40,0	2,52
$\frac{E-Д}{Д-A}$			4,2
$\frac{E-Д}{Д-Б}$			6,6
$\frac{E-Д}{Д-B}$			8,0
$\frac{E-Д}{Д-Г}$			15,4

Silver chloride and other crystals with coatings on them have long been studied [9].

Thus, the main problem in developing a radiation thermoelement -- making measurements of a comparatively weak flux in the 2.5 - 40 μ range of waves with a powerful radiation present in the form of 0.3 - 2.5 μ waves -- is not very accurately resolved in using various filters. Hence, searches were undertaken and studies made of such coverings of the receiving platforms which aided

through the principle of reflection in isolating the 2.5 - 40 μ band of waves from the total radiation striking the r.t.e. Such a project could be set up because blackening coatings have long been studied [10], even for the far infrared portion of the spectrum [11], and the only thing necessary was to use the existing apparatus for measuring the spectral coefficients of diffuse reflection and begin studying new coatings. In this, the main stress was placed, naturally, on white, finely-dispersed materials because of their non-susceptibility to the visible and infrared waves and absorption in the more distant zone of the spectrum. After testing a large number of different substances, the basic results were formulated in one of the latter works [12]. It appears that magnesium oxide mixed with a binder of BF-2 cement in the proportion of 10:1 in a dried state and deposited on silver in a layer with a thickness of the order of 6 mg/cm^2 has a very strong absorption action on infrared radiation (Fig. 5) (up to 90%) -- second to practically no other blackening agents -- in the 2.5 - 25 μ band, and it is a good reflector (about 80%) in the 0.3 - 2.5 μ interval (Fig. 6). However, we should pay special attention to the need for depositing MgO in a layer sufficiently thick, because from the curves in Fig. 5 it is apparent that in passing over from a layer 6.8 mg/cm^2 thick to one 3.2 mg/cm^2 thick absorption in the 3.7 and 8 - 14 μ wave band decreases markedly. Since the blacking customarily used is made according to an old method and consists of a mixture of soot and BF-2 cement with a weight-thickness of 4 mg/cm^2, a thickness of 6 mg/cm^2 for MgO will result in increasing the inertia, but this will not be very considerable because the silver layer has been decreased to 2.5 microns [10,11]. Despite the difficulties in the technology of depositing a covering of MgO on such a thin layer of silver -- the difficulty lies in having to repeat several operations of forming a thick layer from a series of thinner layers -- this method of producing a thermic indicator which acts with sufficient non-selectiveness

only on waves in the 2.5 - 40 μ interval is, thus far, the only possible one, and successfully resolves one of the more complex problems in designing an r.t.e. The use of KRS-5 for making hemispheric input windows for these indicators makes them more reliable and convenient than is the case with other crystal materials; this is due to the more effective moisture-proof qualities of KRS-5.

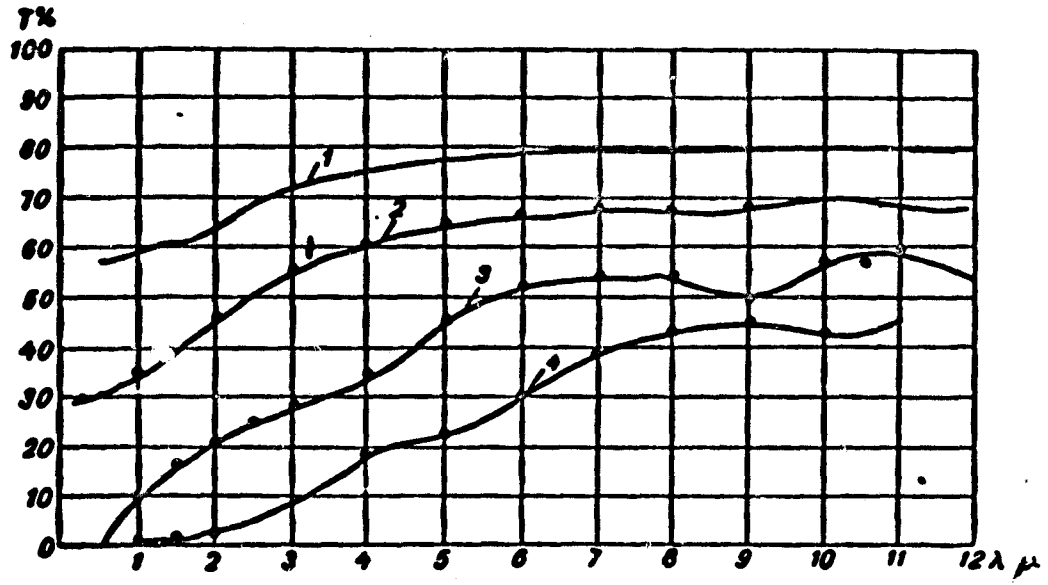

Fig. 4. Transmissivity of AgCl with various coverings in the 1.0 - 24.0 μ range.

1 - AgCl (0.77 μ). 2 - AgCl + Se (0.134 μ). 3 - AgCl + Te (0.019 μ). 4 - AgCl + Te (0.04 μ).

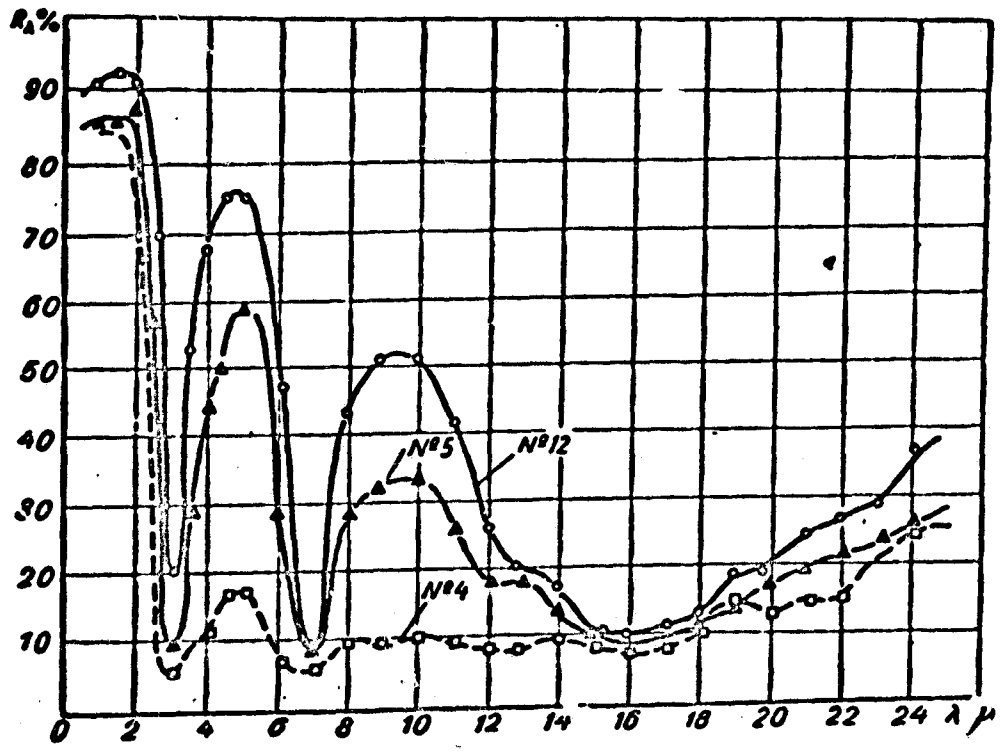

Fig. 5. Spectral reflection of coating of MgO in the 1.0 - 24.0 μ range. No. 12 - 3.0 mg/cm^2 MgO with BF-2 cement on silver (10:1); No. 5 - 3.2 mg/cm^2 MgO with BF-2 cement on Ag (10:1); No. 4 - 6.8 mg/cm^2 MgO with BF-2 cement on Ag (10:1).

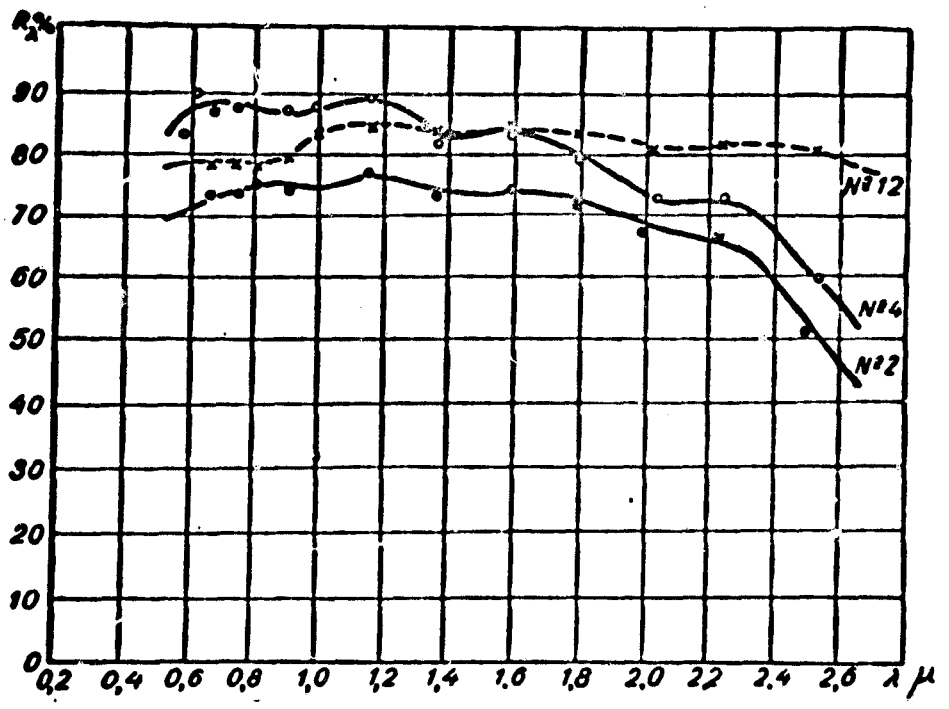

Fig. 6. Spectral reflection of coatings of MgO in the 0.4 - 2.5 μ range. No. 12 - 3.0 mg/cm^2 MgO with BF-2 cement on Ag (10:1); No. 4 - 6.7 mg/cm^2 MgO with BF-2 cement on Ag (10:1); No. 2 - 3.2 mg/cm^2 MgO with BF-2 cement on Ag (10:1).

4. During the process of designing the radiation thermoelements and just before they were turned over to be tested, the equipment was subjected to laboratory investigation in order to make a most careful determination of their parameters. The spectral sensitivity of all kinds of r.t.e. was determined with the infrared spectrometer IKS-12 in which monochromatized radiation alternately fell either on the basic, standard radiation thermoelement or on the one being tested; the latter was set up on the outside of the IKS-12 and was receiving radiation after its emergence from the side window. Shown in Fig. 7 are the curves of spectral sensitivity of all three types of radiation thermoelements developed, pointing to the non-selectivity of each of the three r.t.e. in a specific wave zone.

It should be mentioned that these measurements are quite complex because in setting up the work for greatest accuracy and precision we had to deal with two FEOU-18 amplifiers connected to two radiation thermoelements, and in the more simplified form we occasionally used two highly sensitive galvanometers;

however, in this, the deviations in the zone of short and slightly longer waves proved small. The curves shown in Fig. 7 pertain to the overall surfaces of receivers of the radiation thermoelements being tested, which determine the magnitude of deviations obtained.

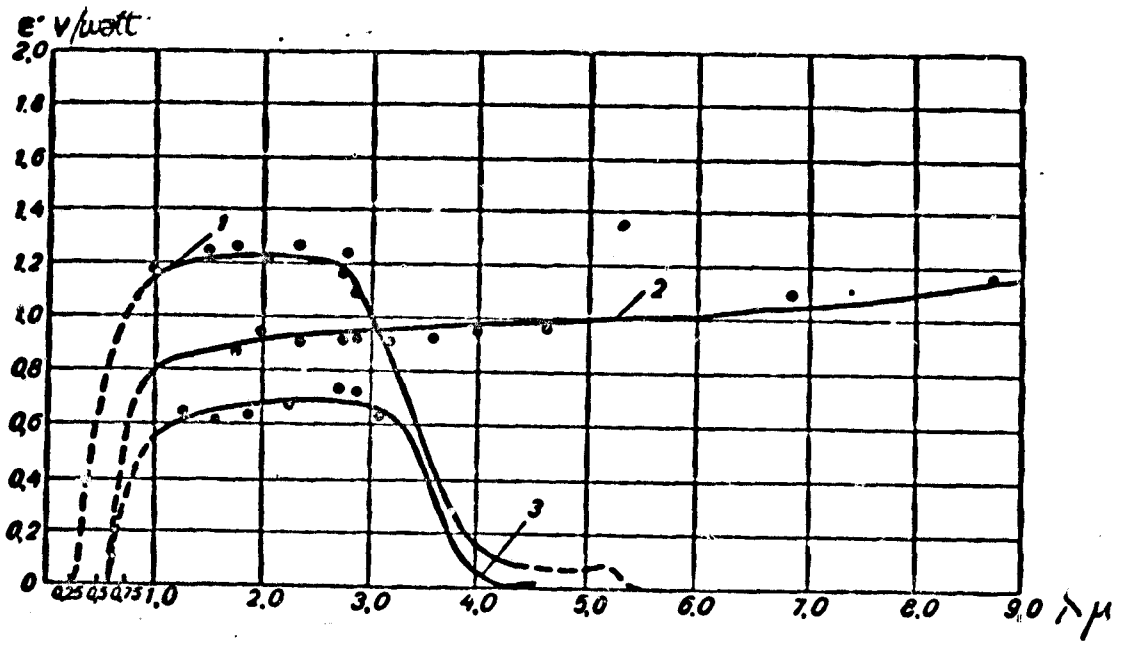

Fig. 7. Spectral sensitivity of various types of radiation thermoelements.

1 -- with filter of UV, ε'_o = 0.475 volts/watt;
2 -- with filter of KRS-5, ε' = 0.41 volts/watt;
3 -- with combination filter, ε'_o = 0.382 volts/watt.

The proportionality of thermal currents in the radiation thermoelement circuit when there is a change in the incoming irradiation rate was repeatedly confirmed in irradiations ranging from 0.07 watt/cm^2 and lower by using the method of lattice sets placed in the path of solar rays. Recently, in addition, some special experiments were carried out in the laboratory in which the thermoelement was irradiated by a powerful two kilowatt lamp set up at various distances from the r.t.e. In this experiment, it was assumed that the overall irradiation rate of the incandescent coil and heated vessel, when provided a stable supply of power from the network voltage, remains unchanged and hence the variations in rate of flux striking the receiver vessel can be computed by the square of the distance law. Fig. 8 gives the relationships in the uviol r.t.e. circuit and its specific sensitivity ε' as a function of large values

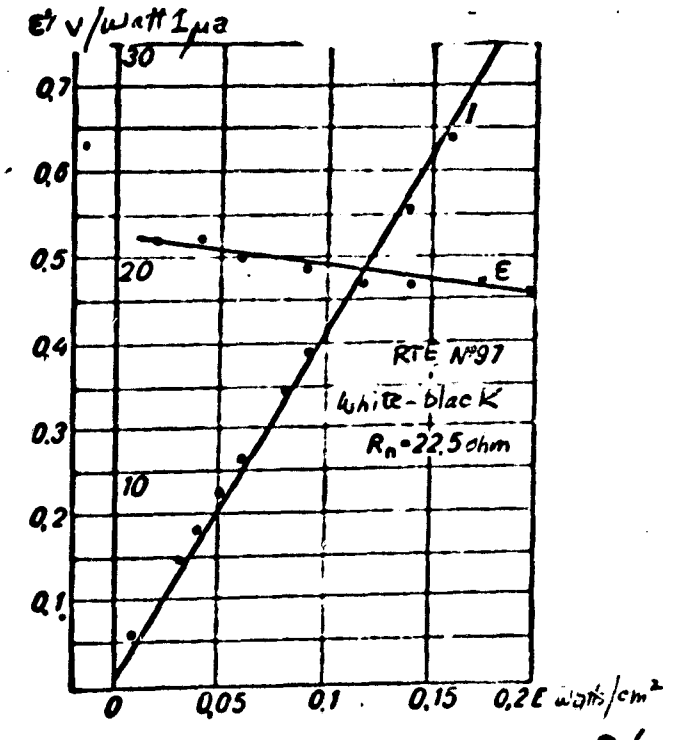

Fig. 8. Specific sensitivity ε' and thermal current of radiation thermoelement as a function of the irradiation rate.

of incoming radiation power changing within the limits of from 0 to 0.2 watts/cm^2. As we can see, the value of the thermal current remains linearly related with the dropping power in the entire power band extending beyond the limits of the problem (0.07 - 0.14 watt/cm^2); the specific sensitivity ε' shows a slight decrease (by 4% within the limits of 0 - 0.07 watt/cm^2), which is probably determined by Peltier effect losses and is, in general, close to the limits of accuracy set up for the experiment. Thus, on the basis of all tests made, we can deem as well confirmed the proportionality of the signals from the thermoelements being developed to the radiation values striking these r.t.e.

Since the radiation thermoelements were designed for measuring radiation fluxes from half space, it appeared essential to study the relationship of the sensitivity of an r.t.e. to the angle of incidence of the beams and the extent to which Lambert's law was observed in this. Fig. 9 shows some curves resulting from measurements of the specific overall sensitivity for a uviol r.t.e. with black and white surfaces and, in addition, the ε' for just the black areas

alone. As we can see, the departure of results from the cosine law, described by broken lines, is very slight, and it is manifested only at large angles of incidence in the form of a difference ε' to zero at 90° when the reflection of radiation from the walls of the hemispheric window begins to have effect. In developing the thermoelements special attention was directed, of course, to the vacuum inside their vessels, inasmuch as the sensitivity of

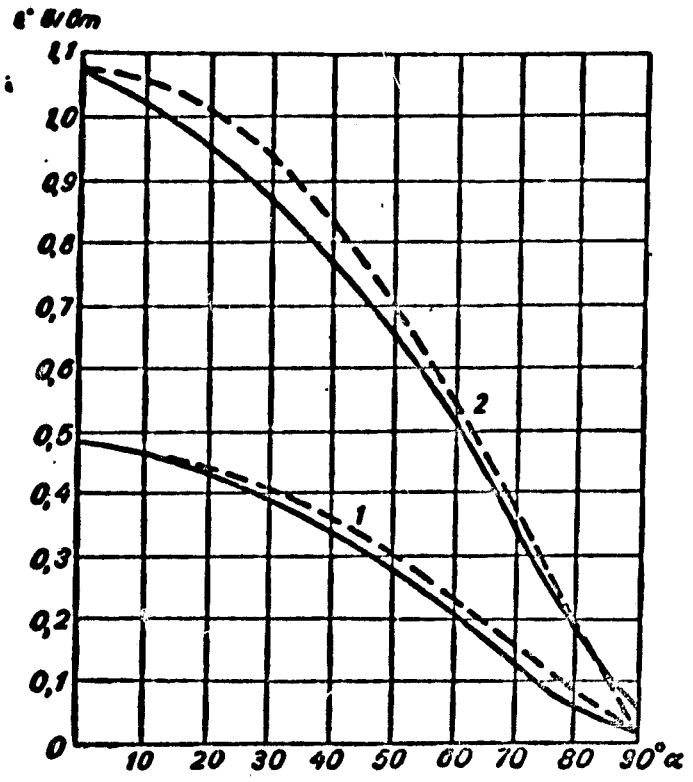

Fig. 9. Relationship of specific sensitivity ε' of radiation thermoelement to angle of incidence of rays.
1 - black and white, 2 - black.

the r.t.e. depends on the amount of vacuum. Specially undertaken experiments to determine the relationship of ε' to the pressure p of the black-white and of the black-shining thermoelements to the uviol window gave results which are shown as curves in Fig. 10. Moreover, in addition to their general sensitivity, special tests were made on the ε' for black, white (MgO), and shining (Ag) platforms. As we can see from Fig. 10, as well as from figures, the sensitivity ε' is a function of the pressure only in the interval from 10^{-3} to 10^{-1} Torricelli vacuum, the ε' in a high vacuum exceeding by approximately a factor of 4.5 the ε' at atmospheric pressure, as is the case both with black surfaces

and black-white surfaces. Although it was confirmed in this manner that a very high vacuum inside the vessel proper was not required, and that at times some generation of gas is permissible increasing the pressure almost to 10^{-3} Torr., nevertheless, the use of a vacuum regime, regardless of the presence of a getter, always entails the possibility of a variation in pressure and instability in the specific sensitivity ε', especially in the case of an r.t.e. with bonded windows. For that reason, a serious study was made on the possibilities of filling a thermoelement with xenon gas instead of evacuating the vessel. The effect of gas pressure on changes in sensitivity of the r.t.e. can be computed from the general relationships of the kinetic theory of gases by a formula for the relationship of heat losses W for a gas from a 1 cm^2 surface with an excess temperature of τ° of this surface with respect to the surrounding area

$$W' = 3k\alpha\tau \frac{p}{2mc} \cdot 1340 \cdot 10^{-7} \cdot 4{,}18, \qquad (6)$$

where k is the Boltsmann's constant, m is the mass of the molecule, c is the mean square velocity of the molecules, α is the coefficient of accommodation.

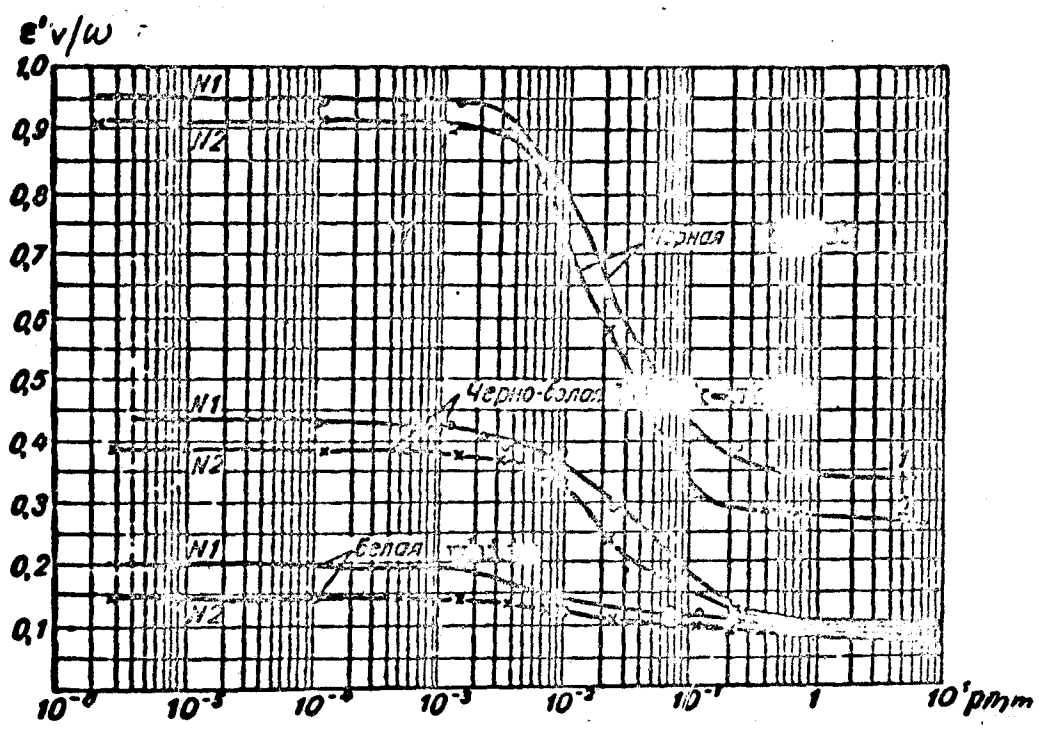

Fig. 10. Relationship of specific sensitivity ε' of radiation thermoelement to air pressure.

Assuming $\alpha \approx 0.5$ and $\tau = 1^\circ$, at an air temperature of $T_0 = 290^\circ K$ we get

$$W_1 = 6 \cdot 10^{-3} p \quad \text{watt/cm}^2.$$

whence for p = 0.5 Torr. we have $W_1 = 3 \cdot 10^{-3}$ watt/cm^2.

For 1 cm^2 area of the receiver, i.e., for 2 cm^2 of its surface, it is clear that the losses to gas will be equal to $W = 2W_1 = 6 \cdot 10^{-3}$ watts/cm^2; this value corresponds not only to p = 0.5 Torr., but also to the total pressure of the atmosphere, because the thermal conductivity of a gas does not depend on pressure from approximately 0.5 Torr. In the early part of this work there were indicated heat losses due to back radiation from 1 cm^2 of the receiving surface of a radiation thermoelement at $\tilde{\iota} = 1^\circ$ as $O_1 + O_2 = 6 \cdot 10^{-4}$ watts/cm^2 degree. It appears that the transition from a vacuum to atmospheric pressure is accompanied by the addition of ten-fold flow-off of power compared with back radiation. Since the molecular weight of xenon is $\frac{131.3}{29} = 4.5$ times greater than air, then, obviously we can write

$$\frac{W_{air}}{O_1 + O_2} = 10; \quad \frac{W_{air}}{W_{Xe}} = 4,5,$$

from which we get

$$\frac{W_{Xe}}{O_1 + O_2} = \frac{10}{4,5} = 2,2,$$

i.e., replacing the high vacuum in the vessel of the r.t.e. with xenon gives additional losses which exceed by 2.2 the losses in power to back radiation. The specific sensitivity $\mathcal{E}'$ of the radiation thermoelement will not depend linearly on losses of W because in the thermoelement there are losses of heat outflow to the traverses along chromel and kopel' wires; the coefficient k entering into formula (5) is of great importance. However, knowing W for xenon we can introduce this value into formula (5) and compute all basic parameters of a thermoelement filled with xenon. Given in Table 2 are the results of such computations for two r.t.e. with 16 blackened surfaces each with dimensions of 2.2 and 3.3 mm.

Table 2

		$\varepsilon' V/\omega$	$T_{0.63}$ sec.	εV	τ^0
$s = 2{\cdot}2$ мм^2	Vacuum	0,95	2,4	0,042	41,5
$l = 4$ мм	Atmosphere	0,214	0,54	0,0094	9,4
$k = 1,6$	Xe ($p = 600$ Torr)	0,645	1,65	0,0288	28,4
$s = 3{\cdot}3$ мм	Vacuum	0,635	3,6	0,063	62
$l = 4$ мм	Atmosphere	0,1	0,57	0,01	10
$k = 0,71$	Xe ($p = 600$ Torr)	0,37	2,1	0,037	36,4

After such r.t.e. were made, they were subjected to various tests which confirmed with sufficient accuracy the correctness of the computed values. For example, for a xenon-filled radiation thermoelement with surfaces 3 • 3 mm we got $\mathcal{E}' = 0.32$ volts/watt (by computation $\mathcal{E}' = 0.37$ volts/watt), and for an r.t.e with a surface of 2•2 mm it was found through experimentation $\mathcal{E}' = 0.5$ volt/watt (by computation $\mathcal{E}' = 0.645$ volt/watt). The transition from a vacuum in an r.t.e. to a xenon-filled device is accompanied by a comparatively low loss in sensitivity and is compensated for by a certain decrease in the time constant. If the envelope of the r.t.e. contains xenon, it is immaterial if there is any leakage through the walls of this envelope and from the cement layer near the window because the pressure of the xenon $p \approx 600$ Torr. and the pressure of the gases given off ordinarily does not exceed 0.1 Torr. Therefore, such an r.t.e. does not have to be vacuum pumped nor does it require a getter; it holds its sensitivity very stably, and that is very important in its operation. External blowing of the hemispheric input window by sudden blasts of air, as shown by tests, had absolutely no effect on the sensitivity of the radiation thermoelement.

5. In discussing the conditions formulated on page 372 we remarked that in this investigation it was necessary to do much work in analyzing the various methods of calibrating r.t.e. and developing new methods for measuring

their sensitivity and evaluating possible errors herein. As a result, it appeared that a single method of calibration for all types of r.t.e. developed cannot be used, and the sensitivity can be determined most simply and precisely only for a thermoelement with a window which is transparent for the longer waves, i.e., one of KRS-5 or some other crystal. In that case a low temperature, absolutely black body ($T = 100 \div 200^{\circ}$) should be used as a standard of beamed radiation; in recent years, it was rather frequently recommended as a source of radiation for work dealing with thermic and long wave photoelectric receivers [5,7]. A classic radiator of this type can be made using either a tube surrounded by the steam from slowly boiling water or, when higher temperatures are used, heating this tube with coils of wire with a current of electricity flowing through them. Schematically represented in Fig. 11 is the disposition of an absolutely black body and an r.t.e. being calibrated; also, there is given a formula for evaluating the rate of irradiation flowing to the receiving platform of the r.t.e. In this method the essential thing is knowing this power precisely, if in designing an absolutely black body we have observed conditions for an adequate ratio of the cell length to its diameter and if appropriate diaphragms are installed in front of the opening of the absolutely black body [5]. Since we ordinarily select a short distance from the absolute black body to the radiation thermoelement being tested, the absorption of radiation in the air can be disregarded, particularly since, for example, at $T = 100^{\circ}$ the maximum flux is for a wavelength of 8 μ, which is in general well transmitted by the atmosphere. However, if necessary, we can introduce corrections for absorption in the air, making use of studies presently available [13]. By using formula

$$W = \frac{5{,}7 \cdot 10^{-12}}{\pi} \frac{(T_{ch}^4 - T_P^4)}{l^2} S_{ch} S_P \qquad (7)$$

we evaluate the radiation power directed to the receiving platform of the r.t.e. and not the power received by the receiver, which will be less than W

due to the absorption by the material contained in the input window and in part, though a small part, reflection by the black surface. But the radiation thermoelement will be placed in the same conditions with respect to the radiation flux measured by it during the operating process.

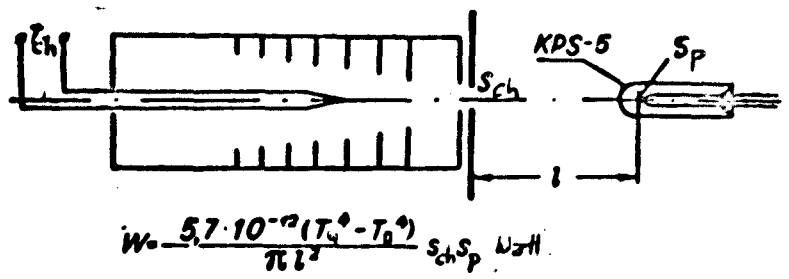

Fig. 11. Diagram showing disposition of instruments in calibrating a radiation thermoelement relative to a cylindrical, absolutely black body.

Since the radiation thermoelement with a window of KRS-5 is designed for receiving radiation from half space there was a requirement for calibrating it under the action of a radiation flux coming from a solid angle 2π and not from a small angle in the above-described situation with an absolutely black body. We, therefore, set up the arrangement shown in Fig. 12 consisting of a spherical, high-vacuum chamber with a diameter of 300 mm in the lateral cylindrical opening of which (diameter - 30 mm) we mounted a radiation thermoelement with a window of KRS-5; the walls of this opening were surrounded by a conical vessel for water at a temperature of T = 293°. The spherical portion of this device was surrounded by a tank in which water at a temperature of T = 333°K was poured in at a specific moment. Since the amount of power radiated from a 1 cm^2 spherical and absolutely black body is $5.7 \cdot 10^{-12} T_1^4$, then a receiver of area s_n and a temperature of T_o will receive an amount of power equal to $5.7 \cdot 10^{-12} (T_1^4 - T_o^4) s_p$ and yields a thermo emf of $\mathcal{E}$ in the process. Hence, its specific sensitivity will obviously be equal to

$$s' = \frac{\mathcal{E}}{5.7 \cdot 10^{-12}(T_1^4 - T_0^4) s_p}. \qquad (8)$$

Due to the high ratio of diameters of the spherical container (diameter 300 mm) and the hemisphere of the r.t.e. input window (diameter 22 mm) we can

assume that the radiation on the receiving platforms of the r.t.e. comes from half space. Heat transfer to the window of the r.t.e. by gas molecules is excluded because the high vacuum pump maintained the pressure inside the sphere at all times at not more than 10^{-5} mm of mercury.

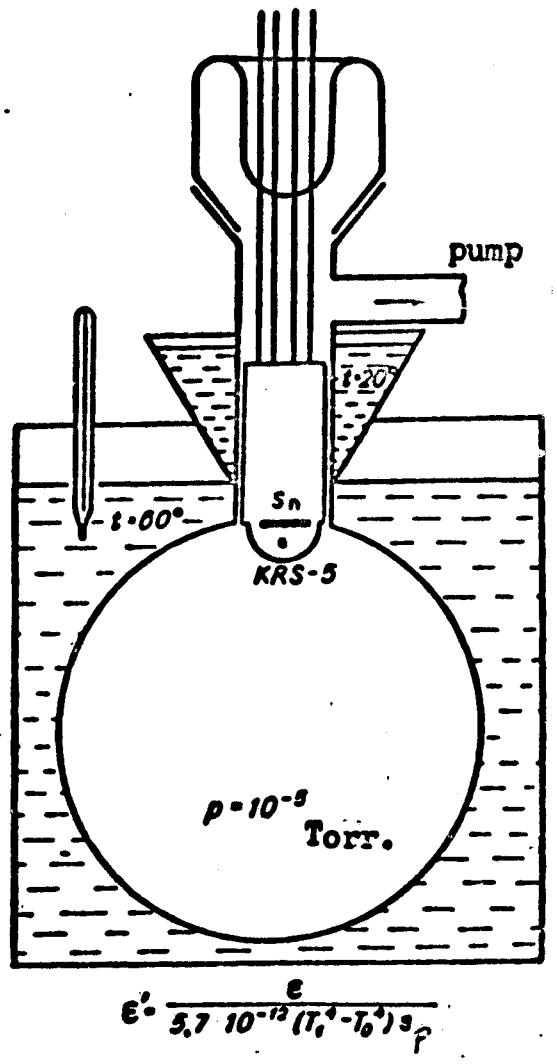

Fig. 12. Diagram showing disposition of instruments in calibrating a radiation thermoelement with respect to a spherical absolutely black body.

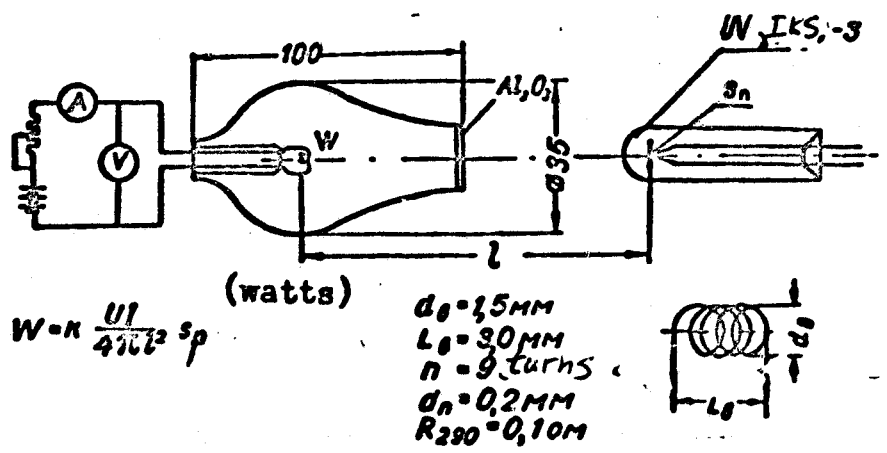

Fig. 13. Schematic diagram showing disposition of instruments in calibrating a radiation thermoelement with respect to a lamp with sapphire window.

The results of measuring the sensitivity ε' for an r.t.e. with a window of KRS-5 in a set-up with the usual absolutely black body and spheres proved to be practically the same at all times. However, whereas the error of the first method did not exceed 1 - 2% in the second method, due to the gradual transfer of heat to the water poured into the conical vessel, the accuracy of measurements did not exceed 5%.

However strange this may seem, nevertheless it proved considerably more difficult to determine the sensitivity of the thermoelements with a uviol window as well as an r.t.e. with KRS-5 and uviol. The fact is that it was absolutely impossible to calibrate them according to a low temperature, absolutely black body due to the non-transparency of uviol glass to waves in excess of 2.5 μ; and in principle it was necessary to use an absolutely black body with a temperature of the order of 3,000°K or higher in order that the greatest part of the flux of this body be made up of waves shorter than 2.5 μ. Unfortunately there is no technically well-developed absolutely black body for temperatures of $T \geqslant 3000^{\circ}K$ in laboratories, and for that reason it was necessary to use a highly heated ($T \approx 3100^{\circ}K$) tungsten coil mounted inside the evacuated envelope equipped with a brazed sapphire window (Al_2O_3) with a transparency in the infrared portion of the spectrum up to 6 μ (Fig. 13). The "sapphire" lamp developed in this manner had a spiral with a power of the order of 6 watts and, depending on the voltage fed, permitted a temperature zone of 2800 - 3100°K. To eliminate the effect of tungsten dusting of the interior surface of the Al_2O_3 the spiral was moved from the window a distance of 5 cm, and, in addition, it was connected only for the comparatively short periods of time of measurement.

In evaluating the radiation power directed to the receiver platform of the r.t.e. it is essential to introduce a correction. If the power taken by the spiral from the power supply is UI, only 0.95 UI will be radiated, because according to calculations, only 5% will flow to the cross-arms of the spiral

and flow to the base of the lamp. After that, it is necessary to take into account the radiation losses due to reflection from two bounding surfaces of the sapphire window with an index of refraction of n = 1.75 for wave lengths of 1 μ; from this we get a transmissitivity for the window of $k_0 = 1-0.13 = 0.87$ from Frenkel's formula. Finally, we should also take into account the presence in the tungsten spiral emission of a radiation which cannot pass through a sapphire window (with $\lambda > 6\ \mu$) or through the input of the r.t.e., i.e., for KRS-5 with $\lambda > 0.6\ \mu$, for IKS-1 with $\lambda > 0.8\ \mu$, and for uvi-1 with $\lambda > 2.5\ \mu$. Since the radiation of non-black bodies is always at a maximum, which is shifted toward the shorter waves, with respect to the maximum radiation of an absolutely black body at the same temperature, then the radiation of tungsten at 3100°K will correspond, from this point of view, to the radiation of an absolutely black body with a temperature of approximately 3200°K, and tungsten at 2800° will correspond to the radiation of an absolutely black body at 2900°K. The percentile content of power radiated by an absolutely black body for the different wave regions (0-0.6; 0-2.5 μ, etc.) can be recognized from the tables mentioned in reference /8/, and on the basis of all these data we can construct Table 4 for computing the coefficients k_1 which take into account the disparity in radiation of the tungsten spiral in different kinds of r.t.e. designs. For coefficient k'_1 in Table 3 we mean $k_1' = \frac{W_{0-\lambda T}}{W_{0-\infty}}$ for an absolutely black body at T = 3200°K or T = 2900°K. By introducing all such corrections we can write down the magnitude of the radiation power directed toward the receiver as

$$W_p = 0{,}95 k_0 k_1 \frac{UI}{4\pi l^2} s_p, \qquad (9)$$

in which U is the drop in voltage on spiral, I is the current flowing through the spiral, l is the distance from the spiral to the receiver platforms.

In Table 3 the products $0.95\ k_0 k_1$ are computed for various types of r.t.e. and, as we can see, in certain instances they reach considerable dimensions.

Table 3

		λ μ				Window	k_1	0,95 $k_0 k_1$
		0,6	0,8	2,5	6,0			
T = 3100 °K	λ T	1926	2560	8000	19200	UV UV + KRS-5	0,86 0,805	0,71 0,67
Absolutely black body, 3200 °K . .	k_1'	0,055	0,175	0,86	0,98	UV + IKS-1 KRS-5	0,685 0,925	0,57 0,765
T = 2800 °K	λ T	1720	2320	7000	17200	UV UV + KRS-5	0,82 0,85	0,68 0,7
Absolutely black body, 2900 °K . .	k_1'	0,03	0,125	0,82	0,98	UV + IKS-1 KRS-5	0,695 0,95	0,575 0,785

The use of formula (9) presupposes uniformity of distribution of radiation by the tungsten spiral in the limits of solid angle 4π ; this is confirmed by an experimental check with the aid of a photo-element with sealing layer. An estimate of the accuracy in determining the specific sensitivity of the r.t.e. with a sapphire lamp can be made taking into account the errors made only in measurements of U, I, l, because the correction coefficients are based on computations using Plank's formula for an absolutely black body. The disparity in values of k_1 to the real situation of the experiment can be due only to the non-equivalences of transition from radiation of tungsten at 3100°K to the radiation of an absolutely black body at 3200°K. On the whole, if we estimate the error at 1% upon introducing the coefficient 0.95, and 2% for $\frac{UI}{4\pi l^2} s_p$ and consider k_0 and k_1 to be precise, we get an overall error for the method of calibrating receivers with a sapphire lamp not exceeding 3%, i.e., practically the same as in the first method with a low temperature, absolutely black body. However, the introduction of correcting coefficients 0.95, k_0, k_1, which attain great values in individual cases, is undoubtedly the weak point of the method of using sapphire lamps. Of course, uviol and combination type radiation thermoelements can be calibrated, if meteorological conditions permit, with solar radiation, using a standard radiometer in the process.

References

1. Kozyrev, B. P. Raschet i vybor parametrov odnospaynogo valuumnogo radiatsionnogo termoelementa s vydelennoy prieyemnoy ploshchad'yu. Izv. LETI, 30, 37, 1956.
2. Kozyrev, B. P. Osnovy rascheta i konstruirovaniya radiatsionnogo termoelementa. Izv. LETI, 44, 22, 1960.
3. Gill, T. P. Some Problems in Low-Temperature Pyrometry. JOSA, 47, 1000, 1957.
4. Kortum, H. Zur Leistungsfahigkeit der Thermoelemente bzw. Thermosaulen, uber Bedeutung und Messung der Zeitkonstante. Jenaer Rundschau, No. 3, 67, 1957.
5. Conn, G. K. and Avery, D. G. Infrared Methods. Academic Press, 1960.
6. Hackforth, H. L. Infrared Radiation. McGraw Hill, 1960.
7. Smit, R., Dzhons, F., Chesmer, R. Obnaruzheniye i izmereniye infrakrasnogo izlucheniya. IL., 1959.
8. Harrison, T. R. Radiation Pyrometry and its Underlying Principles of Radiant Heat Transfer. John Wiley and Sons, 1960.
9. Kozyrev, B. P. Prozrachnost' materialov dlya voln 0.8 ÷ 15.0 μ. Izd. LETI, 1959.
10. Kozyrev, B. P., Vershinin, O. E. Opredeleniye spektral'nykh koeffitsiyentov diffuznogo otrazheniya infrakrasnoy radiatsii ot zachernennykh poverkhnostey. Optika i Spektroskopiya, 6, 542, 1959.
11. Kozyrev, B. P., Kropotkin, M. A. Issledovaniye koeffitsientov spektral'nogo otrazheniya poktrytiy termicheskikh priyemnikov izlucheniya dlya oblasti dlin voln ot 10 do 200 μ. Optika i spektroskopiya, 10, 657, 1961.
12. Kozyrev, B. P., Kropotkin, M. A. Issledovaniye diffuznogo otrazheniya belykh pokrytiy, sil'no pogloshchayushchikh infrakrasnoye izlucheniye. Optika i spektroskopiya, 14, 152, 1963.
13. Zuyev, V. E., El'yashberg, M. E., Safonova, G. A. Prozrachnost' malykh tolshch atmosfery v oblasti 1 ÷ 13 μ. Izv. VUZ, seriya fizika, No. 5, 77, 1960.

V. A. Katulin, M. S. Malkevich, I. P, Malkov,
G. V. Rozenberg, and L. I. Yurkova

AN AIRCRAFT INSTRUMENT FOR MEASURING RADIATION BALANCE AND CERTAIN RESULTS OBTAINED IN ATMOSPHERIC SOUNDINGS

A description is offered of an instrument designed for making simultaneous measurements of ascending and descending radiation currents in two intervals of the spectrum: 0.3 - 2.5, and 2 - 40 μ , as well as in areas of the 0.3 - 2.5 μ portion of the spectrum. This makes it possible to obtain separately a balance of short and long wave radiation, as well as a complete radiation balance at any level in the atmosphere.

As a result of aircraft measurements, we obtained some basic rules on the vertical distribution of rising and descending radiation currents, the albedo and of the balance in two sections of the spectrum. It was established that radiation heating of the atmosphere is due to a greater extent to aerosol absorption than to absorption by water vapor. Studies were also made of radiation characteristics in the presence of clouds.

1. INTRODUCTION

The study of radiation balance in a free atmosphere is of great importance in the solution of many problems in atmospheric physics, especially problems dealing with the circulation of the atmosphere and weather forecasting.

Thus far, the experimental studies of quantitative variations in radiation balance and its components have been too inadequate. This is due to the fact that existing actinometric apparatus (pyranometers, balance meters /1/) do not permit us to make reliable simultaneous measurements of short wave solar radiations (0.3 - 2.5 μ) reflected by the earth, and the flux of long wave radiation of earth origin (2.5 - 20 μ)[1].

1. In the spectral intervals indicated practically all the radiant energy of the sun and earth, respectively, are contained.

In the laboratory of atmospheric optics IFA AN SSSR [Institute of Physical Analysis, Academy of Sciences, USSR] there was developed a sensitive, low-inertia type of apparatus for measuring radiation fluxes in the spectral intervals 0.3 - 2.5 and 2 - 40 μ, designed for making measurements from an aircraft, aerostat or the earth. Structurally, the instrument consists of two sensing elements and a commutator unit with amplifier (Fig. 1). The sensing units contain three radiation receivers each which make it possible to measure radiant energy fluxes in the 0.3 - 2.5, 2 - 40 μ and in the 0.6 - 2.5 μ or the 0.9 - 2.5 μ interval in which are concentrated the atmospheric gas absorption bands (water vapor and carbon dioxide). The commutator unit contains a mechanical commutator for the purpose of interrogating the signals and amplifier successively.

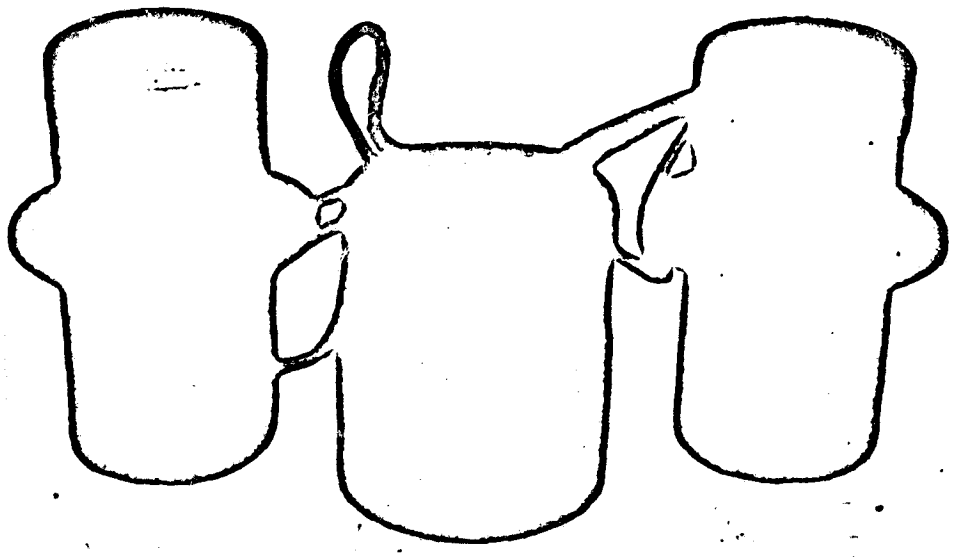

Fig. 1. General view of instrument.

Radiation Receivers

Serving as radiation receivers in the instrument are vacuum-type thermoelements (Fig. 2), developed and constructed in the Leningrad Electrotechnical Institute on the basis of instructions given by the IFA AN SSSR.

The thermoelements are thermic batteries with a black covering, and they are contained in vacuum envelopes. Serving as the input windows of the vessels are hemispherical filters of KRS-5, uviol glass, and combinations of these.

The window and the envelope are vacuum connected. The temperature of the housing is controlled by a resistance thermometer connected into the bridge circuit. A description of the construction, operating characteristics, and methods of calibration are given in an article by B. P. Kozyrev [2].

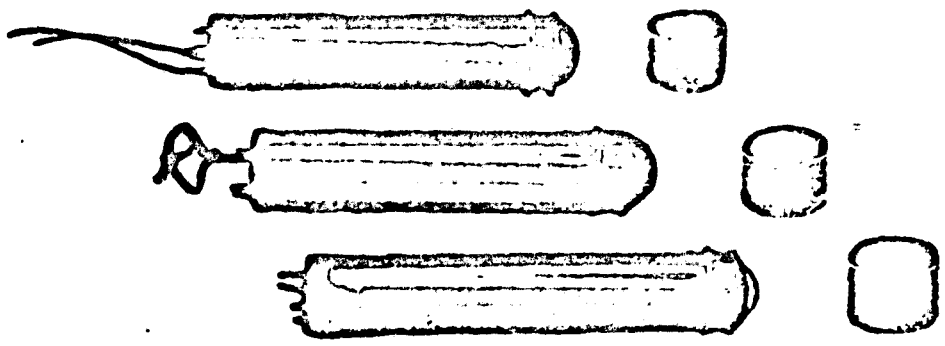

Fig. 2. Radiation Receivers

Commutator

The mechanical commutator consists of a 24 volt d.c. motor which successively closes 60 commutator segments. For reliability in commutation, there are three rows of segments which can be connected in parallel.

Amplifier

The signals from the radiation receivers are amplified by a direct current amplifier built on semi-conductors. The electrical circuit of the amplifier is shown in Fig. 3.

The signal is fed to a balanced switch. If there is no signal at the emitter of triode $P T_3$, the potential on collectors $P T_3$ and $P T_4$ is equal to zero. When the signal appears on emitter $P T_3$ there is an unbalanced voltage on the collectors in the form of rectangular shaped pulses which are proportional to the signal voltage. The unbalanced pulses are amplified by transistors P 102, & P106, and rectified at the output into d.c. voltages.

The circuit is fed by a d.c. net. The 20-volt direct current is fed to the pulse converter. The converter consists of a semiconductor pulse generator of relaxation oscillations with inductive coupling. The P 101 triodes

operate on a switchover system, i.e., they are quickly changed over from a cut-off operating rate (the collector current is close to zero) to saturation (the voltage of the collector-emitter is close to zero).

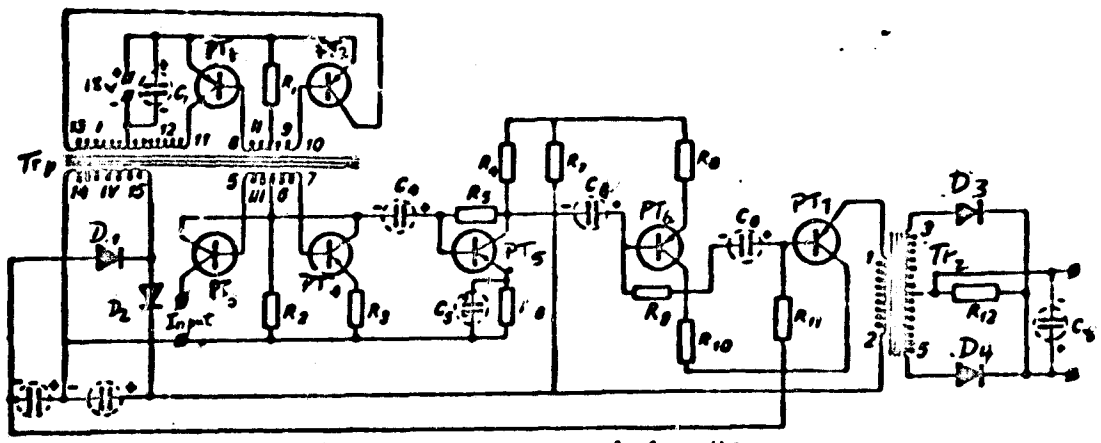

Fig. 3. Schematic diagram of amplifier.

The core of the transformer Tr_2 is made of a material with sharply expressed saturation induction (permalloy 79 NM). The shape of pulses of the collector current and the voltage on the transformer windings is close to rectangular.

The switch is built on the two triodes P 102. For normal operation of the switch the triodes should be similar; and in coil III of transformer Tr_1 points 5 and 7 should be symmetrical with respect to point 6.

The first and second stages of amplification are built on a circuit with a common emitter. The third stage of amplification is built on a common collector (emitter repeater). The load of the emitter repeater is the primary winding of transformer Tr_2. The two-cycle rectifier is connected into the secondary winding of the transformer. To fee the triodes of the amplifier, transformer Tr_2 has a winding IV to which is connected a circuit with double voltage yielding 24 volts of d.c.

The amplifier boosts the signals from the radiation receivers on the linear portion of the curve. The coefficient of amplification has a certain complex relationship to the temperature of the surrounding medium. To increase the accuracy of measurement, the instrument circuit is provided with a means

of checking the zero position and gain of the amplifier before interrogating each radiation receiver; this is done by feeding a zero and standard signal to its input. All this makes it possible to amplify the radiation receiver signals with an error of only about 3%. Hence, the maximum error in the measurement of radiation currents with this instrument is between 7 and 10%.

Construction of Instrument

The sensor unit consists of a duralumin cup with three thermoelements disposed in parallel fashion within it. A sweep of about 180° is insured by the thermoelements. There is an opening in the bottom of the cup for securing the sealed section through which the sensor unit is coupled with the commutator and amplifier unit.

The small dimensioned amplifier is assembled in the commutator housing in the free space under the cover, making a single unit with the commutator.

Interrogation of the sensors is done in a very definite sequence. Each cycle of interrogation includes 37 elements of interrogation (12 emf, 12 cold-joint resistance thermometers, 12 standard signals, 1 zero signal). The frequency of interrogation is set, depending on the experiment, by feeding a certain voltage (within permissible limits) to the motor which turns the commutator rotor. After amplification the signals in the amplifier go to the loop oscillograph.

Provision is made in the instrument for recording signals without preamplification with sensitive loops or galvanometers.

The sensor units are secured to the aircraft fuselage (one on top and one on the bottom) using special securing devices designed to keep the thermoreceiver platforms horizontal in horizontal flight.

2. PRELIMINARY TESTS OF AIRCRAFT INSTRUMENT IN OPERATION AND METHODS OF MEASUREMENT

The great sensitivity of radiation receivers and the presence of very sensitive loops made it possible to record signals on the loop oscillograph and galvanometers without preamplification.

For radiation receivers we took thermoelements with black covered surfaces and light filters of uviol glass, KBS-5 crystal, and a combination of these light filters. These receivers make it possible to register radiation currents in the 0.3 - 2.5; 0.6 - 2.5; and 0.6 - 40 μ bands of the spectrum.

In contrast to the calibrations described in [2], the thermoreceiver data were power calibrated; their indications were compared with the indications of a high precision actinometer.

The principle of power calibration consists of the following: using light filters we cut out of the solar spectrum that spectral interval of wave lengths which is transmitted by the thermoelement light filter without distortion. This radiation is directed simultaneously to the thermoelement and the actinometer. In this case, the radiation of the same spectral composition falls on the receiving surfaces of both radiation receivers.

The indications of the thermoelements influenced by the incoming radiation in a given portion of the spectrum were compared with the indications of the actinometer affected by the same radiation. Varying the intensity of the incident radiation, we can construct a calibration graph. It is assumed in this that the receiving platforms of the thermoelements and the actinometer are nonselective. The calibration circuit is shown in Fig. 4. In order to determine the effect on the calibration of the solar aureole, tubes with diaphragms were placed on the thermoelements, which produced the same viewing angle with the actinometer. In this, attention was paid to the fact that the indications of the thermoelements (as established in reference [2]) had not great relationship to the radiation incident angles.

3. RESULTS OF INSTRUMENT TESTS

Aircraft tests of the first instrument mockup permitted us to determine the operation of the equipment under realistic conditions. During a month of flights the thermoelements proved themselves as being reliable instruments.

During this period they passed the mechanical (vibration, jolts, commotion) and atmospheric (rain, dust, etc.) tests. However, due to the dissimilar spectral transmission characteristics of filters of one type on the various receivers, the interpretation of measured radiation fluxes encountered serious difficulties. These difficulties were related to the fact that the transmission of the KRS-5 filter does not have a steep drop in the shortwave region of the spectrum, as a result of which both receivers (0.6 - 2.5 and 0.6 - 40 μ) fix the radiation at less than 0.6 μ, but in different proportions. Since a great amount of solar energy is concentrated in this region, the non-identical portion of the visual flux appeared comparable to and sometimes exceeded the flux of the inherent radiation of the earth. Thus, experience has demonstrated that in this case, because of the low quality of the filters, the method of subtracting from the radiation flux measured by a receiver with a KRS-5 filter, that flux which was measured by a receiver with combination filters gives inadmissibly large errors.

As far as an interpretation of the measured fluxes of shortwave radiation 0.3 - 2.5 and 0.6 - 2.5 μ is concerned, there are no particular difficulties. However, in these instances too it is impossible for the same reason to indicate a clear left boundary of the spectral interval in which the radiation flux is measured by the combination receiver. Consequently, if we are to determine the radiation flux in the shortest region of the shortwave band 0.3 - 0.6 μ by subtracting the fluxes we again get an indeterminacy as to which spectral band the current should be referred.

The tests conducted have enabled us also to evaluate the errors in measuring by comparing the measurement data with simultaneous measurements of shortwave radiation fluxes by pyronameter attached to the side of the same aircraft. In Fig. 5, which shows the relationship of the results of measurement by the two instruments, we get a dispersion of data (especially for currents of rising radiation), but nevertheless there appears to be certain order in this

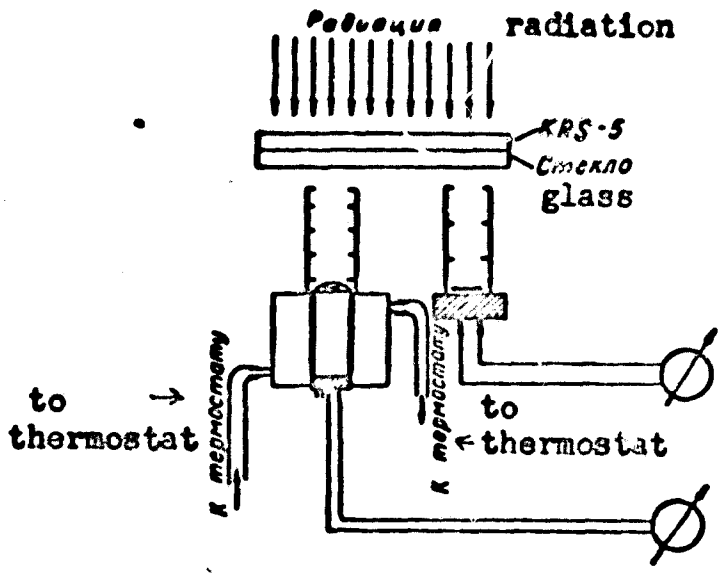

Fig. 4. Schematic diagram showing the calibration of the instrument.

dispersion. Specifically, for descending fluxes the instrument being tested gives results which are lower than those made with a pyranometer, and for ascendant fluxes it is higher. It is not difficult to understand that the most probable reason for these systematic errors is the differing reaction of the parasitic radiation of the filter on the magnitude of the signal. The filter (uviol) for the receiver, which is directed toward the earth's surface and whose receiving surface gets little heat due to the small values of ascending radiation, will be heated because of the absorption of thermal radiation and will radiate toward the receiving surface. In the receiver facing the sun the platform is highly heated and emits radiation to the filter which receives the weak thermal atmospheric radiation from without. The filter, on the other hand, radiates energy into space, thereby decreasing the original signal. In order to avoid this error, it is necessary to measure the filter temperature.

The method of dividing the radiation spectrum into 0.3 - 2.5; 0.6 - 2.5; 0.6 - 40 μ sections leads to great errors in determining the flux of long wave radiation. Hence, it is necessary to use receivers which measure radiation in two basic sectors of the spectrum; 0.3 - 2.5 and 2 - 40 μ. By doing so, we separate visual, direct, and scattered solar radiation from thermal radiation, and the measurement errors decrease markedly. In addition, the radiation

effect of the filter is eliminated by constructing a thermoelement with compensating device.

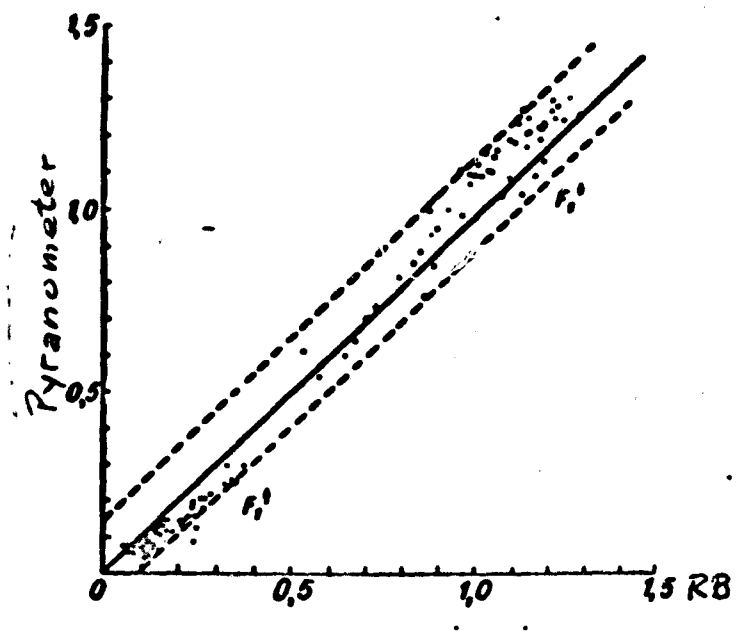

Fig. 5. Relationship of $F_1^{\uparrow}$ and $F_1^{\downarrow}$ fluxes measured with a pyranometer and an RB device.

Fluxes were measured above comparatively uniform surfaces (the sea, desert, solid overcast) and above horizontally non-uniform surfaces (steppes, forest-steppe, broken clouds). The aircraft exposed platforms for four minutes while ascending and descending at the following altitudes: 0.5; 1; 2; 3; 4 and 5 km. On each platform the measurements were made at two positions of the sun relative to the direction of motion of the aircraft: on the right and left. The results were recorded by galvanometers, for the most part.

On each platform five readings were made for each psotion of the sun, and mean values of fluxes determined. In many cases simultaneous observations of fluxes and basic meteorological elements were made on the ground.

In working out the results we took 11 cases of vertical sounding: four flights in clear weather over the ground and two over the ocean; five flights were made over the ground during cloudy weather. The method of processing aircraft measurements of radiation fluxes developed by V. G. Kastrov [3-5] were used.

4. RESULTS OF MEASURING RADIATION FLUXES

We shall consider some of the results of aircraft measurements of fluxes of ascending radiation $F_1^{\uparrow}$ (0.3 - 2.5 μ) and $F_2^{\uparrow}$ (0.6 - 2.5 μ) at different levels in the atmosphere.

Because of the non-uniformity of the underlying surface and atmosphere and because of anisotropy in the field of outgoing radiation there are encountered great difficulties in reducing radiation fluxes measured at high altitudes to those levels of the atmosphere which are actively involved in the transformation of radiation energy [6]. Hence, determining the underlying laws relative to changes in fluxes of outgoing radiation with respect to altitude above various underlying surfaces is one of the important problems in aircraft soundings of the atmosphere. It should be borne in mind here that we are interested not only in soundings over a uniform surface -- and this is usually the case in meteorology -- but also over non-uniform reflecting surfaces which are the more common thing in practice. Of course, in these instances the variation in ascending radiation fluxes will be determined not only by a change in the optical parameters of the atmosphere with altitude, but also by changes in the nature of the underlying surface which come into the receiver field of vision.

The chance of simultaneously getting radiation fluxes in two portions of the shortwave region of the spectrum makes it possible theoretically to study the outgoing radiation in the spectral band where poor absorption and dispersion prevail (0.3 - 0.6 μ), and in that spectral area where we find the main bands of absorption of shortwave radiation by atmospheric gases but where there is little dispersion of radiation (0.6 - 2.5 μ).

It should be mentioned that in our case the division of currents is provisional or conditional in nature to a certain extent because the structural imperfections of the instrument did not [illegible] getting good readings of fluxes in the area of main dispersion; specifically, we cannot establish the boundaries

of the spectral interval to which these fluxes can be ascribed. Hence, all the following results of measurement enable us to make only qualitative comparisons of radiation fluxes and other radiation characteristics of these two intervals of the spectrum. Readings of radiation fluxes $F_1^{\uparrow}$ and $F_2^{\uparrow}$ are within a 10% limit of error of the maximum value.

Shown in Fig. 6 and 7 are examples of the vertical distribution of fluxes of departing radiation at two intervals of the spectrum measured above two types of underlying surface (earth and sea) in an atmospheric layer up to 5 km high, which is important in the transformation of radiant energy. These results pertain to clear weather with rather clear visibility. One of the very characteristic features of the field of ascending radiation over the earth and sea consists in that in the first case (the earth) the fluxes $F_1^{\uparrow}$ and $F_2^{\uparrow}$ practically coincide, and in the second case (the ocean) they differ markedly. This testifies to the difference in spectral composition of the corresponding fields of radiation. Above the ground (steppes or deserts), shortwave radiation is very slight, while over the water it constitutes a considerable portion of the departing flux.

In the 0.5 - 4 km layer of the atmosphere, the ascending flux is weak and, generally speaking, it does not change according to any law with altitude, especially over the ground; at any rate, the variations in fluxes associated with changes in the nature of the underlying surface exceed considerably the vertical changes. Such a vertical motion is apparently characteristic of radiation fluxes over a non-uniform underlying surface. As we know, in the formation of a radiation field there is a superposition of oppositely acting effects: on the one hand the flux should increase on account of the radiation scattered by the increasing layer of atmosphere, and on the other hand, the flux reflected by the underlying surface will weaken due to the back scatter and absorption of radiation in the bands of water vapor, carbon dioxide, and

aerosol. Even over a uniform, strongly reflecting surface the effect of each of the two components can change, and there will be some variation in the ascending radiation flux. If the underlying surface is not uniform, however, there are, at least, small variations near the surface, and this seems to be the case from data obtained.

We will note that the sea is also a non-uniform surface due to the presence of patches during a heavy swell. This can explain the slight subsidence of fluxes above the ocean as the aircraft ascends.

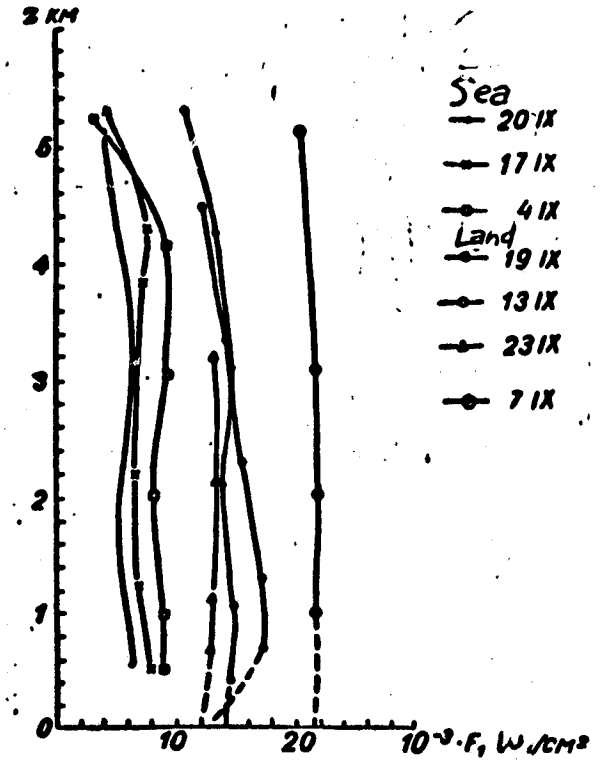

Fig. 6. Vertical distribution of ascending radiation flux $F_1^{\uparrow}$ for various instances of measurement in clear weather - 1961.

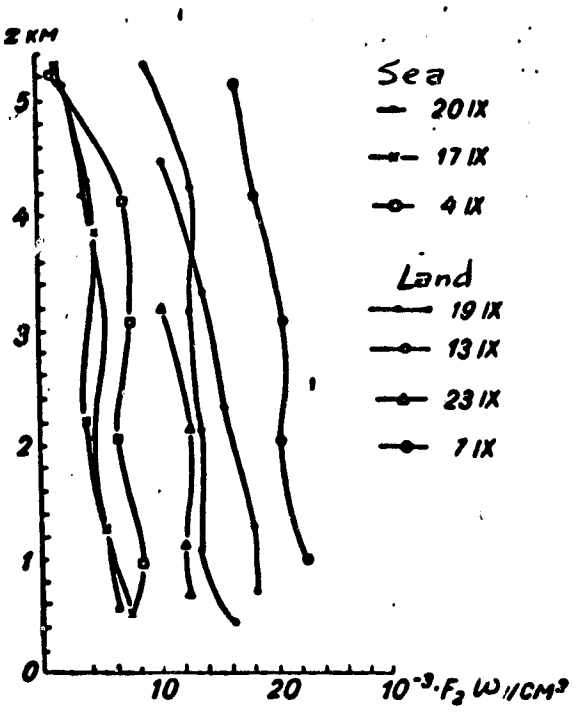

Fig. 7. Vertical distribution of ascending radiation flux $F_2^{\uparrow}$ for various instances of measurement in clear weather - 1961.

A solution of the equations dealing with the transfer of radiation for a case of pure dispersion above a non-uniform, underlying surface [7] shows that the flux of ascending radiation increases with altitude above sectors with a weak reflection (low albedo), and subsides above sectors with strong reflection (great albedo). Near the division boundary we can observe an increase as well as a subsidence in the flux, depending on the dimensions of the reflecting surfaces which appear in the radiation receiver field of vision. With altitude, the influence of the non-uniform underlying surface levels out and

the atmosphere begins to be the main element in the further transformation of radiation. The resulting picture of the vertical distribution of radiation fluxes would be encouraging if such a course were not interrupted due to cloudiness and turbidity of the atmospheric layer at altitudes of 3 - 5 km. Testimony of this is the systematic subsidence of radiation fluxes above 4 km, i.e., the level of the zero isotherm. If we assume that at this level there is an upper boundary of the steam fog layer, the radiation will weaken, after passing through that layer, mainly on account of the increasing absorption of shortwave radiation and the decreasing segment of scattered radiation.

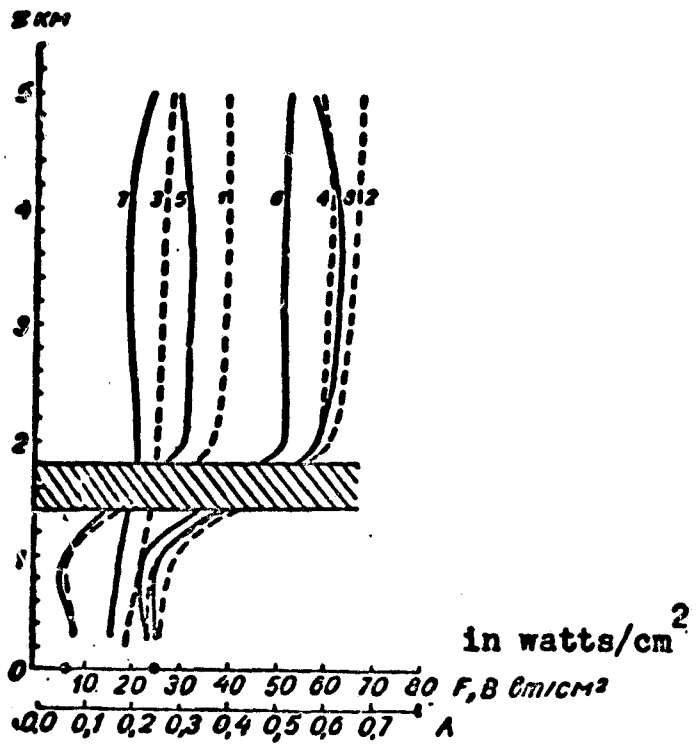

Fig. 8. Vertical distribution of basic radiation characteristics of the atmosphere when layer type clouds are present:

1 – $F_1^{\uparrow}$. 2 – $F_1^{\downarrow}$ – $B_1 = F_1^{\uparrow} - F_1^{\downarrow}$. 4 – A_1. 5 – $F_2^{\uparrow}$ – $B_2 = F_2^{\uparrow} - F_2^{\downarrow}$. 6 – A_2.

The ground value of albedo A_1 is entered on the x scale.

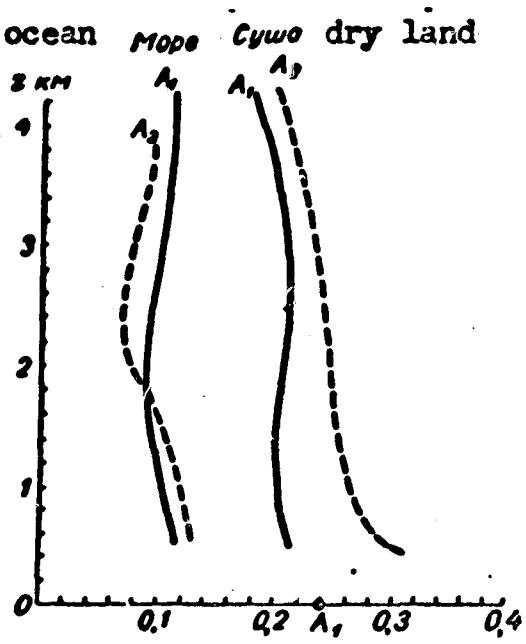

Fig. 9. Vertical distribution of albedo in different portions of the spectrum in clear weather.

The greatest change in the field of radiation and transformation of radiant energy is due to cloud cover [8]. Fig. 8 shows, by way of an example, a case of sounding with a clearly outlined layer of clouds about 400 meters thick. A characteristic feature of this case is the uniformity of the ascending and descending fluxes under the cloud, and the marked increase about the cloud; moreover the ascending flux virtually does not change with altitude. It may be

assumed that above 5 km the flux of ascending radiation will not change markedly. This gives us reason to assume that the flux of shortwave radiation above a uniform extended cloud measured from a satellite or rocket can be reduced to a lower level by mere geometric conversions. Fig. 8 is an example of the vertical distribution of the balance of shortwave radiation.

The results of measurement of radiation fluxes enables us to obtain a variation in the albedo of the underlying surface and layer of the atmosphere above the ocean, dry land, and clouds (Figs. 8 and 9) for the two intervals of the spectrum (A_1 and A_2). It is interesting to note that above cloud A_1 and A_2 they almost coincide; this testifies to the weak spectral relationship of radiation reflection in the shortwave region. In that portion of the spectrum where the water and water absorption bands are concentrated, the reflection will be dependent on the wavelength, but this part of the radiation in the total flux will be small.

The subsidence of the albedo with altitude (Fig. 9) is directly connected with the weak vertical change (subsidence) of the ascending radiation flux which is caused by the previously mentioned effect of absorption of reflected radiation in the atmosphere. This explains the divergence with the theoretical calculations for a purely dispersing atmosphere, [7] from which it follows that the total albedo over a poorly reflecting underlying surface (e.g. the ocean) increases with altitude. It should be mentioned that the error in determining the vertical profile of the albedo will be quite large. A much more reliable characteristic of reflection of shortwave radiation is the value of the albedo averaged out for the entire atmospheric layer.

These values for the two above-indicated intervals of the spectrum and for several types of reflecting surfaces and albedo at the ground A_0 are given in Table 1. A comparison of albedo A_1 and A_2 shows that there is no established relationship between them. As a rule, $A_2 < A_1$ above the sea and clouds,

whereas the opposite is true over deserts. It is easy to see that this is tied in with the spectral course of the albedo of the underlying surfaces [9].

5. SPEED OF RADIATIVE HEATING OF THE ATMOSPHERE

As we know, absorption of solar radiation in the atmosphere results in heating the air, and this is due to the presence in the atmosphere of water vapor and aerosols.

The speed of radiative heating of the air as determined from experimentation is insured by both substances (the values $\left(\frac{\partial T}{\partial t}\right)_1$ for the two portions of the spectrum are given in Table 1). Since the absorption functions of water vapor are sufficiently well known, then, knowing its distribution by height, we can without difficulty compute the contribution of water vapor in the balance of radiation absorbed. Consequently, we can determine the speed of radiative heating of the atmosphere due to absorption of radiation by the aerosol, regarding the latter as the difference of corresponding magnitudes $\left(\frac{\partial T}{\partial t}\right)_1$, obtained directly from measurements and computations $\left(\frac{\partial T}{\partial t}\right)_{H_2O}$.

The data of Table 1 indicate that the experimentally obtained values for the speed of radiative heating exceed the corresponding values of heat caused by the absorption of radiation by water vapor.

The mean values of the residual (aerosol) radiative heating for the 0.5 - 5 km layer are given in Table 1A. Given in this same table are similar values obtained from radiative flux measurements made in an aircraft as carried out by Roach /10/ over southern England.

The values of radiative heating for this particular layer of the atmosphere in the 0.3 - 2.5 μ region of the spectrum will vary from 0.09 to 0.23 degrees/hr, and the average for all flights $\left(\frac{\partial T}{\partial t}\right)_1$ is 0.13 degrees/hour. This result agrees well with Roach's data /10/. In the 0.6 - 2.5 μ region the radiative heating is somewhat greater, the mean value $\left(\frac{\partial T}{\partial t}\right)_2$ for all cases being 0.16 degree/hour.

It is interesting to note that radiative heating due to absorption of radiation by aerosol is comparable to, and in a number of instances exceeds, the corresponding values for water vapor, $\left(\frac{\partial T}{\partial t}\right)_{H_2O}$ being practically constant for all cases of measurement: $\left(\frac{\partial T}{\partial t}\right)_{H_2O} = 0{,}04 \div 0{,}06$ degree/hour; according to [10] $\left(\frac{\partial T}{\partial t}\right)_{H_2O} = 0{,}04 \div 0{,}07$ degree/hour).

Table 1

A. Mean Values According to our Measurements in 1961

	31 VIII	2 XI	4 XI	6 XI	7 XI	13 XI	17 XI	19 XI	20 XI	23 XI
	cloudy	cloudy	clear	cloudy	cloudy	clear	clear	clear	clear	clear
	land		sea	land			sea	land	sea	land
$\left(\frac{\partial T}{\partial t}\right)_1$ degr./hr.	0,18	0,09	0,16	0,10	0,23	0,12	0,12	0,11	0,11	0,11
$\left(\frac{\partial T}{\partial t}\right)_2$ degr./hr.	—	0,15	0,20	0,12	0,25	0,18	0,16	0,14	0,12	—
$\left(\frac{\partial T}{\partial t}\right)_{H_2O}$ degr./hr.	0,04	0,04	0,06	0,06	0,04	0,03	0,04	0,04	0,04	0,04
A_1	0,34	0,49	0,11	0,23	0,29	0,24	0,08	0,24	0,12	0,24
A_2	0,27	0,42	0,10	0,26	0,25	0,19	0,10	0,20	0,12	0,20
A_0	0,19	0,22	—	0,24	0,26	0,24	—	0,21	—	0,20
$10^5 k_1$ cm²/g	19	24	37	25	—	48	30	33	23	—
$10^5 k_2$ cm²/g	62	—	35	33	47	28	26	28	19	—

B. Average Measured Values, According to [10], 1959.

	21 IV	22 IV	17 VI	19 VI	6 VII	15 IX	24 IX	30 IX	5 X	Mean Values
$\left(\frac{\partial T}{\partial t}\right)_1$ degr./hr.	0,20	0,11	0,11	0,12	0,09	0,13	0,07	0,10	0,14	0,12
$\left(\frac{\partial T}{\partial t}\right)_{H_2O}$ degr./hr.	0,06	0,05	0,07	0,06	0,06	0,05	0,04	0,05	0,06	0,05
A_1	0,09	0,06	0,01	0,05	0,02	0,07	0,05	(0,02)	0,03	0,05
A_{relay}	0,12	0,09	0,04	—	0,03	0,11	0,07	0,04	0,05	0,07

Consequently, radiative heating of the 0.5 - 5 km layer is due, to a considerable extent, to absorption by aerosol. This conclusion is important in studies of the heat regime of the atmosphere. Actually, if the aerosol absorbs the solar radiations so powerfully then it is a great storehouse of heat, because there is little radiation of aerosol in the long wave region [11]. Thus, in contrast to water vapor, which produces not only radiative heating of the atmosphere but also radiative cooling, which is approximately equal in amount, the aerosol is capable of contributing considerably to the atmospheric heat balance. But since we find a stratified (and generally non-uniform) distribution of the aerosol in the atmosphere, we can assume that the aerosol is responsible for heating individual layers or volumes of air.

The results obtained enable us to evaluate the coefficient of aerosol absorption k_i [4].

Since there are layers in the atmosphere with differing turbidity, we get a rather variegated picture of changes in the coefficient k_i with altitude. Given in Table 1A are the mean values of coefficients of dust absorption for the 0.5 - 5 km layer. The average values for the coefficient k_i are of the order of $30 \cdot 10^{-5}$ cm^2/gram. This value is comparable to the coefficient of atmospheric scatter in the visible and infrared regions of the spectrum.

It is interesting to note that the coefficients of aerosol absorption of radiation in the 0.6 - 2.5 μ interval of the spectrum and throughout the entire shortwave interval of 0.3 - 2.5 μ were of the same order (cf. Table 1). This testifies to the lack of selectivity in absorption of radiation by an aerosol.

CONCLUSIONS

The above results of processing aircraft measurements of radiation fluxes enable us to make a number of conclusions about the radiation characteristics of the 0.5 - 5 km layer of the atmosphere.

1. Basic underlying laws of the vertical distribution of ascending and

descending radiation fluxes were obtained. The horizontal heterogeneity of the underlying and surface and atmosphere (clouds and vaporous layers) has the greatest influence on fluxes.

2. It was established that in the 0.5 - 5 km layer the radiative heating in two portions of the spectrum will vary from 0.1 to 0.2 - 0.25 degree/hour, and the radiative heating due to water vapor is less by a factor of 2 - 4 than the total radiative heating, i.e., radiative heating of the layer in question is due in large degree to aerosol absorption. The aerosol coefficient of absorption varies rather considerably with altitude but its average for the 0.5 - 5 km layer is of the order of $30 \cdot 10^{-5}$ $cm^2/gram$; this is comparable to the coefficient of dispersion of the atmosphere in the visible and infrared regions of the spectrum.

3. With clouds present the radiation flux, albedo, and balance above the cloud practically do not change.

4. The aircraft version of the instrument with which the data were measured requires additional refinement in the matter of ejecting and taking into account thermal interferences of the surrounding medium and filters.

The authors wish to express their gratitude to V. S. Ivanov, E. M. Kozlov, and V. P. Trusov for their contribution in building the equipment and in processing the results of the measurements.

REFERENCES

1. Yanishevskiy, Yu. D. Aktinometricheskiye pribory i metody nablyudeniy. Gidrometeoizdat, L., 1957.
2. Kozyrev, B. P. Mnogosloynyye radiatsionnyye termoelementy dlya izmereniya moshchnogo izlucheniya iz poluprostranstva v spektral'nykh oblastyakh 0.3 - 2.5 i 2.5 - 40 μ . See this collection.
3. Kastrov, V. G. O nagrevanii atmosfery blagodarya pogloscheniyu solnechnoy radiatsii vodyanim parom. Tr. TsAO, No. 6, 1952.
4. Kastrov, V. G. Izmereniye pogloscheniya solnechnoy radiatsii v svobodnoy atmosfere do 3 - 5 km. Tr. TsAO, No. 8, 1952.
5. Pyatovskaya, N. P. Potoki korotkovolnovoy radiatsii v svobodnoy atmosfere. Tr. GGG, No. 109, 1961.
6. Malkevich, M. S. Uglovoye i spektral'noye respredeleniye radiatsii otrazhennoy zemley v mirovoye prostranstvo. Iskusstvennyye sputniki zemli, No. 14, 1962.

7. Malkevich, M. S. Vliyaniye gorizontal'nykh izmeneniy al'bedo podstilayushchey poverkhnosti na rasseyaniye sveta v odnorodnoy atmosfere. Izv. AN SSSR, ser. geofiz., No. 8, 1958.
8. Chel'tsov, N. I. Issledovaniye otrazheniya propuskaniy i pogloshcheniya solnechnoy radiatsii oblakami nekotorykh form. Tr. TsAO, No. 8, 1952.
9. Krinov, E. A. Spektral'naya otrazhatel'naya sposobnost' prirodnykh obrazovaniy. Izd. AN SSSR, M. 1947.
10. Roach, W. T. Some aircraft observations of fluxes of solar radiation in the atmosphere. Quart. Journ. Roy. Met. Soc., v. 87, N 373, 346-363, 1961.
11. Deirmenjian, D. The role of water particles in the atmosphere transmission of infrared radiation. Quart. Journ. Roy. Met. Soc., v. 85, 1959.

V. L. Gayevskiy and L. N. Guseva

DETERMINATION OF HEIGHT OF UPPER CLOUD BOUNDARY USING METEOROLOGICAL SATELLITE DATA

If we know the air temperature at the surface of the earth and the vertical gradient of air temperature, then from measurement data of the cloud radiation temperature it is possible to determine the height. As shown in reference /1/, the height of the upper boundary of the cloud can be determined with an accuracy of 0.5 km.

This article considers the problem for a case where we do not have the actual vertical gradient of the air temperature (e.g., for the ocean surface where systematic radio sounding of the atmosphere is not organized) and the surface temperature is determined from measurements of radiation temperature from a satellite or from a synoptic chart. For this purpose, it is extremely important to know how reliable is the mean value of the vertical gradient of the air temperature in determining the height of the upper boundary of the cloud.

In this connection, the vertical air temperature gradients were computed for clouds of certain types from atmospheric soundings by aircraft. Fig. 1 presents the values of the vertical temperature gradient for an air layer from the ground surface to the upper boundary of the cloud. In the drawing the abscissa is used for the vertical air temperature gradient, and the ordinate has the altitudes of the upper boundary of the cloud. A total of 923 cases were recorded during the period 1956 - 1959 in the Leningrad area.

Analysis of the materials obtained shows that 80% of all instances of clouding were concentrated within the limits of 0.4 - 0.75° of the vertical temperature gradient. Moreover, a temperature gradient from 0.45 - 0.60° corresponds to As, Ac and Sc type clouds (Sc for the upper boundary higher than 2 km). In the case of Sc clouds with the upper boundary being at less than 2 km, the vertical temperature gradient is within the limits of 0.6 - 0.85°. In

the case of Ns clouds the temperature gradient was from 0.35 to 0.6° in 90% of the cases considered. Only in the case of layered clouds does the vertical temperature gradient have a wide range of from 0.9 to -0.1°.

The mean value of the vertical air temperature gradient, if there are As, Ac, Ns, and Sc clouds, is 55°. The error in determining the height of the upper cloud boundary, using the vertical temperature gradient of 0.55° for clouds whose upper boundary is 3 km high is 0.5 km. The largest error in determining the height of the upper boundary will be for stratified clouds.

The aircraft measurements of cloud surface temperatures we made using the radiation method indicate that radiative temperatures of cloud surfaces, depending on their density and optical thickness in excess of 400 meters differs from the temperature of the air by about 3° whereas the radiative surface temperature of clouds with a thickness of less than 200 meters can differ from the air temperature by 10°.

Such great differences in determining the temperature of the surface by the radiation method restricts the use of the method proposed for determining the height of the cloud cover.

Determining the height of the upper boundary of a cloud with the accuracy indicated is possible for clouds whose thickness is not less than 400 meters. This type of cloud can be identified through television images of cloud cover [2,4]. The mean temperature of the surface for computing the height of the upper boundary of clouds is determined by measurements of the radiative temperature from a satellite in cloud breaks or outside the cloud front. As was demonstrated in studies [3,5], the mean radiative temperature at the surface of the earth is practically equal to the mean temperature obtained for this same surface using weather station data.

If necessary, the air temperature at the ground surface for a region in which we are interested may be obtained from synoptic charts.

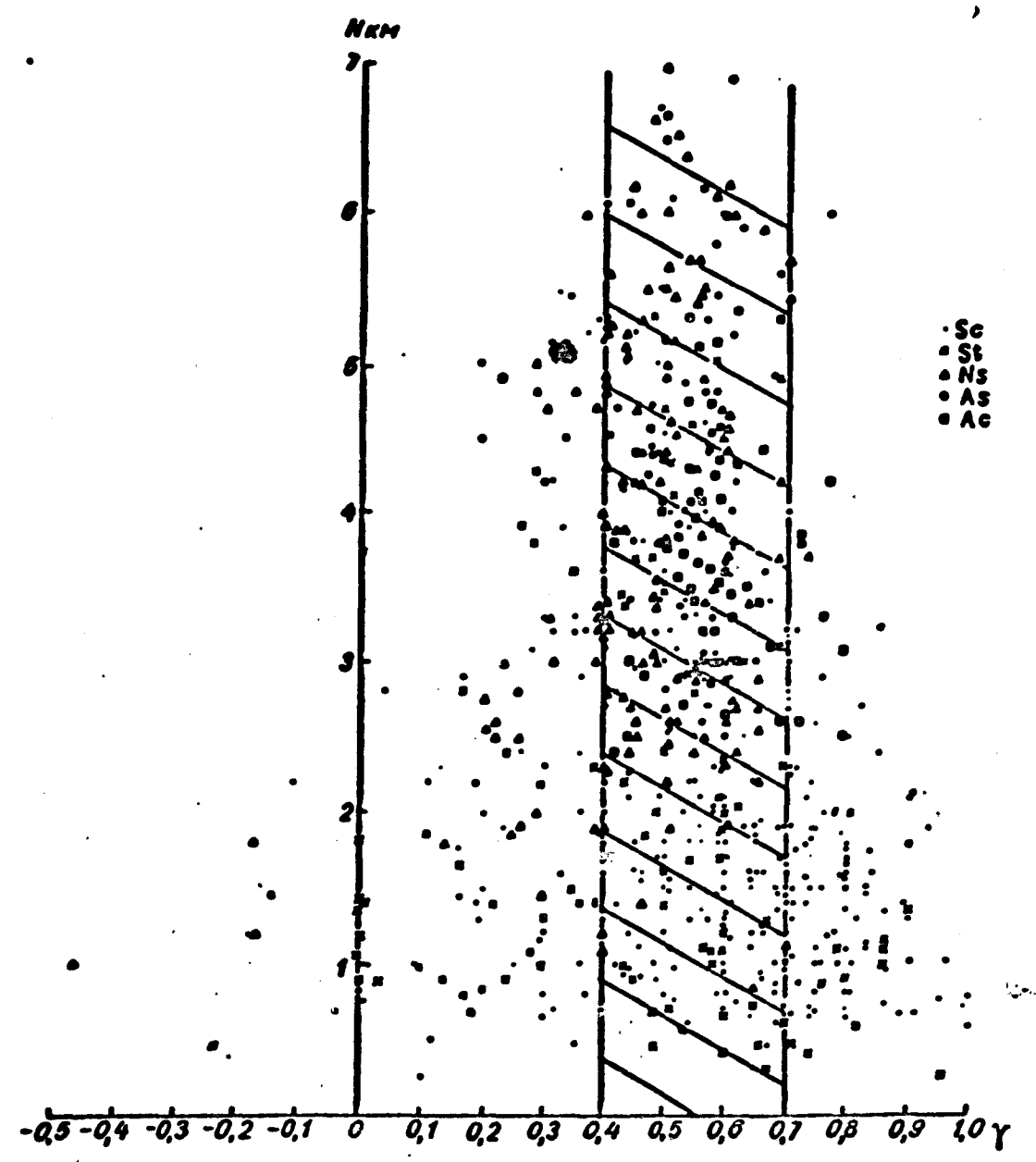

Fig. 1. Vertical gradient of an air layer from the ground to the upper edge of the cloud.

Cited in Table 1 by way of illustration are data for determining the upper boundary of a cloud using the method above described. The radiation temperatures of the cloud and earth surfaces were determined from measurement data from an aircraft for a sector 30 km long.

Table 1

Results of Determining the Cloud Height by the Radiation Method

Date	Cloud height (H) in km	Radiation temperature		Cloud height (H) in km (computed)	Thickness of cloud, meters
		Upper boundary of cloud	Surface		
19 X 62	1,7	5,4	9,4	0,8	200
19 X	2,2	4,2	9,5	1,0	200
21 X	1,2	4,5	11,0	1,2	400
23 X	1,8	2,9	10,0	1,3	400
23 X	2,2	2,7	9,2	1,2	200
27 X	2,7	1,4	16,4	2,7	700
21 X 63	2,0	0,0	12,0	2,2	300

We also considered another method of determining the height of the upper boundary of clouds. In working out this method, we made the basic assumption that corresponding to each type of cloud there is a definite value for the upper boundary, which changes little during the year for a given geographic region. In determining the type of cloud from television image data (obtained from meteorological satellites) we can estimate the height of the upper edge of the cloud. Shown in Table 2 are the mean values of the height of the upper boundary for As, Ac, Sc, St and Ns clouds, using materials obtained from aircraft soundings in the area of Leningrad over a four-year period.

Table 2

Mean Values of the Height of the Upper Edge of Certain Types of Clouds

Type of Cloud	Spring			Summer			Fall			Winter		
	Mean	Maximum	Minimum	Mean	Maximum	Minimum	Mean	Maximum	Minimum	Mean	Maximum	Minimum
As	5,5	6,4	4,6	5,5	6,0	5,0	4,2	5,1	3,5	4,7	6,0	4,0
Ac	3,5	5,5	2,6	3,7	6,0	2,4	3,8	5,0	2,5	3,3	4,6	2,2
Sc	2,5	5,0	0,7	2,5	6,2	1,0	2,0	6,4	0,8	1,6	5,0	1,3
St	2,5	4,6	0,6	3,5	5,0	1,0	2,0	4,5	0,5	1,2	5,5	1,0
Ns	4,4	6,3	2,0	3,5	6,3	1,6	4,2	6,0	1,7	3,0	4,5	1,0

The mean values of cloud heights for each type of cloud change rather little from season to season. The most stable are the mean values for As clouds; their extreme variation from the mean is within comparatively narrow limits.

For the other types of clouds the extreme variations from the mean height of clouds attain greater values (up to 5 km).

The number of cases with a variation from the mean by $\pm$ 1 km for this type of cloud is 50 - 60%.

As we can see, this method does not insure the necessary precision in determining the height of the upper cloud limit. Data on the mean altitude of clouds can be useful in making an analysis of materials on the height of the upper boundary of clouds obtained by other methods.

REFERENCES

1. Boldyrev, V. G. Ob ispol'sovanii radiatsionnykh izmereniy so sputnikov v sinopticheskom analize. Meteorologiya i gidrologiya, No. 10, 1962.
2. Kondrat'yev, K. Ya., Meteorologicheskiye sputniki, Gidrometeoizdat, L. 1963.
3. Gayevskiy, V. L., Babinovich, Yu. I. Ob uchete vliyaniya atmosfery na resul'taty izmereniya radiatsionnoy temperatury poverkhnosti zemli s ISZ. See this collection.
4. Erickson, S. O. and Hubert, L. F., Identification of cloud forms from Tiros I pictures MSL Rep., No. 7, 1961.
5. Wark, D., Jamamoto, G. and Lienesch, I. Methods of estimating infrared flux and surface temperature from meteorological satellites. Journ. Atm. Sci., v. 19, No. 5, 1962.